Active Shortening in the Alpine–Himalayan Belt

David Mackenzie

Thesis submitted to the University of Oxford

for the degree of Doctor of Philosophy

in

Earth Sciences



Department of Earth Sciences,

University of Oxford

Trinity, 2016

Supervised by Prof. Richard Walker and Prof. Barry Parsons

Citation: Mackenzie, D. (2016), Active Shortening in the Alpine–Himalayan Belt, D.Phil. thesis, University of Oxford, Department of Earth Sciences, Oxford, UK.

Keywords: Continental Earthquakes, Faulting, Active Tectonics, Alpine-Himalayan Belt, Turkey, Central Asia.

This thesis has been typeset using LaTeX 2$_\varepsilon$, released under the LaTeX Project Public License (LPPL), and references were compiled using BibTeX. Many of the figures were produced using the open source Generic Mapping Tools (GMT) software, released under the GNU General Public License.

This work is licensed under the Creative Commons Attribution-NonCommercial-ShareAlike 4.0 International License. To view a copy of this license, visit the Creative Commons website.



Printed in the United Kingdom.

Declaration

The contents of this thesis are all my own work, except where otherwise stated. The views and opinions expressed herein are mine and not necessarily those of any other person or body unless so attributed.

Active Shortening in the Alpine–Himalayan Belt

David Mackenzie

St Edmund Hall, Oxford

Trinity Term, 2016

In this thesis, I use a multi-disciplinary approach to investigate the accommodation of tectonic strain within the Alpine–Himalayan Belt by thick-skinned compressional faulting, to constrain seismic hazard potential and probe the earthquake cycle in regions of distributed deformation. A case study on the fault which generated the 2011 Van Earthquake is used to link the instrumentally observed earthquake behaviour to the late Quaternary slip rate and the regional tectonics of the Turkish-Iranian Plateau. At the Van fault, the surface geomorphology and topography are dominated by slip in the uppermost $\sim$10 km, and so models based on surface observations are likely to underestimate the full depth extent of seismogenic structures in the region. A second case study focuses on the Karkara Rangefront of the Terskey Range in the Tien Shan, which regional GPS suggests is creeping at a significant fraction of the total shortening rate across the northern Tien Shan. Dating river terraces along the rangefront, I estimate a late Quaternary slip-rate consistent with the present day creep rate, though it is unclear whether creep is the long-term deformation mechanism. Building on the Karkara Rangefront case study, I construct a transect of late Quaternary slip rates and earthquake recurrence intervals through the Kazakh Tien Shan and Dzhungarian Alatau. I find that deformation is distributed across numerous faults with slip rates of $<$0.6 mm/yr and recurrence intervals of $>$5 ka (and maybe significantly longer). Finally, I develop a new method to exploit the full power of new high resolution digital elevation models in estimating fault slip from surface fault scarps. Combining multiple measurements along strike, I use the variation in surface offset with topographic geometry to solve for the three-dimensional slip vector.

Extended Abstract

This thesis is concerned with the earthquake cycle and the distribution of deformation in low strain-rate continental interiors. Throughout the Alpine-Himalayan Belt the high strain-rate and fast slip-rate faults are relatively well studied geologically and instrumentally, but in lower strain rate regions individual faults are usually unresolved by geodetic methods and deformation is typically distributed across many faults over a large region. I focus on the accommodation of tectonic strain by thick-skinned faulting in such regions. In particular, I have investigated compressional faulting in the Tien Shan of Central Asia, driven by the India–Eurasia convergence and in the Turkish–Iranian Plateau, driven by the Arabia–Eurasia convergence.

Chapter 2 focuses on a case study of a fault that generated a recent large earthquake, tying together an instrumental study of the coseismic and postseismic motion with the late Quaternary fault slip rate and regional tectonics. The 23 October 2011 M_W 7.1 Van earthquake in eastern Turkey caused ∼600 deaths and caused widespread damage and economic loss. The seismogenic rupture was restricted to 10–25 km in depth, but aseismic surface creep, coincident with outcrop fault exposures, was observed in the hours to months after the earthquake. I combine observations from radar interferometry, seismology, geomorphology and Quaternary dating to investigate the geological slip rate and seismotectonic context of the earthquake and assess the implications for continuing seismic hazard in the region. Transient post-seismic slip on the upper Van fault started immediately following the earthquake, and decayed over a period of weeks; it may not fully account for the long-term surface slip-rate estimate of $\geqslant$0.5 mm/yr. Post-seismic slip on the Bostaniçi splay fault initiated several days to weeks after the mainshock, and I infer that it may have followed the 9^{th} November M_W 5.9 aftershock. The Van earthquake shows that up-dip segmentation can be important in arresting seismic ruptures on dip-slip faults. Two large, shallow aftershocks show that the upper 10 km of crust can sustain significant earthquakes, and significant slip is observed to have reached the surface in the late Quaternary, so there may be a continuing seismic hazard from the upper Van Fault and the associated splay. The wavelength of folding in the hanging-wall of the Van fault is dominated by the structure in the upper 10 km of the crust, masking the effect of deeper seismogenic structures. Thus, models of subsurface faulting based solely on surface folding and faulting in regions of reverse faulting may underestimate the full depth extent of seismogenic structures in the region. Measuring cumulative postseismic offsets to anthropogenic structures showed that Structure-

from-Motion can be rapidly deployed to create snapshots of postseismic displacement. I also demonstrate the utility of declassified Corona mission imagery (1960s–70s) for geomorphic mapping in areas where recent urbanisation has concealed the geomorphic markers.

Chapter 3 presents a case study of the previously unstudied Karkara Rangefront Fault on the northern edge of the Terskey Tien Shan. The exceptionally high quality GPS velocity field for Central Asia has allowed me to demonstrate for the first time that a continental interior fault is deforming by creep, without a known historic earthquake. Elastic modelling of the GPS velocity field suggests that the fault is creeping at ∼3 mm/yr (horizontal shortening), the fastest known slip rate in the northern Tien Shan and the only individual structure resolved in the regional velocity field. Combining field studies with a satellite stereo-image derived digital elevation model (2 m resolution), I map a series of fluvial terraces along the rangefront which are uplifted by up to ∼300 m above the present river level. Radiocarbon ages from one catchment constrain the ages of the lowermost two terraces to be ∼4–5 ka and ∼10–15 ka, consistent with prominent, regionally extensive terraces observed in Kyrgyzstan. Based on conservative estimates for the fault dip under the displaced terraces, I estimate a fault slip rate of $3.5^{+1.7}_{-0.4}$ mm/yr on the Karkara Rangefront Fault and a further >0.8 mm/yr on a fold structure in the Kegen basin that I infer is driven by a detachment from the main rangefront. I therefore estimate a minimum shortening rate across the rangefront of 1.1–3.3 mm/yr, encompassing the GPS derived rate to within error. At present the fault is accumulating minimal strain but it remains unclear whether creep is the long term mechanism for deformation of the fault and whether it is capable of generating earthquakes.

Building on the Karkara Rangefront case study, Chapter 4 constructs a transect of late Quaternary shortening rates through the Kazakh Tien Shan and Dzhungarian Alatau, focusing primarily on the E-W oriented thrust/reverse faults. Where possible I have estimated minimum recurrence intervals and the age of the most recent event on each fault. All of the faults which yielded slip-rates show rates of <0.6 mm/yr, suggesting that the 3.5±1.0 mm/yr of shortening between the Kegen basin and the Kazakh platform is distributed relatively evenly across a zone ∼300 km wide. Summing the late Quaternary slip rates, I estimate a total shortening rate of $1.01^{+0.30}_{-0.21}$ mm/yr. Though the errors are large on the geodetic rate, there is a component of slip unaccounted for by the studied faults that may arise from two potential sources. There are several thrust faults for which slip rate is still unconstrained and any contribution from strike-slip faulting was not included. The observed slip rates suggest two different regimes of faulting in the Kazakh Tien Shan; the high Terskey Tien Shan with relatively little internal deformation are bounded on the northern margin by a fast moving frontal thrust fault, whereas the faults from the Kegen Basin to the Kazakh Platform are characterised by low slip rates, distributing deformation over a zone ∼300 km wide. Where assessed, earthquake recurrence intervals were >5 ka, and so seismic hazard assessments based only on instrumental and historic records are likely to be heavily biased. In addition, I have demonstrated the utility of structure-from-motion photogrammetry in assessing fault slip-distributions along strike from palaeo-earthquake scarps, generating a DEM and slip-distribution

covering an unprecedented ∼30 km length of fault scarps.

In Chapter 5, I present a new and inherently 3D approach to the analysis of fault scarps using high resolution digital elevation models. Advances in topographic measurement techniques (e.g. lidar and photogrammetry) have allowed extensive measurement of single and multiple event scarps to draw conclusions about along-strike slip variation and characteristic slip. However, the resulting slip distributions are almost always variable and "noisy". I first present the results of sensitivity analysis to demonstrate the introduction of significant apparent noise by simply varying terrain, fault and measurement geometry (topographic slope attitude, fault dip and slip obliquity). A case study on the Hoshab fault, Pakistan is used to demonstrate that the introduction of a small degree of oblique slip can have a significant effect on the measured apparent slip. I use the variation in apparent offset with marker geometry, with fully 3-dimensional marker surfaces, to constrain the slip vector in 3D. Combining offset measurements along strike, I show that determining the slip vector is reduced to a simple linear formulation. I test my method using a terrestrial lidar dataset from the ruptures on the Borrego Fault from the 2010 El-Mayor Cucapah earthquake, estimating a vertical slip of 1.56±0.02 m and a lateral slip of 1.91±0.34 m. The lateral estimate is less than previous studies suggest and although the extensional component is poorly constrained, it is significantly larger. In regions of significant topography or with oblique slip, my method will give enhanced slip resolution while standard methods will give biased estimates.

Although detailed conclusions are given at the end of each chapter, I make some more general concluding remarks in Chapter 6.

Acknowledgements

First and foremost, I want to thank my supervisors Richard Walker and Barry Parsons, for giving me so much support and guidance over the past four years. Richard, thank you for being so willing to take on someone with little or no prior field experience and teaching me so much. Thank you both for the aid in maintaining a clear overarching thread to the thesis and bringing my focus back to the big picture whenever it drifted. I am grateful to have been supported for this research by a National Environmental Research Council (NERC) Studentship. Fieldwork, satellite imagery and Quaternary dating were funded through a Geological Remote Sensing Group (GRSG) student grant, a successful NERC Cosmogenic Isotope Analysis Facility (CIAF) proposal, the NERC/ESRC Earthquakes Without Frontiers (EWF) consortium, the Centre for Observation and Modelling of Earthquakes, Tectonics and Volcanoes (COMET, COME30001, http://comet.nerc.ac.uk) and the Looking into the Continents from Space (LiCS, NE/K011006/1) large grant. Thanks to the Open Topography team for the data services provided by the OpenTopography Facility with support from the National Science Foundation under NSF Award Numbers 1226353 & 1225810. I am grateful to my examiners Ramon Arrowsmith and David Pyle for great disucssions during my viva and their comments which have helped strengthen this thesis.

I would like to thank all of the COMET group here in Oxford, and also the wider community throughout the UK. In particular, I wish to thank John Elliott for his help during fieldwork, but also an unending supply of GMT tips and tricks and meticulous attention to detail. I would like to thank Austin Elliott, Christoph Grützner, Magali Rizza and Grace Campbell for their aid throughout; in the field; away on conferences and in the office. All have provided inspiration, stimulating conversation and help with preparation of papers, even when their own time was hard pressed by deadlines. I thank the other occupants of 50.03: Tim Middleton for his unending patience when I have struggled to grasp geological concepts and always being willing to answer 'ill-informed' questions; Yu Zhou for his technical help with photogrammetry and the Balochistan dataset even when he had the least time to spare and Eleanor Ainscoe for her help in the field and stimulating discussions. Thank you to all the 4th year students who have joined us for their masters projects. Thanks especially to Emily for the meticulous attention to detail in the analysis of the Toraigyr Fault trench.

Without Quaternary dating, mostly performed by others on my behalf, this study would have been impossible. I want to thank Andrew Carr and Jean-Luc Schwenninger for carrying out the IRSL and

OSL dating. I thank Ángel Rodés, Delia Gheorghiu and Sheng Xu for their help in performing the wet chemistry, AMS and modelling of the ^{10}Be cosmogenic dating samples. I also thank the staff at the Beta Analytics Ltd. labs and the Oxford Radiocarbon Accelerator Unit (ORAU) for their analysis of numerous radiocarbon samples. Lastly, I thank Andrew Mason here in Oxford for his careful work in performing U-series dating on pedogenic carbonate rinds.

Without a doubt, one of the highlights of this research has been the fieldwork in Central Asia and Turkey, both incredibly beautiful and geologically fascinating regions. Without the wonderful field teams this would not have been possible. I would like to thank Kanatbek Abdrakhmatov for his excellent logistical management of our field campaigns in Central Asia and great campfire stories (well, most of them!), and Erhan Altunel for his aid in organising two great field trips to Van, Turkey. I also thank Ivan, Sargun, Ainagul, Aidyn, Azat and Yunus for keeping us safe, fed, watered, entertained and optimistic and even helping dig holes during the many happy, busy and productive weeks in the field.

Outside work, I am fortunate to have a great group of friends keeping me going. Thanks in particular to the St Mary's and Oxford Rd crew and all my friends in the mountaineering club for many happy times – four years has gone by very quickly indeed. Thanks also to my college friends and old friends whom I haven't seen as often as often as I would like, yet continue to invite me to things and are always there if I need someone to talk to.

Thank you to my parents, my brother and grandmother for encouraging me to embark on a DPhil, supporting me when times were hard and for putting up with me being so poor at communication. I doubt you ever expected me to spend so long in education! Last but not least, Alex, thank you so much for putting up with me through this tough time, especially the final few months. Your endless enthusiasm, optimism and love have truly kept me going.

Contents

Declaration . . . ii
Abstract . . . v
Extended Abstract . . . vii
Acknowledgements . . . xi
Contents . . . xvii
List of Figures . . . xxiv
List of Tables . . . xxv

1 Introduction **1**
1.1 Alpine Himalayan Belt . . . 2
1.2 Earthquake Hazard . . . 4
1.3 High Resolution Topography . . . 6
1.4 Thesis Structure . . . 9
1.5 Miscellaneous Notes . . . 10
1.6 Publications arising from this thesis . . . 11

2 2011 Van Earthquake **13**
2.1 Introduction . . . 13
2.2 Background to the Van Earthquake . . . 16
2.2.1 Tectonic Setting . . . 16
2.2.2 Geological Setting . . . 17
2.2.3 The October 23, 2011 Van earthquake . . . 19
2.3 Methods . . . 21
2.3.1 Structure from motion surveying . . . 21
2.4 Postseismic slip: InSAR and field measurements . . . 22
2.4.1 Field measurements of postseismic slip . . . 23
2.4.2 Postseismic InSAR . . . 28
2.4.3 Postseismic slip: summary . . . 32
2.5 Geological Slip Rate . . . 33

2.5.1 Overview . . . 33
2.5.2 Slip-rate measurements . . . 35
2.6 Discussion . . . 40
2.6.1 Fault geometry . . . 40
2.6.2 Postseismic Motion . . . 44
2.6.3 Earthquake Hazard . . . 45
2.7 Conclusions . . . 47

3 High Tien Shan Northern Rangefront: A Creeping Fault 49
3.1 Introduction . . . 49
3.2 Tectonic, Geologic and Geomorphic Setting . . . 51
3.2.1 Regional GPS . . . 52
3.2.2 Terskey Northern Rangefront . . . 53
3.2.3 Late Pleistocene Stratigraphy . . . 53
3.3 Methods . . . 54
3.3.1 DEM Construction . . . 54
3.3.2 Dating . . . 56
3.4 Karkara Rangefront . . . 57
3.5 Results: River Catchment 1, High resolution surveying . . . 58
3.6 Results: River Catchment 2, Kyrgyzstan . . . 65
3.6.1 Terraces . . . 67
3.7 Results: Rangefront Terraces, Rc3–6 . . . 70
3.7.1 River Catchment 3 – Border Valley . . . 70
3.7.2 River Catchments 4–6 . . . 74
3.8 Results: Kegen Basin Fold (KBF) . . . 74
3.8.1 Structure and Geomorphology . . . 74
3.8.2 Dating . . . 77
3.9 GPS Constraints on Fault Creep . . . 81
3.10 Discussion . . . 84
3.10.1 Slip-Rate . . . 84
3.10.2 Creep . . . 86
3.10.3 Seismic Hazard . . . 88
3.10.4 Regional Terraces & Climate . . . 89
3.11 Conclusions . . . 92

4 Compressional Faulting in the Kazakh Tien Shan **93**

4.1 Aims . . . 93
4.2 Geodynamic Context . . . 97
4.3 Modern Strain Rate Field . . . 98
4.4 Methods . . . 100
4.4.1 ^{10}Be Dating . . . 101
4.4.2 U-Series Dating . . . 102
4.4.3 Monte-Carlo Slip Rate Estimates . . . 103
4.5 Kegen Basin . . . 104
4.5.1 Karkara Rangefront Fault (KRF) . . . 104
4.5.2 Kegen Basin Fold (KBF) . . . 104
4.5.3 Kegen Rangefront Fault (KGR) . . . 104
4.5.4 Saryjaz Rangefront (SJZ) . . . 106
4.6 Saty Fault (SF) – 1889 Chilik Earthquake Ruptures . . . 110
4.6.1 Scarp Morphology . . . 112
4.6.2 Palaeoseismology & Geochronology . . . 114
4.6.3 Rangefront Section – Cumulative offsets . . . 116
4.6.4 Summary: Saty Fault (*Abdrakhmatov et al.*, 2016) . . . 118
4.7 Ili Basin (South) . . . 118
4.7.1 Toraigyr Fault (TF) . . . 118
4.7.2 Kemin–Chilik Fault Zone (KCF) . . . 126
4.7.3 Shonzhy Fault System . . . 128
4.8 Ili Basin Northern Margin . . . 131
4.8.1 Ili Basin (North) Cenozoic Folding (NIF) . . . 131
4.8.2 Usek Thrust (UT) . . . 133
4.8.3 Konyrolen Scarps . . . 133
4.8.4 Dzhungarian Southern Rangefront Fault (DZS) . . . 148
4.9 Dzhungarian Alatau Northern Margin . . . 151
4.9.1 Qapal Fault (QP) . . . 152
4.9.2 Sarkand Rangefront Fault (SKR) . . . 153
4.10 Synthesis: Compressional Faulting . . . 157
4.10.1 Role of Thrust Faulting . . . 157
4.10.2 Role of Strike-Slip Faulting . . . 159
4.11 Geodynamic Implications . . . 160
4.12 Synthesis: Earthquake Hazard . . . 161
4.13 Summary . . . 163

5 Disentangling Slip-Distribution and Fault Scarp Geometry in 3D **165**

5.1 Introduction . . . 165

5.2 Offset Landform Geometry . . . 167

5.2.1 Geomorphic Markers . . . 167

5.2.2 Geometric Effects . . . 167

5.2.3 2D profile assumptions . . . 169

5.2.4 Nomenclature . . . 170

5.2.5 Geometry Definitions . . . 170

5.3 Analytical Fault Throw . . . 171

5.3.1 Assumption: Dip-Slip & Fault Perpendicular Aspect . . . 173

5.3.2 2D: Monte-Carlo Error Analysis . . . 176

5.3.3 2D profiles: Case Study - 2013 Balochistan Ruptures . . . 177

5.3.4 2D profiles: Summary . . . 180

5.4 Slip Geometry – 3D Analysis . . . 180

5.4.1 General Solution . . . 181

5.4.2 Validity & Geometric Interpretation . . . 181

5.4.3 Line Markers . . . 182

5.5 3D Example – El-Mayor Cucapah . . . 183

5.6 3D Example – Hoshab Fault, Pakistan . . . 185

5.7 Discussion & Implications . . . 187

5.7.1 A 3D Framework . . . 188

5.7.2 Profiles and Planform-projection . . . 188

5.7.3 Measurement of Slip Distributions . . . 189

5.8 Conclusions . . . 191

6 Concluding Remarks **193**

6.1 Further Work . . . 195

Bibliography **197**

Appendices **217**

A Methods – Technical Specifcations **217**

A.1 Van OSL Dating technical specifications . . . 218

A.2 Karkara Rangefront OSL and IRSL details . . . 219

A.2.1 Sample Preparation . . . 219

A.2.2 Sample properties and analysis protocols . . . 219

A.2.3 Environmental dose rate determination . . . 219

A.3 Karkara Rangefront Seismic Reflection Profiles 220

B Matlab Scripts **223**

B.1 Monte-Carlo Throw Estimation 224

B.2 3D Slip Vector Solving 226

List of Figures

1.1 Continental vs oceanic crustal deformation . . . 3
1.2 The Alpine–Himalayan Belt . . . 5
1.3 Population density, strain rate and hazard in the Alpine–Himalayan belt . . . 6
1.4 Continental vs oceanic crustal deformation . . . 8

2.1 Van regional setting & GPS . . . 14
2.2 Van Coseismic Intergerogram . . . 16
2.3 Van Regional Faulting . . . 18
2.4 Van Fault Overview . . . 23
2.5 Van–Erciş Highway Offsets . . . 24
2.6 Bostaniçi Splay Fault – Corona Imagery . . . 26
2.7 Bostaniçi Splay Fault – Photographs . . . 27
2.8 Postseismic Interferograms . . . 30
2.9 Postseismic Interferogram Profiles . . . 31
2.10 Geomorphology of the Van Fault . . . 34
2.11 S1 Scarps . . . 35
2.12 S2 Scarps . . . 36
2.13 S3 Scarps . . . 38
2.14 Slip-rate Estimate . . . 39
2.15 Perspective Overview of Van Fault . . . 41
2.16 Summary Cross-Section . . . 43

3.1 Northern Tien Shan Overview . . . 50
3.2 Terskey Northern Rangefront – Perspective view . . . 55
3.3 Rc1: Photographs . . . 59
3.4 Rc1: T1 Sampling photographs . . . 61
3.5 Rc1: River terrace profiles . . . 63
3.6 Rc2: Orientation Map, Inset . . . 66

3.7 Rc2: Hammer seismic line C . . . 67
3.8 Rc2: Perspective View & Photographs . . . 68
3.9 Rc3: Terrace map . . . 71
3.10 Rc3: Terrace profiles . . . 72
3.11 Rc4–Rc6: Terrace maps and profiles . . . 73
3.12 Kegen Basin Fold: Overview . . . 75
3.13 Kegen Basin Fold: Profiles . . . 76
3.14 Kegen Basin Fold: Accommodation structures . . . 77
3.15 Kegen Basin Fold: Sampling . . . 78
3.16 Regional GPS profiles . . . 82
3.17 Karkara Rangefront slip rate plot . . . 85
3.18 Karkara Rangefront: Rc1–6, lowest scarps . . . 86
3.19 Karkara Rangefront Conceptual Model . . . 89
3.20 Rangefront terraces: correlations . . . 90

4.1 Tien Shan Overview . . . 94
4.2 Transect Geodynamic Overview . . . 96
4.3 Seismicity depth in the Tien Shan boundaries . . . 97
4.4 Transect Overview . . . 98
4.5 Transect Regional GPS profile . . . 100
4.6 Kegen Basin Map . . . 105
4.7 Saryjaz Site: Orientation Map, Insets . . . 107
4.8 Saryjaz: SR1 . . . 108
4.9 Saryjaz: SR2 . . . 109
4.10 Saty Fault Overview . . . 111
4.11 Saty Ruptures – Trench Site . . . 113
4.12 Saty Ruptures – Photos . . . 114
4.13 Saty Trench Palaeoseismology . . . 115
4.14 Saty Fault Cumulative Offsets . . . 117
4.15 Ili Basin (South) Map . . . 119
4.16 Toraigyr Fault: Site Map . . . 120
4.17 Toraigyr Fault: Trench . . . 121
4.18 Toraigyr Fault: Slip rate sampling . . . 123
4.19 Toraigyr Fault: Depth Profile . . . 123
4.20 Toraigyr Fault: Depth profile multi-episodic deposition . . . 125
4.21 Toraigyr Fault: Slip rate site scarp offsets . . . 126

4.22 Kemin–Chilik Fault Zone . . . 127
4.23 Shonzhy Site: SIT . . . 128
4.24 Shonzhy Site: SH . . . 130
4.25 Ili Basin (north) Map . . . 132
4.26 North Ili Folds – Photograph . . . 133
4.27 Konyrolen Scarps: Model distortion pre-calibration . . . 134
4.28 Konyrolen Scarps: West . . . 136
4.29 Konyrolen Scarps: Central . . . 137
4.30 Konyrolen Scarps: East . . . 138
4.31 Konyrolen Scarps: Photos . . . 139
4.32 Konyrolen Scarps: Intali Site . . . 140
4.33 Konyrolen Scarps: Examples . . . 141
4.34 Konyrolen Scarps: Plane fitting Example . . . 143
4.35 Konyrolen Scarps: Vertical Offset Distribution . . . 144
4.36 Konyrolen Scarps: Slip Distribution . . . 145
4.37 Konyrolen Scarps: Petroglyph Photographs . . . 146
4.38 Dzhungarian Southern Rangefront Fault: Overview . . . 149
4.39 Dzhungarian Southern Rangefront Fault: U-Series Dating . . . 150
4.40 Dzhungarian Rangefront Northern Margin: Overview . . . 152
4.41 Qapal Fault Overview . . . 153
4.42 Sarkand Rangefront – Zhansugirov Site Summary . . . 155
4.43 Sarkand Rangefront – Zhansugirov Site Photos . . . 156
4.44 Geodetic/Geologic rate comparison . . . 159

5.1 (A) A map view diagram for oblique right-reverse slip demonstrates the very different apparent lateral offsets that can be measured on two fences crossing the fault at 45°, even with only a small component of shortening. (B) Cross-section view showing the effect of slope angle on the vertical separation measured by a profile. For the same slip vector and hence throw (s_z), the vertical separation measured will differ. (C) 3D block diagram of a topographic slope displaced by a left-normal fault, resulting in a surface fissure across which the linear stream marker is projected. S_L is the lateral component of slip, correctly measured by projecting the end of the channel across to the free face, in the slope-parallel direction. ϵ is the extra component of apparent lateral slip introduced by the horizontal advection of topography. ω is the vertical component unaccounted for by a profile, due to the advection of topography. The true fault throw is therefore $s_z = \Delta z + \omega$. . . . 168

5.2 (A) Slip vector **s** displaces the hangingwall along the fault plane. The orthogonal separation between planes is $\mathbf{s} \cdot \hat{\mathbf{n}} = d$. (B) After *Ragan* (2009). Example of a marker plane displaced by **s**. The observed strike separation (P) and dip-separation (Q) are much larger than the lateral and dip slip components of the slip vector. The dip-slip component of **s** ($\mathbf{S_D}$) can be further divided into two components, the heave (s_y) and throw (s_z). (C) Geometry definitions. θ = slope angle, ψ = slope aspect, δ = fault dip and $\hat{\mathbf{n}}$ = slope unit normal vector, $-\nabla h$ = down-slope direction. 172

5.3 Definition of slope angle theta under the geometry described in §5.2.5. (left) $\theta > 0$ gives a downhill facing scarp with reverse slip or an uphill facing scarp for normal slip. (right) The opposite is true for $\theta < 0$ 173

5.4 Plot of the relative error $\left(\frac{s_{z,profile}}{s_{z,true}} - 1\right)$ in a profile measurement, assuming pure dip-slip on a fault of known dip, plotted against slope aspect for several cases. Solid lines represent pure dip-slip cases, while dashed lines show the effect of adding lateral slip for the case of $\theta = 10°$. *(Left)* shows the case with a fault dip of 60°, while *(Right)* is 30°, showing a much more pronounced effect at lower fault dips. 174

5.5 Plots of the relative error $\left(\frac{s_{z,profile}}{s_{z,true}} - 1\right)$ for expected ranges in slope aspect (ψ) and slope angle (θ), for three different fault dips (30°, 45°, 60°) and three different degrees of lateral slip (S_L/S_D = 0.1, 0.5, 1.0), with the dip slip held fixed at 1 m. The described rake values are an angular measure of S_L/S_D, indicating the direction of slip in the fault plane $rake = \arctan \frac{S_L}{S_D}$. Each plot is coloured by the error in the measurement due to the assumptions of pure dip-slip and simple measurement geometry, for slope angle and aspect. The contours represent values of 0.05, 0.1 and 0.2, i.e. 5%, 10% and 20% departure from the true value. Dashed lines are the transects shown in Figure 5.4. Following the convention in Figure 5.3, a downhill facing reverse scarp will have $\theta > 0$ while a normal scarp will have $\theta < 0$. The converse is true for uphill facing scarps. 175

5.6 An example of a Monte-Carlo simulation uncertainty analysis with a selection of typical geometric parameters and associated uncertainties. Each of the geometric parameters is assigned an estimated probability distribution function (PDF) based on prior knowledge. The resulting throw PDF (grey) is asymmetric – a normal distribution of the same mean and standard deviation is overlaid (red). Median and 95% intervals shown dashed. 177

5.7 Effects of geometry on profile measurements for an oblique slip case study: the Hoshab Fault, Pakistan. (A) Adapted from *Zhou et al.* (2015a), Figure 2. We take swath profiles through the photogrammetry derived pointcloud along the lines P1–P1' and P2–P2'. Yellow and orange polygons outline the sections of hangingwall and footwall used for estimating slope attitudes and 3D separations. We measure vertical separations of 12.1±1.5 m from profile P1 and 7.3±0.4 m from P2. (B) Throw PDFs for the two profiles P1 and P2 under the assumptions of *Zhou et al.* (2015a). In each case the solid line represents a Gaussian distribution with the same mean and standard deviation, dashed lines show the median and 95% bounds. (C) PDFs for P1 and P2 correcting for the slope angle (estimate from pointcloud), but assuming $\psi = 0$, with a fault dip of 50-70°. (D) Estimated PDFs for the throw at P1 and P2 incorporating the slope aspect, slope angle and an a-priori s_L/s_D estimate along with their associated uncertainties. Both profiles are then consistent at the 1σ level, suggesting a throw of ∼10–11 m. 178

5.8 (A) Solving for the 3D slip vector is equivalent to finding the intersection between a collection of planes. Each plane represents the hangingwall plane displaced from the origin by $(\mathbf{s} \cdot \hat{\mathbf{n}}_i)\hat{\mathbf{n}}_\mathbf{i}$, i.e. each plane actually represents one pair of planes describing an offset planar feature. (B) The intersection of two planes is a line, which can be displaced by some amount d (orthogonal to the line). Thus a line feature can be incorporated under Equation 5.13 as two planes intersecting along the line. In many cases, this can give a less subjective characterisation of a linear feature than other methods relying on a user picking points on the line. 182

5.9 (top) Perspective view of the Site 2 terrestrial lidar dataset of *Gold et al.* (2013) generated in LidarViewer, showing the points selected for fitting planes. Footwall selections are red, hangingwall selections are blue. (bottom) Comparison of our measured perpendicular displacements to those predicted by our average slip vector and the average slip vectors of *Gold et al.* (2013), for both site 1 and site 2. The data points have been sorted by location along strike, but the x-axis is arbitrary. 184

5.10 (A) Illustrative diagram of the geometry for projecting two planar surfaces onto the fault plane. P illustrates a topographic surface, while Q represents a vertical plane through a river channel (river shown as blue line). Black arrows mark the plane perpendicular separations. (B) Fault plane view, of each of the two intersection lines (footwall is dashed, FW), with each plane separation in the correct spatial location. (C) The intersections are shifted to a common origin in the footwalls. (D) The slip vector is then the distance between the footwall intersection point (the origin) and the intersection of the hangingwall lines. 186

5.11 A fault plane normal view of intersection lines. The slip vector is fit to the two planes associated with profiles P1 (blue) and P2 (brown) and the vertical plane (orange) through the river channel at the site on the Hoshab Fault (locations in Figure 5.7), weighted by the errors in the separation measurements. Each line represents a hangingwall-plane – fault-plane intersection line in fault geometry. The dashed line indicates the second plane defining the displaced river channel, which was excluded from slip solution as the channel only records the most recent event in the vertical. Δx_R represents the lateral separation in the river channel. Δz_1 and Δz_2 represent the vertical separation that would be measured by a profile at P1 and P2. 187

A.1 Basharin Site: Hammer seismic lines A and B 221

List of Tables

2.1 Earthquake Source Parameter Estimates 20
2.2 SAR Acquisitions 29
2.3 Van OSL Dates 37
2.4 Van Radiocarbon Ages 37

3.1 Table of Karkara Rangefront Fault Radiocarbon Dates 64
3.2 Table of Feldspar IRSL dates 80
3.3 Table of Quartz OSL dates 80
3.4 Terrace Height Ratios 91

4.1 Saryjaz Rangefront Feldspar IRSL dates 110
4.2 Toraigyr Fault Depth Profile – ^{10}Be Concentrations 123
4.3 U-Th age estimates at the Dzhungarian Southern Rangefront Fault (DZS) 151
4.4 Sarkand Rangefront radiocarbon ages 154
4.5 Summary of the slip-rates, shortening rates, most recent event (MRE) ages and recurrence intervals estimated along the transect studied. R – Reverse slip, LL – Left lateral slip and RL – Right lateral slip. Errors stated with upper and lower bounds are 95% confidence intervals. The error on the DZ slip rate is the 1-σ bound given by *Campbell et al.* (2013) . 158

Chapter 1

Introduction

The characteristics and distribution of earthquakes and faulting within the continents are fundamentally different to those of the oceanic crust (Figure 1.1, *McKenzie*, 1972; *Molnar and Tapponnier*, 1975). Earthquakes in the oceanic crust typically occur within 10–100 km of the plate margins, accommodating strain in narrow bands on the edges of the relatively rigid and undeforming plates (*McKenzie and Parker*, 1967). By contrast, continental margins are characterised by broad zones of deformation distributed over 100s to 1000s km on numerous faults (Figure 1.1, e.g. *Thatcher*, 2009). Continental crust is generally older and has often experienced generations of deformation prior to the present orogenies, which result in pre-existing fault zones. These structures were formed under a different stress regime and can be re-activated under the present strain field in a wide variety of orientations (e.g. *Jackson*, 1980), consistent with the great variety of types of faulting and earthquakes observed (*Wei et al.*, 2011) and lead to the accommodation of tectonic motions by a number of kinematic configurations.

The advancement and densification of GPS networks has given a good constraint on the far-field plate velocities globally and in some regions (e.g. California, Tien Shan, Himalayas) the networks are dense enough to start illuminating the regional strain rate fields on scales of 10s to 100s km (e.g. *Shen et al.*, 2011; *Zubovich et al.*, 2010), i.e. scales at which individual fault zones can often be resolved. However, the links between the earthquake cycle, present day strain rates and longer term deformation of the landscape (>1 Ma) are poorly understood (*Thatcher*, 2009). Understanding the deformation occuring before, during and after an earthquake on a given fault is therefore important both in the study of seismic hazard but also the long term landscape evolution and the underlying rheology and dynamics which drive crustal deformation (e.g. *Burov et al.*, 2006; *Bürgmann and Dresen*, 2008).

The concept of the earthquake cycle developed from studies of triangulation data after the 1906 San Francisco earthquake and originally consisted of two phases (*Reid*, 1910). Strain accumulates on a locked fault above a stably sliding lower crust during an interseismic period, which is released in the coseismic phase upon reaching a critical stress on the fault plane. With the development of improved measurement

techniques, a further postseismic component is generally acknowledged (e.g. *Smith and Wyss*, 1968; *Thatcher*, 1983). A variety of mechanisms for postseismic deformation have been proposed, including afterslip (e.g. *Marone et al.*, 1991), fault rheology (e.g. *Wesson*, 1988), viscoelastic relaxation (e.g. *Nur and Mavko*, 1974) and fluid redistribution (e.g. *Booker*, 1974; *Scholz*, 1974). Most faults display significant cumulative displacements but these models generally cannot account for the long term expression of faults due to unrecoverable off-fault strain (*Copley and Jolivet*, 2016).

It has also become clear that behaviour varies substantially from fault to fault and region to region, both in the coseismic and postseismic behaviour of individual earthquakes and in the long term topographic expression. *Klinger et al.* (2011) found strong evidence for repeating characteristic slip on the Fuyun fault (China) whereas studies have found irregular repeat times on the San Andreas fault (e.g. *Schwartz and Coppersmith*, 1984), suggesting temporal clustering and earthquake 'super-cycles' (*Grant and Sieh*, 1994). There are also suggestions of millennial scale variation in slip rates, possibly due to the switching of motion between different fault strands (e.g. *Dolan et al.*, 2016). A small number of faults even show evidence for stable sliding being the long term deformation mechanism (e.g. the Hayward Fault, *Burgmann et al.*, 2000). This raises the question of how applicable long-term geological measurements are at representing present-day strain accumulation – a question this study touches on in Chapters 2–4. The majority of earthquake cycle studies have focused on high strain rate zones as they naturally give shorter time-scales more accessible by instrumental techniques. These are typically subduction zones and the major continental strike slip faults (e.g. *Hyndman et al.*, 1995; *Klinger et al.*, 2011). The earthquake cycle in more slowly deforming regions is relatively understudied and only poorly understood since the longer time-scales require investigation of the geological record, with the uncertainties that brings.

Individual faults within zones of distributed intracontinental deformation typically have low slip rates and yet can sustain large (M_W>8), destructive and unpredictable earthquakes (e.g. *Jackson*, 2001; *Abdrakhmatov et al.*, 2016). With fault slip rates below the geodetic detection thresholds and earthquake recurrence intervals unpredictable and usually substantially longer than the instrumental records, seismic hazard is often very poorly constrained in slowly deforming continental interiors (e.g. *Bilham*, 2013). Extensive work has been performed in characterising how continental normal faulting (e.g. Basin and Range, *Wesnousky and Jones*, 1994) and strike-slip faulting (e.g. North Anatolian fault, *McKenzie*, 1970; *McKenzie et al.*, 1970) accommodates regional strain, but fewer have discussed the accommodation of shortening by thrust faulting in regions of distributed deformation (e.g. *Thompson et al.*, 2002).

1.1 Alpine Himalayan Belt

Though a zone of general convergence, the Alpine-Himalayan belt exhibits a wide variety of faulting regimes along its 7000 km length that extends from Europe to China (Figure 1.2). In the west, convergence is driven by the collision of Arabia with Eurasia (at ~23 mm/yr with anticlockwise rotation), causing

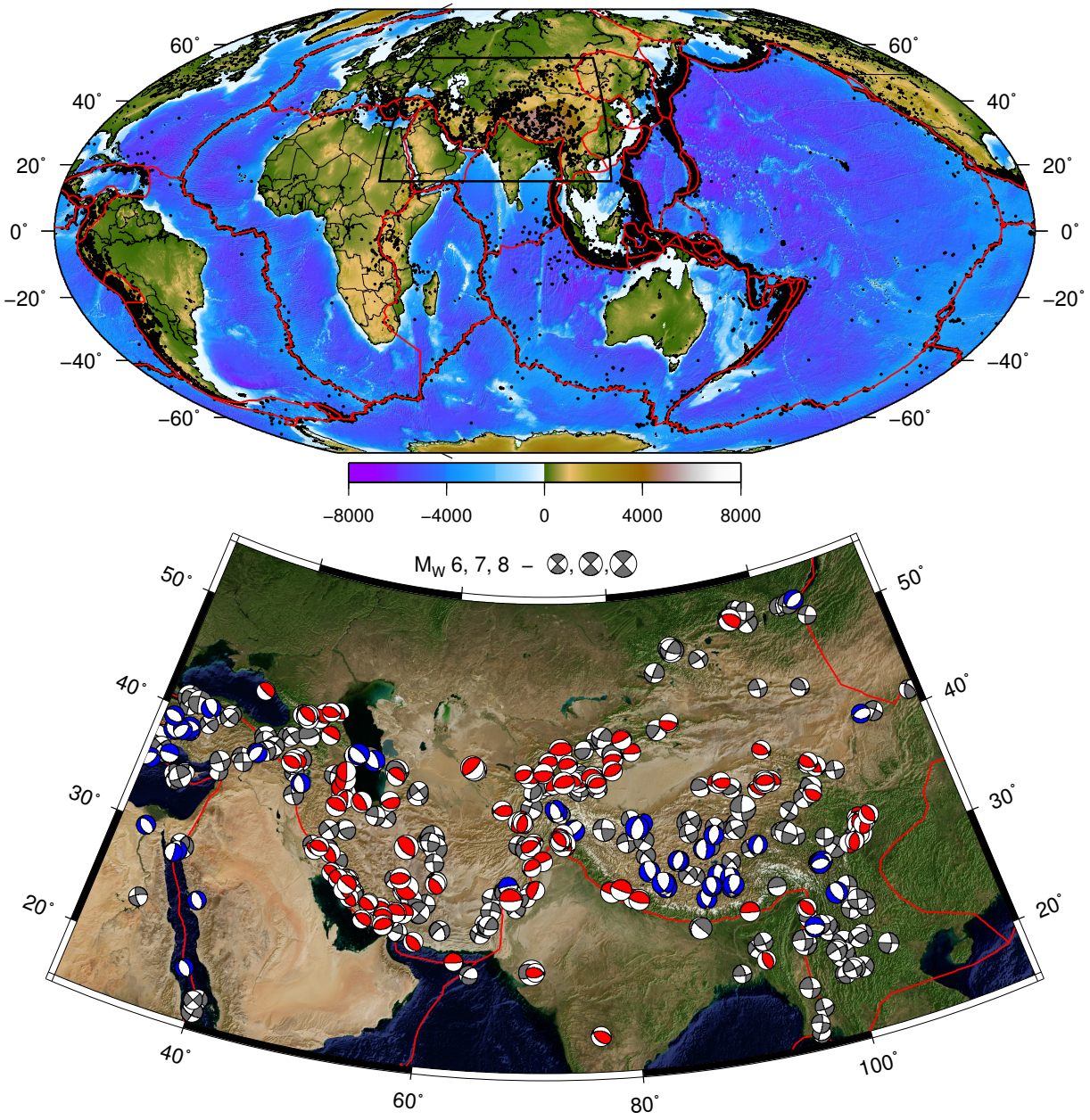


Figure 1.1: (top) A map of global seismicity from the global CMT catalogue showing all the M_W>5.5 since 1976. In the oceans, these cluster around the plate margins (red, *Bird*, 2003) whereas they are spread over broad zones within the continental margins. (bottom) Albers equal area projection map of the Alpine–Himalayan belt (NASA blue marble basemap). Focal mechanisms from the global CMT catalogue are shown for earthquakes since 1976 (M_W>5.5), demonstrating the huge variety of different styles of deformation. Mechanisms coloured by rake: red – thrust/reverse, grey – strike-slip, blue – extensional.

thick-skinned thrust faulting building the Caucasus and the Turkish Iranian plateau and driving the westward extrusion of Anatolia (*McClusky et al.*, 2000; *Reilinger et al.*, 2006), and the thin-skinned fold and thrust belt of the Zagros (*Jackson and McKenzie*, 1984; *Vernant et al.*, 2004). At the longitude of central Iran the Makran subduction zone accommodates ∼30 mm/yr of convergence between Arabia and Eurasia whereas the interior of Iran is only very slowly deforming (*Walker and Jackson*, 2004; *Reilinger et al.*, 2006; *Walpersdorf et al.*, 2014). Although central Iran is relatively undeforming, the northern margin of Iran also shows intense deformation along the Alborz mountains and the Kopet Dag (e.g.

Hollingsworth et al., 2008; *Mousavi et al.*, 2013; *Walters et al.*, 2013). Further east, the India-Eurasia collision is driving a zone of deformation more than ∼1000 km wide (at ∼40 mm/yr, *DeMets et al.*, 1990, 1994; *Wang*, 2001; *England and Molnar*, 2005; *Abdrakhmatov et al.*, 1996; *Zubovich et al.*, 2010). Through Pakistan and Afghanistan, the Chaman fault system accommodates ∼30 mm/yr of left-lateral strain between the western edge of the Indian plate and Eurasia (*Szeliga et al.*, 2012). At the longitude of Tibet, around half the plate convergence is accommodated by thrust faulting along the Himalayan arc and thrust and strike slip faulting on the northern margin of Tibet (*Molnar and Tapponnier*, 1975), while central Tibet displays E-W extension (e.g. *Elliott et al.*, 2010). To the north, the remaining 20 mm/yr of shortening is accommodated by a thin-skinned fold-and-thrust belt at the northern margin of the Tarim basin (*Yin et al.*, 1998; *Allen et al.*, 1999), and thick-skinned faulting through the Tien Shan of Central Asia (e.g *Abdrakhmatov et al.*, 1996; *Thompson et al.*, 2002).

The focus of this thesis is how the thick-skinned faulting in regions of distributed shortening accommodates tectonic strain, with a focus on thrust and reverse faulting in low strain rate regions. To this end, I have investigated two sections of the Alpine Himalayan belt undergoing significant total deformation distributed over numerous relatively slow moving faults: the Turkish-Iranian plateau (TIP, *Copley and Jackson*, 2006; *Reilinger et al.*, 2006) and the Tien Shan of Central Asia (*Abdrakhmatov et al.*, 1996; *Thompson et al.*, 2002). The 2011 Van Earthquake on the TIP gives the opportunity to probe the earthquake cycle in a region of distributed shortening. Geodetic and field observations of coseismic and postseismic slip can be tied to the geological estimates of the late Quaternary slip rate and the permanent topographic expression of the causative fault. In the northern Tien Shan, the excellent environmental preservation presents an opportunity to probe the late Quaternary fault slip rates and earthquake behaviours on numerous faults. The high quality geodetic network of *Zubovich et al.* (2010) gives a well constrained regional strain field on length scales of 10–100s km with which to compare the late Quaternary estimates of shortening rates.

1.2 Earthquake Hazard

Over the past century, the number of deaths associated with earthquakes has increased alongside increasing global population and the increase in population in vulnerable urban environments (*Bilham*, 2009). However, the link between earthquake magnitude and number of deaths is less straightforward. The largest earthquakes (M_W 9+) are observed on subduction zones, so are generally offshore and the exposed populations are in the far-field regime. These earthquakes occur in well defined locations and so countries exposed to the hazard are generally better prepared to deal with the effects. By contrast, intracontinental earthquakes of M_W 7–8 have been significantly more deadly over the past century (*England and Jackson*, 2011). Distributed deformation makes the identification of earthquake sources harder, and lower strain rates give long recurrence intervals and potentially rare but very large magnitude events,

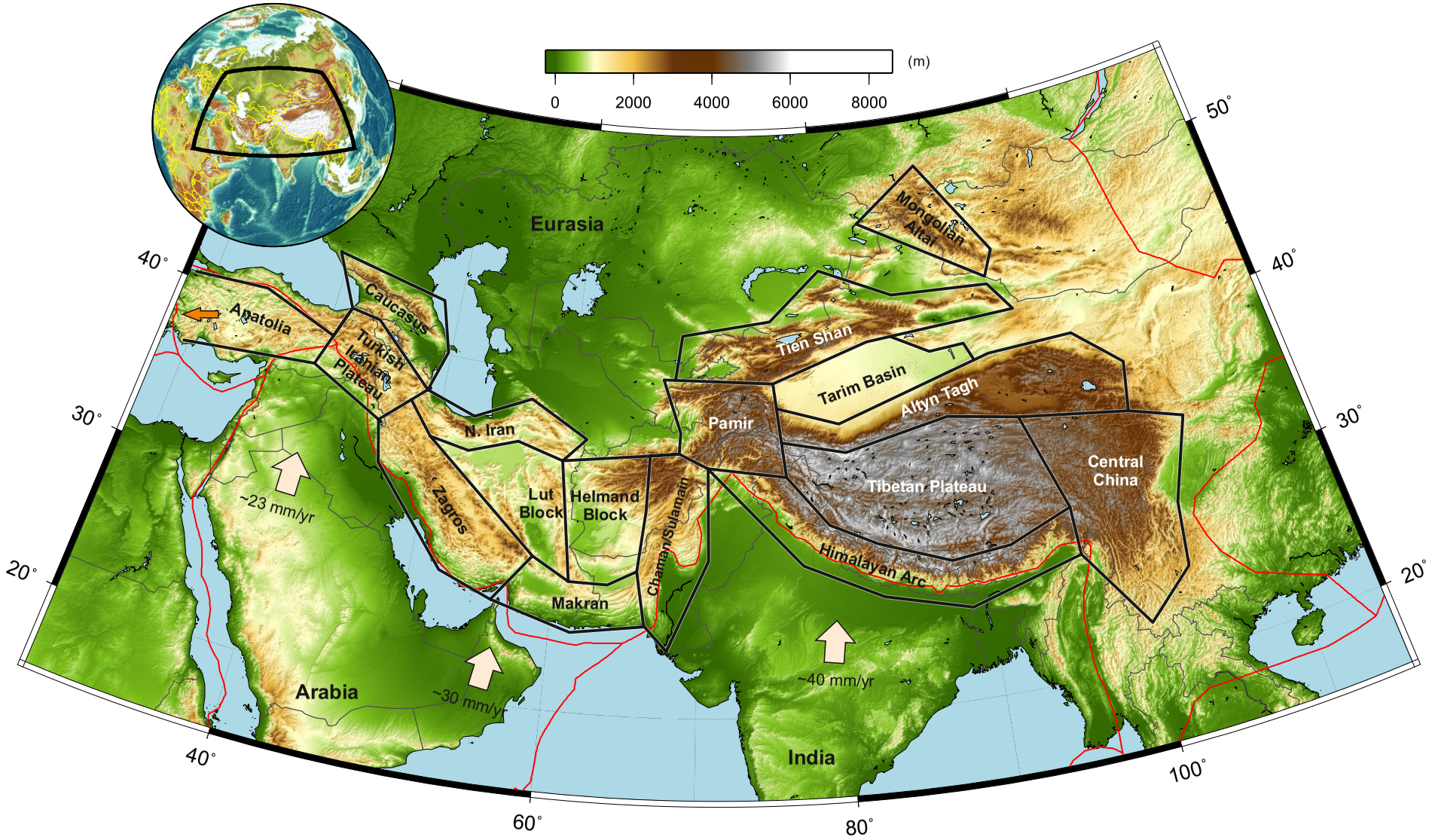


Figure 1.2: Albers equal area projection map of the Alpine–Himalayan belt with an SRTM basemap. Plate velocities of Arabia and India are given relative to a fixed Eurasia (including the anticlockwise rotation of Arabia). The main regions of deformation are shown, along with the rigid (or very low strain rate) blocks of the Tarim basin, the Lut block and the Helmand block. The foci of this thesis are two areas of distributed, thick-skinned thrust and reverse faulting; the Turkish-Iranian Plateau and the northern Tien Shan

leading to lower populational awareness and lower societal resilience. Additionally, maps of population density (Figure 1.3a) show that population tends to concentrate along the borders of mountain ranges for water supply (*Jackson*, 2008). Unfortunately this results in a concentration of people along the regions of higher strain rate and earthquake hazard (Figure 1.3b,c).

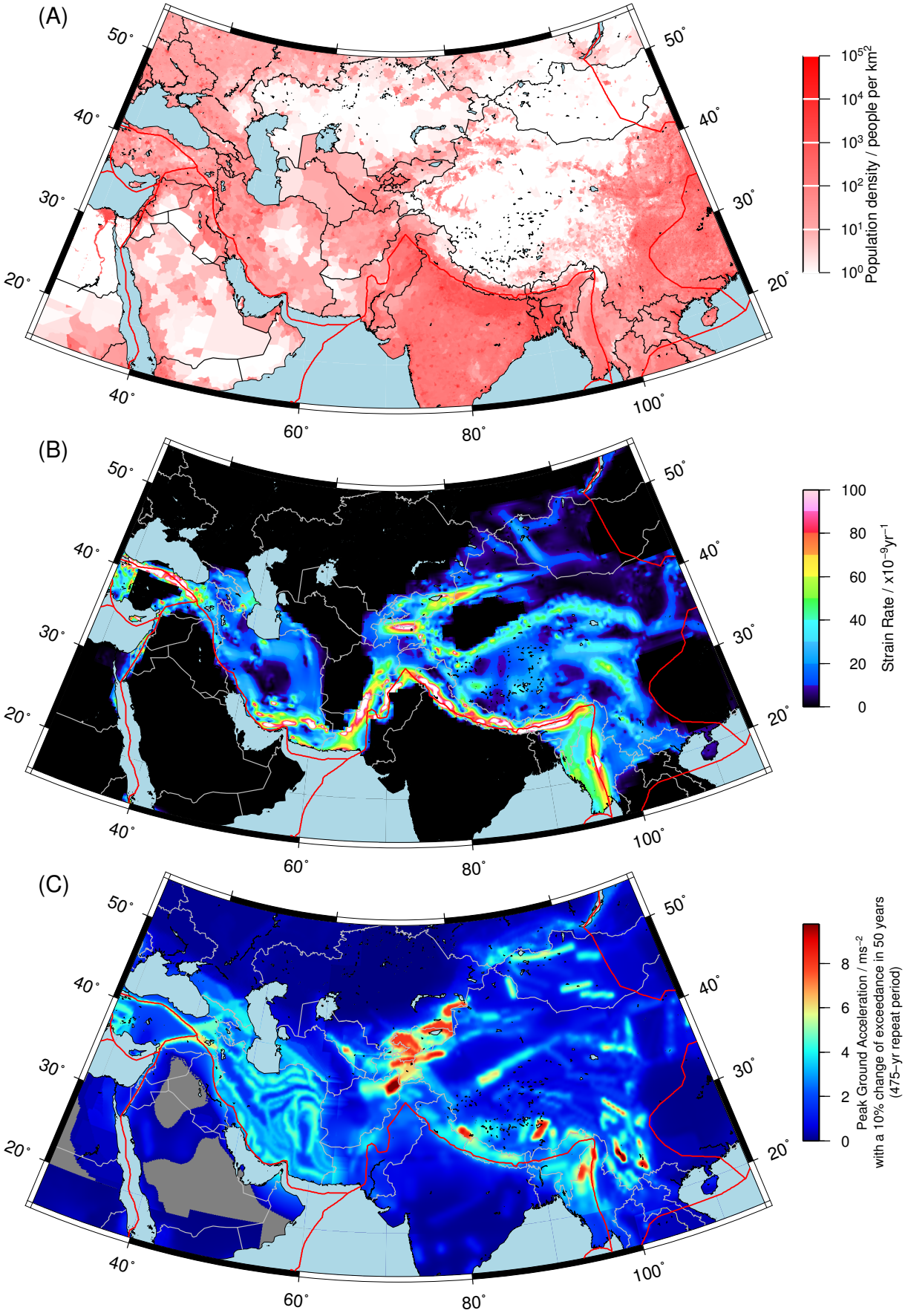
Throughout the Alpine–Himalayan belt, the high slip rate fault zones are well mapped and studied both instrumentally and geologically. However, in the low strain rate regions, individual faults are generally unresolvable by geodetic methods (InSAR, GPS) and have earthquake recurrence intervals far longer (often >1–10 ka, *Thompson et al.*, 2002; *Campbell et al.*, 2015; *Abdrakhmatov et al.*, 2016) than the seismic instrumental record (∼100 yr), and even the historic record in many regions. In the past two centuries, several faults in such regions have generated M_W 8+ earthquakes. For example, the Bogd Fault (*Rizza et al.*, 2011), and the Chilik Fault (*Delvaux et al.*, 2001; *Abdrakhmatov et al.*, 2016), while numerous others have also generated very damaging earthquakes in the M_W 7–8 range (e.g. 1976 Chaldıran, 2008 Sichuan, 2011 Van, *Gülkan et al.*, 1978; *Wang*, 2008; *Erdik et al.*, 2012, respectively). Seismic hazard assessments based on instrumental data alone are therefore likely to be biased (e.g. *Kossobokov and Nekrasova*, 2012). The geological and geomorphological record provides an invaluable method by which to extend the time period of observations. Dating late Quaternary geomorphic features displaced by multiple events on a fault can yield an average slip rate, and palaeoseismic trenching yields estimates for earthquake recurrence intervals and magnitudes (e.g. *Thompson et al.*, 2002; *McCalpin*, 2009).

1.3 High Resolution Topography

A recurring theme throughout this study is the use of high resolution topography in the analysis of fault-displaced geomorphic markers. High resolution elevation models (DEMs) were conventionally acquired using expensive airborne lidar surveys. However, recent improvements in photogrammetry techniques have allowed the production of relatively low-cost, high resolution digital elevation models (Figure 1.4, e.g. *Snavely et al.*, 2006; *James and Robson*, 2012; *Westoby et al.*, 2012; *Johnson et al.*, 2014; *Salisbury et al.*, 2015; *Zhou et al.*, 2015a), revolutionising the study of tectonic geomorphology in a number of ways. For several recent earthquakes, high resolution elevation data has even been available both pre-event and post-event, allowing measurement of the full surface displacement field (*Nissen et al.*, 2012, 2014; *Borsa and Minster*, 2012; *Zhou et al.*, 2015b).

My study has integrated these techniques into the workflow for studying fault scarps at a variety

Figure 1.3 *(following page)*: (a) Population density map of the Alpine–Himalayan belt (*Center for International Earth Science Information Network (CIESIN)*, 2016), plate margins overlain in red (*Bird*, 2003). (b) Strain rate map covering the same region from the GSRM project, combining geodetic rates with earthquake mechanisms (*Kreemer et al.*, 2003). (c) Global seismic hazard assessment program (GSHAP) map of peak ground accelerations with a 10% chance of exceedence in 50 yrs (*Giardini et al.*, 1999).


(A)
50˚
40˚
30˚
20˚
40˚
60˚
80˚
100˚
10^5
10^4
10^3
10^2
10^1
10^0
Population density / people per km^2
(B)
100
80
60
40
20
0
Strain Rate / x10^{-9}yr^{-1}
(C)
8
6
4
2
0
Peak Ground Acceleration / ms^{-2}
with a 10% change of exceedance in 50 years
(475–yr repeat period)

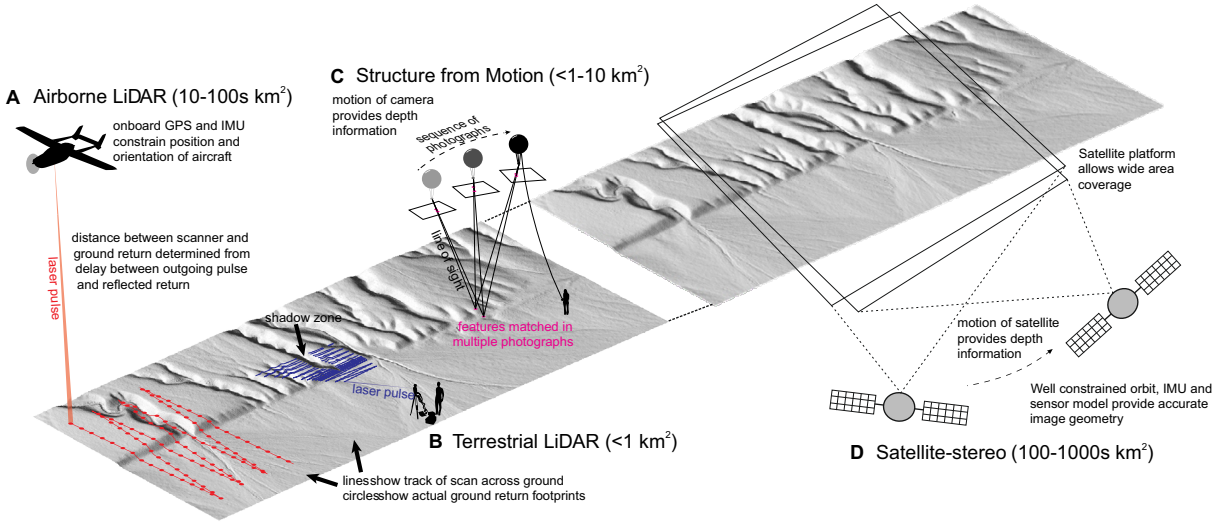


Figure 1.4: Adapted from Figure 1 of (*Johnson et al.*, 2014). The variety of techniques available for generating high resolution digital elevation models of surface fault scarps to measure geomorphic offsets. (A) Expensive airborne LiDAR – large area and very accurate. (B) Terrestrial LiDAR – very accurate, but small area coverage (C) Structure-from-motion – cheap, reasonable coverage at reasonable accuracy. (D) Satellite-stereo photogrammetry – very large area coverage, cheaper than airborne LiDAR.

of scales, tracking the rapid development of the field in two formats: Structure from Motion (SfM) and satellite-stereo photogrammetry. These allow us to map in three dimensions offsets on the scale of millimetres to kilometres. At the millimetre scale, ground based SfM is used to measure coseismic and postseismic offsets well preserved in anthropogenic structures (e.g. kerb-stones, *Wilkinson et al.*, 2010; *Morelan et al.*, 2015; *Lienkaemper et al.*, 2016; *Mackenzie et al.*, 2016). At the metre scale, low-aerial SfM is used to reconstruct geomorphic landforms (e.g. ridge crests, terrace risers, *Johnson et al.*, 2014; *Mackenzie et al.*, 2016). Increasing further in scale, higher altitude (50+ m) aerial SfM is used to build along-strike slip distributions on fault scarps (up to 10s km). At even larger scales of 10–100s km, satellite stereo imagery can be used to generate photogrammetric DEMs covering entire faults (e.g. *Zhou et al.*, 2015a; *Middleton et al.*, 2016), allowing measurement of slip distribution and detailed mapping over areas much larger than is practical in the field.

In addition to geomorphic mapping and offset measurements, SfM has been developed as a tool for generating virtual outcrops. Hand held camera images can be automatically mosaicked into three-dimensional palaeoseismic trench logs, fault exposures or outcrops, allowing detailed post-fieldwork examination and saving on relatively expensive field time (e.g. *Bemis et al.*, 2014; *Reitman et al.*, 2015).

The developments in the photogrammetric techniques have been integrated into the workflows for the investigation of surface faulting throughout this thesis. The availability of such high resolution DEMs also prompted me to develop a method to exploit them in a new and inherently three-dimensional fashion (Chapter 5).

1.4 Thesis Structure

This thesis is concerned with the earthquake cycle and the distribution of strain in low strain rate regions, using the natural laboratory of the Alpine Himalayan belt. Detailed introductions to areas of study are presented in the beginning of each chapter, as are the methods used within each chapter, though each chapter builds upon the methods of the previous ones. The final chapter presents an analysis for uncertainties on techniques for measuring fault slip at the surface and develops several new tools to take advantage of high resolution 3D elevation data. The motivation arises from the potential inadequacies and inaccuracies of the conventional techniques employed in the earlier chapters, but the techniques have not been applied retrospectively. I give here a brief summary of each chapter:

- **Chapter 2:** the 2011 Van Earthquake in eastern Turkey was a modern, instrumentally recorded earthquake on a thrust fault in a continental interior region. This chapter presents a case study of the earthquake, investigating the co-seismic and post-seismic phases related to it and tying the activity into the regional tectonic setting with a late Quaternary slip rate.

- **Chapter 3:** investigates the Karkara Rangefront fault in the northern Tien Shan. Analysis of the modern GPS velocities through two profiles across the fault suggest that it is creeping at a rate (2.9–3.2 mm/yr shortening) which represents a significant fraction of the total strain across the northern Tien Shan (∼10 mm/yr at this longitude). A study of river terraces along the rangefront using a high resolution DEM reveals a geological slip consistent with the geodetic creep rate, suggesting that creep may be the long term deformation mechanism.

- **Chapter 4:** presents a synthesis of the shortening rates and earthquake behaviours of the faults across the Kazakh Tien Shan and Dzungarian Alatau. Drawing on several seasons of fieldwork, extensive mapping, quaternary dating and surveying, a transect of Late Quaternary slip rates are compared to the regional GPS velocity field.

- **Chapter 5:** measurements of surface faulting through the previous chapters highlights several important geometric assumptions on the capturing of surface offsets. Principally a methodology study, Chapter 5 addresses the impact of these assumptions on measuring fault slip, and develops new methods to exploit the full power of high resolution digital elevation models in cases where the geometric assumptions are violated. Test cases suggest that this method is effective at capturing an average slip vector on scarps with significant oblique slip in regions of varied topography.

- **Chapter 6:** draws together the findings of the previous chapters to make broader conclusions on the nature of compressional faulting within the continents.

1.5 Miscellaneous Notes

Photographs are used in figures throughout the thesis. All were taken by myself or other authors of the publications mentioned below during our field campaigns. Care was taken to acquire photographs under reasonable light conditions, but this was not always possible. To improve the clarity and print quality of the resulting figures I have adjusted the brightness and contrast to correct the exposure in many of the images.

Wherever possible I have referred to faults by their labels in earlier publications. On faults previously unrecognised (Chapters 3–4), I endeavour to label them by the name of the range they bound in the case of rangefront faults, or the name of the nearest major river (often the same). These names are drawn primarily from Soviet era topographic maps and so may occasionally be outdated.

1.6 Publications arising from this thesis

The material of Chapter 2 is published in *Mackenzie et al.* (2016):

> Mackenzie, D., J.R. Elliott, E. Altunel, R.T. Walker, Y.C. Kurban, J.-L. Schwenninger, and B. Parsons, Seismotectonics and rupture process of the MW 7.1 2011 Van reverse-faulting earthquake, eastern Turkey, and implications for hazard in regions of distributed shortening, 2016, *Geophys. J. Int.*, 206, 1, 501-524, doi:10.1093/gji/ggw158

The material of Chapter 5 has been resubmitted following moderate revisions for publication as:

> Mackenzie, D. and A. Elliott, Disentangling Slip-Distribution and Fault Scarp Geometry: Rigorous Quantification of Slip in 3D, *revised for Geosphere, 2016.*

The material of Chapter 3 is in preparation for submission as:

> Mackenzie, D., R. T. Walker, G. Campbell, A. Carr, C. Gruetzner, A. Mukambaev, M. Rizza and K. Abdrakhmatov, Geomorphology, Structure and Preliminary Slip-Rate on the Northern Edge of the High Tien Shan: A Creeping Thrust Fault?

I was also involved in the fieldwork contributing to the papers *Campbell et al.* (2015), *Abdrakhmatov et al.* (2016) and *Grützner et al. (in prep)*, material from which is incorporated into Chapter 4 (noted fully as footnotes of that chapter):

> Campbell, G. E., R. T. Walker, K. Abdrakhmatov, J. Jackson, J. R. Elliott, D. Mackenzie, T. Middleton, and J.-L. Schwenninger (2015), Great earthquakes in low strain rate continental interiors: An example from SE Kazakhstan, Journal of Geophysical Research: Solid Earth, 120 (8), 5507–5534, doi:10.1002/2015JB011925

> Abdrakhmatov, K., R. Walker, G. Campbell, A. Carr, A. Elliott, C. Hillemann, J. Hollingsworth, A. Landgraf, D. Mackenzie, A. Mukambayev, M. Rizza, and R. Sloan (2016), Multi-segment rupture in the July 11th 1889 Chilik earthquake (M_W 8.0-8.3), Kazakh Tien Shan, interpreted from remote-sensing, field survey, and palaeoseismic trenching, Journal of Geophysical Research: Solid Earth, pp. 1–16, doi:10.1002/2015JB012763.

> Grützner, C., E. Carson, R. Walker, E. Rhodes, A. Mukambayev, D. Mackenzie, J. Elliott, G. Campbell, and K. Abdrakhmatov (in prep.), Assessing the activity of faults in continental interiors: palaeoseismic insights from SE Kazakhstan.

Chapter 2

Seismotectonics and rupture process of the M_W 7.1 2011 Van reverse-faulting earthquake

2.1 Introduction

On 23^{rd} October 2011, the cities of Van and Erciş in eastern Turkey were severely damaged by a M_W = 7.1 earthquake (Figure 2.1), resulting in the death of 604 people. A further 40 died as the result of an M_W 5.7 aftershock on 9 November 2011, which caused further building damage, primarily in the city of Van (e.g. *Erdik et al.*, 2012; *Elliott et al.*, 2013; *Fielding et al.*, 2013). The earthquake, which occurred on a relatively short (∼25 km) reverse fault (Figure 2.3) and generated no primary surface ruptures, was one of the largest continental reverse faulting events in recent decades (*Wright et al.*, 2013).

The slip solution determined by InSAR for the Van earthquake suggests the fault only ruptured below a depth of ∼10 km (Figure 2.2). As such, there is the potential for another, possibly even more damaging, shallow earthquake if the upper portion of the fault fails seismically (*Elliott et al.*, 2013). Alternatively, the upper sections of the fault may creep aseismically; it is known that at least small amounts of postseismic creep occurred, as was imaged following the mainshock (*Elliott et al.*, 2013; *Doğan and Karakaş*, 2013). However, the largest aftershock (M_W 5.9) ten hours after the mainshock was associated with shallow slip between 3–10 km depth at the eastern end of the main fault rupture, indicating that this shallower portion of the fault still has the potential to be seismogenic (*Elliott et al.*, 2013). Therefore, resolving the depth extent of fault frictional behaviour is important for assessing the potential size of a future earthquake and consequent degree of hazard.

It has long been recognised that there are a range of frictional stability regimes that govern the slip

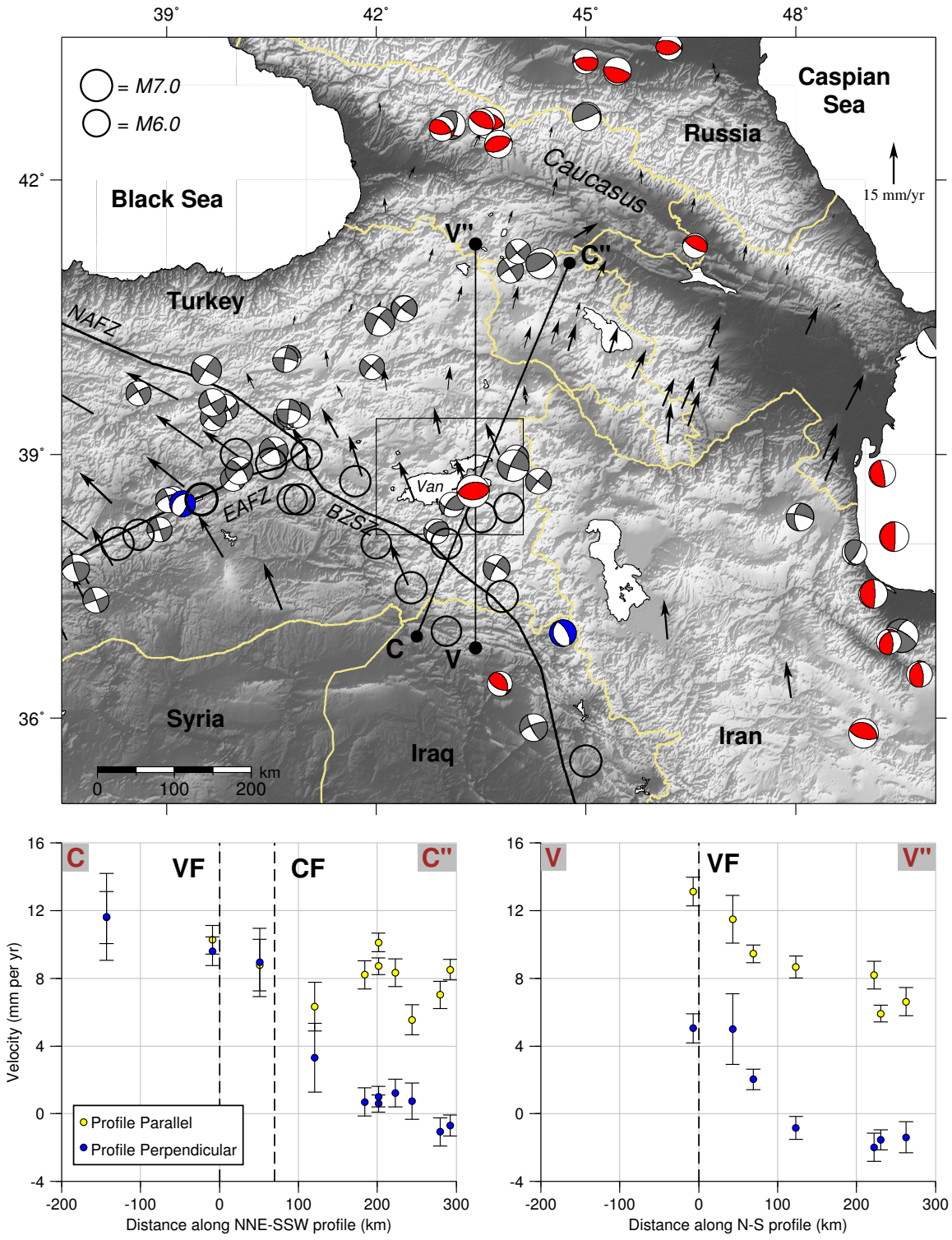


Figure 2.1: *(Top)* Tectonic overview of the Turkish-Iranian plateau, the highlands between Iran and Turkey, where we see the transition from the localised deformation on the north and east Anatolian faults (NAFZ, EAFZ), to distributed shortening and shear accommodated by conjugate strike slip and thrust faulting. BZSZ marks the Bitlis-Zagros Suture zone between Arabia and Eurasia. Modern earthquake focal mechanisms shown for magnitude > 5 from the Global Centroid Moment Tensor catalogue (*Dziewonski et al.*, 1981; *Ekström et al.*, 2012). Thrust mechanisms are shown in red, normal in blue and strike slip in grey. Regional GPS velocity vectors overlaid from *Vernant et al.* (2004), *McClusky et al.* (2000) and *Reilinger et al.* (2006). The box shows the outline of Figure 2.3. *(bottom)* The GPS velocity vectors projected onto the two profiles V–V″ (000°) and C–C″ (022°) demonstrate the distributed nature of shortening and shear across the plateau. The dashed line at zero represents the Van fault (VF). The second dashed line on C–C″ represents the right-lateral strike slip fault, the Çhaldıran fault (CF).

on faults (*Scholz*, 1998), largely varying as a function of depth: deep, stable sliding as a result of quartz plasticity, occurring beneath 15–20 km dependent upon the local geotherm; above this, an unstable (stick-slip) regime in which earthquakes can nucleate and propagate; finally at the shallowest depths an upper transition back to stable sliding occurs in the first few kilometres of the fault, depending on the lithologies cut, the degree of consolidation of sediments and any development of fault gouge due to how mature the fault zone is (*Marone and Scholz*, 1988). A rapidly growing number of faults have been shown to be creeping at shallow depths (*Avouac*, 2015), including the Longitudinal Valley Fault (Taiwan) whose creep rate changed after the 2003 M_W 6.8 Chengkung earthquake (*Thomas et al.*, 2014). Shallow afterslip is observed following a significant number of earthquakes (*Wright et al.*, 2013), and is often considered to be driven by coseismic stress changes, although postseismic shallow afterslip in the recent Napa (California) earthquake (*Elliott et al.*, 2015a) shows a large spatial variability which may also suggest a lithological control on slip behaviour (*Floyd et al.*).

In addition to depth-dependent frictional behaviour, there is the potential for both structural and lithological controls on the depth extent of faulting. Lithological layers such as salt and shale detachment horizons act to compartmentalise slip in narrow depth extents (*Nissen et al.*, 2010; *Elliott et al.*, 2015b), and the intersection of faults at depth has been suggested as a possible (albeit potentially temporary) barrier to rupture propagation (*Elliott et al.*, 2011, 2016). There has been much discussion on the effect of along-strike segmentation on the length of ruptures in strike-slip earthquakes (e.g. *Wesnousky*, 2008), but much less for down-dip segmentation in dip-slip earthquakes in intracontinental settings. The rapid postseismic motion observed with InSAR following the Van earthquake images the faulting in the upper 10 km of the crust, allowing us to probe the influence of structure on slip propagation.

Further south from the Van fault, *Doğan et al.* (2014) noted motion on a splay fault (the Bostaniçi Fault, Figure 2.3) at the surface within the northern limits of the city of Van using postseismic GPS and InSAR data. We add further remote sensing observations and field evidence of the surface expression of this splay fault. In addition, we demonstrate the utility of two novel datasets in assessing and monitoring Quaternary and modern geomorphology within expanding cities – the exploitation of 1960–70s declassified US spy satellite imagery (*Hollingsworth et al.*, 2012); and the rapid, very low cost, photogrammetric mapping using Structure from Motion (SfM) (*James and Robson*, 2012; *Johnson et al.*, 2014).

Combining the tectonic geomorphology across the region with Quaternary dating, we determine the long term slip-rate on the Van fault. Studying the immediate postseismic behaviour and the longer-term slip rate allows us to probe the earthquake cycle in this region of the Arabia-Eurasia collision zone where the cycle is much longer that the instrumental catalogues and often the historical records too.

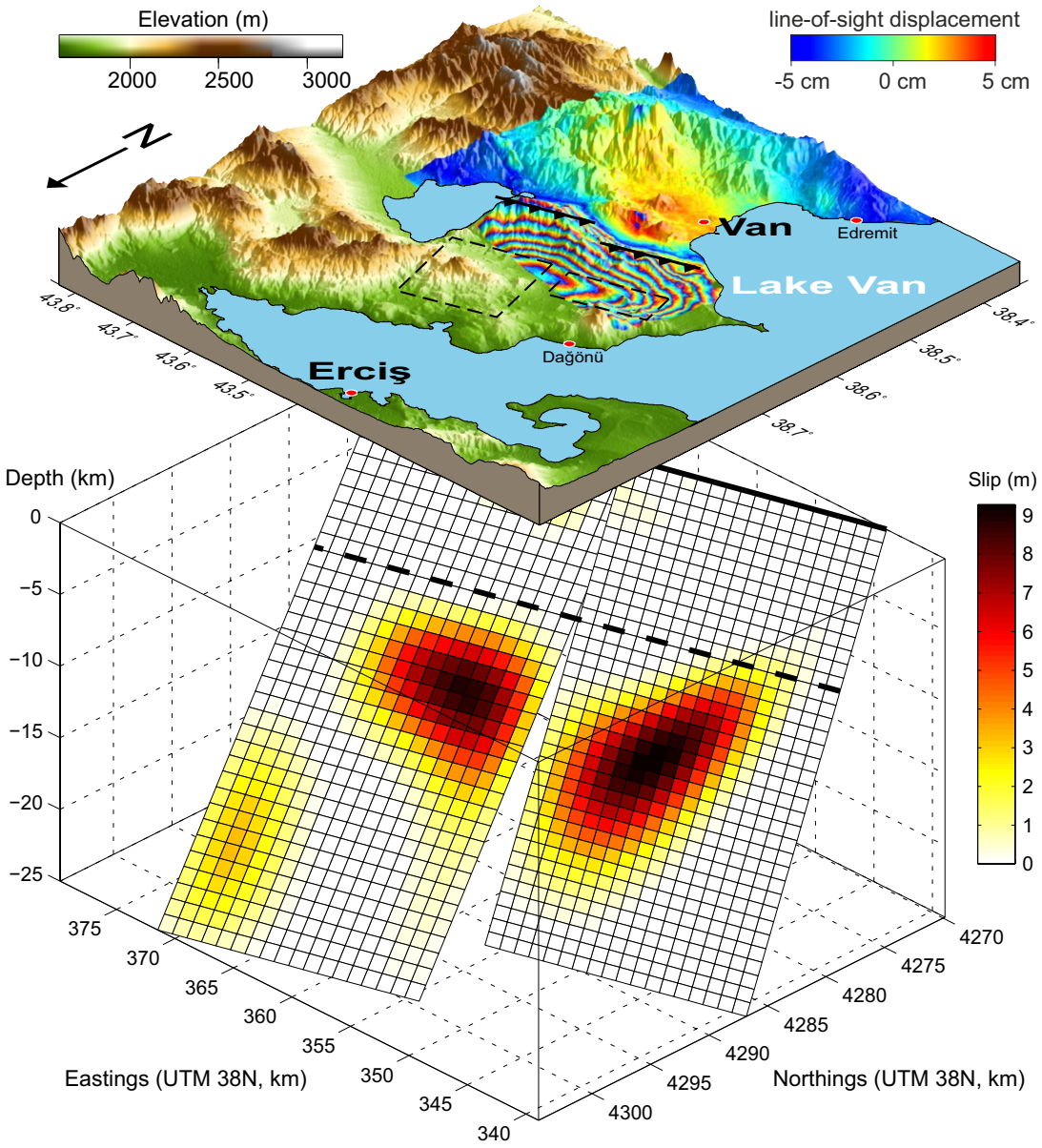


Figure 2.2: Perspective view looking SE, of the coseismic interferogram overlaid on the SRTM topography, above a perspective view of the fault slip distribution for a two plane fault model. Very little slip is observed above a depth of ∼10 km (dashed line). Fringes in the CSK1 interferogram have been re-wrapped to 10 cm line of sight motion with increasing positive values indicating motion towards the satellite. (Adapted from *Elliott et al.* (2013))

2.2 Background to the Van Earthquake

2.2.1 Tectonic Setting

The Van region lies in a zone of general north-south shortening within the continental collision zone between Arabia and Eurasia (e.g. *Copley and Jackson*, 2006). Early estimates suggest that the initial collision was at ∼10 Ma (*Dewey et al.*, 1986), though palaeoclimate studies suggest it may have begun as early as ∼35 Ma (*Allen and Armstrong*, 2008). Much of the current rate of Arabia-Eurasia convergence (23 mm yr^{-1}) is accommodated by shortening in the Caucasus, but around ∼10 mm yr^{-1} is distributed

across the Turkish-Iranian Plateau (TIP) (*Reilinger et al.*, 2006). In western Turkey, Arabia-Eurasia shortening results in the westwards extrusion of Anatolia in a plate-like fashion, bounded by the North Anatolian and East Anatolian faults (e.g. *McClusky et al.*, 2000; *Reilinger et al.*, 2006), whereas eastern Turkey is a zone of distributed crustal shortening (Figure 2.1).

Shortening within the TIP is accommodated by a combination of thrust and conjugate strike-slip faults (Figs. 2.1–2.3 *Altinli*, 1966; *Saroglu et al.*, 1992; *Karakhanian et al.*, 2004; *Ozkaymak et al.*, 2011; *Üner et al.*, 2015). The 2011 Van earthquake occurred on a thrust fault approximately 10 km north of Van which was previously unrecognised as active (*Doğan and Karakaş*, 2013; *Elliott et al.*, 2013; *Fielding et al.*, 2013). There have been a number of large historical earthquakes in the Van region, the most recent of which was the 1976 $M_W = 7.1$ Çhaldıran strike-slip earthquake ∼80 km north east of Van (Figure 2.3), which caused heavy damage in the town of Çhaldıran and much of the surrounding region (*Gülkan et al.*, 1978).

Monastery archives record several damaging historical earthquakes in the region, including the 1648 Van-Hayotsdzor earthquake, estimated to be M ∼6.7, which caused heavy damage in the region from Van south to the Gürpınar valley (Figure 2.3), completely destroying or damaging beyond repair at least 11 different monasteries across the region (*Ambraseys*, 1989). In 1715, a M 6.6+ earthquake occurred south east of Van in the region of Mahmatan, causing damage in the Mehmedik plain (Figure 2.3), ruining the walls of the Hoşap Castle (modern town of Gŭzelsu, ∼40 km south-east of Van), but potentially causing damage as far as Erciş (*Ambraseys*, 1989; *Ambraseys and Melville*, 1982; *Thierry*, 1979). In 1903, the M_S 7.0 Malazgirt earthquake to the north west of Lake Van, was reported to have killed at least 700 people (*Shebalin et al.*, 1997). *Utkucu* (2013) suggest that the 1715 event may have occurred on the same fault as the 2011 event, but it is difficult to associate these historical earthquakes with specific faults with much certainty, as there are no records of surface ruptures.

2.2.2 Geological Setting

Van lies on the eastern shore of the alkaline Lake Van, which has a mean elevation of 1650 m above mean sea level (*Kadioğlu et al.*, 1997). To the north and west of Lake Van, the exposed geology is predominantly composed of Quaternary and Neogene volcanics (*Pearce et al.*, 1990). To the south of Lake Van, the Bitlis mountains rise to ∼3500 m, and are comprised of Palaeozoic and Mesozoic metamorphic and ophiolitic lithologies. Around the city of Van, are regions of Pliocene basin deposits, Quaternary lake sediment deposits and extensive Quaternary volcanics (*MTA*, 2002; *Kuzucuoğlu et al.*, 2010), most of which have been faulted, folded and tilted by tectonic activity.

The presence of soft sediment deformation structures (seismites) in the varved lake sediments provide a rich record of prehistoric earthquakes in the Van region. *Üner et al.* (2012) map several different varieties of seismites at 6 different locations around the south and east shores of Lake Van, which they

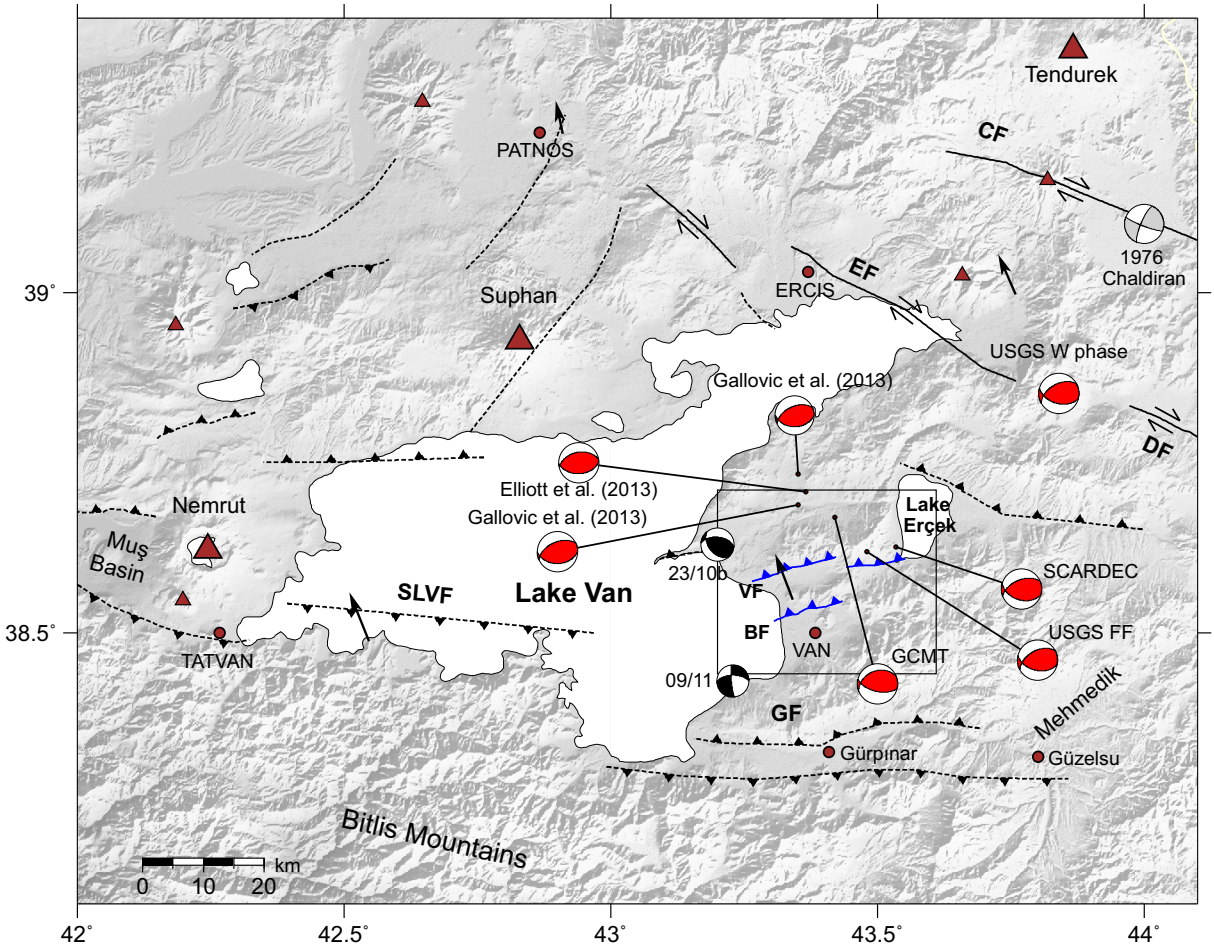


Figure 2.3: Active fault map of the Van region, based on work by *Altinli* (1966); *Saroglu et al.* (1992); *Karakhanian et al.* (2004); *Ozkaymak et al.* (2011); *Üner et al.* (2015) and our own field and remote sensing mapping. Solid lines represent faults for which we have strong evidence of activity from earthquakes and/or displaced Late Quaternary markers. Faults marked in red are those shown to have undergone postseismic motion following the mainshock. Dashed lines represent faults inferred from the broader geomorphic markers, but lacking direct evidence for Holocene activity. The black box marks the region shown in Figs. 2.4 and 2.8. The focal mechanisms in red represent the various fault plain solutions for the 23 October 2011 mainshock. The mechanisms in black are for the two large aftershocks - the 23/10/11 mechanism is from bodywave modelling by *Elliott et al.* (2013), while that of the 09/11/11 aftershock is from the USGS solution. Both locations are from the USGS. Triangles denote Holocene volcanic centers and brown dots show the main population centers. GPS velocity vectors from *Reilinger et al.* (2006). Fault labels: CF - Çhaldıran Fault, EF - Erciş Fault, DF - Dorutay Fault, VF - Van fault, SLVF - South Lake Van Fault, BF - Bostaniçi Fault, GF - Gürpınar Fault.

attribute to occurrence of repeated $M_W > 5$ earthquakes in the Late Quaternary. The recent International Continental Drilling Project (ICDP) PALAEOVAN project has focused on coring the varved sediments from two locations within Lake Van (*Litt et al.*, 2009, 2012; *Litt and Anselmetti*, 2014; *Cukur et al.*, 2014; *Stockhecke et al.*, 2014). Work is ongoing to establish the chronology, but *Litt et al.* (2009) observe extensive seismites in the test drill cores, attributing them to the repeated occurrence of earthquakes throughout the last 500 ka.

2.2.3 The October 23, 2011 Van earthquake

Initial epicentres for the 2011 mainshock were as far apart as ∼20 km, but later solutions incorporating radar interferometry tie the location to ∼22 km due north of Van (Figure 2.3). A summary of the seismological and geodetic solutions is shown in Table 2.1.

InSAR, seismology, GPS and combined solutions (*Zahradnik and Sokos*, 2011; *Irmak et al.*, 2012; *Gallovic et al.*, 2013; *Zahradnik and Sokos*, 2014; *Doğan and Karakaş*, 2013; *Elliott et al.*, 2013; *Fielding et al.*, 2013; *Feng et al.*, 2014; *Moro et al.*, 2014; *Wang et al.*, 2015), broadly agree that the earthquake occurred on a steep north dipping (40–55°) fault, with a small left lateral component. The upper extent of slip is generally agreed to be 7–10 km depth. Chequerboard tests by *Elliott et al.* (2013) show that this top depth is well constrained by the InSAR data. The pattern of uplift is consistent with the field observations of *Emre et al.* (2011), who observed uplift of the lake shore (inferred from the height of shoreline boulder deposits) of up to ∼40 cm near the village of Dağönü. The source models of *Elliott et al.* (2013), *Zahradnik and Sokos* (2014) and *Wang et al.* (2015) go further in breaking the rupture into two smaller discrete patches of slip or sub-events, possibly on two fault segments aligned to two geomorphic scarps.

The majority of well constrained aftershocks were shallow, in the 0–10 km region, and appear to cluster around the uppermost edge of the rupture region (*Fielding et al.*, 2013), but the cumulative moment release from the aftershocks over the entire region is still small compared to that of the mainshock ($< 10\%$ over the first 3-months, based on the ISC bulletin). Two large aftershocks occurred in the hours to days following the earthquake. A M_W 5.9 aftershock occurred towards the northeastern extent of the fault 10 hours after the mainshock with a thrust mechanism similar to the mainshock (*Irmak et al.*, 2012; *Elliott et al.*, 2013). The M_W 5.7 aftershock on 9th November 2015 had a strike-slip/oblique mechanism and was located to the south west of the Van fault, within Lake Van (*Fielding et al.*, 2013).

Source	**Dataset**	**Lat** °	**long** °	**Centroid depth** /km	**M_W**	**Moment** /10^{19} Nm	**Strike** °	**Dip** °	**Rake** °	**Slip** / m	**Top** / km	**Bottom** / km
KOERI	Seismic	38.73	43.43	5	6.6(M_L)							
GCMT	Seismic	38.67	43.42	12	7.1	6.40	246	38	60			
USGS	Seismic	38.69	43.49	16	7.1	6.40	255	50	73			
USGS–W	Seismic	38.69	43.49	16	7.1	5.60	241	51	58			
GFZ	Seismic	38.72	43.55	10	7.0	4.70	268	36	85			
EMSC	Seismic	38.86	43.48	10	7.2	6.80	248	53	64			
Elliott 2013	Seismic	38.67**	43.42**	19	7.0	3.26	243	50	60			
Irmak 2012	Seismic	38.782	43.337	15	7.1		246	46	59	3.6	11	24
Fielding 2013	Seismic	38.69*	43.49*	18	7.1	5.37	258	46	71	3.5	6	29
Utkucu 2013	Seismic	38.69*	43.49*	11	7.1	4.60	255	50	73	5.5	5	20
Gallovic 2013†	Seismic	38.689	43.351	10	7.2	7.40	246	52	75			
Feng 2014	SAR	43.403	38.702	12	7.03		261	49	80	6.5	8	
Elliott 2013-1f	SAR	38.592	43.386	14.1	7.0	4.44	258	45	83	3.7	8.6	19.6
Elliott 2013-2f	SAR			13.7/13.8	6.8/6.8	2.13/2.31	254	40/55	64/93	3.3/6.7	8.3/10.2	19.1/17.4
Fielding 2013	SAR				7.1	5.84	259	42.5			6	30
Wang 2015-2f	SAR			25/25	7.19	6.08	253/253	40/54				

Table 2.1: Table of earthquake mechanisms for the Van Earthquake mainshock from various authors mentioned in the text. 1f and 2f refer to the single fault and two fault models. * Fixed to the USGS location. ** Fixed to the Global CMT (GCMT) location. † Solution used as the assumed fault plane by *Zahradnik and Sokos* (2014) who estimate a total moment release of 3.55–3.87x10^{19} Nm in two subevents.

2.3 Methods

2.3.1 Structure from motion surveying

One of the fundamental measurements in characterising active faulting from geomorphic markers is determining fault offsets in topography, due to motion in single or multiple events. In the simplest case of a uniform fault scarp running through a flat surface, a basic differential GPS (DGPS) profile can be used to measure of the offset in the surface. However, as the surface becomes more uneven, or the strike of the fault changes, it becomes necessary to look at the offset over a larger area and terrain range and take an average. Similarly, if we wish to differentiate between individual events (such as multiple lateral offsets of different amounts), it becomes necessary to take a full three dimensional view of the fault expression at the surface. For small areas, this can still be done with kinematic DGPS, simply by walking the antenna over the ground (e.g. *Campbell et al.*, 2015). But for larger areas, this procedure becomes too time consuming to achieve sufficient resolution. Instead we implement a work flow using photogrammetric reconstruction by Structure from Motion (SfM), based on the methods of *James and Robson* (2012), *Fonstad et al.* (2013) and *Johnson et al.* (2014). This is a highly scalable technique, the utility of which we demonstrate from scales of small (<10 cm) creep offsets to much larger (5+ m) fault scarp offsets.

Structure from Motion uses many photographs taken from a variety of perspectives, to construct a scale-independent 3D model. Supplementing this with accurately determined ground control points, we can make DEMs with centimetric resolution. Traditional photogrammetry relied on a small number of photos from well calibrated metric cameras, with multiple ground control points necessarily visible in every photograph. In contrast, the SfM method uses the redundancy of many highly overlapping photographs to use a new feature identification algorithm (SIFT, Scale Invariant Feature Transform, *Lowe*, 2004) to simultaneously solve for the relative camera positions and calibration parameters, by matching features between photos. This is followed by a multi-view stereo image correlation based reconstruction in a purely relative space, based on the calculated camera orientations. A minimum of three ground control points within the model are required to orient and scale the model.

We use the Agisoft Photoscan commercial software to perform the photogrammetric reconstruction, first using a sparse reconstruction to solve for the internal and external camera parameters, and then a multi-view stereo reconstruction to generate a dense pointcloud. The pointcloud is then scaled and oriented using a small number (typically 5–10) of ground control points consisting of orange plastic squares pegged into position and whose location is measured using realtime kinematic (RTK) DGPS. The pointcloud is gridded using a tensioned minimum curvature algorithm, under the Generic Mapping Tools package (GMT, *Smith and Wessel*, 1990), to generate a digital elevation model (DEM). The gridded data is appropriate for hillshading and display (§2.5.2), but analysis is performed on the raw dense pointcloud. We manually mask any regions of the pointcloud where the geomorphic marker has

been modified, before measuring displacements.

In this study we perform two different types of SfM survey; for small offsets in anthropogenic markers which can easily be viewed from many viewpoints, we use a handheld compact digital camera, while for larger terrain offsets (scarps) we use a camera mounted on a long pole to gain an elevated perspective. The survey design is important in determining the ability of the SIFT algorithm to match features between photos – photos were taken with significant overlap typically >60% and minimal change in orientation (10%). In the case of the pole survey (§2.5.2), we used a compact digital camera (Ricoh GRII) mounted on a 6 m aluminium pole. The camera is oriented downwards but angled forwards at ∼20–30 degrees, just clear of the operator, in order to incorporate a greater depth of field (DOF) in the photographs (and remove the operator from the frame). A 28 mm (full-frame equivalent) focal length camera provides a field of view of ∼11x12 m on the ground, so we walk a grid at 10 m spacing, covering an area of ∼190x150 m. The pole was carried in a rough grid pattern across the scarp, with adjacent (overlapping) "tracks" moving in opposite directions. A simple downward (nadir) looking geometry would provide the easiest approach, with the best photograph overlap and feature matching, but this results in very limited DOF in the photographs. That parallel-axis geometry with limited DOF results in a trade-off between the focal length and radial distortion coefficients when solving for the lens parameters, resulting in uncorrected image distortion that propagates into the whole model as a "bowl" effect (*James and Robson*, 2014). Our opposing geometry with the angled camera and pre-calibration, avoids the special-case of parallel geometry so we can solve for the lens parameters without ambiguity, even in scenes with relatively poor texture (e.g. grassy fields).

2.4 Postseismic slip: InSAR and field measurements

The very rapid first acquisition of post-earthquake COSMO-Skymed data (4hrs), has provided a valuable opportunity to probe the early postseismic motion. The COSMO-Skymed interferogram for the coseismic period (CSK1, Table 2.2) showed minimal surface discontinuities from the earthquake itself. However, interferograms for the period immediately following the earthquake (CSK3, 4 hrs to 3 days after) show a small discontinuity at the surface (*Doğan and Karakaş*, 2013; *Elliott et al.*, 2013; *Feng et al.*, 2014), coincident with surface displacements of up to 10 cm observed in the field (*Emre et al.*, 2011). It is likely therefore that most of the observed surface displacements occurred postseismically, over the two weeks following the mainshock (discussed below). In the following sections we further refine measurements of the postseismic slip, using both field measurements and InSAR. These motions provide important constraints on fault behaviour, as well as providing an insight into the upper crustal structure of the Van fault and associated splay, and potential controls on rupture propagation.

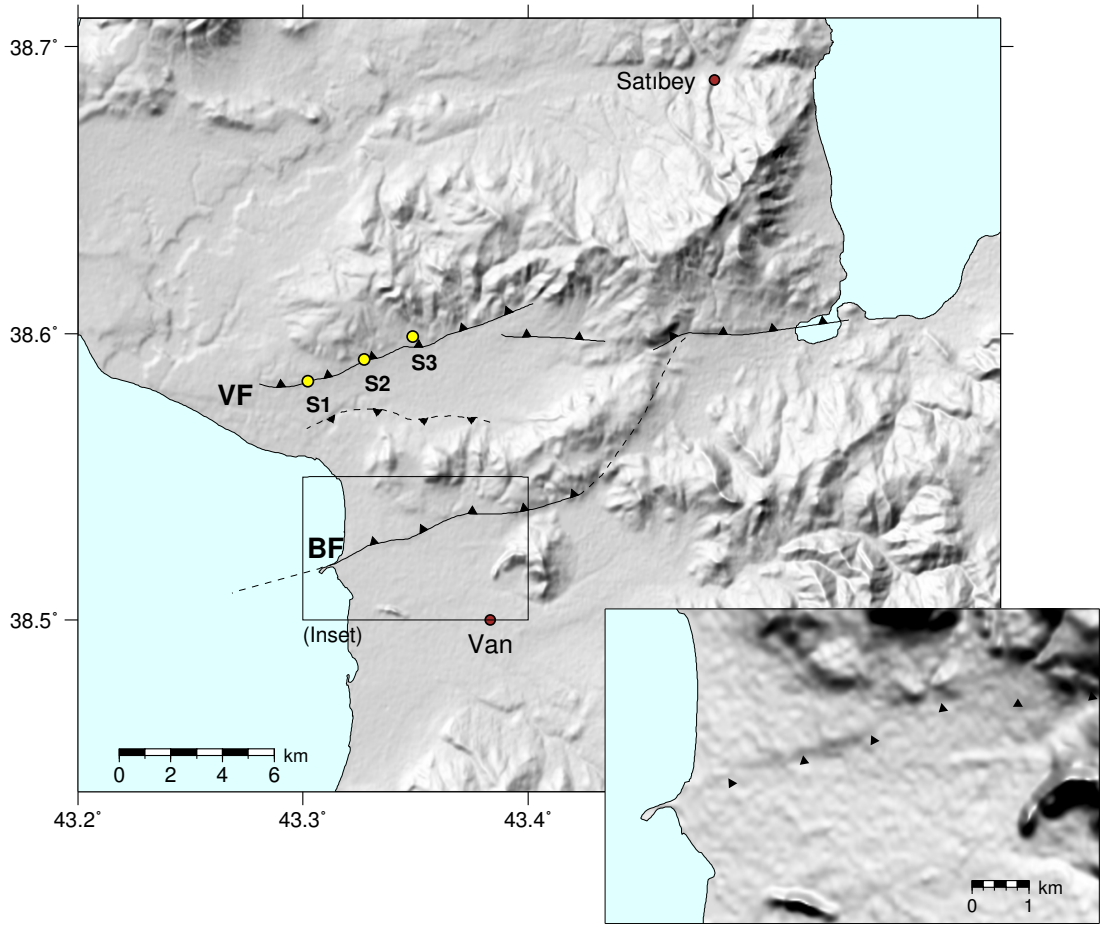


Figure 2.4: Map of the field study region covering the same region as the interferograms in Figure 2.8, on a hillshaded Shuttle Radar Topography Mission (SRTM, 30 m, illuminated from the north west) basemap with the Van fault (VF) and the Bostaniçi fault (BF) marked and the individual field study sites shown (S1, S2, S3). The backthrust is marked as a dashed line, as is the possible lakewards extension of the Bostaniçi fault. We infer from the topography that in the east the fault motion collapses back onto a single strand (connected by a dashed line), consistent with the trace mapped by *Doğan et al.* (2014) and *Wang et al.* (2015),. The inset shows the zoom of the northern Van city, with trace of the Bostaniçi splay fault visible in the SRTM elevation data (marked with black triangles). This splay fault is laterally extensive and cuts palaeo lake shorelines.

2.4.1 Field measurements of postseismic slip

Van-Erciş Highway

Very shortly after the mainshock (1–5 days), a series of small surface ruptures (typically <20 cm) were observed on the main Van–Erciş highway (S1 in Figure 2.4). The ruptures are indicative of oblique shortening, including cracking and folding of tarmac, displacement of kerbstones and paved surfaces, and shallow cracking and moletracks across agricultural fields (*Doğan and Karakaş*, 2013; *Emre et al.*, 2011; *Ozkaymak et al.*, 2011; *Elliott et al.*, 2013). The ruptures are along strike from a fault exposure at the Van–Erciş highway, which dips 45–50°N in late Pleistocene deposits (photograph in Figure 2.5c). The fringe rate in the coseismic (CSK1) interferogram is too high to distinguish phase discontinuities at the level of 1–2 fringes (<3 cm LOS) so, reinspecting the coseismic interferogram, we cannot rule out motion during the earthquake. However, we know from the postseismic interferograms (see below) that

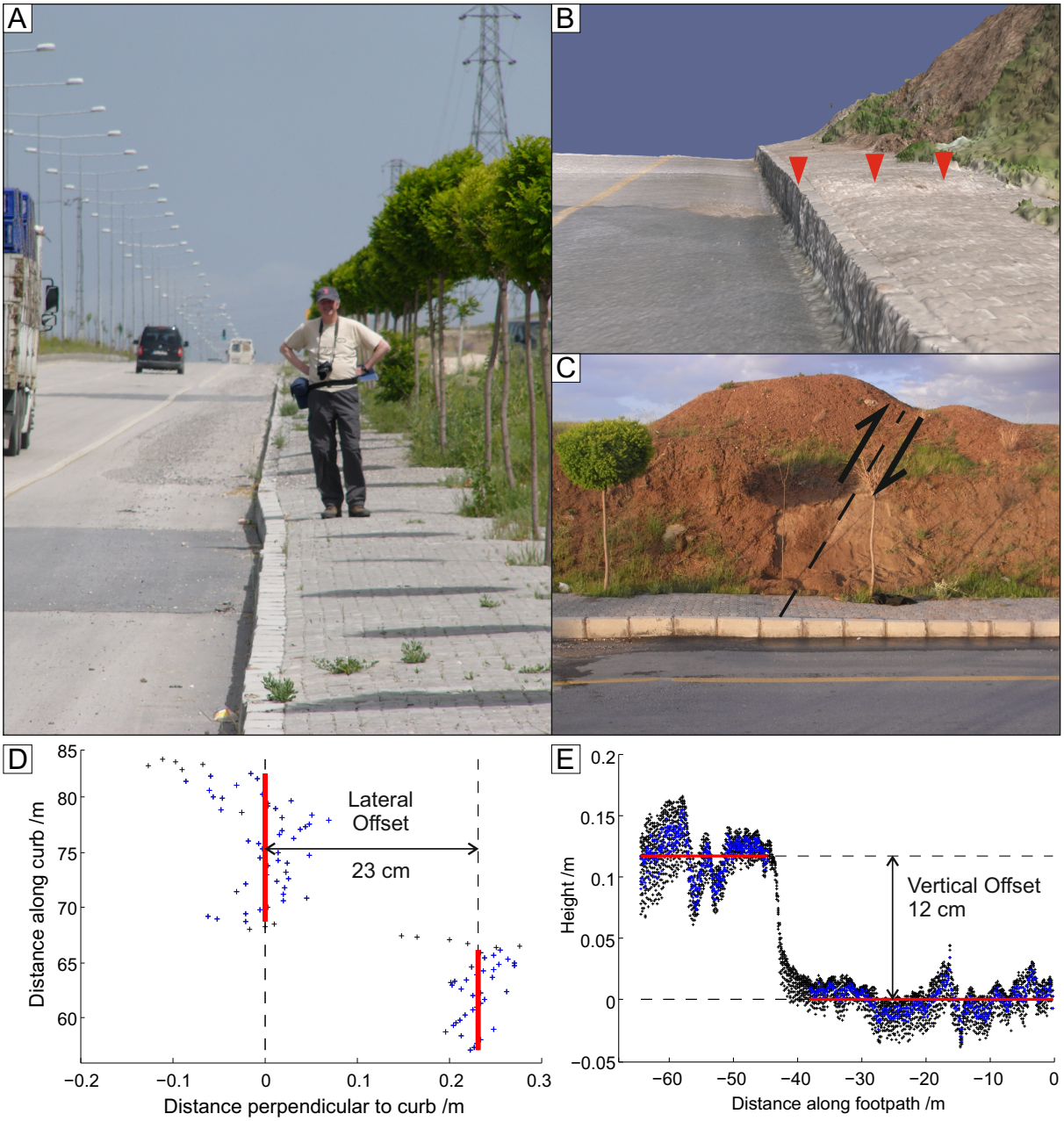


Figure 2.5: *(a)* Photograph looking along kerbline (May 2013), person for scale, showing left lateral displacement. *(b)* Oblique 3D perspective view of the structure-from-motion reconstruction, showing a vertical offset in the same kerbline. Red arrows denote the displacement line. The poorly correlated trees have been removed from the model (3 x vertical exaggeration to aid visualisation). *(c)* Photograph of the cleaned road cutting, with contrast between hangingwall and footwall sediments and coincident displaced kerbstones in the foreground. Dashed line and arrows mark the visible fault dipping 45°N. *(d)* Horizontal profile along the top edge of the kerbline in the SfM pointcloud showing ∼23±3 cm lateral offset. Points shown in blue are those used for least squares fit. *(e)* Vertical profile along the top edge of the kerbline in the SfM pointcloud showing ∼11.7±1.0 cm vertical offset. A gradient has been removed to de-trend the profile and aid visibility of the vertical offset.

significant motion did occur postseismically.

The road surface has since been repaired, but the kerbstones record the full displacement (Figure 2.5a). Using Structure from Motion (SfM, see §2.3.1), we created a 3D terrain model (Figure 2.5b) of the road and pavement in order to accurately quantify the displacement at the surface, such that we can compare the observed slip with that imaged in the postseismic interferograms. The length of six kerbstones

measured in the field was used to accurately scale the model. We measure an offset of 23±3 cm laterally and 11.7±1.0 cm vertically (Figure 2.5) in the kerbline, as of 24th May 2014. The displacements are consistently observed in each of the four kerblines of the dual-carriageway and are coincident with the exposed fault in the road cutting. They are also along strike from a topographic scarp of probable Holocene age (§2.5.2).

Splay fault

Postseismic slip on a southern fault strand, within the northern suburbs of Van city, was imaged using the TSX1 interferogram by *Doğan et al.* (2014) and *Wang et al.* (2015). Reprocessing this interferogram with minimal downsampling (below) enabled us to show that this displacement occurred within a zone no more than ∼200 m wide, which we targeted for field investigation. Using the approximate location derived from InSAR we examined optical imagery and topographic datasets. The Shuttle Radar Topography Mission (SRTM) and the Global Digital Elevation Model (GDEM) datasets both show a low south-facing scarp running E-W through the Altintepe and Iskele districts on the northern edge of Van (Figure 2.4), roughly paralleling the train tracks and reaching the coast at the port.

We use declassified Corona reconnaissance imagery from one of the Key Hole satellite missions (KH-4B, data available from the U.S. Geological Survey, nadir ground resolution of 1.8 m) to view the region prior to the northward urban expansion of Van. Figure 2.6 shows the Corona scene from 20 July 1970, on which we identify the faint trace of a scarp from minor stream incision and shadowing on its uplifted northern side. By comparing the historical imagery to the modern WorldView-2 imagery (0.5 m), we identified several sites for field study where the fault cuts modern roads and buildings. From inspection of high-resolution optical imagery on the Google Earth historical archive, we can see that the majority of the roads in a narrow band along the scarp (coincident with the postseismic deformation imaged with InSAR) were re-surfaced approximately 1–2 yr after the earthquake. Most of the current road surfaces are therefore not an appropriate record of the total postseismic deformation. Though the reason for resurfacing is not clear, it is likely that the roads were re-surfaced due to damaged tarmac as a result of postseismic motion. The only exception is the main road leaving Van to the north, which does not appear to have been resurfaced (24 May 2014), but showed signs of needing repair from cracking in the tarmac (Figure 2.7d, location in Figure 2.6).

In order to measure the total discrete postseismic surface slip, we primarily focussed our field investigation on the kerblines, walls, and buildings. Examples of deformed kerbstones and walls are shown in Figure 2.7. Verbal reports from local residents suggest that the wall in Figure 2.7a (location in Figure 2.6), which was built in 1993, was intact immediately after the earthquake, and that the visible extensional cracks have occurred between 2011 and 2014, i.e. postseismically. The cracking in this wall is consistent with uplift on the northern block. In contrast to the surface displacements on the main Van fault, we find no clear evidence for lateral displacements on this fault. The damaged walls and buildings

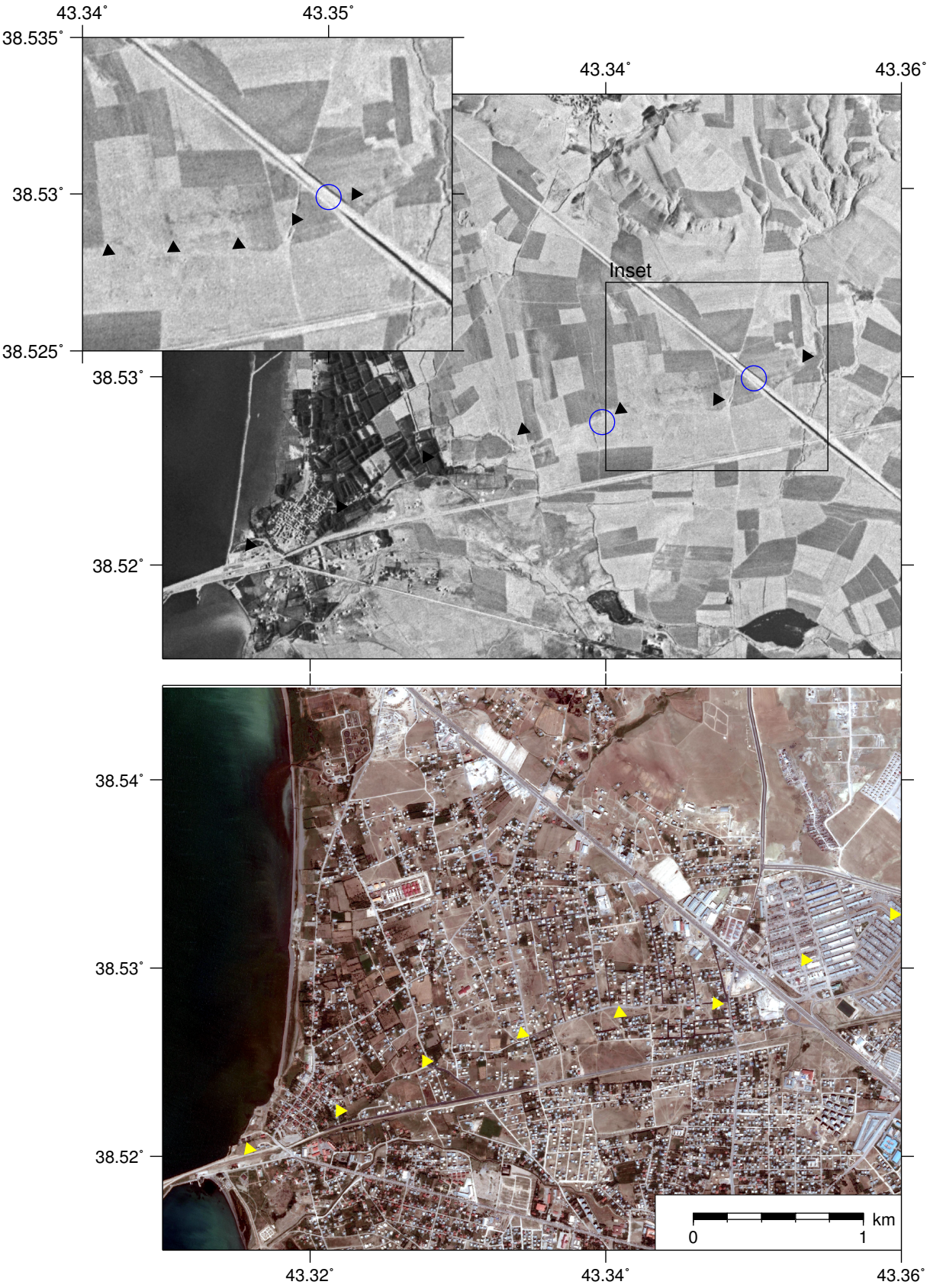


Figure 2.6: *(top)* Declassified satellite photograph from the Corona mission, 20 July 1970, prior to much of the urban sprawl of Van. Circles show the field sites shown in photos in Figure 2.7. Black triangles denote the trace of the fault scarp on the Bostaniçi Fault. *(bottom)* Modern satellite image (Google Earth, Imagery from CNES/Astrium, Image date:19/07/2013) showing the same region, with much of the morphology covered by urban dwellings. Yellow triangles denote the same trace.

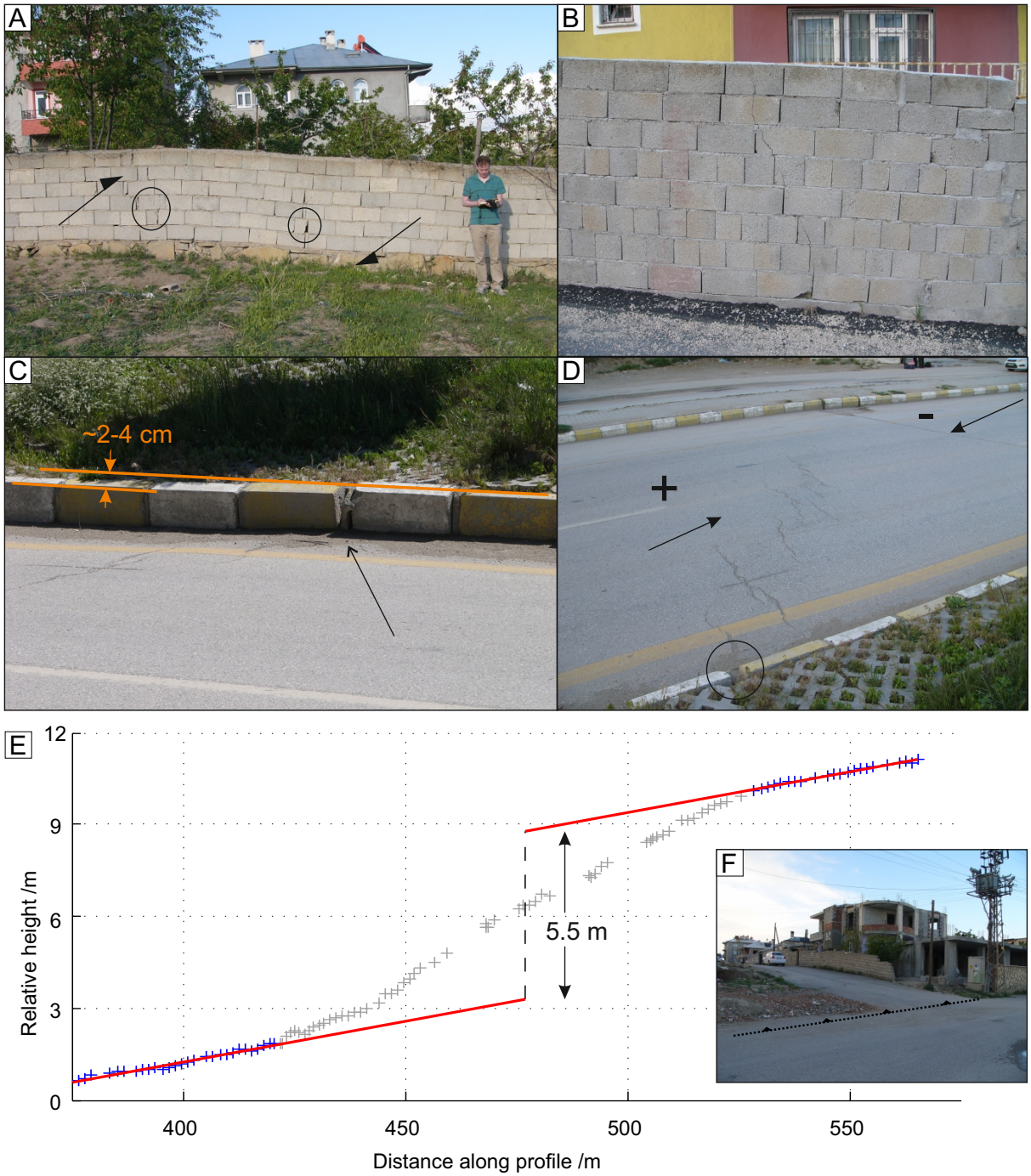


Figure 2.7: *(a)* Photo of a wall distorted by a few centimetres through postseismic motion on the splay fault. The wall was constructed in 1993, but was undisturbed immediately following the earthquake. A tension gap and a cracked block are circled. Person for scale. Arrows indicate the sense of displacement of the wall. View east, location: 38.5283°N 43.3472°E. *(b)* A second wall featuring cracks likely caused by the same postseismic motion. The obvious crack has split individual blocks, but a second crack on the right has been repaired too. The orientation of these cracks is consistent with uplift on the north (left). View east, location: 38.5279°N 43.3438°E. *(c)* Curb stones on the central reservation are displaced vertically, and gaps have developed between stones. The vertical displacement is ∼2–4 cm. *(d)* Distorted tarmac on the Van–Erciş highway. Note that the displacement here has likely been exaggerated by the action of vehicles travelling over the displaced tarmac. Location (c-d): 38.5295°N 43.3501°E. *(e)* Kinematic DGPS profiles across the scarp reveal a throw of ∼5.5±0.5 m, Location: 38.5278°N 43.3460°E. Points in grey were excluded from line fitting. *(f)* A view of a tarmac road ascending the scarp on the splay fault. On top of the scarp is a new building being rebuilt following the earthquake. Location: 38.5276°N 43.3397°E.

are superimposed on the pre-existing scarp shown in Figure 2.7f. Using kinematic DGPS, we measured the total vertical offset across the scarp to be ∼5.5±0.5 m.

The kerbstones of both carriageways of the main road leaving Van to the north showed clear displacements with the north side uplifted where they cross the splay fault, and the tarmacked surfaces are distorted (see Figure 2.7c,d). The road does not appear to have been resurfaced post-earthquake and the deformation of the tarmac road surface is coincident with the displacement gradient imaged in the post earthquake InSAR. Despite not being resurfaced, we suspect that deformation of the tarmac will still have been modified by the impact of vehicles driving over it in the intervening years. However, the kerbstones also appear not to have been replaced since the earthquake, and so are more likely to reliably represent the total postseismic motion on the splay fault since the earthquake. We constructed a digital surface model of the road section around the kerb offsets, using structure-from-motion (SfM, see §2.3.1) with a hand held compact camera. The resulting 3D model was scaled from tape-measure length measurements of two sets of six kerbstones, agreeing to within 1%. From the scaled surface model we measured 2–4 cm of discrete vertical displacement and negligible lateral displacement.

2.4.2 Postseismic InSAR

In order to place firm constraints on the timing, spatial variability and magnitude of postseismic slip, we re-processed the postseismic interferograms CSK3, TSX1, TSX2 and TSX3 (first 3 months after the earthquake, described in Table 2.2). The InSAR data were processed using the ROI_PAC software (*Rosen et al.*, 2004), multilooked to four looks in range and azimuth (5 m final pixel size), with branch cut unwrapping. We use minimal down-sampling in order to constrain the location of the splay fault for field study. Further InSAR data from the TerraSAR-X mission were available, with regular acquisitions through to the end of January 2012 (through the Supersites webpage http://supersites.earthobservations.org/van.php), but these interferograms generally showed very poor coherence – most likely due to winter snow cover, confirmed by inspection of the Landsat ETM+ archive. The four interferograms processed show good coherence near the shores of Lake Van, but poor coherence to the east in the areas of higher topography due to topographic decorrelation and localised snow cover.

Figure 2.8 shows the wrapped and unwrapped interferograms, in which we observe significant deformation following the earthquake, localised on two different faults: the Van fault, and the Bostaniçi splay in the northern suburbs of Van. The faults are identified by high phase gradients and phase discontinuities that correlate well from scene to scene and map closely to the observed surface displacements. Note that both the large aftershocks mentioned in §2.2.3 are captured by these interferograms. The M_W 5.9 aftershock 10 hrs after the mainshock is within the CSK3 scene and is likely responsible for the enhanced uplift at the eastern end of the Van Fault (*Elliott et al.*, 2013). The second aftershock, M_W 5.7 on 9th November 2011, is captured by both TSX1 (ascending) and TSX2 (descending), and is visible as a series

Interferogram	**Orbit**	**Date 1** yyyy-mm-dd	**Date 2** yyyy-mm-dd	**Perpendicular Baseline** (m)	**Incidence Angle** (°)	**Postseismic period** (Days)
CSK1	dsc	2011-10-10	2011-10-23	194	28	0–0.167
CSK2	dsc	2011-10-10	2011-10-26	115	28	0–3
CSK3	dsc	2011-10-23	2011-10-26	309	28	0.167–3
TSX1	asc	2011-10-31	2011-11-11	194	33	8–19
TSX2	dsc	2011-11-09	2011-11-20	14	26	17–28
TSX3	dsc	2011-12-01	2012-01-03	29	26	39–72
ASAR1	dsc	2010-11-05	2011-10-31	138	41	0–8
ASAR2	dsc	2011-07-22	2011-11-19	221	41	0–27

Table 2.2: Acquisition dates of the various interferogram pairs discussed in the text. CSK – COSMO-Skymed, TSX – TerraSAR-X, ASAR – Envisat (the latter in the period after loss of orbit stability). Asc refers to ascending tracks, while dsc refers to descending tracks. The perpendicular baseline is the average between that at the top and bottom of the scene.

of concentric fringes in the wrapped image of TSX2 (Figure 2.8).

To study the spatial and temporal variability of the uplift associated with the fault motion, we take three fault perpendicular profiles (swath width 1.5 km) through the interferograms, A–C (Figure 2.9). The CSK3 interferogram (0–3 days) shows a line-of-sight (LOS) displacement signal associated with the Van Fault across all three profiles, with a wavelength of ∼6–7 km, a magnitude of ∼3 cm and a discontinuity at the mapped fault trace (2–3 cm in LOS). There is little motion on the Bostaniçi splay fault in this interval.

The TSX1 ascending pass interferogram shows a small discontinuity of ∼1 cm at the Van Fault and a larger step of 2–3 cm at the splay fault, with a broad signal of ∼4 cm LOS displacement over a wavelength of 6–8 km north from the splay fault, associated with postseismic displacement on the splay fault. Though this interferogram spans the 9th November aftershock, there is no evidence of displacement in this line of sight. The TSX2 descending pass interferogram shows a LOS displacement towards the satellite at the southern end of the profiles B,C, due to the 9th November aftershock, masking the effect of the splay fault. Superimposed on the aftershock deformation, we also see small discontinuities at both the Van Fault and the Bostaniçi Fault (∼1 cm). At both faults, all four interferograms show LOS displacement towards the satellite on the north block and away from the satellite on the south block, consistent with thrust or oblique left lateral fault slip.

The 9th November aftershock signal shows displacements of up to 4–5 cm LOS displacement in TSX2, but almost none in TSX1, both of which span the earthquake. However, the USGS bodywave mechanism for the aftershock has a strike-slip mechanism with a small oblique component, on an approximately E–W or N–S striking fault plane. A simple elastic half-space model (*Okada*, 1992), resolved into the look direction shows that for the north dipping, right lateral slip fault plane, the expected surface deformation pattern matches closely that observed, with very little motion in LOS for the TSX1 look direction, but significant motion in the TSX2 line of sight. Thus it is likely that the M_W 5.7 on 9th November occurred on a north dipping fault plane off the shore of Lake Van near the town of Edremit, though the fringes we observe suggest a location closer to Van city than the published seismological locations from the USGS

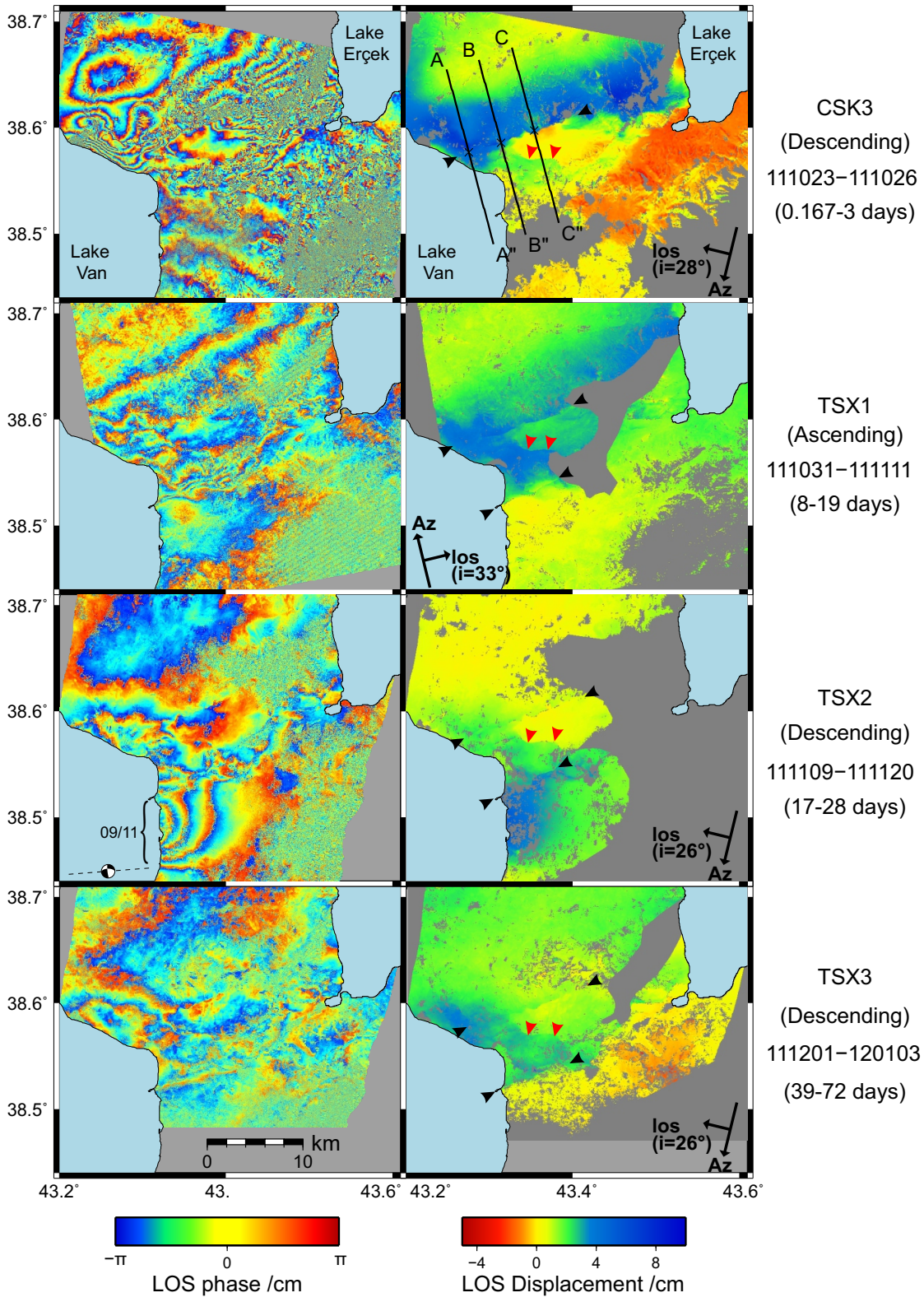


Figure 2.8: Series of COSMO-Skymed and TerraSAR-X interferograms for the period up to 2.5 months after the mainshock, in temporal order top to bottom (outline shown in Figure 2.3). Both the wrapped phase (left) and unwrapped interferogram (right) are shown – unwrapped LOS displacement is positive towards the satellite. We see clearly delineated both the Van and Bostaniçi faults (black arrows), along with a small backthrust (red arrows). There is a general uplift signal across the 5-8 km region associated with topography, with discontinuities at both faults. The locations of the profiles A-C of Figure 2.9 are shown on the top right. The two middle interferograms (TSX1 and TSX2) also capture the edge of the displacement field for the 9th November 2011 M_W5.9 aftershock near the edge of Lake Van (as identified by *Doğan et al.* (2014)).

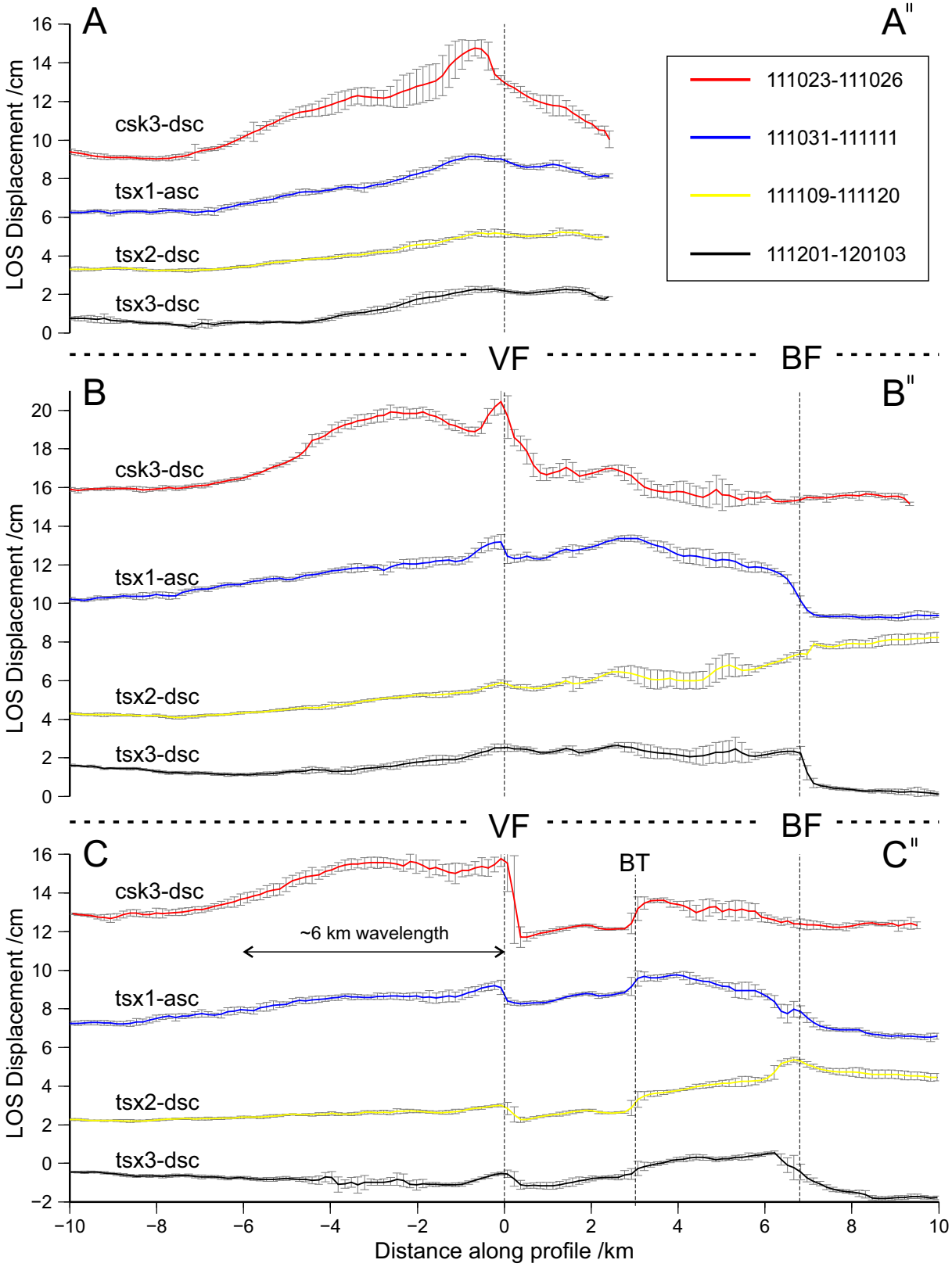


Figure 2.9: Profiles across the Van and Bostaniçi faults through the postseismic interferograms in Figure 2.8. LOS displacement is positive towards the satellite. Error bars represent the one sigma standard deviation in values of the points across the 1.5 km swath width of each profile, with the data binned in 100 m increments along profile. Note, a constant offset has been applied to each profile for clarity. Labels: VF – Van Fault, BF – Bostaniçi Fault, BT – Backthrust.

and *Irmak et al.* (2012). This is consistent with the model of *Wang et al.* (2015) based on the TSX1 and ASAR2 interferograms.

Another common feature of all the interferograms is a small discontinuity between the Van fault and the Bostaniçi splay fault in profile C–C", south side uplifted. This feature appears in both the wrapped and unwrapped interferograms (Figs. 2.8–2.9), so we suggest that it is a small backthrust accommodating the transfer of motion between the two faults. There is no geomorphic signature associated with this structure however, so we expect it to be a minor feature.

In summary, the sequence of interferograms show early shallow slip on the upper section of the Van fault resulting in uplift over a wavelength of ∼6–7 km that is well correlated with the hangingwall topography, but decays very rapidly over the days to weeks after the mainshock. This is followed by an aftershock under the easternmost edge of Lake Van, for which the interferograms show motion consistent with right-lateral strike-slip/oblique faulting on an offshore fault near Edremit, striking E-W and dipping to the north. Either shortly before or following this aftershock, we observe creep on the Bostaniçi fault. Superimposed is the continued creep on the Van fault at shallow depths (1–2 km). The final interferogram shows that both faults were still moving aseismically at least until the start of December (+39 days), though more slowly than in early interferograms (∼1 cm over the 1 month period). The signal associated with the Van fault has a wavelength of only ∼1 km, so only very shallow motion remained in this period, whereas the signal associated with the Bostaniçi has a wavelength of ∼6 km suggesting deeper slip was still continuing over the final period. Both faults show a slightly longer wavelength signal in the west suggesting that deeper slip was occurring there in all four interferograms.

Akinci and Antonioli (2013), *Moro et al.* (2014) and *Wang et al.* (2015) estimated the Coulomb stress changes on the fault planes of the 9th November M_W 5.7 aftershock predicted by the centroid moment tensor solutions; they suggest that the aftershock fault may have been brought closer to failure by the mainshock as the transferred stress values generally exceeded 1 bar for both possible fault planes. The fringes associated with this aftershock in TSX2 suggest a centroid location significantly north and east of the USGS location. This suggests that the stress transfer values of *Moro et al.* (2014) and *Akinci and Antonioli* (2013) are likely to be underestimated, making it even more likely that the aftershock was triggered by stress transfer following the mainshock.

2.4.3 Postseismic slip: summary

Projecting the field measurements into satellite line-of-sight (LOS), the offset at the Van-Erciş highway is equivalent to 14 cm towards the satellite for the descending pass interferograms (CSK3, TSX2, TSX3) and 4 cm away from the satellite for the ascending pass (TSX1). However, TSX1 displays motion towards the satellite in the hangingwall, suggesting that the large lateral offset may partly be a local site effect. This echoes the findings of *Elliott et al.* (2013) and *Emre et al.* (2011) who noted that the strike-

slip:dip-slip ratio at the highway was much larger than was seen at most other locations. The descending interferograms are less sensitive to the lateral component, so we can still compare the observed thrust offset to the InSAR data. The CSK3 interferogram for the period of 4 hrs – 3 days after the mainshock shows an offset of ∼4 cm at the highway, almost a third of the total measured in 2014, while the later interferograms show decreasing offsets of 2–0.5 cm over longer temporal baselines (finally, 0.5 cm over the period 39–72 days), suggesting that the aseismic slip-rate at the surface decayed very rapidly over at most the first 8 days.

At the Bostaniçi fault, projecting the field measurements into radar LOS, we expect displacements of at most ∼5 cm, which is less that the cumulative displacement measured in the interferograms (which do not cover the full time period). This is most likely because the surface displacement is more diffuse on this fault, with only a proportion localised at the pre-existing scarp – the InSAR profiles are generally smoother across this fault, with a length scale of 100–200 m.

2.5 Geological Slip Rate

2.5.1 Overview

The postseismic surface breaks on the main Van fault and the Bostaniçi fault were superimposed on pre-existing fault scarps. The surface trace of the Van fault bounds the southern margin of a range of east–west striking hills with a steepened southern slope, rising up to ∼900 m above the level of Lake Van (Figure 2.4). The relief is highest in the east, tapering down to the lake level in the west. These hills form an anticline in the hangingwall of the fault, with a wavelength of ∼7.5 km (further discussion in §2.6.1). Many sections of the Late Quaternary fault scarp have been strongly altered by human influence, but we identify several points where clear Quaternary scarps are visible, with heights of ∼3–20 m. Both the fault and the range it bounds are characterised by two distinct geomorphic segments, an eastern and a western segment (Figure 2.10).

The eastern segment of the Van fault extends from ∼43.44°E to Lake Erçek, though lack of surface observations in the lake make it difficult to determine how far under the lake the fault extends and the rupture continued. This segment is characterised by a continuous scarp of typically ∼30–50 m, consisting of an uplifted bedrock terrace (Figure 2.10d). The fault trace is shown in Figure 2.10a – there is a clear change from incision to deposition in crossing from the hangingwall to the footwall, but no coseismic surface displacements were observed in this section. During our brief field survey we did not find any Quaternary sediments on the terrace surface suitable for determining a slip-rate, but the well preserved, extensive and large scarp suggests it is likely that the fault extends to the surface in this segment. The relief associated with this section of the fault rises to ∼900 m above the level of Lake Van, and is flanked by Pliocene sediments on the backlimb of the fold in several locations (see §2.6.1).

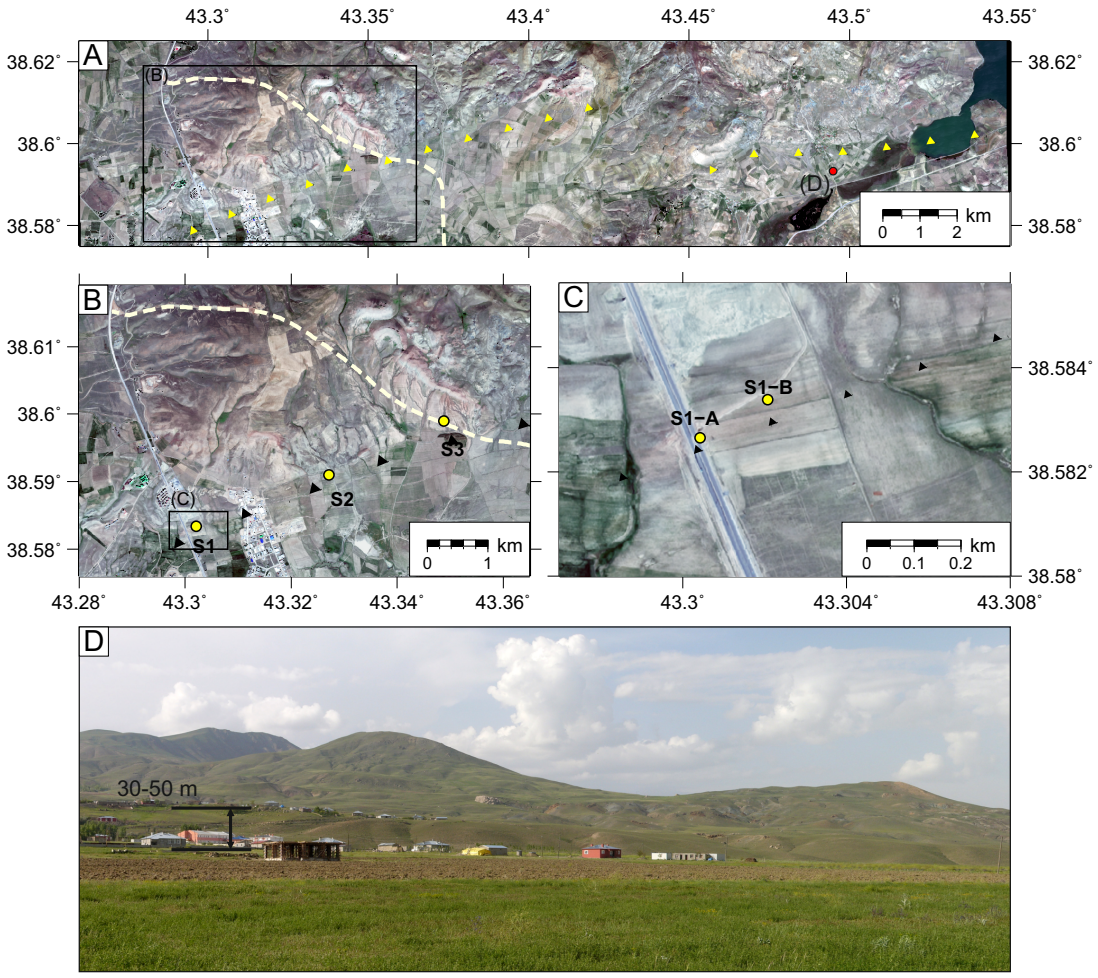


Figure 2.10: WorldView-2 Multispectral RGB true colour 0.5 m pansharpened imagery of the Van fault (May-June 2011). (a) An overview of the Van fault showing both the eastern and western segments, denoted by yellow arrows. In the east, the scarps are primarily bedrock, but in the west they cut Quaternary sediments. (b) The western section of the scarp, with the three field sites discussed in §2.5.2–2.5.2 shown in yellow, and the new highway, which provides the cutting for sampling at S3, shown as a dashed line. (c) Close up of the site S1, divided into two, S1-A - the road cutting in which we see a fault exposure and displaced pavements (Figure 2.5), S1-B a shallow scarp of 2.7±0.3 m in Quaternary deposits (Figure 2.11). (d) Photograph of the ∼30–50 m bedrock scarp of the eastern segment of the Van Fault, near lake Erçek. Photo looking North, location: 38.5948° N, 43.4943° E

The western segment of the Van fault extends from the shore of Lake Van to ∼43.44° E (Figure 2.10). It is unclear whether the fault continues under the lake, though the decrease of the hangingwall relief suggests that the fault ends near the edge of the lake. This asymmetry is not seen in the coseismic displacement field, suggesting that the fault may be growing westwards. This western section of the fault has cut through a series of the Quaternary alluvial and lake deposits, forming a semi-continuous rangefront scarp. The scarps are developed primarily in volcanoclastic alluvial deposits and lacustrine deposits. They have generally been modified by agriculture, but we found a number of sites where the scarps are well-preserved. The three sites (S1, S2 and S3) that we selected for slip-rate measurements, where we see scarps of ∼3 m, ∼5 m and ∼18 m respectively, are shown in Figure 2.10. We use a combination of optically stimulated luminescence (OSL) dating and radiocarbon dating to estimate the deposition age of two surfaces at sites S2 and S3. We use kinematic DGPS and structure-from-motion to

generate digital elevation models of the scarp in two separate locations, and DGPS profiles in a third, to estimate fault throw at the surface.

2.5.2 Slip-rate measurements

Site S1

The Van fault continues eastwards along strike of the deformation of the Van–Erciş highway (described in §2.4.1) as a low scarp tracking across agricultural fields (Figure 2.11a). Despite significant ploughing having occurred, the scarp is clearly visible in the Late Quaternary volcanoclastic alluvial sands and gravels with a 10–20 cm soil developed at the surface. DGPS profiles across the scarp show 2.7±0.3 m of vertical throw (Figure 2.11b). Quartz optically stimulated luminescence (OSL) samples collected from a pit in the upthrown side of the scarp have unfortunately not been possible to date due to the insensitivity of the quartz. It is however still clear that at site S1 significant Late Quaternary fault slip has reached the surface to generate the scarp.

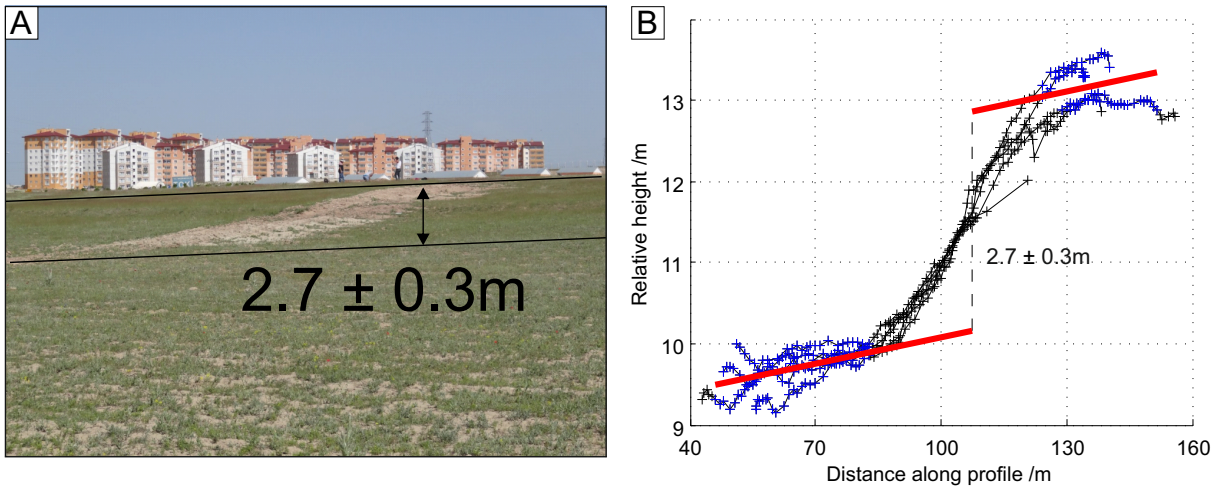


Figure 2.11: *(a)* At site S1b, near the main road we observe a 2.7 m scarp in Quaternary material. Immediately behind the scarp, new apartment blocks have been constructed on the hanging wall of the fault, built after the earthquake to replace some of the damaged building stock. Photo looking NW from 38.5826°N, 43.3029°E. *(b)* Four stacked kinematic DGPS profile across the scarp at S1, showing an offset of 2.7±0.3 m Points in black were excluded from line fitting.

Site S2

Immediately east of site S1, the land has been heavily modified by building, but ∼2 km further east, at site S2 (Figure 2.10), we found further scarps in similar materials (Figure 2.12a). We use SfM (see §2.3.1) to quantitatively assess topography of this site, using photographs from a digital camera mounted on a 6 m-pole, to create a DEM of a 200 m stretch of the scarp (Figure 2.12c,d). Fitting parallel planar surfaces to the pointcloud above and below the scarp, we measure a vertical offset of 4.7±0.3 m on this section of the scarp (Figure 2.12e).

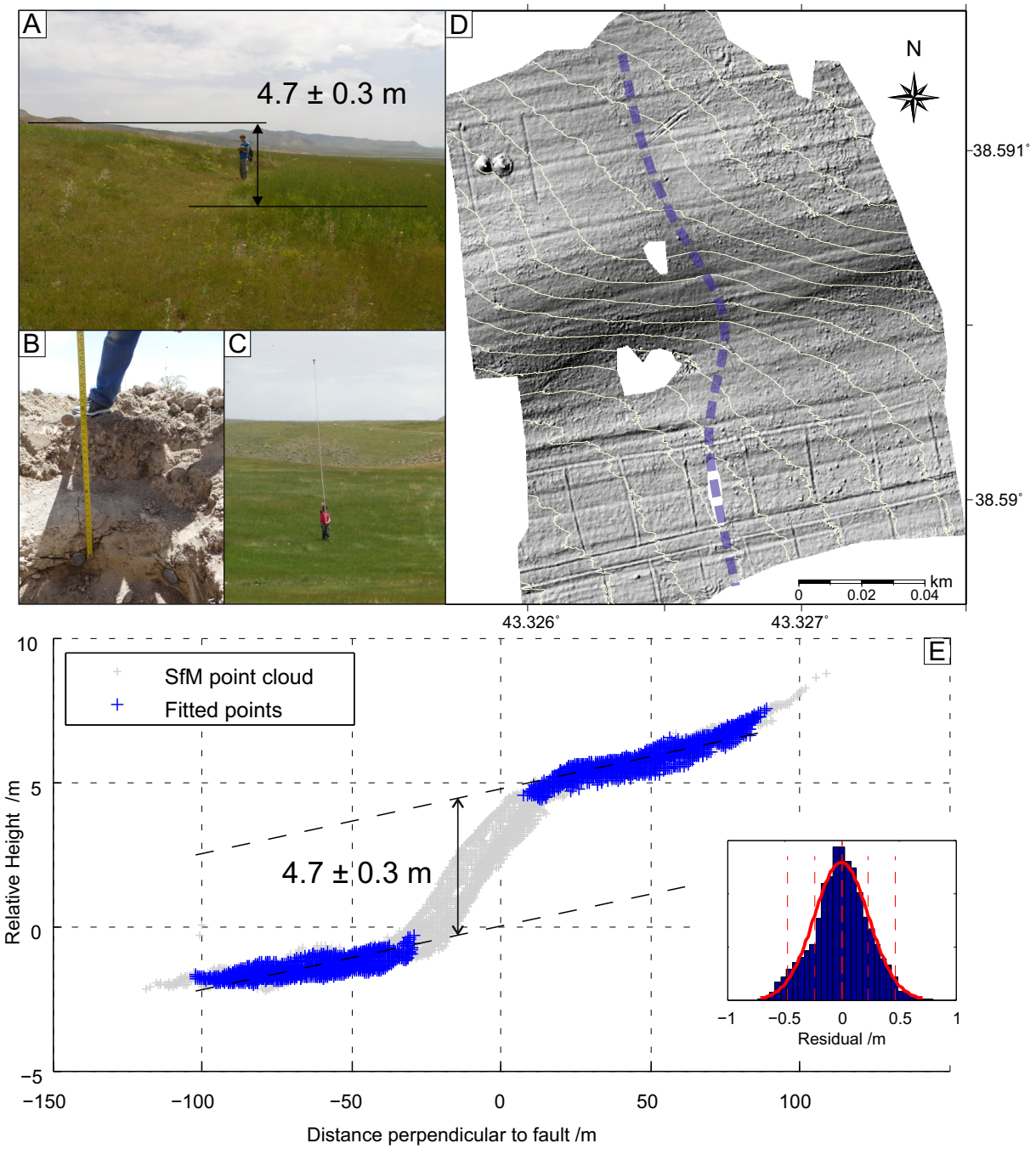


Figure 2.12: *(a)* Scarp visible at Site S2 running through agricultural fields, person for scale. Photo taken looking E at 38.5909°N, 43.3282°E. *(b)* Sample pit at S2 in the hanging wall, two OSL samples (OSL5 and OSL6, Table 2.3) collected from a depth of 58 cm. *(c)* Compact digital camera mounted on a 6 m pole to collect photographs for structure from motion. *(d)* Shaded relief DEM of a 200 m stretch of the scarp at the S2 site, overlaid with 1 m contours, generated from ∼1100 photos by SfM. The horizontal banding in the image represents the individual plough furrows and irrigation channels of the agricultural field. Three small patches with poor photograph coverage have been masked out. The small channel (dashed blue line) running through the middle of the scarp has also been masked out for the purpose of measuring an offset. *(e)* The fault throw here was measured by fitting parallel planes in the hangingwall and footwall and measuring the vertical offset between them. This plot shows the points projected along the plane into a fault perpendicular profile. The inset shows the residuals to fitting the planes, compared to a gaussian of the same mean and standard deviation. We find rms misfits of 0.22 m and 0.25 m for the footwall and hangingwall respectively, giving an uplift of 4.7±0.3 m. Points in grey were excluded from plane fitting.

Name	Sample	Site	Site offset /m	Offset Error /m	Age B.P. /ka	Age error /ka
OSL3	X6333	S1	2.7	0.3	fail	-
OSL4	X6334	S1	2.7	0.3	fail	-
OSL5	X6335	S2	4.8	0.5	9.2	2.6
OSL6	X6336	S2	4.8	0.5	8.9	2.6
OSL1	X6331	S3	18	1	7.2	2.3
OSL2	X6332	S3	18	1	7.0	1.5
OSL7	X6337	S3	18	1	11.1	4.0

Table 2.3: Table of Optically stimulated luminescence (OSL) dates. The vertical throw for each site (locations in Figure 2.10) is also shown. Quoted errors are 1-σ uncertainties.

Sample	Conventional Age /ka	1-σ Error /ka	$\delta^{13}C$ $^{0}/_{00}$	Calibrated Age B.P. 95% Confidence Interval /ka
Shell_A	37780	280	1.5	41684–42519
Shell_B	39990	460	0.4	42888–44521
Shell_C	42710	620	-0.1	44892–47395

Table 2.4: Radiocarbon ages for the three gastropod shell samples collected from site S3 (Figure 2.10b). Ages calibrated using the IntCal13 atmospheric curve (*Reimer*, 2013).

We collected two OSL samples from the upthrown side of the scarp to date the deposit (OSL5 and OSL6 in Table 2.3, Figure 2.12b, OSL measurement protocol described in Appendix A.1). These two samples give close agreement at 9.0±2.7 ka for the age of the offset surface. However, as we discuss in §2.5.2, the quartz OSL in the region is generally dim for all samples and does not agree well with radiocarbon dating at site S3, so we are cautious in our interpretation of these dates.

Site S3

Site S3 is situated 2 km east of S2 (Figure 2.10a). Here the fault is expressed as a much larger cumulative scarp within a series of alluvial fans, as shown in Figure 2.13a. A vertical throw of 18±1 m was measured at this site from multiple DGPS profiles (Figure 2.13b). Our measurement of vertical displacement neglects footwall sedimentation since surface abandonment, so the offset measurement here is considered a minimum fault throw since the abandonment of the upthrown surface.

The hangingwall deposits again consist of volcanoclastic alluvial sands and gravels which are well exposed in a new road cutting (Figure 2.13b). Most of the deposits are composed of well-rounded clasts up to ∼10 cm, consistent with a high-energy alluvial setting. However, we also found a few localised deposits consisting of fine-grained sand and silt. The fine-grained deposits were laminated in places, and contained abundant freshwater gastropod shells. These fine units were interbedded within the gravel deposits and, due to their restricted extent, we interpret them to have formed as small ponds perched on the aggrading alluvial fan surface.

We collected three OSL samples (OSL1, OSL2, OSL7 in Table 2.3) and several gastropod shells for radiocarbon dating (Table 2.4) from the fine-grained units. The sampled gastropod shells were found in

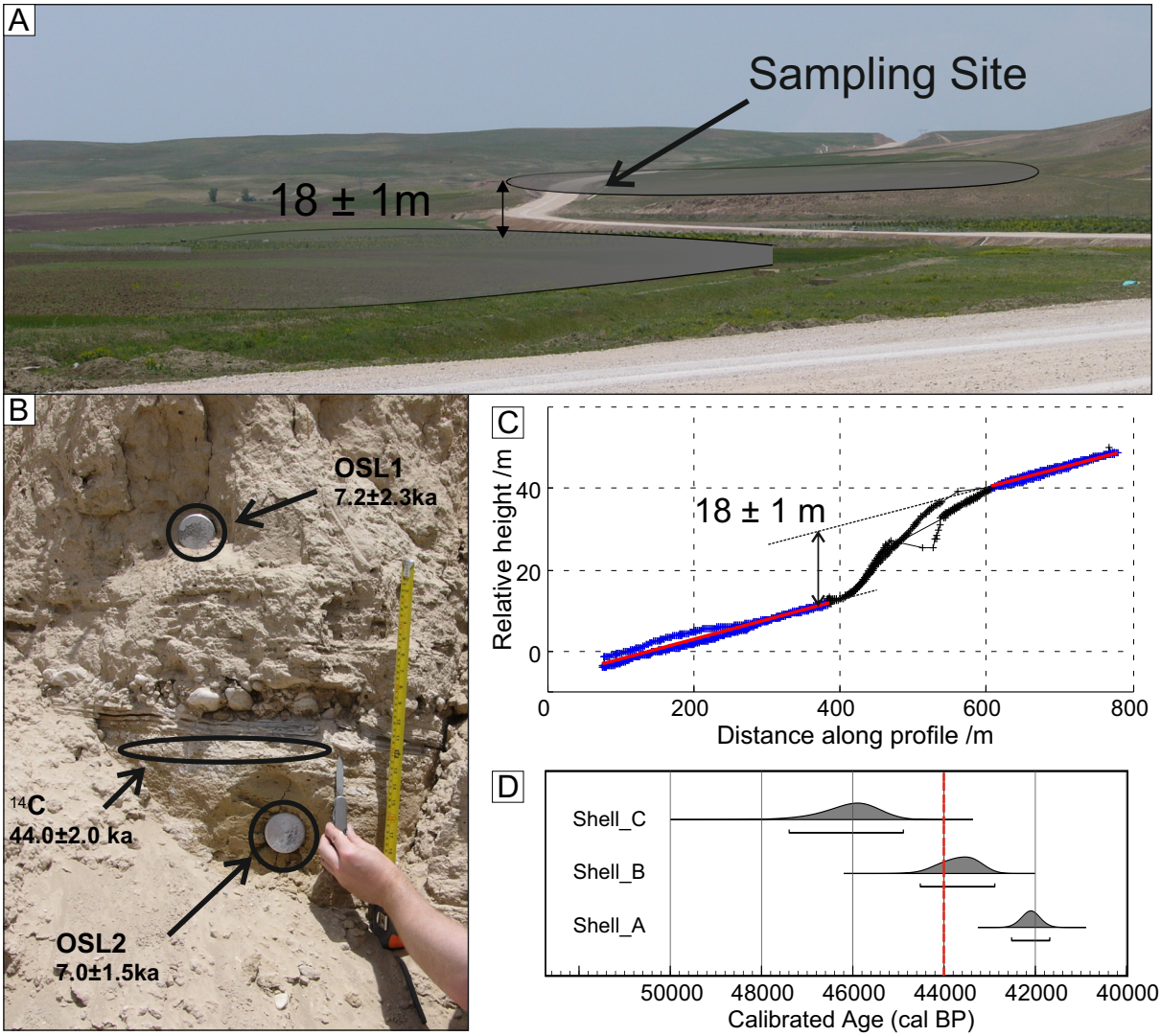


Figure 2.13: (a) Larger scarp at site S3, with a minimum throw of ∼18 m. This location provides the main basis for our preliminary slip-rate. Photo taken looking NW from 38.5874°N, 43.3732°E. (b) Setting of the two OSL samples and gastropod shells (^{14}C) found at site S3. The two OSL samples are from fine grained silt beds above and below that containing the gastropod shells. Note the presence of the occasional gravel layer interspersed, suggesting the presence of occasional higher energy flows. The gastropod shells (including Shells A–C listed in Table 2.4) are found in abundance in a sandy layer beneath silt and gravel beds. The abundance of shells suggests that are unlikely to have been redeposited. (c) Three stacked DGPS profiles used to estimate the minimum offset on this surface. Points in black were excluded from line fitting. (d) Radiocarbon ages for three shells from the same horizon at site S3. Dates are presented using the OxCal program V4.2 (*Bronk Ramsey*, 2009), and calibrated using the IntCal13 atmospheric curve (*Reimer*, 2013). Dashed line represents the unweighted mean age.

a single continuous layer in an undisturbed stratigraphic sequence, suggesting they were living in place prior to an extinction event – it is unlikely that they were transported there after death of the organisms. The shells yield a mean calibrated radiocarbon age of 44.0±2.0 ka (Shell_A, Shell_B and Shell_C in Table 2.4). Each sample represents an individual shell and the individual probability density functions based on the IntCal13 calibration (*Reimer*, 2013) are shown in Figure 2.13d. The OSL samples give ages of ∼7.0, 7.2 and 11.1 ka (Figure 2.13), which are much younger than the radiocarbon ages obtained from the same outcrop. We attribute the mismatch to low sensitivity of the quartz to OSL (e.g. *Rhodes*, 2015). Low quartz sensitivities have been found in studies in nearby Iran, similarly resulting in anomalously

young burial ages (*Fattahi et al.*, 2007; *Walker and Fattahi*, 2011). The low quartz content also reduced measurement reliability due to a small quartz sample size.

Slip-rate estimates: Summary

Taking the mean radiocarbon age at Site S3 as a reasonable estimate of the age of the displaced surface we calculate a minimum throw rate of 0.4±0.1 mm/yr. Figure 2.14 shows a plot of offset against age for each of the samples at site S3, with a line indicating an uplift rate of 0.4 mm/yr, calculated based on the mean radiocarbon age at Site S3. The two OSL ages from site S2 (OSL 3 and 4) are consistent to within error of this line, suggesting that those two samples ages may be reliable, though as we have no independent age constraint on the sediments at site S2 we cannot confirm it.

We note that 0.4±0.1 mm/yr is a minimum bound on the throw rate, as the measured offset assumes no post-formation deposition in the footwall of the scarp, and we do not account for any folding or off-fault deformation occurring in the near-surface. Taking the fault dip of 45–50 degrees as estimated from the road cutting on the Van–Erciş highway (consistent with the InSAR solution, though this may differ from the shallow sub-surface dip), we find a minimum fault slip-rate of 0.5±0.2 mm/yr.

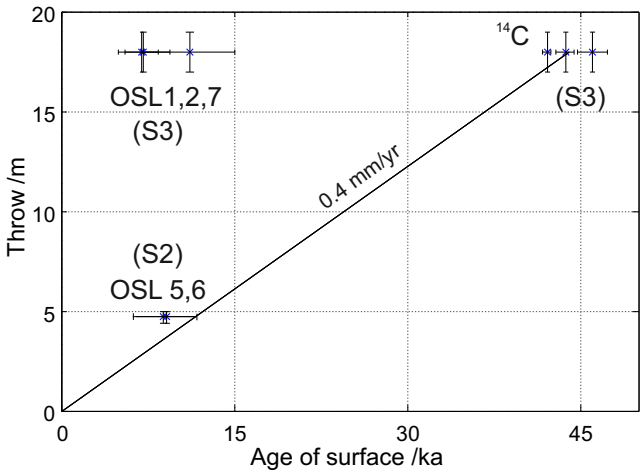


Figure 2.14: Vertical offset against age for each of the samples. Line represents an uplift rate of 0.4 mm/yr, based on the Site S3 ^{14}C sample only. Note that this line is consistent to within error of the OSL ages observed for site S2 (OSL 5,6).

2.6 Discussion

2.6.1 Fault geometry

The co-seismic geodetic models for the 2011 mainshock broadly agree, but there are a few key differences. The solution from *Elliott et al.* (2013), based on the earliest co-seismic pair (10/10/2011–23/10/2011, CSK1 in Table 2.2), shows no clear discontinuities at the surface and gives evidence for two fault segments, with only the lower sections (below 10 km) failing in the earthquake. The west/east segments strike approximately east-west and dip at 40°/55°, with top depths of 10/8 km and bottom depths of 19/17 km respectively. In their distributed slip model, they resolve a strong up-dip gradient in slip, suggesting an abrupt arrest at the upper limit of rupture at ∼10 km. The up-dip projections of the two fault segments are tied to the location of small ground displacements mapped in the field, so the geometry is not entirely free, though the authors note that their tied location gives a minimum misfit to the data. The coseismic model of *Wang et al.* (2015), combining all of the available geodetic data, finds a similar two-fault geometry, with two distinct patches of intense slip up to a maximum of ∼6.3 m.

Fielding et al. (2013), *Moro et al.* (2014) and *Feng et al.* (2014) instead prefer single fault models for simplicity and lacking primary surface ruptures to tie segments to. These models incorporate additional azimuthal displacements from multiple aperture interferometry (MAI) or amplitude image pixel correlation. They show slip and significant moment release is restricted to depths below ∼6–8 km, consistent with a high density of aftershocks at this depth due to a strong slip gradient. *Feng et al.* (2014) present the CSK1 coseismic interferogram, which includes only the first four hours of the postseismic period. In contrast, the CSK2 interferogram used by *Fielding et al.* (2013) and *Wang et al.* (2015) includes the three days following the mainshock, during which time a significant (M_W 5.9) aftershock occurred in the epicentral region and significant shallow postseismic slip occurred (§2.4). Thus, their coseismic models will contain a small amount of postseismic slip as well as the mainshock coseismic slip. We note that studies using the CSK2 interferogram consistently estimate a larger cosesimic moment release than those modelling the CSK1 interferogram (Table 2.1), likely due to the inclusion of a large fraction of the total postseismic motion.

Similarly, the seismological models broadly agree. Modelled source-time functions from low-frequency teleseismic data are generally triangular with a total length of 10–15 seconds, though the position of the peak varies between models (*Zahradnik and Sokos*, 2011; *Elliott et al.*, 2013; *Fielding et al.*, 2013). Using a higher frequency range with regional to near-regional stations and a multiple point source model, *Gallovic et al.* (2013) and *Zahradnik and Sokos* (2014) resolved a source-time function consisting of two distinct sub-events separated by 3–4 seconds, with locations corresponding well to the two fault segments resolved with InSAR by *Elliott et al.* (2013). Finite fault models by *Irmak et al.* (2012) and *Fielding et al.* (2013) show close agreement in the source time functions, with the majority of the moment released in a triangular source-time function spanning the first 10 seconds, and a subsidiary peak at around 14–

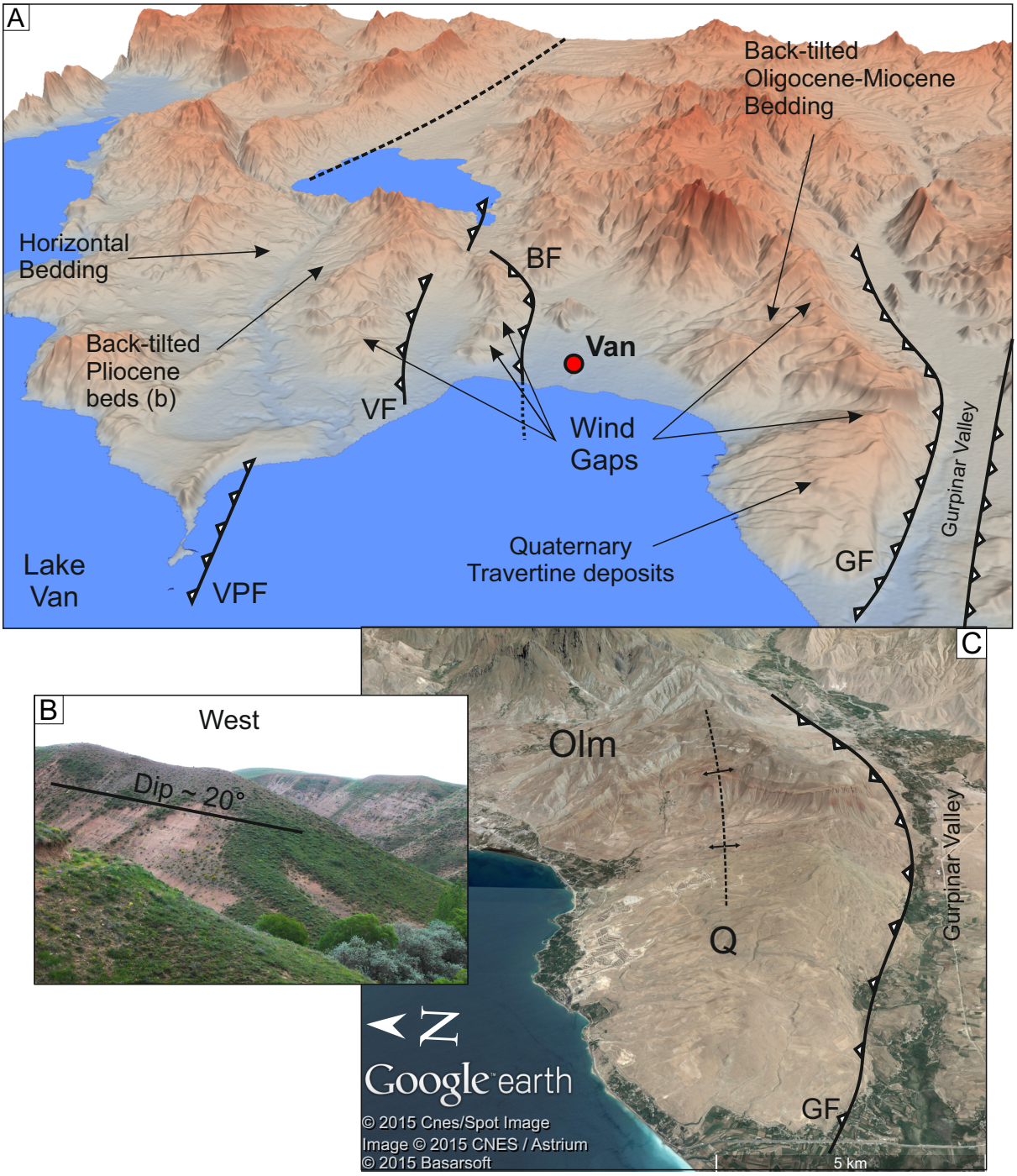


Figure 2.15: (a) 3D perspective view looking East along the Van fault and the Bostaniçi fault. Also marked are the Gürpınar (GF) and Peninsula (VPF) faults. Arrows indicate the location of several prominent windgaps in the ridges and folded sedimentary units. (b) Back tilted Pliocene beds near the village of Satıbey, dipping ∼20° N. Photo looking West, location: 38.6843° N, 43.4823° E. (c) Oblique view of the Quaternary travertines (labelled in (a)) and folded Oligocene-Miocene sediments in the hangingwall of the Gürpınar thrust.

15 seconds. Using backprojection of strong motion waveforms, *Evangelidis and Kao* (2013) image two distinct sources of high frequency radiation at depths of 10–12 km in locations corresponding well to the two fault segments, which are attributed to stopping phases or rupture propagating through geometric complexities (possibly linking between the two fault segments).

The seismological and geodetic models agree that coseismic slip does not extend to the surface, with

little significant moment release above depths of 7–10 km. In addition there is strong evidence for geometric complexity, with the two-fault models giving a good fit to the SAR data and two discrete pulses of slip observed in the source time functions and multiple-point source models.

Figure 2.15a shows an overview of the Van Fault and surrounding structures. From the large-scale topography it appears that the main Van Fault (VF) and the Bostaniçi Fault (BF) merge to form a single trace in the east, consistent with the model of *Wang et al.* (2015). In the west, the two faults are characterised by a footwall basin and a narrow range of hills in their immediate hangingwalls, which we attribute to folding of the hangingwall. In both ranges, we see a series of prominent windgaps likely resulting from earlier drainage across the folding axis. Approximately 7 km north of the Van fault, near the village of Satıbey, we observed back tilted Pliocene sedimentary units (*MTA*, 2002) dipping north at ∼20° (Figure 2.15b). However, ∼1 km further north across the valley, the same Pliocene sediments are horizontal. The wavelength of folding therefore stretches ∼7.5 km north from the fault, corresponding closely to the observed topography (Figure 2.16a,b).

The coseismic uplift associated with the 2011 earthquake was distributed over a wavelength of 20–25 km, much wider than the hanging-wall uplift preserved in the large-scale topography (Figure 2.16a). It is unlikely, therefore, that repeated earthquakes of the style of that in 2011 are responsible for generating the hangingwall topography. Discrete slip on the deeper section of the Van Fault in 2011 must give rise to a deficit of slip in the uppermost 8 km, and our observations of Quaternary scarps at the surface suggest that at least some of this motion is localised onto the two faults. By contrast the topography and wavelength of folding at the surface is closely correlated with the observed postseismic displacement (CSK3). This suggests therefore that displacement in the upper ∼8 km is responsible for the observed topography; a simple 2D elastic halfspace model (Figure 2.16a) gives a good fit to the CSK3 profile, with 8 cm of slip on a 55° dipping fault plane (0.6–7 km depth). It is likely, however, that some of this topography is due to fold growth, so a 2D elastic model may not be entirely appropriate. Indeed, scaling this model to the observed topographic relief gives net rotations of <1° near Satıbey, so to achieve the observed Pliocene bed rotations over the 7–8 km wavelength, significant anelastic off-fault deformation must also occur.

Figure 2.16c presents our schematic model of the Van Fault, which builds on a model produced by *Doğan et al.* (2014), in which we have brought together our observations from the co-seismic and post-seismic InSAR, field observations of surface faulting, and of long-term folding observed in the topography and bedrock geology. Our model is for a profile orthogonal to the western segment of the Van fault in order to compare results with our Late Quaternary slip rate (§2.5.2). The model consists of a ∼45° N-dipping reverse fault within the depth range of 8–25 km, which steepens at a depth of ∼7–8 km beneath the northern edge of the observed fault related topography. The steeply-dipping Van Fault reaches the surface at the observed Quaternary scarps and small postseismic surface displacements, while the splay follows a shallower dipping detachment to steepen under the northern edge of Van city, reaching

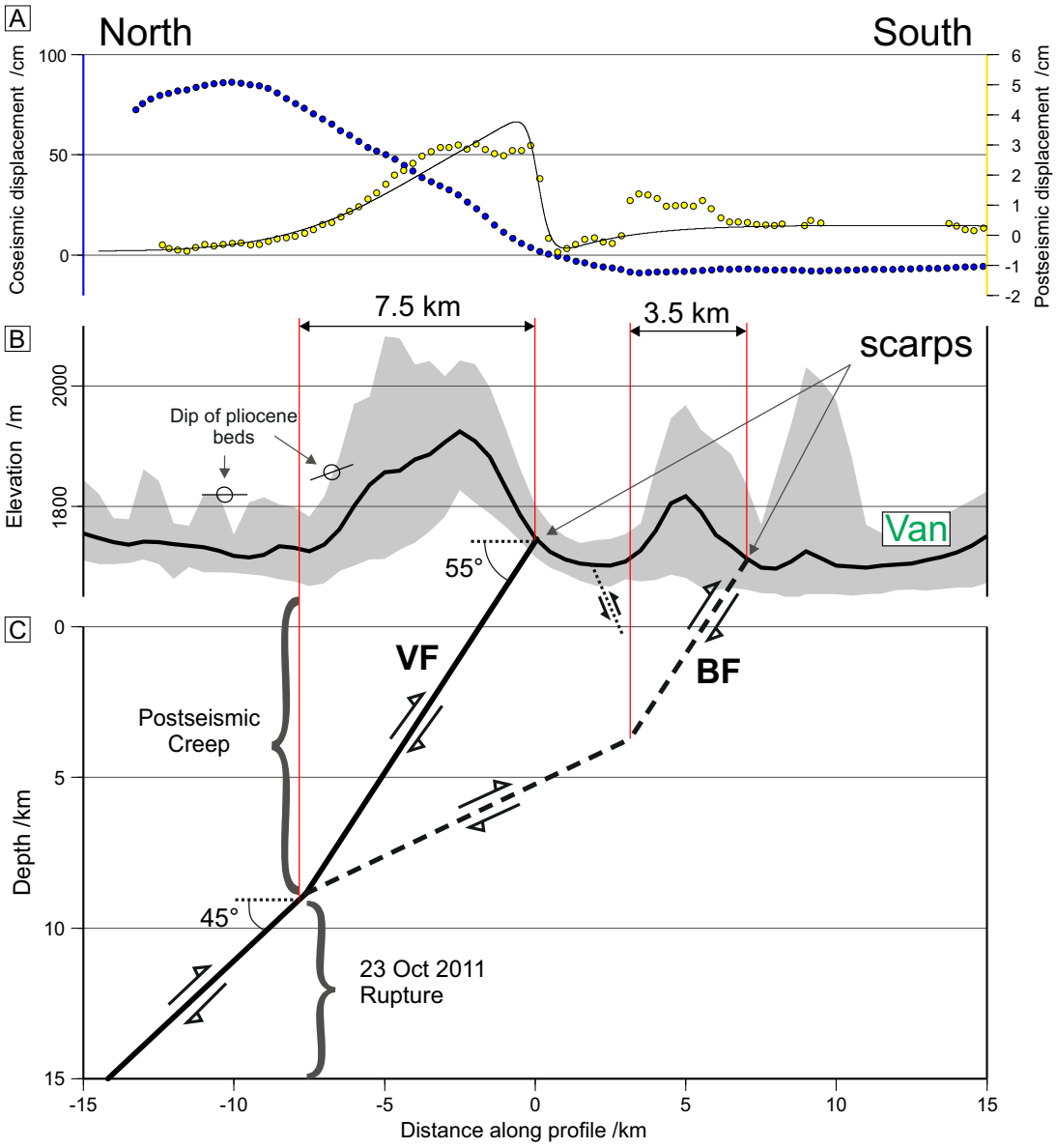


Figure 2.16: (a) Coseismic (blue, 10/10/2011–23/10/2011, CSK1) and early postseismic (yellow, 23/10/2011–26/10/2011, CSK3) line-of-sight displacement profiles. The thin black line shows a simple forward model for 8 cm slip on the uppermost 7 km of the fault, closely fitting the wavelength observed in the postseismic InSAR. (b) The same profile through SRTM topography, average elevation in black, with minimum/maximum bounds shaded grey. The locations of the tilted/undisturbed Pliocene units are also shown. (c) Structural cross-section based on the observed topographic wavelength associated with each fault north of Van. This transect is taken through the western segment of the fault where we observe two distinct faults, the Van Fault (VF) and the Bostaniçi Fault (BF).

the surface where we observe further postseismic displacements. We mark the splay fault dashed as, although it is likely to meet the main Van fault at depth, the precise depth at which it does is poorly constrained. The change in dip at depth on the Van fault (possibly the same depth at which the fault splays) may have provided a barrier to rupture propagation during the 2011 earthquake, consistent with the observations of *Doğan and Karakaş* (2013), *Elliott et al.* (2013), *Fielding et al.* (2013), *Feng et al.* (2014) and *Wang et al.* (2015) who all observed a strong slip gradient and rupture termination. This is also consistent with *Evangelidis and Kao* (2013) who imaged a high frequency (HF) source at this

depth and location which they relate to rupture termination or geometric complexity. A similar trend was observed in the location of the HF seismic radiation sources in the 2015 Gorkha Earthquake, Nepal (*Avouac et al.*, 2015); *Elliott et al.* (2016) show that the HF sources were co-located with a change in dip of the fault plane, though in that case, they were in the middle of the ruptured zone.

2.6.2 Postseismic Motion

Combining field observations with quantitative measurements from the postseismic InSAR interferograms, we have evidence of shallow, postseismic creep on both the Van fault and the Bostaniçi fault, consistent with previous estimates of postseismic motion imaged with GPS (*Altiner et al.*, 2013; *Doğan et al.*, 2014) and InSAR (*Elliott et al.*, 2013; *Fielding et al.*, 2013; *Feng et al.*, 2014; *Moro et al.*, 2014; *Wang et al.*, 2015). The mainshock occurred on the Van fault, which breaks the surface ∼8 km north of Van, but *Doğan et al.* (2014) and *Wang et al.* (2015) use postseismic regional GPS and TerraSAR-X data (TSX1 and TSX2, Table 2.2) to identify a second, splay fault (the Bostaniçi Fault), which reaches the surface in the northern suburbs of Van. Thus, in the weeks following the mainshock, a small amount of slip reached the surface, both at the surface projection of the main Van fault, and on the splay fault ∼7 km to the south. *Doğan et al.* (2014) also identify fringes in the TSX1 and TSX2 interferograms relating to the M_W 5.9 aftershock on 9th November (strike-slip mechanism). *Wang et al.* (2015) go further to model slip on both faults based on the timeseries of TSX scenes – estimating as much as 0.7 m of slip.

Postseismic surface displacement due to slip on the Van fault occurs over a wavelength of ∼6–7 km – the simple 2D forward model for fault slip on the upper Van fault closely matches the observed postseismic surface displacement (Figure 2.16a), suggesting the creep is confined to the upper, largely locked section of the Van fault. This is in agreement with the suggestions of *Wang et al.* (2015) and *Altiner et al.* (2013) who find that the majority of the postseismic motion occurs over a broader region than the coseismic rupture. Shallow postseismic slip is also consistent with the observations of *Acarel et al.* (2014) from cross correlation of ambient seismic noise, which show a velocity decrease at the mainshock that does not recover for the higher frequency bands which sample the shallower crust, suggesting continued shallow slip. Combining the observations from both CSK3 and the TSX scenes, we observe creep on the Van fault decaying over a very short timescale of hours to days, whereas the Bostaniçi fault does not creep during the 3 days following the earthquake, but is clearly creeping following the M_W 5.7 aftershock, with a slower decay constant (evidenced by significant displacement in the TSX3 interferogram, more than 24 days after the aftershock). This is consistent with the suggestions of both *Doğan et al.* (2014) and *Wang et al.* (2015), that there was a time delayed migration in postseismic motion from the Van fault plane onto the splay fault, possibly due to static stress change or fluid migration. We do not observe a longer wavelength signal that would suggest significant afterslip in the coseismic rupture region.

In the recent 2014 Napa Earthquake, significant rapid postseismic motion was also shown to occur in

the hours to days following the earthquake (e.g. *Hudnut et al.*, 2014; *Brocher et al.*, 2015), though the first post-event InSAR pass was not until three days after the event. *Lienkaemper et al.* (2016) estimate that up to around on quarter of total expected afterslip motion may have been taken up within the first day on some sections of the fault. Both the Napa and Van earthquakes have shown very rapidly decaying postseismic motion after the event, declining over periods of hours to days. Inclusion of this short-term postseismic displacement in InSAR-derived slip models could give systematic overestimates of coseismic moment release and shallow fault slip. In order to accurately characterise this shallow afterslip and to differentiate between coseismic and postseismic slip, we need very rapid and easily deployed measurement techniques. Shortened revisit times with new radar satellites will improve InSAR capabilities (*Elliott et al.*, 2015c), but postseismic acquisitions are still likely to be multiple days after events instead of hours. We have shown that a single person with minimal training can generate a DEM of a ∼200x200 m area in under an hour with minimal cost – this can be achieved even faster with a small quadcopter or fixed wing drone as was performed by several teams following the Napa earthquake (*Morelan et al.*, 2015). Thus observations are limited only by time required to travel to the event location and re-visits can be near continuous. In the future, with the increase in availability of cheap and rapid observation, we expect to see much higher temporal sampling of postseismic motion particularly in the acquisition of near zero-delay type observations, giving the chance to better constrain the evolution and behaviour of surface and near-surface faulting both in the coseismic and postseismic phases.

2.6.3 Earthquake Hazard

We have imaged a postseismic transient on the Van Fault which decayed rapidly after the mainshock, amounting to <20 cm of measurable aseismic fault slip. Transient slip on the Bostaniçi splay fault is also imaged, and likely decayed with time.

Wang et al. (2015) estimate up to 0.7 m (34% of mainshock moment) of postseimic slip on the fault plane, over the first 3 months of the postseismic period, and hence suggest that the fault does not represent significant future seismic hazard. Although we do not model the fault slip, the total surface displacements we observe amount to less than 15% of those observed after the deeper mainshock in the radar line of sight. The solution of *Wang et al.* (2015) requires larger lateral slip on the upper fault, which the InSAR measurements are less sensitive to, but there still remains a slip deficit if one considers the thrust component of slip. As such, the maximum thrust slip we estimate on both the upper Van fault and the splay fault in the earthquake and the first 2.5 months of postseismic motion is still only a small fraction of the average slip modelled at depth (though a much longer timeseries is needed to determine the full postseismic behaviour). The two large, shallow aftershocks, combined with the presence of fault gouge at the surface (*Elliott et al.*, 2013) suggests that the upper crust is capable of sustaining earthquakes. Palaeoseismic trenching is required to characterise the earthquake behaviour of the upper fault. It is

clear, however, that significant slip does reach the surface on a discrete fault plane (⩾0.5 mm/yr) and that the upper 8–10 km of crust is capable of sustaining earthquakes.

Considering the unruptured upper part of the Van fault, the fault length of ∼25 km and a bottom depth of 10 km gives a fault plane of similar area to that which failed in the 2011 earthquake. Assuming the same average slip (∼3.7 m, *Elliott et al.*, 2013) modelled at depth (or equivalently that average slip scales with fault area e.g. *Wells and Coppersmith*, 1994), would yield another earthquake of M_W 7.1. The slip would be equivalent to 2.6–2.8 m uplift at the surface (assuming a dip of 45–50°), suggesting that the scarp at site S3 is comprised of at least ∼6–7 earthquakes, with recurrence intervals of <8 ka if the fault fails in characteristic earthquakes. It is likely however, that some of the slip at depth is accommodated as folding, giving rise to the anticlinal ridge that forms the hangingwall topography (see §2.6.1, Figure 2.15). An earthquake on the upper section of the fault would have a centroid 10 km shallower than the 2011 event, and would also be ∼10 km closer to the city of Van, and hence would likely result in much heavier damage to the city than the 2011 earthquake.

The 2011 Van earthquake occurred on the fault below a depth of ∼8–10 km, with a magnitude M_W 7.1. As discussed, the coseismic uplift does not correlate with the topography, and so the surface topography reflects the structure of the upper ∼7–8 km of the crust. Thus the Van earthquake illustrates difficulties for palaeoseismic and geomorphic investigations in regions of thick skinned faulting, as we see that large (M>7) earthquakes can be generated by deep ruptures which do not affect the surface geomorphology. The lack of primary surface ruptures also means that palaeoseismic trenches on reverse faults in the region can 'miss' earthquakes of at least M_W 7.1 and estimates of earthquake hazard in the region based on surface data will underestimate the depth extent of seismogenic faulting and hence maximum earthquake magnitudes.

Using the diagnostic features of uplift observed in the hanging-walls of the Van and Bostaniçi faults, we map several more faults across the region (see Figure 2.3), complementing previous studies (e.g. *Altinli*, 1966; *Saroglu et al.*, 1992; *Özkaymak et al.*, 2003; *Karakhanian et al.*, 2004; *Ozkaymak et al.*, 2011; *Üner et al.*, 2015). These include the Gürpınar fault to the south of Van city (Figure 2.15a,c) on which we identify a series of wind gaps in the ridge line and north-dipping tilted sedimentary units on the backlimb (Quaternary Travertines and Oligocene-Miocene sediments). An earthquake on this fault would also be damaging to the city of Van, as the inferred north-dipping fault plane projects directly beneath the city given similar dip ranges. The Gürpınar fault ridge is ∼50 km in length, longer than the Van fault, and from scaling relationships one could expect slip in even larger magnitude events to occur on this structure (*Wells and Coppersmith*, 1994).

2.7 Conclusions

The M_W 7.1 Van earthquake involved rupture of a reverse fault over a depth range of 10–25 km and did not break the surface. The mainshock was followed by postseismic slip on two upper crustal splays above the seismic rupture. We suggest that a change in dip and possible splaying of the fault at a depth of 7–8 km created a structural barrier to propagation of the main earthquake rupture. It is clear from aftershocks that the upper fault has the potential to fail seismically and we have shown that at least 0.5 mm/yr of discrete slip reaches the surface averaged over the long-term. However, palaeoseismic trenching is required in order to characterise the likely slip and magnitude of earthquakes occurring on this upper segment. The Van example is also important more generally, as we have shown that in cases of sub-surface structural complexity, the effects of deeper parts of the structure on bedding-dip and topography may be masked by the larger amplitude, shorter wavelength and possibly anelastic effects arising from the shallower parts of the structure. Therefore, models of sub-surface structure built solely on surficial and upper-crustal measurements may underestimate the seismogenic depth of faulting, and might underestimate possible earthquake magnitudes or cause hazardous deep faults to remain hidden. Additionally, we have demonstrated the utility of two new techniques; Structure-from-Motion, a very low cost tool for accurate measurement of 3D fault displacements, both for small creep type offsets of cm's and fault scarps of meter displacements, and the declassified Corona mission imagery for geomorphic mapping in areas where urbanisation has removed geomorphic markers. In particular Structure-from-Motion can be deployed very rapidly following an event in order to capture offsets due to rapidly decaying shallow afterslip and is inexpensive enough to allow frequent re-surveying.

Chapter 3

Geomorphology, Structure and Preliminary Slip-Rate on the Northern Edge of the High Tien Shan: A Creeping Thrust Fault?

3.1 Introduction

Contemporary studies of the late-Quaternary faulting in the Tien Shan have mostly focused on the western and northern ranges of Kyrgyzstan (e.g. *Burtman et al.*, 1996; *Burbank et al.*, 1999; *Abdrakhmatov et al.*, 2002; *Thompson et al.*, 2002; *Oskin and Burbank*, 2007; *Selander et al.*, 2012; *Goode et al.*, 2014; *Landgraf et al.*, 2016) and the Chinese Tien Shan (e.g. *Burchfiel et al.*, 1999; *Hubert-Ferrari*, 2005). Not many studies have focused on the Tien Shan of SE Kazakhstan (e.g. *Arrowsmith et al.*, 2016; *Abdrakhmatov et al.*, 2016) and there are few known slip rates on the active faults in the region (*Campbell et al.*, 2013; *Cording et al.*, 2014). It is likely that many more faults are unmapped or unrecognised as active.

Establishing the spatial distribution of shortening within continental interiors can yield insight into the processes forming the mountains, but also holds important conclusions for earthquake hazard assessment - for example, in the late 19th and early 20th centuries there were a number of large ($M_W > 7$) destructive earthquakes which caused extensive damage around Almaty and Bishkek (Figure 3.1, *Bogdanovitch et al.*, 1914; *Delvaux et al.*, 2001; *Abdrakhmatov et al.*, 2002; *Kalmetieva et al.*, 2009; *Krüger et al.*, 2015; *Kulikova and Kruger*, 2015; *Arrowsmith et al.*, 2016; *Abdrakhmatov et al.*, 2016). However, only a small fraction of the known active faults have failed in recorded history and recurrence intervals may be in the order of thousands of years (e.g. *Thompson et al.*, 2002; *Carson et al.*, 2015; *Abdrakhmatov et al.*, 2016). Thus,

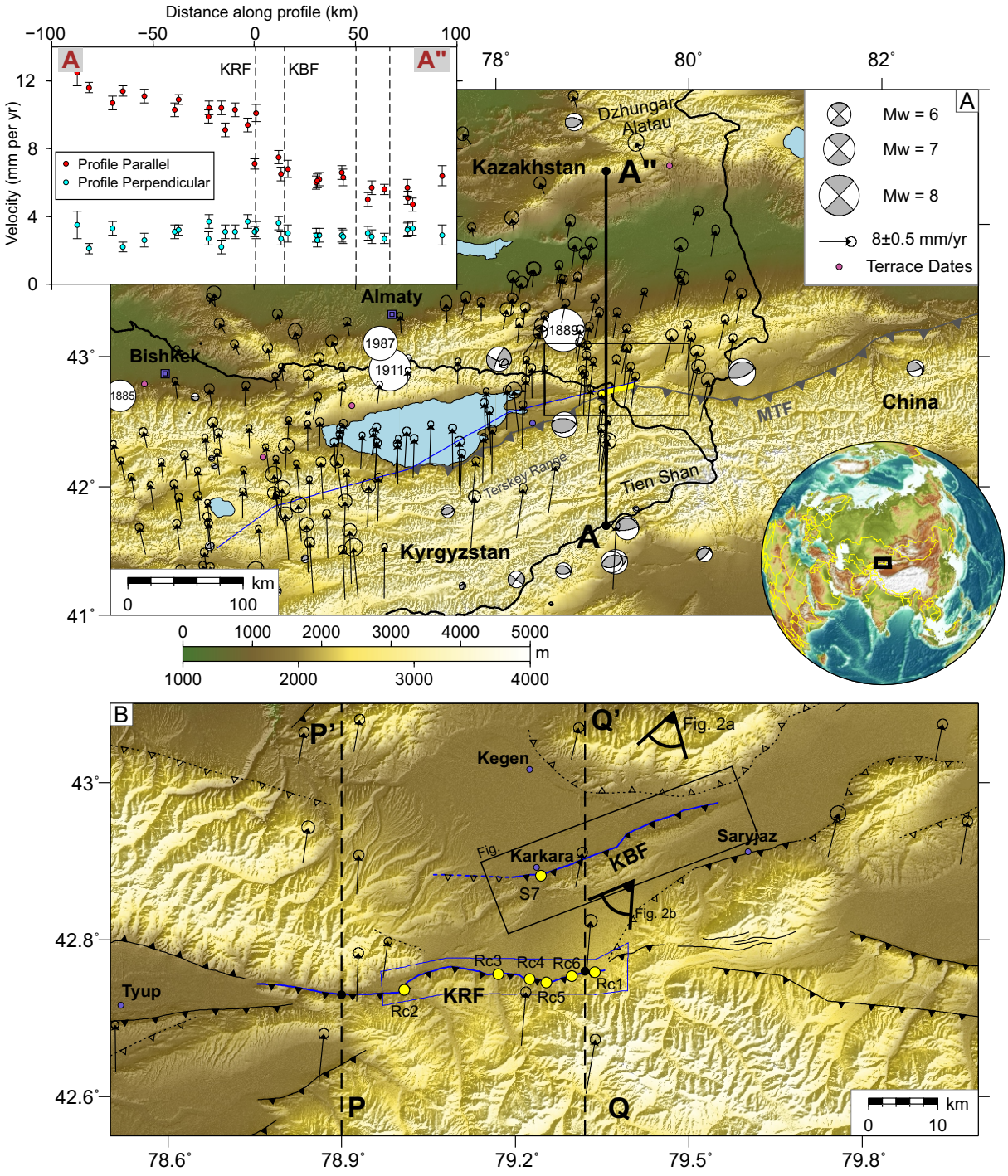


Figure 3.1: *(top)* An overview of the NE Tien Shan. Historic earthquakes of M>6 are shown as open circles, and focal mechanisms show modern instrumental earthquakes of M>6 from the global centroid moment tensor (GCMT) catalogue. GPS velocity vectors are from *Zubovich et al.* (2010) and ellipses indicate the 95% confidence interval. The blue line represents the discrete step in the northwards regional gps velocities identified by *England and Molnar* (2015). (inset) GPS velocity vectors over a swath width of ±40 km projected on to the line A–A'. Dashed line indicates the surface fault location. Error bars indicate the 95% confidence interval. Modified after *Mackenzie et al.* (2015). *(bottom)* Inset showing the Karkara Rangefront (KRF), the Kegen Basin Fold (KBF), and the individual study sites Rc1–6. Blue outline shows the extents of the stereo Pléiades derived DEM. Profiles P–P' and Q–Q' are the two profiles taken through the regional GPS velocity field, modelled to estimate the fault creep rate (Figure 3.16).

the present seismic hazard assessments, based on instrumental records covering the last ∼100 yrs, are likely to be incomplete (e.g. *Pittore et al.*, 2011).

We present a case study of the northern rangefront fault of the high Tien Shan at the longitude of the highest peaks of the range (Figure 3.1). Regional GPS (*Zubovich et al.*, 2010) shows that faults along this rangefront accommodate a significant portion of the regional convergence at the present day (Figure 3.1), so understanding how the shortening is accommodated by faulting is important both for seismic hazard and regional tectonics. Applying Quaternary geochronology and generating high resolution digital elevation models (DEMs), we investigated a series of fluvial river terraces crossing the rangefront to estimate a late Quaternary slip-rate on the main rangefront fault (KRF). We have also studied a foreland fold structure (KBF) running through the middle of the Kegen Basin which we infer to be a detatchment off the main rangefront (Figure 3.1).

We combine displacement measurements with Quaternary dating from radiocarbon and postIR-IRSL and a structural model, to estimate slip rates on both faults (§3.8). Compiling the Quaternary terrace ages we estimate from each of the sites, we compare the ages to those of *Thompson et al.* (2002) who identify key terrace-forming events in Kyrgyzstan, attributing widespread terrace formation in particular time intervals with climatic events. Based on the correlation between sites, we infer estimated ages at the sites in which we were unable to obtain samples for Quaternary dating.

Noting a discrete step in northwards regional GPS velocity at the rangefront (observed by *England and Molnar*, 2015), we fit an elastic dislocation model to the data demonstrating a rapid creep rate across the fault in the late Holocene. We assess the capacity of this fault to produce large earthquakes, comparing the observed creep rate to our preliminary late Quaternary slip rate.

3.2 Tectonic, Geologic and Geomorphic Setting

The Tien Shan ("Celestial Mountains") extend ∼2000 km along the northern edge of the Tarim Basin, from the north-eastern edge of the Pamir to the Gobi Altai (Figure 3.1). They form an actively deforming intracontinental region between two relatively stable blocks, the Tarim Basin and the Kazakh Platform, with convergence driven by the Eocene–present India–Eurasia collision. This shortening is accommodated by a series of E-W oriented thrust faults and conjugate strike slip faulting, with faults extending up to several hundred kilometres in length (*Tapponnier and Molnar*, 1979; *Thompson et al.*, 2002; *Selander et al.*, 2012).

The basement records several generations of Palaeozoic deformation (*Burtman*, 1975; *Windley et al.*, 1990), but the topography associated with those deformations was planed off prior to the late Cenozoic reactivation (*Abdrakhmatov et al.*, 2001; *Korjenkov et al.*, 2007; *Oskin and Burbank*, 2007), giving a widespread peneplain erosion surface. Apatite fission track (AFT) and apatite U–Th–Sm/He (AHe) ages suggest that the widespread late Cenozoic deformation initiated at ∼25 Ma (e.g. *Hendrix et al.*, 1992;

Yin et al., 1998), though recent studies in the vicinity of some of the major inherited structures suggest that tectonic deformation may have begun to occur as early as ∼45–55 Ma(*Glorie et al.*, 2011). There was however an intensification at ∼26–20 Ma, and again at ∼10–3 Ma (e.g. *Charreau et al.*, 2005; *Sobel et al.*, 2006; *De Grave et al.*, 2007; *Glorie et al.*, 2010; *Li et al.*, 2011; *Macaulay et al.*, 2014; *Glorie and De Grave*, 2016), driven by increased regional shortening (*Sobel et al.*, 2006; *Selander et al.*, 2012; *Macaulay et al.*, 2014). The AFT data show spatially variable initiation ages and, though poorly constrained, *Sobel et al.* (2006) suggest deformation started in the south and east, propagating north and west. *Macaulay et al.* (2014) suggest that deformation initiated on the inherited structures best able to accommodate the regional deformation, including the Main Terskey Fault (MTF) on the northern front of the Terskey Range.

Cenozoic sediments lie unconformably on the peneplain surface, but uplift of the material by late-Cenozoic to present thrusting resulted in the stripping off of these sediments, frequently leaving flat-topped mountains flanked by tilted Cenozoic deposits (e.g *Oskin and Burbank*, 2007). Faulting and folding of the Cenozoic sediments has resulted in rotated and deformed stratigraphy. Overlying the Cenozoic deposits, Quaternary alluvial gravels and sands record deformation since deposition, often recording Quaternary fault slip over multiple earthquake cycles.

3.2.1 Regional GPS

Situated ∼1000 km from the main Himalayan collision zone, the Tien Shan accommodate ∼20±2 mm/yr of shortening (at the longitude of this study), amounting to around half the total India–Eurasia plate convergence (*Tapponnier and Molnar*, 1979; *Abdrakhmatov et al.*, 1996; *Zubovich et al.*, 2010). Approximately half of this, ∼10 mm/yr, is taken up across the northern and central Tien Shan, with the other half accommodated along the margin of the Tarim Basin.

The majority of the faults in the region are not well resolved in the regional GPS velocity field. The only exception is a discrete step in the velocity field observed by *England and Molnar* (2015), extending from Song-Kul lake in Kyrgyzstan at least as far as the Kegen Basin, roughly paralleling the Terskey Range (Figure 3.1). The velocity field of *Zubovich et al.* (2010) only extends as far as the Kazakh-Chinese border, so it is possible that the step extends eastwards into China. *England and Molnar* (2015) suggest that this step is probably due to a creeping or very shallowly locked fault. At the Kegen basin, this step is a 3-4 mm/yr drop in northwards velocity, the location of which coincides very closely with the northern rangefront of the Terskey Tien Shan. Fault slip rates in the Tien Shan are typically <1–2 mm/yr (e.g. *Thompson et al.*, 2002; *Campbell et al.*, 2013; *Cording et al.*, 2014), so this northern rangefront and associated structures must accommodate a significant fraction of the strain within the north-eastern Tien Shan.

3.2.2 Terskey Northern Rangefront

The high Tien Shan are a series of major ranges running through the border regions of China, Kazakhstan and Kyrgyzstan. On the northern margin, strain is accommodated by thick-skinned faulting, characterised by fault bounded Palaeozoic basement-cored ranges interspersed with small intramontane basins (*Selander et al.*, 2012). The northern rangefront of the Terskey range, the Main Terskey Fault (MTF), extends E-W for over 500 km forming the southern boundary of the Kegen, Issyk Kul and Narynkol Basins, though it is segmented along its length. Though mapped as an active fault by several authors (*Tapponnier and Molnar*, 1979; *Delvaux et al.*, 2001; *Deng et al.*, 2003, 2004; *Macaulay et al.*, 2013; *Campbell et al.*, 2013), there are no published slip-rate studies and no recorded geomorphological or structural observations on the MTF. We focus on an individual segment of ∼40 km in the Kegen basin of Kazakhstan, which we term the Karkara Rangefront Fault (KRF), where flights of well preserved river terraces record fault displacement through the late Quaternary. The KRF strikes approximately E-W and dips to the south (Figure 3.1). The foreland basin is at an elevation of ∼2000 m and the hangingwall range of the KRF reaches ∼4000 m, though the highest parts of the Terskey Tien Shan reach ∼7000 m (∼80 km to the south east). The range is cored with Palaeozoic basement, but the surface expression of the KRF has propagated 2-3 km north from the Palaeozoic contact and Tertiary basin deposits are uplifted in the hanging wall.

3.2.3 Late Pleistocene Stratigraphy

Late Pleistocene/Quaternary climatic variation caused time varying stream power, causing rivers to change from aggradation to degradation or vice versa, resulting in the deposition or abandonment of fluvial and alluvial surfaces. In many areas, especially those driven by glaciation/deglaciation, river terraces have been shown to form in response to climatic change events; and hence occurred simultaneously across wide regions. Therefore if correlation can be established between terraces at different locations, terraces of known ages can be used to estimate abandonment ages at other locations (e.g. *Avouac and Peltzer*, 1993; *Molnar et al.*, 1994; *Burbank and Anderson*, 2011).

In Kyrgyzstan, late Pleistocene terraces are divided into morphological classification of four major eras, QI–QIV (oldest–youngest), each of which is further broken into several subdivisions (e.g. QII(1)–QII(3), oldest–youngest). Extensive work has been carried out dating river terraces to estimate fault slip rates, highlighting two terraces well correlated across multiple drainage networks. *Thompson et al.* (2002) estimate an age of 13.5–15.7 ka for the QIII(3) terrace from multiple radiocarbon dates, and 140±9 ka for the QII(2) surface from thermoluminescence dates. The authors link the abandonment of QIII(3) to the end of the last glacial maximum (LGM). *Bowman et al.* (2004) estimate a minimum age of 96±9 ka for a high terrace observed on the north-west shore of Issyk Kul, which is also likened to the QII(2) surface. *Selander et al.* (2012) suggest an age of 100±30 ka for the QII(2) surface, encompassing both

their measurements from cosmogenic Beryllium-10 dating and those of previous studies. In Kazakhstan, very few terrace surfaces have been dated with modern geochronology. *Cording et al.* (2014) estimate the age of an old terrace surface at 360±60 ka from a cosmogenic Beryllium-10 depth profile on the southern margin of the Dzhungarian Alatau.

Further east, in the Chinese Tien Shan, *Molnar et al.* (1994) identify a prominent terrace at <20 ka, and another at 120±10 ka (coinciding with those observed in Kyrgyzstan), which they correlate to the last two glacial maxima. In addition, the authors identify older terraces at approximately periodic offsets. They suggest that these correlate well with the ∼100 ka climate oscillations observed in the δO^{18} record (e.g. *Imbrie et al.*, 1984), the most recent two of which were at ∼15 ka and ∼120 ka corresponding to the LGM and the penultimate glacial maximum.

We use fault-displaced terraces as markers of late Quaternary slip, dating the terrace abandonments in an attempt to constrain the fault slip-rate. We compare our terrace ages to those published in nearby regions, but we also attempt to correlate terraces at a local scale. Along the KRF, flights of terraces are preserved in each valley; correlating them along strike we investigate changes in slip-rate and fault geometry along strike.

3.3 Methods

3.3.1 DEM Construction

We employ a number of techniques to constrain the geometry and offset of geomorphic markers displaced by faulting. For small scarps with simple geometry, we use simple kinematic DGPS profiles, projecting them onto a vertical plane and fitting lines above and below the fault to estimate vertical offsets. For more complicated marker geometries over larger scales we employ photogrammetry to capture the full topography field.

Over the scale of a single valley, we used Structure-from-Motion (SfM) to generate a digital elevation model (DEM), implementing a workflow based on methods by *James and Robson* (2012) and *Johnson et al.* (2014). At catchment Rc1 on the Karkara Rangefront (§3.5) we surveyed a 1x4 km area covering fluvial terraces uplifted by up to ∼60 m. We used a compact digital camera (Ricoh GR Digital II) suspended from a 2 m^3 helium filled Helikite[1] to collect ∼1650 aerial photographs for the reconstruction. The Helikite was tethered to a controller by a lightweight spectre line and dragged in tracks along the long axis of the survey, from the highest terrace wherever possible to maintain maximum survey altitude (height limited by tether weight[2]). Ground control was provided by control points (orange plastic squares of 0.5 m and 1 m) located using kinematic DGPS. The resulting DEM has a resolution of ∼0.3 m, with a

[1] A Helikite (Allsopp Helikite Ltd.) offers significant advantage over a traditional balloon. The kite structure provides significant additional lift in a gentle breeze and greater stability in wind that would be prohibitively strong for conventional balloons.

[2] A 2 m^3 balloon is just sufficient to carry a small compact camera (220g) at altitudes up to ∼2200 m and a flying height of 60–80 m.

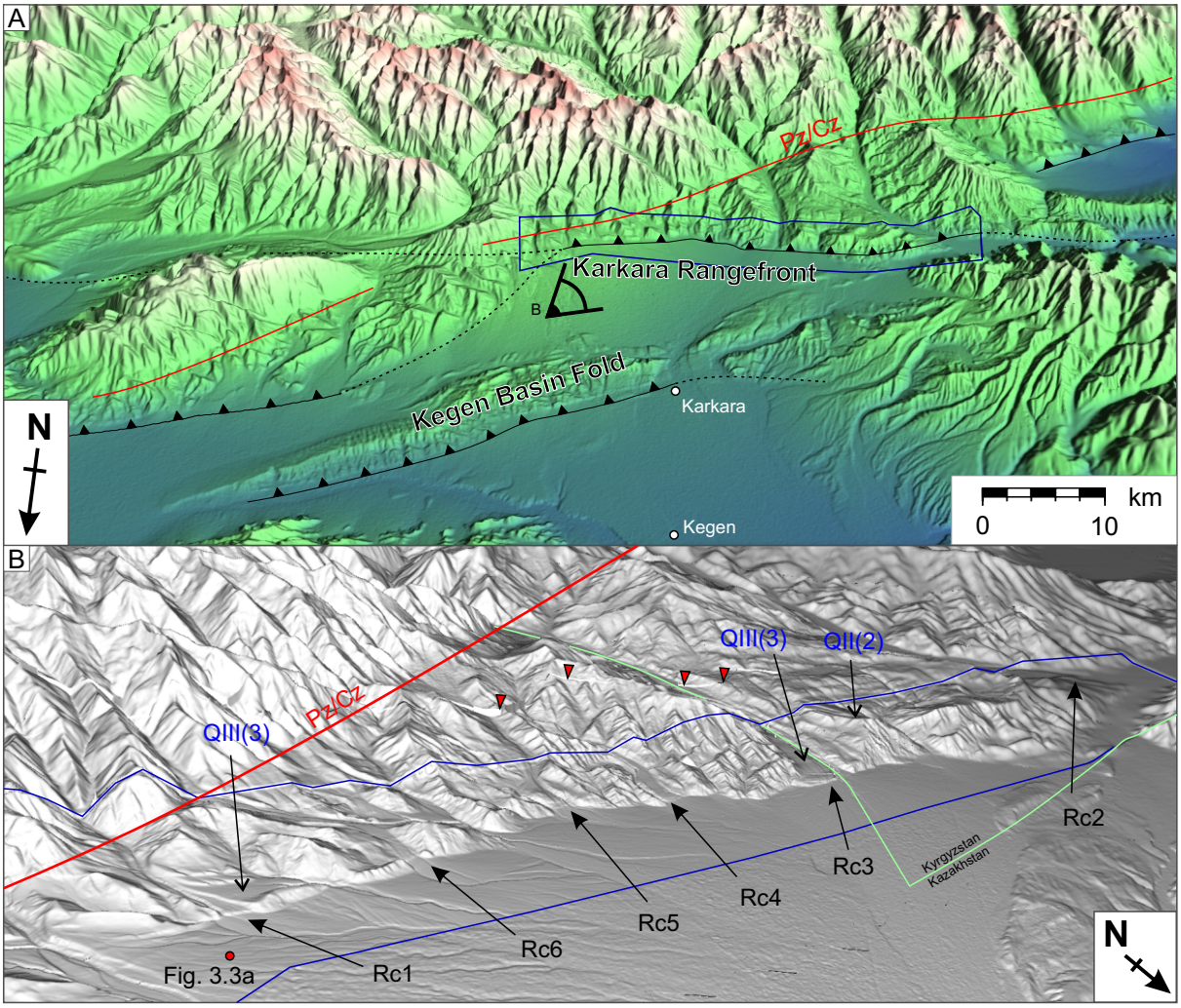


Figure 3.2: (a) Perspective view of the Terskey northern rangefront, showing the major structures studied here. Basemap elevation data from the SRTM 1-second dataset. 2x vertical exaggeration. Red line indicates the Palaeozoic–Cenozoic contact at the surface for the Karkara Rangefront. (b) Perspective view looking SW along the KRF, from the Pléiades derived DEM on top of the AW3D30 DEM (*Takaku et al.*, 2014), showing the individual river catchments studied. Blue lines indicate an artefact due to minor mis-registration between the DEMs, and form the outline of the high resolution dataset.

scale accuracy of ∼1%, demonstrating the utility of this method in assessing geomorphic structures. Due to time constraints and weather conditions, the aerial survey was conducted over two days. Unfortunately, changing light conditions and heavy rain overnight made automated feature matching between the two datasets impossible, so the pointcloud and resulting DEM presented are two independent sections which have been coregistered manually.

In addition to the SfM DEM of our primary field site (Rc1), we used 0.5 m resolution stereo Pléiades satellite imagery to generate a wider area DEM in order to study the rangefront and terrace morphology over the whole fault segment (Figure 3.2). We process the stereo imagery using the Leica Photogrammetry Suite module within the ERDAS IMAGINE software package. Tie points were used to refine the rational polynomial coefficients which approximate the interior and exterior image geometry, then pixel by pixel correlation was performed. We used a 9x9 pixel correlation window, starting with a correlation threshold

of 0.3 and refining up to 0.7. An identifiable ground control location from the SfM survey was used to co-register the two datasets. The Pléiades DEM covers catchments Rc1–Rc6 (§3.4), a 30 km stretch of the rangefront[3], with an average point density of 0.25 pts/m^2.

The resultant pointclouds from both datasets were gridded using a continuous spline minimum curvature algorithm (under GMT, *Wessel and Smith*, 1998) to generate raster DEMs at 0.3 m and 2 m resolution for the SfM and Pléiades datasets respectively. In the following sections the raster DEMs are used for visualisation, but all analysis (profiles etc.) are performed directly on the pointcloud to avoid biasing results by gridding interpolation. Both photogrammetric methods also generate a high resolution orthoimage aiding detailed mapping.

We test our topographic analysis of uplifted river terraces with the high resolution survey at catchment Rc1 and then use area Pléiades DEM to extend the analysis along the entire rangefront. Using the terrace morphologies, we correlate the river terraces between valleys along a large portion of the fault (§3.7).

3.3.2 Dating

Wherever possible, we collected detrital organic material for radiocarbon dating to estimate terrace and fan ages. Samples were analysed by the Beta Analytics laboratories and calibrated using the OxCal utility (*Bronk Ramsey*, 2009), based on the IntCal13 calibration (*Reimer*, 2013); a full list of the measured isotope concentrations and calibrated dates is given in Table 3.1. Dates are quoted in ka before present (BP), as ranges covering the 95% confidence interval based on the measurement and calibration uncertainties.

Away from the main rangefront the environment is relatively arid with minimal organic material, so we also use a combination of quartz and K-feldspar luminescence dating[4]. An outline of the luminescence techniques is given below, but the full details of sample preparation and instrument specifications are given in Appendix A.2. The environmental dose rate D_e was estimated from the ∼5 cm of material at the ends of the sample tubes, assuming that this material is representative of the surrounding material; in some cases such as narrow sand lens' or near contacts this may introduce further unaccounted for errors.

Quartz OSL

From each luminescence sample, we derive a measure of the equivalent dose using the quartz single aliquot regeneration (SAR) protocol (*Murray and Wintle*, 2000, 2003). For samples where sufficient quartz was recovered, dose recovery (DR) experiments were first conducted to test whether the SAR protocol derives an appropriate estimate of the equivalent dose following the application of a known radiation dose (*Murray and Wintle*, 2003). DR experiments were carried out across a range of preheat

[3]Pointclouds to be available for download from OpenTopography (www.opentopograph.org) after publication of this work

[4]Quartz OSL and Feldspar post-IR IRSL analysis was carried out by Andrew Carr at the University of Leicester.

temperatures (160-260°C) to optimise the SAR measurement protocols. Each aliquot within the SAR cycle was tested for recycling and recuperation; aliquots showing recycling ratios significantly departing from 1, or significant recuperation were discarded.

The samples from the Kegen Basin Fold (OSL3,4, §3.8) gave reasonable results, with good recycling ratios and dose recovery experiments getting broadly consistent doses. We acquired further OSL samples from the Karkara Rangefront Fault (catchment Rc1, §3.5), but initial measurements indicated that grains were insensitive ("dim"), lacking a bright and rapidly bleaching "fast" component to the signal – these samples were not pursued further for quartz OSL analysis. This is not an unusual feature in many tectonically active alpine continental settings (e.g. *Steffen et al.*, 2009; *Rhodes*, 2015).

Feldspar post-IR IRSL

In light of the poor OSL properties of quartz demonstrated by the KRF samples, we also determined burial ages for the K-feldspars separates for each sample, using the post-IR IRSL (pIRIR) single aliquot regeneration method (*Murray and Wintle*, 2000; *Thomsen et al.*, 2008; *Buylaert et al.*, 2009). K-feldspar typically produces bright luminescence signals with infra-red stimulation (IRSL), characterised by dose-response curve that saturates at much higher doses than quartz. It has however, been shown to suffer from the problematic phenomenon of "anomalous fading" – the "leakage" of electrons from traps that ought to be stable at field/room temperature (*Wintle*, 1973; *Huntley and Hancock*, 2001). While fading correction procedures have been developed, these are not always suitable and add additional uncertainty to the final age estimate (*Reimann et al.*, 2011; *Kars et al.*, 2012).

The post IR-IRSL (pIRIR) feldspar measurement protocol isolates a non-fading (or at least much more slowly fading) component (*Huntley and Hancock*, 2001). This approach comprises an initial low temperature (50°C) IR stimulation to remove the fading affected electrons, immediately followed by a higher temperature (225°C or 290°C) stimulation that accesses an electron population less affected by fading (*Jain et al.*, 2015). The trade-off is that signal derived from the second IR stimulation tends to be less rapidly bleached on exposure to sunlight (*Colarossi et al.*, 2015). Two samples were exposed to daylight for 48 hrs, then tested at 290°C, but showed residual doses in excess of 10%. By comparison the same samples showed average residuals of less than 10% under the $pIRIR_{225}$ protocol – we therefore calculate ages using the 225°C preheat.

3.4 Karkara Rangefront

Near the town of Karkara, in the vicinity of the Kyrgyz–Kazakh border, uplift in the hangingwall of the Karkara Rangefront Fault has resulted in the preservation of flights of fluvial terraces in each river valley crossing the fault. With the assumption that the terraces formed at steady river gradient at the time of formation, we measure the present day shape of the terraces to estimate the underlying fault

structure and the uplift and hence fault slip since abandonment (e.g. *Thompson et al.*, 2002; *Burbank and Anderson*, 2011).

The terraces are cut into Neogene sediments and generally capped with fluvial gravels, followed by a post-abandonment soil development. Unfortunately the Neogene deposits are very weakly bedded so we were unable to estimate bedding plane orientations in any of the river catchments. We study the morphology of the terraces along the rangefront; we map flights of terraces at six river valleys crossing the fault along a ∼30 km stretch of the fault (catchments Rc1–6, Figures 3.1b, 3.2b). At the eastern end (Rc1), the fault trace reaches the surface ∼2 km from the Palaeozoic–Cenozoic contact, but the contact strikes SW while the fault continues E-W, giving a separation of ∼15 km at catchment Rc2, suggesting a change in the shallow fault geometry (Figure 3.2). The hangingwall uplift maintains a change from incision to deposition where each river crosses the fault. The terraces generally extend from the fault trace most of the way to the Palaeozoic contact. In the west, the river catchments are larger and the active trace is further from the contact, giving the largest terraces sequences with individual terraces uplifted by up to ∼300 m (Figure 3.2b).

In the following sections we present site studies from two locations along the rangefront (Rc1, Rc2, Figures 3.1b,3.2b), where we have attempted to date the abandonment of the terrace surfaces through radiocarbon and OSL dating. Using the high resolution study at Rc1 as a calibration point, we extend the terrace mapping along the rangefront to Rc2–6, using the satellite derived DEM to cover a much larger area than is practical in the field.

3.5 Results: River Catchment 1, High resolution surveying

At the eastern end of the Karkara fault section, we chose a river valley site with a well developed flight of terraces (Figure 3.3a) as a case study for high-resolution surveying; we used SfM to construct a 1x4 km DEM of the valley (Figure 3.3c). In addition we attempted to date the formation of each terrace through radiocarbon and OSL dating.

In it's upper catchment, the river runs S to N in a deeply incised valley in the Palaeozoic bedrock. Approximately 2 km south of the main surface trace of the fault, the river crosses into the Neogene sediments, in which terraces have developed. Where exposed, the Neogene sediments are homogeneous fine grained, dark red in colour, with a clay-like consistency and show little stratigraphy, so we were unable to extract any bedding information. The poorly consolidated material and generally only thin gravel cap on the terraces, does not preserve exposures well and we found no fault plane exposures. Widespread landsliding has occurred in the Neogene sediments right along the rangefront (Figure 3.3b,d), obscuring terraces in several places.

Using the combined elevation datasets, we map four discrete major terrace levels at Rc1 (T1–4), of which three are preserved on both sides of the river (Figure 3.3b-d). We determine the elevations of

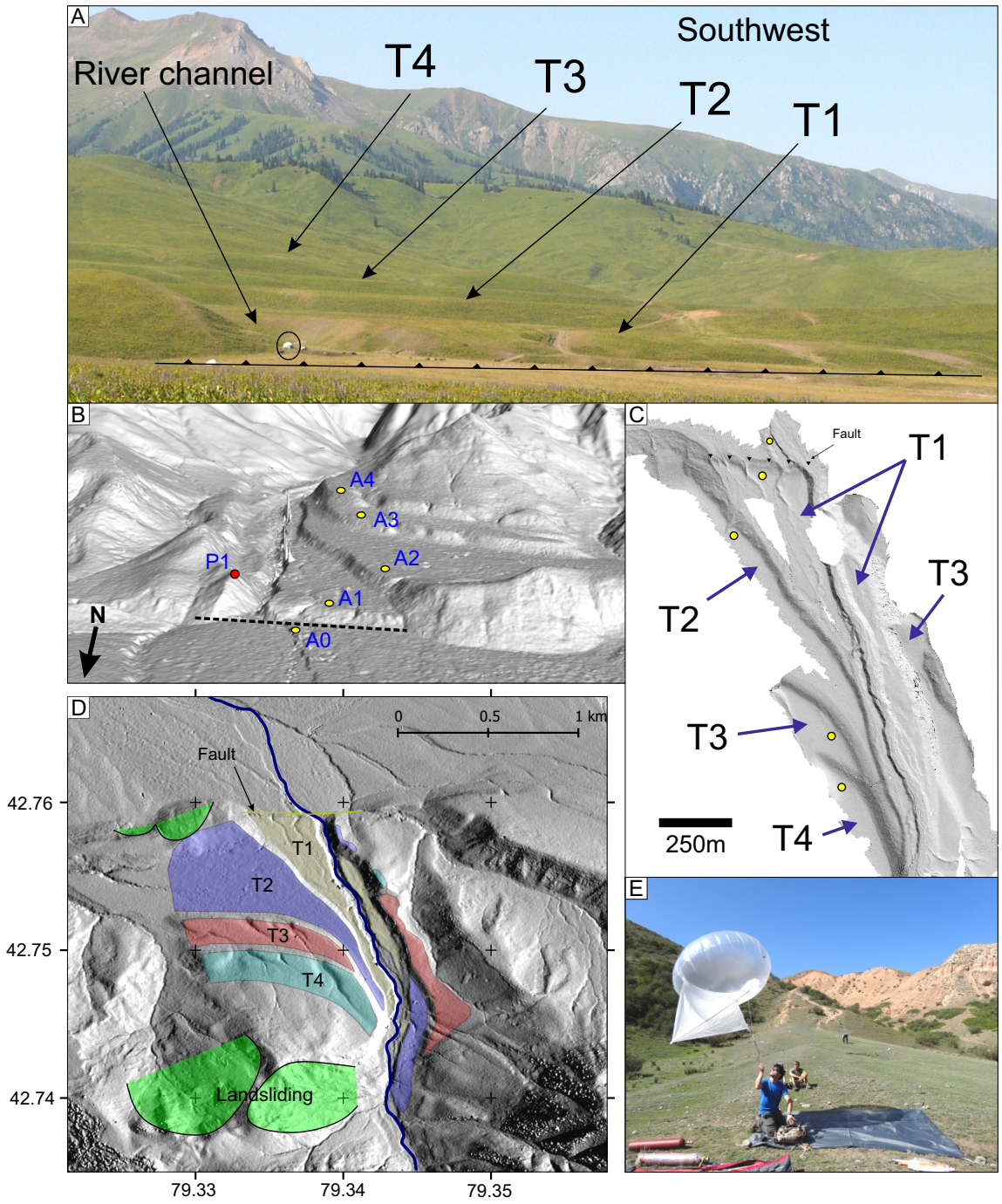


Figure 3.3: (a) Overview of the stepped terraces, T1-4, with the fault in the foreground. (b) Perspective view looking south at the flight of terraces, based on shaded relief of the Pléiades 2 m DEM. Sampling sites are marked as yellow dots. Red dot marks location of photo in Figure 3.4. 2x vertical exaggeration. (c) Shaded relief of the 30 cm SfM DEM, with terraces and sampling locations labelled. (d) Map of the terraces at Rc1. T1–4 shown as coloured polygons with colours consistent with the terraces shown in later figures. Green line marks the fault surface trace in the most recently abandoned terrace. Landslides shown as green polygons. (e) The Helikite used to obtain aerial photos for photogrammetric reconstruction to produce an elevation model of the river valley (photograph taken in different location *Abdrakhmatov et al.*, 2016).

these terraces above the current footwall surface and the river level. There are several locations where subsidiary terraces were also noted, but as they have minimal extent we do not analyse them further. A kinematic GPS profile along the river base was used to constrain the present-day longitudinal river profile as this provides a better constraint on the river elevation than the photogrammetry DEMs, which decorrelate on water.

Dating

We excavated a pit into each terrace surface, choosing locations to minimise the likelihood of post abandonment deposition or erosion i.e. well away from up-slope risers or stream channels (locations in Figure 3.3). We also sampled from a stream cut exposure in the footwall surface.

We collected samples for Luminescence (Optical and PostIR-IR) dating and radiocarbon dating. Though attempts were made to measure quartz OSL and feldspar postIR-IRSL ages from the luminescence samples, the sample material proved extremely unreliable for both methods in both samples, so we only present radiocarbon ages from this site. As there was no discrete identifiable organic matter available, we were restricted to bulk dating of organic rich sediment samples from within the terrace deposits – in a number of locations, dark consolidated palaeo-soil clasts were used (Table 3.1).

Rc1: T1

The most recent major terrace (labelled T1, Figures 3.3) is observed as a pair of well preserved surfaces on both sides of the present river channel, though only western side is preserved at the fault trace. The terrace surface in the hangingwall consists of a ∼30 cm soil cap on top of gravels, which were estimated to be ∼2–4 m thick, lying unconformably on top of the red Neogene sediments (observed in river cuttings below, Figure 3.4). The surface is generally planar, with the exception of two steepened sections, ∼220 m and ∼750 m from the fault surface trace (Figure 3.5), which we attribute to step changes in fault dip below these regions (e.g. *Le Béon et al.*, 2014).

In the footwall, a river cut exposes the uppermost stratigraphy which consists of a soil cap of ∼30 cm overlying angular gravels up to ∼15 cm with occasional coarse sand lenses; however only the uppermost 2 m is exposed, so the depth of the Neogene contact in the footwall is unknown. Given the similar gravel cap in the footwall and hangingwall, it is likely that the surface in the footwall represents the correlated T1 surface. We measure the displacement of the T1 surface since abandonment relative to the downthrown fan surface as 12.9±0.5 m in the immediate 50-100 m of the hangingwall, reducing to 10.0±0.5 m ∼200 m from the scarp (Figure 3.5, discussed below).

Figure 3.3 shows the location of the sampling sites in the downthrown (A0) and upthrown (A1) sides of the terrace. Our only successful age constraint comes from radiocarbon bulk samples, which provide estimates of the pre and post abandonment ages. Sample C3 from the base of the soil layer (depth ∼35–41 cm, Figure 3.4) at A1 consisted of a very dark organic rich soil layer, which yielded a calibrated age

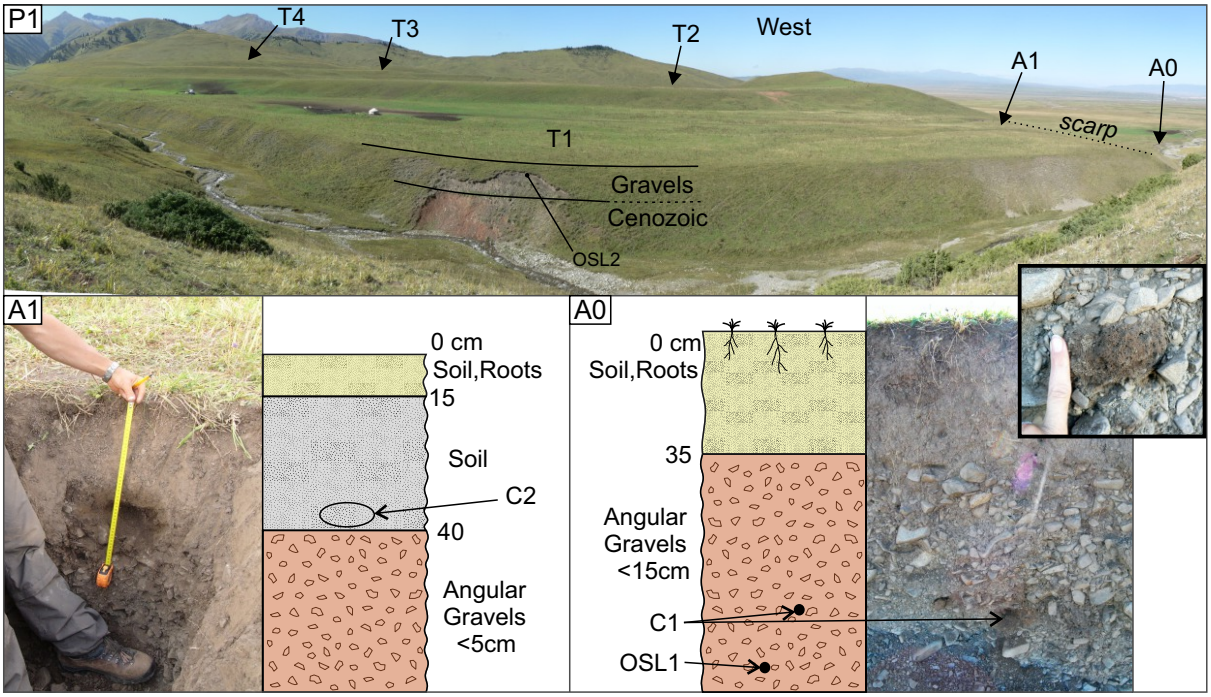


Figure 3.4: *(top)* Panorama looking across the T1 surface from the opposite side of the river (location in Figure 3.3). The contact between the red Neogene sediments and the terrace gravels is visible in the terrace riser in the foreground. (A1) Stratigraphy of the Pit in T1 in the hangingwall, ∼0.40 cm soil, overlying fluvial gravels. (A0) Stratigraphy of the stream cut exposure in the footwall deposits. ∼0.45 m Soil thickness, overlying fluvial gravels interspersed with occasional sand lenses. Locations of the radiocarbon and OSL/IRSL samples are shown. Radiocarbon ages are described fully in Table 3.1.

of 4.0–4.2 ka BP. *Thompson et al.* (2002) suggest that samples from the base of the post-abandonment deposits generally give a tight post-date on terrace abandonment. Sample C4 from a depth of ∼58 cm at A0 consisted of a ∼6 cm soil clast embedded within the gravel matrix, which yielded a calibrated age of 9.6–9.7 ka BP, a pre-date on terrace abandonment. As these gravels cover the footwall remnant of T2, this must also post-date the abandonment of T2.

Rc1: T2

The second terrace at Rc1, (labelled T2, Figures 3.3–3.5) is also preserved on both sides of the river, though only a small remnant remains on the eastern side around ∼1.3 km upstream from the fault. This terrace consists of a thicker soil development of ∼60 cm overlying red clay, with a poorly defined interface. The red clay contains occasional gravels (<10 cm). Given the thick soil development on the T1 terrace, a significant proportion of the soil development on this terrace is likely to post-date T1 too.

Coincident with the steepened sections of T1, the T2 surface has two sections that steepen towards the fault; one at 800–900 m from the fault with a gentle slope of ∼1.5°S and a second in the 100-200 m closest to the fault, with a slope of ∼4°S. Near the fault, the T2 surface is ∼36.3±1.7 m above the current river level (Figure 3.5). However, projecting the river-parallel part of the terrace gradient to the current fault trace suggests a minimum uplift for the stable part of the terrace of ∼21.8±1.4 m since

abandonment. The different degree of uplift on each section of the terrace surface is likely to be due to changes in the fault dip, with a steeper dip under the section nearest the fault trace (discussed below). We note that the fan aggradation during T1 formation will have buried the footwall remnant of T2, so the observed uplift is a minimum since abandonment.

Sampling was performed on T2 at pit A2 marked in Figure 3.3. Sample C5, a consolidated organic rich soil clast, was a bulk sediment sample from within the mixed gravel and clays at a depth of ∼124 cm, that yielded a calibrated age of 14.2–14.9 ka BP. Given that this sample was within the uppermost pre-abandonment deposits, this suggests that the terrace was abandoned after ∼14.5 ka.

Rc1: T3

T3 is mainly preserved on the eastern bank, though there is a small remnant on the western side (Figures 3.3–3.5). The terrace is not preserved in the vicinity of the fault scarp, so estimating the total displacement requires significant extrapolation giving large associated errors. At the location of the pit, the eastern and western terrace remnants are at heights of ∼42 m and ∼35 m above the modern footwall surface respectively; we attribute this difference to the asymmetry of the drainage and the river not being perpendicular to the fault, but they may also be two separate sub-terraces. Projecting the gradient of the terrace to the present fault surface trace, we estimate a minimum uplift of 45±5 m since abandonment for the larger remnant.

Similar to T2, no well defined gravel cap was observed, only a gradual transition from soil to Neogene sediment derived clays. Below a soil cap of ∼40 cm, there was a further ∼40 cm of very uniform red clay without clasts. Beneath 80 cm depth, there were sparse fine gravels (<3 cm) in a clay matrix, with occasional cobbles up to ∼20 cm.

Radiocarbon ages from this surface, collected at A3 (Figure 3.3), give mixed ages. Sample C6, a soil clast embedded in the bottom of the uniform clay at a depth of ∼76 cm, yielded a calibrated age of 28.2–28.7 ka BP. Sample C7 at a depth of 88 cm yielded a calibrated age of 10.4–10.7 ka BP. These two samples are in reverse stratigraphic order, with a very large difference in age and one of similar age to C5 on T2. This suggests that either C6 was eroded from up-slope and redeposited here during soil development or post-depositional contamination has occurred for one or both samples.

Rc1: T4

Only a small remnant of T4 exists at a significant distance from the surface trace so the uplift is poorly constrained. Scaling the T1 profile up to T4, we estimate a minimum displacement of 53±5 m. Similar to T2 and T3, there is a 30 cm soil cap, merging slowly into a uniform red clay band, which becomes interspersed with occasional small clasts below ∼85 cm. Two bulk samples, C8 of bulk soil and C9 of bulk clay, yielded calibrated ages of 8.8–9.0 ka BP and 12.7–12.8 ka BP respectively – similar to samples from T2 and T3.

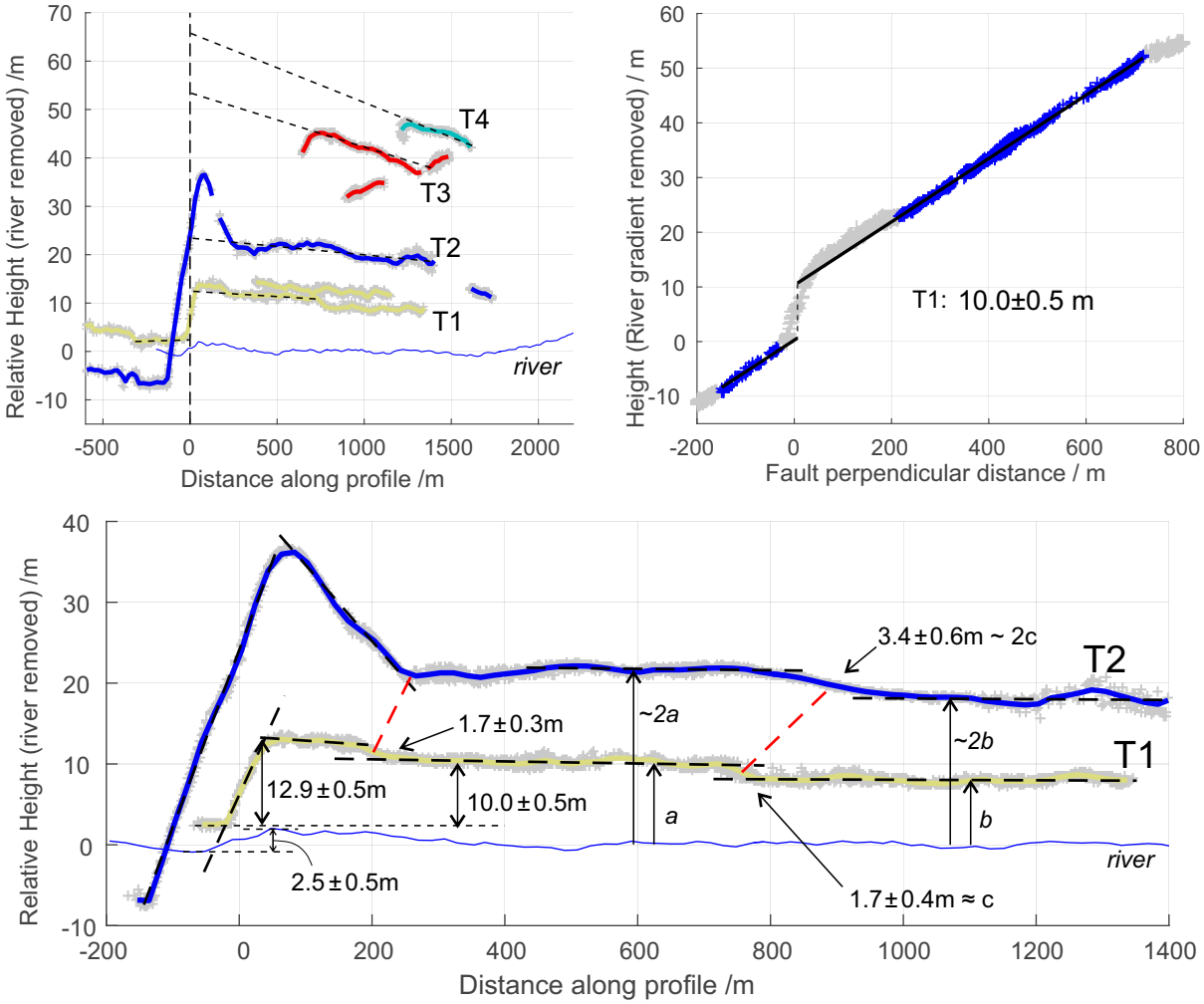


Figure 3.5: (a) Profiles along each of the identified river terraces. The present river gradient has been removed from all profiles (residuals in blue). Colours correspond to the polygon colours in Figure 3.3d. (b) Profile across the most recent terrace T1 (without river gradient removed). Offset: 10.0±0.5 m, though this is larger in the ~200 m nearest the fault trace. (c) Zoomed section of terraces T1 and T2 in (a). Two steps in the T1 and T2 terrace surfaces are well correlated (dashed red lines), and approximate offsets shown. The offset in the river gradient at the fault is visible, with an offset of ~2.5 m.

Terrace Deformation

Approximately 200 m south of the scarp, T1 shows a kink down in height by 1.7±0.3 m over a distance of ~70 m. At the corresponding point in T2, the remainder of the terrace south of the kink, changes gradient from approximately river parallel to 4.5° relative to the river gradient, dipping to the south (away from the fault trace). We attribute this feature to a steepening of the fault dip towards the surface in the uppermost 50–100 m of sediments. This step preserved in both terraces closely resembles fold scarps generated by fault-bend folding (e.g. *Le Béon et al.*, 2014). The step has resulted in a distinctive short wavelength (~100 m) raised topographic feature in the immediate hangingwall of the fault (Figures 3.3b). This small fold is visible in the topography along much of the rangefront (Figure 3.2b), increasing in wavelength to the west though it has been eroded in places by landsliding of the soft Neogene sediments.

N	Lab code	Rc	Material	Terrace	Depth *(cm)*	Delta-13C *(o/oo)*	Conventional Radiocarbon Age (yr BP)	Calibrated Age *(yr BP)*
C1	397882	Rc2	Organic rich sediment	II	86	-19.3	4280±30	4.82–4.96
C2	395357	Rc2	Organic rich sediment	II	105	-10.7	22850±90	26.99–27.45
C3	397881	Rc1	Bulk organic rich soil	I	35-41	-23.9	3750±30	3.99–4.23
C4	395371	Rc1	Peat/Soil clast	I	58	-20.8	8710±30	9.55–9.76
C5	397880	Rc1	Peat/Soil clast	II	124	-20.4	12440±50	14.22–14.94
C6	395348	Rc1	Peat/Soil clast	III	76	-20.7	24400±100	28.2–28.7
C7	395350	Rc1	Peat/Soil clast	III	88	-21.7	9340±30	10.44–10.66
C8	397883	Rc1	Bulk organic rich soil	IV	67	-21.8	8050±30	8.78–9.03
C9	404173	Rc1	Bulk clay	IV	80	-22.8	10860±40	12.69–12.80
C10	35584*	Q7	Amalgamated gastropod shell fragments	–	150	-6.3	32230±190	35.7–36.5
C11	35585*	Q7	Amalgamated gastropod shell fragments	–	160	-8.6	34110±210	38.2–39.1

Table 3.1: Full description of the Radiocarbon ages obtained at each of the sites studied along the Karkara Rangefront. Rc1–6: Karkara Rangefront, Q7: Kegen Basin Fold. Ages are reported as radiocarbon years before present where present = AD 1950. Sample analysis was performed by Beta Analytics except for those marked * which were analysed at the Oxford Radiocarbon Accelerator Unit (ORAU). Ages calibrated based on the IntCal13 atmospheric curve (*Reimer*, 2013), using the OxCal utility (*Bronk Ramsey*, 2009). Errors on the radiocarbon age are 1-σ analytical uncertainties. The calibrated age range presented is the 95% confidence interval based on the analytical uncertainty and the uncertainty in the calibration curve.

Further into the hangingwall, we see a second back-tilted section in both T1 and T2, which we again attribute to a steepening of the fault under this section (∼800 m from the fault trace). Under this model, we would expect the ratio of the step offset in T1 to the step offset in T2 to equal the ratio of total fault slip since abandonment of each terrace. Significant noise in the terrace surface gives large errors, but we estimate a ratio of 1.9±0.4 i.e. T2 records twice as much slip as T1 (Figure 3.5). For comparison, we estimate the ratio of the elevation of the terrace surfaces relative to modern river level either side of the fold scarp giving 2.16±0.09 (north) and 2.25±0.15 (south), the same as the ratio of slip estimated from the fold scarps (within error). Thus the elevation of the T2 terrace above present river level is a good measure of the total uplift of T2 since abandonment (within error), so there has been minimal burial of this surface in the footwall (<20% of the uplift).

In addition to the deformation of the terrace surfaces, we also note a deflection of the river gradient. The river shows a short wavelength step of $\sim 2.5 \pm 0.5$ m (significant against the noise level, Figure 3.5), which has not migrated back upstream significantly from the fault. There is no bedrock visible in the modern stream bed and the Neogene sediments are very soft and unlikely to generate a material contrast strong enough to cause this deflection purely due to a change in lithology. It seems likely therefore that this deflection arises from motion on the fault, though given the relatively diffuse nature of the deflection, it is not possible to distinguish whether it has been generated by continuous creep or a palaeoearthquake.

Rc1 Terraces - Summary

Profiles through the DEM of the Rc1 river valley with the present river gradient removed (Figure 3.5), reveal that T1, T2, T3 and T4 are offset vertically by ∼10, ∼22, ∼45 and ∼53 metres respectively, relative to the present day footwall surface (Figure 3.5). In both T1 and T2, we also note the back-tilting of the terrace surface in two locations, suggesting a progressive steepening towards the fault trace in the

uppermost 500 m of sediments, though we cannot constrain the absolute dips. The small fold in the 100–200 m south of the fault trace suggests a steep dip in the near surface, while the sinuosity of the fault trace along the rangefront suggests that although the uppermost ∼100 m may be relatively steep, the section beneath most of the terraces should have a relatively low dip.

Radiocarbon samples constrain the age of the T1 surface to 4.1–9.7 ka, though as suggested by *Thompson et al.* (2002), we take the lower end of this as forming a close post-date on terrace formation, at ∼4.1 ka. This is similar to the prominent terrace dated at 4.2-5.2 ka in Kyrgyzstan by *Campbell* (2015). Radiocarbon samples from the higher terraces proved more contextually difficult to interpret, but a sample from the gravel–clay interface on T2 gave an age of ∼14 ka. This would be consistent with T2 being the widespread QIII(3) terrace observed in Kyrgyzstan which is dated at 13.5–15.7 ka (*Thompson et al.*, 2002; *Landgraf et al.*, 2016).

With the exception of C6 which is out of apparent stratigraphic order, the ages from T3 and T4 are not significantly older than those observed for T2, suggesting that there was a major period of soil development at ∼9–12 ka, responsible for all of these soil deposits; consistent with soil formation in the stable period after the demise of the LGM. Equivalently, this may also have been due to a period of intense rainfall, resulting in extensive groundwater flow, which can result in post-depositional exchange of the carbon content, especially in bulk soil samples such as these. Estimates of uplift and shortening rates based on the terrace sequence are discussed in §3.10.1.

3.6 Results: River Catchment 2, Kyrgyzstan

Catchment Rc2 is at the opposite end of the Karkara fault segment, across the border into Kyrgyzstan. Although we still see a well developed flight of terraces here, the fault takes on a different character in this region, with the terraces generally warped over a longer wavelength, though this is still relatively short (1–2 km, Figure 3.6), suggesting folding within the uppermost 1–2 km. The fault surface trace is further (∼15 km) from the Neogene/Palaeozoic contact (Figure 3.2). To the west, the fault splits into several strands, one following a relatively young fold structure to the edge of lake Issyk Kul (and likely underneath *Gebhardt et al.*, 2016), while the other follows the main rangefront of the high topography south of the lake (Figure 3.1b).

The river at Rc2 has a large catchment (∼360 km^2) and low river gradient (0.9°), giving rise to large fan structures, and hence terrace surfaces. The net result is a large flight of terraces preserved here on the eastern bank, raised by up to ∼150 m relative to the modern river channel (Figure 3.6d).

In addition to topographic surveying and Quaternary dating, we attempted to constrain the shallow fault dip at this site using hammer seismic profiles to estimate the seismic velocity structure of the uppermost sediments. Using a line of 24 geophones, we constructed two velocity profiles (A, B) across the main fault strand in T1 on the western bank, and a third (C) across the secondary scarp, in (locations

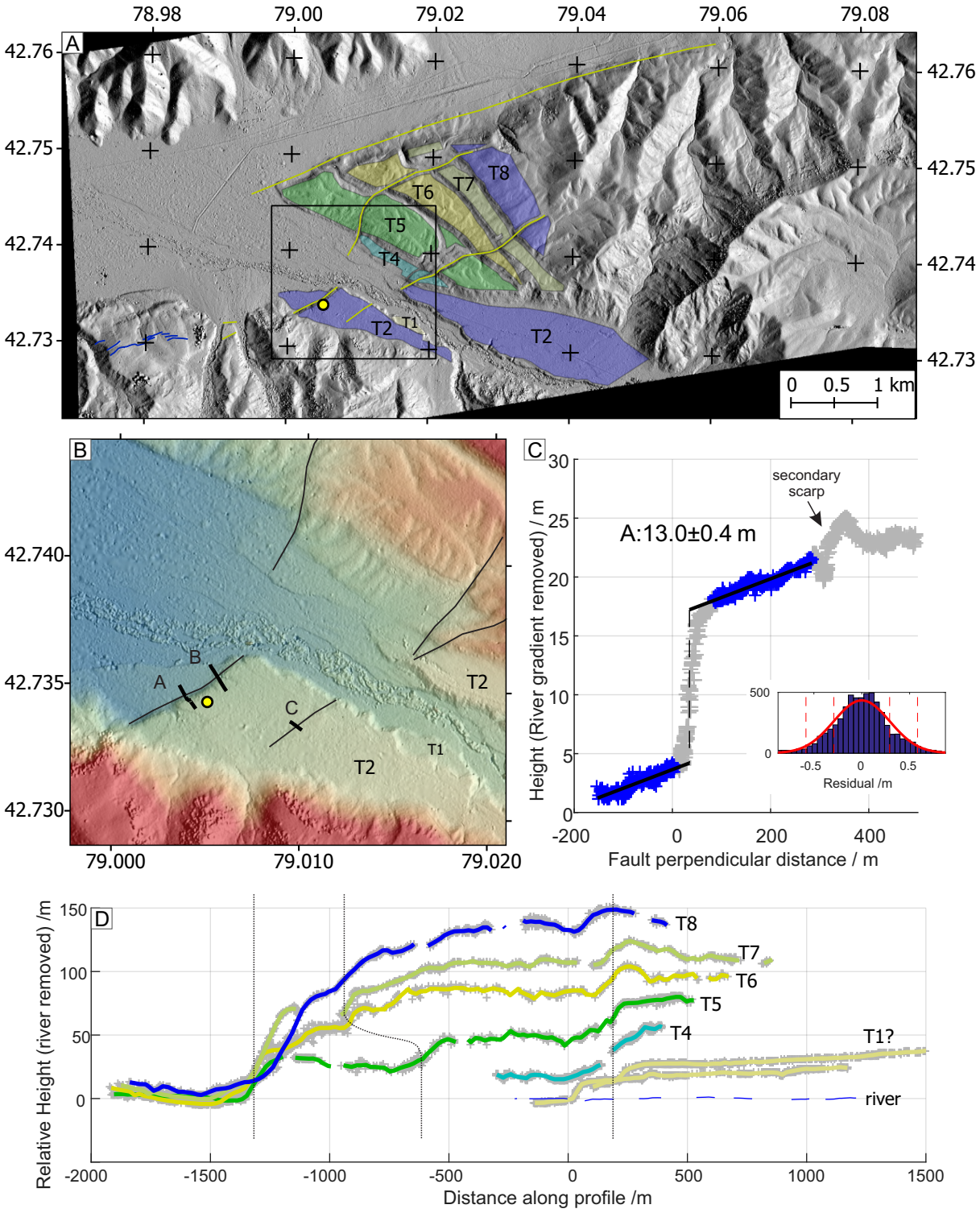


Figure 3.6: (a) Map of the Basharin site, highlighting the series of terraces observed. Labels correspond to the correlated terraces at other sites (§3.7). (b) Zoom near the scarp, showing the location of the three shallow hammer seismic refraction/reflection lines across the scarps, and the sampling pit location. (c) A profile across the most scarp in the most recent displaced terrace (T1), in the vicinity of profiles A and B. (d) Long profiles through the flight of terraces collapsed onto an azimuth of 070°, show displacements of up to 150 m relative to the modern river channel; the older terraces mark fault displacement in several locations (dashed lines). The older terraces with greater maximum displacement show more displacement further north, while the more recent terrace only shows displacement on the southern fault strand.

in Figure 3.6b). Unfortunately, due to the size of the primary scarp, the depth penetration of this method was insufficient to resolve faulting in profiles A and B. Profile C (Figure 3.7) resolved an offset of ~2±0.5 m across the secondary scarp in the Neogene sediments, similar to the topographic offset (below), but due to the low resolution and homogeneous nature of the sediments, the fault interface was unresolved.

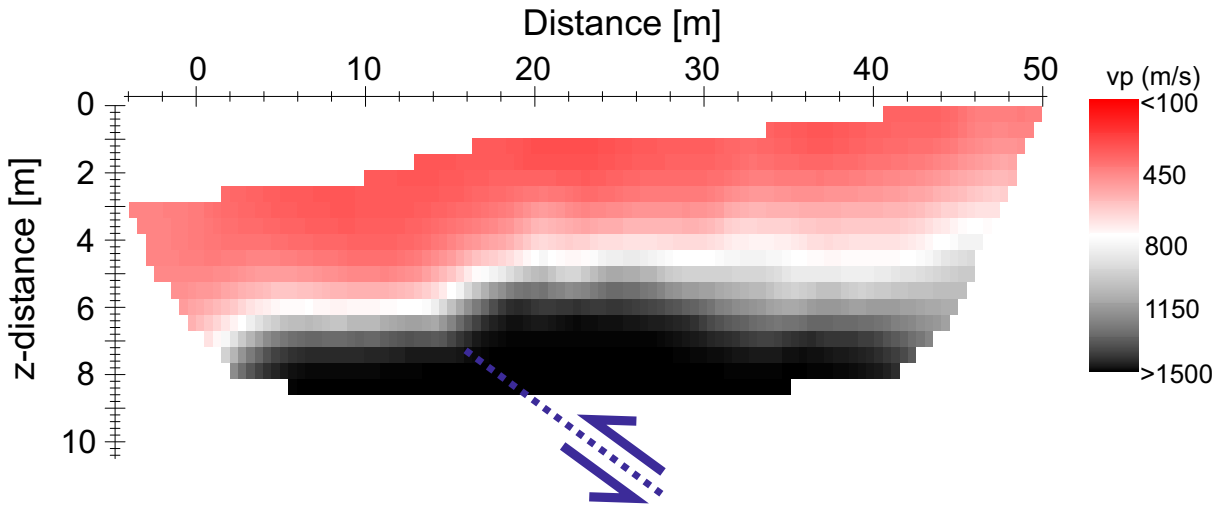


Figure 3.7: Hammer seismic refraction model for profile C (Figure 3.6). We see a displacement in the high velocity deeper material (most likely consolidated Neogene) of ~2 m. 2x vertical exaggeration. Possible fault orientation and location shown in purple (20°).

3.6.1 Terraces

Figure 3.6 shows a detailed map of the major terrace surfaces observed at Rc2. Correlating terraces with other sites along the rangefront, we maintain the same labels used for the other catchments for those inferred to match (§3.7). Of the Rc2 terraces, T2 is the youngest easily observable in the field, and erosion of T4–8 meant that these were more easily identified using the Pléiades DEM (Figure 3.8a). We also identify a remnant of T1 ~700 m from the fault trace, with an offset of approximately half that of T2.

Rc2: T2

The paired T2 terrace is well preserved, extending ~10 km upstream from the main fault trace (though only ~4 km is captured within the DEM, Figure 3.6a). On the western bank, we see a well defined fault scarp in the most recent major terrace surface (Figures 3.6–3.8). A profile across the primary scarp through the Pléiades derived point cloud (Figure 3.6c), shows a displacement of 13.0±0.4 m relative to the modern footwall. In addition to the main fault strand, we also observe a smaller scarp ~400 m behind the main scarp with an offset of 2.4±0.4 m (Figure 3.8d). Incorporating the secondary scarp displacement, we estimate a total vertical displacement since abandonment of 15.4±0.8 m. On the eastern side of the river channel, the fault trace splits in the older surfaces, forming a number of smaller strands spread over

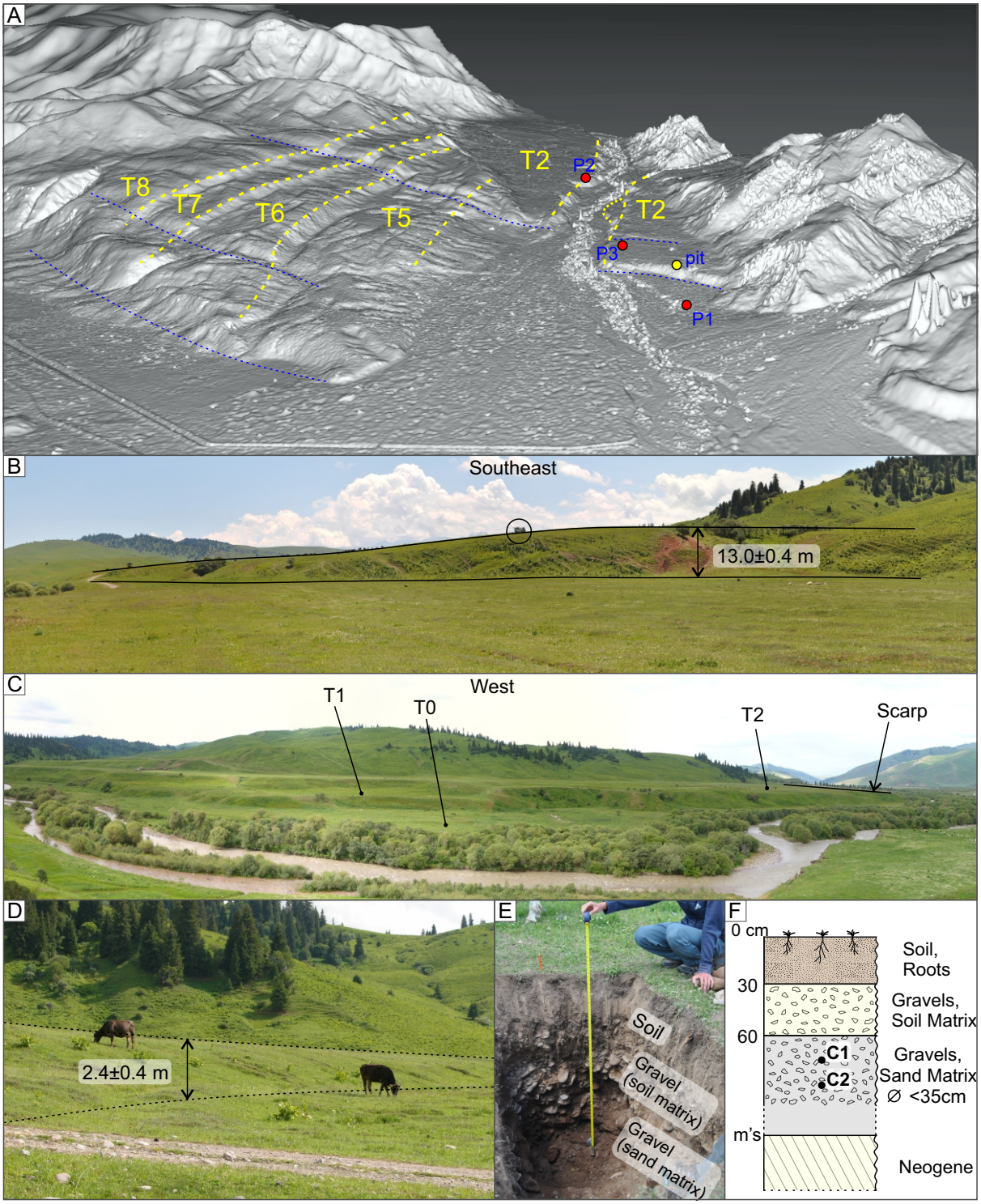


Figure 3.8: (a) Perspective view of the flight of terraces at Rc2. Note the tilting of the terraces away from the river channel. P1, P2 and P3 mark the locations of the photos in (b), (c) and (d) respectively. Blue dashed lines mark fault scarps. (b) Panoramic view (3 photos stitched in cylindrical projection) of the fault scarp in the T2 terrace surface, with an offset of ∼13 m. Car for scale. (c) Panoramic view of the terraces on the western bank (5 photos, stitched in stereographic projection). (d) The smaller secondary scarp (cows for scale), ∼400 m from the main scarp in the terrace surface of T2 has an offset of ∼2.4 m. (e) Sampling pit in the T2 surface. (f) Stratigraphy of the T2 terrace surface. Both radiocarbon samples came from within the gravels with a sand matrix. The presence of Neogene sediments at several metres depth is inferred from outcrops in the present river bed and the seismic reflection profile.

∼1.5 km.

The terrace consists of a gravel bed deposited on a Neogene strath (exposed only in the river bed) capped with a thin (∼30 cm) post-abandonment soil development. We sampled the surface via a pit near the primary fault trace, well away from any hillslopes above to minimise chance of redeposited material. At the pit the terrace gravels could be broadly divided into two units; the upper with a soil matrix and the lower with a coarser sandy matrix, both with rounded clasts up to <35 cm (Figure 3.8e,f). As at Rc1 (§3.5), we found two pockets of dark, organic rich sediment embedded within the gravels. C1 at a depth of ∼86 cm yielded a calibrated age of 4.82–4.96 ka, while C2 at a depth of 105 cm yielded a calibrated age of 26.99–27.45 ka. These dates are very different, suggesting either post depositional mixing or significant groundwater leeching. Inspecting high resolution optical imagery available after the field investigation (Bing Maps), we note that there are remnant plough furrows on the majority of the terrace surface. This suggests the large, flat terrace surfaces were intensively farmed in the Soviet era so the upper part of the terrace may have undergone significant mixing in the last ∼100 years. However, with little opportunity for the arrival of older material at this site, the C1 sample may still impose a weak minimum age constraint on the terrace of ∼5 ka.

Rc2: T4 – T8

On the eastern riverbank, a flight of four higher terraces is preserved, uplifted to ∼150 m above the current river channel. However, the fault is split into several strands (Figure 3.8) propagating further into the foreland, so each terrace surface shows scarps in several places. A perspective overview of the terrace system (Figure 3.8a) shows that these higher terraces are also tilted away from the main river channel, resulting in small channels which have formed at the base of the riser for each terrace. This might be due to curvature in the initial terrace surface at abandonment or differential uplift across the terrace system i.e. the terraces are folded but the fold axis plunges eastwards. We estimate maximum displacements of 56 m, 78 m, 100 m, 120 m and 150 m for the T4, T5, T6, T7 and T8 surfaces respectively. We note that all the old terraces show similar displacement on the southern fault strand, while the older terraces show progressively more uplift on the northern strand than the younger ones; T2 shows no displacement in line with the northern strand. This suggests that fault motion used to be accommodated by the northern strand, but switched to the southern strand since the abandonment of T4. Due to the tilting away from the river channel of these terraces and the degree of incision, the higher terraces were not visible on the ground – the high resolution Pléiades imagery derived DEM allows us to map and measure these terraces that were not easily mapped in the field or satellite imagery. We were unable to collect samples from these terraces, so the ages remain unknown, but by correlating terraces with others in Kyrgyzstan and those at the other catchments along the rangefront, we infer ages for the terraces (see §3.10.4).

3.7 Results: Rangefront Terraces, Rc3–6

In sections §3.5–§3.6 we showed examples from two locations along the Karkara rangefront with well developed flights of fluvial terraces, and obtained several age estimates. Using the remote sensing derived DEM, we remotely map the terraces at each major catchment along the rangefront and estimate their elevations above the modern river level. This allows us to extend our survey over a much larger area than is easily achievable by field survey, but also gains access to areas which are physically or logistically difficult to gain access to in the field (e.g. border regions). We measure terraces at four further river catchments shown in Figure 3.1; Rc3 – a major river on the Kyrgyz-Kazakh border with an especially well developed sequence, and Rc4–Rc6, smaller rivers in Kazakhstan

3.7.1 River Catchment 3 – Border Valley

The catchment Rc3 lies on the border between Kazakhstan and Kyrgyzstan, and is therefore difficult to investigate thoroughly with a field survey. However, the Pléiades DEM reveals the exceptional level of preservation at this site, with 7 separate terrace levels identified (Figure 3.9), sequentially uplifted by up to ∼300 m (Figure 3.10). The degree of preservation is likely due to the river having the largest catchment of any along the rangefront (∼1000 km^2).

There is a large scarp at a primary fault strand at the rangefront, but the T2 surface also shows a series of smaller offsets in the hangingwall, suggesting that a fraction of the motion is distributed across the terrace surface. Each of the terraces also show a broad warping signal over a wavelength of ∼1.5 km, suggesting the fault dip flattens slightly towards the surface in the uppermost 1–2 km (Figure 3.9, 3.10).

Rc3: T0–T1

In the lowest terrace surface T0, we see a vertical offset of just 4.8±0.6 m (Figure 3.10b), the smallest observed along the rangefront. This young terrace is only well preserved within ∼500 m of the fault, so we are unable to assess any contributions due to folding. Additionally, we see a remnant of an intermediate terrace further upstream, displaying an offset approximately half that of T2, which may be the T1 surface. This surface is displaced to 16.7±2.5 m above the present river level. Given the warping of the terrace surfaces, T0 could instead be the T1 surface, but with the surface slip reduced by faulting and slip on the secondary structures.

Rc3: T2

The T2 terrace at Rc3 is very well preserved, extending ∼2.5 km upstream, with very little incision/degradation. Given the similar level of preservation and degree of uplift, we liken this terrace to the T2 terrace at Rc1 (see §3.10.4). Near the fault, we note a smaller sub-terrace likely cut shortly after the primary terrace abandonment (T2b, Figure 3.9a). At the fault trace, we estimate a vertical offset of ∼20 m,

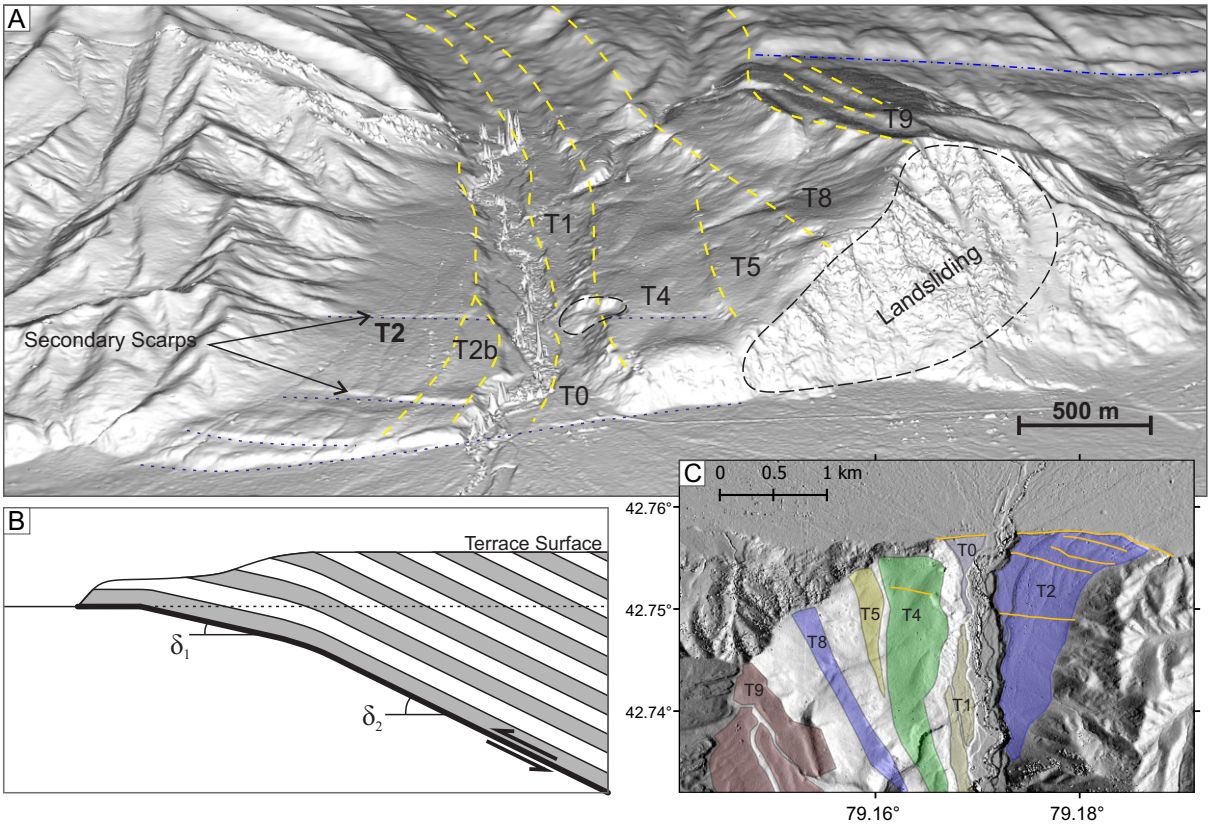


Figure 3.9: (a) Perspective view of the DEM at the border site at Rc3 (looking S, illuminated from viewpoint). The background low resolution DEM is from the AW3D30 dataset, in which the larger terraces are still visible. Terrace riser tops are highlighted with yellow dashed lines. Fault scarps are shown as blue dashed lines. (b) Hypothetical model of the subsurface based on the terrace deformation (see Figure 3.10). (c) Map of the terraces observed at Rc3, on top of shaded relief from the Pléiades DEM (illuminated from the East). Terrace polygon colours are consistent with those correlated at the other catchments.

but given the general folding of the terrace over it's 2 km wavelength, we estimate a maximum uplift of 26±1.8 m for T2.

Rc3: T3–9

The upper terraces T3–9 show similar shapes, though with a general progression towards the basin of the point of maximum uplift of the terrace; we attribute this progression to the advection of topography by fault motion. We estimate maximum displacements of 75±7 m, 102±4 m, 190±11 m, 304±22 m for terraces T5, T6, T8 and T9 respectively.

We estimate the total horizontal displacement between abandonment of different terraces by considering the location of point of maximum uplift on each terrace assuming that this peak has migrated through the advection of topography as slip occurs on the underlying fault. The point of maximum uplift is relatively poorly defined on each terrace, however, so this horizontal displacement measurement carries a large uncertainty. We estimate 270–550 m horizontal displacement between the abandonment of T8 and T2 (Figure 3.10c). Given a minimum vertical displacement of 165±10 m between abandonment of these surfaces, this suggests a lower bound on the fault dip of ∼20°. If the change of base level has been

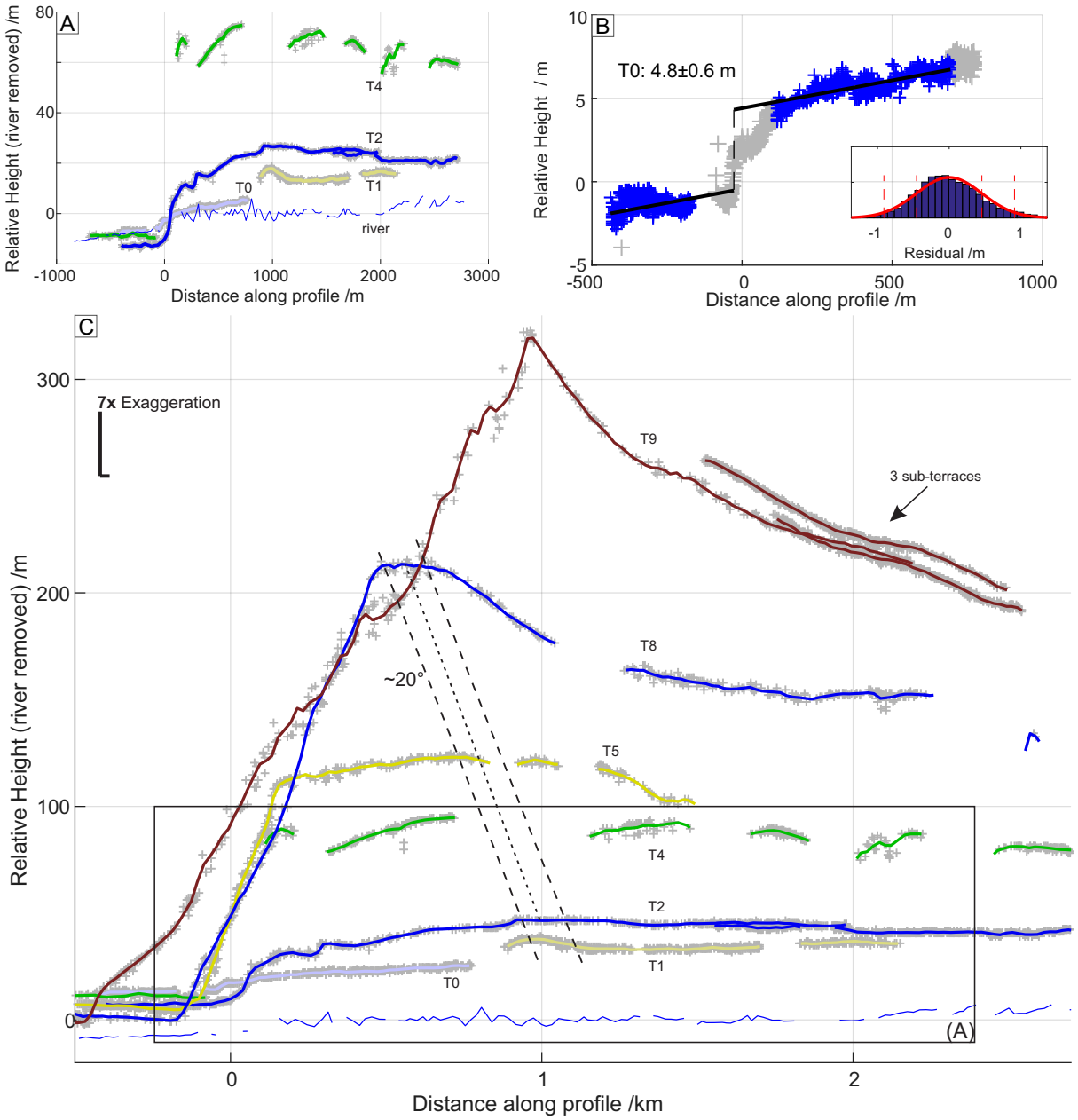


Figure 3.10: (a) Profiles across the lowest four terraces at the Rc3 catchment show a broad warping. It is unclear whether T1 and T0 are the same terrace. (b) Profile across the unique low scarp (T0), measuring a vertical offset of ∼4.8 m at the fault trace (inset shows histogram of residuals). (c) Long profiles along all of the terraces, collapsed onto an azimuth of 80°. All of the terraces show an increase in displacement relative to modern river level towards the basin, suggesting the fault dip flattens upwards. Dashed lines mark an envelope of the peak height of the terraces where visible; dotted lines show the extrema linking these displacement peaks, suggesting a low fault dip of ∼ 20° (provided that change in river base level between terrace abandonment is small).

relatively small compared to the total uplift, this will be close to the true dip, so unless there has been major footwall deposition since abandonment of T8, the fault most likely has a gentle dip (∼20–30°) under the terraces.

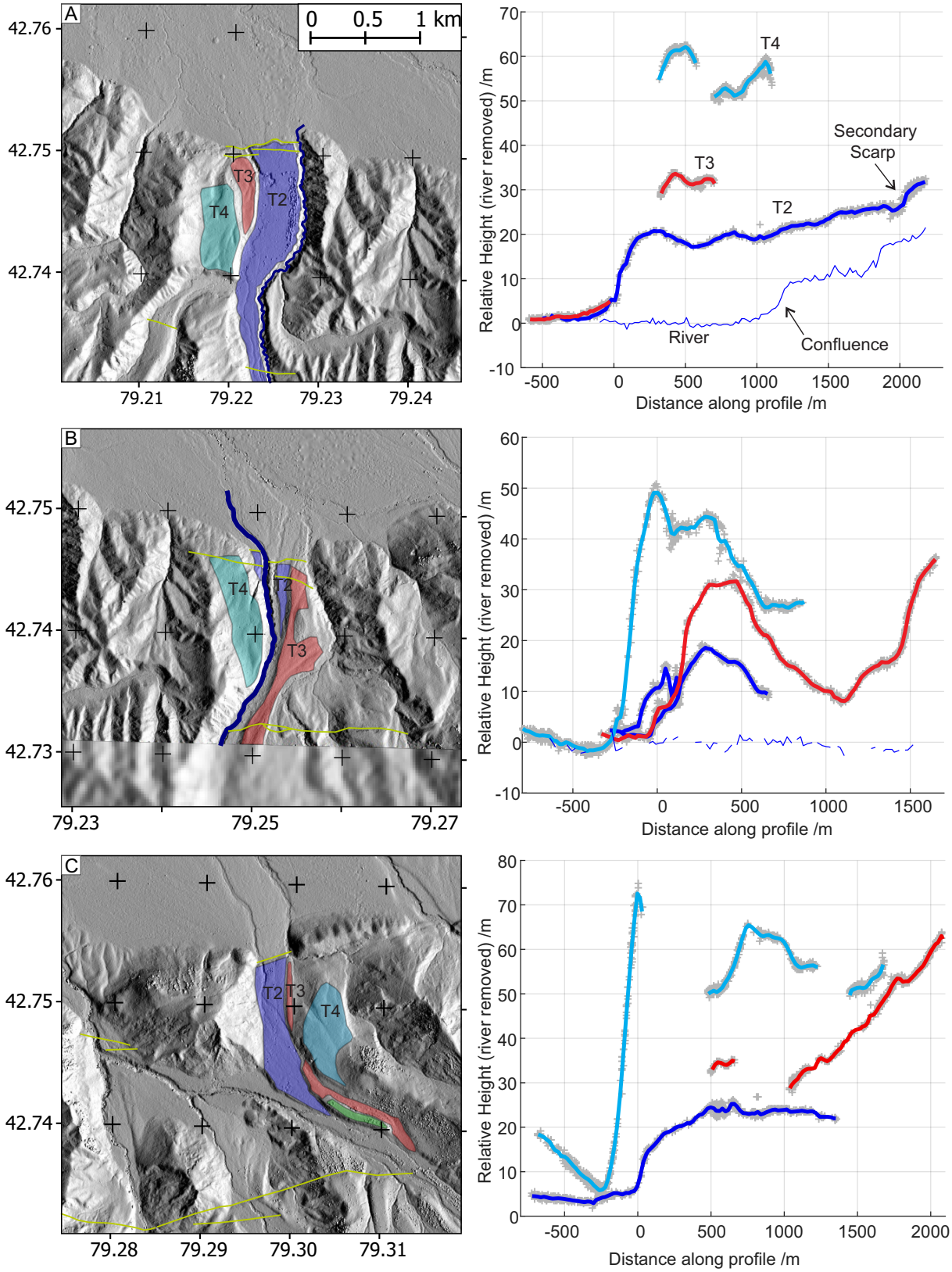


Figure 3.11: Maps and profiles for each of the sites Rc4–Rc6. The mapped terrace colours correspond to the profile smoothed lines, and common colours indicate terraces correlated between catchments. Fault scarps are shown in green – at each site, secondary scarps are seen 1–2 km further back from the primary scarp.

3.7.2 River Catchments 4–6

Catchments Rc4–6 are much smaller than Rc2–3, so the terrace lengths are shorter and fewer terraces are preserved. However, in each case we identify at least three well defined terraces, the lowest of which is uplifted by ∼15–20 m in all three cases and shows similar degrees of post-abandonment incision. Figure 3.11 shows a small map and series of profiles for each site. Rc4 has only small remnants for the older terraces, but appears to show relatively little folding. Rc5 shows three terraces, which have been more altered by folding, over a short wavelength of ∼1 km. At Rc6, the primary river is drained through a different break in the rangefront so the terraces are further from the river axis – here we can only estimate an approximate modern river gradient to subtract from the profiles; further upstream, a significant change in terrace gradients is observed that we attribute to a change in the downstream catchment that the terrace surface drains to. We also observe more secondary scarps in the hangingwall at all three sites. The maximum uplift of each terrace is summarised in §3.10.4 where we discuss how these terraces correlate from catchment to catchment along strike.

3.8 Results: Kegen Basin Fold (KBF)

Approximately 12 km north from the main rangefront, a low fold structure runs NE-SW through the middle of the Kegen Basin (KBF, Figures 3.1, 3.2, 3.12, 3.13). This is a less well developed structure than the Karkara Rangefront, with relief of 200–300 m. It may represent a foreland propagation structure from the main rangefront in a style similar to many basin folds observed in nearby Kyrgyzstan and China (e.g. *Thompson et al.*, 2002; *Charreau et al.*, 2008; *Goode et al.*, 2011), though it could be another thick-skinned structure with little cumulative displacement. However, the degree of bed rotation (below) suggests that significant total slip has occurred, and the lack of Palaeozoic outcrop suggests that slip is primarily within the basin sediments. We also note the presence of salts in the river bed at several points along the core of the fold, identifiable in the satellite imagery as highly reflective in all bands. The presence of salts in the core of the fold is consistent with slip occurring along a detachment in a weak salt layer at depth (e.g. *Bullen and Burbank*, 2001). We investigate the KBF, identifying Quaternary scarps along the northern edge and broad warping of a river terrace which crosses a large portion of it.

3.8.1 Structure and Geomorphology

Near the town of Karkara the fold is cut by the Karkara river (large 1500 km^2 catchment), which has eroded a deep channel through the fold. River cut exposures into well bedded, steeply dipping, Cenozoic deposits are preserved widely along the eastern riverbank and in several locations on the west (Figures 3.13a,b, 3.15a). We measured bedding orientations of the Cenozoic sediments, in a profile nearly perpendicular to the fold, covering the first 3.5 km from the surface fault trace. The beds dip

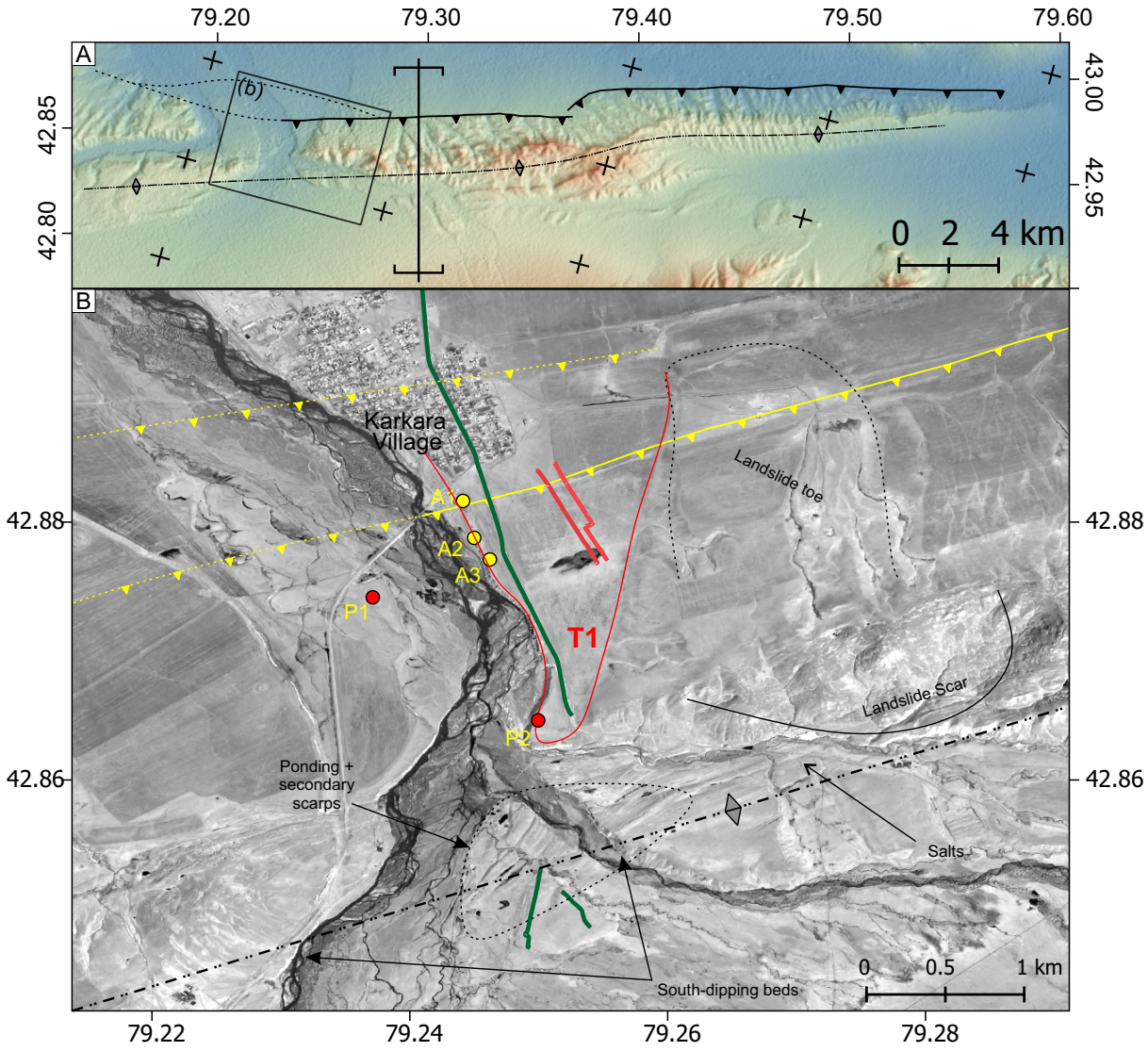


Figure 3.12: (a) Map of the Kegen Basin Fold, which runs approximately NE-SW across the Kegen Basin. The estimated fold axis is shown, along with the mapped fault at the surface along the northern edge of the fold. B–B' marks the location of the topography swath profile in Figure 3.13 (b) Map of site Q7, where the Karkara River cuts the Kegen fold. Basemap is 1 m resolution panchromatic Kompsat-2 imagery. Locations of the GPS profiles are shown as red and brown lines. Sampling sites are shown as yellow dots, and the locations of the photos in Figures 3.13a,b, 3.15a, are shown as red dots.

north near the fault, steepening south along the profile and switching to dip south at ∼3.4 km S of the fault trace (Figure 3.13c). Further south, the Cenozoic beds are no longer well exposed because the river is less constrained by the channel through the fold core, splitting into a number of smaller tributaries each with less incision such that there are no natural exposures. Comparing the observed bedding dips to the topographic section (Figure 3.13), we estimate a folding wavelength of ∼6.5 km, though the main topography is only ∼4 km across, implying that much of the backlimb of the fold has been eroded.

Climatic variation has resulted in the abandonment of several terraces along both sides of the river. We focused on the most prominent of these terraces on the eastern bank (Figure 3.15a), which is well preserved in both the footwall and approximately 2 km into the hangingwall. There are a number of smaller remnants from different generations preserved on the eastern bank too (Figure 3.15b). Unfortunately,

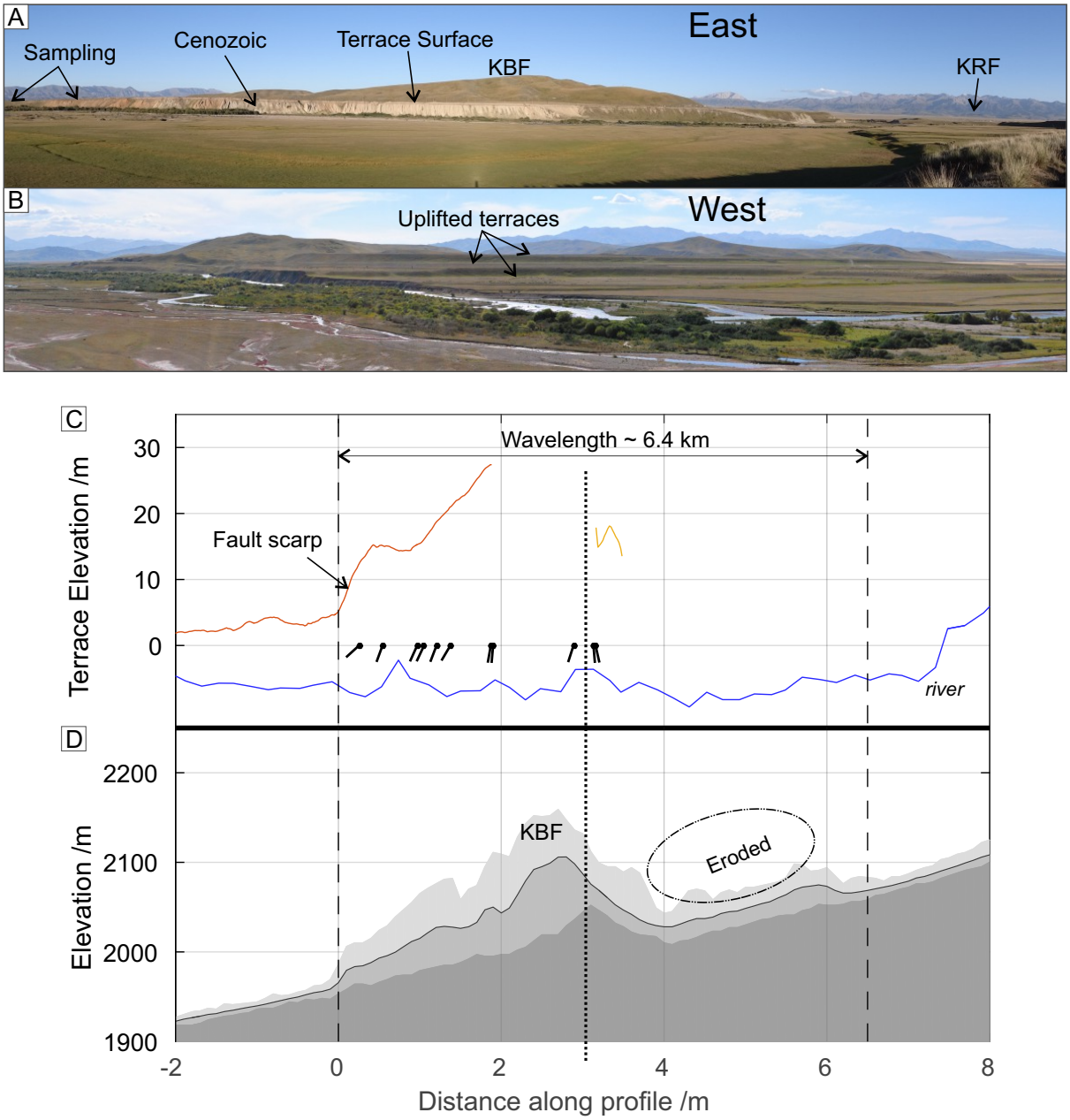


Figure 3.13: (a) Photograph looking east across the Karkara river to the long continuous terrace surface on the eastern side. The terrace consists of a thin gravel layer lying unconformably on steeply dipping Cenozoic sediments. Behind the terrace, the profile of the fold can be seen. (b) Photograph looking west across the Karkara river to the flight of terraces on the western side. (photo locations in Figure 3.12). (c) Long terrace profile with kinematic GPS along the terrace warped by folding is shown in red. Two shorter sections of terrace remnant are also shown, but appear to be different terrace surfaces. The present river gradient, estimated from SRTM, has been removed from the profiles. The residuals to a linear fit to the present river channel over the wavelength from the fold is shown in blue. The apparent bedding dips are marked in black, showing a clear change from north dipping to south dipping at ~3 km from the fault trace (markers not scaled to the vertical axis). (d) Cross section through the minimum, mean and maximum topography across the fold in the swath profile shown in Figure 3.12.

only one short terrace remnant was observed to the south of the fold axis, which we are unable to correlate to other terraces so we can only estimate the deformation in the fore-limb of the fold.

The terraces consist of a strath cut into the Cenozoic beds overlain unconformably by river gravels (Figure 3.15). Post terrace-abandonment, a loess cap (typically 0.5–2 m) accumulated, followed by a

soil development (0.1–0.5 m). We use kinematic GPS to measure a long profile of the terrace surface on both sides of the fault trace (Figure 3.13c, location in Figure 3.12b). This was performed by car along the road on the terrace surface, so the road embankment has resulted in an artificial smoothing of the surface scarp. The terrace surface does not capture the crest of the folding deformation, but we can see that folding has generated at least ∼16 m of uplift. Figure 3.15f also shows a higher resolution pair of profiles across the fault scarp at the surface trace, from which we estimate vertical offsets of 10.0±0.5 m, giving a minimum total uplift of $\gtrsim$26 m for the terrace.

In addition to the primary scarp at the northern edge of the fold, we note a series of minor scarps parallel to the fold axis through the core of the fold. Each has reverse offsets of $\lesssim$1 m in the underlying Cenozoic beds and displaces the Quaternary gravel deposits (Figure 3.14); the array of parallel scarps at the surface has generated a series of small ponds between them on the terrace surfaces (Figure 3.12). These scarps are only observed in the young terraces at the core of the fold, and are suggestive of a degree of distributed faulting at the surface. However, given the small total offsets, we suggest that these are secondary structures that play a minor role in accommodating the folding, but the exact relation to underlying fault motion is unclear.

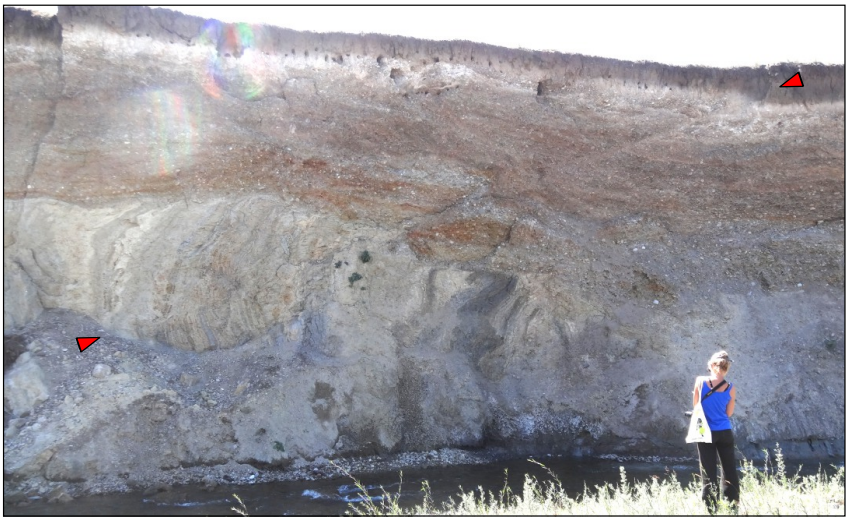


Figure 3.14: A small thrust fault exposed near the centre of the KBF. The gravels are displaced by ∼50 cm vertically, but the offset in the underlying sediments is difficult to constrain.

3.8.2 Dating

Radiocarbon and OSL/IRSL samples were collected to date the prominent river terrace at the KBF (sampling locations in Figure 3.12). A summary of the protocols used to carry out the quartz OSL and feldspar postIR-IRSL (pIRIR) is given in Section §3.3.2, and the individual luminescence and radiocarbon ages are summarised in Tables 3.1–3.3. At location A1, we have two samples OSL3 and C10, while further south along the profile we collected samples OSL4 and C11 at locations A2 and A3 respectively; the terrace surface is continuous across all three sites.

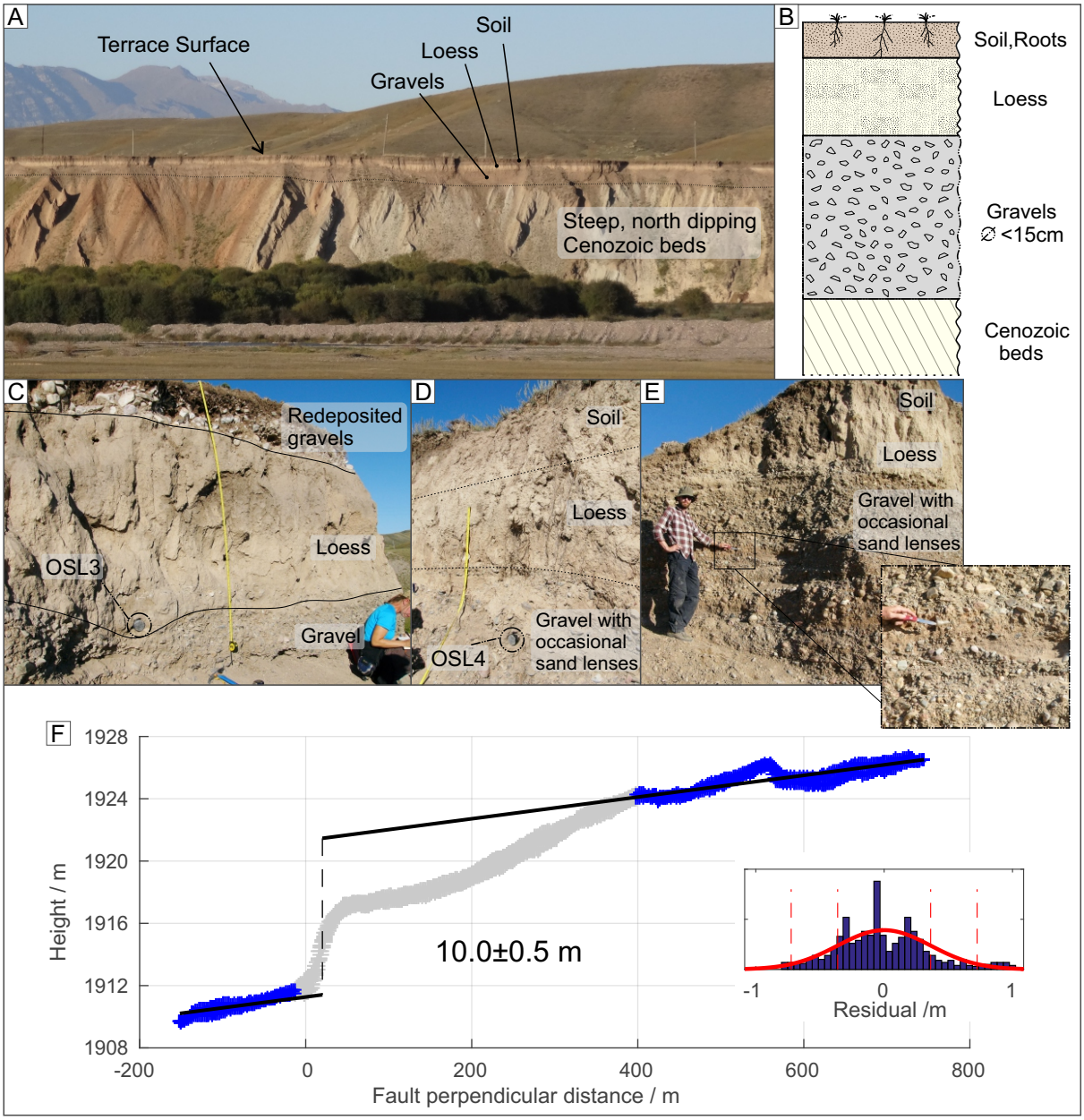


Figure 3.15: (a) View east across the river. Steeply north-dipping Cenozoic sediments are capped with terrace deposits. (b) Approximate profile of the terrace stratigraphy. A thin soil cap sits on top of a thick (1–3 m) loess layer. Beneath this, ∼1-5 m of gravels, lie unconformably on the the Cenozoic sediments. (c) Setting of sample OSL1. With an age of 15–17 ka (Tables 3.2– 3.3) we interpret this as being within post abandonment channel fill. (d) Sample OSL2, from a coarse sand lens within the terrace gravels. (e) Sample C10, amalgamated gastropod shell fragment sample from a shell containing lens of sand within the terrace gravels. Sample C11 was collected from a similar setting ∼500 m further south. (f) Two stacked kinematic GPS profiles across the fault scarp near the town of Karkara show an offset of 10.0±0.5 m in the terrace surface at the fault scarp.

Radiocarbon Ages

Samples C10 and C11 (sites A1, A2, Figure 3.12) consisted of amalgamated small fragments of gastropod shell from a sand lens within the gravels (Figure 3.15e), and yielded calibrated ages of 35.7–36.5 ka BP and 38.2–39.1 ka BP respectively. Gastropod shell has been shown to sometimes have significant inheritance due to the incorporation of calcium carbonate from the surrounding environment, or failure

to behave as a closed system after burial (e.g. *Pigati et al.*, 2010). In the nearby Saty valley, several modern (live) shells were dated at equivalent radiocarbon ages of 0–1000 yrs BP (*Abdrakhmatov et al.*, 2016). Additionally, in dating amalgamated fragments, there is no well well defined heritage, so there may be further inheritance due to post-death redeposition – dating of amalgamated shell samples by *Abdrakhmatov et al.* (2016) yielded ages of 4.5 ka and 8 ka for samples embedded in a medieval soil. As both C10 and C11 are within the terrace gravels and likely have significant inheritance, they only pose an upper limit on the abandonment age of the terrace.

Luminescence Ages

OSL3 was collected from the base of the loess layer in a small channel of mixed loess/silt, cut into the terrace gravels (Figure 3.15c). OSL4 was collected from a coarse sand lens in the uppermost terrace gravels, deposited prior to terrace abandonment (Figure 3.15d). Both samples exhibited reasonably bright quartz OSL signals and dose recovery tests showed that in most cases a known dose could be recovered within 10% of the administered value without a systematic or strong trend with preheat temperature (see Appendix A.2). Though OSL4 was able to broadly recover a consistent dose, it showed significantly more scatter than OSL3. Of the 37 aliquots measured for OSL3, 17 were rejected on the basis of poor recycling ratio and a further 2 for recuperation; the remaining 18 were used to calculate the equivalent dose. The poor recycling and recuperation were most likely due to the dominating of medium and slow components in those aliquots (see §3.3.2). OSL4 performed better, with only 1 of 25 aliquots rejected. We estimate quartz ages of 15.2±1.1 ka BP for OSL3, and 22.6±1.4 ka BP for OSL4 (Table 3.2).

In light of the poor performance of the quartz OSL samples for samples from Rc1, IRSL and post-IR IRSL (pIRIR) measurements were carried out on feldspar extracts from the same samples (see methods in §3.3.2). The $pIRIR_{225}$ approach (§3.3.2) yielded ages of 16.6±0.9 ka for OSL3 and 33.0±2.1 for OSL4.

KBF Summary

The feldspar pIRIR, fading corrected IRSL and quartz OSL agree closely for sample OSL3 within error, giving a post-date on the terrace abandonment of 14.1-17.5 ka BP. Samples C10, C11, and OSL4 are all expected to predate the terrace abandonment and range from 22–39 ka. However, given the poorer dose recovery rates for the quartz OSL of OSL4 and the significant departure from the feldspar pIRIR results, the quartz age may be anomalously young. Our tightest pre-dating estimate is therefore the feldspar pIRIR age of 33.0±2.1 ka BP, consistent with samples C10 and C11 having significant inheritance of ∼3.1 and ∼5.6 ka respectively. Thus our age estimate for the terrace abandonment is 14.1–35 ka, though as discussed by (*Thompson et al.*, 2002) the date from the base of the post-abandonment deposits commonly gives the closest estimate to the terrace age so we might expect an age of ∼15–17 ka, similar to the age of QIII(3) (§3.2.3).

Name	**Site**	**Depth** *(cm)*	**Material**	**Water** *(%)*	**Feldspar grain size** *(μm)*	**Feldspar total dose rate** *(Gy ka-1)*	**Feldspar CAM D_e $pIRIR_{255}$** *(Gy)*	Aliquots n_{255}	**OD** (%)	**Uncorrected IRSL 50°C Age** (ka)	**Fading corrected IRSL 50°C age** *(ka)*	**$pIRIR_{225}$ Age** *(ka)*	**$pIRIR_{290}$ Age** *(ka)*
OSL1	Rc1	70	sand	3.2±3	180-250	5.89±0.23	106±6[a]	21	20	9.0±0.5	15.5±1.5	18.0±1.2	–
OSL2	Rc1	75	sand	7.8±3	180-250	5.37±0.21	127±9[b]	18	26	11.6±0.7	22.3±3.6	23.7±1.9	–
OSL3	S7	180	loess/silt	1.1±3	180-212	4.43±0.18	74±3	16	9	14.4±0.8	17.1±0.9	16.6±0.9	17.4±1.0
OSL4	S7	215	coarse sand	0.8±3	180-212	4.21±0.17	139±7[c]	15	13	27.0±1.8	33.0±2.2	33.0±2.1	40.2±3.1

[a] One high outlier removed
[b] Two high outliers removed
[c] One high and one low outlier removed

Table 3.2: Feldspar pIRIR ages for the luminescence samples, labels are consistent with those for the same samples analysed for quartz OSL. Samples OSL1 and OSL2 showed large overdispersion, generally dim signals and exhibits a significant residual dose after bleaching, suggesting incomplete bleaching may have occurred prior to deposition – they are not used in calculating slip rates. Errors represent 1-σ uncertainties.

Name	**Site**	**Depth** *(cm)*	**Material**	**Water** *(%)*	**Grain size** *(μm)*	**Total dose rate** (Gy ka-1)	**Palaeodose D_e** *(Gy)*	**Aliquots**	**OD** (%)	**Quartz age** *(ka)*
OSL3	S7	180	loess/sand	1.1±3	180-250	3.55±0.16	53.8±2.8	18	15.1	15.2±1.1
OSL4	S7	215	coarse sand	0.8±3	212-250	3.33±0.16	75.3±3.2	24	12.6	22.6±1.4

Table 3.3: Quartz OSL dates for the OSL3–4 samples from the folded terrace at Kegen. OSL3 is believed to be loess fill in a channel cut into the terrace surface, giving a post-date on terrace abandonment. OSL4 was coarser sand material, yields a quartz age significantly younger than the pIRIR age for the same sample and the ^{14}C estimates. Errors represent 1-σ uncertainties.

3.9 GPS Constraints on Fault Creep

To estimate a present day, geodetic slip-rate on the Karkara rangefront and investigate the possibility of fault creep, we fit an edge dislocation model to two N–S profiles through the regional GPS velocity field (*Zubovich et al.*, 2010). The solution for the horizontal displacements (u_x) at the surface due to a dipping semi-infinite edge dislocation at depth d in a uniform elastic halfspace (e.g. *Segall*, 2010), is described by:

$$u_x = \frac{s}{\pi}\left(\cos\delta \arctan\eta + \frac{\sin\delta - \eta\cos\delta}{1+\eta^2}\right) \quad , \tag{3.1}$$

$$\eta = \frac{x - d\cot\delta}{d} \quad , \tag{3.2}$$

where s is the fault slip, d is the depth to the edge dislocation, δ is the fault dip and x is the surface coordinate relative to the fault surface projection. This solution predicts surface displacements for a fault plane locked down to a depth d and stably sliding below. As the problem is linear, the case of a partially locked fault (e.g. with a slower slip rate on the upper section than the lower section) can be treated as two planes slipping at different rates superimposed to add to the correct slip rates. Similarly, changes in fault geometry can be modelled as multiple edge dislocations superimposed.

We investigate profiles P and Q (Figure 3.1b) through the regional GPS data of *Zubovich et al.* (2010), chosen to coincide with the highest density of stations within a swath of ±10 km. Before fitting the data, we subtract the regional strain rate of 0.6x10^{-15} s^{-1} observed for this region by *England and Molnar* (2015).

Profile Q–Q'

Profile Q shows little or no curvature on either side of the fault, suggesting minimal locking. We know from Rc1 (§3.5) that the geometry of the fault in the uppermost ∼1 km of sediments is not entirely constant, so the exact surface projection of the fault plane at seismogenic depths is unlikely to coincide with the surface fault trace. The "worst" case scenario for determining the locking depth is that the fault projects to half way between the two gps stations either side of the fault, so we use that fault location in order to put an upper bound on the locking depth.

We first perform a linear inversion for the slip rate with a zero locking depth and an assumed fault dip of 45°, to estimate an approximate slip rate. This is refined by a grid search in locking-depth – slip-rate space across a reasonable range. Our model estimates a shortening-rate of 3.2±0.3 mm/yr, with a maximum locking depth of ∼1.5 km. The uppermost 1–2 km is primarily Cenozoic sediments, which are unlikely to be able to store significant elastic strain so the fault is most likely creeping right to the surface. Figure 3.16a shows the regional gps data projected onto the line Q–Q', with our best fit model overlain in red. The point in grey was excluded from the inversion, though the model prediction is still within the

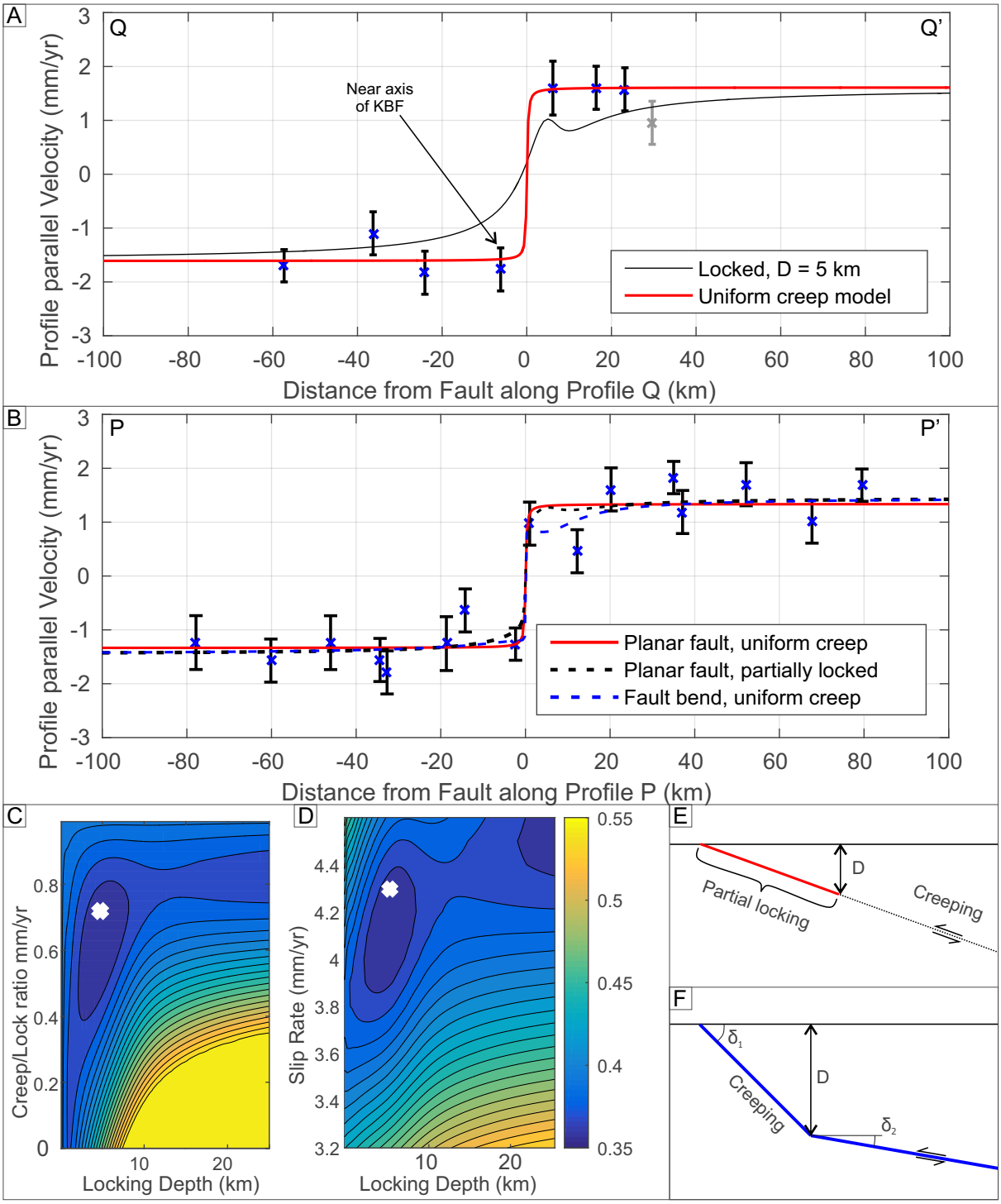


Figure 3.16: (a–b) Modelling of profiles Q and P through the regional GPS field of *Zubovich et al.* (2010), perpendicular to the KRF. Errorbars indicate the 95% confidence interval. Profile Q is well fit by a single planar fault creeping right to the surface, whereas profile P is better fit either by a partially locked upper segment, or a change in geometry at ∼5–10 km depth. Map locations of stations shown in Figure 3.1. (c) Rms well for the locking ratio with locking depth in the partially locked model for profile P. (d) Rms well for the slip-rate with locking depth in the partially locked model for profile P. (e-f) Schematic diagrams of the partially locked model and flat-ramp model giving the fits in (b).

95% error bound; the resultant rms misfit is 0.28 mm/yr. The black line shows a model locked to a depth of 5 km, demonstrating that even relatively shallow locking is a poor fit to the data. This model was validated against the Coulomb model (*Lin and Stein*, 2004; *Toda*, 2005) using a very long and deep fault (under the Coulomb 3.3 program available at http://earthquake.usgs.gov/research/software/coulomb/). As creep appears to reach the surface at the full rate, this profile is insensitive to the fault dip, so an estimate of the slip-rate is dip dependent, but a minimum of ∼3.2 mm/yr makes it the one of the fastest known in the Tien Shan.

Profile P–P'

Profile P shows a large step offset at the fault (location well constrained), but it also shows a broader deflection towards the fault over a wavelength of ∼10 km either side. This could arise from two potential sources; partial locking of the upper fault plane, or changes in fault geometry. We test both of these cases and compare to that of a planar fault creeping all the way to the surface.

Figure 3.16b shows the regional gps data projected onto the line P–P' with our three best fit models overlaid. The black dashed line shows the fit for a simple planar fault creeping to the surface at the full slip rate. This yields a shortening rate of 2.7±0.6 mm/yr, but does not give a good fit to the near fault stations (rms misfit 0.36 mm/yr). The red line represents the same planar fault, but we allow partial locking above a depth D; we solve for the degree of locking (ϵ) and D. This model predicts a shortening rate of 2.9±0.7 mm/yr, with ϵ=0.7±0.2, a poorly resolved locking depth of 6^{+3}_{-2} km, and an rms misfit of 0.36 mm/yr. Lastly, we superimpose a hypothetical model of changing geometry, with the same slip rate creeping right at to the surface. The blue dashed line is the predicted displacement for a 45° fault at depth, which steepens to 60° in the uppermost 7 km. This model gives an rms error of 0.34 mm/yr, lower than either discussed above.

We conclude that a single creeping fault does not provide a particularly good fit to the available data here and underestimates the slip rate, whereas a partially locked fault (slipping at 70% of the full slip rate) or a flat-ramp geometry provide a better fit, with a shortening rate of 2.9±0.7 mm/yr. Given the very close proximity of the stations either side of the fault on this profile, a significant fraction of the fault slip is unambiguously reaching the surface at the mapped fault strand. It is clear from both of the profiles discussed here that the KRF is creeping, most likely at the full slip-rate resolvable from GPS at the present day (discussed further in §3.10.2).

3.10 Discussion

3.10.1 Slip-Rate

We have inspected two fault segments in this study; the KRF (Rc1–6) and the KBF (Figure 3.2). As discussed below, these two surface structures likely link to the same primary fault at depth (Figure 3.19), which is accommodating a large fraction of the motion across the northern edge of the Tien Shan. Dating the displaced Late Quaternary river terraces, we estimate the relative importance of these structures in accommodating the tectonic strain over longer time-scales and compare to the present-day GPS rate.

KRF Slip Rate

Figure 3.17 summarises the terrace ages we have constrained at Rc1 and Rc2 through radiocarbon dating, plotting terrace uplift against age. At catchment Rc1 the ages of T1 and T2 are relatively tightly constrained, at 4–5 ka and 9.6–14.6 ka. Based on the amount of uplift in T1 and T2, we estimate an uplift rate of ∼1.5–2.6 mm/yr (dashed lines, Figure 3.17). The ratios of the heights of T1 and T2 above the present river levels (§3.5) suggest that there was minimal burial in the footwall of the T2 surface, though the uplift of the T2 surface may still be underestimated by up to 20% within the errors observed. It is therefore unsurprising that T2 yields a lower uplift rate – thus we expect an uplift relative to the buried T2 in the footwall at the upper end of the bracket. Also shown are the ages from the upper terraces T3 and T4 at Rc1 (grey points), which are mostly anomalously young and suggest a period of enhanced soil formation after the abandonment of T2. However, C6 would be consistent with a similar uplift rate to those suggested from T1 and T2, suggesting that it may be correct but unaffected by post-depositional carbon exchange.

Estimating a slip-rate and shortening rate for the fault remains difficult as we were unable to find fault exposure to estimate the fault dip. The relatively sinuous fault trace suggests a gentle dip in the shallow sediments, though this may steepen within the basement (c.f. basement faults are often found to be >45° at depth, *Avouac and Tapponnier*, 1993). Using Monte-Carlo simulations (*Thompson et al.*, 2002), we estimate probability distribution functions (PDFs) for the slip-rate and shortening rate based on conservative estimates for the fault dip. We assume that T1 is well dated by sample C3, while T2 is bracketed with a uniform probability density function by the ages of C4 and C5. Taking a dip range of 25–45° (uniform PDF) in the shallow subsurface, this would result in a slip-rate of $3.5^{+1.7}_{-0.4}$ mm/yr (or $2.8^{+1.4}_{-0.7}$ mm/yr based on T2, Figure 3.17). The fault most likely steepens at depth onto an inherited basement structure, so we estimate the shortening accommodated by this fault based on the same slip rate PDF, on a steeper dip of 45–60°, yielding $2.3^{+1.0}_{-0.6}$ mm/yr from T1 ($1.6^{+1.1}_{-0.5}$ mm/yr based on T2, 95% confidence bounds based on estimated PDFs, Figure 3.17).

At catchment Rc2, the age of T2 is not well constrained (red points, Figure 3.17), but assuming an age of 9–14 ka consistent with T2 at catchment Rc1, the uplift rate must be much lower (∼1.0 mm/yr,

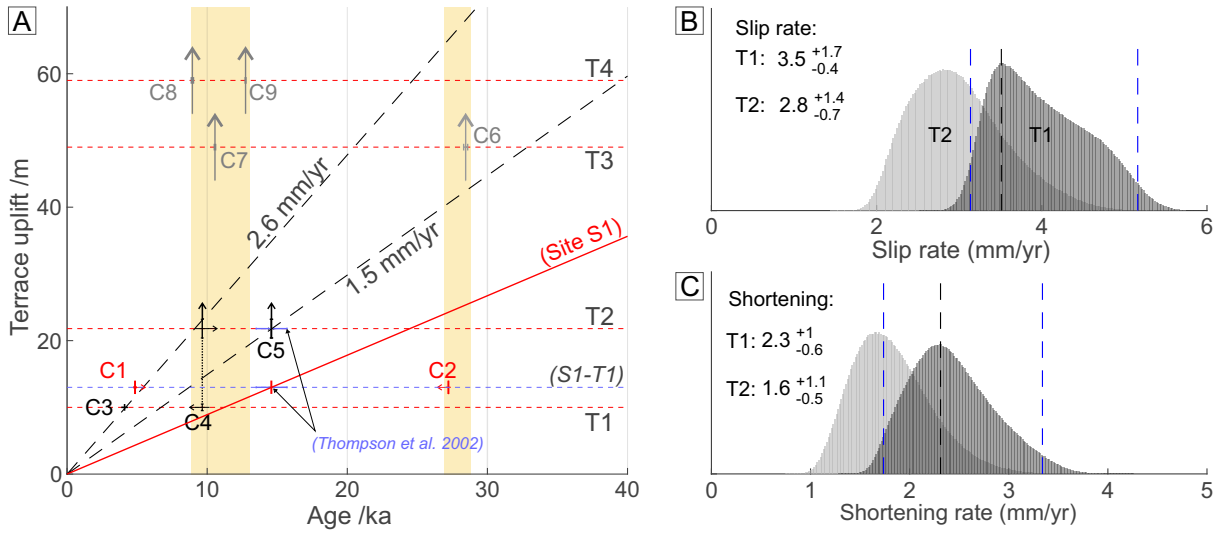


Figure 3.17: (a) Plot of uplift against age for the terraces at Rc1. Points in black represent those used to estimate uplift rates at Rc1. Grey points represent anomalously young ages, possibly due to accelerated soil development or excessive groundwater in the post-LGM period. Red points are those from catchment Rc2, so we might expect a different uplift rate. Horizontal dashed lines represent the estimated minimum terrace uplifts relative to the modern river level. (b-c) Monte-Carlo simulation generated PDFs for the shortening rate and slip rate based on the uplift rates for T1 and T2.

Figure 3.17). This may be due to variation in the slip rate along strike or the fault has a much gentler dip along on this stretch of the fault – consistent with the surface trace splaying further from the rangefront and more folding of the Neogene sediments.

KBF Slip Rate

At the KBF, we observe a broad terrace uplifted by >26 m over a ∼6 km wavelength. OSL, post-IR IRSL and radiocarbon samples constrain the abandonment age of this surface to 14.1–33 ka, suggesting a minimum uplift rate of >0.8 mm/yr. If however, the terrace at Q7 is the QIII(3) terrace of ∼14 ka, it would suggest a much higher minimum of >1.8 mm/yr.

Unfortunately, there is no exposure of fault driving the KBF and we only have structural observations in the core and forelimb of the fold so estimating a slip rate is difficult. The minimum uplift does suggest however a conservative minimum slip-rate of 0.8 mm/yr (or 1.8 mm/yr if QIII(3)). This is still a moderately fast rate for the Tien Shan, so it is likely that this fold also accommodates a significant portion of the regional shortening.

A careful inspection of the regional GPS station locations shows that for profile Q (Figures 3.1), the only station between the KBF surface trace and the KRF is a single one on the folded related topography, very close to the core of the fold. Therefore fault motion on the underlying thrust would translate into mostly vertical displacements, so at this profile we cannot distinguish from the GPS field whether the KRF is creeping or the KBF is growing by creep. As we discuss below though, the scarp morphology at the rangefront is more consistent with creep than those at the basin fold. Regardless, the Kegen fault

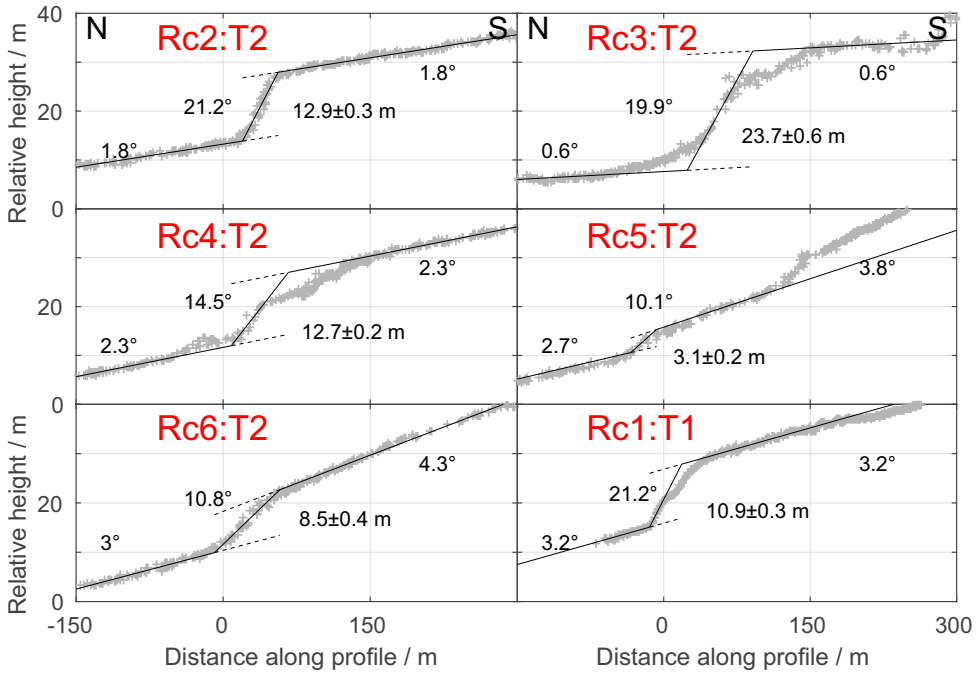


Figure 3.18: Scarps in the lowest main terrace from each catchment Rc1–6. Angles are given for the upthrown and down thrown sides, along with the scarp face angle. Vertical scale is maintained throughout.

accommodates a significant fraction of the regional strain over geological time scales.

Summary – Comparison to Regional GPS

Elastic halfspace modelling of the regional GPS velocity along profiles P and Q gave a consistent shortening rate estimate of 2.9–3.2 mm/yr for both profiles. Both profiles include any motion accommodated by both the KRF and the KBF. We estimate that the KRF has accommodated 1.1–3.3 mm/yr of shortening in the late Quaternary. Without further estimates of the folding geometry at the KBF, we cannot convert our uplift estimate into a corresponding shortening rate – however, given its clear expression in the geomorphology, it is likely that it contributes a further component of shortening. Given the significant error margins in geochronology and fault geometry, our estimates of the shortening in the Late Quaternary are consistent with the geodetic rate, suggesting that the majority of the present-day shortening is accommodated by aseismic creep on these two faults. Apatite fission track data shows that rapid bedrock exhumation has occurred in the Terskey Range over the late Cenozoic (5–3 Ma, *Sobel et al.*, 2006; *Selander et al.*, 2012; *Macaulay et al.*, 2014), our results show a rapid slip-rate through the late Quaternary, and the regional GPS suggest rapid slip at the present. The MTF appears to have played and be playing a major role in the development of the Tien Shan.

3.10.2 Creep

Inspection of the regional GPS velocity field shows a very strong gradient in the northwards velocities at the KRF. Modelling of the two profiles P–P' and Q–Q' (§3.2.1) suggest that the KRF is either creeping

or locked to depths of <3-5 km. However, as discussed by *Marone et al.* (1991), the uppermost few km of basin sediments are generally weak and therefore likely to be in a velocity strengthening regime and unable to nucleate earthquakes. It is likely therefore that creep extends all the way to the surface.

In addition to the GPS data, the shape of the Late Quaternary fault scarp shape also hints at formation by creep. The shape of the scarp in T1 at catchment Rc1 does not conform to a typical scarp diffusion model (e.g. *Wallace*, 1977; *Avouac*, 1993). The upper limb of the scarp shows a broadly curved shape as might be expected, but the lower limb shows very little curvature where it meets the footwall and the face of the scarp is very steep ($\sim 21°$, Figure 3.5). This scarp shape instead fits the profile of a fresh scarp, with mild folding of the hangingwall and a gravity-controlled face at the base (e.g. *Carretier et al.*, 2002). Similarly, the youngest scarp at Rc2 also shows a very steep face ($\sim 21°$, Figure 3.18) As the scarp would be excessively large for a single event and there are no known events over the past hundred years on this fault, the scarp shape is consistent with continuous formation by fault creep, maintaining the 'fresh' appearance and gravity controlled face.

The observed shortening rate makes the Karkara Rangefront one of the fastest faults in the Tien Shan, though even faster rates are observed further SW in the Pamir (*Arrowsmith and Strecker*, 1999). Our observations show that most or all of that slip is reaching the surface as creep, suggesting that strain accumulation across the fault is likely to be minimal at present. This fault may therefore not pose significant seismic hazard compared to the majority of locked faults across the region. Seismic hazard assessments based on the regional strain rate field (e.g. *Holt et al.*, 2005) will overestimate the seismic hazard in the area, as a significant fraction of the strain is being released aseismically. However, the time period of GPS observation is very short compared to the seismic cycle in the region (typically 1–5 ka, e.g. *Abdrakhmatov et al.*, 2001) so it is unclear whether the present creep is indicative of the long term fault behaviour. Most known creeping faults are observed creeping in the decades to centuries following major earthquakes upon them (e.g. *Cohn et al.*, 1982; *Reilinger et al.*, 2000; *Lienkaemper et al.*, 2001). A number of major plate margin faults are also known deform by creep without associated earthquakes, for example sections of the North Anatolian fault (e.g. *Kaneko et al.*, 2012), the Longitudinal Valley Fault (e.g. *Thomas et al.*, 2014) and the San Andreas Fault (e.g. *Steinbrugge et al.*, 1960; *Titus et al.*, 2006). However, very few intraplate faults are observed to creep without a known prior earthquake (e.g. *Jolivet et al.*, 2012; *Copley and Jolivet*, 2016). Except for the 1889 Chilik earthquake attributed to the Saty fault (*Abdrakhmatov et al.*, 2016), there are no known earthquakes which have occurred in the region of the Karkara Rangefront in the last few hundred years, but historic records in the region are generally short and poorly documented (*Campbell et al.*, 2015). The MTF is almost 600 km long, and at the latitude of the KRF it has considerable relief across the fault. In combination with thermochronology observations that suggest early activation of the MTF (*Macaulay et al.*, 2014) we interpret the MTF to be a very mature fault that has accommodated significant total displacement. This is consistent with the other major examples of long term creep on intraplate faults (e.g. San Andreas, North Anatolian

Fault), suggesting that the fault maturity is linked to its strength (*Bürgmann and Dresen*, 2008), allowing deformation by aseismic creep (e.g. *Chester et al.*, 1993; *Kaneko et al.*, 2012; *Carpenter et al.*, 2011).

It is important to note that the GPS velocities of *Zubovich et al.* (2010) give exceptionally dense coverage and the duration of the campaigns has resulted in small errors – there are few surveys of equivalent quality elsewhere. It is therefore quite possible that other intracontinental faults such as this are creeping, but we are unable to resolve them with present geodetic data. Further work is needed along the KRF to further characterise the spatial extent and temporal evolution of the observed fault creep – it offers a unique opportunity to probe the frictional behaviour of a mature fault in an intracontinental setting.

3.10.3 Seismic Hazard

While it appears from the GPS data that the fault is creeping at the full slip-rate at present, the resolution of GPS is limited. By comparison, none of the other faults across the Tien Shan are well resolved in the GPS velocity field and yet have accommodated several large (M8+) earthquakes in the past few hundred years (Figure 3.1, e.g. *Delvaux et al.*, 2001; *Campbell et al.*, 2015; *Abdrakhmatov et al.*, 2016). Thus, there may still be a small amount of strain accumulation below the resolution limit of GPS, which could result in earthquakes. In addition, faults such as the Longitudinal Valley Fault have been shown to sustain earthquakes which nucleate in non-creeping velocity-weakening regions but propagate into velocity strengthening regions that deform primarily by creep (e.g. *Thomas et al.*, 2014).

The greater rangefront of the Terskey Range is almost 600 km in length. It is unclear how far along this structure ruptures could propagate, though the section we primarily focus on in this study is ∼40 km without significant stepovers, suggesting a lower bound. If multiple segments can rupture together however, we could expect very large magnitude events. The evidence suggests that creep is accommodating a large fraction of the fault slip rate at present, which may be the long term mechanism for slip on this fault, but palaeoseismic excavation is required to ascertain whether the fault can sustain earthquakes. The majority of the primary scarps observed along the Karkara rangefront are too large to be attributable to single earthquake events – most terraces are uplifted by >10 m. The only exceptions are the river knick point at Rc1 with a relatively diffuse deflection of 2.5±0.5 m (§3.5) and a terrace offset by 4.8±0.6 m at Rc3 (§3.7). In most locations (Rc1–6) we map multiple small secondary scarps south of the main fault trace with offsets of 1-2 m; these are consistent with hangingwall accommodation structures but it is unclear whether they are formed seismically.

At Rc3, the small scarp of ∼5 m and the numerous secondary scarps warrant further field investigation despite access issues. The secondary scarps in particular present possible targets for palaeoseismology, where there may be access to an earthquake record on a rangefront where the primary scarps are generally too large for trenching.

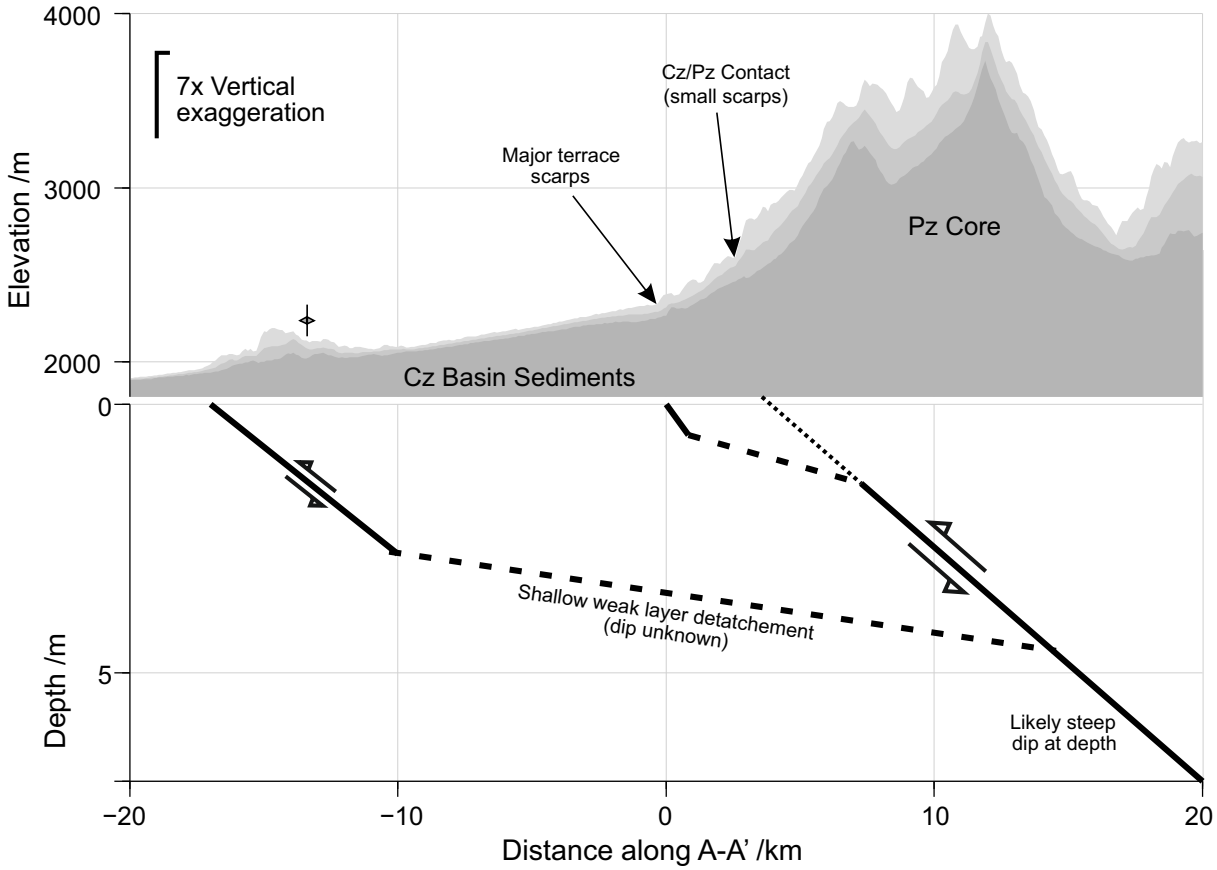


Figure 3.19: Conceptual model of the Karkara Rangefront Fault (KRF) and associated splay structure, the Kegen Basin Fold (KBF).

3.10.4 Regional Terraces & Climate

At Rc1, we constrained the age of the T2 terrace as 9.6–14.9 ka, consistent with this terrace being the QIII(3) terrace in the generalized Tien Shan stratigraphy (§3.2.3). The T1 surface at the same site yields an age estimate of ∼4.1 ka. However, in order to compile the full terrace history, we need to correlate the terraces between valleys along the Karkara rangefront and assign age estimates.

Using the degree of incision and uplift, we attempt to correlate the terraces between valleys along the rangefront. The surface trace of the fault varies in location perpendicular to strike along the range so we expect some variation in fault geometry and hence uplift from site to site. This is accounted for by identifying a common terrace between each river valley and scaling the other terraces relative to it. The most widespread terrace, typically uplifted by ∼20–30 m appears to be the T2 surface, coloured blue in Figures 3.3d, 3.6, 3.9, which we identified at Rc1 as the QIII(3) terrace; we scale the other terraces based on the peak offset of this terrace at each site.

At each site we estimate the maximum uplift for each terrace relative to the modern river channel. If the maximum uplift point is not preserved, we scale the nearest terrace to estimate the shape of the terrace at the peak point. Where a terrace surface is poorly defined or heavily modified, large uncertainties are assigned. We also exclude the very short wavelength (<200 m) feature showing enhanced uplift very

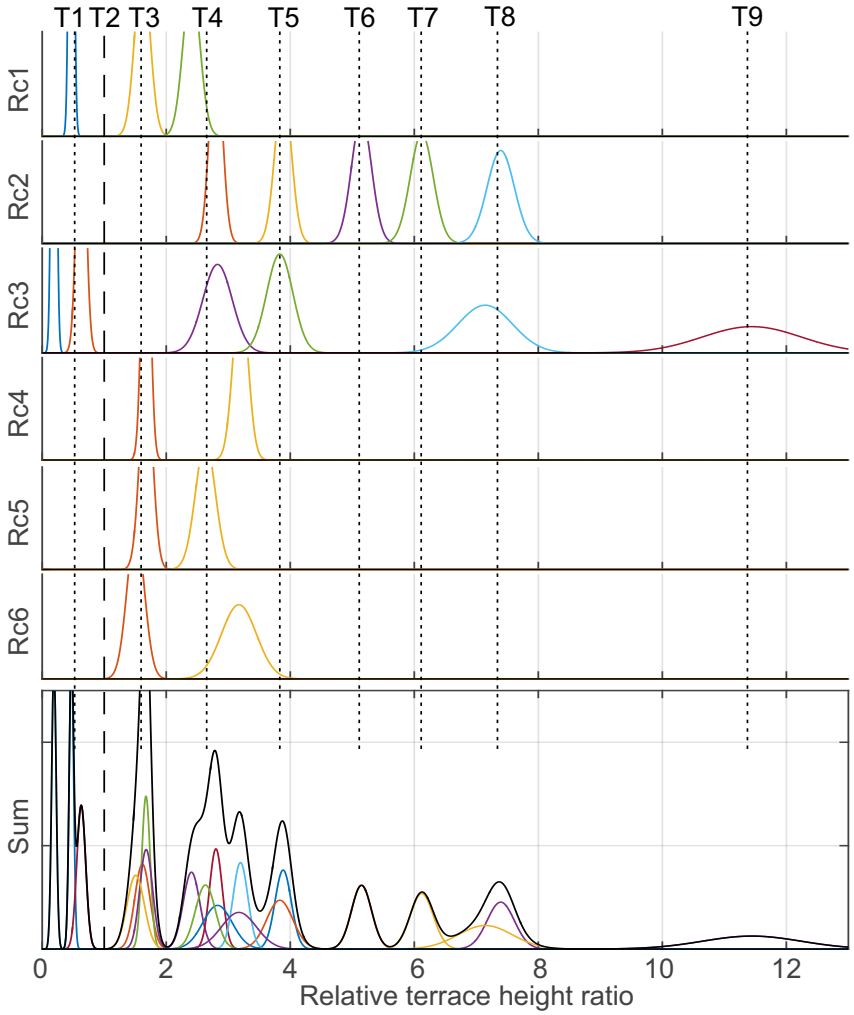


Figure 3.20: (a) The probability distribution functions for each terrace at each site, scaled by then height of the assumed T2 above present river level at each location. Each measurement is assumed to be gaussian distributed. (b) Summed probability distribution functions from (b). Despite some variation between sites, we see several reasonably well correlated terraces between the valleys.

close to the fault trace in the T1 and T2 terraces at catchment Rc1 as this likely reflects a steepening of the fault in the very shallow subsurface only. Figure 3.20 shows the resulting probability distribution functions (PDFs) for the relative uplift ratios for each site and the summed PDF. Though noisy, we get good correlation at ∼1.6, ∼3.9, ∼5.2 and ∼7.3 times the height of the T2 surface, with more weakly constrained terraces at ∼0.5, ∼2.8, ∼6.1 and ∼11.5 times. Scaling the age of T2, we estimate the ages of each of the 8 other terraces assuming a constant uplift rate (Table 3.4).

Despite being uplifted by >300 m at Rc3, T9 is very well preserved over a large area (including several sub-terraces) and visible extending westwards along the rangefront (Figure 3.9a). Given the well preserved nature and the age estimate of 100–180 ka, we suggest that this is the QII(2) terrace in the generalized Tien Shan stratigraphy dated elsewhere to be 100–140 ka (§3.2.3).

Similar to *Molnar et al.* (1994) we observe prominent terraces which coincide well with the past two glacial maxima, T1 and T9, and we further note a weak periodicity of ∼12–15 ka in the terrace formation,

though this scales with the assumed age for the T2 surface (here 9.6–14.6 ka). In the Qilian Shan of China, *Pan et al.* (2003) and *Pan et al.* (2007) observe sequences of terraces which they date up to 1.24 Ma, the most recent of which is dated at ∼10 ka. Based on the tight correlation with the 100 ka cycles in the $\delta^{18}O$ record, they conclude that the cold-to-warm transitions following the major glacial periods play a major role in controlling terrace formation across the region. Along the southern edge of the Tarim Basin, extensive slip-rate and palaeoearthquake investigations have dated numerous Late Quaternary fluvial terraces along the Altyn-Tagh and Kunlun faults (e.g. *Van Der Woerd et al.*, 2002; *Mériaux et al.*, 2004; *Cowgill*, 2007; *Elliott et al.*, 2015a). In particular, *Van Der Woerd et al.* (2002) compare the ages of 31 displaced terraces to the $\delta^{18}O$ record, also finding evidence for correlation with the 100 ka climate cycles; the authors extend their analysis along the fault to estimate the ages of numerous other offset landforms along strike. The majority of these studies observe a prominent terrace at ∼10 ka and ∼100-140 ka in close agreement with our results, consistent with climatic formation mechanism. It is less clear how well the intermediate terraces correlate regionally, as they are typically less well preserved and generally only a subset are preserved at any one site.

Terrace	Min. Ratio	Max. Ratio	Age (ka)
T0	0.15	0.23	1.4–3.4
T1	0.43	0.63	4.1–9.2
T2	-	-	-
T3	1.5	1.8	14–26
T4	2.4	3.2	23–47
T5	3.7	4.0	36–58
T6	5.0	5.3	48–77
T7	6.0	6.3	57–91
T8	6.9	7.7	67–112
T9	10.8	12.2	104–178

Table 3.4: Correlated terrace heights relative to the T2 terrace estimated from the summed PDFs (Figure 3.20). Ages are based on the estimate for T2. Age ranges represent the minimum–maximum plausible age based on the reconstruction.

If the assumption of a constant uplift rate holds over the last few hundred ka, then the terraces could provide a proxy for the ages of periods of climatic change, as suggested by *Thompson et al.* (2002) and *Van Der Woerd et al.* (2002). Further work needs to be carried out to validate this hypothesis, but based on the observed ages for T1 and T2, the terrace correlation suggests periods of increased fluvial output at the periods given in Table 3.4. However, the large errors in the abandonment ages combined with the errors in the displacement measurements give large error bounds on these ages, so further geochronology is necessary to strengthen the correlation.

3.11 Conclusions

We estimate the slip rate of the Karkara Rangefront Fault as $3.5^{+1.7}_{-0.4}$ mm/yr and a minimum uplift rate of 0.8 mm/yr (though possibly as large as 1.8 mm/yr) for the Kegen Basin Fold. Based on a conservative estimate of a steeply dipping basement fault, we estimate a minimum equivalent shortening rate of 1.1–3.3 mm/yr across the rangefront. This is the fastest known fault slip-rate in the northern Tien Shan, but elastic halfspace modelling of the regional GPS shows that at present this is mostly accommodated by creep, suggesting that there is minimal strain accumulation at present within GPS resolution. Major earthquakes (M8+) have occurred in the past two centuries on other faults in the region that are completely unresolved in the regional GPS velocity field, so this fault may still be capable of earthquakes – further palaeoseismic investigation is necessary as the rangefront length suggests the potential for very large magnitude events. We have also demonstrated the utility of structure-from-motion and satellite-stereo photogrammetry, allowing accurate quantification of offsets in features displaced by faults at a variety of scales, and correlation of terraces along the rangefront. We find evidence for a major terrace surface displaced to ∼300 m above present river level which based on a constant slip-rate, may be the QII(2) surface of the general Tien Shan stratigraphy.

Chapter 4

Active Shortening in the Kazakh Tien Shan

4.1 Aims

The mountain ranges of central Asia (Pamir, Tien Shan, Borohoro Shan, Dzhungarian Alatau, and the Kazakh and Mongolian Altai) represent the northernmost expression of the India-Eurasia collision zone (*Molnar and Tapponnier*, 1975; *Tapponnier and Molnar*, 1979; *Bullen and Burbank*, 2001). Regional GPS velocities show that the Tien Shan account for almost half (∼15–20 mm/yr, §4.3) of the total India–Eurasia plate convergence at present, distributed across numerous faults, generally with slip rates of <1 mm/yr (*Abdrakhmatov et al.*, 1996; *Thompson et al.*, 2002; *Zubovich et al.*, 2010). Central Asia is an under-studied area of potentially high seismic risk; deep in the continental interior, the strain rates are low and faults have long recurrence intervals (typically >1–5 ka), but the potential for large, rare earthquakes (*Delvaux et al.*, 2001; *Campbell et al.*, 2015; *Abdrakhmatov et al.*, 2016). The lack of slip-rate data and incomplete mapping of active faults, mean that current seismic hazard assessments (*Giardini et al.*, 1999; *Abdrakhmatov et al.*, 2003; *Bindi et al.*, 2012) are based on instrumental seismic and geodetic observations that only sample a small fraction of the seismic cycle. As the historic and instrumental records are much shorter than the seismic cycle, exploit the geologic and geomorphic records of surface faulting.

Here I perform an investigation of compressional faulting through the Kazakh Tien Shan, the Ili Basin and the Dzhungarian Alatau (Figure 4.1), presenting a collection of geological slip-rate studies and palaeo-earthquake behaviour estimates wherever possible, to construct a transect of geological shortening rates (line A-A" in Figure 4.4). Comparing my geological shortening rate estimates to those indicated by geodetic data (§4.3), I aim to determine which faults are likely to be the most seismically active and, in combination with palaeoseismology wherever possible, estimate possible earthquake magnitudes and

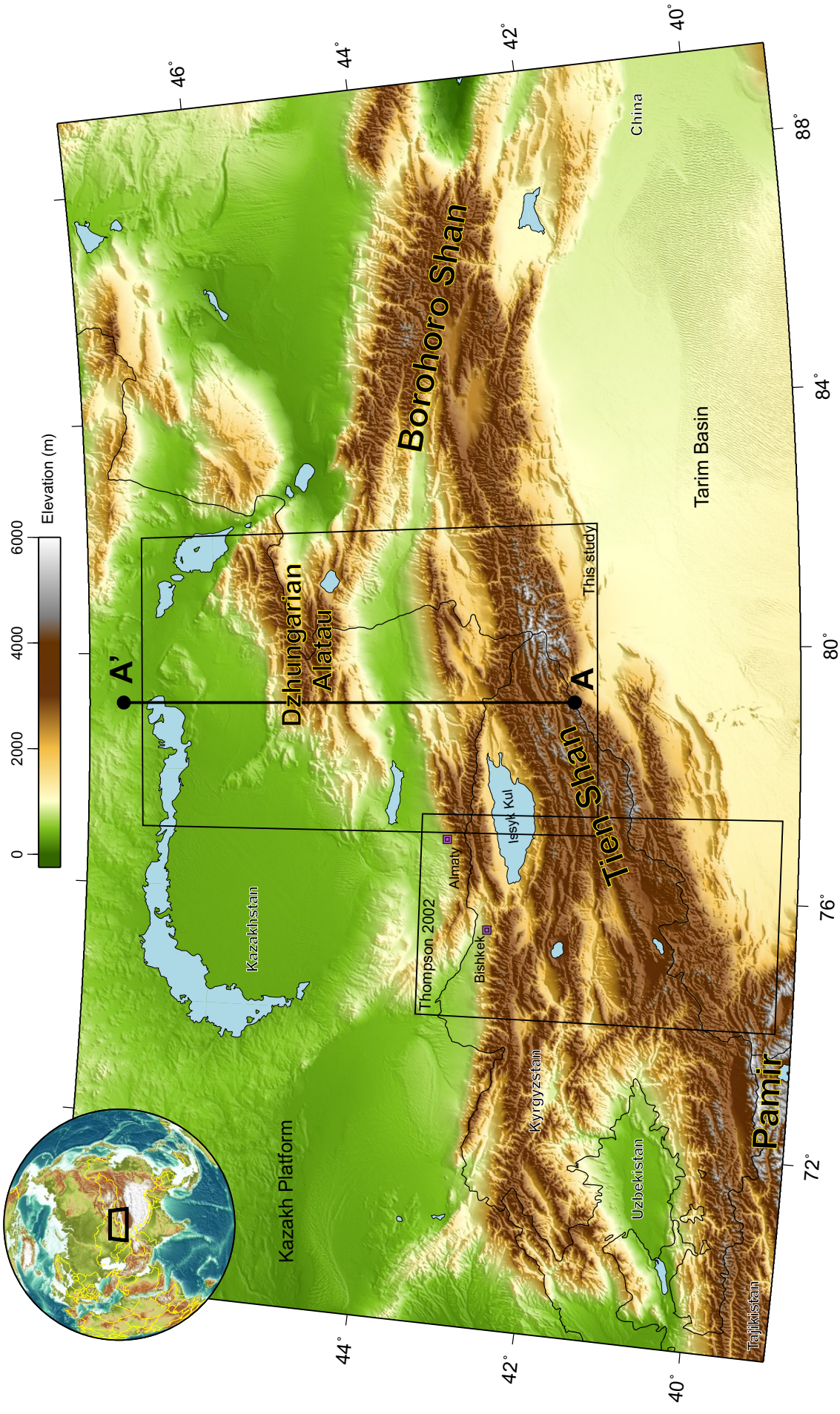


Figure 4.1: Overview of the Tien Shan of central Asia. At the longitude of my transect, the mountain belt has quite a different structure to that at the transect studied by *Thompson et al.* (2002).

recurrence intervals on the faults. Much of the background tectonic and geologic setting of the Tien Shan was covered in Chapter 3, so here I summarise the regional velocity field and introduce the Dzhungarian Alatau only.

I break the transect into four distinct sections (Figure 4.4); the Kegen Basin (mostly covered in Chapter 3), the southern half of the Ili Basin (§4.7), the northern half of the Ili Basin (southern margin of the Dzhungarian Alatau, §4.8), and the northern margin of the Dzhungarian Alatau (§4.9). I step through the transect from south to north, introducing each fault and range in turn, drawing from earlier chapters and introducing previous work where it exists. Section §4.10 draws together all of the findings, discussing the implications for the distribution of shortening, while §4.12 summarises the implications for seismic hazard.

My study complements a previous study carried out further west, in Kyrgyzstan, by *Thompson et al.* (2002) (Figure 4.1). Several older studies have also estimated shortening rates on individual faults further east in the Borohoro Shan, China, based on alluvial fan ages estimated from climate records and several radiocarbon ages (e.g. *Avouac and Tapponnier*, 1993). Along my transect, only two faults have documented slip rates (*Campbell et al.*, 2013; *Cording et al.*, 2014) and only one is believed to have failed in a historic earthquake (*Abdrakhmatov et al.*, 2016).

At the longitude of the *Thompson et al.* (2002) study, the Tien Shan are characterised by well distributed 'quasi-periodic' ranges separated by intramontane basins. By comparison, at the longitude of A–A' they are comprised of two discrete series of ranges separated by the intermontane Ili Basin. The Terskey Ranges and the Dzhungarian Alatau are each characterised by a high, mountainous core, flanked by a series of smaller ranges each separated by small intramontane basins (Figure 4.1–4.4). This suggests a different distribution of shortening at this longitude compared to the ranges further east and west.

The main focus of this work are the E-W striking thrust faults that exist throughout the study area. I pay less attention to the strike-slip faults, though they may also play a role in accommodation of shortening (*Campbell et al.*, 2013, discussed in §4.10.2). Initial reconnaissance was performed by remote sensing using high resolution optical satellite imagery (Kompsat-2 1 m, Pleiades 0.5 m, GoogleEarth® and BingMaps®), to map the active faults and identify well situated sites for field studies. Two faults on the transect have been studied previously: the Lepsy fault, (*Campbell et al.*, 2015) and the Usek Thrust (*Cording et al.*, 2014), LP and UT in Figure 4.4. At each of the other faults, I have studied both single event and multiple event late Quaternary scarps (wherever preserved), employing a variety of dating techniques to constrain (a) the age of the last event, (b) the slip rate on the fault, and (c) earthquake recurrence intervals.

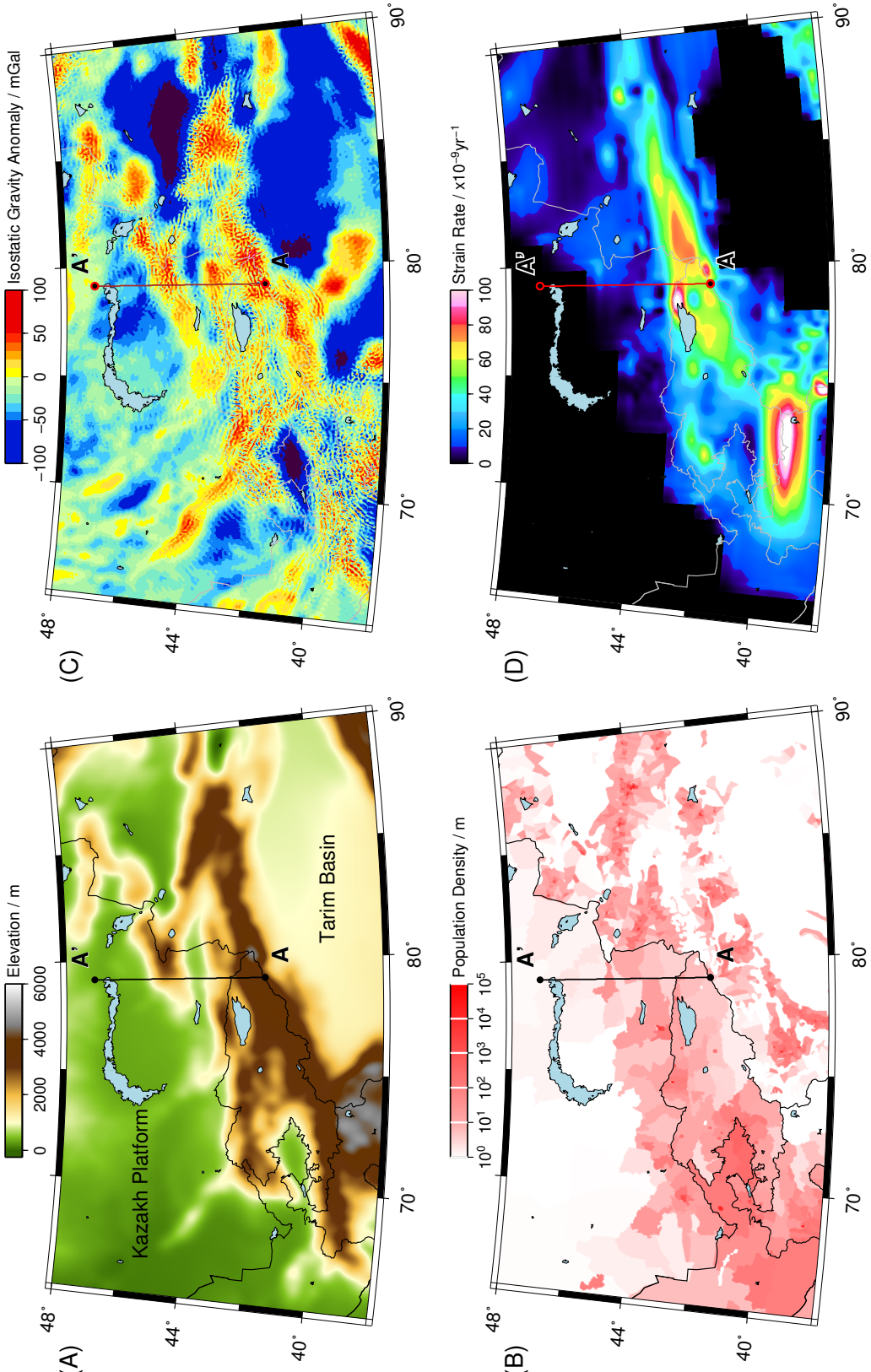


Figure 4.2: (a) Long wavelength topography of the Tien Shan and Pamir ranges (ETOPO smoothed at a 100 km wavelength). (b) Population density map of Central Asia (*Center for International Earth Science Information Network (CIESIN)*, 2016). (c) WGM-2012 Isostatic gravity anomaly map of the same region, showing a relatively strong positive anomaly over the eastern Tien Shan (*Balmino et al.*, 2012) (d) Strain rate map covering the same region from the GSRM project, combining geodetic rates with earthquake mechanisms (*Kreemer et al.*, 2003). The high strain rate spot at the eastern end of Lake Issyk Kul relates to the KRF (Chapter 3). Other focus points may exist, but the resolution of the geodetic networks is insufficient to observe them.

4.2 Geodynamic Context

The Tien Shan (TS) Orogen is a zone of intense deformation between the relatively strong, old and rigid cratonic crust of the Tarim Basin and the Kazakh Platform. Lithospheric thickness maps compiled from surface wave tomography (*Priestley et al.*, 2006) and ambient noise tomography (*Gao et al.*, 2014; *Gilligan et al.*, 2014) suggest a thin lithosphere beneath the TS, in contrast to the Tarim Basin and Kazakh platform which exhibit a much thicker, and hence stronger lithosphere. The lithospheric heterogeneity is suggested as a reason for the intense deformation within the Tien Shan; to the weaker lithosphere allows substantial deformation, whereas the stronger platforms on either side show relatively little internal deformation (e.g. *Roecker et al.*, 1993; *Zubovich et al.*, 2010). This is consistent with the earthquake sources observed within the TS and surrounding forelands; *Sloan et al.* (2011) and *Alinaghi and Krüger* (2014) observe only shallow (<20–30 km), upper crustal earthquakes within the TS, whereas deeper (>20–30 km), lower crustal earthquakes occur within the platforms, suggesting a strong lower crust (Figure 4.3).

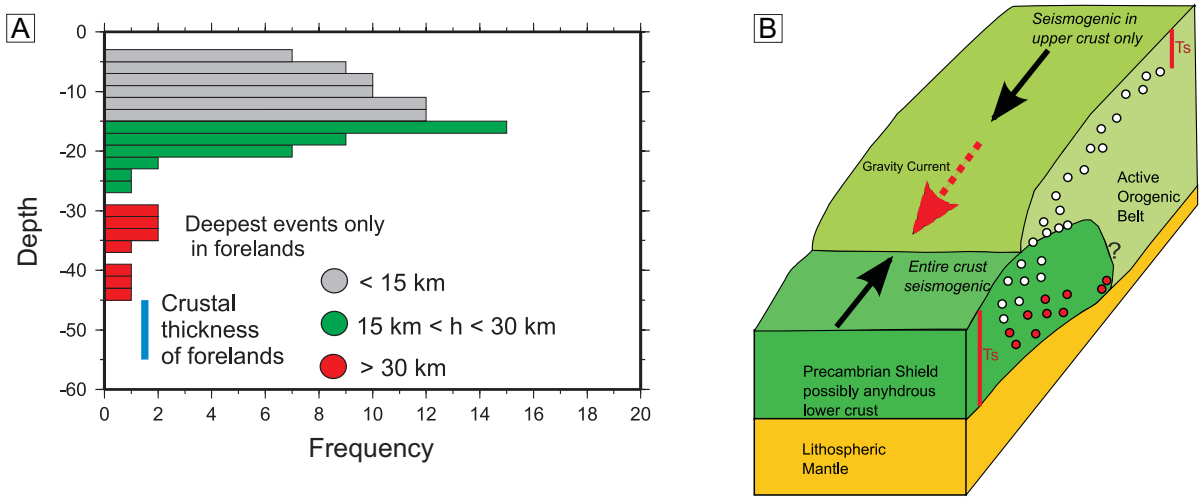


Figure 4.3: (a) Adapted from *Sloan et al.* (2011), Figure 3D. Depth histogram for earthquakes in the Tien Shan and its forelands. Lower crustal earthquakes are only observed in the forelands. (b) Schematic model of the crustal structure on the margins of the Tien Shan, Adapted from *Sloan et al.* (2011), Figure 9.

Seismic tomography (e.g. *Zhiwei et al.*, 2009), receiver function and surface wave studies (*Vinnik et al.*, 2004, 2006; *Makarov et al.*, 2010; *Gilligan et al.*, 2014; *Li et al.*, 2016) and gravity studies (*Burov et al.*, 1990; *Steffen et al.*, 2011; *Kaban and Yuanda*, 2014) suggest a deep cold root on the southern margin of the TS, suggesting underthrusting or subduction of the Tarim Basin beneath the belt (e.g. *Mattauer*, 1986; *Poupinet et al.*, 2002). The northern margin is more poorly resolved, but there is suggestion of underthrusting of the Kazakh platform beneath the northern TS also (e.g. *Zhiwei et al.*, 2009; *Zabelina et al.*, 2013). Within the central TS, receiver function studies and shear wave splitting analysis suggests an anomalous high velocity zone beneath the central part of the TS, indicating high temperatures and suggesting that the Tarim lithosphere may have delaminated and the range may be supported by hot

asthenospheric material, potentially arising from small scale convection under the TS (e.g. *Roecker et al.*, 1993; *Liu et al.*, 2007; *Cherie et al.*, 2016).

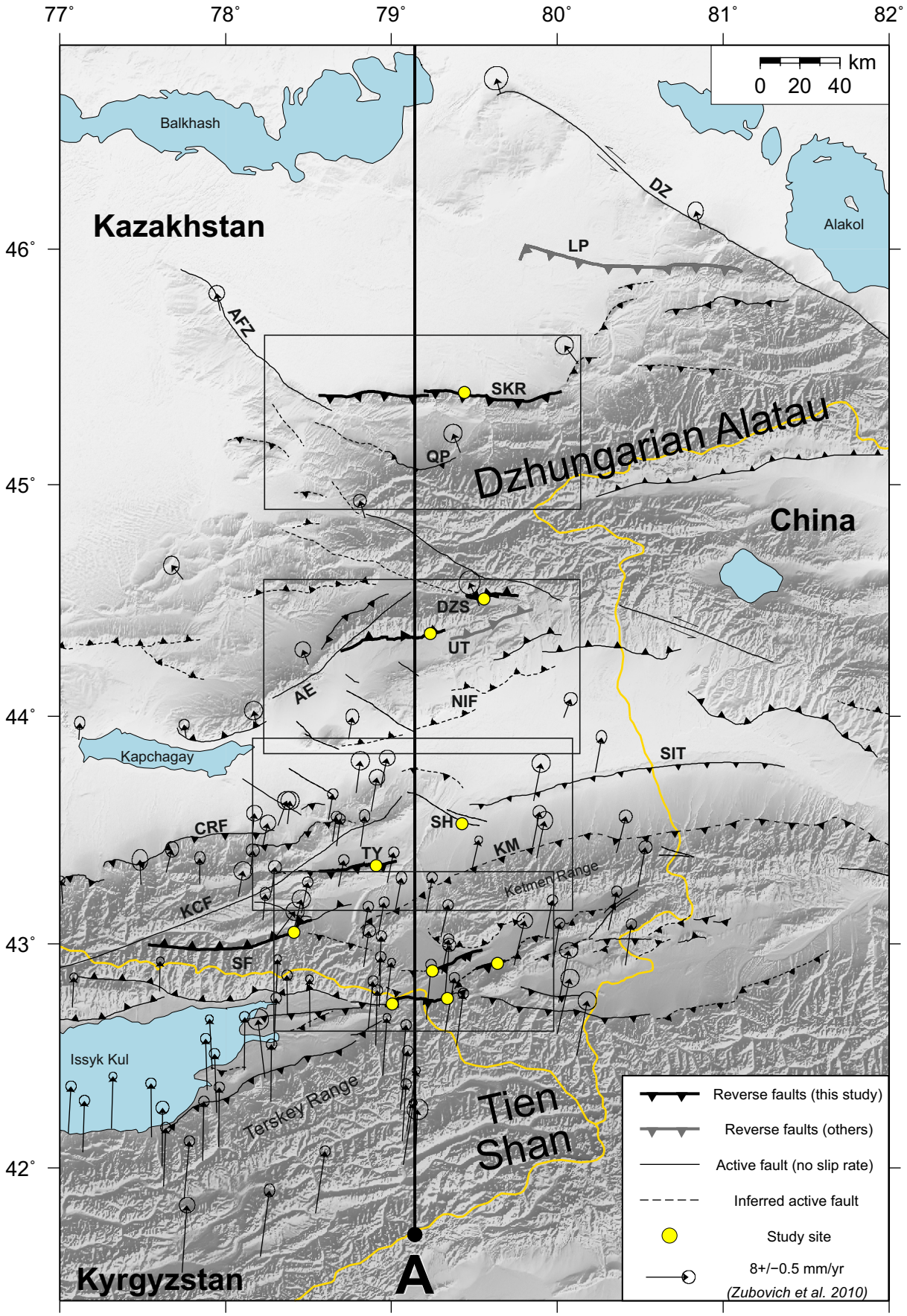
The resolution of these seismic and gravitational methods have very coarse resolution, making it difficult to associate the geodynamics with surface structures. However many authors observe strong lateral variations in the geodynamic observations along the length of the TS (*Burov et al.*, 1990; *Roecker et al.*, 1993; *Priestley et al.*, 2006; *Lei*, 2011; *Zabelina et al.*, 2013; *Gao et al.*, 2014; *Kaban and Yuanda*, 2014; *Cherie et al.*, 2016), especially between the Western and Central TS, but also to a lesser degree between the Eastern and Central TS. The isostatic gravity anomaly (Figure 4.2c), modern strain rate field (Figure 4.2d), long wavelength topography (Figure 4.2a) and tomography observations all show significant variation E-W across the Tien Shan, yet the mechanism reason for this change is not yet understood. The transect of slip rates measured by *Thompson et al.* (2002) cover the western TS; by comparison the central/eastern TS are in a substantially different geodynamic regime. Thus, differences in the distribution of faulting between our transect and that of Thompson et al. may help to better resolve and understand the difference in the underlying geodynamics.

4.3 Modern Strain Rate Field

The modern strain rate field in the Tien Shan (Figure 4.2d) shows a strong correlation with the topography field. The transect studied in this chapter was chosen to coincide with the narrow region showing a particularly high strain rate at the eastern end of lake Issyk Kul but lower strain rates to the north and south. This is in contrast to the wide region of moderate strain rates at the Thompson et al. transect in Kyrgyzstan. Comparing the strain rate field to the population density map for Central Asia (Figure 4.2b,d) highlights the strong correlation between the population centers and zones of active deformation, likely due to water demand (e.g. *Jackson*, 2008). Establishing the distribution of faulting and accommodation of regional strain is therefore vital for the characterisation of seismic hazard. Wherever possible we also attempt to constrain the recurrence intervals and magnitudes of the faults studied.

Figure 4.5 shows the regional gps velocities along the transect A–A' projected from a ±40 km swath.

Figure 4.4 ***(following page)*:** An overview of the Kazakh Tien Shan and Dzhungarian Alatau in shaded relief from SRTM elevation data (outline in Figure 4.1). Faults shown in bold are those I have performed slip-rate studies on, with individual field sites shown in yellow. Other known active faults are also marked, with inferred faults shown dashed. The *Zubovich et al.* (2010) regional GPS vectors (relative to fixed Eurasia) are shown with 95% confidence ellipses and the line A-A" is the profile onto which the GPS is projected in Figure 4.5. Boxes show the locations of Figures 4.6, 4.15, 4.25 and 4.40 (S to N respectively). Labels: SF – Saty Fault, KCF – Kemin-Chilik Fault Zone, TY – Toraigyr Fault, KM – Ketmen Rangefront Fault, SH – Shonzhy Faults, SIT – South Ili Thrust, CRF – Chilik Rangefront Fault (not discussed), NIF – North Ili Fold system, UT – Usek Thrust, AE – Altyn Emel Fault, DZS – Dzhungarian Alatau Southern Rangefront, QP – Qapal Fault, AFZ – Aktas Fault Zone, SKR – Sarkand Rangefront Fault. Mapped but not labelled (see Figure 4.6): KRF – Karkara Rangefront Fault, SJZ – Saryjaz Rangefront Fault, KBF – Kegen Basin Fold, KG – Kegen Rangefront. The active fault mapping is based on maps of *Tapponnier and Molnar* (1979); *Delvaux et al.* (2001); *Deng et al.* (2003, 2004); *Macaulay et al.* (2013); *Campbell et al.* (2013) and my own field and remote sensing mapping, and forms a component of the COMET (Center for Modelling of Earthquakes and Tectonics) Active Fault compilation for Central Asia.


77˚
78˚
79˚
80˚
81˚
82˚
46˚
45˚
44˚
43˚
42˚
km
0 20 40
Balkhash
Kazakhstan
DZ
Alakol
LP
AFZ
SKR
QP
Dzhungarian Alatau
China
DZS
UT
AE
NIF
Kapchagay
SIT
CRF
SH
KM
TY
Kelmen Range
KCF
SF
Issyk Kul
Terskey Range
Tien Shan
Kyrgyzstan
A
Reverse faults (this study)
Reverse faults (others)
Active fault (no slip rate)
Inferred active fault
Study site
8+/−0.5 mm/yr
(Zubovich et al. 2010)

The total shortening accommodated by the Tien Shan and Dzhungarian Alatau at this longitude is around 15-20 mm/yr, though further east in China this drops to ∼10 mm/yr in in the Borohoro Shan due to the clockwise rotation of the Tarim basin (*Zubovich et al.*, 2010).

With the exception of the the KRF (Chapter 3), the northwards velocities show no major steps, indicating distributed shortening right across the region i.e. no of the other faults (shown dashed in Figure 4.5) are resolved. The westward components of the velocities in general show very little profile-perpendicular motion, except at the latitude of the Ili Basin where there is a step of 2–3 mm/yr – also visible as a rotation in the velocity vectors (Figure 4.4). The spatial sampling of the GPS in this region is relatively low (∼60 km), so it is difficult to ascertain which structures accommodate this. In addition, this profile may not be optimally oriented to capture the maximum principle strain in either component in this region. The accommodation of this shear is discussed in §4.10.2.

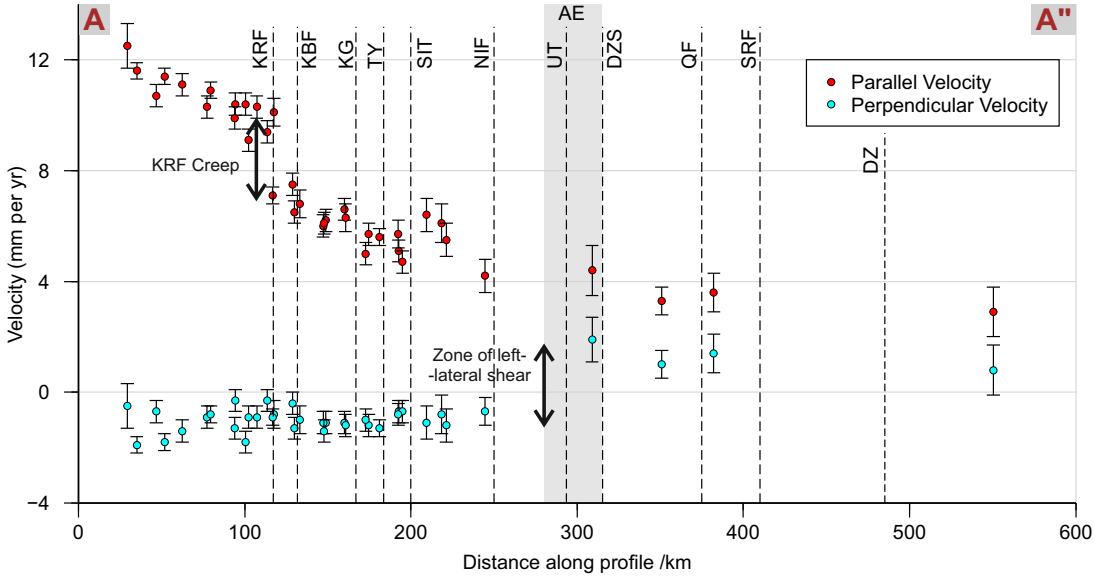


Figure 4.5: Regional GPS data from *Zubovich et al.* (2010) projected onto the line A-A", resolved into profile-parallel (red) and profile-perpendicular components. Stations from within 40 km either side of the profile are shown. Faults mapped in Figure 4.4 are shown as dashed lines (see Figure 4.4 caption for fault labels). Shown as a shaded region is the approximate projection of the sub-perpendicular Altyn Emel (AE) strike slip fault. I observe a significant drop of ∼3-4 mm/yr in the northwards (parallel) velocity across the Karkara rangefront, but the majority of the faults are unresolved. The Altyn Emel fault (AE, Figure 4.4) may be responsible for the change in profile perpendicular (Westward) velocity at 250-300 km.

4.4 Methods

In order to accurately quantify morphological offsets, I use aerial photos acquired from a Helikite or quadcopter drone to construct digital elevation models (DEMs) by structure-from-motion (SfM) based photogrammetry (described fully in §3.3.1). I have used these DEMs to quantify earthquake surface slip distributions along strike, in order to estimate palaeo-earthquake magnitudes and discern between single event and cumulative fault scarps. While rasterised DEMs were used for visualisation, all analyses were

performed directly on the pointcloud to avoid gridding interpolation.

For the majority of our sites, I date the displaced markers by a combination of radiocarbon dating and quartz/feldspar optically/infrared stimulated luminescence (OSL/IRSL). For a surface at the Toraigyr fault (§4.7.1) without material for radiocarbon/OSL/IRSL dating, I used cosmogenic Be-10 dating. In one further location, I also used Uranium-Thorium dating on stratified carbonate cements within an alluvial deposit. The techniques used for OSL, IRSL and radiocarbon dating were described in previous chapters (§3.3.2 and Appendix A.2), but I outline below (§4.4.1, §4.4.2) the methods used for ^{10}Be and U-Th dating.

4.4.1 ^{10}Be Dating[1]

The incidence of high energy cosmic rays on the earth surface gives rise to the production of cosmogenic radionuclides (CRNs) within common rock minerals. The basic evolution of the concentration of CRNs for a parcel of rock is governed by the differential equation balancing production and decay:

$$\frac{dN}{dt} = P - \lambda N \quad , \tag{4.1}$$

where P is the production rate, N is the number of CRNs and λ is the decay constant ($\lambda = \log \frac{0.5}{t_{1/2}}$, for isotope half life $t_{1/2}$). The CRN 'clock' therefore saturates once sufficient CRNs have accumulated such that the production rate is balanced by isotopic decay.

Charged cosmic rays are guided towards the geomagnetic poles by the Earth's magnetic field, so incidence rates and hence production rates are strongly dependent on geomagnetic latitude, with reduced flux near the poles. The attenuation length of cosmic rays in the lower atmosphere is ∼1.5 km, so the production rate is also strongly altitude dependent. The production rate contains the complexity arising from geomagnetic latitude and altitude, but also environmental shielding – the orientation of the surface relative to the surrounding topography must be accounted for in a 'shielding' calculation based on the surrounding topography. Production rates are calibrated by latitude and altitude from sites such as glacially polished bedrock surfaces, with ages constrained by other methods (e.g. *Clark et al.*, 1995). If erosion is negligible, the isotope half life is known, and the production rate can be estimated, geomorphic surfaces exposure ages can therefore be estimated through the measurement of CRN concentrations in a surface rock parcel (e.g. *Burbank and Anderson*, 2011).

Quartz is a common target mineral, with ^{10}Be being produced from ^{18}O and ^{26}Al being produced from ^{32}Si at reasonable rates with appropriate half-lives and decay chains, though other target minerals can be used (*Benedetti et al.*, 2003, e.g. ^{36}Cl in limestone,). Given the minerals available in this study, I have exploited ^{10}Be production in quartz rich granites (e.g. *Gosse and Phillips*, 2001). ^{10}Be has a half life

[1]Initial crushing, sieving and magnetic separation was performed by myself, but the wet chemistry and AMS were performed by Angel Rodés and Sheng Xu, at the Scottish Universities Environmental Research Center (SUERC) Cosmogenic Isotope Analysis Facility (CIAF) funded under a successful NERC CIAF-SC proposal.

of ∼1.5 Ma (*Holden*, 1990), a timescale appropriate for measuring exposure dates from several thousand years (to accumulate measurable quantities) out to the late Pliocene (saturation due to isotope decay).

In general, a simple rock parcel exhumed instantaneously from depth to a stationary non-eroding surface, is not a sufficient model for a given feature – the material (bedrock or alluvium) will have had some exposure prior to deposition/emplacement. In this study I have dated an alluvial fan surface displaced by faulting; prior to exhumation the material will generally have been buried for a long time relative to the half life so any ^{10}Be will have decayed. However, the material will generally have some unknown exposure between exhumation and deposition. Cosmic rays attenuate exponentially with depth through sediment (e-folding length of ∼50–60 cm), so by measuring a depth profile of ^{10}Be concentrations down to depths of 1.5–2 m, I can fit an exponential decay assuming instead that all the samples have been exposed to similar pre-burial transport, and hence have the same inheritance. In the case of an eroding surface, further corrections can be added to model the erosion rate. If the uppermost 10's cm has been significantly bioturbated, the uppermost sample will not fit the exponential decay well, and is often disregarded in fitting the exposure age (e.g. *Nissen et al.*, 2009; *Burbank and Anderson*, 2011).

4.4.2 U-Th Decay Chain Dating[2]

^{238}U–^{234}U–^{230}Th dating (U-series) can be used to date the age of deposition of pedogenic carbonate (e.g. *Ku et al.*, 1979; *Sharp et al.*, 2003). Uranium is relatively soluble in ground water, and is therefore incorporated into carbonate as it is deposited, in a similar ratio to the U/Ca^{2-} in the water. By contrast, ^{230}Th is insoluble, so fractionation occurs (e.g. *van Calsteren and Thomas*, 2006) with (ideally) only the Uranium incorporated. The radioisotope decay of U to ^{230}Th through well defined pathways of known half-life, allows the time of deposition to be estimated.

In practice, detrital contamination occurs due to the incorporation of silicic particles within the carbonate, introducing an amount of ^{230}Th and uranium with a different ^{234}U/^{238}U ratio, generally biasing the age estimate to older values. This is accounted for by using the ^{232}Th/^{238}U ratio as a proxy for the amount of contaminant (*van Calsteren and Thomas*, 2006). The isotopic composition of the contaminant is assumed to be approximately that of continental crust, using a U-series archive dataset from the EarthChem dataset (http://www.earthchem.org), the uncertainties of which are propagated to the final ratios.

In this study, I utilise U-series dating to estimate the deposition age of layered carbonate rinds that have formed on the undersides of pebbles within alluvial fans. Carbonate is deposited only on the undersides of the pebbles, so where rinds are observed consistently in the correct orientation, they must have been deposited after emplacement within the fan – typically this occurs within 2 m of the surface (*Birkeland*, 1984). The rinds grow progressively outwards, so the innermost rind therefore provides a

[2]Carbonate milling and U-series chemistry and analysis was performed by Andrew Mason in the Oxford Earth Sciences Department.

minimum age constraint on the fan surface. Where sufficient thickness of rind is present, a progression series can be measured to improve the reliability of the result (e.g. *Gregory*, 2012).

4.4.3 Monte-Carlo Slip Rate Estimates

For many of the faults discussed their dip is poorly known and has to be estimated in order to convert feature uplift rates into slip rates and shortening rates. In order to quantify the uncertainties in the resulting rates, I use Monte-Carlo methods following *Thompson et al.* (2002). Estimating the probability distribution functions (PDFs) of all the geometric parameters and ages, I sample them 10^6 times to estimate PDFs for the fault slip rate and shortening rate. I have used the same conventions as Thompson et al. for the choice of PDF shape in each case. It should be noted however that this will not always be appropriate; *Scharer et al.* (2014) suggest that strong justification is required for non-uniform distribution function. This method naturally lends itself to the characterisation of slip rates and shortening rates as PDFs instead of numerical values, an important step forward in estimating the rates and associated uncertainties (*Zechar and Frankel*, 2009).

The faults in this study generally have sinuous traces, suggesting relatively shallow dips – I therefore assume a dip of 25–45° with a uniform probability density function (PDF). However, reverse faults in the Tien Shan are generally observed to be steeply dipping at depth (>45° *Avouac and Tapponnier*, 1993; *Sloan et al.*, 2011; *Selander et al.*, 2012; *Kober et al.*, 2013; *Campbell et al.*, 2013; *Abdrakhmatov et al.*, 2016), so in order to calculate the rate of shortening accommodated by a fault, I assume a fault dip of 45-60° at depth.

For markers which only record slip in a moderate number of earthquakes (<10), the elastic strain stored prior to the formation of the surface and at the present can contribute a further component of slip not captured by the surface offset measurement (*Lavé and Avouac*, 2000; *Thompson et al.*, 2002). I incorporate this as an extra component of uplift of $u_z = \delta z_1 - \delta z_0$. δz is the uplift that would have accumulated since the most recent event if the fault slipped continuously and δz_0 is similarly the uplift that would have accumulated prior to the abandonment of the surface. This component is especially important for events where I might suspect scarps only record 1–3 earthquakes. If we can estimate the uplift in a single event (δz_{quake}), I assume that δz_1 and δz_0 are uniformly distributed between 0 and δz_{quake}, otherwise I assume a maximum value of δz_{quake}=5 m. The sum $u_z = \delta z_z - \delta z_0$ is therefore has a triangular distribution between -1 and 1 with a peak at 0.

4.5 Kegen Basin

The Kegen Basin is the southernmost and highest basin within the transect. Situated right on the northern margin of the high Tien Shan, the basin slopes gently down to the north, from 2200 m at the Karkara Rangefront to 1800 m at the Kegen rangefront (Figure 4.6).

4.5.1 Karkara Rangefront Fault (KRF)

The Karkara Rangefront is a segment of the main northern rangefront of the Terskey Range (MTF) – a full investigation on this fault was presented in Chapter 3. This fault is the only one resolvable in the regional GPS velocity field (Figure 4.5), suggesting that is likely to be a significant fault in the region. Our study focused on flights of fluvial river terraces progressively offset by fault motion, by up to 300 m above modern river levels. Radiocarbon dating of the river terraces yielded a preliminary slip rate of $3.5^{+1.7}_{-0.4}$ mm/yr. Elastic dislocation modelling of the regional GPS velocity field showed that this is accommodated by creep at present, so this fault does not pose any greater hazard than the other faults along this transect which are unresolvable in the GPS velocity field. It is unclear whether there is any strain stored elastically on the fault at present, and hence whether it can generate large earthquakes.

4.5.2 Kegen Basin Fold (KBF)

The Kegen Basin fold runs NE-SW through the middle of the Kegen basin and is bounded on it's northern side by fault scarps, suggesting a south dipping fault. A full investigation on this fault was also presented in Chapter 3; it appears to be a splay structure associated with the Karkara Rangefront to the south. A terrace surface extending from the surface trace ∼2 km towards the core of the fault records an uplift of at least 26 m. Radiocarbon, OSL and IRSL ages suggest a minimum uplift rate of 0.8 mm/yr (though possibly as high as 1.8 mm/yr). The location of the individual regional GPS stations mean this fault cannot be distinguished from the Karkara rangefront with the GPS velocity field.

4.5.3 Kegen Rangefront Fault (KGR)

The northern edge of the Kegen basin is defined by the broad Ketmen range, which has uplifted a Palaeozoic bedrock core generating a relief of ∼1100 m. The shape and width of the range varies significantly along it's length; a series of topographic profiles through the range (Figure 4.6a-c) show a narrow (∼13 km, profile A) range in the west, with a steep northern flank, while near the centre of the Kegen basin (profile B), the range is much broader (30 km) with a very steep southern limb and a gently sloping northern limb. In the east, the range narrows again to ∼20 km before merging with the NE continuation of the series of stepped ranges that bound the eastern end of the Kegen basin (Figure 4.6).

The southern margins of the range do not show clear, continuous fault scarps, but several features suggest that the range bounding faults may be active. In the central (broader) section of the range,

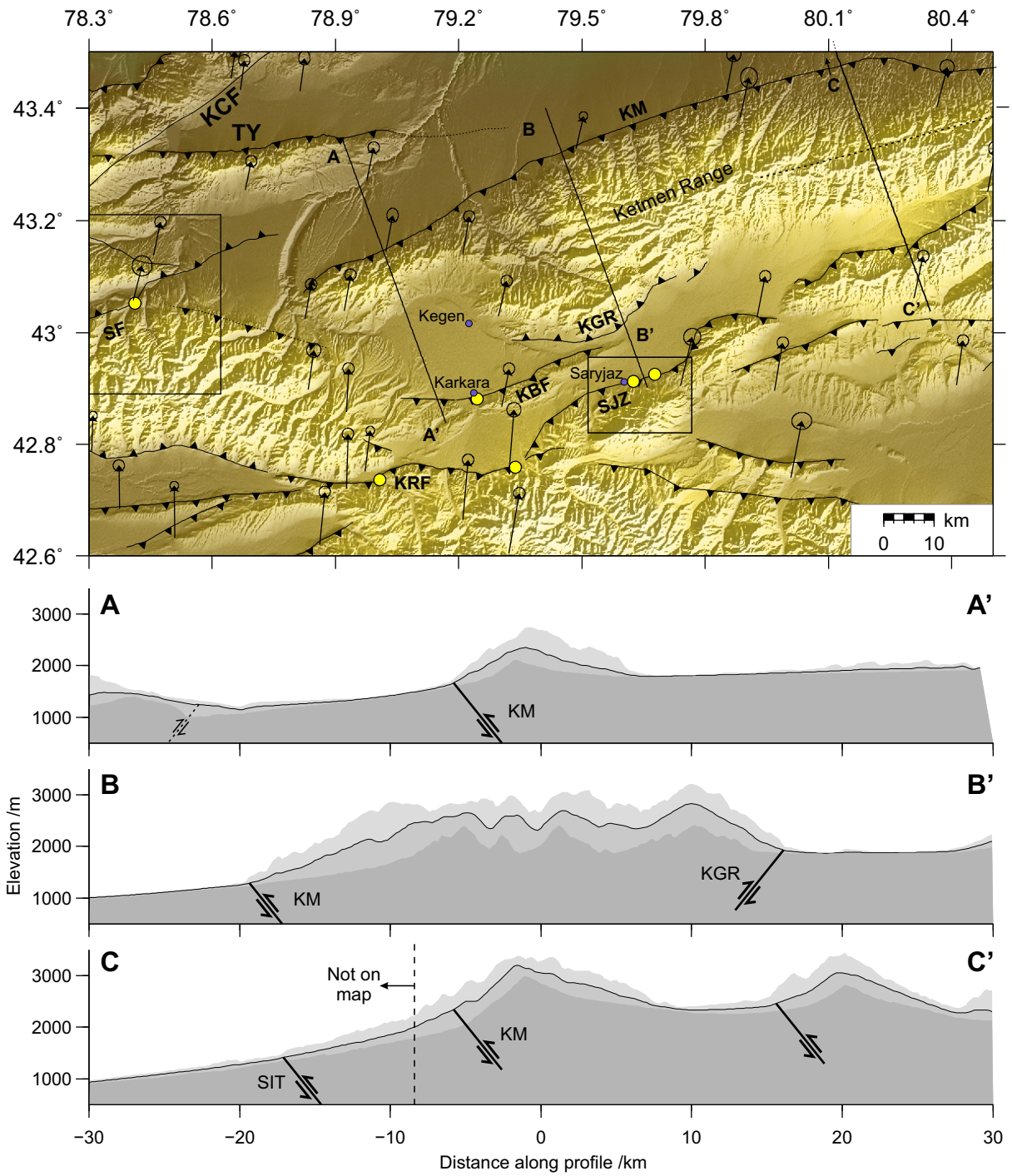


Figure 4.6: (map) An overview of the Kegen Basin, bounded on the north by the Kegen rangefront (KGF) and the south by the Karkara Rangefront (KR). Running up the middle is the Kegen Basin Fold (KBF), bounded on the north sided by a south dipping fault that is most likely a basinwards propagating detachment from the main KRF. Yellow dots mark field sites discussed in Chapter 3, plus Saryjaz sites SR1 and SR2. For full fault labels see caption for Figure 4.4. (a-c) Profiles through the Ketmen Range, showing the minimum, mean (black line) and maximum elevation within a swath width of ±5 km. The central section of the range is broad, with faults bounding both sides, while the eastern and western parts show a much narrower range, likely only bounded on the northern front.

I observe several alluvial fans with significant offsets in them, which rise through the topography at a different gradient to the main river channel, suggesting that they may not be terrace risers. However, the major range-parallel river, and heavy modification for irrigation makes it hard to find conclusive evidence

of activity on this fault, and any field investigation is difficult – I therefore have no geological constraint on the slip rate on this fault. Given the lack of major surface expression in Quaternary sediments, I expect this to be a relatively slow moving fault in the late Quaternary, though the high relief across the range implies significant total displacement. Also, as I note from the Saty fault in the next section, low slip-rate faults can still generate very large earthquakes with a long recurrence interval (similar to resetting timescale of the landscape).

To the east and west of the central segment where the range is much narrower, the southern limb is generally less steep, and I observe no signs of active faulting in Quaternary materials, suggesting there is no active fault on the southern range margin along these stretches. I discuss the northern margin of the Ketmen range in §4.7.

4.5.4 Saryjaz Rangefront (SJZ)

At the eastern end of the Karkara segment of the Terskey Rangefront, the primary rangefront divides into two major strands, one striking ESE past Narynkol into China, and the other stepping northwards in a left-stepping fashion, in a series of short (∼20 km) sections (Figures 4.4, 4.6). This stepped arrangement may accommodate a component of left lateral slip, consistent with the SW-NE trend of the ranges. Each section of the NW trending strand is characterised by a roughly symmetric diamond shaped range, with a relatively planar top, representing the basement peneplain, flanked on either side by tilted and deformed Cenozoic sediments.

I study the northern strand, near the town of Saryjaz (Figure 4.6). The Saryjaz rangefront consists of a contact between the Cenozoic sediments and Palaeozoic basement at the sharpest change in topography, but the primary active surface faulting is sited 3–4 km basinwards, where I observe displaced river terraces and alluvial fans. I focus on two sites (SR1, SR2, Figure 4.7): at SR1, a river leaving the rangefront and crossing the fault has left a flight of three terraces abandoned and uplifted in the hangingwall, and at SR2 the fault has displaced an alluvial fan.

We found no material suitable for ^{14}C dating so I rely on IRSL samples from the base of the loess cap at both sites; OSL5 at SR1 and OSL6 at SR2 (Table 4.1). I expect complete bleaching prior to deposition in the wind-blown deposits. I estimate ages with the post-IR IRSL (pIRIR) protocol[3], as this gave the most reliable results at the nearby Kegen Basin Fold (Chapter 3). In samples from the KBF study, the lower fading pIRIR_{290} signal was found to exhibit high residual doses, so all measurements here utilised the pIRIR_{225} signal. Both samples gave acceptable dose recovery ratios well within 10%, and the interpolated equivalent doses were all well below saturation. The samples also responded well to the SAR protocol, with all aliquots giving recycling ratios within 5% of unity, and recuperation of <0.5% of the natural sensitivity-corrected IRSL for all aliquots.

[3]IRSL sample preparation, measurement and analysis was carried out by Andrew Carr at the University of Leicester. Full method described in Chapter 3 and Appendix A.2.

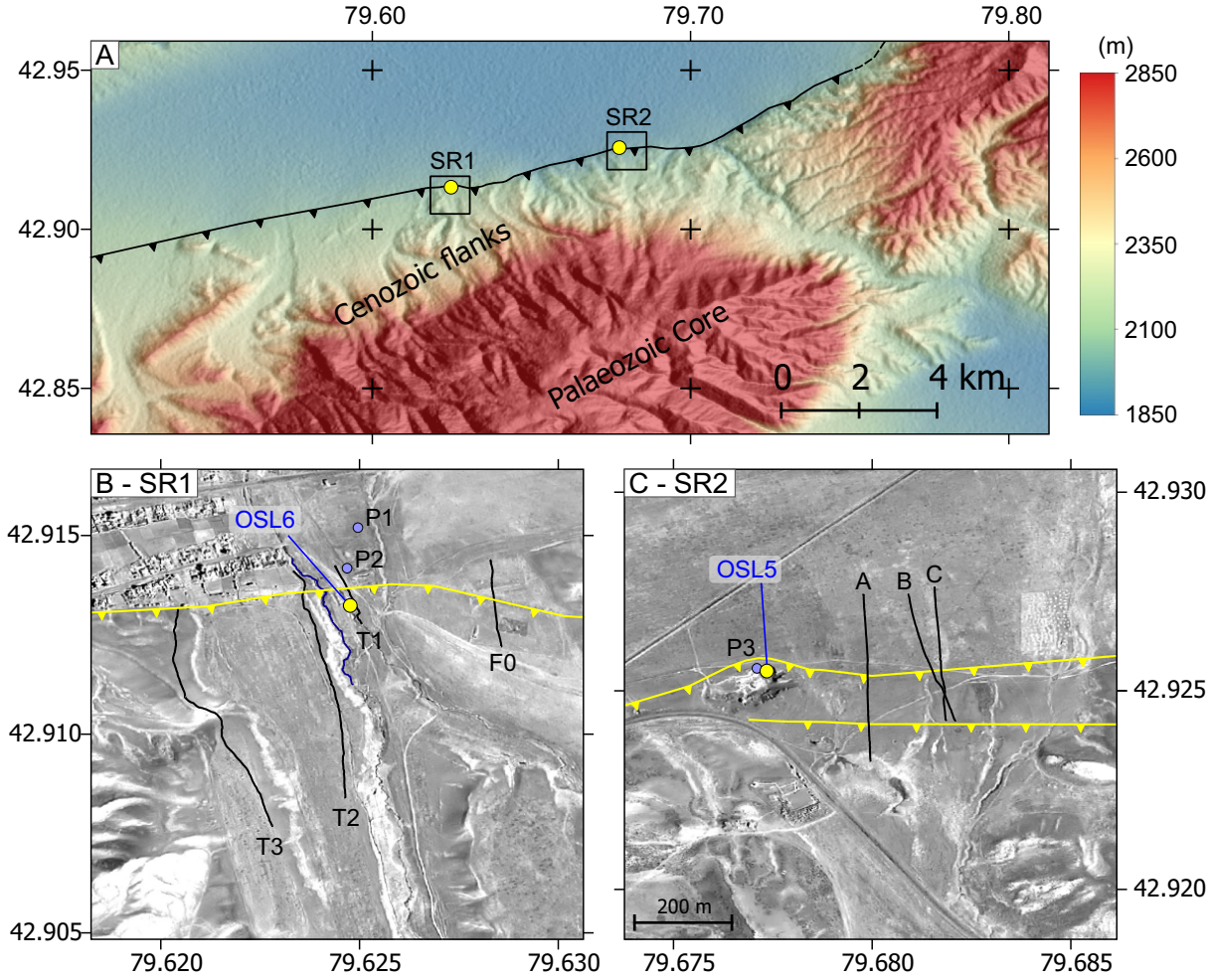


Figure 4.7: (a) Map of the Saryjaz rangefront showing locations of sites SR1 and SR2. Shaded relief SRTM-90m basemap. (b) Overview of SR1 near the edge of the Saryjaz village, showing the location of the GPS profiles displayed in Figure 4.8a. Yellow dot indicates the location of the OSL3 sample. Purple dots show the photograph locations. Basemap is 1 m resolution panchromatic Kompsat-2 imagery. (c) Overview of SR2 showing the location of the GPS profiles displayed in Figure 4.9b. Yellow dot indicates the location of the OSL4 sample. Purple dots show the photograph locations. Basemap is 1 m resolution panchromatic Kompsat-2 imagery.

SR1

Figure 4.8a shows a photograph looking south west at the main flight of terraces preserved near the eastern edge of the Saryjaz town. The youngest well preserved terrace, T1, is uplifted by 3.5±0.1 m relative to the footwall surface (Figure 4.8b,e); river cut exposures allowed us to collect samples and date the abandonment of this terrace (below). The older two terraces (T2–3) are preserved over a longer distance, and are tilted away from the fault trace after a distance of 300–500 m, suggesting that the fault steepens in the uppermost few 100 metres. T2 and T3 are uplifted by 9.9±1.4 m and 24.4±1.5 m respectively, relative to the modern footwall surface (Figure 4.8). It is unclear how much deposition has occurred in the hangingwall, so these estimates constitute minimum terrace uplift values. A further small scarp is seen ∼100 m east of the main river channel, in a small fan surface, with a displacement of 2.1±0.1 m (labelled F0 in Figure 4.8c), which may represent the most recent earthquake on the fault.

Sample OSL5 from the base of the loess cap overlying the T1 gravels yielded an age of 9.5±0.5 ka. The

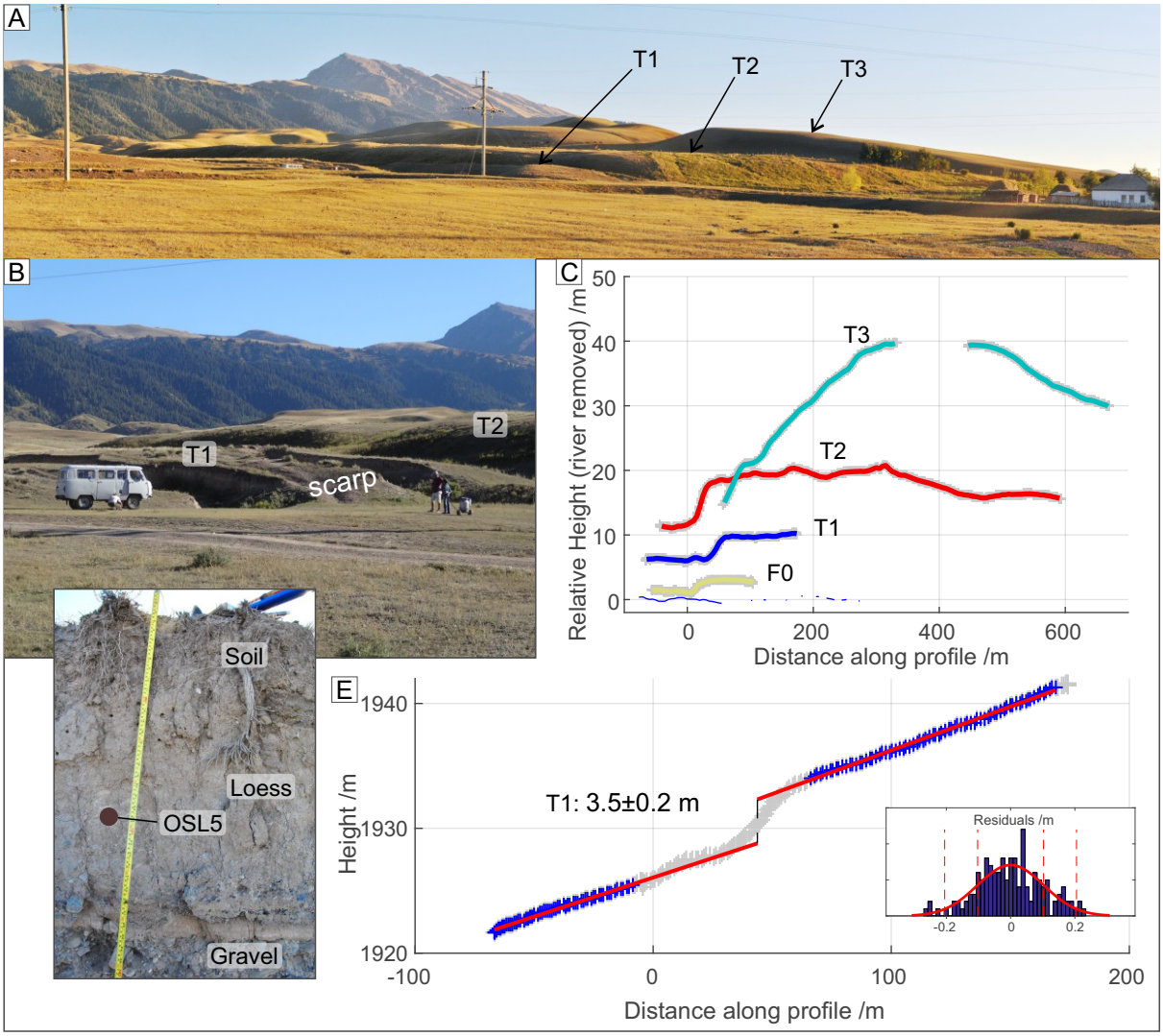


Figure 4.8: (a) Panoramic view of the rangefront near the town of Saryjaz, with the flight of terraces shadowed by light from the west. The Palaeozoic core of the range is visible rising behind (∼3 km to the S). Photo looking SW, location in Figure 4.7. (b) Closer view of the scarp in the T1 terrace at SR1 (car for scale). (c) Profiles along each of the terraces. Successive terraces have been offset by 5 m vertically to aid readability. In T2 and T3, the terrace heights decrease relative to the modern river at 350 m and 400 m from the fault trace respectively, suggesting that the fault steepens in the uppermost few hundred meters. (d) OSL5, sample from the base of the loess cap on T1, provides a postdate on the abandonment of the terrace. (e) Enlargement of a profile along T1; I measured a displacement of 3.5±0.1 m.

scarp in T1 may only represent 1–2 earthquakes, so any slip rate would not be representative. However, 3.5 m of uplift has occurred since ∼10 ka BP, suggesting that at least one earthquake occurred here in the Holocene (if the fault fails seismically).

SR2

At SR2, the fault cuts an alluvial fan sourced from the rangefront, which has been quarried for gravel at location P3 (photo, Figure 4.9). With 1 m resolution panchromatic Kompsat imagery, I identify two generations of scarps cutting the fan surface. Using kinematic GPS profiles I estimate the total offset of the fan surface to be 12.9±0.2 m (Figure 4.9c). The lower scarps yielded vertical offset estimates of 3.7–

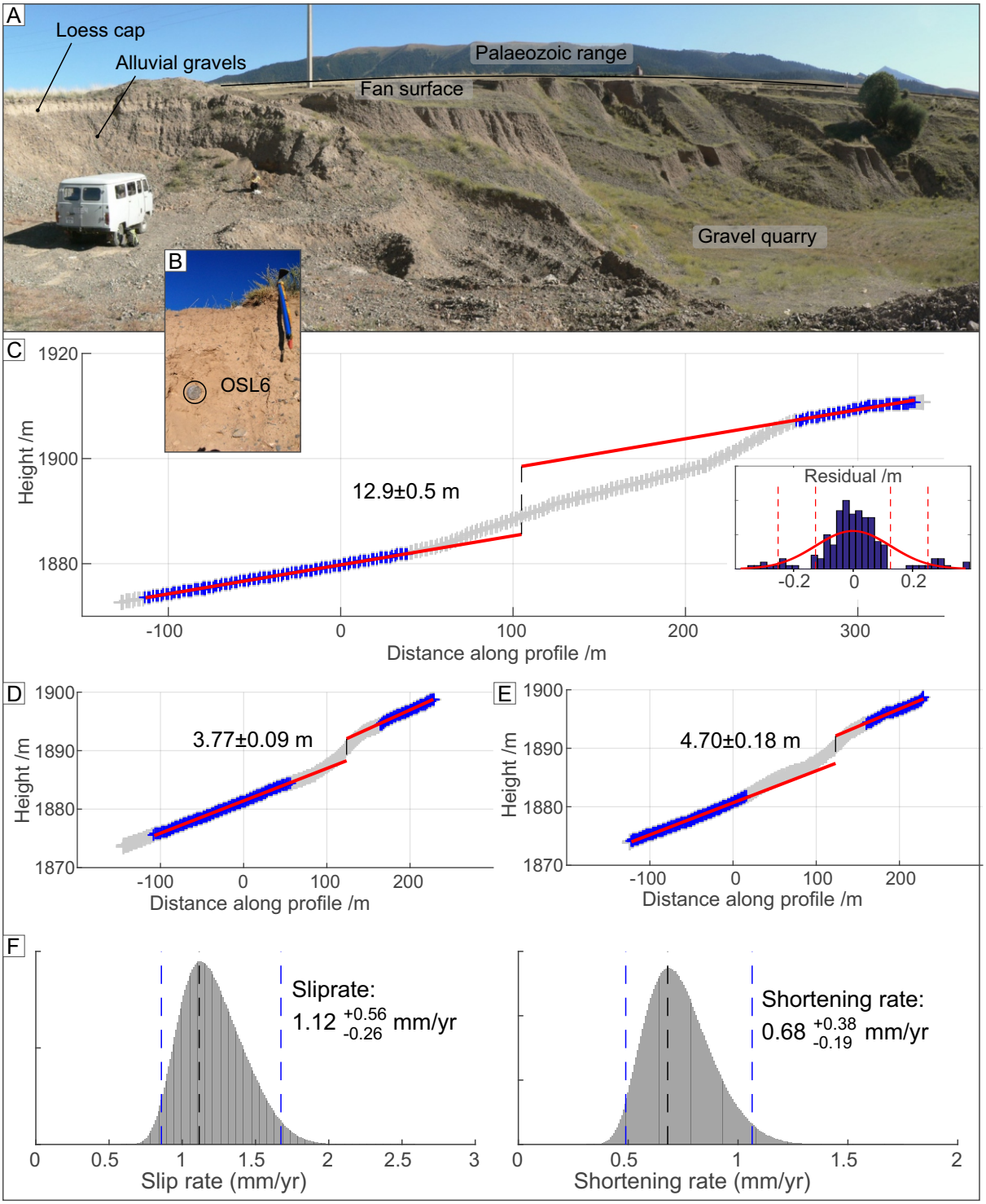


Figure 4.9: (a) Panoramic view of the gravel quarry sampling site at SR2. (b) Sample OSL6 collected from the base of the loess (also containing occasional gravels <2 cm). (c) A long profile through both scarps in the fan, suggests a total offset of 12.9±1.5 m. (d) Profiles through the smaller northernmost (freshest) scarp show ∼3–5 m offsets, but considerable variation along strike. (e) Monte-Carlo simulation probability density functions for slip rate and shortening rate based on offset in (c) and the age of OSL6.

4.7 m. From the fan exposures in the gravel quarry, sample OSL6 from the base of the loess cap yielded an age of 17.4±1.0 ka (Table 4.1). Given the vertical displacements of the fan surface, this suggests an uplift rate of ∼0.7 mm/yr.

Name	Site	Depth *(cm)*	Material	Water *(%)*	Feldspar grain size *(μm)*	Feldspar total dose rate *(Gy ka-1)*	Feldspar CAM D_e $pIRIR_{255}$ *(Gy)*	Aliquots	OD (%)	$pIRIR_{225}$ Age *(ka)*
OSL5	SR1	58	loess	2.5	63-90	4.91±0.19	46.8±1.79	18	8.4	9.5±0.5
OSL6	SR2	56	loess	2.3	63-90	4.38±0.16	76.4±3.3	15	11.6	17.4±1.0

Table 4.1: Feldspar pIRIR ages for the luminescence samples at the Saryjaz Rangefront Fault (SF). Analysis carried out by Andrew Carr at the University of Leicester. Quoted errors are 1-σ.

I have no constraint on the fault dip at this site, but the sinuosity of the fault trace and folding of the terraces at SR1 suggest it may be relatively shallow in the near-surface sediments. Assuming a fault dip of 25–45° in the shallow subsurface, I use Monte-Carlo simulations to estimate a slip rate PDF, including a term to allow for stored elastic strain both at the time of abandonment and at present (up to 3 m uplift). I estimate a slip rate of $1.12^{+0.56}_{-0.26}$ mm/yr and, assuming a deep fault dip of 45–60°, a shortening rate of $0.68^{+0.38}_{-0.19}$ mm/yr (Figure 4.9e). Exhumed Cenozoic beds in the hangingwall between the active trace and the Paleozoic basement are tilted, suggesting a component of folding in the hangingwall, so shortening rates based purely on scarp heights may be underestimated.

The slip rates at Saryjaz are smaller than those observed at the KRF, suggesting a partitioning of strain between the eastwards continuation of the MTF and the left stepping ranges trending NE along the eastern edge of the Kegen Basin. However, this rate is still significantly faster than the majority of faults observed along the transect – palaeoseismic investigation is needed to establish the significance for seismic hazard.

4.6 Saty Fault (SF) – 1889 Chilik Earthquake Ruptures

At the south-western-most corner of the Ili basin, there is a zone of complex surface ruptures, which we infer to have failed in the 1889 M∼8.0–8.3 Chilik earthquake (Figure 4.10). This is the only fault along our transect thought to have generated surface ruptures in historic times; it therefore provides a case study by which to tie the behaviour of faults in earthquakes to the long term fault morphology. Importantly it is also a precautionary case for the study of active faulting in the region, as we found that prior to the 1889 earthquake there would have been very little evidence for significant activity on the fault, yet it failed in a M_W 8+ earthquake. The work in this section is fully described in *Abdrakhmatov et al.* (2016); I outline here the important findings we made[4]. In addition I present work from the 2015

[4] This work was performed as a collaboration for *Abdrakhmatov et al.* (2016). KEA, RTW, GEC, CH, JH, AL, DM, AM and MR all participated in the 2013 field campaign. Field logistics were organised by KEA and AM. AL and MR constructed the trench log. I acquired and processed the aerial survey of the site, and AE interpreted the resulting digital topographic model. ASC undertook infrared-stimulated luminescence analyses. All authors contributed to the text, which was compiled into the final manuscript by RTW. KEA and RTW were responsible for the overall scientific concept and project design.

field campaign with observations of a site on the north side of the Saty river where cumulative scarps were found and measured[5].

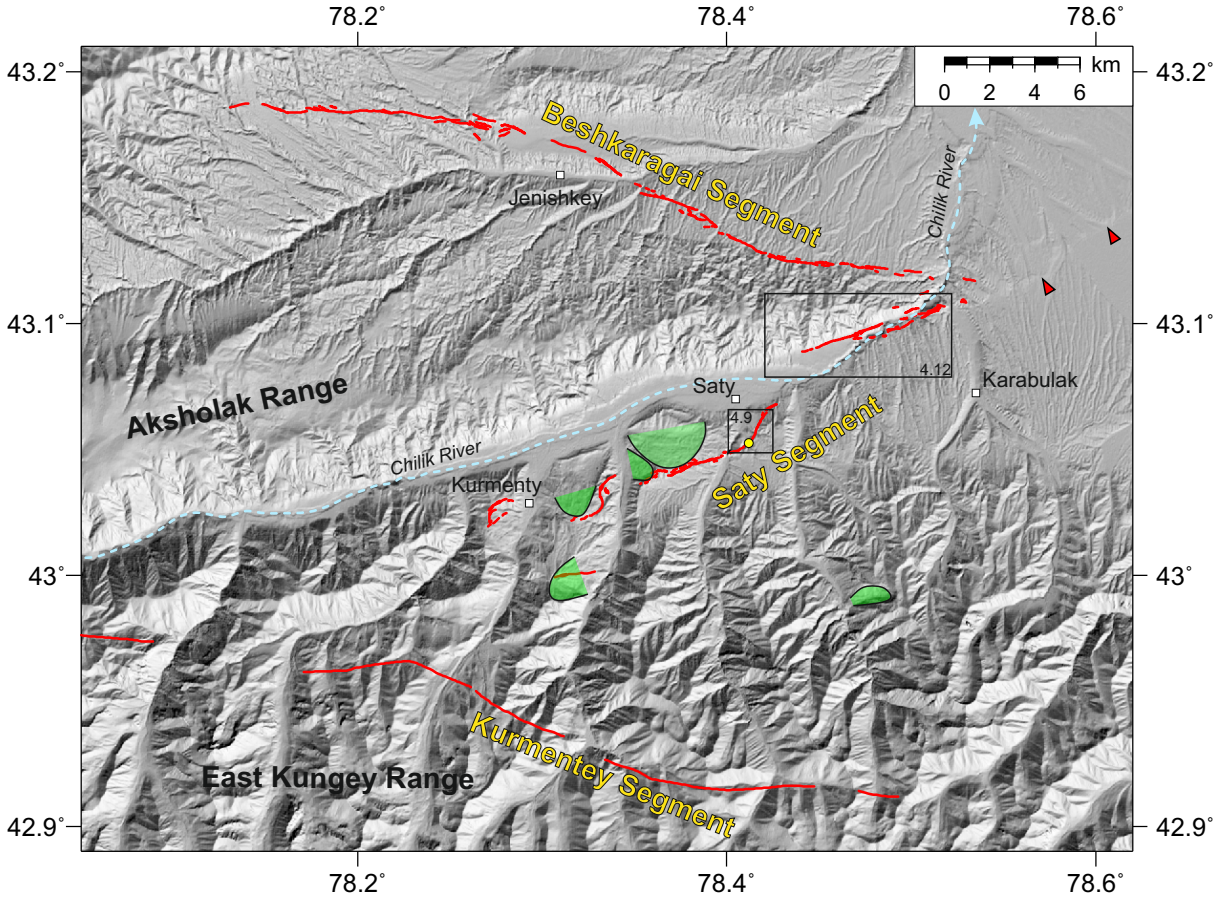


Figure 4.10: Adapted from Figures 3–4 of *Abdrakhmatov et al.* (2016), location in Figure 4.6. The Saty fault and surrounding structures are believed to have been activated in 1889 Chilik earthquake. Mapped ruptures are in red and landslides in green. The yellow dot shows the trench site. Arrows mark the section extending E into the basin sediments which did not rupture in the most recent event. Boxes show the outline of Figures 4.11, 4.14.

Analysis of early seismograms, magnetograms and macroseismic damage suggests a magnitude of 8–8.3 for the 1889 earthquake (*Mushketov*, 1981; *Bindi et al.*, 2013; *Krüger et al.*, 2015). Though several sets of surface ruptures were observed in the epicentral region (*Tibaldi et al.*, 1997; *Tibaldi*, 1998; *Crosby et al.*, 2007) the combined length is substantially shorter than might be expected for a M8+ from classical scaling relations (*Krüger et al.*, 2015). In addition to the scarps observed near the village of Saty (*Tibaldi et al.*, 1997; *Tibaldi*, 1998; *Crosby et al.*, 2007), we attempted to find and assess a series of other possible surface ruptures associated with the 1889 event, identifying in satellite imagery and field observations further scarps along the Beshkaragai segment to the north and the Kurmenty Segment to the south (Figure 4.10). The combined length of this z-shaped collection of scarps on three separate fault segments brings the total length of scarps within the epicentral zone to ∼175 km, close to what might be expected from a M 8+ event, though the kinematics of such a rupture were not considered. Due to the mountainous terrain, the Kurmenty scarps were mapped from remote sensing data only, so although they are a plausible source

[5] Carried out in collaboration with Austin Elliott (lead), Christoph Gruetzner and Eleanor Ainscoe

of the 1889 event, their link to that event remains speculative. In this section, I focus on the detailed case study of scarps along the Saty fault segment, (first described by *Tibaldi et al.*, 1997), as they carry important implications for the study of active faulting in the Tien Shan.

4.6.1 Scarp Morphology

The Saty scarps run approximately east-west, with the north side consistently upthrown, for about 25 km along the Saty valley and can be split into three distinct sections. The western section extends westwards from the trench site showing mainly reverse offsets (north side up), with a small component of left-lateral offset. The central section runs SW–NE from the trench site to the rangefront showing large left-lateral offsets and a smaller vertical throw. The eastern section runs along the front of the Aksholak range with primarily reverse motion again. The stepped orientation of the scarps, is consistent with the central section transferring motion from the rangefront to the mid-basin scarps. The very linear nature of the scarp as it cuts through steep topography is indicative of a very steep fault dip, consistent with the observations of *Tibaldi et al.* (1997) who observed an 80° NNW dipping fault plane near the Saty river gorge placing Palaeozoic rocks against Quaternary sediments.

We performed Helikite SfM surveys (as for §3.3.1) along the majority of the scarps on all three sections of the Saty fault, creating a 20 cm DEM of a 100–200 m swath along the ruptures. Scale and orientation for each section was provided by control points whose location is measured with DGPS. Along the western and central sections, the north side-up offsets have resulted in a scarp against the hillslope, causing extensive ponding behind the scarp. I first describe the scarps and findings from the palaeoseismic study in the central section above Saty village, where we see only single event scarps. I then present observations of the scarps on the northern side of the Chilik river where we note several cumulative offsets.

SF – Central Section

Figure 4.11a shows the central stretch of the fault south of Saty village, with the predominantly strike-slip section in the northern part of the image, bending at the trench location to become primarily thrust in the western part. At the trench site the fault cuts though a small alluvial fan within a small river valley approximately where the fault strike changes by 30°. Uplift of the north side, temporarily dammed the river drainage causing ponding behind the scarp – an ideal location for palaeoseismology (below). Figure 4.11b shows the DEM of the trench site, where the scarp cuts the T1 surface. Piercing lines show left lateral offsets of 3-6 m, while vertical profiles show a stable offset of 6-8 m both in the T1 and T2 surfaces, suggesting a net slip of 6.7-10 m.

Figure 4.11c shows the DEM of the stretch of scarp cutting a series of colluvial deposits at the edge of the T2 surface. Three NW flowing stream beds (Figure 4.12d,e) show left-lateral displacements of 6.8±1.0

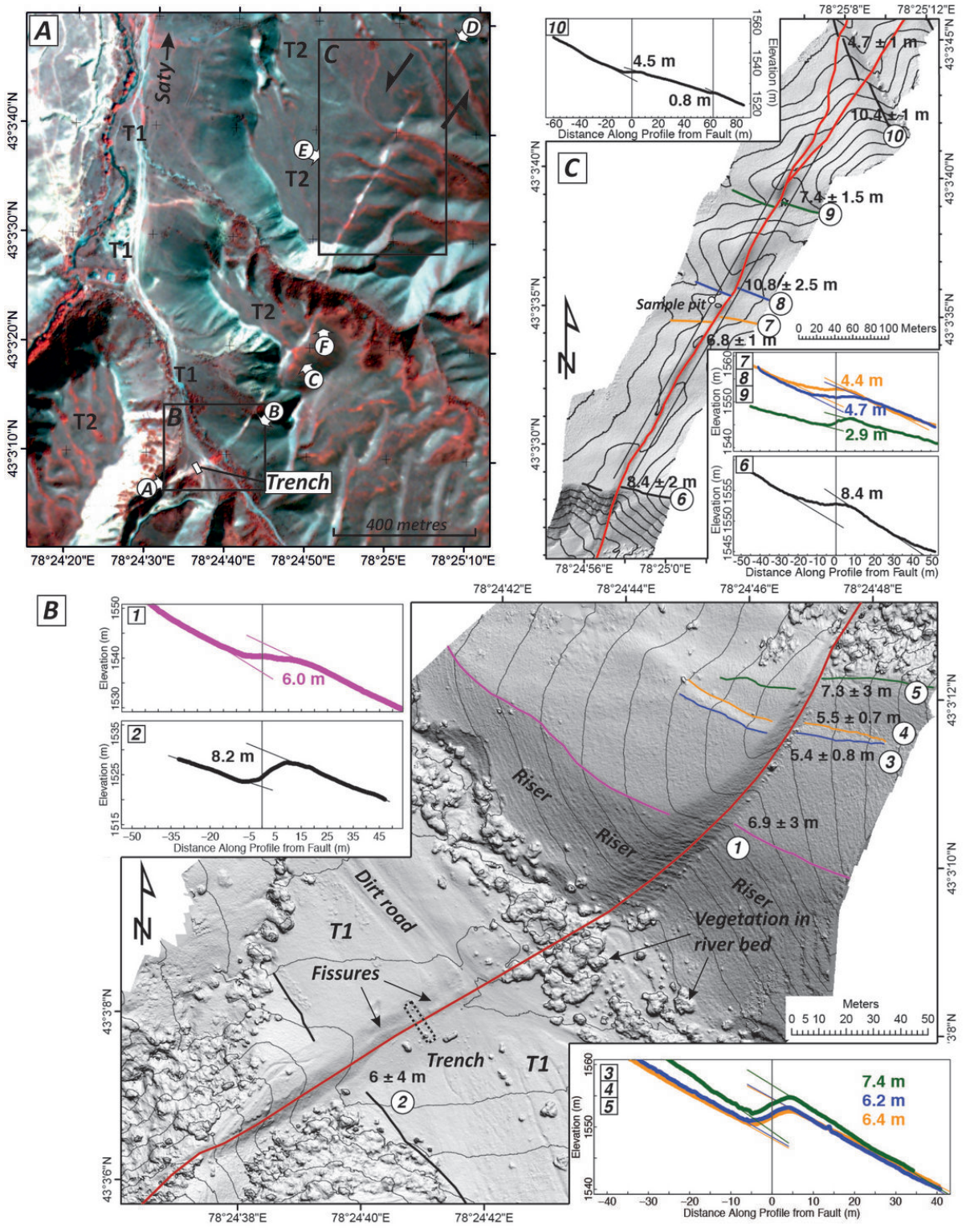


Figure 4.11: Figure 4 from *Abdrakhmatov et al.* (2016). (a) Map of the scarps above Saty Village, showing the location of the trench and photographs in Figure 4.12. (b) The locality of the palaeoseismic trench. The scarp uplift has dammed the river channel, resulting in a flattened area behind the scarp. Vertical offsets are larger here and to the west, while lateral offsets are smaller. (c) SW-NE oriented stretch of the scarp, on which we see primarily lateral motion with a small vertical component.

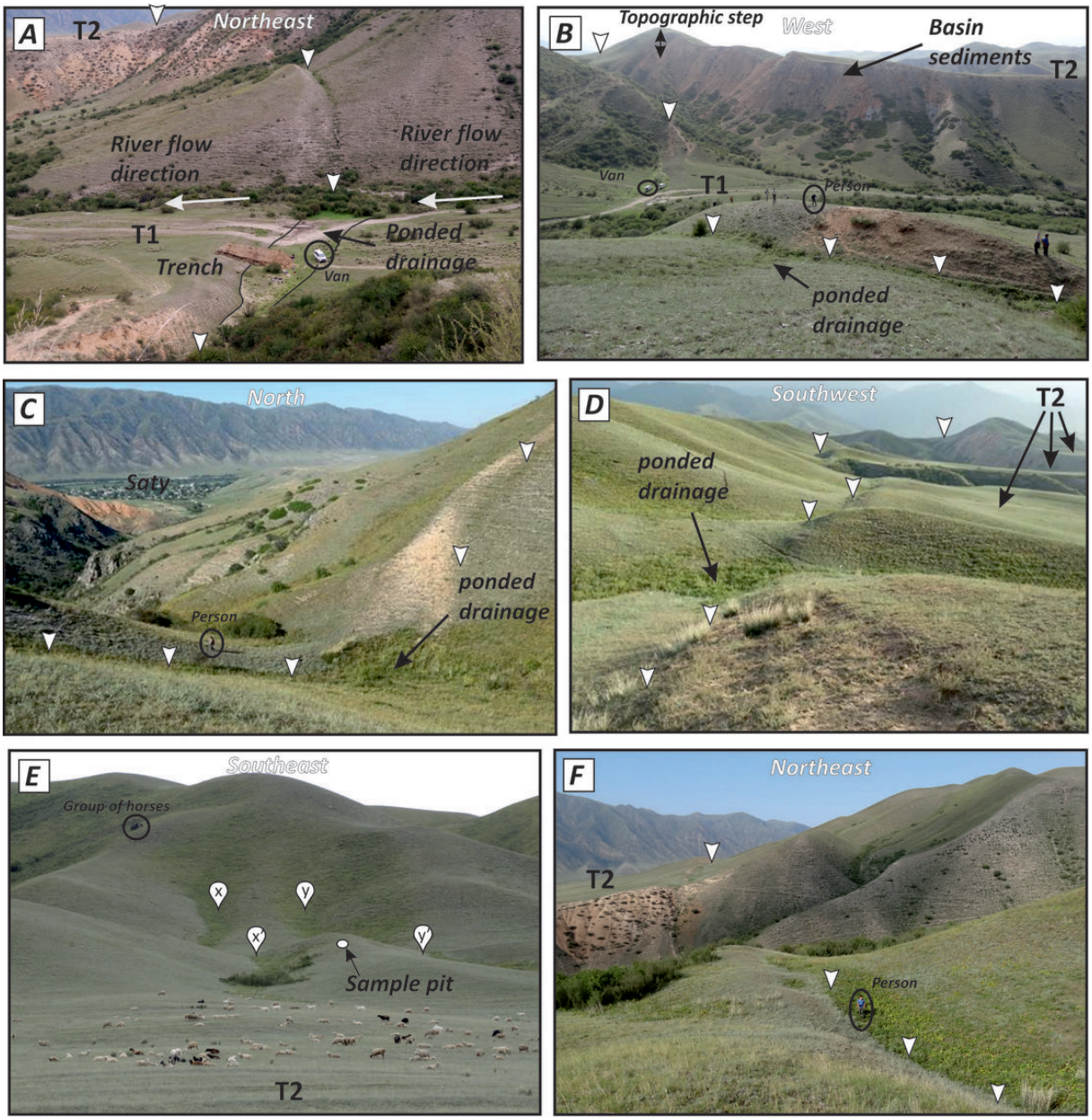


Figure 4.12: Figure 5 from *Abdrakhmatov et al.* (2016), locations in Figure 4.11. (a) Scarp crossing the T1 surface at our trench site. A north-flowing stream was blocked by scarp formation, leading to the development of a pond. (b) Looking west along the scarp, showing the steep un-vegetated scarp, and a small gully that has been blocked by scarp formation. Cenozoic basin sediments are exposed in the upthrown northern side of the fault. A topographic step of ∼50 m is visible at the horizon, coincident with the fault. (c) Displacement and ponding of minor drainage channel at the scarp. Saty village and the Aksholak range-front are visible in the distance. (d) View south west along the scarp showing it displacing the T2 terrace. (e) View of ∼10 m left-lateral stream displacements. IRSL ages of 86-87 ka were obtained from colluvial hillslope deposits in the sample pit indicated. (f) View north east showing the scarp in the T2 terrace.

m, 10.8±2.5 m, and 7.4±1.5 m, and are displaced vertically by 4.4 m, 4.7 m, and 2.9 m, respectively.

4.6.2 Palaeoseismology & Geochronology

At the site in Figure 4.11b, a north-flowing river has been blocked by the scarp, resulting in ponding behind the scarp which was subsequently abandoned when the river re-established northwards flow (Fig-

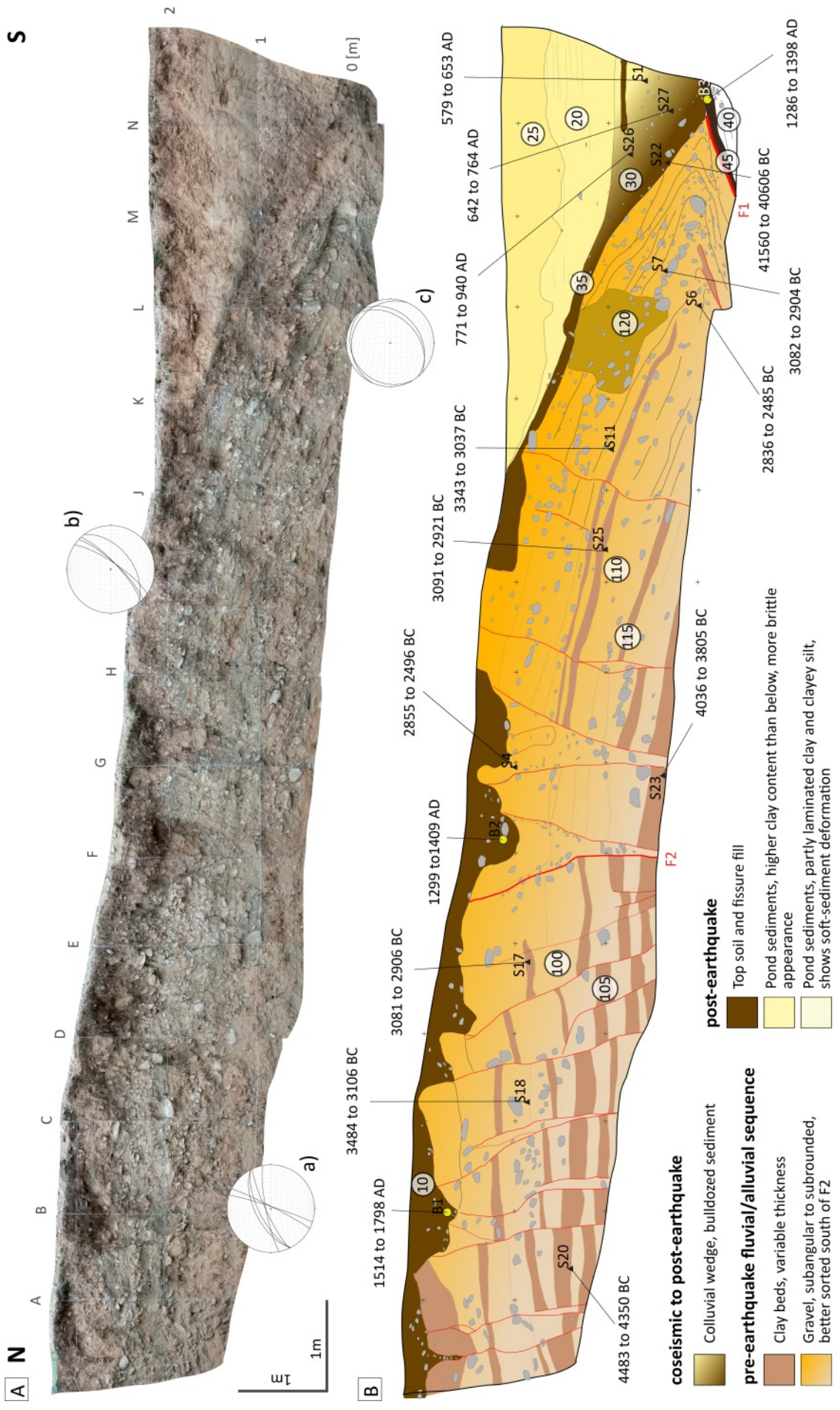


Figure 4.13: Figure from *Abdrakhmatov et al. (2016)*. (top) Orthomosaic of the Saty Trench. (bottom) Interpreted trench log, dating samples shown in with age estimates (95% confidence intervals). The uphill facing scarp caused ponding, resulting in laminated silts sealing the rupture tip and colluvial wedge material.

ure 4.12a,b). We excavated a 10 × 3 m trench to a depth of 3 m through the fault scarp, unearthing the main fault interface near the bottom of the trench (Figure 4.13). I briefly outline of the main findings, but the full trench log and lithological and structural description is given in *Abdrakhmatov et al.* (2016).

The gravels of the hangingwall are drag-folded and thrust over a thin dark palaeosol unit which we interpret to represent the palaeosurface soil horizon immediately before the earthquake. Fissures in the hangingwall cut the full depth of the trench down to ∼2 m, and are filled with loose unsorted pebbles; these fissures are consistent with extension in the hangingwall accommodating a small degree of folding. They remain visible on the surface as slight depressions, attesting to the relatively recent formation of the scarp. South of the scarp (up-slope), the initial fill is interpreted as gravitationally fed polymict sediments from the free face of the scarp during or shortly after the earthquake. The upper section of the pond is filled with laminated clays. A series of radiocarbon ages provide some constraint on the date of the scarp forming event; a bulk soil sample from the organic rich palaeosol which predates the event yielded an age of 1342±56 AD. Apart from the 1889 event, no other large event is observed in the historic records for the Chilik valley region, so although not certain, it is likely that the Saty rupture formed in the 1889 event.

The fan material at the trench site was dated at the base of the trench to ∼5–6 ka BP, and the fan records no displacement from any previous events, placing a minimum age on the penultimate event. However, the scarps cutting through the older valley sides and the older T2 surface show similar displacements, suggesting that the penultimate event may have been substantially older.

4.6.3 Rangefront Section – Cumulative offsets

To the north and east of Saty village, the fault crosses the river and joins the southern front of the Aksholak Range becoming a more classical rangefront thrust scarp (Figure 4.14). It is unclear whether there is significant strike slip motion along this section – though there is definitely less than the central section. We observe a series of continuous smaller scarps along the range which we attribute to the 1889 event, but also a set of larger offsets in an older alluvial fan remnant. Further east, where the river has incised a deep gorge, the scarps cross back to the southern side of the river and are preserved for ∼2 km (Figure 4.14a) before fresh scarps are no longer visible (though the longer-term expression of the fault continues eastwards into the basin, Figure 4.10).

Helikite and quadcopter drone aerial surveys for SfM along the rangefront (Figure 4.14a,b) were used to estimate offsets from the most recent event scarps, and the cumulative scarps. Figure 4.14 shows a perspective view along a stretch of the rangefront where we see three different generations of scarps preserved. Using profiles through the pointcloud, we estimate offsets of 3.3±0.5 m (P1) for the most recent event, 6.7±0.5 m for the intermediate scarp (P2) and 32±5 m (poorly constrained, P3) for the largest offsets. To the west along the rangefront, the slip tapers to zero at the end of the survey, suggesting

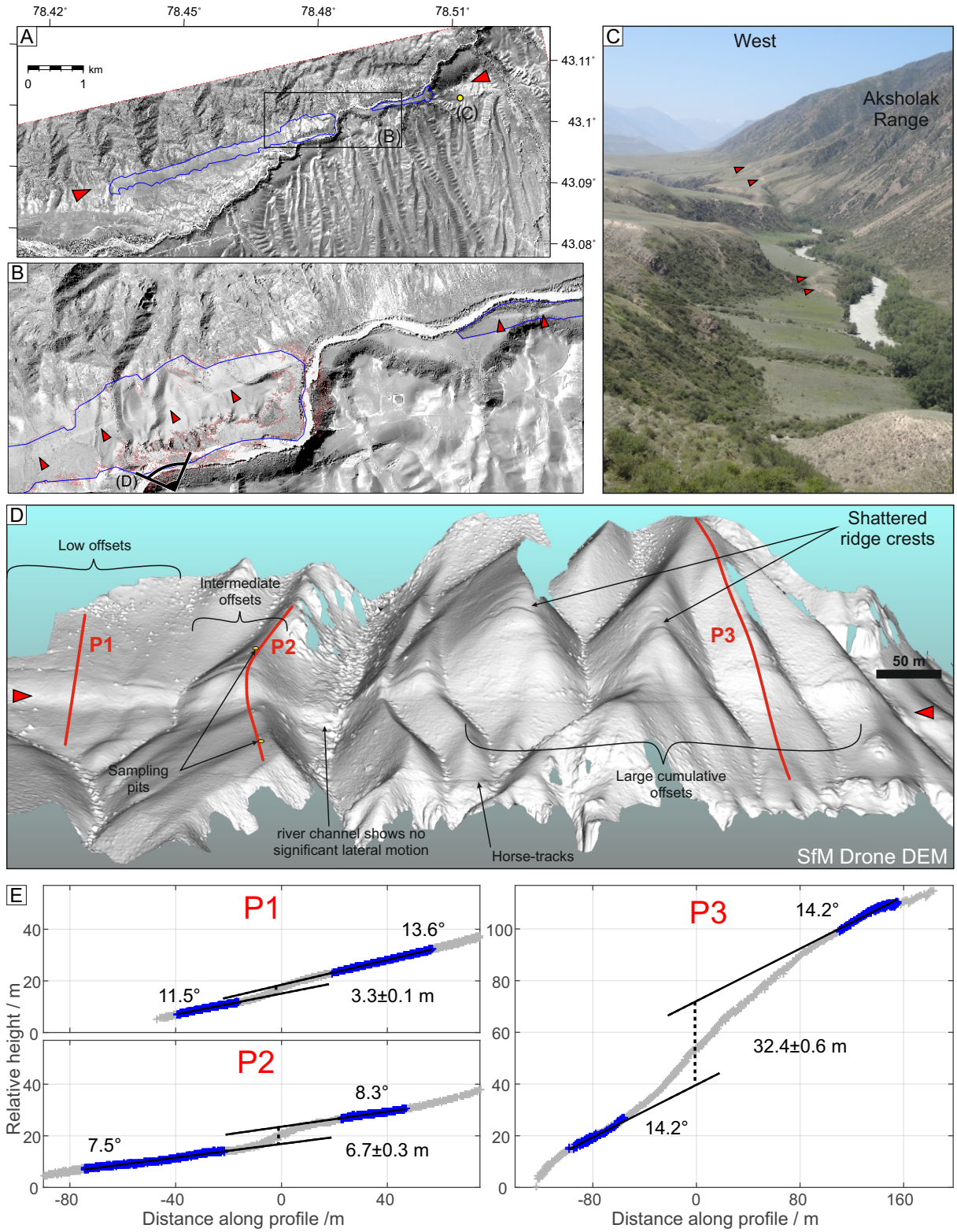


Figure 4.14: (a) Map of the Saty fault along the northern side of the Chilik river, where it bounds the Aksholak Range. Outline of the aerial surveys shown in blue. Basemap is 1 m resolution panchromatic Kompsat-2 imagery. (b) Zoomed section from (a), showing the shaded relief DEMs overlain. The scarps are visible as a bright ribbon when illuminated from the SE. (c) Photograph looking west along the fault. Scarps are visible near the river in the middle distance, then cross the river, and displace the older fans at the rangefront in the far distance. Location in (a). (d) Perspective view looking northwards at the series of cumulative scarps, we see three generations of scarp formation. The older offsets have the more recent scarps on top. (e) Profiles P1, P2 and P3 through three different (increasing size) generations of scarps. Locations in (f). P2 shows the vertical offset across the fan sampled for a slip rate study.

that there is a gradual southwards transfer of slip onto the central section of the fault. The offsets at P1 are much smaller than the typical vertical offsets observed on the central section of the Saty fault. No significant lateral offsets were visibly preserved at this rangefront site (Figure 4.14), suggesting that the fault is primarily dip slip there.

Excavating a pit in the upthrown surface which displays the intermediate offsets (∼6.7 m, Figure 4.14), we collected OSL samples from the base of the loess cap to put a minimum age constraint on the fan surface. A second pit in the downthrown surface yielded several small gastropod shells embedded within the loess cap. Sample analysis is in progress at time of writing, but these samples should constrain the maximum slip rate on this fault.

4.6.4 Summary: Saty Fault (*Abdrakhmatov et al.*, 2016)

At Saty, there is evidence for a very large earthquake which generated surface scarps with offsets of up to 10–14 m, most likely the 1889 M_W 8+ Chilik earthquake. The penultimate earthquake on the Saty fault was at least 5-6 ka BP, suggesting the fault fails in very large events but with a long recurrence interval. Only one location on the north side of the river shows scarps which we can attribute to multiple event offsets, so prior to 1889 there would have been very limited evidence for the activity of this fault in the geomorphology.

4.7 Ili Basin (South)

I divide the study of the faulting around the Ili Basin into the parts south and north of the Ili river. The southern margin of the Ili basin is comprised of a single large range in the east, the Ketmen range, but in the west the Ketmen and Kemin-Chilik fault zones overlap, in the southern part of the basin. Thus within the transect being considered, there are a series of major faults to consider (Figure 4.15); the rangefront of the Ketmen range (KM), the Toraigyr Fault (TF), the Kemin-Chilik Fault (KCF), and the Chilik Rangefront Fault (CRF). There are also a series of short NW-SE faults, which I infer from their orientation to be primarily right-lateral strike slip faults. Careful mapping has further revealed another structure running E-W through the basin sediments, which I label the South Ili Thrust (SIT).

4.7.1 Toraigyr Fault (TF)[6]

In the SW corner of the Ili Basin, the geomorphology of the Toraigyr Fault retains evidence to investigate both its slip-rate and its behaviour in earthquakes. TY therefore provides a second opportunity to link the long term fault evolution with the behaviour in individual earthquakes. The close proximity to the Bartogai reservoir and dam means that the seismogenic activity of this fault is also of importance for seismic hazard assessment.

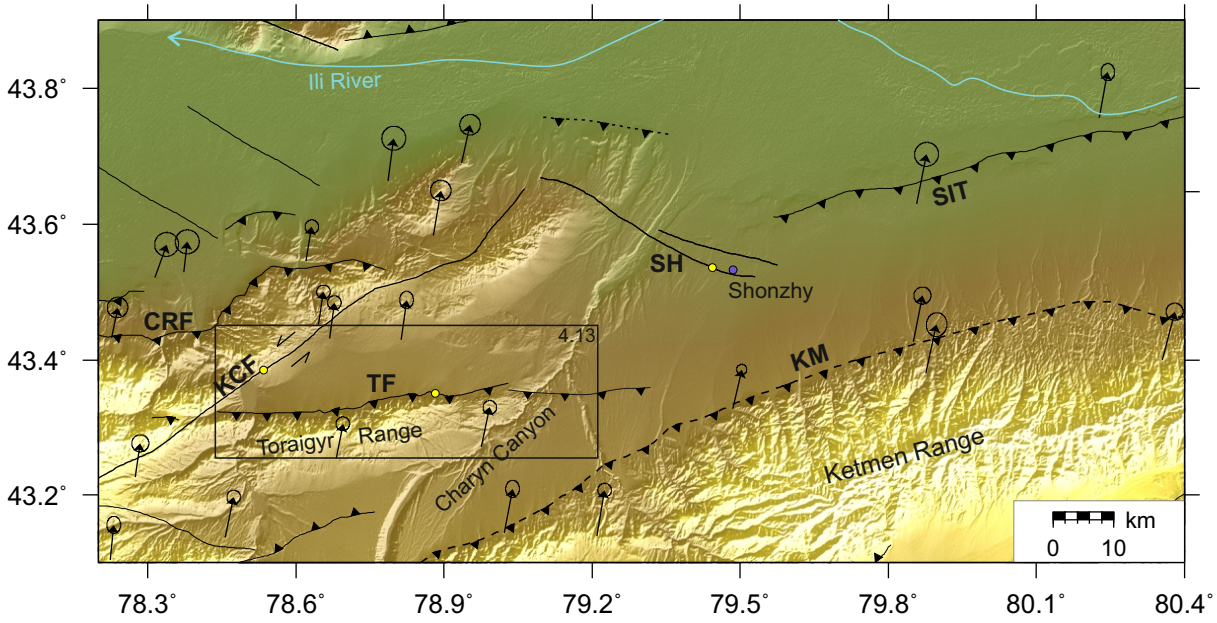


Figure 4.15: Map of the Ili Basin to the south of the Ili River. Yellow points mark location of field studies. Box shows location of Figure 4.16a. See Figure 4.4 caption for fault labels.

The south dipping fault (TF, Figure 4.15) bounds the Toraigyr range, running ∼60 km from the Chilik left-lateral fault zone in the west to the Charyn Canyon. The fault has displaced Quaternary alluvial fans, forming fault scarps of up to ∼12 m (Figure 4.16). For most of the length of the range, however, the fault is marked by a single continuous scarp of 1.5–2 m which we confirm from trenching to have formed in a single earthquake. The younger fans, offset by only a single event were targeted for palaeoseismic investigation, while the older fans show cumulative offsets from multiple events, providing targets for estimating the slip-rate.

We performed a field investigation along the majority of the fault, with detailed site studies at B1 and B2 (Figure 4.16). At B2 we perform a slip-rate study, while at B1 we excavated a palaeoseismic trench across the fault, and used Helikite SfM survey to estimate fault displacements in two generations of alluvial fans.

B1: Palaeoseismology

We excavated a trench across the youngest generation scarps in T1 at 43°20.776'N 78°54.543'E, from which we confirmed that the scarps formed in a single event and we estimate the magnitude of that event. Kinematic DGPS profiles across the scarp in the vicinity of the trench show a vertical offset of 1–1.5 m (mean 1.3 m) with no evidence for significant folding of the hangingwall. Figure 4.17 shows the trench log documenting lithology, grain size, colour, bedding and deformation observed within the eastern wall of the trench; this was mapped on an orthomosaic of the trench wall generated by structure from motion

[6]The trench work and scarp offset measurements on the Toraigyr Fault was carried out primarily by Emily Carson for her MSci Thesis, and prepared for publication in *Grützner et al., (in revision)* by Christoph Gruetzner. The slip-rate study was carried out by myself, with the wet chemistry and AMS for ^{10}Be dating performed by CIAF at SUERC. Here I summarise the main findings, and add a slip-rate estimate.

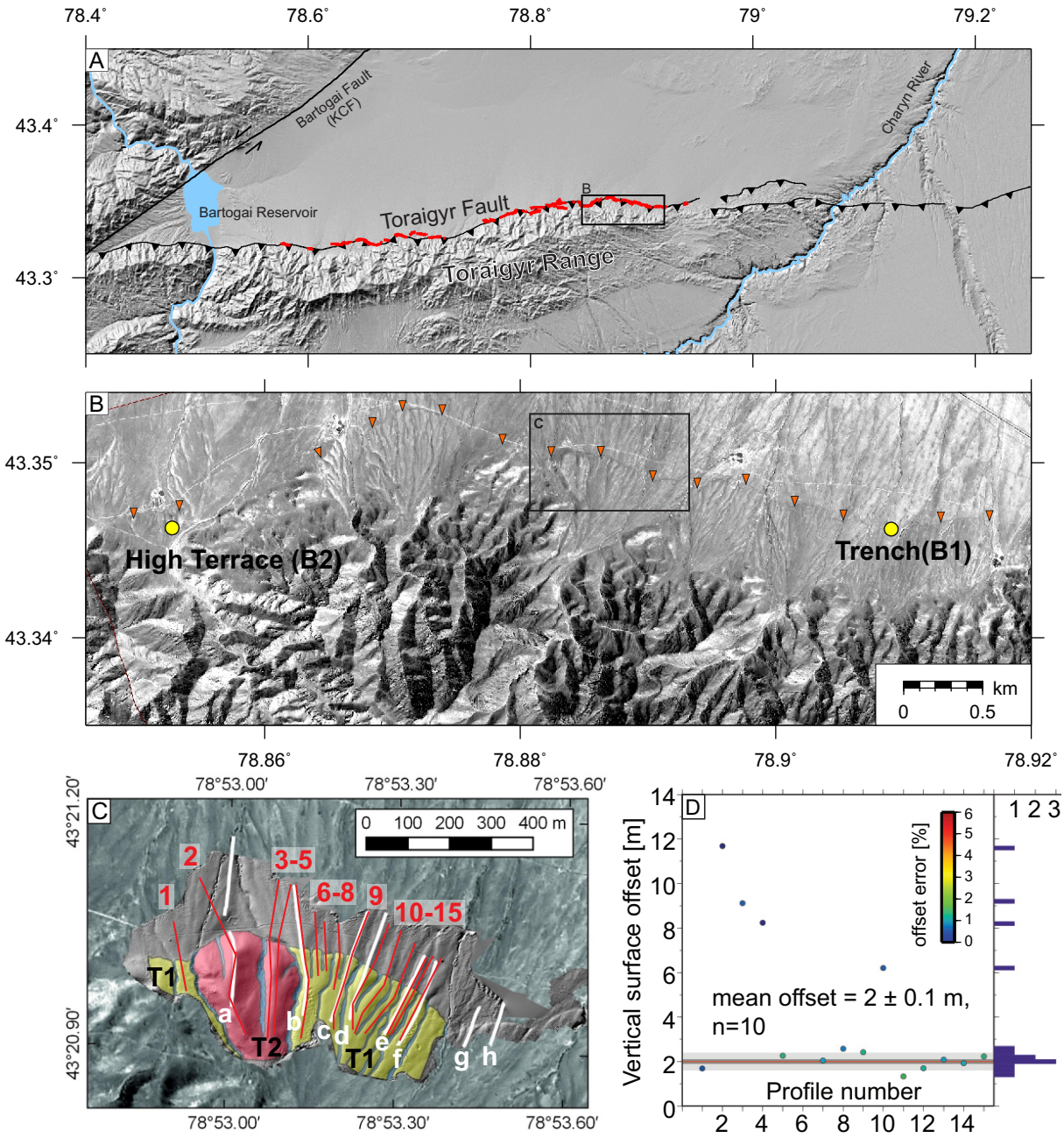


Figure 4.16: Adapted from Figures 1,2 of *Grützner et al., (in revision)*. (a) Overview of the Toraigyr fault. Fresh surface scarps attributed to the most recent event are shown in red, while black lines show the rest of the mapped fault. At the western end, the fault is in very close proximity to the Bartogai reservoir. (b) The locations of both the high (∼10 m) scarp dated to estimate the fault slip-rate, and the palaeoseismic trench, on basemap of 1 m resolution panchromatic Kompsat-2 imagery. (c) High resolution Helikite survey of the short stretch of ruptures where we see two generations alluvial fans preserving different amounts of fault slip. (d) Profiles across the high-resolution DEM, show numerous offsets of 1–2 m attributed to the most recent event (T1), but also larger cumulative offsets up to 11–12 m (T2).

(e.g. *Bemis et al.*, 2014; *Reitman et al.*, 2015).

We observed two faults within the trench wall, F1 and F2, both of which offset marker horizons. Fault F1, on which the most recent even occurred, dips 25° S at the base of the trench and flattens toward the surface, coinciding with the modern scarp. F2, located further south, dipping 18° S only offsets the lowermost units. Based on the observed stratigraphy, we build a retro-deformation scenario to reconstruct

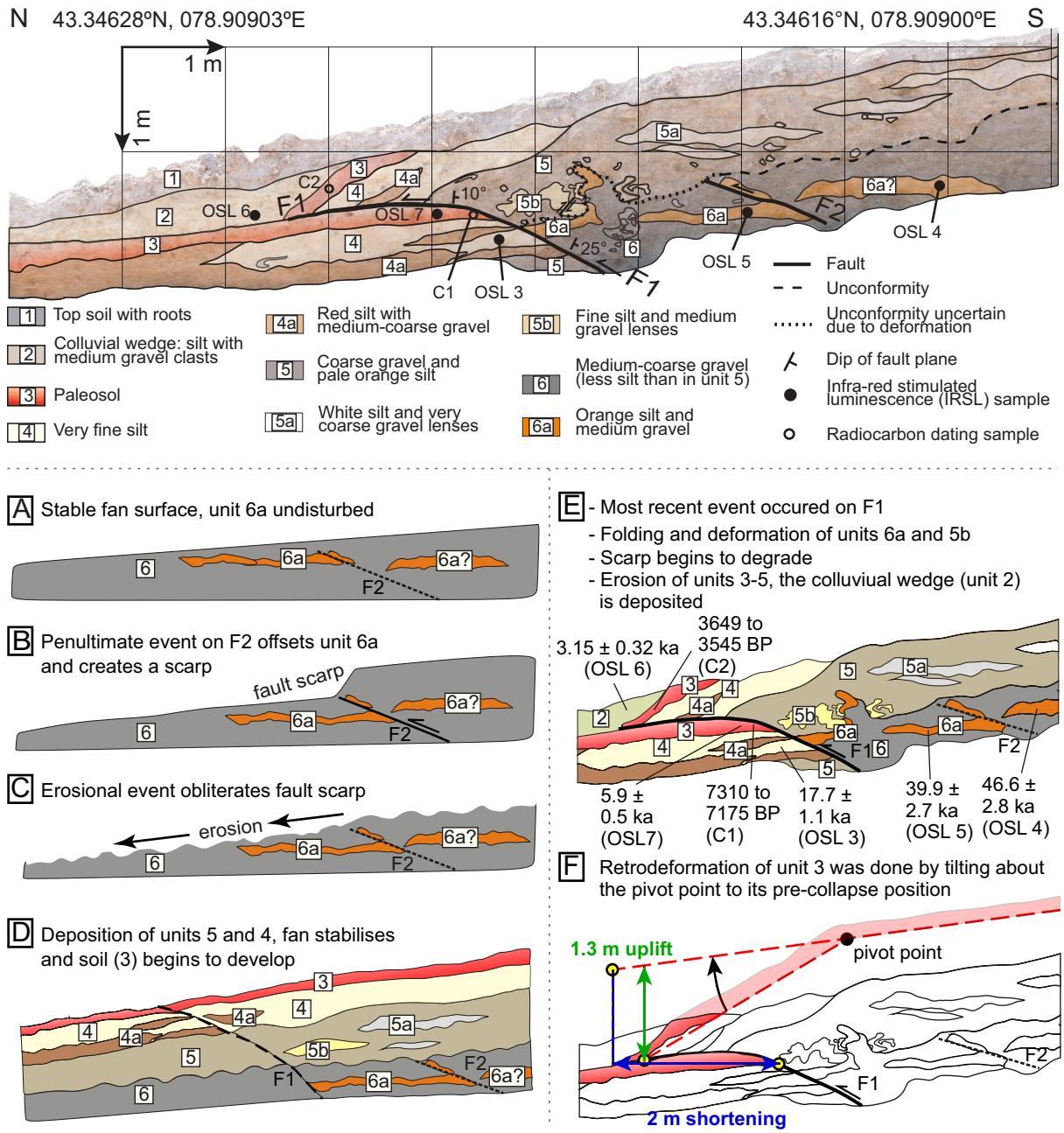


Figure 4.17: Adapted from Figures 6,7 of *Grützner et al., (in revision)*. (top) Palaeoseismic trench log with the main lithological units, interred faults, bulk deformation structures and locations of the Quaternary dating samples marked. (a-e) Retro-deformation of the trench wall, comprising of two surface-rupturing events. Radiocarbon constraint from the pre-MRE palaeosol are shown in years BP, while IRSL ages for the other silt lens' are shown in ka BP. (f) Sketch illustrating how the vertical and horizontal offset in the most recent event were determined.

the earthquake history on the fault (Figure 4.17a-e). The penultimate surface rupturing event occurred on F2, offsetting units 6 and 6a, followed by a period of erosion that erased the surface scarp. After the erosional event, a period of fan deposition emplaced units 5-4 followed by the formation of a palaeosol (unit 3) on the fan surface. The most recent surface rupturing event occurred on F1, displacing this palaeosol and all units stratigraphically below it (Figure 4.17e). Following this event, erosion of the units 3-5 occurred in the hangingwall, and a colluvial wedge was deposited against the scarp.

The silt unit 6a displaced by F2 yields a minimum slip estimate of ∼0.63 m of slip in the penultimate event, though the offset wedge of unit 6a could have come from a stratigraphically similar unit below, so this is a minimum bound. On F1, restoring the base of the palaeosol to its original planar geometry by extrapolating its gradient (Figure 4.17f) yields a vertical offset estimate of ∼1.3 m, in agreement with estimates from DGPS profiles on the fan surface. Combining this with the observed dip of 25° S gives an estimate of total slip of ∼3 m in the shallow subsurface.

Two bulk sediment samples from the palaeosol yielded calibrated radiocarbon ages of ∼7.2 ka BP and ∼3.6 ka BP (Figure 4.17e), a unit that should give a close pre-date on the last surface rupturing event. We attribute this variation to the palaeosol forming from deposition over a wide timespan, and potentially inclusion of older material by redeposition. The younger age of ∼3.6 ka therefore most likely marks the youngest stage of soil development and immediately pre-dates the earthquake. IRSL samples back this up, with a date of 3.15±0.32 ka from the colluvial wedge, and 5.9±0.5 ka from within the palaeosol – both of which fall within the range bracketed by radiocarbon ages for the palaeosol formation. An IRSL sample from unit 4 yielded an age of 17.7±1.1 ka indicating that the penultimate surface rupture occurred prior to the end of the LGM. Finally, samples from unit 6a in the footwall and hangingwall of F2 yielded IRSL ages of 39.9±2.7 ka and 46.6±2.8 ka respectively, pre-dating the penultimate surface rupturing event.

Therefore the most recent surface rupturing event occurred on F1 between ∼3.6 ka and 3.15 ka BP. The penultimate event occurred on F2 between 18–40 ka BP. Estimates of palaeo-earthquake magnitudes from the observed displacements suggest M_W 6.9–7.3 based on scaling relations of *Wells and Coppersmith* (1994), though we note that the correlation between offset and magnitude for thrust events is low. While there are large uncertainties, it is clear that this fault generated a large M∼7 earthquake in the 3-4 ka BP. The penultimate earthquake observed on this section of the fault occurred 18–40 ka BP, suggesting a recurrence interval of >10 ka for the fault.

B2: Slip-rate

4.5 km west of the trenching site, we observe further short remnants of cumulative scarps, displacing older alluvial fan surfaces (Figures 4.16, 4.18). With a granitic catchment, this fan is a good target for dating with a cosmogenic ^{10}Be depth profile for a slip rate study. Kinematic DGPS profiles across the scarp show a vertical offset of 12.4±0.4 m (Figure 4.18a,4.21a). If the offsets observed at the trench site are characteristic for events on this fault, it suggests that this is a cumulative scarp comprised of at least 6–8 events.

A pit in the surface shows relatively uniform stratigraphy of coarse sand, with occasional clasts up to 3 cm (Figure 4.18a). Low erosion rates and the dry environment suggest that sediment mixing and bioturbation should be minimal. Animal burrows were not observed at the surface or in the pit walls. Most root penetration is restricted to ∼25cm, though a few roots extend to ∼50cm depth. Any resultant

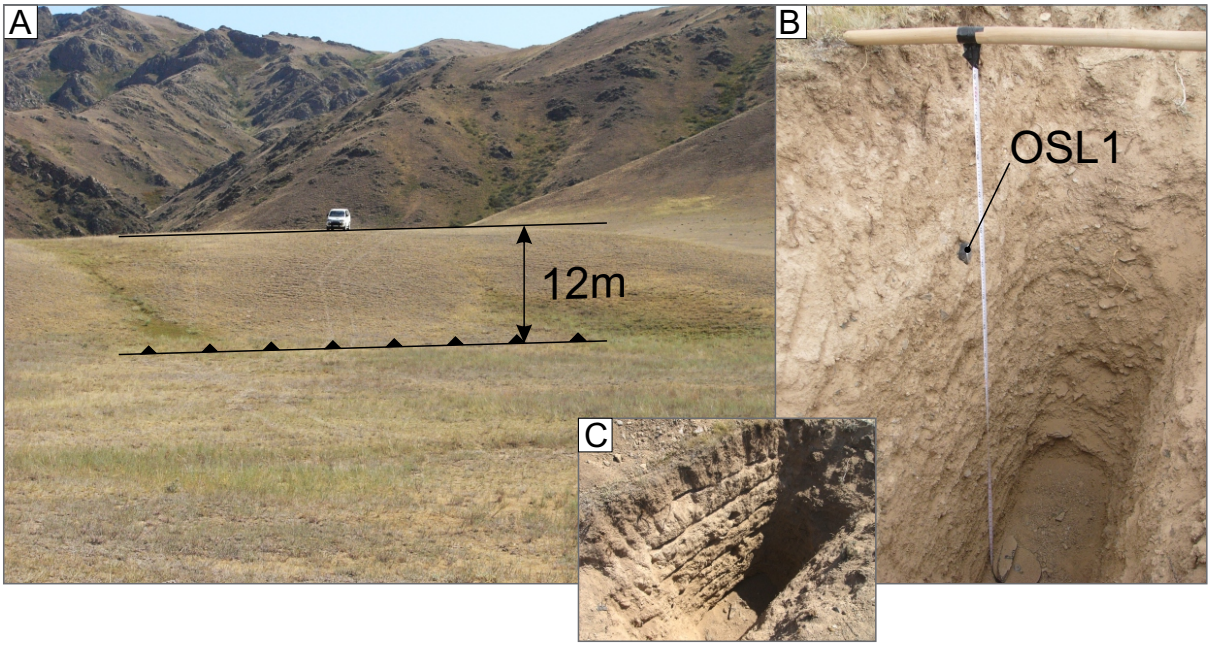


Figure 4.18: (a) 12 m scarp at the slip rate site on the Toraigyr Fault (b) Sampling pit for the ^{10}Be depth profile. (c) layers of ±2 cm were mined to collect 2 kg of material at 25 cm intervals.

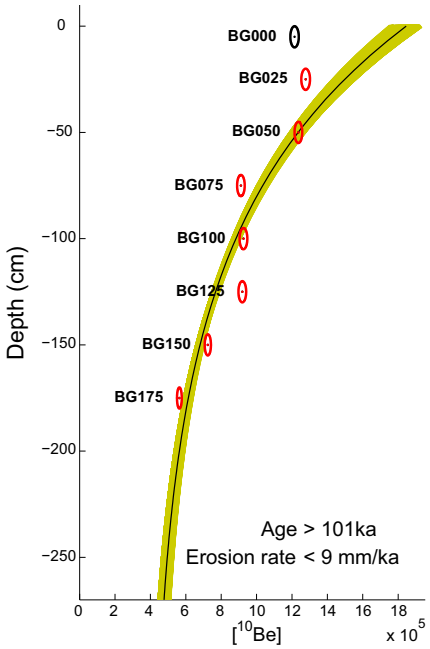


Figure 4.19: Depth profile of ^{10}Be concentrations. Monte-carlo simulations for the depth dependence assuming uniform instantaneously deposited material are shown in green (best fit in black).

Sample	AMS ID	^{10}Be (atoms/g)[1]
BG000	b10267	1214672 ± 23928
BG025	b10268	1277335 ± 24621
BG050	b10269	1236248 ± 21827
BG075	b10311	911432 ± 21494
BG100	b10312	925816 ± 21933
BG125	b10427	919404 ± 21888
BG150	b10429	724498 ± 17642
BG175	b10430	563795 ± 13501

[1] based on 2.79x10^{-11} ^{10}Be/Be ratio for NIST SRM4325 standard.

Table 4.2: ^{10}Be concentrations for the samples from the depth profile (Figure 4.18), The processed blank ratios were between 0.26 and 0.49% of the sample ^{10}Be/Be ratios. The uncertainty of this correction is included in the stated standard errors.

mixing in these uppermost regions is accounted for by reducing the weighting of the top two samples in the age modelling. Though the stratigraphy is reasonably uniform, I noted a slight reduction in grain size below a depth of ∼60 cm, but the material is the same quartz rich fine gravels and sand.

Eight samples were collected, each composed of ∼2 kg of amalgamated coarse granitic sand (<1cm),

collected at 25cm depth intervals, centred on a band of 2–4 cm thickness. One further sample of 10x10x10 cm was collected to estimate the sediment density (1.93±0.15 g/cm^3). ^{10}Be concentration measurements from sand-sized fractions have yielded well-resolved depth profiles in recent studies, particularly as the amalgamation of a large number of grains is effective in yielding averaged inheritance (e.g. *Schmidt et al.*, 2011). Initial preparatory work crushing and sieving yielded grains in the range 250-500 μm, was followed by magnetic separation to leave primarily quartz grains. I obtained a minimum of 200 g of quartz grains within the designated fraction for each sample.

After wet chemistry separation and AMS[7], we obtain ^{10}Be concentrations for each sample (Table 4.2). However, the concentrations do not show the expected clean exponential decrease with depth; there are two 'steps' down to ∼1.25 m, below which the concentration decreases more monotonically. Thus, the simple model of an instantaneously deposited unit exposed continuously since deposition (Figure 4.19) does not give a good fit to the data (χ^2=38), even if the uppermost sample is excluded because of suspected surface mixing and bioturbation.

Given the relatively uniform strata, and the presence of roots in the uppermost 30–50 cm, there is probably significant bioturbation within the upper 25–50 cm. Sample OSL1 (∼65 cm depth, Figure 4.18) also showed large inter-aliquot spread and failed to yield a robust age, also consistent with mixing at this depth. The change in stratigraphy observed at a depth of ∼60 cm combined with the stepped ^{10}Be concentrations therefore inspires a multi-stage depositional model for the surface (Figure 4.20a): We suggest the following sequence:

1. the deeper stratigraphy of the surface was deposited relatively rapidly as t0 before abandonment.
2. fault slip generates a cumulative scarp, while erosion smooths the profile (∼70–15 ka).
3. at 15-20 ka BP, a second period of intense deposition overtops the previously abandoned surface, draping a further 60 cm thick unit on top of the scarp (t1). The level of deposition in the footwall relative to that in the hangingwall is unknown, so the vertical offset estimate is only approximate.

Both t0 and t1 are comprised of very similar fine gravel and coarse sand of a similar origin, with only a minor difference in grain size differentiating them; I therefore assume the same inheritance for both to minimise the degrees of freedom. Fitting this model to the data suggests an age of >65 ka for the t0 surface, erosion rates of <30 mm/yr and ^{10}Be inheritance of 0.29–0.38 million atoms per gram (Figure 4.20b-e). While reasonably consistent with the observed concentrations, this deposition and evolution model is only one possible solution, so I am cautious in the interpretation of the age estimates. By comparison however, several other plausible models (three units, one unit, changing the number of samples excluded for mixing) all give similar minimum age constraints of >55-100 ka.

Attributing landscape evolution to periods of major climatic change (discussed in Chapter 3) can also provide a useful order of magnitude constraint on the surface age. Previous studies have noted especially

[7]Initial crushing, sieving and magnetic separation was performed by myself, but the wet chemistry and AMS were performed by CIAF at SUERC, see §4.4.1 for further details. Modelling of the ^{10}Be concentrations to estimate ages and erosion rates was performed by Angel Rodes at CIAF.

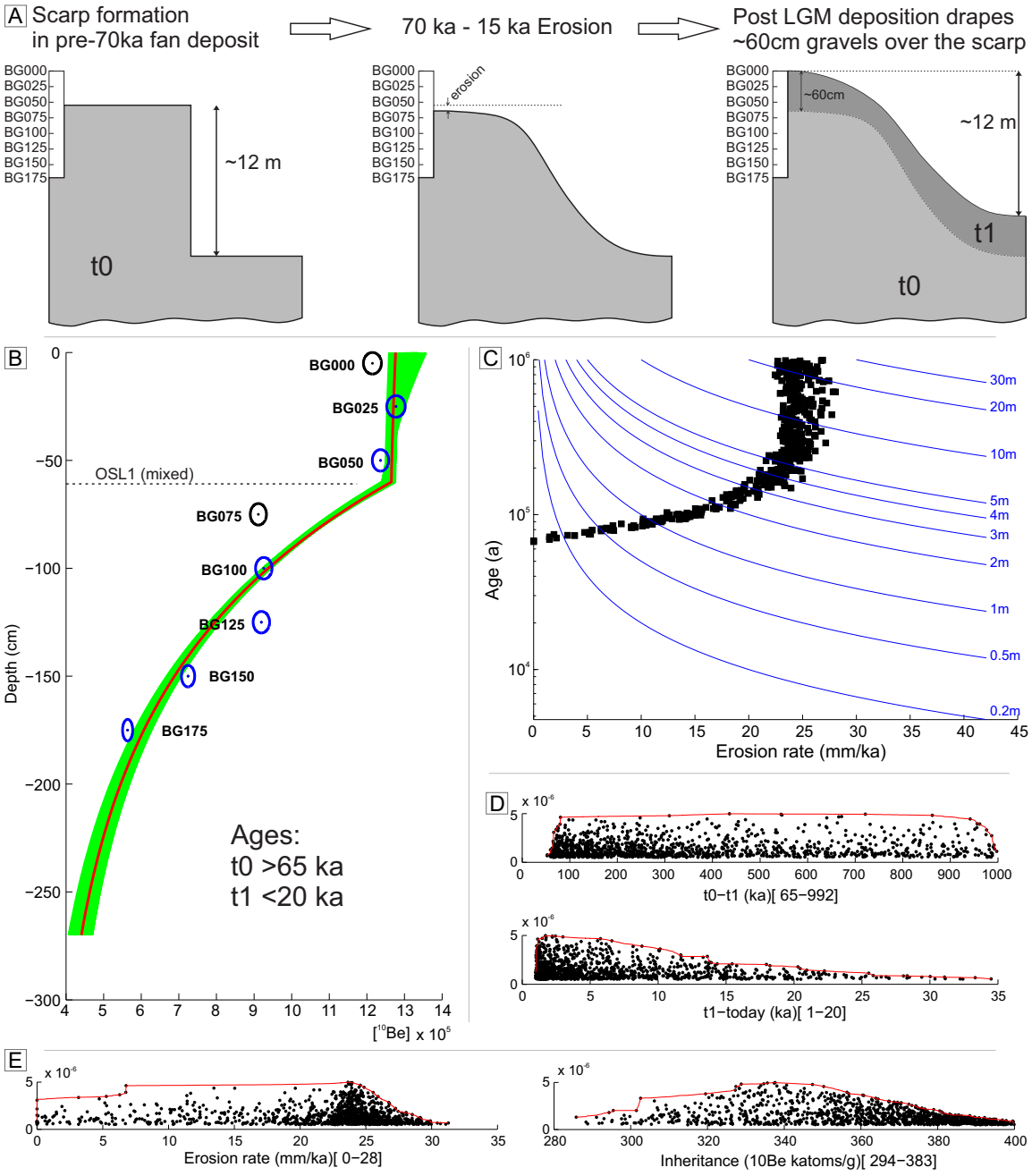


Figure 4.20: (a) Schematic site evolution suggested to give two episodes of deposition. The thin uppermost unit (t1, ∼60 cm) was draped on a pre-existing scarp in an older fan surface (t0). (b) Monte-Carlo simulations for the ^{10}Be concentration depth dependence based on the model in (a). Red shows the best fit model. Samples BG000 and BG075 were excluded from the fitting as we might expect surface mixing at these depths. Also noted is the relative location of sample OSL1 which showed strong inter-aliquot scatter suggestive of mixing. (c) The Monte-Carlo simulations (black) plotted in Age–Erosion Rate space suggest a maximum erosion rate of ∼30 mm/ka and a minimum age of ∼65 ka (models fitting at the 1-σ level shown in red). (d) Monte-Carlo simulation estimates for the exposure age of the t0 unit (>65 ka) and the t1 unit (<20 ka. (e) Monte-Carlo simulation estimates for the erosion rate and ^{10}Be inheritance.

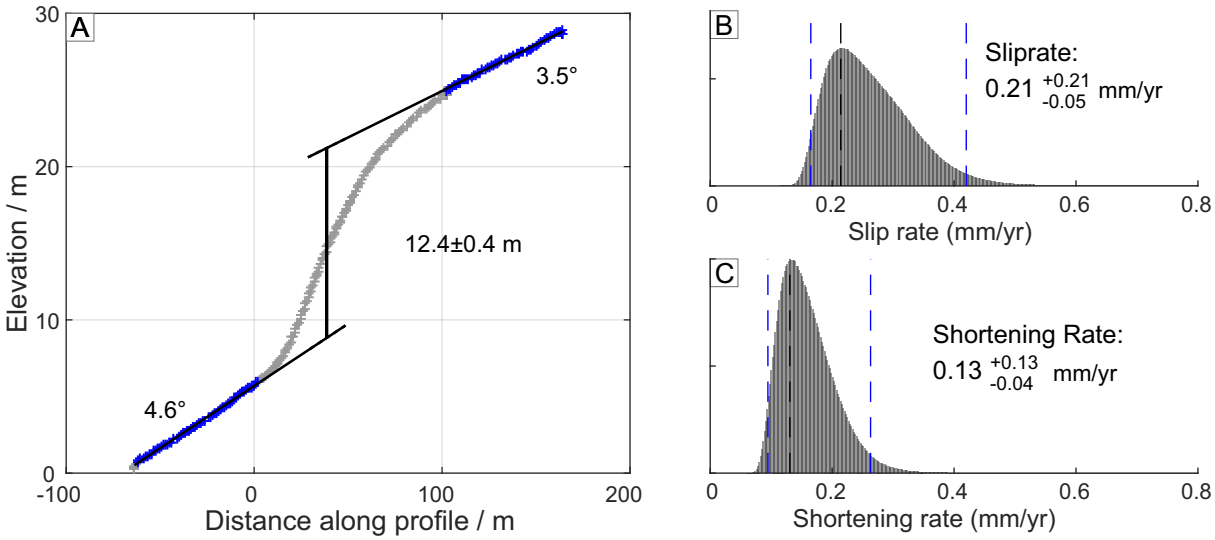


Figure 4.21: (a) A kinematic DGPS profile across the scarp at the slip rate site reveals a vertical offset of 12.4±0.4 m. (b-c) Monte-Carlo modelling of the slip rate and shortening rate based on a shallow dip of 26±5°, a deep dip of 45-60° and the minimum age from the ^{10}Be date gives maximum rates.

strong periods of landscape change associated to the demise of the last two glacial maxima at ∼14 ka and ∼120 ka. In particular, deposition following the LGM has erased fault scarps in many places through the Tien Shan; in general, only short stretches of cumulative scarps are preserved from prior to the LGM, with fewer still from prior to the previous maxima. It is likely therefore that the t0 surface was abandoned after ∼120 ka BP. I note also that our estimated age for the deposition of the t1 unit (poorly constrained) corresponds closely to the end of the LGM in the region (*Thompson et al.*, 2002), consistent with the emplacement of this unit during a later period of intense deposition. As we only observed a single earthquake in the past >17 ka at the trench site, it is very unlikely that the observed scarp was entirely formed since the deposition of t1.

Given the estimated age range of ∼65–120 ka, with a fault dipping at 25±5° S (from the trench), I use Monte-Carlo simulations to estimate a preliminary slip rate of $0.21^{+0.21}_{-0.05}$ mm/yr (Figure 4.21b). For a steep 45-60° on the deep fault, this suggests a geological shortening rate of $0.13^{+0.13}_{-0.04}$ mm/yr (95% confidence bounds, Figure 4.21c).

4.7.2 Kemin–Chilik Fault Zone (KCF)

To the north and west of the Toraigyr fault, the Kemin–Chilik Fault zone (KCF) runs NE-SW for over 280 km through the Za'Ilisky Range (*Delvaux et al.*, 2001; *Selander et al.*, 2012), the local section of which is labelled the Bartogai Fault (BF) in the vicinity of the Bartogai reservoir (Figure 4.16). The 1911 M 8 Kemin earthquake occurred the Kyrgyz section of this fault zone, rupturing the Chon-Kemin and Chon-Aksu fault segments, but no earthquakes are reported on the Kazakh portion of the fault zone. This long, inherited Palaeozoic structure shows large cumulative left-lateral offsets of up to 350±50 m, to the west of the Bartogai reservoir. There are no known slip-rate estimates on this fault, and there are

almost no surface scarps in Quaternary materials.

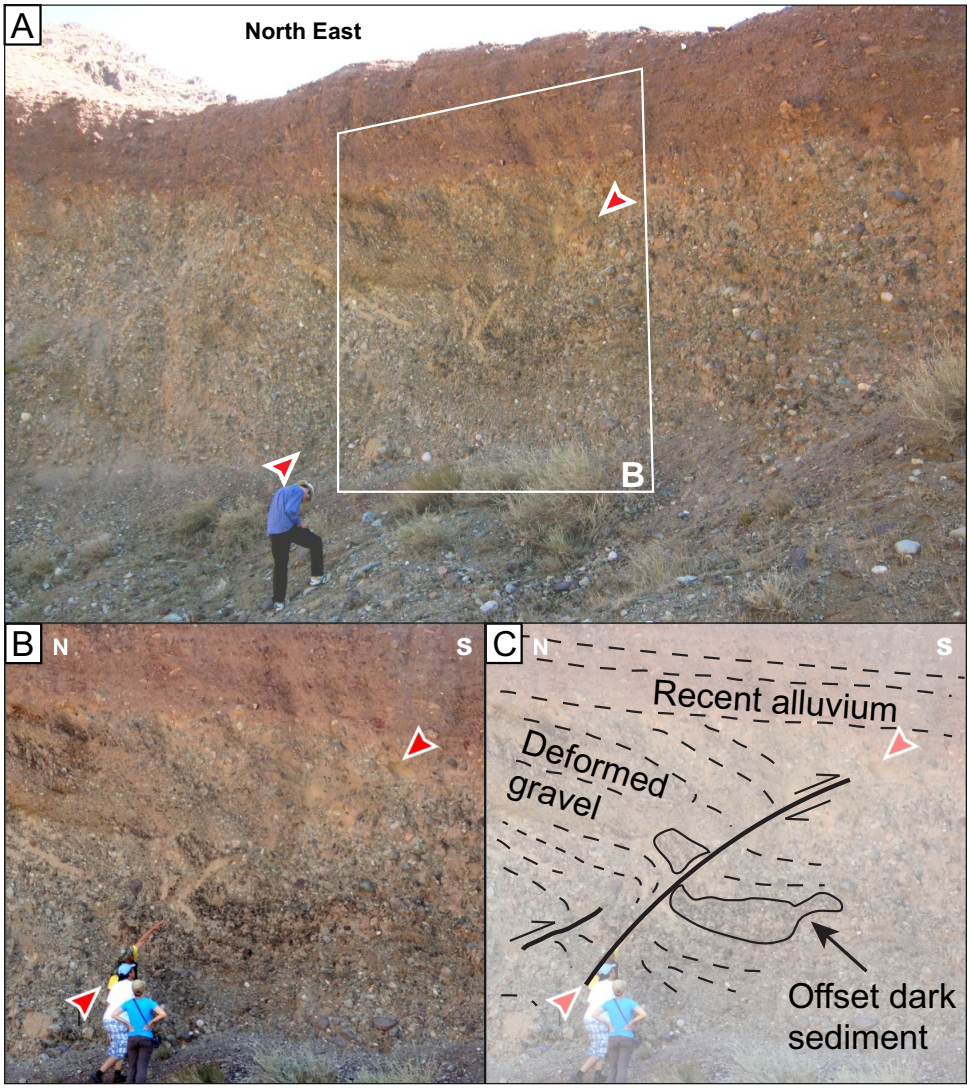


Figure 4.22: Figure 8 from *Grützner et al., (in revision).* (a) Photo of the deformed units at the Bartogai Fault (location in Figure 4.15). Photo looking east.

Near the eastern shore of the Bartogai reservoir (Figure 4.16a), the fault is exposed in a small gravel Quarry (Figure 4.22). Alluvial deposits are offset with a significant reverse component (lateral slip unconstrained), on an interface dipping at $\sim 45°$ N. However, the uppermost deformed units are capped with a further ∼2 m of alluvial sands and gravels, suggesting that this fault strand has not had a surface rupturing event in the late Holocene, consistent with the suggestion of a low slip rate. Further work is necessary to properly constrain the activity of this fault, especially given the close proximity of the Bartogai reservoir dam. It is clear though that this fault is accommodating at least a small component of the geodetically observed shortening. However, compared to the TY scarps across the basin, the surface scarps have been removed by ∼15 ka of deposition, suggesting no earthquakes in the Holocene. Combined with the lack of cumulative scarps, this suggests a low slip rate and hence shortening rate. Though as observed on the Saty and Toraigyr faults, prior to the most recent event on each, there would have been

very little indication of activity.

4.7.3 Shonzhy Fault System

Near the town of Shonzhy in the south of the Ili Basin, we map a complex interaction of faults (Figure 4.23). The most prominent geomorphic scarps are two near-parallel fault scarps on a NW-SE orientation and a broad zone of surface scarps extending eastwards along the Ili Basin from near Shonzhy. These scarps are visible both in the optical satellite imagery due to the vegetation changes across the scarp, and as topographic steps in the global AW3D30 (*Tadono et al.*, 2014) global 30 m DEM (Figure 4.23). Here I describe each set of faults, both of which demonstrate significant late Quaternary activity, though neither are marked on existing active fault maps of the region.

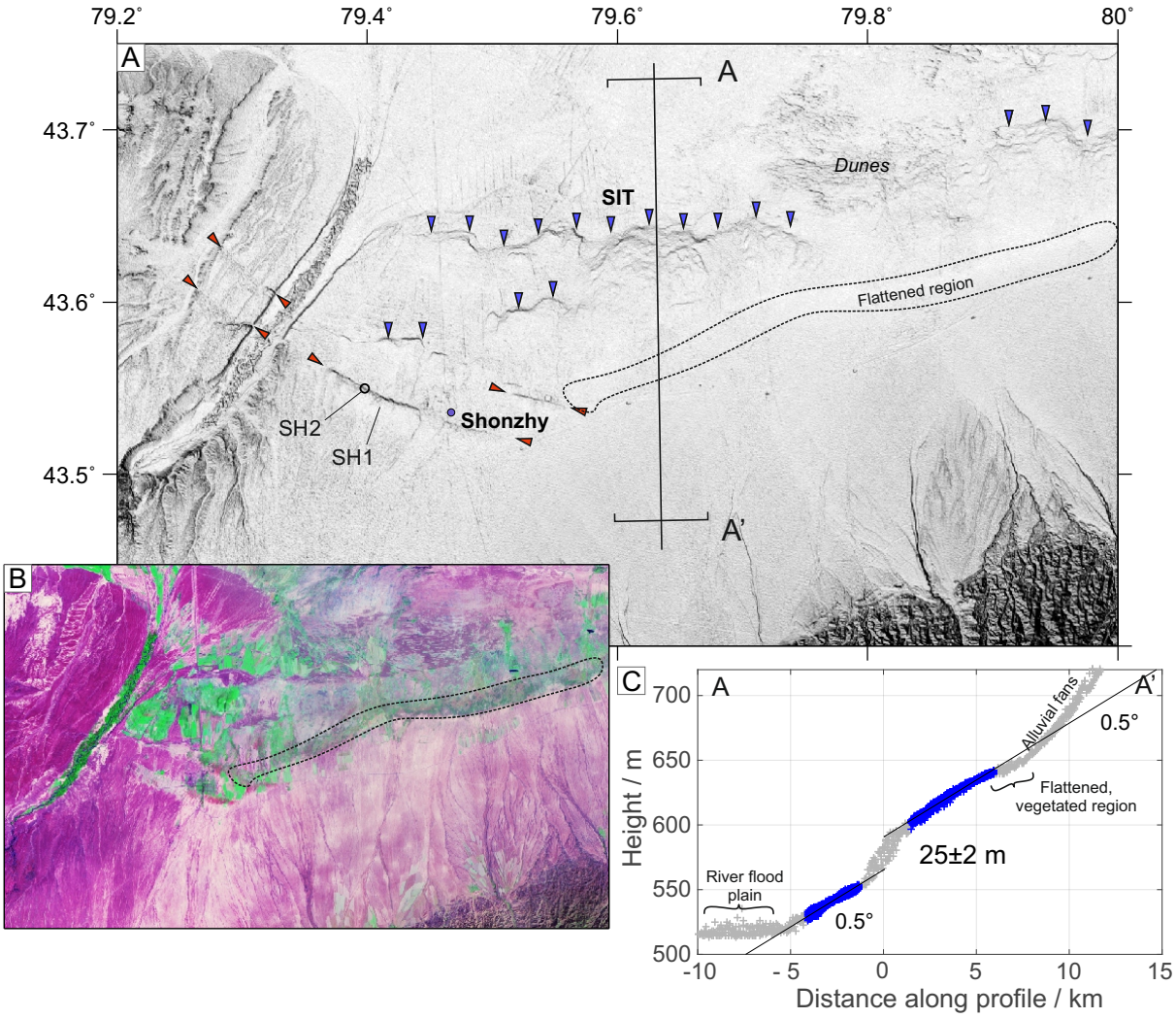


Figure 4.23: (a) Shaded relief of the southern margin of the Ili Basin near the town of Shonzhy (AW3D30 elevation data, illuminated from the SE at a low angle to exaggerate the shading). Orange arrows mark the distinctive Shonzhy faults, two parallel strike slip faults with significant thrust component. Blue arrows denote the South Ili Thrust (SIT). (b) Landsat ETM+ 542 mosaic of the same region as (a), showing the enhanced vegetation within the dashed polygon. Fault uplift has back-tilted this region, inhibiting drainage. (c) Projecting the AW3D30 DEM onto the profile A–A" (marked in A, swath width ±2 km) shows a cumulative vertical offset of ∼25 m on the SIT.

South Ili Thrust (SIT)

The thrust fault running east of Shonzhy is visible in a shaded relief of the AW3D30 topography (Figure 4.23a), with low angle illumination from the south. It forms a sinuous fault scarp, running relatively continuously for 160 km, parallel to the rangefront of the Ketmen range. In contrast to the river terrace risers of the Ili river which are very straight, well defined and of fairly uniform height, this scarp varies in offset along strike, and has a characteristic asymmetry consistent with a degree of shallow folding.

Figure 4.23c shows a swath profile across one of the clearer sections of the scarp; there is a discrete step in the gradient of the alluvial fan material emanating from the rangefront, with an offset of ∼25 m here. Where the scarps cross younger fan material and drainages, they are smaller. In the immediate hangingwall, fault displacement has resulted in a southwards-tilting of the surface over a wavelength of ∼5–10 km, resulting in an almost entirely flat region (Figure 4.23). This flat region collects water from the rangefront, resulting in more vegetation – the vegetated band is visible for most of the length of the Ketmen range, as are the topographic scarps. Given the consistent location of this fault relative to the range to the south (20–30 km), I suggest that this fault is a splayed detachment from the Ketmen rangefront fault. Similar to the Kegen basin fold (§4.5.2), this is likely to be a low angle detachment within the basin sediments (estimated to be 4–5 km thick, *Kober et al.*, 2013). The surface scarp shows back-tilting over a wavelength of 5–10 km, consistent with a shallow detachment steepening to the surface in the uppermost ∼5 km. Therefore, although I have noted that the fault at the rangefront itself has a low slip rate inferred from lack of scarps in late Quaternary fans, the active slip may instead reach the surface near the middle of the Ili basin. The SIT is clearly a significant active fault, with displacements of 25+ m displacements in the Quaternary sedimentary cover.

Shonzhy Town Scarps (ST)

At the town of Shonzhy, two NW-SE trending fault scarps run through the edges of the town (Figure 4.23a). Both scarps show south side up displacement, with a large offset (Figure 4.24b) – there are no well defined markers to measure lateral offsets on the faults, but the fault orientation suggests a component of right-lateral slip too. At site SH1, I investigated the southern strand in the field; Figure 4.24 shows a photo of the scarp with a person for scale. We estimate the vertical offset of the scarp by a combination of kinematic DGPS profiles, and a drone SfM survey DEM of a 500 m stretch of the scarp.

Figure 4.24a shows a shaded relief map of the DEM. Strong winds adversely affected the photographs from this survey, so the survey area has been cropped heavily, and we grid the pointcloud at a horizontal resolution of 0.6 m as we observe motion-blur related artefacts in the data at higher resolutions. This resolution is still sufficient to measure scarp offsets; Figure 4.24b shows four profiles through the dense pointcloud from which we estimate vertical offsets of 20–25 m. A further 2.5 km NW along the scarp, at SH2, we estimate a smaller offset of ∼10 m from two kinematic DGPS profiles (Figure 4.24d).

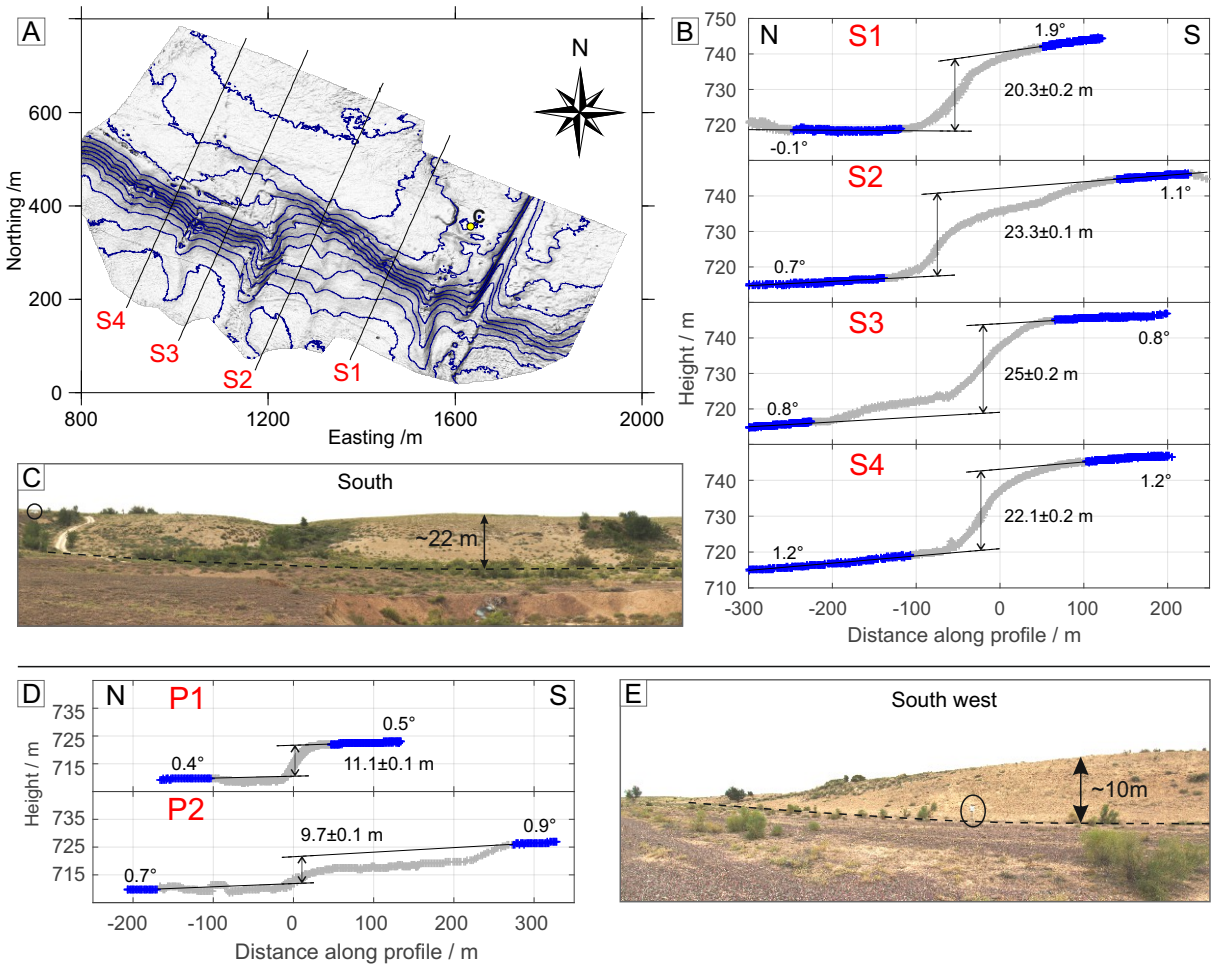


Figure 4.24: (a) Shaded relief of the drone SfM DEM at site SH1, contoured at 2 m intervals, showing the locations of the profiles S1–S4. (b) Profiles across the scarp at SH1, yielded vertical offsets of 20–25 m. (c) Panoramic photo of the scarp (location in A). (d) Two kinematic DGPS profiles across the scarp at SH2, ∼2.5 m NW from SH1. The scarp is smaller here, with an offset of ∼10 m (e) Photo of the scarp at SH2, person for scale (circled).

In the hangingwall, the scarp material at the surface has a thick loess cap, while in the footwall, we observe compacted gravels (<15 cm) in a loessic matrix; this change in composition is indicative of post scarp-formation loess deposition. It is unclear how much loess has been deposited on top of the scarp, but as the topographic step is maintained over a large wavelength (visible in AW3D30), the majority of the measured offset is likely to be fault displacement related. The thick loess makes access to the gravels in the hangingwall difficult, making it tricky to provide fault relation for any samples collected within the loess deposits. As such, a further more detailed investigation is needed to constrain the slip-rate on this fault, but is likely to be hampered by site conditions.

The northern of the two strands (Figure 4.15) displaces similar material in the same sedimentary setting, south side up, suggesting a very similar structure though the scarps are generally smaller so we expect a lower slip rate on this strand.

4.8 Ili Basin Northern Margin

The Dzhungarian Alatau form the northern margin of the Ili Basin, where shortening is accommodated by a series of thrust faults, and possibly a contribution from strike-slip rotation (discussed in §4.10.2). There are three main E–W oriented structures; the southern rangefront of the Dzhungarian Alatau (DZS), the Usek Thrust (UT) bounding the Koyandytau Range, and the North Ili Folding sequence (NIF) in the foreland (Figure 4.25).

The major rangefront (DZS) at the southern edge of the high topography has not been studied in the past and the difficult access prevented palaeoseismic trenching, but we attempt to constrain the slip-rate on this fault through dating of alluvial fans offset by cumulative scarps. The Usek thrust has a previous study documenting the slip rate (*Cording et al.*, 2014), but not the behaviour of this fault in past earthquakes – we investigate a series of relatively fresh single and cumulative event scarps to estimate likely recurrence intervals and a bound on the age of the most recent event. The folding extending into the foreland basin has been partially documented by *Cording et al.* (2014) and *Kober et al.* (2013); we add further observations and note the presence of discrete fault scarps along the southern margin of the folds. Significant shortening is accommodated by these folds, but further detailed structural mapping is required to ascertain the actual rate of shortening. In this section I describe each structure, summarising the observations of previous authors and presenting my estimates of slip-rates and earthquake histories.

4.8.1 Ili Basin (North) Cenozoic Folding (NIF)

Although the Usek Thrust and the Dzhungarian southern rangefront bound the main ranges, faulting and folding has propagated southwards into the Ili Basin. *Kober et al.* (2013) and *Cording et al.* (2014) map two major fold structures and a push-up range.

The basement cored Duyantau Range is ~6.5 km wide and has generated ~500 m relief. *Cording et al.* (2014) map active, steep dipping reverse faults on both the north and south boundaries, and an eastwards continuation in the form of the Lesnovka anticline in Cenozoic sediments (Figure 4.25). Immediately south of the Duyantau Range, *Kober et al.* (2013) and *Cording et al.* (2014) map two small anticlines near the Usek River (informally labelled Ibex and Beknazar anticlines), and the larger Aktau anticline to the west.

The folds have uplifted the Cenozoic sediments, resulting in deep incision in the soft, well bedded material (Figure 4.26). In addition, *Kober et al.* (2013) and *Cording et al.* (2014) note a flexure/scarp in the piedmont on the southern side of both the Aktau, Ibex and Beknazar anticlines, suggesting that discrete fault slip reaches the shallow subsurface at least. The degree of incision and the surface scarps suggests that these anticlines are accommodating significant slip on the underlying faults – more work is needed to quantify the geometry of the folding deformation and the ages of the surfaces displaced by the scarps along the southern margins. The potential role of these structures in accommodating shortening

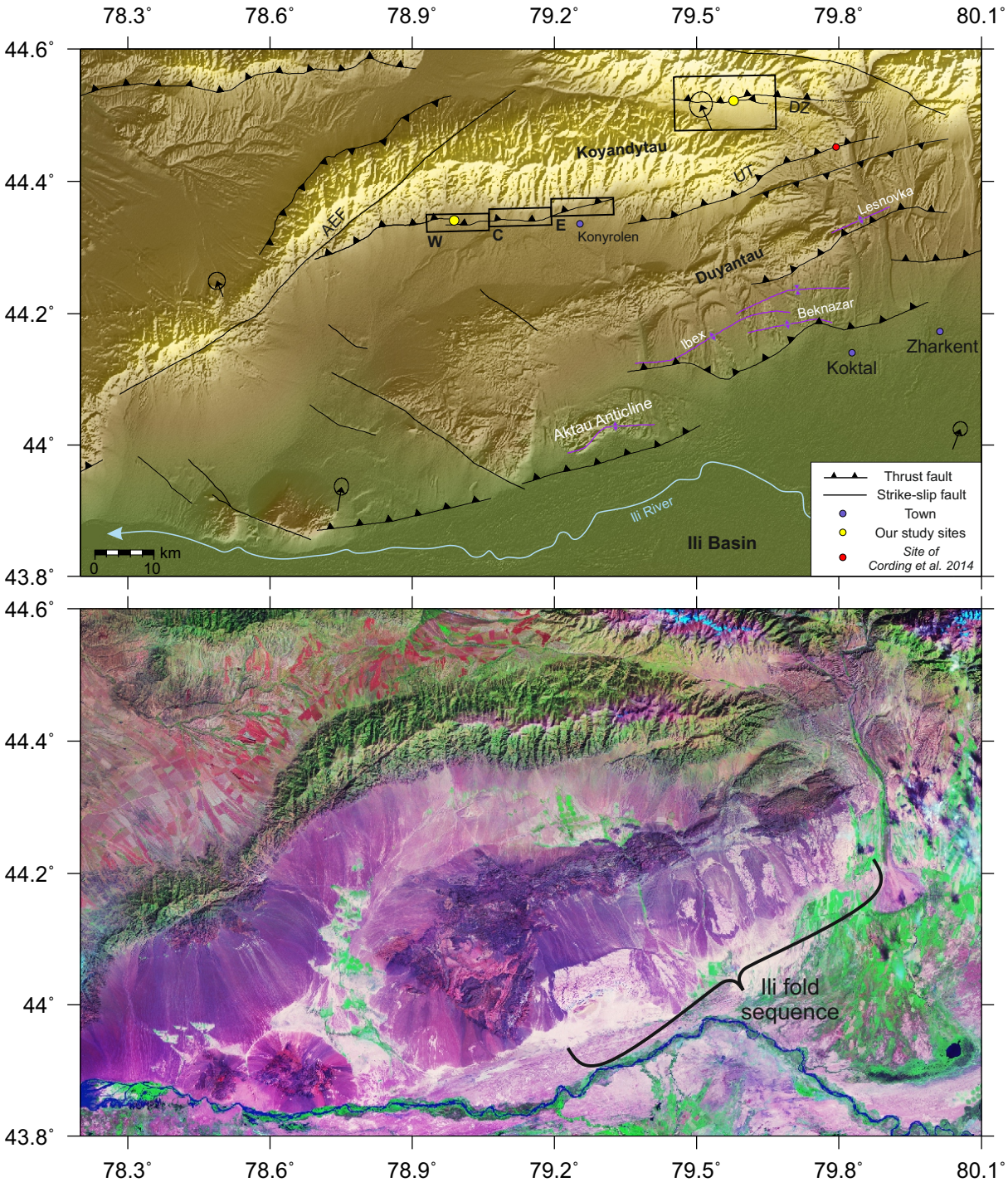


Figure 4.25: (top) Map of the active structures on the southern margin of the Dzhungarian Alatau and the Northern half of the Ili Basin. Fault and fold mapping based on *Kober et al.* (2013); *Cording et al.* (2014); *Campbell et al.* (2013); *Abdrakhmatov et al.* (2016), with additions from our own field and remote mapping. Boxes W, C, E mark the regions covered in Figures 4.28, 4.29 and 4.30 respectively. Fault labels: AEF–Altyn Emel Fault, DZS–Dzhungarian Alatau Southern Rangefront, UT–Usek Thrust. (bottom) Landsat 7 ETM+ 542 False colour composite mosaic image of the northern Ili basin (same area). The Cenozoic sequence is visible as very bright, light colours where folding in the NIF has exposed it. The Palaeozoic basement of the Duyantau Range appears magenta. The inherited structure of the Altyn Emel Fault is also clearly visible cutting through the Koyandytau Range.

is discussed in §4.10.

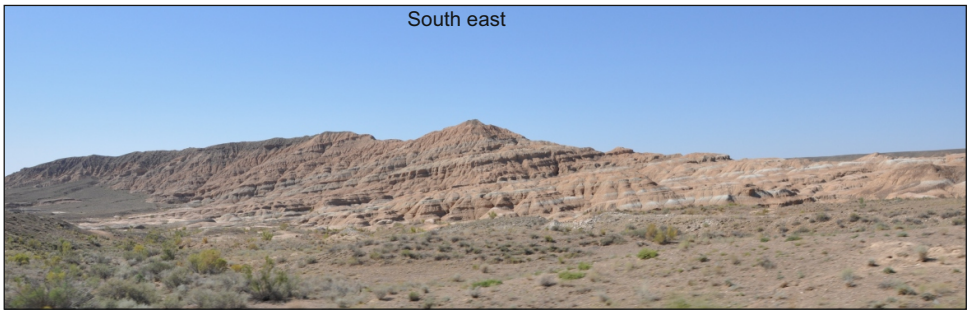


Figure 4.26: Example of the tilted, uplifted and incised Cenozoic sediments in the Ibex Anticline of the North Ili fold (NIF) system. Location: 44.172°N, 79.538°E.

4.8.2 Usek Thrust (UT)

The Usek thrust runs approximately E-W along the southern front of the Palaeozoic basement cored Koyandytau range (Figure 4.25). This range is flanked by Neogene sediments, topped with Quaternary deposits.

Slip rate – *Cording et al.* (2014)

At the longitude of 79.8°E, adjacent to Koktal town, the Usek river has incised a deep gorge through the Palaeozoic core of the Koyandytau range, but on the flanks the river has left a flight of large late Pleistocene terraces up to ∼300 m above the present river level (Location in Figure 4.25). *Cording et al.* (2014) studied this series of terraces to estimate the fault slip rate. They estimate the age of their T_4 terrace (offset by ∼140 m) using a ^{10}Be depth profile and ^{10}Be surface boulder ages. The two methods independently estimate the abandonment of the surface as ∼360±60 ka, giving an uplift rate of 0.36±0.07 mm/yr. Based on the dip of the contact between the Palaeozoic basement overthrusting the Neogene sediments in the sides of the Usek river valley, they estimate a dip of 45-70°, yielding a shortening rate of $0.25^{+0.09}_{-0.08}$ mm/yr. The authors also estimate an erosion rate of ∼0.5 mm/yr based on the ^{10}Be depth profile and qualitative observations of the degree of incision in the terrace surfaces.

4.8.3 Konyrolen Scarps

To the west of the site on the Usek Thrust studied by *Cording et al.* (2014), the Koyandytau Range increases in height, with peaks up to ∼3200 m. This large, Palaeozoic basement cored range runs approximately E-W as far as the Altyn Emel strike slip fault (AE, Figure 4.25), where it turns SW, stretching to the Kapchagay reservoir. Along the rangefront between the villages of Konyrolen and Intali (Figure 4.25), there are a series of very continuous fault scarps. The scarps break the surface mainly in granite boulder alluvial fans at a distance of 1–3 km basinwards from the rangefront Palaeozoic-

Quaternary contact, and are visible for >35 km. There are, however, no known earthquakes in the historic records attributed to this region. These scarps present an opportunity to probe the earthquake behaviour on this fault of a known slip rate, though the rate estimate of *Cording et al.* (2014) was near the end of the fault, so it may be higher here. Surveying a long stretch of the fault, we estimate the offsets of two different heights of scarps, which we infer to represent slip in the past two events. Based on an approximate age estimated from anthropomorphic petroglyphs, we infer a minimum age and slip of the most recent event.

Survey

Using a Helikite aerial survey, I constructed a DEM covering the majority of the visible surface scarps (∼30 km). Carried out on two separate days, the eastern half in the 2014 field season and the western half in the 2015 season, this comprises the longest fault scarp survey to have been carried out on a single fault trace with SfM to date. The capacity for SfM to perform such surveys is rivalled only by airborne lidar, but at many times the cost.

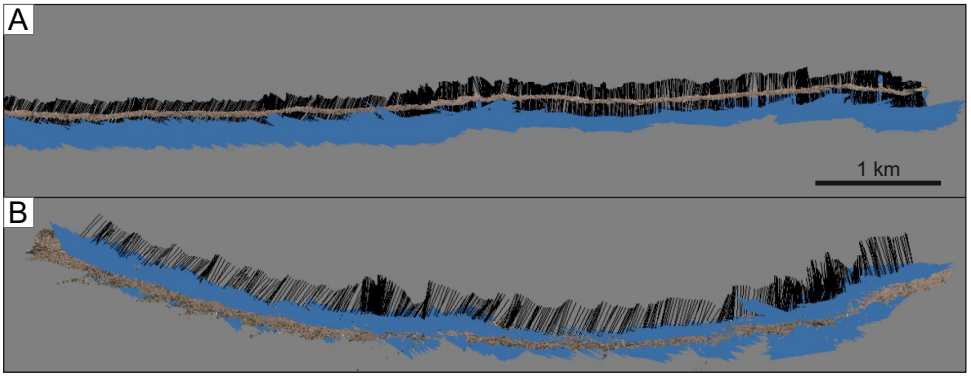


Figure 4.27: (a) Model after using an initial pre-calibration. (b) Model without pre-calibration for the eastern section, showing a long-wavelength 'bowl' effect due to an error in the estimated radial distortion and focal length parameters.

As with the previously mentioned surveys, we used the RICOH GR Digital II camera suspended from a 2 m^3 Allsopp Helikite. Using a line length of ∼150 m, we achieved a swath width of ∼200 m. With the balloon attached to a backpack, the operator walked along the fault scarp, choosing where to walk based on the wind direction, to ensure the fault scarp was near the centre of the field of view. With relatively little experience, the operator was able to estimate approximately the area visible from the camera, however a second person at some distance from the primary operator also helped to guide the location of the balloon via instructions. Given the length of the survey, we used rolling ground control i.e. one person placed ground control points ahead of the Helikite, while a second measured the location of each point with a kinematic DGPS and then collected the target once the Helikite has passed over. We used orange plastic squares for targets; with the balloon at this altitude (50–100 m, wind dependent), targets of at least 1 m^2 were necessary in order to identify them in the images during processing. Each

control point has one corner marked with black tape to denote the 'target' point, as the corners are the easiest to define on the images, but we also consistently utilised the southernmost corner of each control point as it is occasionally difficult to visually identify the active corner on the photographs.

The photographs were all taken with a 'forward tilt' on the camera, i.e. looking slightly toward the operator from nadir, with the operator just outside of the edge of the frame. This enlarges the individual field of view and helps introduce more depth of field into the frame, which is necessary to break the trade-off between focal length and radial distortion in solving for the internal camera parameters (*James and Robson*, 2014). A further aid in breaking the radial distortion – focal length trade-off comes from an initial camera model; we used the Agisoft Lens utility to estimate the lens parameters with the same aperture and fixed (∞) focal length. The first attempt to build a model from these photos without the initial estimate of the camera parameters illustrates exceptionally well the effect of this trade-off; Figure 4.27 shows the SfM model with and without the initial estimate for the internal camera parameters. As the model is build sequentially, with photos added one at a time followed by a bundle adjustment after every few additions, errors in the solved lens distortion model can propagate through the entire model, giving a 'bowl' effect (*James and Robson*, 2014).

Due to the scale of the model we were unable to have dense ground control along the entire stretch, so we used the ground control from the first half of the survey to orient the model, and then the points at the end to estimate the total warping due to lens calibration errors. The result is a good fit to the ground control <1% over the 10 km baseline for each half of the survey. The errors in the model are likely to be much smaller than errors in fitting lines/surfaces and interpreting the geometry. As we only measure local offsets at sites along the fault, the long wavelength warping of the model is negligible on the length scales of interest.

Figures 4.28–4.30 show the hillshaded DEM from the survey, and the scarps mapped from both the elevation dataset and panchromatic Kompsat-2 imagery (1 m resolution). Due to a camera battery failure, a short stretch between the two halves of the survey is missing. There are also several stretches where no fault scarp is visible, where it has been covered by post-earthquake deposits, or due to step-overs in the fault. In addition to the two Helikite surveys, we extended the western end of the survey by a further 1 km with a high resolution drone survey (Figure 4.28).

Focus Survey – Intali Site

At the western end of the Konyrolen scarps, near the village of Intali, we used the high resolution survey as a case study of a stretch of fault where we observe multiple generations of faulting in neighbouring fan deposits. Figure 4.32a shows the resulting 3D model and DEM from the high resolution survey, in which we observe two distinct sets of vertical offsets; at the western end the fan deposits are only lightly incised, and are displaced by 1–2 m (profiles 1–4, Figure 4.32d, Figure 4.31a), whereas in the centre the fans are much more heavily incised and profiles yield vertical offsets of 4–7 m (profiles 5–8, Figure 4.32d,

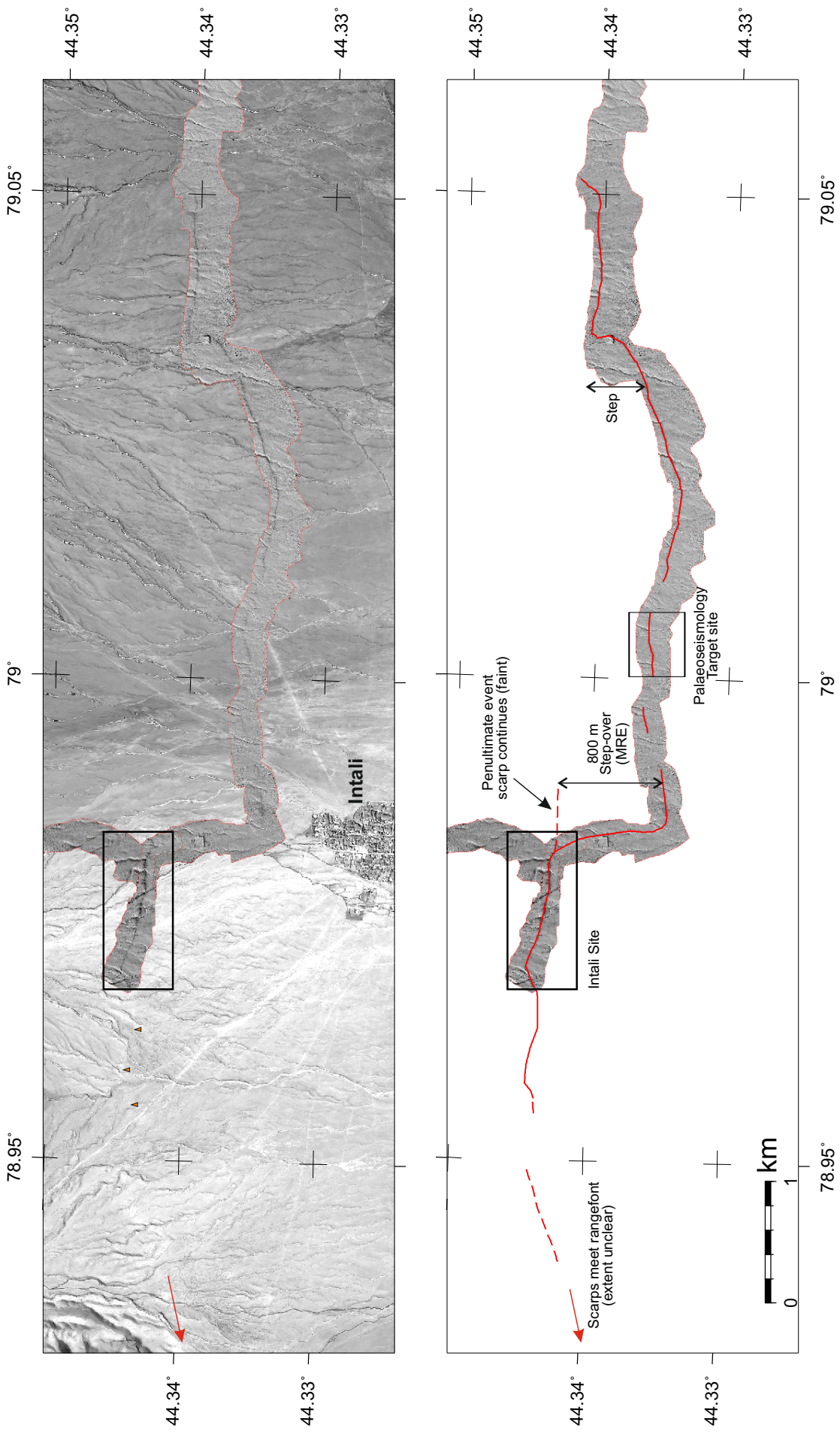


Figure 4.28: Western stretch of the SfM survey; (a) Shaded relief DEM overlain on 1 m resolution panchromatic Kompsat-2 imagery. (b) Map of the observed scarps (red) along this section of the fault. Black boxes show the outline of the Intali site (Figure 4.32) and the potential site for palaeoseismic trenching.

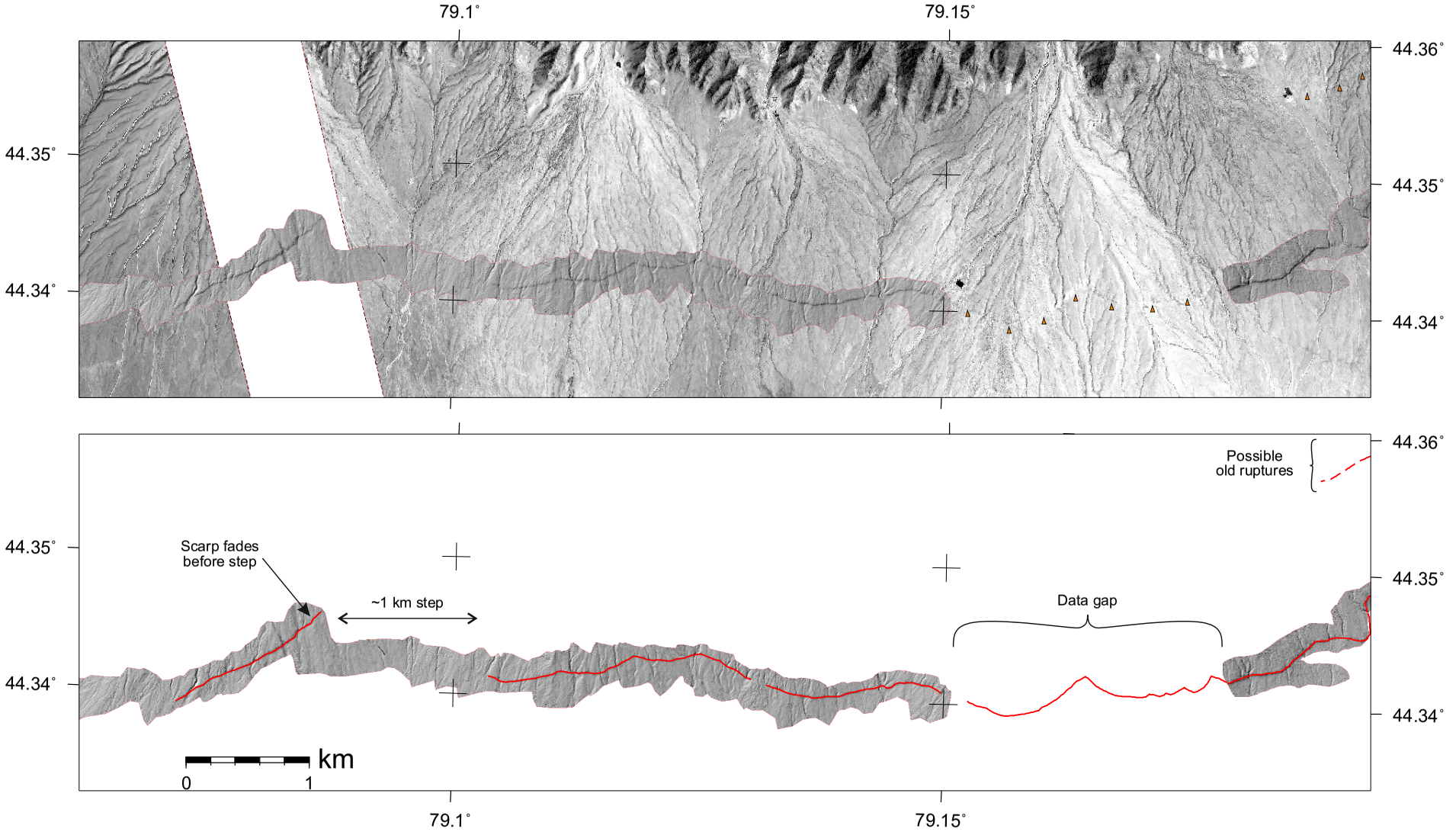


Figure 4.29: Central stretch of the SfM survey; (a) shaded relief DEM overlain on 1 m resolution panchromatic Kompsat-2 imagery. Orange triangles denote the scarp through the section not covered by the DEM due to battery failure. (b) Map of the observed scarps (red) along this section of the fault. Dashed lines indicate other scarps mapped from satellite imagery only – generally less fresh, these may be due to the penultimate event. It is unclear whether the step of 1 km in the observed scarps is due to post-event fan deposition, or a rupture step-over.

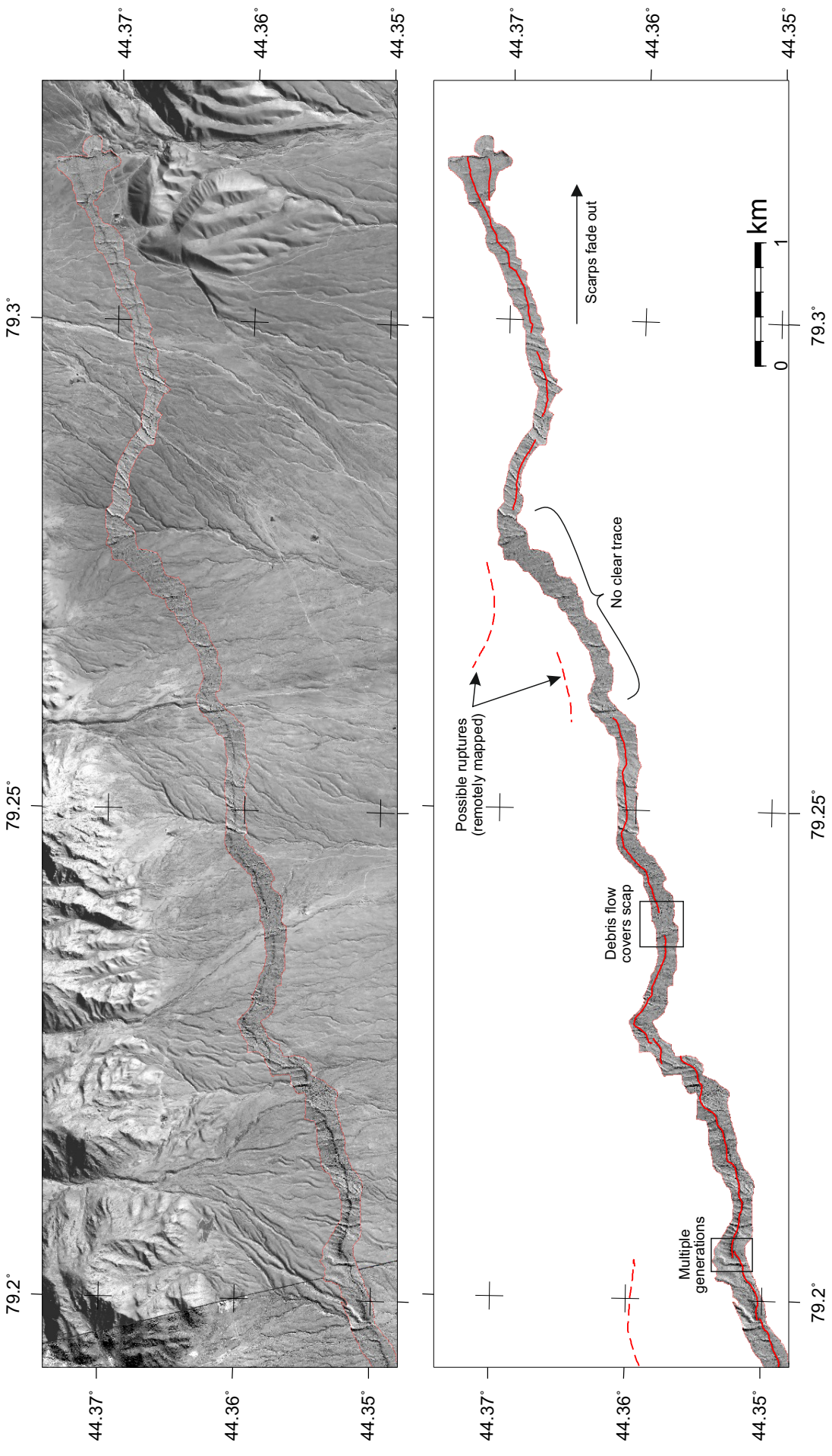


Figure 4.30: Eastern stretch of the SfM survey; (a) shaded relief DEM overlain on 1 m resolution panchromatic Kompsat-2 imagery. At the eastern end of the survey, the scarp height reduces, with scarps no longer visible after a further 500 m. (b) Map of the observed scarps (red) along this section of the fault. Dashed lines indicate other scarps mapped from satellite imagery only – generally less fresh, these may be due to the penultimate event. Black boxes show the outlines of the sites in Figure 4.33.

Figure 4.31b,c). We infer that the fan at the centre of this survey is significantly older, recording 2–3 events, while the fan deposit at the western end is younger and only records a single event (Figure 4.32b). Given the very continuous and uniform nature of the lower scarp, it is likely that it represents only a single event, but palaeoseismic investigation is needed confirm this.

At the eastern extreme of Intali site, the rupture trace splits, with one strand continuing east, while the other trends south. The east trending strand has an offset of ∼1.6 m (profile 9), similar to those on profiles 5–8, and extends only ∼80–100 m. This strand is not visible carrying on further east, suggesting it has been erased from the landscape; it may represent the penultimate surface rupturing event. The southwards strand is poorly defined and has been heavily modified by anthropogenic construction, so I make no quantitative offset measurements, but it coincides well with a southwards step of ∼800 m in the mapped scarp traces (Figure 4.28).

Focus Sites – Helikite Survey

Figure 4.33a shows another example at which we see evidence for multiple generations of faulting, along the central portion of the fault (location in Figure 4.30). Two profiles P1 and P2 (Figure 4.33b) show

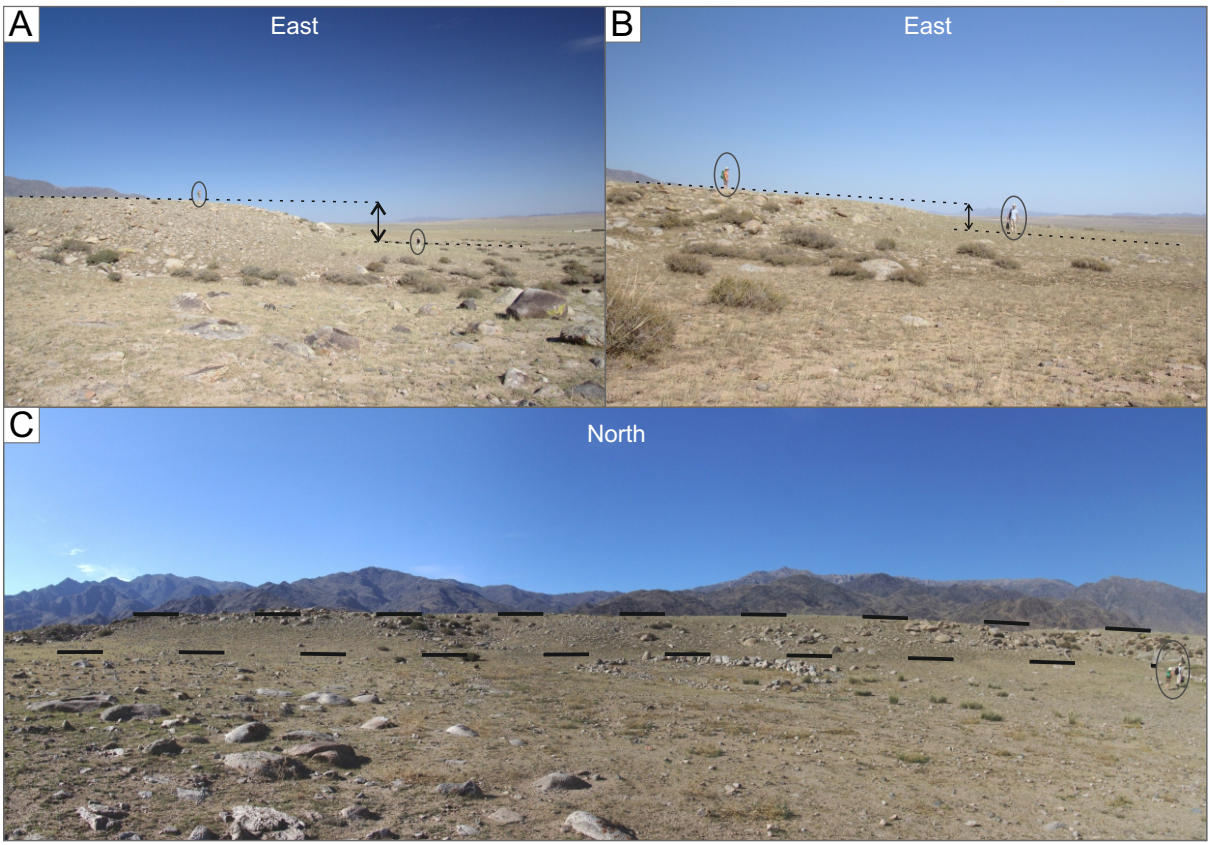


Figure 4.31: Scarp photos at the Intali site (locations in Figure 4.32). (a) Large, cumulative scarp of ∼6 m vertical offset, person for scale. Location: 78.9749°E 44.3433°N. (b) Smaller scarp, possibly formed in the most recent event, with a vertical offset of ∼1.5 m, person for scale. Location: 78.9728°E 44.3437°N. (c) Cumulative scarp of ∼6–7 m in the foreground, with the Altyn Emel behind. Location: 78.9776°E 44.3429°N.

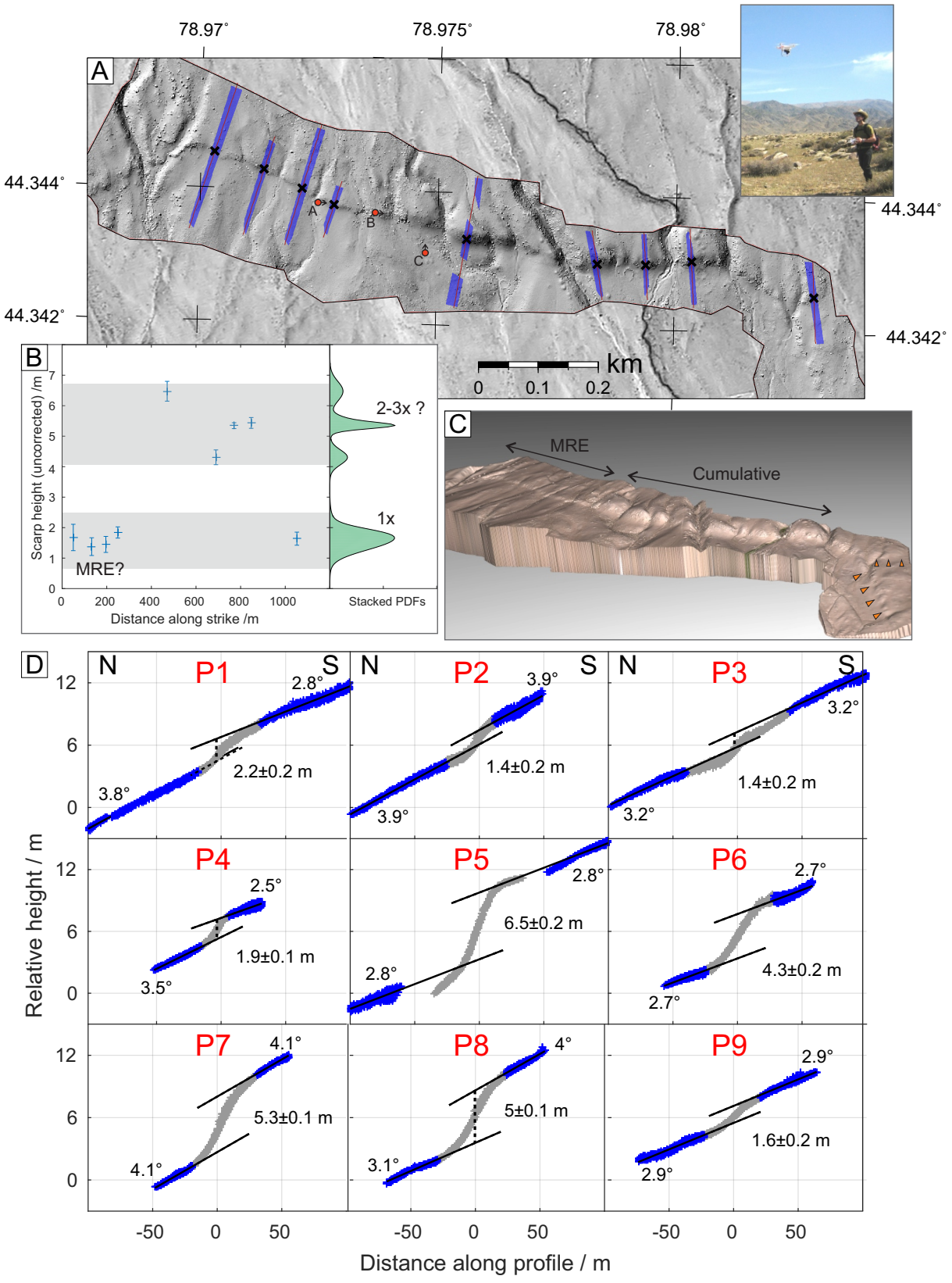


Figure 4.32: (a) High resolution drone survey of a section of the scarps near the Intali Village. We observe two distinct different generations of scarps, at ∼1–2 m and ∼5–6 m. Red dots labelled A,B,C show the locations of the photos in Figure 4.31. (b) Summary of the offset estimates from the profiles 1-9 (uncorrected for hillslope), with a stacked probability distribution function. (c) Profiles P1–P9 across the scarp.

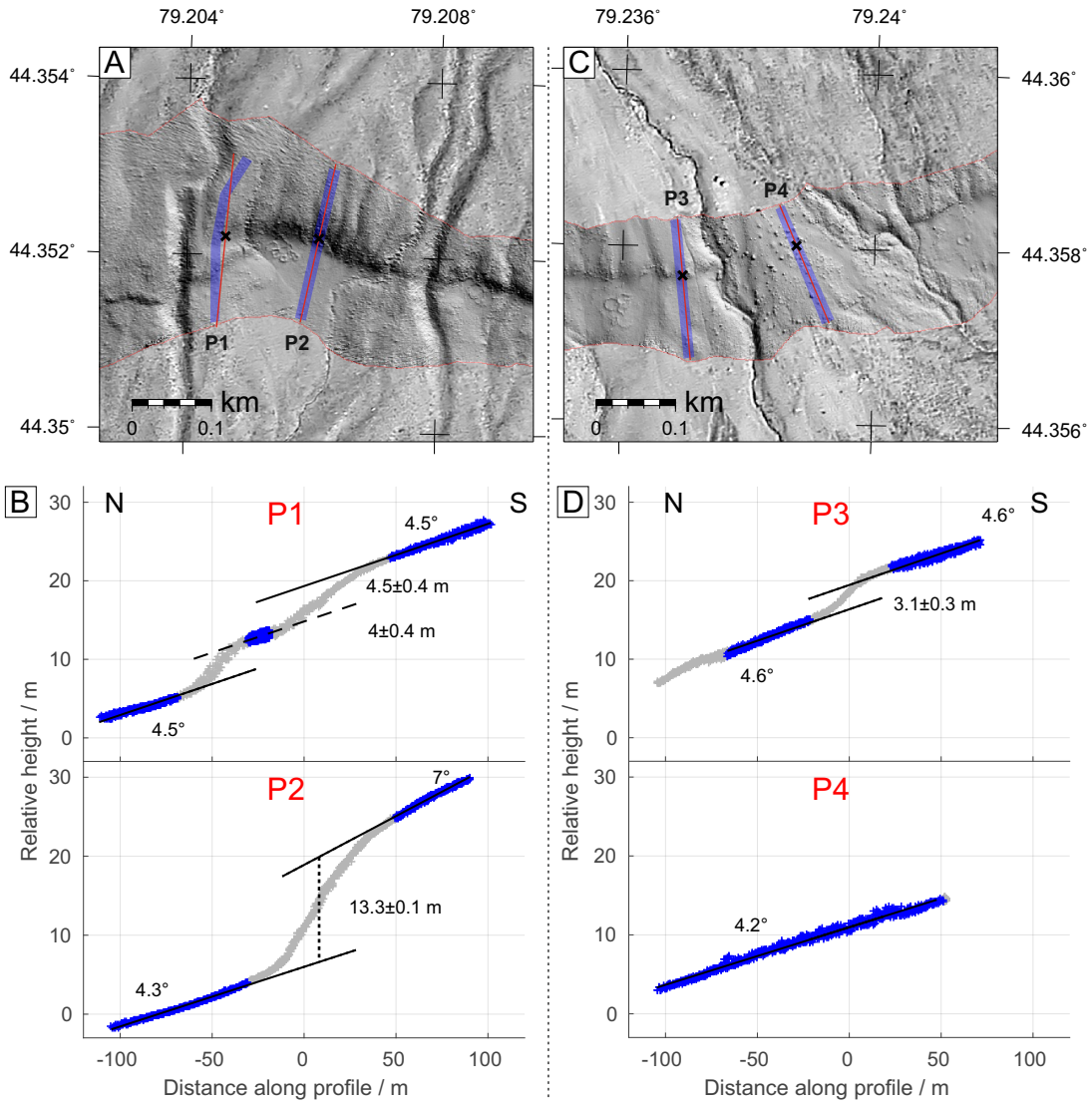


Figure 4.33: (a) An example where we see two generations of scarps in close proximity. (b) Two profiles across the scarps in (a). P2 shows a single cumulative scarp, while P1 shows two discrete steps. (c) An example of a debris flow which has covered the scarp entirely. (d) Profiles across the scarp and debris flow (c).

the scarp splitting; P2 shows a cumulative scarp of ∼13 m vertical offset, while P1 shows two distinct sub-scarps of ∼4–4.5 m vertical offset. These sub-scarps are substantially larger than the single event offsets at the Intali site, though as we see below, this may be due to larger slip on this more central section of the fault; Intali is near the western tip of the fault where the offsets are generally smaller.

In Figure 4.33c,d, a debris flow has covered the fan entirely. On either side of the flow, we see a scarp of ∼3 m vertical offset, but none within it. There are however petroglyphs on large boulders embedded within the debris flow, confirming that at least some of the petroglyphs were drawn since the most recent event on the fault (discussed further below).

Slip Distribution

Our topographic dataset covering the ruptures gives an opportunity to investigate the along-strike distribution of slip on the fault, a rare opportunity for palaeo-earthquake thrust scarps. Given the large scale of the dataset, covering almost the entire length of the Konyrolen scarps, I developed a semi-automated procedure for measuring surface offsets from the photogrammetry pointcloud over the full extent of the fault. As discussed further in Chapter 5, profiles aren't necessarily the most suitable tool for estimating fault offsets; instead I chose to fit parallel planar surfaces to the 3-dimensional photogrammetry pointcloud on either side of the fault, using the following procedure:

1. Using the hillshade DEM, create a mask polygon, covering all the eroded regions of the hangingwall and footwall (river channels, anthropomorphic features etc., mapped under classical GIS software). Also carefully map the location of the fault.

2. Apply the masking polygon to the pointcloud, selecting only the unmodified points (Performed with Generic Mapping Tools, GMT, *Wessel and Smith*, 1998).

3. Break the fault trace up into regular sections (in this case chosen to be 50 m sections).

4. Step along the fault sections. At each step, select all the points within a rectangular area in the hangingwall, and in the footwall, ignoring any within a chosen tolerance distance from the fault trace (i.e. those on the scarp itself).

5. For each pair of footwall and hangingwall point sets, fit a pair of parallel planes through them (Performed under Matlab). I also fit each set of points independently (i.e.. non-parallel planes) – if the solutions disagree by $>1.5°$, then the pair is discarded.

6. Both the normal vector, and the perpendicular offset between the planes are recorded, preserving information on the orientation of the hillslope. The rms misfit to the planes is used as an estimate of the error in the offset – this is not the strict error in the mean, but experience (Chapters 2–3) shows that it better captures errors generated by non-planarity and roughness of the geomorphic surfaces.

For each pair of planes, I plot the residuals in the two orthogonal directions within the plane, along with the histograms of the residuals; if the residuals show obvious bias, then the observation is discarded. I also plot a view of the shaded relief DEM and orthophoto with the point selection polygon overlaid to check for adequate pointcloud coverage and potentially biasing features. Figure 4.34 shows an example of these analytics generated for each section. Significant operator input is required at three stages; masking the pointcloud, mapping the fault trace and choosing sites to disregard due to erosion, poor fit or poor DEM coverage. Thus there is still some subjectivity, but this method is more objective than choosing

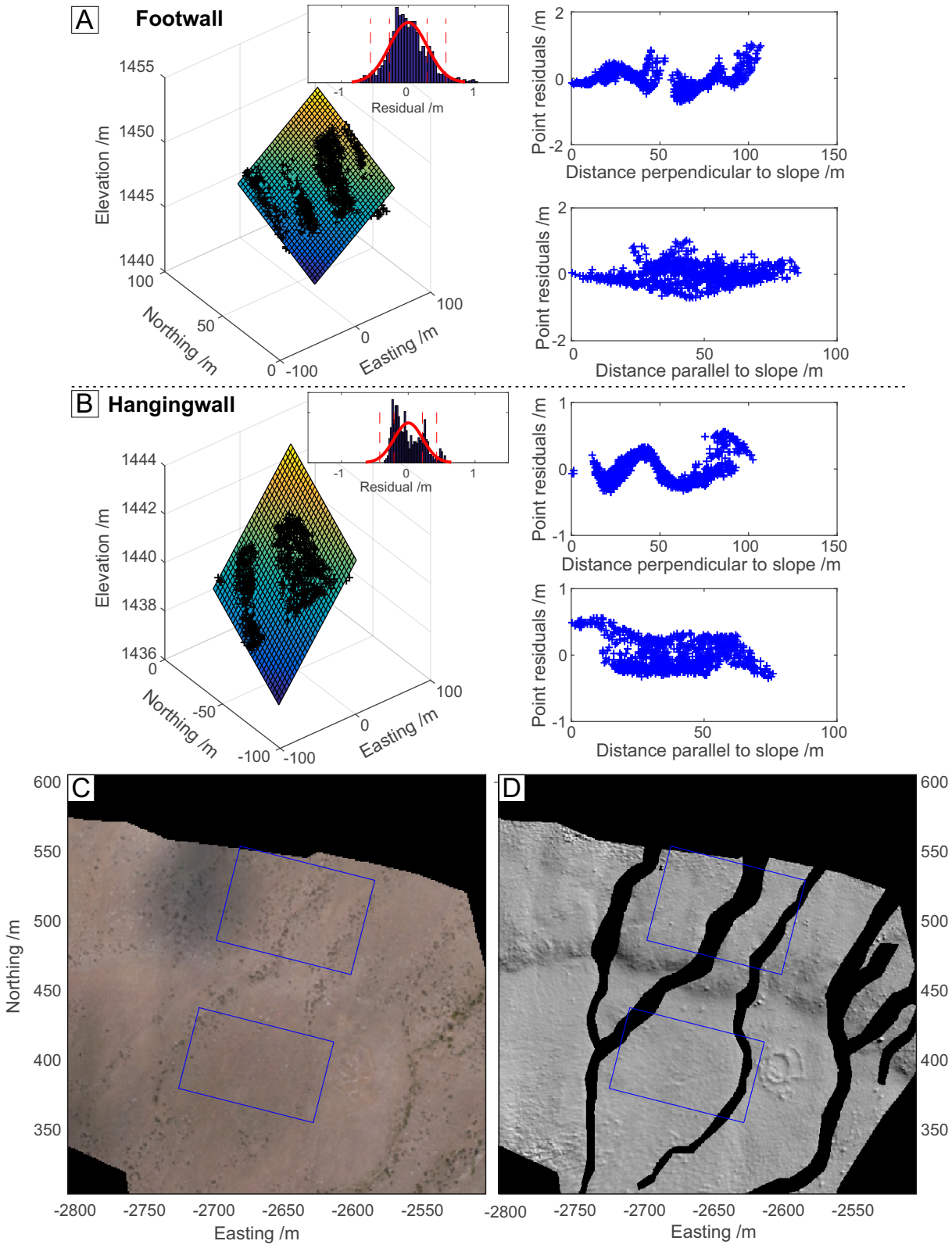


Figure 4.34: The visual analytics used to decide whether to discard an observation. For each of the footwall (a) and the hangingwall (b) I generate a 3D plot (interactive) showing the points and the plane fit through them. Also shown are the residuals in the across slope and down-slope directions – non parallel planes show up through biased residuals in one/both directions. (c) SfM orthophoto of the regions with the point selection polygon overlain. (d) Masked shaded relief DEM with the point selection coverage. Points from black regions (streams here) are ignored.

explicitly where to measure profiles. The fitting of planes retains the full surface geometry, allowing a more rigorous characterisation of fault slip (see Chapter 5).

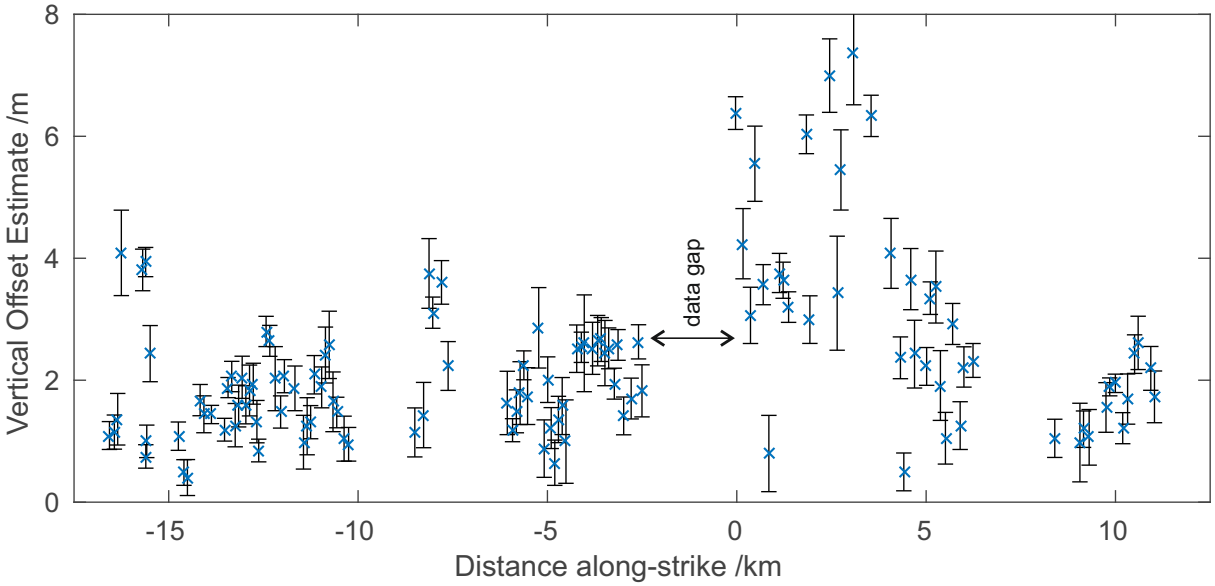


Figure 4.35: Vertical offset distribution along strike. The gap between -2 km and 0 km represents the gap where the camera battery failed, so no photographs were acquired.

Figure 4.35 summarises the vertical offset estimated for each section measured along strike. There is a general trend for larger offsets in the central section, with typical offsets of ∼3 m, tapering to 1–2 m at either end. There are also several sections in which we see offsets much larger than other nearby measurements, most likely multiple event scarps, with vertical offsets up to ∼7 m. I note that there are several observations of very small vertical offsets – these are typically at the locations where the scarp tapers out and steps closer to the rangefront or further out.

However, vertical offset is not necessarily a good proxy for fault slip, as it is affected by the geometry of the fault-hillslope intersection. The variation in hillslope angle and aspect is insufficient to invert for the 3D slip vector (Chapter 5), but we can remove some of the geometric effects if we make assumptions about the slip geometry. Assuming a pure dip-slip vector, and a fault plane dip, I estimate a fault throw based on each measurement. Figure 4.36 plots the throw estimates, for two cases of fault dip; 20° and 45°. Approximating the probability distribution function (PDF) for each observation as a normal distribution about the mean, I stack the PDFs for windows of 2 km along strike. Inspecting the stacked PDFs (Figure 4.36), several locations show multiple distinct peaks, which may suggest different generations of scarps recording different numbers of events (as noted above). Based on these stacked PDFs, I estimate an approximate slip distribution function (red dashed line) – scaling this up by a factor 2, gives a relatively close match to the cumulative offsets along the central stretch of the fault (for both dip cases). This might suggest that these scarps may be comprised of two events if the fault ruptures in so-called 'characteristic', repeated events.

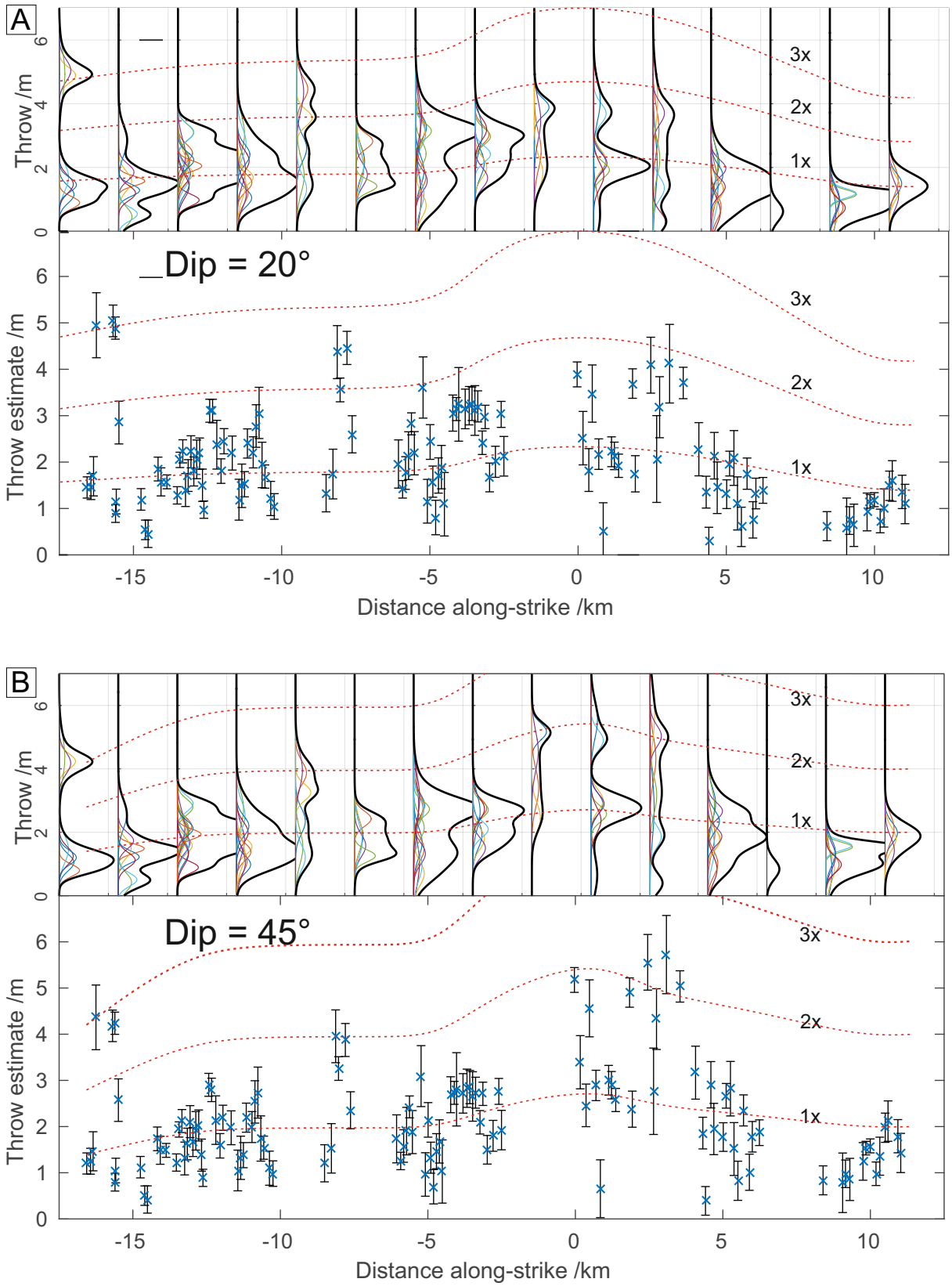


Figure 4.36: Throw estimates based on an assumed fault dip, with a pure dip-slip slip vector. Thick black lines in the upper plot represent the stacked PDFs for the observations within a 2 km window in the corresponding plot below. Coloured lines represent the individual observations. Dashed red lines represent one possible slip distribution function based on the stacked PDFs – each successive line represents the same distribution scaled up by a factor of 2,3 and 4. (a) 20° fault dip. (b) 45° fault dip.

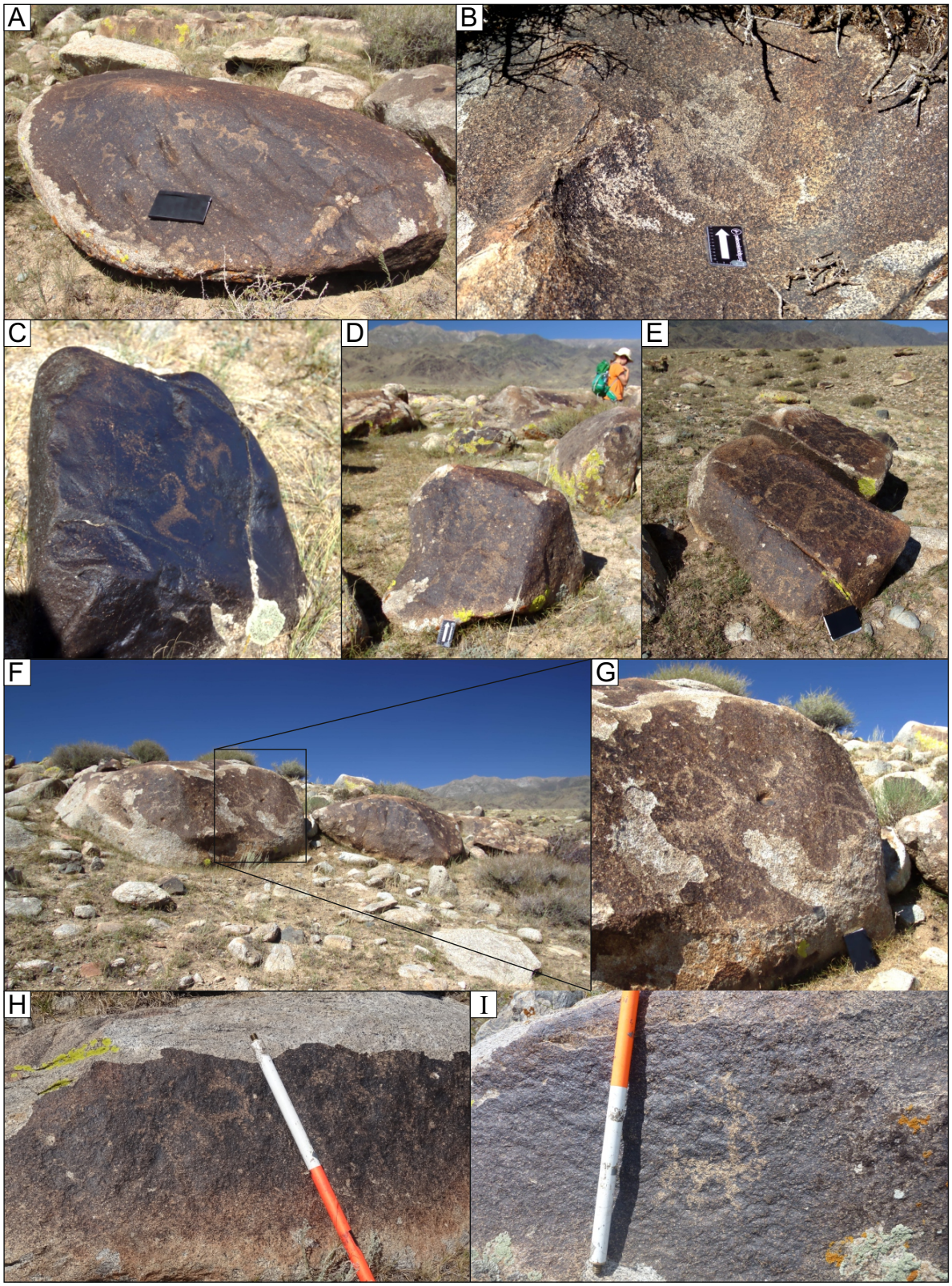


Figure 4.37: (a) Riders hunting ibex, along with numerous other ibex images. Location 44.34153°N, 78.95074°E. (b) Two depictions of camels, one with a rider. Location 44.34153°N, 78.95074°E. (c) Two Ibex, on a very dark varnished surface – a boulder of a different lithology to the majority of boulders. Location 44.34355°N, 78.95646°E. (d) A man standing with a shepherd's crook. Location 44.34355°N, 78.95646°E. (e) Ibex. Location 44.34353°N, 78.97412°E. (f-g) Boulders right on the face of the scarp, with several Ibex images. Location 44.3435°N, 78.9471°E. (h-i) Ibex glyphs on boulders embedded in a debris flow that covers the scarp (Figure 4.33). Location 44.3541°N, 79.2211°E. Note: photos (a-g) were taken using a circular-polarising filter angled to reduce reflections and enhance contrast.

The slip distribution suggests a peak fault throw of 2–3 m for the most recent event. It is possible that these scarps have been built up in multiple events, rupturing only small portions of the fault, however the extremely continuous nature of the scarps and lack of significant >500 m step overs is suggestive of a single through-going rupture.

Petroglyphs

The majority of the scarps cut granite boulder alluvial fans; unfortunately the large boulders ($\lesssim$5 m) prevented excavation, and the friable surface of the granite boulders is generally too eroded to allow surface boulder cosmogenic isotope dating. We were therefore unable to date the surfaces displaced by faulting through conventional geochronology. However, we observed numerous petroglyphs etched in the desert varnish of the boulders on the scarp (e.g. Figure 4.37). Many hundreds of these glyphs exist along the entire length of the scarp; the scarp itself has resulted in these boulders standing clear of the surrounding fans presenting a canvas for prehistoric rock-artists. Glyphs were not restricted to the scarp, but the greatest concentration was in the immediate vicinity. Of the hundreds we observed, none appeared to be overturned and there were several locations where we saw petroglyphs on boulders within debris flows which have buried the scarp (e.g. Figures 4.33c and 4.37h,i). We therefore infer that the petroglyphs were emplaced after the most recent earthquake event on this fault.

The majority of the images are indicative of the Saka period (early Iron Age), based on the diagnostic representation of riders and the style of the Ibex, and are therefore from ∼3000 yrs BP (pers. comms. E. Jacobson-Tepfer, *Sala and Deom*, 2005). Given the very dark varnish surface that the glyphs have been etched into, the surface may have been undisturbed for a significant period prior to this, but it is unclear whether this could have formed pre-earthquake. The most recent earthquake on this fault was therefore over 3 ka BP. In earlier sections I have noted observations of major landscape resetting following the LGM (§4.7.1). Given the similar environment here (to that around the Toraigyr Fault) it is likely that many of the rangefront fans were deposited post LGM. However, the scarps are continuous across most of the fans so I infer an upper bound on the age of the most recent event of 13–15 ka.

Konyrolen Summary

I have generated a DEM which covers ∼30 km of surface ruptures on the Konyrolen fault of the Usek thrust system, mapping and measuring offsets over the full length of the observed scarps; this demonstrates the utility of the Helikite for fault mapping over large areas (5+km) which has not been achieved before. There are at least two generations of faulting preserved in the offset alluvial fans, the youngest of which most likely represents the most recent event (MRE). The scarps attributed to the MRE show a peak throw of 2–3 m and petroglyphs suggest they were formed >3 ka BP, though it may be much longer. If the uplift rate is the same as that measured at the Usek river terraces (0.36±0.07 mm/yr), an uplift-per-event of 2–3 m would suggest a recurrence interval of ∼5–8 ka. This is a fault on which there have been

large surface rupturing events but with a very long recurrence time.

4.8.4 Dzhungarian Southern Rangefront Fault (DZS)

The Dzhungarian Southern Rangefront Fault (DZS) bounds the southern edge of the high topography of the Dzhungarian Alatau. The fault has generated a relief of 1500 m and reaches the surface within a high (altitude ∼2000 m) intramontane basin. Two parallel scarps cut a series of alluvial fans on the northern side of the basin, with different generations of fans displaying different offsets (Figure 4.38).

On the western stretch of the fault, we observed the southern strand cutting through young (likely Holocene) deposits, with scarps of ∼1–4 m vertical offset (Figure 4.38d,e). The lowest of these, running through the relatively flat youngest fans, we attribute to the most recent event; it presents a good target for future palaeoseismic investigation. The eastern section of the fault cuts a series of large fans issuing from the rangefront; both strands have similar large offsets of ∼15 m in each fan (Figure 4.39d).

To constrain the fault slip rate, we dated a large fan surfaces in which a total offset of ∼30 m is recorded (Figure 4.39d). With such large offsets it is likely that the fans are beyond the range of radiocarbon dating and we found no organic material. The coarse boulder material also prevents any luminescence dating. Instead we found well-developed pedogenic carbonate rinds on the undersides of boulders embedded at depths of ∼0.6 m within the fan (Figure 4.39b,c). These rinds are deposited from the flow of meteoric water through the gravels, forming on the undersides of pebbles where the water collects. They are generally assumed to indicate soil formation and hence fan abandonment (*Sharp et al.*, 2003). As the rinds were systematically observed on the undersides of the pebbles, in a well defined stratigraphic layer, they must have been deposited after fan emplacement. The age of the innermost layer of carbonate rind is therefore a lower bound on the age of the fan surface.

U-Th Dating[8]

We collected six pebbles from each of the two sampling pits within the displaced fan surface (Dz1 and Dz2, Figure 4.38). After slabbing the pebbles, we selected the six with the thickest and hardest rinds (PB22,24 from Dz2 and PB1,2,3,6 from Dz1, Table 4.3), milling a sample from the base of the carbonate rind. Due to the minimal rind thickness, we were unable to reliably sample multiple horizons within any rinds. After finding significant spread within these samples, we also attempted to construct an isochron for the most promising pebble (PB2), taking 6 samples from various locations around the pebble.

Table 4.3 shows the $^{230}Th/^{238}U$ and $^{232}Th/^{238}U$ ratios for each sample analysed and the resulting ages. Unfortunately the results show significant spread, leading to two possible interpretations: either the closed system assumption has been violated, with mixing occurring with external material, or the spread represents real ages taken from different horizons within the rind. Figure 4.39 plots the $^{232}Th/^{238}U$ ratio

[8]Carbonate milling and U-series chemistry and analysis was performed by Andrew Mason in the Oxford Earth Sciences Department.

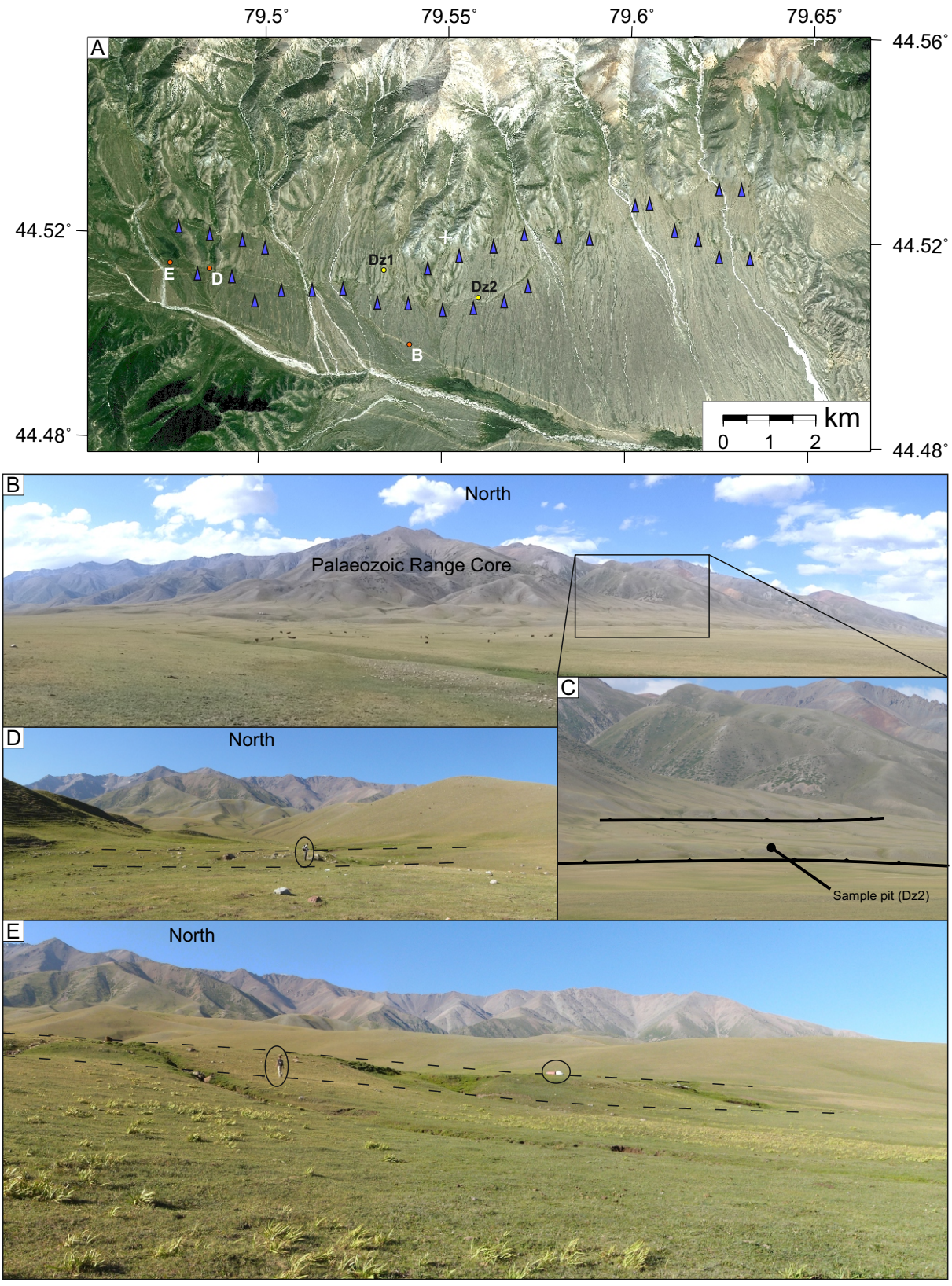


Figure 4.38: (a) Map of the multiple strands of the DZS scarps. (b) Panoramic view, looking north across the basin to the Dzhungarian Alatau southern rangefront. (c) Annotated view of the cumulative offsets in the old fan targeted for a slip-rate study. (d) Smallest scarps observed, with vertical offset of ∼1 m (person for scale). (e) Scarps of ∼2–3 m at location shown in (a). The flattened surface behind the scarp has resulted in ponding and increased vegetation cover and green, vegetated stream channels incising the scarp. Person and yurt circled for scale.

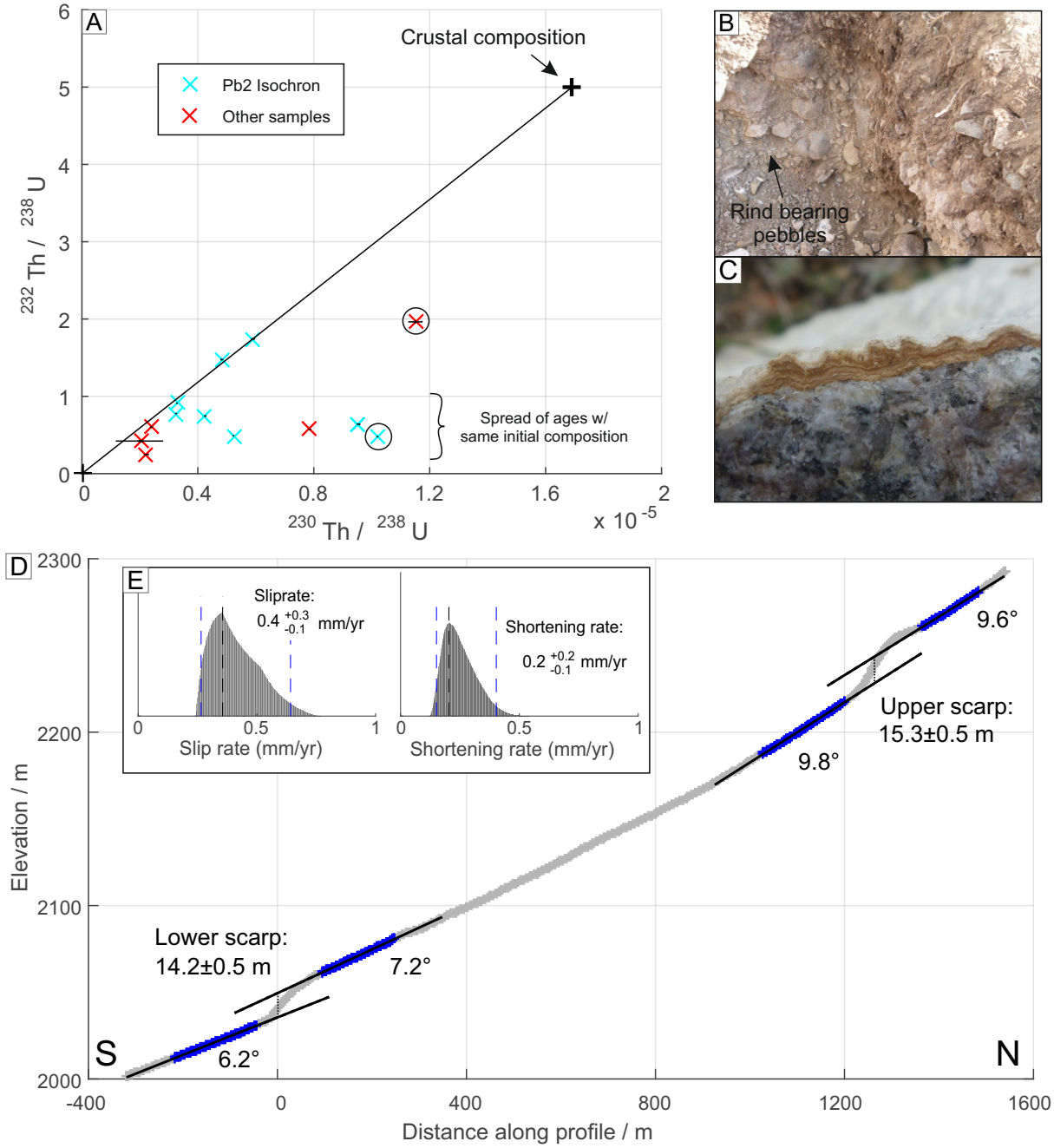


Figure 4.39: (a) Plot of the ^{232}Th/^{238}U against ^{230}Th/^{238}U for each sample measured. Black line represents 'modern' equilibration; decay of the uranium content shifts points to the right, increasing the ^{230}Th/^{238}U, up to saturation once the ^{230}Th/^{238}U reaches that of (old) continental crust. Analytical errors are generally too small to be displayed. Circles denote the two samples which possible give a minimum age for the fan surface. (b) Sampling pit S1 (location in Figure 4.38a). Carbonate rind bearing pebbles were found at a depth of ~60 cm. (c) Example of the carbonate rinds observed (rind thickness here is ~3 mm. (d) Kinematic DGPS profile down the fan surface showing a total offset of ~29.5 m. (e) PDFs for fault slip rate and shortening rate from Monte-Carlo simulations.

against the ^{230}Th/^{238}U ratio for each sample. Many of the samples cluster around the equilibration line, suggesting that they are either modern, or have undergone recent re-equilibration. However, there are also a series of samples which show a spread along a relatively constant ^{232}Th/^{238}U. This spread can be achieved either by mixing occuring with "old" material with the same ^{232}Th/^{238}U ratio, or by different

ages for each sample i.e. decay of uranium, driving the $^{230}Th/^{238}U$ ratio back towards the saturation ratio. If the latter is correct, then the apparent oldest sample yields an age of ∼70.7 ka, suggesting a maximum uplift rate of ∼0.4 mm/yr. However, I stress that this is only one of two equally viable interpretations of the observed isotope ratios – given this uncertainty, I am cautious in the interpretation of these rates.

Lab Code	Sample Name	Th232/U238	Th230/U238 x10^6	Th230/U238 age
AM36_6	KAZ14-DZ-PB22	0.248±0.001	2.22±0.09	
AM36_7	KAZ14-DZ-PB24	0.421±0.007	2.03±0.82	
AM36_2	KAZ14-DZ-PB6	0.573±0.002	7.86±0.04	
AM36_3	KAZ14-DZ-PB3	0.745±0.003	4.25±0.05	
AM36_4	KAZ14-DZ-PB1	0.600±0.002	2.40±0.05	
AM36_5	KAZ14-DZ-PB2	0.640±0.003	9.54±0.06	**63600±600**
AM39_1	KAZ14-DZ-PB2	0.912±0.005	3.28±0.03	18100±200
AM39_2	KAZ14-DZ-PB2	0.490±0.002	5.23±0.03	30500±200
AM39_3	KAZ14-DZ-PB2	0.478±0.003	10.20±0.03	**70700±400**
AM39_4	KAZ14-DZ-PB2	1.743±0.011	5.91±0.07	35700±500
AM39_5	KAZ14-DZ-PB2	0.777±0.004	3.25±0.03	17900±200
AM39_6	KAZ14-DZ-PB2	1.475±0.007	4.83±0.05	27800±300

Table 4.3: U-Th ratio estimates and ages for the pebbles collected at the Dzhungarian Southern Rangefront Fault. 95% percent confidence interval shown. Quoted errors are 1-σ uncertainties.

Attributing the alluvial fans to the different periods of landscape reset can also provide approximate bounds on the slip rate; the continuous, large offsets of ∼30 m in the older alluvial fans may have been deposited in the penultimate glacial period (∼120–150 ka). Combining this with the possible minimum age from the U-series dating, we use Monte-Carlo simulations to estimate a preliminary slip rate and shortening rate. Assuming a fault dip of 25–45° in the shallow subsurface, steepening to 45–60° at depth, we estimate a slip rate of $0.35^{+0.29}_{-0.09}$ mm/yr, or equivalently a shortening rate of $0.21^{+0.20}_{-0.05}$ mm/yr.

Small scarps of the sort observed within the younger alluvial fans and modern river channels (Figure 4.38d,e) would likely have been erased by the LGM in this high elevation setting (c.f. TY and SF examples), suggesting that the fault has generated earthquakes in the Holocene. I suggest therefore that this fault accommodates a significant amount of shortening across the southern margin of the Dzhungarian Alatau, $0.21^{+0.20}_{-0.05}$ mm/yr if the U-Th data are correct – similar to that observed across the Usek thrust.

4.9 Dzhungarian Alatau Northern Margin

The northern rangefront faults of the Dzhungarian Alatau separate the actively deforming range from the relatively rigid Kazakh platform. I map two main structures accommodating shortening on this margin (Figure 4.40); the Qapal fault (QP) and the Sarkand Rangefront (SK). In addition to these major range-bounding thrusts, a further component of shortening may be accommodated by anticlockwise rotation

accommodated by the platform strike slip faults (discussed in §4.10.2, *Campbell*, 2015).

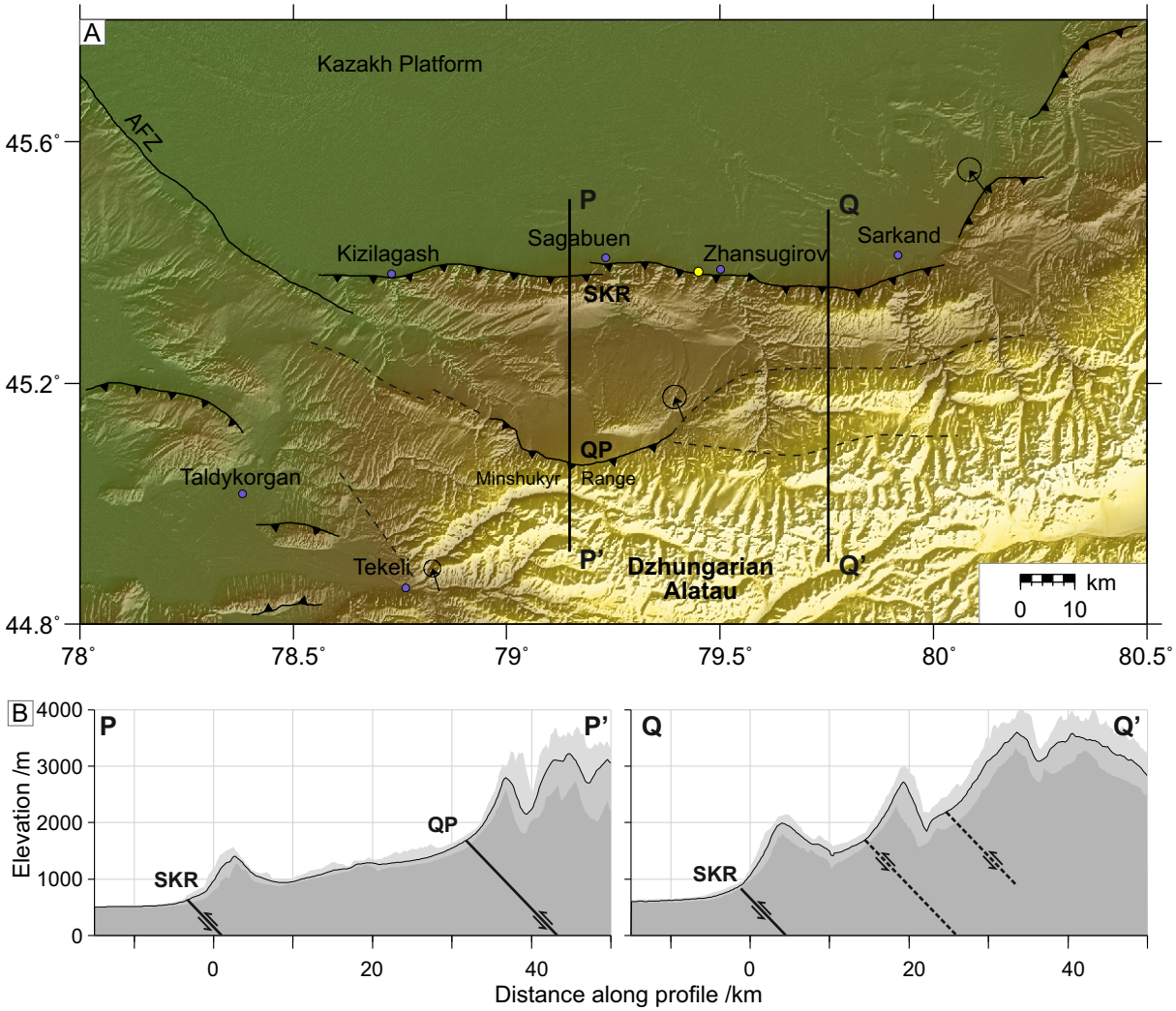


Figure 4.40: (a) Overview of the northern margin of the Dzhungarian Alatau. Fault labels in the text and caption of Figure 4.4. (b) Profiles through the range margin topography (SRTM), showing the minimum, mean (black line) and maximum elevation within a swath width of ±5 km.

4.9.1 Qapal Fault (QP)

The main stretch of the south dipping Qapal Fault extends ~30 km along the northern front of the Minshukyr range and has generated ~1600 m of relief. It has a sinuous trace, changing strike substantially in the west (Figure 4.40) and possibly merging into the Aktas Fault Zone (AFZ, Figure 4.40). In the east (profile B, Figure 4.40b), the fault splits into two strands, extending a further 50–60 km.

For most of its length, QP reaches the surface at the contact between the Palaeozoic and the basin sediments, so the majority of fault offsets are preserved in the form of uplifted bedrock terraces. However, in several locations, satellite imagery shows scarps cutting Late Quaternary alluvial deposits. Figure 4.41 shows a strand of the fault cutting an alluvial fan immediately along strike from a larger bedrock offset terrace. Uplift in the hangingwall has caused incision and a north-facing scarp. Though I was unable to

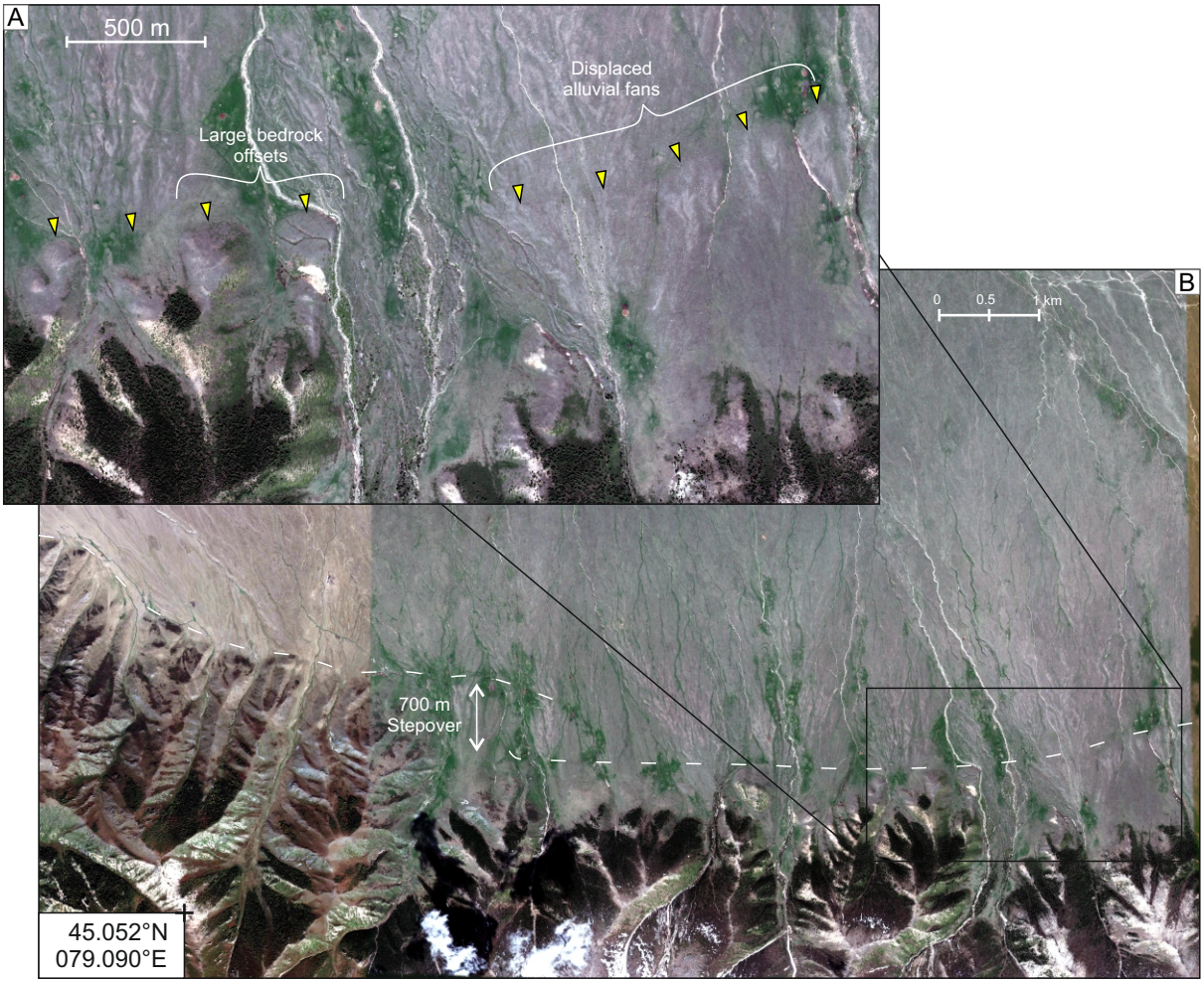


Figure 4.41: (a) A section of the Qapal fault (QP) displacing late Quaternary alluvial fans. Bedrock offsets are also visible on the western side. (b) Wider stretch of QP, the northern rangefront of the Minshukyr Range, with a sinuous trace bounding the bedrock core of the range.

visit this fault, offsets in late Quaternary deposits suggest that it is active.

4.9.2 Sarkand Rangefront Fault (SKR)

The Sarkand rangefront bounds the northern side of the Ayrakkol range, with a hangingwall relief of 1100 m in the east, reduced to ∼500 m in the west. The range is generally topped with the uplifted and gently back-tilted peneplain erosion surface, suggesting that this difference is due to a difference in total slip along the fault – greater in the east. The rangefront is very linear for ∼100 km, with one significant step-over of ∼2 km near the town of Sagabuen (Figure 4.40).

The SKR shows less signs of activity than most of the faults on the southern margin of the Dzhungarian Alatau; in the few locations that scarps are visible, they are heavily degraded, suggesting a long recurrence interval and/or a low slip rate. However, given the length of the rangefront, scaling laws (e.g. *Wells and Coppersmith*, 1994) suggest the potential for large earthquakes, so understanding the role of this fault in regional strain accommodation is important. In this study, I have focused on one of few sections of

scarps still preserved in late Quaternary material, near the town of Zhansugirov.

Zhansugirov Site

Near the town of Zhansugirov, ∼4 km of scarps are preserved but heavily dissected and eroded (Figure 4.42a). I used a Helikite aerial survey of ∼2500 photos to construct an SfM DEM of a ∼2.5 km section of the scarp (Figure 4.42a). Taking a series of profiles through the pointcloud (Figure 4.42c), we note two distinct generations of scarps; one with offsets of 2–4 m and another with offsets of 6–8 m, suggesting that this site may record the two most recent events on the fault, each with an offset of 2–4 m.

Lab Code	N	Site	Material	% Modern Depth (cm)	delta-13C (o/oo)	Conventional Radiocarbon Age (yr BP)	Calibrated Age (yr BP)
404174	B1	1	organic sediment	335	-21.0	19550 ± 70	23830–23280
395356	S6	3	Gastropod shell, species 1	250	-7.2	1560 ± 30	1530–1390
395355	S3	3	Gastropod shell, species 2	250	-6.4	1600 ± 30	1550–1410
395354	C2	2	bone collagen	135	-20.9	520 ± 30	630–610
395353	C1	2	charred material	175	-25.3	2230 ± 30	2330–2150

Table 4.4: Radiocarbon ages for the samples at the site on the Sarkand rangefront fault. Ages are reported as radiocarbon years before present where present = AD 1950. Sample analysis was performed by Beta Analytics Ltd. Ages were calibrated based on the IntCal13 atmospheric curve (*Reimer*, 2013), using the OxCal utility (*Bronk Ramsey*, 2009). Errors on the radiocarbon age are 1-σ analytical uncertainties. The calibrated age range presented is the 95% confidence interval based on the analytical uncertainty and the uncertainty in the calibration curve.

A recent flooding event caused by a breach in the wall of a canal which contours the fan surface in the hangingwall of the fault, has incised deep gulleys, exposing the stratigraphy in the fan deposits which the scarp displaces. In the hangingwall fan, the canal-breach channel incised through the older fan material, which we observed displaced by 6–8 m. The fan material is composed largely of loess, with occasional thin gravel units, but I also observed a darker palaeosol unit at a depth of 3.35 m. The bulk organic sediment sample, B1, from this palaeosol yielded a calibrated age of 23.3–23.8 ka (Table 4.4), which is necessarily a pre-date on the abandonment of the displaced fan surface, though given how deep the palaeosol is, this may significantly pre-date the abandonment. I use Monte-Carlo simulations to estimate a shortening rate from this estimate, assuming a relatively shallow dip of 30–45° in the shallow subsurface, steepening at depth to 45–60° (both uniform PDFs). As this surface most likely only represents 2–3 events, I include a term for the stored elastic strain of 0–3 m vertical offset (i.e. a single event, §4.4.3). This approach yields a broad PDF, with a slip rate estimate of $0.44^{+0.21}_{-0.16}$ mm/yr and a shortening rate of $0.26^{+0.15}_{-0.10}$ mm/yr. Though the errors are large, the slip rate is comparable to the others considered along the transect, and accommodates a significant amount of regional shortening.

Where the same canal-breach reaches the main scarp, it has incised through a much younger fan. This small fan has formed in the stream channel mouth, but extends across the scarp and remains undisturbed by faulting (Figure 4.43b-d). The young undisturbed fan consists primarily of fluvially reworked loess, with occasional fine gravel layers (Figure 4.43b). A charred plant material sample (C1) from within the loess at a depth of 175 cm yielded a calibrated age of 2330–2150 yrs BP, and a small bone (most likely

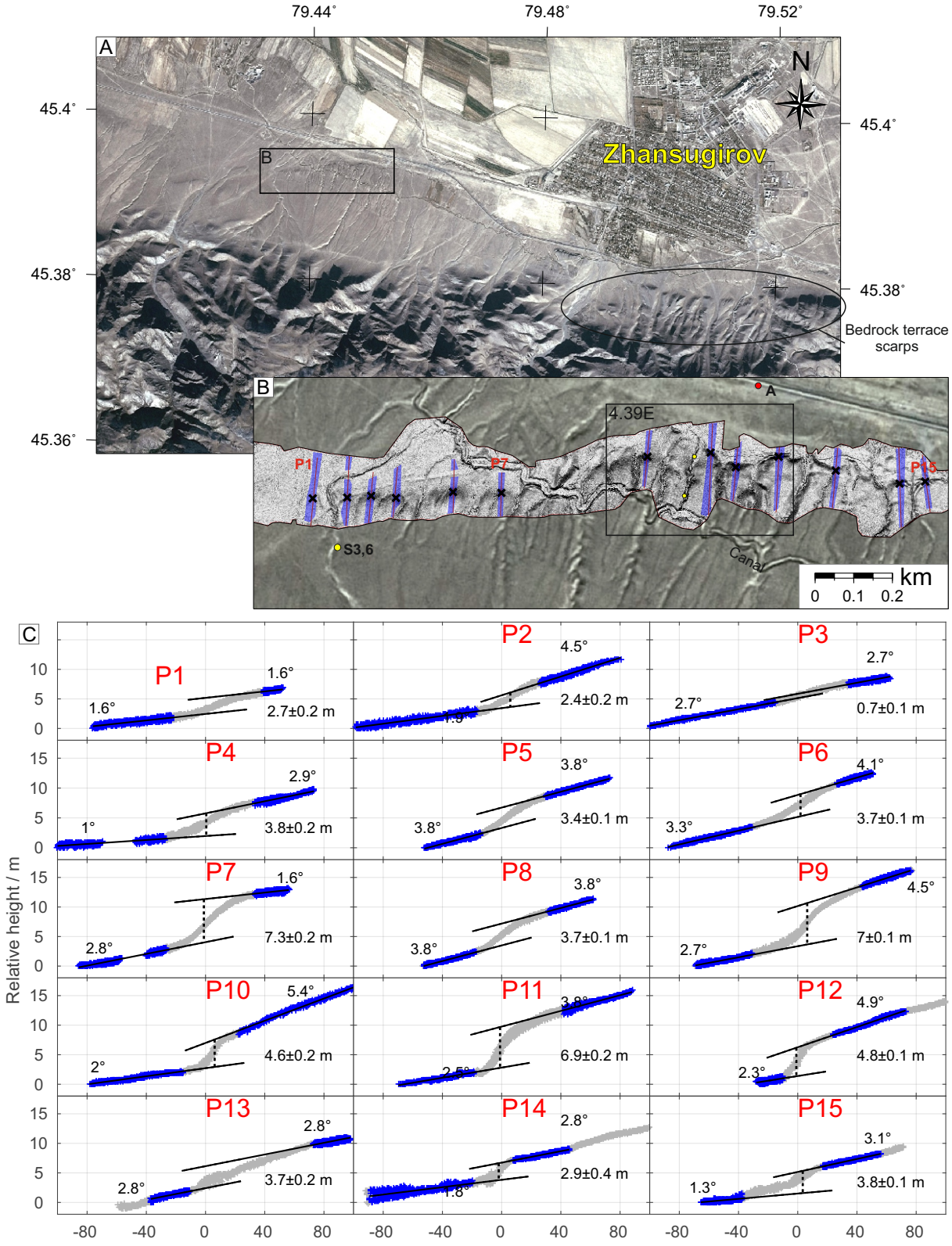


Figure 4.42: (a) Map of the rangefront near Zhansugirov, based on GoogleEarth® imagery. (b) Shaded relief of the SfM DEM of the field site. Blue polygons show the sections of the pointcloud projected onto the profiles in C to measure fault offsets. The sampling sites are shown as yellow points, and photographs in Figure 4.43 are marked as red points. (c) Profiles 1-15 showing two distinct classes of offsets, at 1–4 m and 6–8 m.

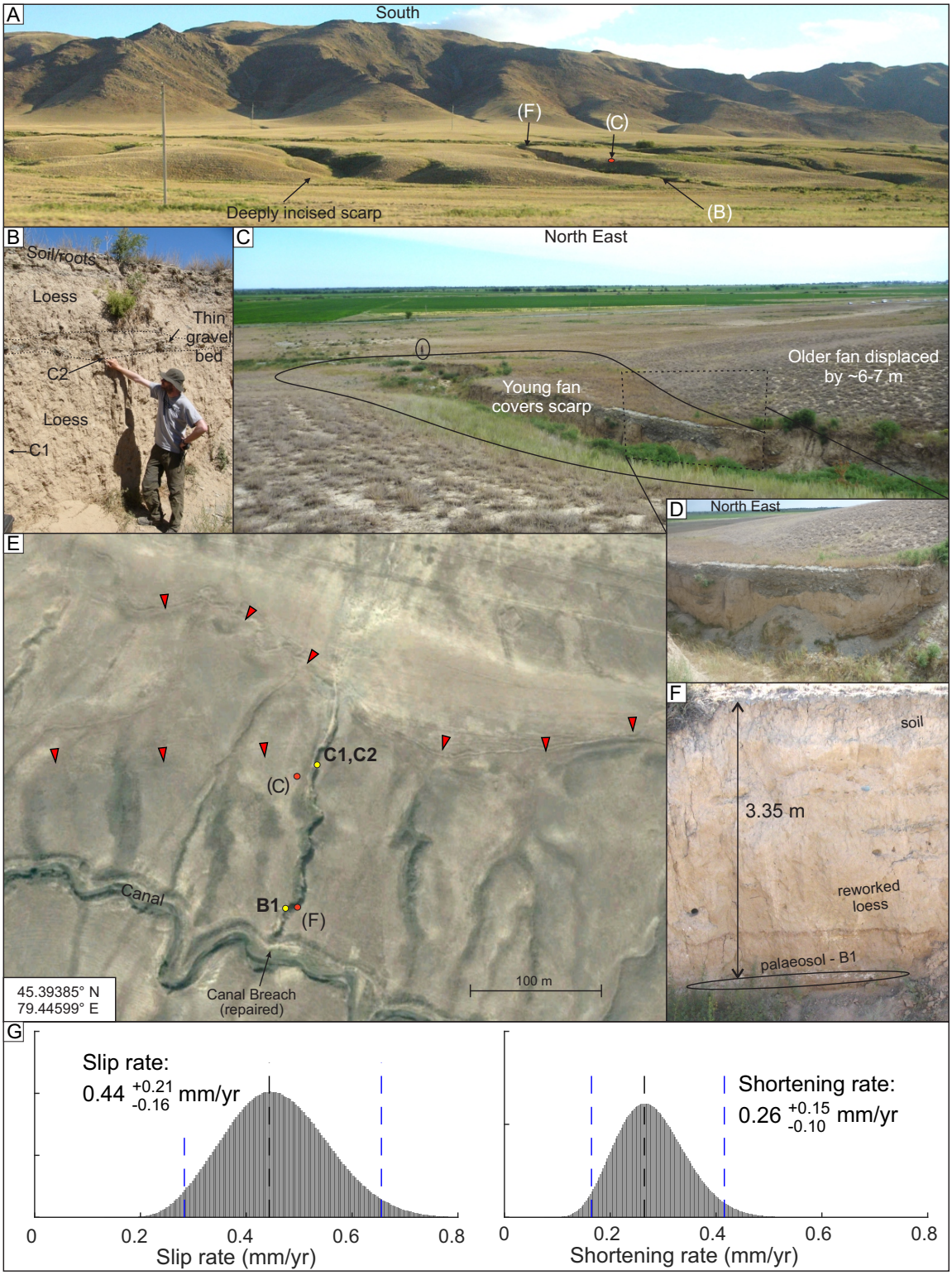


Figure 4.43: (a) Panoramic view of the large section of scarp at the breach-channel. The deep incision of the river channels in the scarp further attest to the relatively low slip rate and/or a long recurrence interval. Location in Figure 4.40. (b) Sampling site in the undisturbed young fan – a thin soil layer caps loess deposits broken with occasional fine gravel lenses. Location in (e). Location of sample C2 shown. Sample C1 is just out of frame, in the unit marked. (c) Photograph looking over the young undisturbed fan surface. Location in (e). (d) Stratigraphy of the young fan. In places gravel filled channels cut into the loess deposits. (e) Close-up map of the breach-channel showing the location of the sampling sites (ages in Table 4.4) (f) Exposure into the old fan deposit, marking the sampled palaeosol at 3.35 m depth. (g) Monte-Carlo simulation estimated PDFs for the slip rate and shortening rate.

rodent, C2) from within one of the thin gravel layers at a depth of 135 cm yielded a calibrated age of 630–610 yrs BP (Table 4.4). C1 and C2 are therefore consistent with the formation of the deposit since ~2.3 ka BP, though it has been active since 630 yrs BP. As the deposit is undisturbed by faulting on the surface and in cross-section, the most recent event on the fault must have occurred at least 2.3 ka ago.

At the western end of the study site, another young fan has partially covered the scarp. I collected a number of gastropod shells from a small river cutting within the fan deposit; two different species of gastropod shells yielded consistent calibrated radiocarbon ages of 1550–1410 yrs BP and 1530–1390 yrs BP (S3 and S6, Table 4.4, location in Figure 4.42b). These must post-date the most recent event, consistent with the observations for C1 and C2.

4.10 Synthesis: Compressional Faulting

4.10.1 Role of Thrust Faulting

In this study I have investigated a series of thrust faults throughout the northern Tien Shan and Dzhungarian Alatau. With the exception of the Karkara Rangefront Fault (KRF) and associated structures (SJZ, KBF), all those for which I have measured rates (BG, DZS, UT, SKR) yielded slip rates of <0.6 mm/yr, with long earthquake recurrence periods (see §4.12). The rates, event timings and recurrence intervals from this study and previous studies are summarised in table 4.5. This suggests that north of the Terskey Tien Shan, shortening is not focused on any one range-bounding fault, but instead distributed throughout the mountain belt, with numerous faults accommodating 0.1–0.4 mm/yr of shortening similar to that described by *Thompson et al.* (2002) in Kyrgyzstan. The ~4-5 mm/yr of shortening between the Kegen Basin and the Kazakh platform is distributed across at least eight discrete faults and folds (Figure 4.4).

At the southern end of the transect, the KRF (a segment of the Main Terskey Rangefront, MTF) exhibits a different behaviour. Combining with the Kegen Basin Fold (KBF) at depth, this segment of the MTF has a slip rate similar to the sum of the rest of the faults along the profile combined, of $\gtrsim$4.3 mm/yr (Chapter 3).

I therefore suggest that several different regimes are present across the Tien Shan and Dzhungarian Alatau. The high Tien Shan are bounded on the north and south by zones of intense deformation; the well documented thin-skinned fold and thrust belt along the margin of the Tarim Basin (e.g. *Yin et al.*, 1998; *Allen et al.*, 1999) to the south, and the thick-skinned MTF on the north (Chapter 3). North of the MTF however, deformation transitions to distributed, thick-skinned faulting on a series of thrust and conjugate strike-slip faults. As discussed by *Selander et al.* (2012) the locations and orientations of these are generally prescribed by the inherited structures of the Palaeozoic basement. Faulting is not well mapped or studied within the interior of the high Tien Shan, but the GPS velocity field (*Zubovich et al.*, 2010) shows relatively little shortening at this longitude, with no discrete steps or zones of high

Fault	Acronym	Slip Sense	M.R.E. (ka BP)	Recurrence interval (ka)	Slip Rate (mm/yr)	Shortening Rate (mm/yr)
Karkara Rangefront	KRF	R	Q	-	$0.44^{+0.21}_{-0.16}$	-
Kegen Basin Fold	KBF	R	Q	-	$0.44^{+0.21}_{-0.16}$	-
Saryjaz Rangefront*	SJZ*	R	<9	-	$1.12^{+0.56}_{-0.26}$	$0.68^{+0.38}_{-0.19}$
Kegen Rangefront	KG	R	Q	-	-	-
Saty Fault	SF	R	0.1	>5-6	pending	-
Ketment Rangefront	KM	R	?	-	-	-
Toraigyr Fault	TY	R	3.2	>13.8	$< 0.42^{+0.21}_{-0.08}$	$< 0.26^{+0.14}_{-0.07}$
South Ili Thrust (+Shonzhy Faults)	SIT(+SH)	RV(+RL)	Q	-	-	-
Kemin-Chilik Fault Zone	KCF	LL	Pre-LGM	-	-	-
North Ili Folds	NIF	R	-	-	-	-
Usek Thrust[1] (+Altyn Emel)	UT[1](+AE)	RV (+LL)	>3	>M.R.E.	$0.37^{+0.23}_{-0.09}$	$0.25^{+0.09}_{-0.008}$
Dzhungarian Southern Rangefront	DZS	R	post LGM	-	$0.35^{+0.29}_{-0.09}$	$0.21^{+0.20}_{-0.05}$
Qapal Fault	QP	R	post LGM	-	-	-
Sarkand Rangefront	SKR	R	>2.1	>M.R.E.	$0.44^{+0.21}_{-0.16}$	$0.26^{+0.15}_{-0.10}$
Lepsy Fault[2]	LP[2]	R	0.4	<5	-	-
Dzhungarian Fault[3]	DZ	RL	post LGM	-	2.2 ± 0.8	?

[1] *Cording et al.* (2014)

[2] *Campbell et al.* (2015)

[3] *Campbell et al.* (2013)

* Along strike from the KRF, so not included in the along-transect summation.

Table 4.5: Summary of the slip-rates, shortening rates, most recent event (MRE) ages and recurrence intervals estimated along the transect studied. R – Reverse slip, LL – Left lateral slip and RL – Right lateral slip. Errors stated with upper and lower bounds are 95% confidence intervals. The error on the DZ slip rate is the 1-σ bound given by *Campbell et al.* (2013)

strain rate, suggesting there is minimal but distributed shortening within the high Tien Shan.

Summing all of the shortening rate estimates from the Kegen Basin to the Kazakh platform (BG, DZS, UT, SKR, excluding the KRF and KBF), I estimate a PDF for the maximum total geological shortening rate, $0.9^{+0.29}_{-0.21}$ mm/yr (95% confidence interval). Differencing the northwards component of the regional GPS, I estimate a present day shortening rate of 3.5±1.0 mm/yr (1-σ). Though the error on the geodetic rate is large, it is significantly larger than the determined geological rate sum, at the 2-σ level. This suggests that there is a further 1–3 mm of shortening occurring across this region on faults which we have not accounted for. I suggest two possible reasons for this: there are a number of faults which we do not have slip rates for (KG, KM, SH, SIT, QP and NIF), and/or the strike-slip faults are playing an important role (below). It is likely to be a combination of both – further work is needed to characterise the slip-rates on the remaining faults along the profile. I also note that my slip rate estimates are based on one site along each fault – variation in slip rate along fault strike could introduce further uncertainty into this estimate.

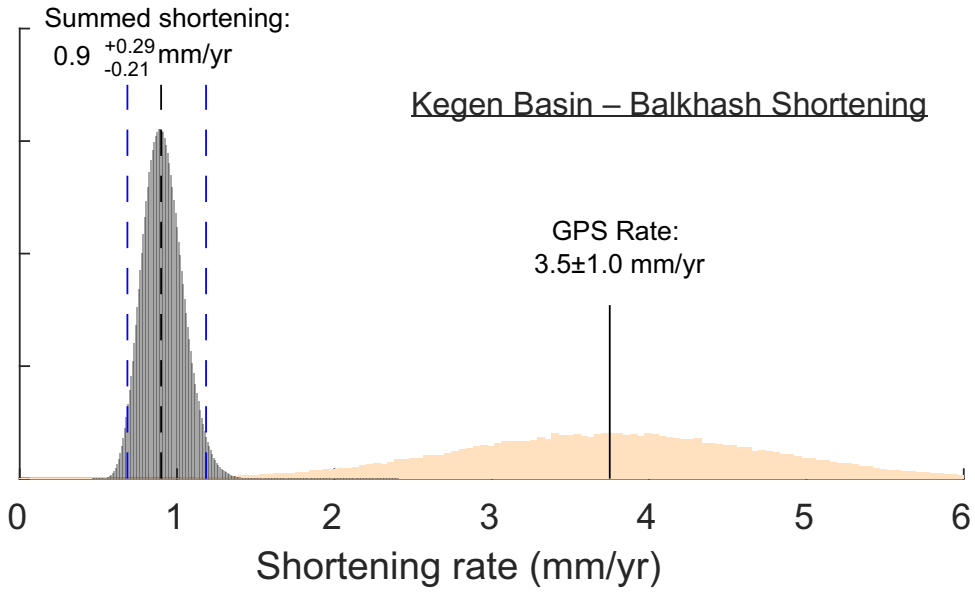


Figure 4.44: Comparison of the summed geological shortening rates to the geodetic rate. The geodetic rate carries a large error, but is still significantly bigger than the geological rate sum at the 2-σ level. The geological rates were summed from their respective PDFs.

4.10.2 Role of Strike-Slip Faulting

The main focus of this study has been the E-W thrust faults along the transect, but it is important to note the contribution of the strike-slip faulting to the overall accommodation of strain within the Tien Shan. Indeed, *Zubovich et al.* (2010) estimate ∼3–4 mm/yr of left-lateral shear running through the Kazakh Tien Shan. Strike slip faults occur along two prominent orientations in the Tien Shan; NE-SW left-lateral faults and NW-SE right lateral faults (e.g. *Tapponnier and Molnar*, 1979; *Burtman et al.*, 1996; *Selander et al.*, 2012), though most also have a component of shortening across them (e.g. *Delvaux et al.*, 2001; *Campbell et al.*, 2013).

The most prominent left-lateral faults along the transect are the Kemin-Chilik Fault zone (KCF, §4.7.2) and the Altyn Emel Fault (AE, Figure 4.4) Neither have known slip rates, though both have a component of offset visible, displacing Late Quaternary alluvial fan deposits, but also generating bedrock hangingwall ranges. Near the Bartogai reservoir, the Bartogai section of the KCF is observed displacing Quaternary gravels in a thrust sense on a $\sim 45°$ interface in the shallow surface; however, the displaced fan is capped by a further 2 m of undisturbed material, suggesting that the fault has not ruptured in the late Holocene. While it exhibits large long term (bedrock) displacements, the minimal late Quaternary offsets suggest a relatively low slip rate (§4.7.2). The Altyn Emel fault has displaced late Quaternary alluvial deposits, but the ages and hence slip rate are not constrained.

The most prominent of the right lateral faults is the Dzhungarian Fault (DZ, Figure 4.4). Running over 350 km from the Chinese Borohoro Shan to Lake Balkhash in the south, the main sense of motion is right-lateral, but it has uplifted a Palaeozoic basement cored range generating a relief of ∼2300 m. *Campbell et al.* (2013) estimated a minimum lateral slip rate of 2.2±0.8 mm/yr, but do not constrain the

shortening rate. However, as vertical offsets are <20% of the lateral offsets, we might expect a dip-slip rate of ∼0.4 mm/yr.

A second prominent right-lateral fault cuts the Dzhungarian Alatau at Taldykorgan, the Aktas Fault Zone (AFZ, Figure 4.4, *Suvorov*, 1964). The zone of right lateral faulting extends all the way from the Ili Basin to Taldykorgan and then ∼100 km NW into the Kazakh platform from the end of the Sarkand rangefront. Though clear in the topography, few Quaternary deposits are disturbed, suggesting a relatively low slip-rate, though no slip rate studies are published.

The role of these major strike-slip faults in accommodating the regional strain field is not well understood. Most directly accommodate small amount of shortening as well as strike slip motion. *Campbell et al.* (2013) suggested that the strike slip motion on the Dzhungarian fault (DF) either accommodates block rotation or allows shortening by lateral extrusion in combination with conjugate left-lateral faulting, or some combination of both processes.

En-Echelon Strike-Slip Faulting in the Ili Basin

From Almaty to the Chinese border, the Ili basin is cut by a series of short, parallel faults (Figure 4.25), each with a component of thrust motion (*Kober et al.*, 2013; *Cording et al.*, 2014; *Campbell*, 2015; *Abdrakhmatov et al.*, 2016, supplemented by my own mapping). Based on their orientations, we infer a component of right lateral slip too. Due to the very low relief nature of the displaced surfaces, lateral offsets are generally not visible, except in the bedrock of the folds in the Duyantau range, where the time period of such offsets is unclear (*Kober et al.*, 2013; *Campbell*, 2015). Vertical offsets are however preserved in the late Quaternary basin deposits, with typical displacements up to ∼10–20 m (e.g. Shonzhy faults, §4.7.3). These short parallel faults are appropriately arranged such that they may accommodate anticlockwise rotation. Located between the large left-lateral faults, the KCF and the AEF, this rotation may accommodate both the transfer of left-lateral shear between the two structures, and internal shortening of the Ili Basin.

At the Ili Basin, the westwards component of the GPS velocities shows a marked increase of 2–4 mm/yr (Figure 4.5), and the northwards component also shows a relatively steep gradient. This is consistent with a zone of left-lateral shear running SW–NE (KCF and AE) through the basin.

4.11 Geodynamic Implications

In general the large scale geodynamics of the Tien Shan (TS) is too poorly resolve at present to establish a concrete link with the evolution and distribution of faulting. However, as discussed in §4.2, observations suggest strong lateral contrasts in the geodynamics along the Tien Shan (*Burov et al.*, 1990; *Roecker et al.*, 1993; *Priestley et al.*, 2006; *Lei*, 2011; *Zabelina et al.*, 2013; *Gao et al.*, 2014; *Kaban and Yuanda*, 2014; *Cherie et al.*, 2016). In the western Tien Shan, *Thompson et al.* (2002) observed distributed faulting

throughout the mountain belt, over a distance of ∼350 km from the Kazakh Platform to the southern Tien Shan, with no one fault having a slip rate of >1–2 mm/yr. By contrast, we find that the Karkara Rangefront Fault accommodates almost half of the convergence at the longitude of my study, but the remaining deformation is distributed across a zone over 500 km wide.

There are several well defined differences in the lower crust. *Steffen et al.* (2011) show that the Isostatic overcompensation increases from west to east within the TS, leaving the region at the KRF overcompensated by almost 30%. In the west, *Oreshin* (2002) and *Gilligan et al.* (2014) note a high velocity region within the upper mantle at depths of ∼90 km, which may be a lithospheric lid. Oreshin et al. suggested that this lid may inhibit shortening and allow for stress transfer N-S across the ranges of the TS at this longitude, giving a broad structure to the range at this point. In the upper crust, *Zabelina et al.* (2013) found strongly negative p-wave velocity anomalies at upper to mid crustal depths (<35 km) beneath the localised beneath the Terskey range at the longitude of my study, compared to weak positive anomalies at the longitude of the Thompson et al. study. At deeper depths, they suggest a much less pronounced high velocity region in the upper mantle that in the western TS, suggesting that such a smaller and/or thinner lithospheric lid. The change in deformation pattern laterally along the TS may therefore be due to the variation in the strength of the mantle lithosphere. At the longitude of my transect, weaker mantle lithosphere could allow the MTF (likely an inherited structure from previous orogens) to accommodate the majority of the strain between the Tarim basin and the Kazakh platform. Only a small degree of strain would therefore be transmitted further north to the Ketmen Range and the Dzhungarian Alatau. On the broader scale, weak lithosphere beneath the Tien Shan is also a suggested reason for the location of the orogen (e.g. *Roecker et al.*, 1993). However, the resolution of the present seismic velocity structures is very coarse in this region and few studies extend further north than the southern edge of the Ili Basin, so further work is needed to properly resolve the dynamics of the structures beneath the Tien Shan at this longitude.

4.12 Synthesis: Earthquake Hazard

Both historic and prehistoric evidence has shown that the Tien Shan have the capacity to generate very large earthquakes (*Tibaldi et al.*, 1997; *Delvaux et al.*, 2001; *Krüger et al.*, 2015; *Campbell et al.*, 2015; *Landgraf et al.*, 2016). At the Saty fault, we tied the regional faulting to a historic earthquake of magnitude >8, with fault slip of up to 10 m, and found a recurrence interval of >5.6 ka (and possibly much longer, *Abdrakhmatov et al.*, 2016). At the Toraigyr fault, we found evidence for a surface rupturing prehistoric earthquake, which generated surface slip of 3 m, but again, the penultimate earthquake was likely to have occurred pre-LGM. On the southern front of the Dzhungarian Alatau, the Konyrolen scarps show vertical offsets of ∼2–3 m in the most recent event which is dated at >3 ka BP, also with the penultimate event likely to have occurred prior to the LGM. Here the slip rate of *Cording et al.* (2014) suggests a

recurrence interval of 5–8 ka. Further north, *Campbell et al.* (2015) observed two events on the Lepsy fault (LP, Figure 4.4), one at ∼400 yrs BP, and another at >5 ka, suggesting a recurrence interval of $\gtrsim$5 ka. They also estimate magnitudes of 7.5–8.2 for the most recent event, with fault slip of 6.0-14.7 m.

At the southern end of the transect, the regional GPS field and my Late Quaternary slip rate show that the Karkara Rangefront Fault (KRF, Figure 4.4) is one of the fastest faults in the northern Tien Shan. However, present day creep at the GPS slip rate suggests that strain accumulation at present is minimal – no faster than any of the other faults through the transect. It is unclear however, whether creep is the long term mechanism for deformation on this fault. Given the length of the extended rangefront (>500 km), if the fault is capable of earthquakes, multi-segment ruptures could have the potential to generate very large earthquakes.

In general, I note therefore that recurrence intervals for surface rupturing events are typically on the order of 5–10 ka, in concordance with those observed further west in the Kyrgyz Tien Shan (*Abdrakhmatov et al.*, 1996; *Thompson et al.*, 2002), and consistent with low slip rates (<1 mm/yr) and large slip per event. Instrumental seismic records covering the last century, therefore only cover a very small fraction of the seismic cycle. The low slip rates mean that strain is generally unresolved in the GPS velocity field. Thus seismic hazard assessments based on instrumental records are likely to be incomplete, and heavily biased by regions which have suffered major earthquakes in the past century.

Unfortunately, these long recurrence intervals also approach the timescale of landscape reset in the region, which is on the order of 10–20 ka. Thus despite the excellent environmental preservation due to low erosion rates, low slip rates and long recurrence intervals make it easy to miss active faults even with the best field and remote sensing observations – this should be taken into account when mapping active faults through the region. For example, prior to the last earthquake on the Saty Fault (SF, §4.6), there would have been very little evidence of activity on the fault, and yet it generated an extremely damaging M_W 8+ earthquake. Similarly, prior to the last event on the Toraigyr fault (TF), there would have been minimal evidence for recent faulting.

4.13 Summary

In this chapter, I have constrained the slip rates and earthquakes on a number of faults (unless stated otherwise, errors are 95% confidence intervals). The Saryjaz rangefront slip rate is $1.12^{+0.56}_{-0.26}$ mm/yr and the most recent event <9 ka BP. The most recent event on the Saty fault was most likely the great 1889 M8+ Chilik earthquake[9] and the slip rate is pending sample analysis. The slip rate on the Toraigyr fault is $0.21^{+0.21}_{-0.06}$ mm/yr, and the most recent event occurred ∼3.2 ka BP while the penultimate event was at least 17 ka BP[10]. The most recent earthquake on the Usek Thrust was >3000 ka BP with a throw of 2–3 m, while the penultimate event was most likely post-LGM, complementing the published slip rate estimate (0.44±0.18 mm/yr). The preliminary slip rate on the southern rangefront fault of the Dzhungarian Alatau is $0.4^{+0.3}_{-0.1}$ mm/yr, and the fault shows signs of activity since the LGM. I found a preliminary slip rate on the Sarkand Rangefront fault of $0.44^{+0.21}_{-0.16}$ mm/yr and the most recent event was >2.1 ka BP. In addition, I have improved upon maps of active faulting along the transect, through both field and remote sensing based mapping.

I have highlighted two different regimes of faulting in the northern Tien Shan; the high Terskey Tien Shan, with relatively little internal deformation are bounded on the northern margin by a fast-moving frontal thrust fault, whereas the faults from the Kegen basin to the Kazakh platform are characterised by low slip-rates, distributing the deformation across a zone 300 km wide.

Of the faults for which we could assess the earthquake recurrence interval in this region of distributed deformation, all were greater than 5 ka (with slip rates of <0.5 mm/yr). Therefore seismic hazard assessment based on instrumental and historic records, which only capture a small fraction of the seismic cycle, will be incomplete.

Generating a DEM covering an unprecedented ∼30 km length of fault scarps has demonstrated the utility of structure-from-motion photogrammetry in assessing an along-strike slip distribution from earthquake scarps.

[9] Work carried out collaboratively for *Abdrakhmatov et al.* (2016), compiled by RW, see §4.6 for details.
[10] Work carried out collaboratively for *Grützner et al.*, *(in revision)*, compiled by EC and CG, see §4.7.1 for details.

Chapter 5

Disentangling Slip-Distribution and Fault Scarp Geometry: Rigorous Quantification of Slip in 3D

5.1 Introduction

Fault displacement estimates from landform offsets are used in a number of applications: estimating fault slip rates in combination with Quaternary dating (e.g. *McCalpin*, 2009), determining earthquake repeatability or fault slip history (e.g. *Lindvall et al.*, 1989; *Kondo et al.*, 2010; *Klinger et al.*, 2011), and estimating maximum earthquake magnitudes through application of scaling laws (e.g. *Scholz et al.*, 1993; *Scholz*, 1994; *Wells and Coppersmith*, 1994; *Manighetti et al.*, 2007; *Leonard*, 2010; *Stirling et al.*, 2013). Additionally, repeat surveys have been used to study temporal variation in fault morphology, for example scarp degradation (e.g. *Elliott et al.*, 2012a) and postseismic tectonic deformation (e.g. *Wilkinson et al.*, 2010; *Lienkaemper et al.*, 2016; *Mackenzie et al.*, 2016).

In the last few years, there has been a major increase in the availability of high resolution topographic data (sub-meter sampling, e.g. Structure-from-Motion (SfM), terrestrial lidar, airborne lidar and satellite stereo-photogrammetry), providing access to the full 3D topography. Such high resolution datasets show great potential for the reconstruction of landform offsets (e.g. *Hudnutt et al.*, 2002; *Salisbury et al.*, 2012; *Zielke et al.*, 2015; *Zhou et al.*, 2015a; *Haddon et al.*, 2016). However, analysis of landform displacements using these data is usually still performed using profiles, reducing the data to two dimensions to measure offsets. This approach has arisen from conventional profile based triangulation survey techniques, for example by topographic profiles (x-z) across a scarp to estimate fault throw, or planform projection (x-y) to estimate lateral slip. In each case a straight line is fit on either side of the fault, and projected to

the fault to measure an offset. This generally requires strong assumptions that any effects arising from the geometric configuration are negligible (often not stated explicitly, e.g. *Zhou et al.*, 2015a, discussed below).

Efforts have been made to account for epistemic and aleatoric uncertainties in piercing line offsets (e.g. *Lienkaemper*, 2001; *Salisbury et al.*, 2015), but even these fail to account for (and capitalise on) the error introduced by the confounding geometries of slip, slope and profile azimuth.

Standardised tools exist for using topography datasets to reconstruct lateral offsets (e.g. *Zielke and Arrowsmith*, 2012; *Haddon et al.*, 2016) or dip-slip vertical offsets (e.g. *Thompson et al.*, 2002; *McCalpin*, 2009; *Burbank and Anderson*, 2011), but these measurements generally lack a rigorous three dimensional framework, and the uncertainty introduced by unaccounted-for geometry is usually poorly constrained. There are no standard methods for characterising the 3D displacements associated with oblique slip and/or imperfect geometry, which necessitate solving for multiple components of the slip-vector simultaneously.

Scalar offset measurements are commonly used to build along-strike slip distributions (e.g. *Kondo et al.*, 2010; *Klinger et al.*, 2011) on the principle that each individual measurement can capture the throw or lateral slip. While these measurements are sufficient if the geometry is very simple (e.g. a vertically displaced horizontal surface, or near-horizontal channel offset laterally), in the case of rough or steep topography, the geometry of the fault-topography intersection can give rise to an apparent slip much larger or smaller than the actual slip (Figure 5.1). This is often mitigated by very careful choice of measurement location, but this filtering limits the amount of information gathered and potentially introduces a sampling bias. Furthermore it does not make use of the information provided by the full topography field. The resulting slip distributions are almost always variable and "noisy" and it is often unclear whether this reflects real slip variation or artefacts of measurement noise, erosion, and slip geometry (e.g. *Haeussler et al.*, 2004; *Klinger et al.*, 2006; *Elliott et al.*, 2012b; *Schwartz et al.*, 2012; *Rockwell and Klinger*, 2013).

We aim to lay out the assumptions associated with present techniques for calculating fault slip distributions and slip-vectors using profiles whether measured directly by differential GPS or total station, or from a high resolution digital elevation model (DEM). We derive an analytical expression linking the vertical separation a profile measures to fault slip under a generalised surface geometry. We use it to test the validity of the geometric assumptions and quantify the errors associated with breaking them. Based on the analytical expressions for fault offset, we suggest a Monte-Carlo approach to uncertainty analysis of fault offset measurements similar to that of *Thompson et al.* (2002), but taking into account the 3D topography-fault intersection geometry.

Given the variation of apparent landform offset caused by fault-topography intersection geometry, we derive a new, inherently three-dimensional method to solve for the full slip-vector. Utilising the variation of apparent offset with topographic attitude and slip-geometry this allows us to fully exploit

high resolution topographic datasets. We test the method on the terrestrial lidar data from the 2010 El-Mayor Cucapah earthquake ruptures (*Gold et al.*, 2013), and the satellite-photogrammetry elevation model of the scarps on the Hoshab Fault, Pakistan (*Zhou et al.*, 2015a).

5.2 Offset Landform Geometry

Conventional methods will not always provide an accurate measure of fault slip. In general, measured separations are sensitive to the orientation of the displaced feature, so without a-priori information or assumptions about the slip orientation, an individual displaced landform will often not be a good proxy for total fault slip (examples below).

5.2.1 Geomorphic Markers

Fault offsets are measured using geomorphic markers—features of known or estimatable prior geometry, displaced by surface faulting. These can generally be divided into two classes; quasi-linear features such as ridge crests or stream channels, and correlative surfaces such as alluvial fan surfaces or river terraces. Linear features provide the tighter constraint on fault slip as there are fewer degrees of freedom – they are only ambiguous along the line of the feature e.g. a horizontal line perpendicular to a dip-slip fault cannot constrain the horizontal shortening/extension across the fault. Correlated planar surfaces are ambiguous along two directions within the plane and therefore give a slightly weaker constraint on fault slip, e.g. a planar slope with an aspect perpendicular to a pure strike-slip fault will not record fault offset.

In both cases, the separation vector in the direction orthogonal to the marker is the only measurement that can be uniquely made with no additional information or geometric assumptions. This is conventionally estimated with profiles in the case of marker surfaces, and more sophisticated 3D line fitting for line markers. In order to relate this separation to the slip vector, the geometry of the fault plane relative to the separation vector must be known. In the case of non-parallel markers (lines or surfaces) the marker separation is measured at the estimated location of the fault surface trace, between the projected markers (e.g. *Thompson et al.*, 2002).

5.2.2 Geometric Effects

Markers forming a simple geometry relative to the fault can provide a good measure of fault displacement, e.g. a line feature perpendicular to a fault trace will provide an accurate measurement of lateral slip without being affected by any dip-slip motion. However, for less "perfect" geometries the orientation of the fault relative to the topography affects the apparent offset measurement, disguising the slip-vector.

The effect of marker geometry on the apparent offset for a given slip vector can be illustrated by several simple cases. Figure 5.1A shows a example map of two perpendicular fences intersecting an oblique right-lateral thrust fault, each at an orientation of 45° to the fault. The fences give apparent

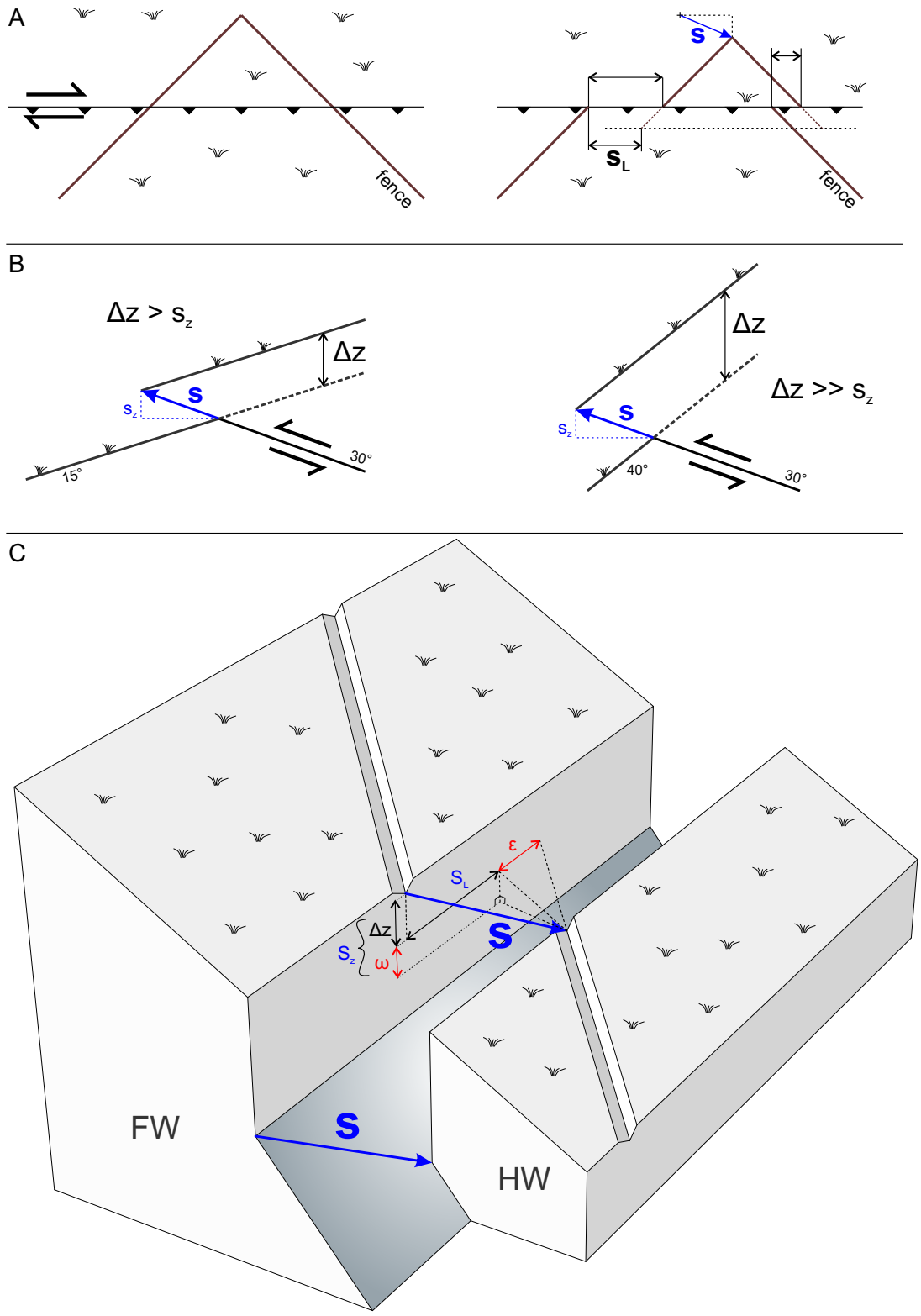


Figure 5.1: (A) A map view diagram for oblique right-reverse slip demonstrates the very different apparent lateral offsets that can be measured on two fences crossing the fault at 45°, even with only a small component of shortening. (B) Cross-section view showing the effect of slope angle on the vertical separation measured by a profile. For the same slip vector and hence throw (s_z), the vertical separation measured will differ. (C) 3D block diagram of a topographic slope displaced by a left-normal fault, resulting in a surface fissure across which the linear stream marker is projected. S_L is the lateral component of slip, correctly measured by projecting the end of the channel across to the free face, in the slope-parallel direction. ϵ is the extra component of apparent lateral slip introduced by the horizontal advection of topography. ω is the vertical component unaccounted for by a profile, due to the advection of topography. The true fault throw is therefore $s_z = \Delta z + \omega$.

lateral offsets which depart from the true value of lateral slip (S_L) substantially as fault-perpendicular motion increases (in this case shortening). Similarly, Figure 5.1B shows a profile view example of a pure dip-slip thrust fault intersecting two different topographic slopes. The vertical separation (Δz) measured with a profile is the sum of two components: the fault throw (s_z) and a component contributed by the horizontal advection of the topography. Unless the second component is accounted for, two different vertical throw estimates will be made for an identical slip vector. The slope angle and the fault dip must therefore be known in order to accurately estimate the throw from a profile across a pure dip-slip scarp (e.g. *Baljinnyam et al.*, 1993; *Thompson et al.*, 2002).

Figure 5.1C shows a perspective diagram of a left-normal fault scarp cutting a slope with fissuring at the base of the scarp, demonstrating the effects of slope angle, fault dip and oblique slip on the slip measurement. A profile across this scarp would measure a vertical separation of $\Delta z = s_z - \omega$, underestimating the throw because the horizontal component of slip contributes its own apparent vertical separation by the advection of topography. Projecting the channel thalweg along its axis to the scarp free-face results in an overestimate of the lateral component of slip ($S_L + \epsilon$). Projecting the end of the channel to the free face in the fault-perpendicular direction gives the correct lateral measurement, but relies on a precise identification of the 'end' of the channel, a measure which is often difficult to identify in practice, and very sensitive to erosion and scarp degradation. Particularly with dipping faults, the strike-perpendicular component of slip will distort the apparent offsets of fault-oblique landforms, which should therefore be avoided unless further constraints are available. This example shows a slope with an aspect perpendicular to the fault strike – non-perpendicular aspects lead to further complication.

In the general case, a marker can only constrain slip in the direction orthogonal to the marker; slip parallel to the marker is not recorded. Thus an individual marker separation is only a proxy for total fault slip in ideal or geometrically constrained cases.

5.2.3 2D profile assumptions

In using profiles to measure lateral slip or throw, several important assumptions are inherently made, though not always stated and often overlooked. Slope/fault geometry is usually assumed to be 'simple', with fault strike perpendicular to slope aspect. Slip is usually taken to be pure dip-slip or strike-slip unless oblique motion is evident. The azimuth of the profile is chosen by the operator and assumed to be either perpendicular to the fault strike, or parallel to the slope aspect. In addition, the geometry of the fault (strike and dip) is usually taken as moderately well known. Not all of these assumptions are made every time, but usually at least one is. Plots of separation against profile azimuth and/or local fault strike are sometimes employed to check for geometric variation (e.g. *Middleton et al.*, 2016). In §5.3 we form analytical expressions to test the effect of breaking the methodological assumptions. However, alongside the methodological assumptions, it is also generally assumed that the surfaces measured are

well preserved and linear or planar—markers are usually carefully chosen to avoid areas of erosion and deposition around the scarp adding a degree of subjectivity and potential operator bias (e.g. *Scharer et al.*, 2014; *Salisbury et al.*, 2015). §5.4 presents an alternative to measuring profiles which may reduce the sensitivity to scarp degradation using a more three-dimensional approach.

5.2.4 Nomenclature

In this paper we use a number of terms related to slip geometry which have different meanings and interpretations between communities. Our usage is based on *Ragan* (2009), extended to incorporate further mathematical terms and described here to avoid ambiguity. The fault slip vector is the slip in the fault plane, comprised of three components—lateral slip (S_L, horizontal, along strike), heave (s_y, horizontal, strike perpendicular) and throw (s_z, vertical). The vector sum of heave and throw is the dip-slip component of slip, $S_D = \sqrt{s_y^2 + s_z^2}$, in the up dip direction on the fault plane (Figure 5.2).

A planar marker displaced by a fault can be described by its attitude: the dip (θ) and aspect (ψ) of the surface. The apparent offset of the marker in a specified direction is termed the separation and can be measured in a number of directions (*Hill*, 1959): strike separation and dip separation in fault-plane space (P and Q in Figure 5.2B) and so-called stratigraphic separation when measured to orthogonal to bedding planes. In our geomorphic focus on offset fluvial and alluvial surfaces we primarily refer to the latter, which for generality we term the "orthogonal separation", the orthogonal distance, d, between the displaced planes (Figure 5.2A,B). Similarly, a displaced line marker is described by its attitude and the orthogonal separation. Where the fault geometry is well known, linear and planar markers are commonly projected to the fault plane intersection, defining piercing points and piercing lines respectively (e.g. *Gold et al.*, 2013).

5.2.5 Geometry Definitions

The simplest test case for fault geometry is a planar topographic slope displaced by a discrete fault, giving two parallel surfaces offset by fault motion (Figure 5.2). We define the geometry using the slope unit normal vector $\hat{\mathbf{n}}$ and choose the fault to strike east, in the positive x-direction (Figure 5.2C). We follow the convention that fault dip is to the right of strike, i.e. in the negative y-direction ('south'). The slope unit normal, $\hat{\mathbf{n}}$, and the slip vector, $\mathbf{s}$, are:

$$\hat{\mathbf{n}} = \begin{pmatrix} \sin\psi \sin\theta \\ \cos\psi \sin\theta \\ \cos\theta \end{pmatrix} = \begin{pmatrix} n_x \\ n_y \\ n_z \end{pmatrix} , \tag{5.1}$$

$$\mathbf{s} = \begin{pmatrix} s_x \\ s_y \\ s_z \end{pmatrix} = \begin{pmatrix} S_L \\ S_D \cos\delta \\ S_D \sin\delta \end{pmatrix} \begin{matrix} lateral \\ heave \\ throw \end{matrix} \quad , \tag{5.2}$$

where ψ = slope aspect relative to the fault, the angle between the topographic gradient and the normal to the fault trace measured in the horizontal (-90–90°), θ = slope angle (-90–90°), δ = fault dip (0–90°) and S_L and S_D are the lateral and dip slip components of $\hat{\mathbf{s}}$. Under this geometry left-lateral and reverse slip are positive. For a left-lateral/reverse fault, a positive slope angle (theta>0) gives a typical downhill-facing scarp and a negative slope angle (theta < 0) describes an uphill facing scarp. For a right-lateral/normal fault, the opposite is true (diagram in Figure 5.3).

For a point $\hat{\mathbf{r}}$ on a plane, the plane is described by $(\mathbf{r} - \mathbf{a}) \cdot \hat{\mathbf{n}} = 0$ where the plane passes through the point $\mathbf{a}$. Fixing the footwall plane to pass through the origin ($\mathbf{a} = \mathbf{0}$), we write the footwall surface as:

$$\mathbf{r}_{FW} \cdot \hat{\mathbf{n}} = 0 \quad . \tag{5.3}$$

The hangingwall is the same plane, displaced by slip vector $\mathbf{s}$:

$$\mathbf{r}_{HW} \cdot \hat{\mathbf{n}} = \mathbf{s} \cdot \hat{\mathbf{n}} \quad . \tag{5.4}$$

These two planes, $\mathbf{r}_{FW}$ and $\mathbf{r}_{HW}$, are a simplified representation of a natural topographic slope offset by discrete fault slip (Figure 5.2A,B).

5.3 Analytical Fault Throw

Using the idealised geometry defined above, we find an expression for the vertical separation that a profile would measure. Considering a profile in the vertical plane, the basic measurement is the vertical separation between the two planes (lines on the projected profile). Considering the point at x=0, y=0, we write the vertical separation, Δz, between the hangingwall and footwall planes as:

$$\Delta z = \frac{\mathbf{s} \cdot \mathbf{n}}{n_z} \quad . \tag{5.5}$$

Expanding, and dividing by the vertical component of slip ($s_z = S_D \cos\theta$), we write this as:

$$\frac{\Delta z}{s_z} = 1 + \tan\theta \left(\frac{S_L}{S_D} \frac{\sin\psi}{\sin\delta} + \frac{\cos\psi}{\tan\delta} \right) \quad . \tag{5.6}$$

In the case of pure dip-slip with the slope aspect perpendicular to fault strike ($\psi = 0$), this reduces to:

$$\frac{\Delta z}{s_z} = 1 + \frac{\tan\theta}{\tan\delta} \quad . \tag{5.7}$$

Equivalently, the total slip on the fault is:

$$s = \frac{\Delta z \cos\theta}{\sin(\delta + \theta)} \quad , \tag{5.8}$$

exactly as described by *Thompson et al.* (2002) for the case of thrust scarps. Thus, assuming pure dip-slip, a known slope angle (θ), and a known fault dip (δ), we can calculate the fault slip (e.g. *Baljinnyam et al.*, 1993, pp. 29). Similarly, in the more general case, if the slope aspect is known the fault slip can

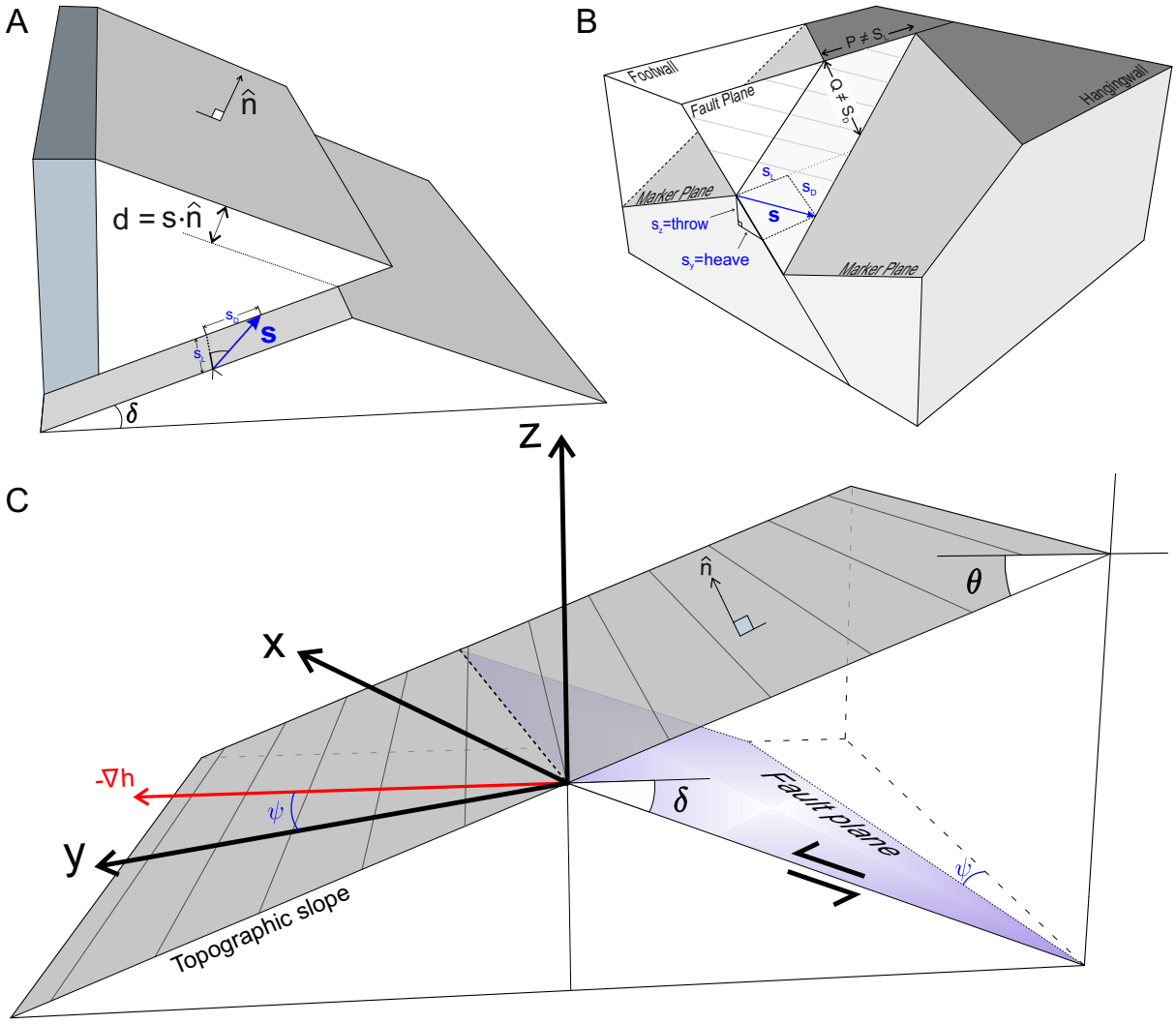


Figure 5.2: (A) Slip vector **s** displaces the hangingwall along the fault plane. The orthogonal separation between planes is $\mathbf{s} \cdot \hat{\mathbf{n}} = d$. (B) After *Ragan* (2009). Example of a marker plane displaced by **s**. The observed strike separation (P) and dip-separation (Q) are much larger than the lateral and dip slip components of the slip vector. The dip-slip component of **s** ($\mathbf{S_D}$) can be further divided into two components, the heave (s_y) and throw (s_z). (C) Geometry definitions. θ = slope angle, ψ = slope aspect, δ = fault dip and $\hat{\mathbf{n}}$ = slope unit normal vector, $-\nabla h$ = down-slope direction.

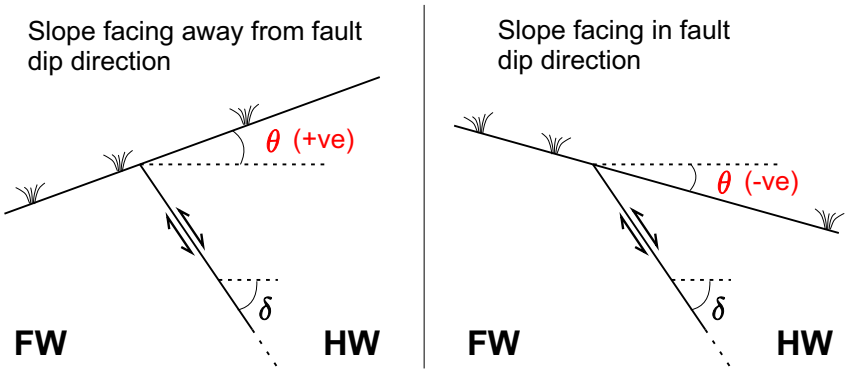


Figure 5.3: Definition of slope angle theta under the geometry described in §5.2.5. (left) $\theta > 0$ gives a downhill facing scarp with reverse slip or an uphill facing scarp for normal slip. (right) The opposite is true for $\theta < 0$

be calculated without further assumptions. The above equations require us to know the entire geometry of the system to calculate the fault slip. Instead, it is often assumed that the geometry is close enough to "simplest" case with fault strike perpendicular to slope aspect ($\psi \approx 0$). It is also commonly assumed that the fault dip is well known. In the next section we test the effects of breaking these assumptions.

If a profile (in a vertical plane) is measured across these two slopes, we expect to measure the same vertical separation between them regardless of the azimuth of the profile. However, such a profile will generally give a biased estimate of the slope angle θ; a profile at an azimuth of β relative to aspect will give an apparent slope angle θ':

$$\frac{\tan\theta'}{\tan\theta} = \cos\beta \quad . \tag{5.9}$$

Thus the slope angle will be systematically underestimated by a profile, except in the ideal case where the profile is in the direction of the slope aspect.

5.3.1 Assumption: Dip-Slip & Fault Perpendicular Aspect

A typical set of assumptions is that the slip vector is purely dip-slip ($S_L/S_D = 0$) on a fault of known dip and that the slope aspect is perpendicular to fault strike ($\psi = 0$). We derive analytical expressions linking the estimated throw under these assumptions ($s_{z,profile}$) to the true throw ($s_{z,true}$). Plotting this function for several different cases of fault geometry and fault slip, we investigate where such profiles can reasonably be used with these assumptions and where they should not be used directly. The measured fault throw can be written as:

$$s_{z,profile} = \frac{\Delta z}{1 + \tan\theta\cot\delta} \tag{5.10}$$

Taking the ratio of $s_{z,profile}$ to $s_{z,true}$, this becomes:

$$\frac{s_{z,profile}}{s_{z,true}} = \frac{1 + \tan\theta \left(\frac{S_L}{S_D} \frac{\sin\psi}{\sin\delta} + \frac{\cos\psi}{\tan\delta} \right)}{1 + \tan\theta \cot\delta} \tag{5.11}$$

Where this expression is close to 1, a profile will give a good estimate for the fault throw (still assuming the fault dip is known well). As this expression departs from 1, we get a systematic measurement error.

Figure 5.4 shows plots of the ratio $s_{z,profile}/s_{z,true}$ for several different cases. Under these assumptions, with fault-perpendicular aspects ($\psi = 0$), a profile can perfectly recover the throw, provided that the fault dip is known and the profile gives a good estimate of slope angle. However, the measurement error increases with aspect, ψ, as it moves away from fault-perpendicular, becoming larger with steeper slope angles and shallower fault dip. The dashed lines demonstrate that even a small degree of lateral slip significantly exacerbates this discrepancy. If we are willing to accept 5% errors in throw, then for steeply dipping (∼60°) dip-slip faults, a slope aspect varying by up to ∼40°, even with reasonably steep slope angles, does not significantly affecting the throw estimate. However, for shallower faults (e.g. ∼30°) this is reduced to 20–30°, or even less if there is a small component of lateral slip (e.g. *Zhou et al.*, 2015a, §5.3.3).

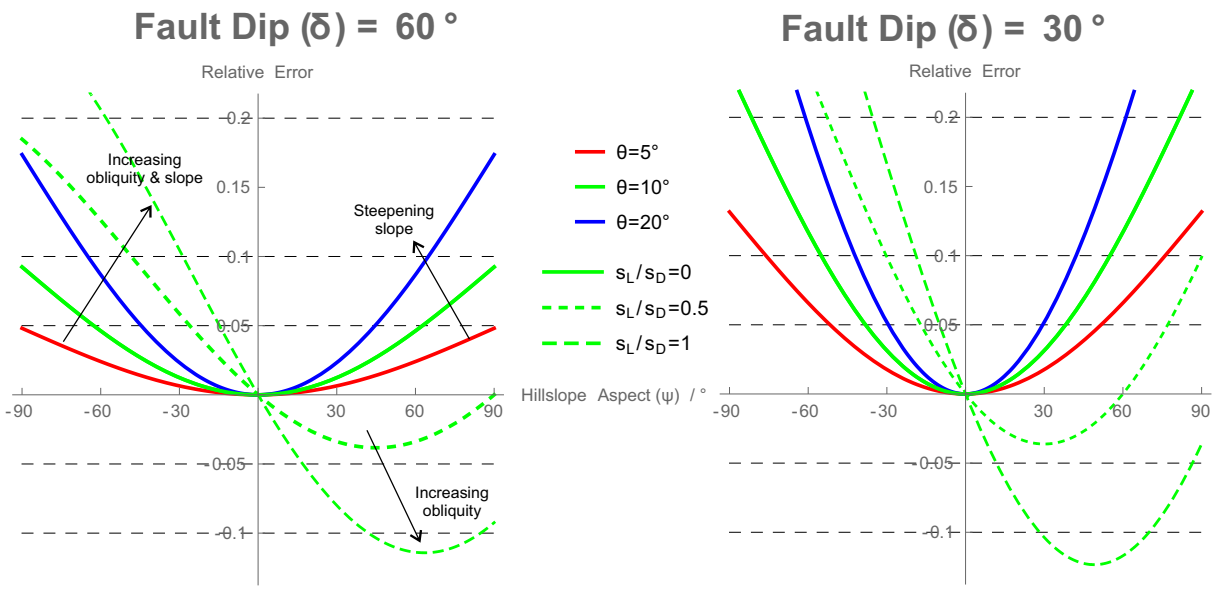


Figure 5.4: Plot of the relative error $\left(\frac{s_{z,profile}}{s_{z,true}} - 1\right)$ in a profile measurement, assuming pure dip-slip on a fault of known dip, plotted against slope aspect for several cases. Solid lines represent pure dip-slip cases, while dashed lines show the effect of adding lateral slip for the case of $\theta = 10°$. *(Left)* shows the case with a fault dip of 60°, while *(Right)* is 30°, showing a much more pronounced effect at lower fault dips.

Full parameter space

The plots of Figure 5.4 show several specific cases, but it is worth considering the full parameter space of Equation 5.11. Figure 5.5 shows a series of density plots for different cases of fault dip (30°, 45°, 60°) and different degrees of oblique slip (S_L/S_D = 0, 0.5, 1). For steeply dipping dip-slip faults the effect

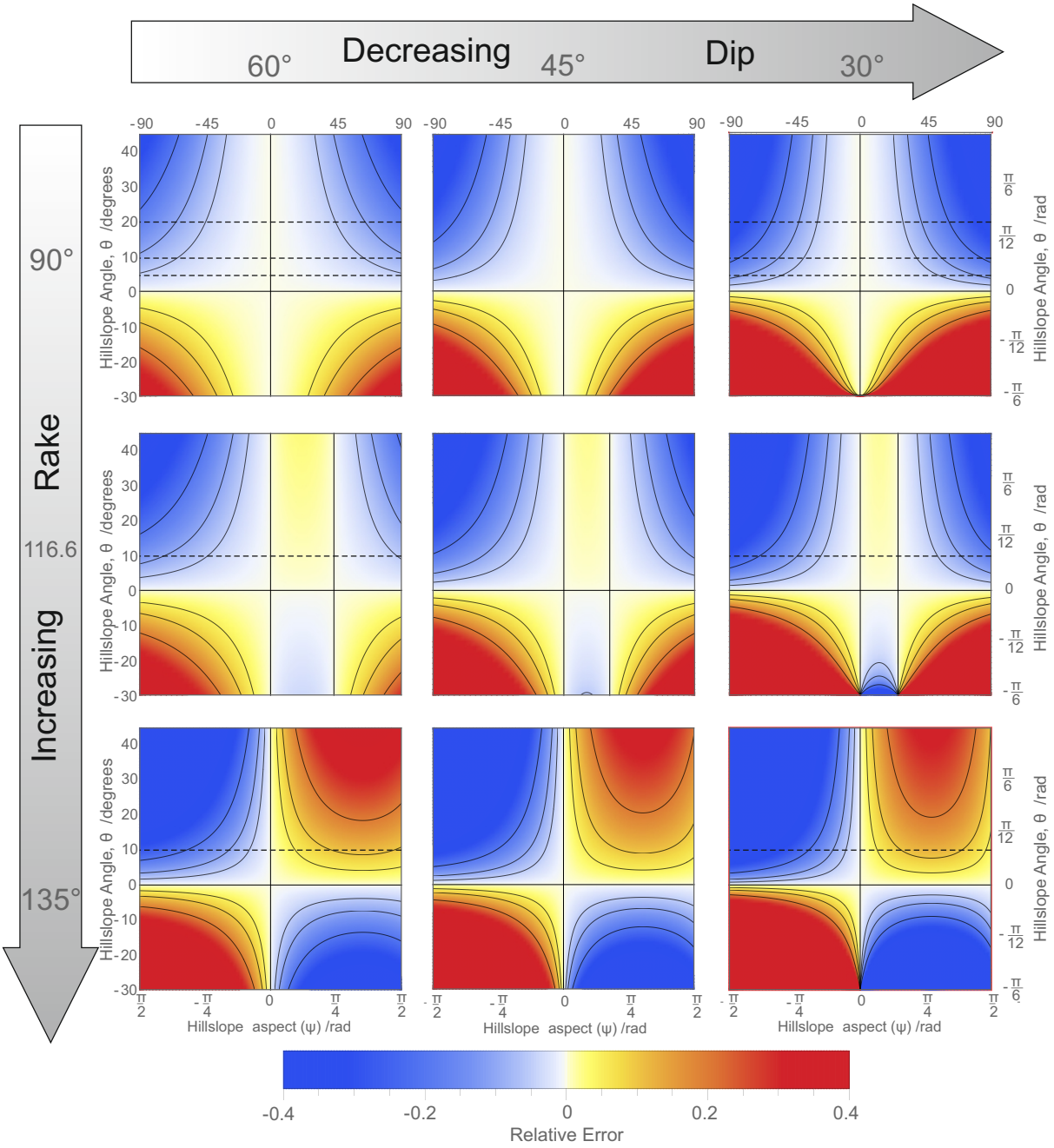


Figure 5.5: Plots of the relative error $\left(\frac{s_{z,profile}}{s_{z,true}} - 1\right)$ for expected ranges in slope aspect (ψ) and slope angle (θ), for three different fault dips (30°, 45°, 60°) and three different degrees of lateral slip (S_L/S_D = 0.1, 0.5, 1.0), with the dip slip held fixed at 1 m. The described rake values are an angular measure of S_L/S_D, indicating the direction of slip in the fault plane $rake = \arctan \frac{S_L}{S_D}$. Each plot is coloured by the error in the measurement due to the assumptions of pure dip-slip and simple measurement geometry, for slope angle and aspect. The contours represent values of 0.05, 0.1 and 0.2, i.e. 5%, 10% and 20% departure from the true value. Dashed lines are the transects shown in Figure 5.4. Following the convention in Figure 5.3, a downhill facing reverse scarp will have $\theta > 0$ while a normal scarp will have $\theta < 0$. The converse is true for uphill facing scarps.

of the slope attitude is relatively small; with $\delta = 60°$ with slope angles up to $\theta \sim 20°$, varying the slope aspect relative to global fault strike by $\sim 40°$ does not affect the measured value at the 5% level.

However, as we might expect from the conceptual models (§5.2.2), introducing a small component of lateral slip significantly reduces this range, an effect which is enhanced by shallower fault dips. Shallower

fault dips and increased obliqueness of slip results in very narrow geometric tolerance, e.g. with $S_L/S_D = 1$ on a 30° dipping fault, and slope angles of >5°, a slope aspect deviating by as little as ∼10° yields a >5% systematic error. Therefore, with gentle slopes, measurements will be quite tolerant of breaking the assumption of simple geometry ($\psi = 0$), but even a small component of lateral slip can cause significant errors in the throw estimate. Importantly, these errors are systematic, and so cannot be characterised by a simple Gaussian uncertainty.

5.3.2 2D: Monte-Carlo Error Analysis

In cases where slopes are close to flat ($\theta \approx 0$) and/or fault-perpendicular ($\psi \approx 0$), profiles can still provide a good constraint on fault slip, but we need a rigorous way to characterise the uncertainty in the measurements due to the fault, topography and slip geometries. The geometric formalism laid out above (Equations 5.5–5.9) can provide this framework.

On scarp profiles, *Thompson et al.* (2002), *Davis et al.* (2005), *Amos et al.* (2010) and *Gold et al.* (2012) use Monte-Carlo simulations to model the errors associated with estimating fault offsets in 2D. Assigning probability distribution functions (PDFs) to each of the important 2D geometric parameters, they sample the PDFs 100,000 times to estimate the probability distribution for the fault throw. Using the geometry defined in §5.2.5, we extend this method to a full three-dimensional approach, providing a means to quantify the effect of imperfectly known 3D geometry on estimates of landform offsets.

In order to estimate the PDF for the fault throw (or total slip etc.), each component of the fault scarp geometry must be attributed a PDF (Figure 5.6). In the case of surfaces fitted with a least squares regression (e.g. slope angle and intercept), a normal distribution with standard error can generally be used. Similarly, parameters known from direct measurement (e.g. dip from fault exposure) are generally also assigned a measurement PDF. Parameters with asymmetric or otherwise constrained distributions, (e.g. fault dip if unknown) are generally given uniform, triangular or trapezoidal distributions depending on the individual case, though (*Scharer et al.*, 2014) note that non-uniform PDFs must be carefully justified. Generalising to 3D, we incorporate two further parameters (compared to *Thompson et al.* (2002)): the slope aspect (ψ) and the dip-slip:strike-slip ratio (S_L/S_D).

As seen above, we can relate vertical separations (Δz) to throw (s_z) with equation 5.6. Similarly we could write this in terms of total fault slip, or lateral slip in the case of a strike slip fault. Thus, provided we can constrain the PDFs of all the geometric parameters, we can estimate the PDF of the fault throw. Figure 5.6 shows a hypothetical case for profile measurements across a reverse fault scarp. In this case the fault dip is unknown but a possible range is estimated, which we represent with a uniform PDF. The slip is taken to be dip-slip, but the rake is allowed to vary, introducing up to 10% lateral slip, as we might expect such small amounts of lateral slip to be missed on inspection. We take the slope aspect and the dip-slip:strike-slip ratio to be normally distributed with zero-mean (though other distributions

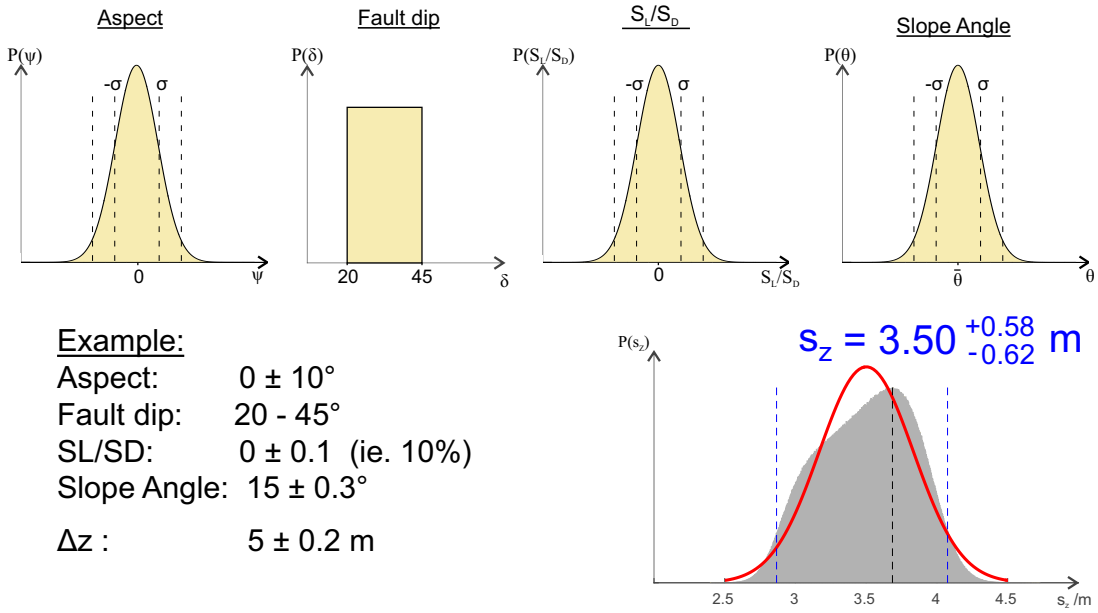


Figure 5.6: An example of a Monte-Carlo simulation uncertainty analysis with a selection of typical geometric parameters and associated uncertainties. Each of the geometric parameters is assigned an estimated probability distribution function (PDF) based on prior knowledge. The resulting throw PDF (grey) is asymmetric – a normal distribution of the same mean and standard deviation is overlaid (red). Median and 95% intervals shown dashed.

could be used). The resulting throw PDF is asymmetric as a result of the trigonometric relations between the geometric parameters. The median and 95% confidence intervals are shown dashed. The MATLAB script for generating the throw PDF in Appendix B.1. We suggest that this full error analysis should be carried out for any slip estimate from profiles in order to accurately characterise the geometric error.

5.3.3 2D profiles: Case Study - 2013 Balochistan Ruptures

An example of the errors associated with varied geometry can be seen from the fault scarps on the Hoshab fault in Pakistan, the source of the 2013 M_W 7.7 Balochistan earthquake (e.g. *Avouac et al.*, 2014; *Jolivet et al.*, 2014). The 2013 earthquake generated ~200 km of surface ruptures, with up to 11-14 m of lateral slip and 1–4 m vertical slip (*Zinke et al.*, 2014; *Gold et al.*, 2015; *Zhou et al.*, 2015a). *Zhou et al.* (2015a) used post-earthquake stereo-imagery to generate a high resolution (1 m) digital elevation model of the entire fault zone. They used planform-projection to measure lateral offsets and profiles to measure vertical offsets, both for the 2013 event and cumulative scarps formed over multiple earthquake cycles.

We reassessed the fault displacement at the site described in Figure 2 of *Zhou et al.* (2015a), focusing on a set of cumulative scarps in an old alluvial fan (Figure 5.7A). Using the elevation pointcloud (full dataset to be made available through OpenTopography, www.opentopography.org), we take swath profiles along the profile lines P1 and P2, and fit parallel lines above and below the scarp (Figure 5.7A), estimating vertical separations of 12.1±1.5 m and 7.3±0.3 m respectively. Incidentally our estimate for P1 is much larger than that of *Zhou et al.* (2015a), highlighting both the subjectivity of profile measurements and the tendency towards confirmation bias in expecting neighbouring profiles to have similar apparent offsets.

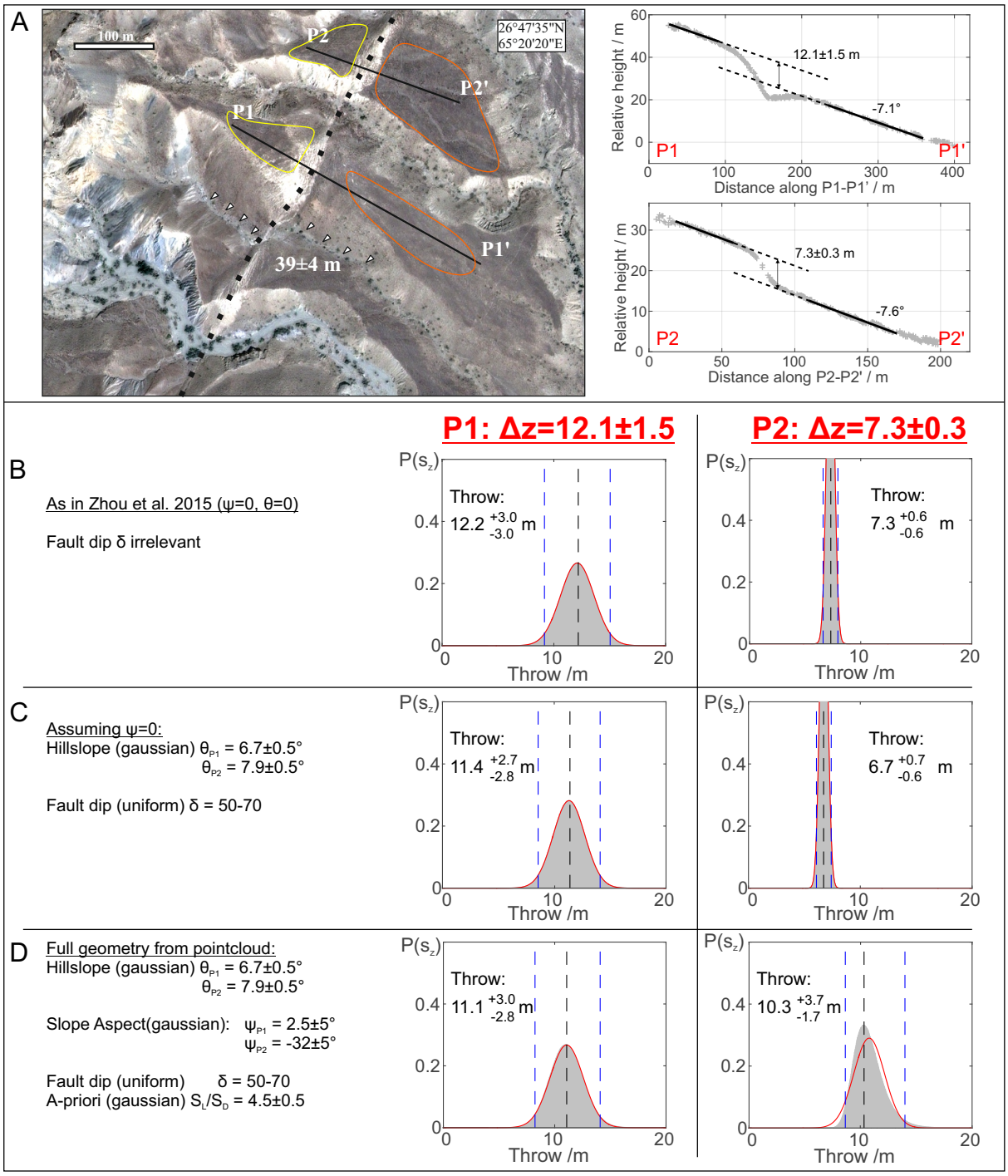


Figure 5.7: Effects of geometry on profile measurements for an oblique slip case study: the Hoshab Fault, Pakistan. (A) Adapted from *Zhou et al.* (2015a), Figure 2. We take swath profiles through the photogrammetry derived pointcloud along the lines P1–P1' and P2–P2'. Yellow and orange polygons outline the sections of hangingwall and footwall used for estimating slope attitudes and 3D separations. We measure vertical separations of 12.1±1.5 m from profile P1 and 7.3±0.4 m from P2. (B) Throw PDFs for the two profiles P1 and P2 under the assumptions of *Zhou et al.* (2015a). In each case the solid line represents a Gaussian distribution with the same mean and standard deviation, dashed lines show the median and 95% bounds. (C) PDFs for P1 and P2 correcting for the slope angle (estimate from pointcloud), but assuming $\psi = 0$, with a fault dip of 50-70°. (D) Estimated PDFs for the throw at P1 and P2 incorporating the slope aspect, slope angle and an a-priori s_L/s_D estimate along with their associated uncertainties. Both profiles are then consistent at the 1σ level, suggesting a throw of ∼10–11 m.

Fitting a plane to the hangingwall slope in each profile (yellow polygons, Figure 5.7), we estimated the slope attitude for the surface represented by each. At P1, the hangingwall surface has an aspect close to fault-perpendicular ($\psi = -3°$) with a slope angle of $\sim 7°$, so we expect measured separations to be relatively insensitive to lateral motion. The hangingwall surface at P2 has an aspect of $\sim$32° and a slope angle of $\sim$7°, so we must consider the contribution of lateral slip to the vertical separation. Using these slope attitudes and the profile separations, we apply the Monte-Carlo method (§5.3.2) to investigate the site with a rigorous treatment of the errors, comparing them to estimates made under simple-geometry assumptions.

In Figure 5.7 we plot estimated PDFs for the fault throw under three different cases. We represent the measurement uncertainties on the vertical profile separations as Gaussian distributed with 1σ errors. Figure 5.7B shows the PDF for the approach of *Zhou et al.* (2015a), where it is implicitly assumed that the geometry is 'simple', i.e. $\theta \approx 0,\ \psi \approx 0$, so the throw is exactly the vertical separation measurement. The two estimates of throw disagree at the 95% confidence level.

Figure 5.7C shows the PDF for the case of assuming $\psi \approx 0$, but accounting for the slope angle θ. The fault dip is assumed to be 50–70° covering the values estimated by *Barnhart et al.* (2014) and *Zhou et al.* (2016) for this reach of the fault; lacking any further information, we assume a uniform probability distribution across this range. The estimated throw is systematically smaller than the measured separation (in this case by $\sim$0.5 m), and the resultant PDFs still disagree at the 95% confidence level between the two profiles.

Figure 5.7D shows the PDFs for the fault throw in both profiles taking account of the full orientation of the slopes measured. We assume a value of $S_L/S_D = 4.5 \pm 0.5$ based on the estimate of *Barnhart et al.* (2014) for this stretch of fault in the most recent event, which is consistent within error to the average ratio based on measurements of *Gold et al.* (2015) and *Zhou et al.* (2015a). The orientation of the topographic surface at P2 is such that lateral slip reduces the vertical separation, so a larger ($10.3^{+3.7}_{-1.7}$ m) throw would be consistent with the measured vertical separation, while P1 is largely unaffected by lateral slip ($11.1^{+3.0}_{-2.8}$ m), but the measurement error is larger. These estimates for the throw agree well within the 1σ error bound, confirming that the change in vertical separation is primarily due to the change in orientation of the surface topography.

We conclude that in locations where slope aspect is approximately perpendicular to fault strike, profiles are a reasonable tool to estimate fault throw, with a mild (<10%) overestimate if the fault dip is unaccounted for. However, where slope aspects are not fault-perpendicular, profiles do not well constrain the throw – further geometric information is necessary. In §5.6 we describe an alternative 3D method to solve for the components of slip using the two slopes described and an offset river channel.

5.3.4 2D profiles: Summary

In general, for shallow slope angles and steep fault dips, variation in the expected vertical separation is relatively small with varying slope geometry (equivalent to moving along strike over different landforms). Therefore profiles can recover fault throw well and Monte-Carlo simulations can give a reasonable estimate of the associated errors. However, with steeper slope angles and shallower faults, there is significant variation in vertical separation with change in slope aspect for a given fault slip, so individual 2D-projected profiles are insufficient to constrain fault motion. Similarly, adding even a small degree of oblique slip further increases the discrepancy. While this analysis was carried out for the case of throw estimates from profiles, a similar analysis can be performed for estimating lateral slip from planform-projections.

To resolve statistically significant slip variation along strike, a rigorous assessment of these errors should be completed. Monte-Carlo simulations based on our geometric framework provide a much needed method to rigorously characterise the uncertainty arising from poorly constrained 3D geometry in fault offset estimates from profiles or planform-projection.

5.4 Slip Geometry – 3D Analysis

Instead of taking profiles, we can exploit the availability of high resolution digital elevation models, by approaching the analysis of surface faulting in an inherently 3D fashion. *Elliott et al.* (2012b) combined pairs of nearby planform markers across the Darfield fault to calculate the magnitude and orientation of the horizontal component of the slip vector, assuming that both markers were subjected to the same slip vector. We extend this concept to exploit the change in apparent landform offset with varying marker geometry to constrain the 3D slip vector by combining multiple along-strike measurements. We start from a base assumption of a constant slip vector over the region of interest. This assumption is unlikely to be valid at the entire fault scale, but may be applicable at the scale of individual/neighbouring geomorphic features (e.g. alluvial fans and moraines). It should be noted that this will not always be applicable, as there are good examples of short wavelength variations in fault offsets which are not due to geometric effects (e.g. *Rockwell et al.*, 2002; *Rockwell and Klinger*, 2013). However, even where there is minor variation over the region of interest, an average slip vector is still a useful constraint, for example in estimating palaeo-earthquake magnitudes.

Instead of profiles, we use correlative surfaces on either side of the fault as these provide a natural estimate of the topographic slope attitude. Again, the simplest case is to approximate the surfaces on either side of the scarp as two parallel planar surfaces, as defined in §5.2.5. Non-planar (e.g. conical fan surfaces) and non-parallel surfaces could similarly be used, but they require more free parameters, so we illustrate the concept with the simplest case. The incorporation of line markers under this model is discussed in §5.4.3.

5.4.1 General Solution

With parallel planar surfaces, the unique separation measurement at any point along the fault is the orthogonal separation vector between the hangingwall and footwall planes, $d\hat{\mathbf{n}}$. A well oriented 2D profile (in the down-slope direction) through the same planar surfaces could measure the same orthogonal separation (d), but in general a 2D profile is an inappropriate tool to constrain the slope normal vector ($\hat{\mathbf{n}}$), as it requires the user to "choose" the profile azimuth. Projecting the slip onto the normal direction, the component of slip orthogonal to the planes (Figure 5.2) is described by:

$$\mathbf{s} \cdot \hat{\mathbf{n}} = d \quad . \tag{5.12}$$

Assuming a constant slip vector over a region of interest, several measurements can be combined along strike, which can be written as a linear problem:

$$\hat{\mathbf{N}} \cdot \mathbf{s} = \mathbf{d} \quad , \tag{5.13}$$

$$\hat{\mathbf{N}} = \begin{pmatrix} n_{x,1} & n_{y,1} & n_{z,1} \\ n_{x,2} & n_{y,2} & n_{z,2} \\ \vdots & \vdots & \vdots \\ n_{x,m} & n_{y,m} & n_{z,m} \end{pmatrix}, \quad \mathbf{s} = \begin{pmatrix} s_x \\ s_y \\ s_z \end{pmatrix}, \quad \mathbf{d} = \begin{pmatrix} d_1 \\ d_2 \\ \vdots \\ d_m \end{pmatrix}, \tag{5.14}$$

where m is the number of observations. Provided the problem is well constrained (see below), this can be solved by least squares minimisation. Generally each observation will have an associated uncertainty, which can be incorporated using weighted least squares. Thus we have a mathematical formalism to resolve the full three dimensional slip-vector by combining along strike measurements.

5.4.2 Validity & Geometric Interpretation

Each row of Equation 5.13 represents a single observation, independent of the measurement location – a hangingwall plane displaced by $d\hat{\mathbf{n}}$ from the footwall. A point from the footwall plane translated by the slip-vector ($\mathbf{s}$) must lie in that hangingwall plane. Introducing a second observation ($d_i\hat{\mathbf{n}}_i$ from a common origin), the end of the slip-vector must lie along the line of intersection between the two hangingwall planes; with a third observation, the slip-vector is uniquely constrained.

Thus, the problem is equivalent to solving for the intersection between all of the hangingwall planes superimposed, where each plane is displaced from the origin by $(\mathbf{s}\cdot\hat{\mathbf{n}}_i)\hat{\mathbf{n}}_i$ (Figure 5.8A). For Equation 5.13

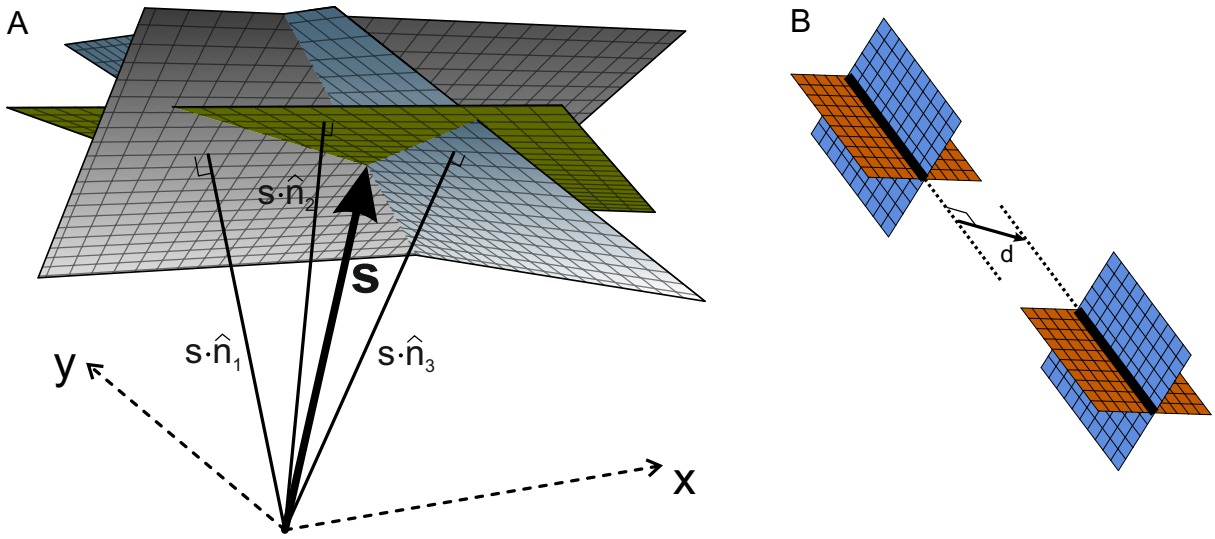


Figure 5.8: (A) Solving for the 3D slip vector is equivalent to finding the intersection between a collection of planes. Each plane represents the hangingwall plane displaced from the origin by $(\mathbf{s} \cdot \hat{\mathbf{n}}_i)\hat{\mathbf{n}}_\mathbf{i}$, i.e. each plane actually represents one pair of planes describing an offset planar feature. (B) The intersection of two planes is a line, which can be displaced by some amount d (orthogonal to the line). Thus a line feature can be incorporated under Equation 5.13 as two planes intersecting along the line. In many cases, this can give a less subjective characterisation of a linear feature than other methods relying on a user picking points on the line.

to have a unique solution, there must be at least three independent rows in the matrix $\hat{\mathbf{N}}$. Thus, there must be significant geometric variation between the measurements, i.e. at least three different slope aspects and/or dips. If all of the observation planes are parallel, the problem is completely unconstrained as the planes will not intersect. Similarly, if all the observed planes share an axis (or equivalently their normals all lie within a single plane), then the slip-vector is only constrained to lie on that axis.

In §5.3, we showed that changing various geometric parameters results in different apparent vertical separations, confounding slip estimates – this same variation is necessary for solving for the slip-vector in 3D. In areas with very shallow slope angles, slope aspects entirely perpendicular to fault strike or steep fault dips and no lateral slip, the problem will likely be under-determined. In these cases, with additional assumptions, or geometric knowledge (e.g. direct measurement of fault dip), we may still be able to solve a constrained problem as we demonstrate for the Hoshab fault (§5.6).

5.4.3 Line Markers

Alongside planar surfaces, line features such as ridge crests, moraine crests or terrace risers are often displaced by faulting.. These can provide a tighter constraint on the slip vector than a planar surface – they provide information equivalent to two intersecting planar surfaces (Figure 5.8B). As such, a line feature (fully captured in 3D) can be incorporated into the formalism of Equation 5.13 as two rows of $\hat{\mathbf{N}}$, i.e. two planes intersecting along the line of the marker.

For a simple straight line feature, the choice of intersecting plane pairs is arbitrary. Two parallel lines must lie within a plane—in the following case studies, we choose the first pair of planes such that

the line feature in both the hangingwall and footwall lies within the same plane, i.e. two planes with an separation of zero. The second pair of planes is then perpendicular to the first, with the maximum orthogonal separation. Incidentally however, many anthropogenic or geomorphic line markers may often be better defined by the intersection of two planes on either side than as a line directly, as this is is less sensitive to erosion/modification (e.g. Ridge crests or curb-stone crests).

As a 3D line marker provides a tighter constraint than a planar marker, only one more offset feature is required to fully constrain the slip vector, provided that it is not a plane in which the line marker lies. Importantly though, a single line feature still does not constrain any component of slip along the line itself. Knowing the precise orientation of the fault plane can provide this third constraint as the slip vector must lie in the fault plane ($\mathbf{s} \cdot \hat{\mathbf{f}} = 0$, for fault plane unit normal $\hat{\mathbf{f}}$).

5.5 3D Example – El-Mayor Cucapah

The scarps on the Borrego Fault from the 4th April 2010 El-Mayor Cucapah earthquake provide an excellent test case for the methods described above and verify the method as a means of assessing palaeoearthquake scarps. *Gold et al.* (2013) studied the Borrego Fault using terrestrial laser scans of two ~200 m sections of the fault cutting a variety of different terrain geometries, and make very precise slip measurements throughout. We used the same terrestrial lidar data available through OpenTopography (http://dx.doi.org/10.5069/G9B85622, http://dx.doi.org/10.5069/G96H4FBB) for two of their sites, applying our method directly to the bare-earth pointcloud. We attempt to measure an average slip vector on this stretch of the fault, with the assumption that it remains approximately constant. This is an inherently different approach to *Gold et al.* (2013), who looked for the change in slip across the sites, but we expect to measure similar slip to their average.

Using the KeckCAVES open-source virtual reality software, LidarViewer (*Kreylos et al.*, 2013), we selected sets of points on the raw pointcloud in 3D, from correlated, approximately planar geomorphic surfaces in the footwall and hangingwall (Figure 5.9A). We then fit parallel planes to each correlative pair of point sets, and determine the orthogonal distance between them. We discard pairs for which a parallel model does not give a good fit, i.e. apparently correlative surfaces with different attitude in the hangingwall and footwall. The varied slope angle and aspect along strike provide sufficient independent rows of $\hat{\mathbf{N}}$, so we solved for the slip vector $\mathbf{s}$ with a simple least squares fit. MATLAB script used to fit parallel planes and solve for the slip vector is provided in Appendix B.2. We find a vertical slip (throw) of 1.56±0.02 m, lateral slip of 1.9±0.3 m and fault perpendicular horizontal component (heave) of 0.8±0.2 m. The errors quoted are the statistical error on the mean; the individual measurements vary by much more, but this represents the error in mean estimated from all the observations together. This captures the aleatoric uncertainties, and highlights those components well or poorly constrained, but does not account for any epistemic uncertainty.

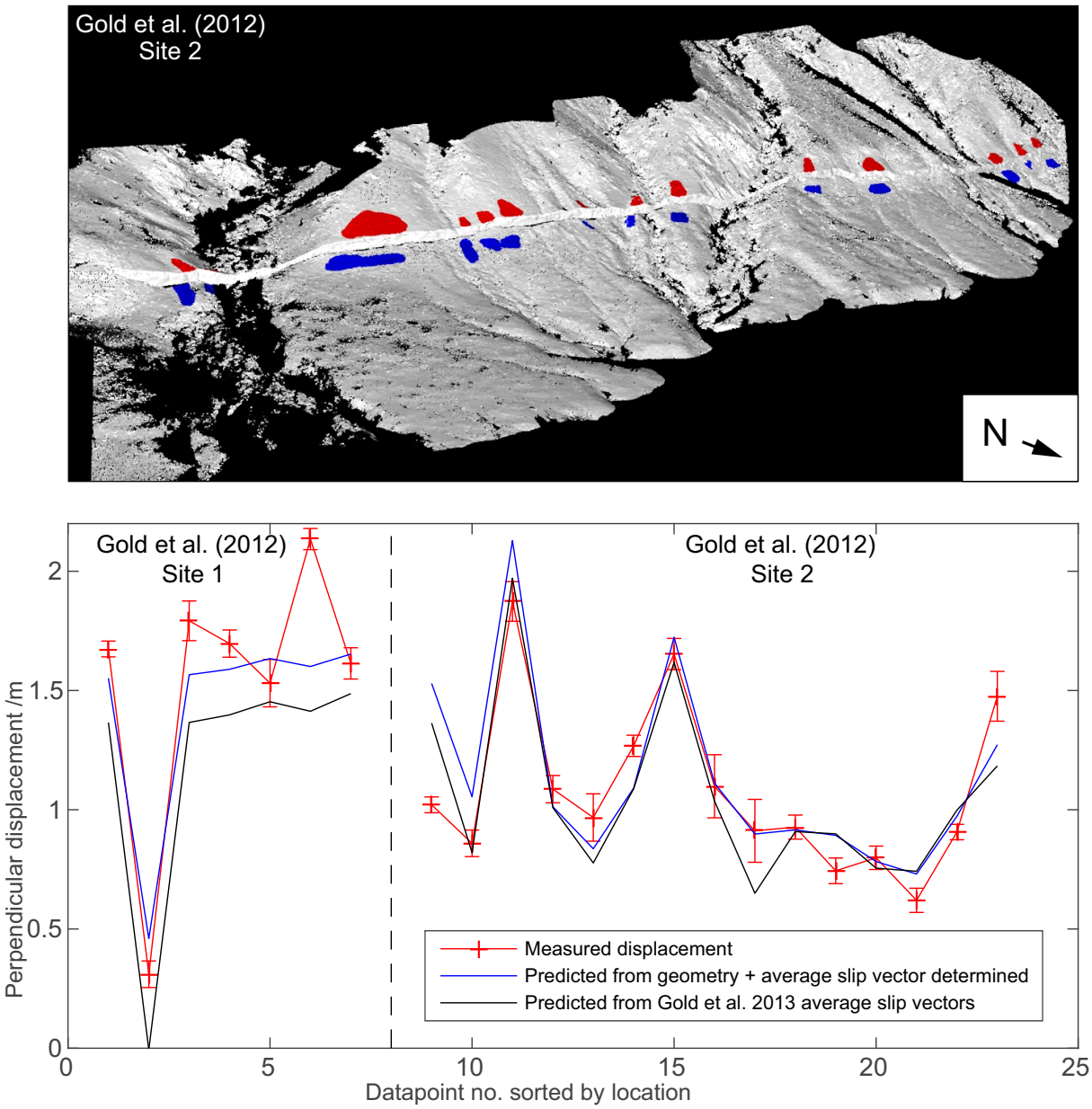


Figure 5.9: (top) Perspective view of the Site 2 terrestrial lidar dataset of *Gold et al.* (2013) generated in LidarViewer, showing the points selected for fitting planes. Footwall selections are red, hangingwall selections are blue. (bottom) Comparison of our measured perpendicular displacements to those predicted by our average slip vector and the average slip vectors of *Gold et al.* (2013), for both site 1 and site 2. The data points have been sorted by location along strike, but the x-axis is arbitrary.

Figure 5.9B shows a plot of the surface-orthogonal separations measured (red), and those predicted (blue) for the best-fit slipvector applied to the surface orientation at each location. Though the data is noisy, the model provides a reasonable fit, with an rms misfit of 20 cm. The black line shows the expected separations based on the average slip vector for each section measured by *Gold et al.* (2013) (Site 1: Vertical 1.4 m, Lateral 2.5 m, Site 2: Vertical 1.2 m, Lateral 2.1 m), giving a larger rms misfit of 25 cm .

Examining the variance of our three slip vector components, we find the vertical component very well

constrained and in agreement with the previous estimate at the 2σ level. The lateral and extensional components are more poorly constrained but differ from those estimated by *Gold et al.* (2013) at the 3σ level, with less lateral motion but a larger heave.

In particular, the main difference in fit between the prior slip vector and our estimate occurs at Site 1, where there was significant scarp collapse and secondary faulting in the hangingwall. The average slip vector of *Gold et al.* (2013) suggests a consistently smaller separation than we measure, likely arising from the wavelength of the problem. Projection of channel thalwegs etc. to the fault plane measures the offsets at ∼10s cm away from the fault, whereas our estimate measures the offset of surfaces 1–10 m from the fault plane, capturing any distributed slip in the region closest to the fault.

A further reason for the discrepancy may be the absence of a measurement of the extensional component (heave) by *Gold et al.* (2013) who project linear features on either side of the fault to the exposed near-vertical footwall fault plane. This approach assumes a slip vector in the near surface fault plane. Along the rupture itself, fissures of up to ∼30 cm were observed, so significant extension did occur and the free face at the surface does not necessarily reflect the fault plane on which slip occurred. Therefore, in projecting non-fault-orthogonal linear features (channel thalwegs etc.) across the fissure to the scarp-face plane, some of the heave can contaminate the apparent lateral and dip-slip measurements (Figure 5.1C).

5.6 3D Example – Hoshab Fault, Pakistan

For the site on the Hoshab fault described in §5.3.3 (Figure 5.7A), we can carry out a similar analysis, demonstrating the solution to the constrained problem with a known fault dip. Previous studies estimated a fault dip of 50–70° on this stretch of the fault (*Barnhart et al.*, 2014; *Zhou et al.*, 2016), so we assume a dip of 60° to demonstrate the method.

The geometric interpretation of the known dip case is very similar to that of the full 3D case; the fault plane itself forms an extra plane in which the slip vector must lie – we can therefore project each observation plane to the fault plane. Each hangingwall plane is displaced from the footwall plane by $d\hat{\mathbf{n}}$, and intersects with the fault plane along a line (Figure 5.10A). Figure 5.10B shows the intersection lines of each hangingwall and footwall surface, in fault geometry and in their correct spatial locations. Shifting each pair to a common origin (Figure 5.10C), the slip vector is measured from the origin to the intersection point, in analogy to the 3D case in Figure 5.8A. Solving for the best fit slip vector required to give the observed separations is therefore equivalent to finding the intersection between the projected lines. We solve for the intersection under Equation 5.13 using weighted least squares, requiring the slip vector $\mathbf{s}$ to lie in the fault plane ($\hat{\mathbf{f}}$), by setting $\hat{\mathbf{f}} \cdot \mathbf{s} = 0$ with a large weight (though a dip uncertainty could be used to weight the constraint relative to the observations).

At the site on the Hoshab fault (see §5.3.3), we consider three markers; two pairs of parallel planes measuring the separation of the slopes at P1 and P2 and the displaced channel which forms a line feature

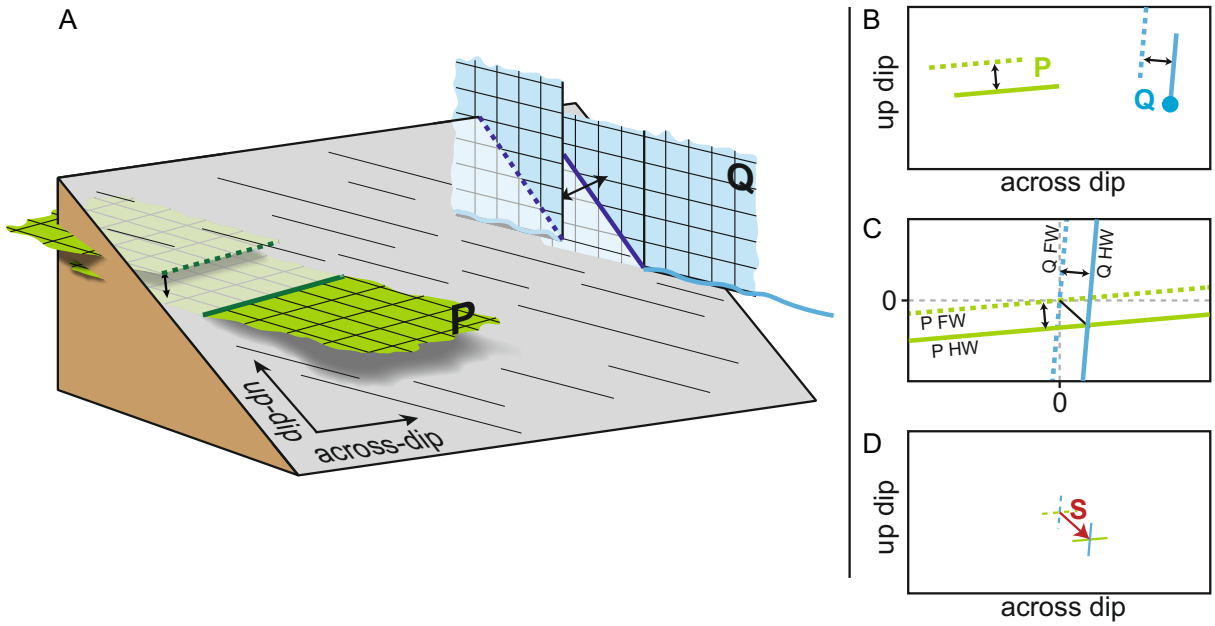


Figure 5.10: (A) Illustrative diagram of the geometry for projecting two planar surfaces onto the fault plane. P illustrates a topographic surface, while Q represents a vertical plane through a river channel (river shown as blue line). Black arrows mark the plane perpendicular separations. (B) Fault plane view, of each of the two intersection lines (footwall is dashed, FW), with each plane separation in the correct spatial location. (C) The intersections are shifted to a common origin in the footwalls. (D) The slip vector is then the distance between the footwall intersection point (the origin) and the intersection of the hangingwall lines.

(Figure 5.7A). At profiles P1 and P2, we select sets of points from the raw pointcloud in the hangingwall and footwall of the correlated alluvial fan surface (yellow and orange polygons respectively, Figure 5.7A), fitting parallel planes through the points. We fit parallel lines to points picked in the river channel from which the lateral offset is estimated by *Zhou et al.* (2015a). The river channel has incised since the abandonment of the P1/P2 fan surface, so the vertical offset in the channel only represents slip in the most recent event. However, the position provides a measure of horizontal slip as the river channel location was "locked in" after the abandonment of the fan surface. We therefore represent the channel thalweg as a pair of vertical planes in the hangingwall and footwall (assuming the river has not migrated laterally since the abandonment of the fan surface). The river therefore constrains a single component of offset (one row of **N**). If each surface/line for each observation pair is fitted independently, the slope-normals change by less than 2° justifying the use of parallel planar markers in all three cases.

We project each marker to the fault plane (Figure 5.11), and solve for the slip vector using a weighted least squares fit (weighted by plane separation uncertainties), estimating a lateral slip of 39±4 m and 14.2±2.0 m of up-dip slip (12.3±1.7 m Throw). This throw matches our earlier best estimates from the two profiles at the 1σ level (§5.3.3). Incorporating the assumed fault dip, this gives a ratio of lateral to vertical slip of 3.1±0.6 (or equivalently 2.7±0.5 strike-slip to dip-slip), significantly lower than that estimated by *Zhou et al.* (2015a) and that of the most recent event *Barnhart et al.* (2014); *Gold et al.* (2015); *Zhou et al.* (2015a).

Thus, the extra constraint of the fault geometry can give a tightly constrained slip vector with fewer

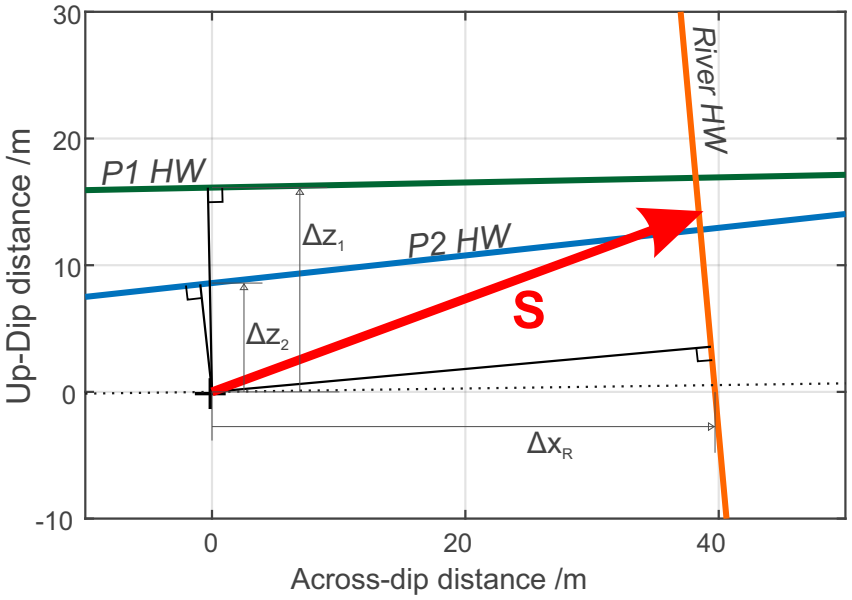


Figure 5.11: A fault plane normal view of intersection lines. The slip vector is fit to the two planes associated with profiles P1 (blue) and P2 (brown) and the vertical plane (orange) through the river channel at the site on the Hoshab Fault (locations in Figure 5.7), weighted by the errors in the separation measurements. Each line represents a hangingwall-plane – fault-plane intersection line in fault geometry. The dashed line indicates the second plane defining the displaced river channel, which was excluded from slip solution as the channel only records the most recent event in the vertical. Δx_R represents the lateral separation in the river channel. Δz_1 and Δz_2 represent the vertical separation that would be measured by a profile at P1 and P2.

observations necessary compared to the unconstrained case. However, given that we only have three observations, the uncertainty is not well constrained. We also note that the slip estimate is quite strongly dependent on the fault dip – we have chosen a fixed dip of 60° to demonstrate the dip-constrained method, but allowing a range of dips would increase the uncertainty.

5.7 Discussion & Implications

Salisbury et al. (2015) discuss the influence of operator decisions on the measurement of offsets on strike-slip faults concluding that discrepancies generally arise from misinterpretation of the feature and its pre-event geometry. They also find that standardising remote measurement methods is crucial in obtaining useful and repeatable offset measurements. In this paper we have provided solutions to standardise two elements of fault offset measurement: the rigorous characterisation of errors in 2D profiles, and a method to characterise fault slip in the case of non-optimal slope geometry and/or oblique slip when the assumptions are violated for conventional methods. Both approaches still require the user to identify correlated surfaces on either side of the fault scarp, but we hope that they provide a framework under which measurements can be standardised.

5.7.1 A 3D Framework

In cases where profiles do not perform well, measurements have generally been very limited. In some cases, with very fresh ruptures, distinct point-to-point vector displacements can be measured (e.g. *Treiman*, 2002), or where the entire geometry is well constrained, features may be projected appropriately to estimate offsets (e.g. *Gold et al.*, 2013). In an increasing number of cases, the full topography field is available both pre-event and post event, allowing the measurement of the full surface displacement field (*Borsa and Minster*, 2012; *Nissen et al.*, 2012, 2014; *Glennie et al.*, 2014; *Zhou et al.*, 2015b).

We suggest an alternative to profiles or planform-projection for measuring discrete fault offsets at the surface. Combining multiple measurements along strike (without reference to their individual locations), we can solve for the best fit slip-vector to give these separations, based on an assumption of constant slip over the region of interest. Such a method can be used over regions in which it is reasonable to assume an approximately constant slip vector, such as individual gullies, ridge crests, or anthropogenic buildings, roads and curbs. Using multiple planes to represent offset linear markers permits constraint by more sample points and will often be a better representation of the marker; for example discrepancies among measurements of an offset curbline in the 2014 South Napa earthquake (*Morelan*, 2015) could be mitigated by capturing the line as the intersection between the planes on either side.

The El-Mayor Cucapah earthquake scarps on the Borrego fault provide a case study demonstrating the utility of combining multiple offset planes to estimate an average slip vector in contrast to using individual line markers. However, even in this case of relatively varied and steep topography, we note large errors on two components of the slip, suggesting that the unconstrained problem may often be poorly resolved. It may therefore often be more appropriate to use a constrained form to characterise fault slip with some prior geometric constraints, as demonstrated by the Balochistan ruptures example (§5.6). The formalism described here is a mathematically rigorous framework under which the constrained problem is a special case.

5.7.2 Profiles and Planform-projection

A detailed understanding of the 3D surface geometry highlights a number of common pitfalls associated with landform offset measurement. We have shown that in the case of relatively simple geometries, the common assumptions hold well. For dip-slip faults of known dip and surfaces which have fault-perpendicular aspect, 2D topographic profiles provide an easy and accurate method by which to estimate fault throw. Similarly, for pure strike-slip faults planform-projection of linear markers can provide an excellent measure of fault slip. Numerous previous studies have used these methods to good effect, using careful selection parameters to choose sites with good geomorphic preservation and simple geometries (*Scharer et al.*, 2014). Where the assumptions hold, profiles and planform-projection can give a good estimate of fault displacement, justifying their continued use provided that the assumptions and limitations

are recognised.

In general however, profile surveys do not characterise the errors associated with these assumptions. We provide a best-practice recommendation for rigorously characterising fault slip and associated uncertainties using a Monte-Carlo simulation method. Using analytical geometric relations a probability distribution function (PDF) can be generated for the component of fault slip based on the uncertainties in all the geometric parameters. Previous studies (e.g. *Baljinnyam et al.*, 1993; *Thompson et al.*, 2002) performed this analysis in an inherently 2D framework, but our sensitivity tests show that incorporating uncertainty in the full 3D geometry is also important. The resultant fault displacement PDFs will generally be asymmetric, so uncertainties should generally be reported either as a PDF or a range covering the possible values (or 95% confidence bounds). Use of this Monte-Carlo method will naturally highlight cases where a profile or planform-projection based approach is inappropriate, presenting as large uncertainty (broad PDF), e.g. in cases of non-zero slope aspects ($|\psi| >> 0$) and significant oblique slip ($|S_L/S_D| > 0$).

5.7.3 Measurement of Slip Distributions

Many studies compile offset measurements along strike to estimate a fault slip distribution (e.g. *Haeussler et al.*, 2004; *Klinger et al.*, 2011; *Haddon et al.*, 2016). This treats measured marker offsets as independent proxies to the local fault slip at the surface. Strictly however, any marker only constrains the component of slip in directions perpendicular to the marker (e.g. Figure 5.1A-C). The method we present combines multiple markers to constrain more components of the slip vector but still requires operator judgement in feature selection.

Scharer et al. (2014) and *Salisbury et al.* (2015) discuss the effects of operator biases and experience in the quality of the measurements made. In particular, they found that the quality of the geomorphic reconstruction is often the largest source of uncertainty and introduce a qaulity measure, whereby each observation is assigned a quality rating (1-3, 1 being highest quality). *Salisbury et al.* (2015) note that in general, the more experienced researchers can make more consistent estimates from a given feature, but the preservation and shape of the geomorphic marker itself often limits the reconstruction quality. Thus, both the quality of the reconstruction and the measurement error must be taken into account when comparing landform offset measurements. The methods we describe reduce or characterise the uncertainties associated with the measurement geometry but do not account for uncertainty arising from a poor quality geomorphic markers. In practice, the operator must still identify suitably correlated surfaces on either side of the fault, with the uncertainty that introduces.

Scharer et al. (2014) also note that a significant trade-off exists in building a slip-distribution from multiple observations along strike, between making as many observations as possible and the quality of those observations. Our methods allow the inclusion of sites that would traditionally be excluded due to

poor marker geometry, enabling more measurements along strike. Under this framework, markers that are not fault-perpendicular or slopes that are cut obliquely are incorporated in a mathematically rigorous manner to provide additional constraints on fault slip.

With the availability of high resolution topographic data with point uncertainties of <5-10 cm (e.g. *Gold et al.*, 2013), the formal measurement uncertainties are typically very low (often <10 cm), excluding any errors due to the geometric assumptions. However in slip distributions compiled along strike, we typically see much greater variation over short wavelengths (100s m) and it is unclear whether this reflects slip variation or reconstruction quality, measurement errors or geometric errors. Our sensitivity tests show that significant noise can arise from the breaking of the geometric assumptions and therefore be removed by correctly accounting for the geometry. However, noise arising from the marker reconstruction must still be evaluated on a site by site basis (*Scharer et al.*, 2014). Using our methods with careful identification of high quality markers should allow slip variation to be resolved over a variety of length scales.

5.8 Conclusions

The recent explosion in availability of high resolution topography data presents great potential for the measurement of fault slip at the surface. In general, for shallow slope angles and steep fault dips, conventional analysis tools can capture fault offsets accurately. However, with steeper terrain and shallower fault dips, we get significant change in apparent offset as the slope attitude changes – this is worsened by even a small (e.g. 10%) component of oblique slip. The rigorous 3D framework described here can be used to characterise fault slip uncertainties through Monte-Carlo methods, incorporating geometric uncertainty into the resultant slip estimate. A case study for this method on the obliquely slipping Hoshab Fault, Pakistan demonstrates that profile measurements can recover the fault throw well when the slope aspect is fault perpendicular, but give biased estimates when this assumption is violated.

Where the assumptions of conventional profile based methods are violated, we propose to exploit new high-resolution topographic datasets, combining multiple measurements to solve for a 3D slip vector. With 3D marker surfaces (here planar) we use the variation in apparent offset with terrain and measurement geometry to determine the slip vector under a simple linear formulation. We have demonstrated the method in estimating a slip vector from the El-Mayor Cucapah rupture scarps on the Borrego Fault – where we estimate a similar throw to previous authors, but less lateral slip and greater (though poorly constrained) heave. A further example from the Hoshab fault, Pakistan, demonstrates the constrained case where the fault dip is relatively well known. The geomorphic marker surfaces can be projected to the fault plane and an analogous 2D problem solved.

In regions significant topography or oblique slip, 2D-projected measurements will generally give biased estimates of fault slip. In contrast, our inherently three-dimensional approach can resolve the true slip-vector and is enhanced by oblique slip and topographic variation.

Dataset Acknowledgements: The data acquisition and data processing and classification of the Borrego Fault dataset at the UC Davis KeckCAVES was supported by the Southern California Earthquake Center, which is supported by the United States Geological Survey (USGS) and the National Science Foundation (NSF). http://dx.doi.org/10.5069/G96H4FBB and http://dx.doi.org/10.5069/G9B85622. The data acquisition and processing of the Hoshab Fault photogrammetry derived dataset at the University of Oxford was supported by the UK Natural Environment Research Council (NERC) through the Looking Inside the Continents (LiCS) project (NE/K011006/1), and the Centre for the Observation and Modelling of Earthquakes, Volcanoes and Tectonics (COMET, COME30001, http://comet.nerc.ac.uk). We thank Yu Zhou for providing us with the Hoshab Fault dataset (to be made available via OpenTopography shortly) and his aid in examining the Hoshab Fault case study. This material is based on data services provided by the OpenTopography Facility with support from the National Science Foundation under NSF Award Numbers 1226353 & 1225810.

Chapter 6

Concluding Remarks

The aim of this thesis was to better understand the earthquake cycle and the accommodation of tectonic shortening by thick-skinned faulting in the Alpine-Himalayan belt. Although detailed conclusions are given at the end of each chapter, there are a number of recurring themes through the thesis, from which I draw a few further conclusions.

In particular I note the importance of drawing together techniques and approaches from a wide variety of disciplines in order to understand the earthquake cycle and the distribution of faulting within the continents. Chapter 2 combines the power of InSAR and field observations in studying short term postseismic afterslip (days-months), with Quaternary dating, high resolution topography and tectonic geomorphology to study the longer term (1-10s ka) evolution of the fault. Amalgamating these data, I was able to set the recent earthquake in the context of the wider regional faulting and estimate the impact of the 2011 earthquake on future seismic hazard – though the need for palaeoseismic trenching highlights the potential for future studies to take this even further. Similarly in Chapter 3, I combine geomorphic field observations with high and very high resolution topography, regional GPS data and Quaternary dating, not only to demonstrate that the fault must be creeping, but also estimate both a geodetic and a geologic slip-rate and present evidence for episodic evolution of climate in the Tien Shan within the past 100 ka. In Chapter 4 I employ palaeoseismology, Quaternary dating, high resolution topography, field observations, and all the results of Chapter 3 to establish the distribution of deformation within the Kazakh Tien Shan and link it to the crustal and upper mantle geodynamics. Finally, Chapter 5 develops a new method which adds to the toolbox of approaches used in the previous chapters.

The Alpine-Himalayan Belt represents a vast region of distributed continental deformation running the length of stable Eurasia. I have shown that within the two focus areas of thick-skinned faulting, the Turkish–Iranian Plateau and the Tien Shan of Central Asia, a wide variety of regimes are present. In Turkey, I have observed that up-dip segmentation of fault planes can terminate rupture propagation.

Off-fault deformation within the uppermost 10 km of crust has generated short wavelength folding which masks the effect of the deeper structure, and so models of the subsurface built on surficial observations may underestimate the depth extent of seismogenic structures. In the Tien Shan, I have observed two distinct regimes of faulting: a high slip-rate creeping fault at the northern margin accommodates almost half of the shortening across the northern Tien Shan, and the remaining half is distributed across at least 6–8 faults over a width of ∼300 km, with contributions from both E-W thrust faulting and conjugate strike-slip faulting.

However, these studies have also suggested a more precautionary note for palaeoseismology and tectonic geomorphology in low strain rate continental interiors. In Central Asia large (M_W 7–8+) earthquakes are noted in the historic records, but the recurrence intervals for these large but rare events are typically on timescales of >5–10 ka. The environmental preservation is excellent in the dry climate but these recurrence intervals are of a similar order to the timescale of landscape reset, and so many of the scarps preserved only represent the most recent event on the fault – there may also be faults which show minimal expression in Quaternary deposits simply because they have not experienced an earthquake since the last glacial maximum. The Van earthquake (Chapter 2) also highlights the limitations of palaeoseismology in these regions – the M_W 7.2 event did not generate surface ruptures, suggesting that the magnitude threshold for surface scarps is high. Despite the difficulties with palaoeseismology in Central Asia and Turkey, the concept of landscape resetting also raises a more positive point. The observations I have made across the Kazakh Tien Shan suggest are consistent with periods of widespread intense deposition and erosion which have lead to fan and terrace surfaces of common age. These present a powerful tool with which one can sometimes establish the activity or lack thereof, of a fault in the landscape, even when we are unable to find datable deposits suitably offset by faulting; further work is needed to establish a fully rigourous chronology, but our studies suggest great potential.

Another common thread to this thesis is the application of photogrammetry to the study of faulting. I have shown that high resolution digital elevation models (DEMs) can give us new insight into faulting on a wide range of scales. Structure from motion has enabled the measurement of millimetre-scale postseismic offsets, metre scale single event offsets, the generation of fault slip distributions over distances of up to ∼30 km and the generation of accurate palaeoseismic trench orthomosaics. Satellite-stereo photogrammetry extends this even further, enabling mapping terraces and measuring offsets over many 10's km along strike, often reaching locations too difficult and timeconsuming to survey in the field. This toolkit of photogrammetry techniques covers a huge range of scales (mm – 100s km) providing a much lower cost alternative to lidar measurements, revolutionising the study of surface faulting.

To take full advantage of the new high resolution data, I have developed new methods for the characterising of surface slip from elevation models. Using high resolution DEMs, I have assessed the errrors associated with measurement geometry for conventional profile based measurements and suggest a Monte-Carlo simulation based approach to characterising the uncertainties. Though developed in the context of

analysing new high resolution topographic datasets, the mathematical framework is also appropriate to apply to more conventional profile base methods too. In situations where such profiles break down due to geometric complexity, I have developed a method to solve for the full 3D slip vector by combining multiple offset measurements along strike. Testing these methods against datasets from the 2011 El-Mayor Cucapah rupture scarps and cumulative scarps on the Hoshab Fault, Pakistan, demonstrates that the method can retrieve the slip-vector well for faults with oblique slip or cut steep topography.

6.1 Further Work

There are several important lines of further work which arise from this thesis. In both Turkey and Central Asia I have characterised the late Quaternary slip rates numerous faults but there remain many more for which the slip rates are unknown. I only have one estimate of the slip rate for any individual fault. Further work is need to both extend the study to the remaining faults and further geochronology needs to be performed to better constrain the preliminary rates estimated in this thesis. In addition, extensive palaeoseismology is needed to ascertain the earthquake behaviour of many of the faults. At the Van Fault (Chapter 2), palaeoseismology is needed to fully conclude the study of the Van Fault. This could reveal whether the upper segment of the fault has sustained earthquakes in the past and potentially whether it remains a significant seismic hazard following the 2011 earthquake on the lower segment.

The Karkara rangefront epsecially needs significant further investigation. In particular, palaeoseismological trenching and InSAR studies (Chapter 3) could help to reveal whether creep is the long term mechanism for deformation. Regardless of whether creep is the long-term mechanism, if the present fault creep can be resolved further this fault presents an excellent target for understanding the rheology of the crust. It also presents an opportunity to probe the devlopement of mountain ranges; the along-range variation of the upper mantle and crustal geodynamics may allow the investigation of the relationships between surface faulting, crustal deformation and mantle/crustal rheology and dynamics. In addition, if the chronology of the terracing sequence can be improved, and the correlations between sites enhanced by further fieldwork, the flights of river terraces preserved along the KRF hold a potentially important climatic record for the region.

Central Asia especially remains a relatively understudied region tectonically – with low slip rates and long recurrence intervals, seismic hazard is difficult to constrain. The mapping performed during this work has contributed to the COMET (Center for Modelling of Earthquakes and Tectonics) compilation of Active Faults in Central Asia, yet many faults likely remain unmapped and many more poorly understood. The series of large earthquakes at the turn of the 19th/20th century highlights the potential for the faults in this region to generate very large earthquakes. Significant work is still needed to well constrain seismic hazard in the region and given the length of the seismic cycle (>5–10 ka), understanding the Quaternary geomorphological record is vital.

Bibliography

Abdrakhmatov, K., R. J. Weldon, S. C. Thompson, D. W. Burbank, C. Rubin, M. Miller, and P. Molnar (2001), Onset, style and current rate of shortening in the central Tien Shan, Kyrgyz Republic, *Russian Geology and Geophysics*, *42*(10), 1585–1609.

Abdrakhmatov, K., H.-B. Havenith, D. Delvaux, D. Jongmans, and P. Trefois (2003), No Title, *Journal of Seismology*, *7*(2), 203–220, doi:10.1023/A:1023559932255.

Abdrakhmatov, K., R. Walker, G. Campbell, A. Carr, A. Elliott, C. Hillemann, J. Hollingsworth, A. Landgraf, D. Mackenzie, A. Mukambayev, M. Rizza, and R. Sloan (2016), Multi-segment rupture in the July 11th 1889 Chilik earthquake (Mw 8.0-8.3), Kazakh Tien Shan, interpreted from remote-sensing, field survey, and palaeoseismic trenching, *Journal of Geophysical Research: Solid Earth*, doi:10.1002/2015JB012763.

Abdrakhmatov, K. E., K. D. Djanuzakov, and D. Delvaux (2002), *Active Tectonics and Seismic Hazard of the Issyk-Kul Basin in the Kyrgyz Tian-Shan*, pp. 147–160, Springer Netherlands, Dordrecht, doi:10.1007/978-94-010-0491-6_11.

Abdrakhmatov, K. Y., S. A. Aldazhanov, B. H. Hager;, M. W. Hamburger, T. A. Herring, K. B. Kalabaev, V. I. Makarov, and P. Molnar (1996), Relatively recent construction of the Tien Shan inferred from GPS measurements of present-day crustal deformation rates, *Letters to Nature*, *384*.

Acarel, D., F. Bulut, M. Bohnhoff, and R. Kartal (2014), Coseismic velocity change associated with the 2011 Van earthquake (M7.1): Crustal response to a major event, *Geophysical Research Letters*, *41*(13), 4519–4526, doi:10.1002/2014GL060624.

Adamiec, G., and M. J. Aitken (1998), Dose-rate conversion factor: update, *Ancient TL*, *16*(2), 37–50.

Aitken, M. J. (1985), *Thermoluminescence dating*, Academic Press.

Akinci, A., and A. Antonioli (2013), Observations and stochastic modelling of strong ground motions for the 2011 October 23 Mw 7.1 Van, Turkey, earthquake, *Geophysical Journal International*, *192*(3), 1217–1239, doi:10.1093/gji/ggs075.

Alinaghi, A., and F. Krüger (2014), Seismic array analysis and redetermination of depths of earthquakes in Tien-Shan: Implications for strength of the crust and lithosphere, *Geophysical Journal International*, *198*(2), 1111–1129, doi:10.1093/gji/ggu141.

Allen, M. B., and H. A. Armstrong (2008), Arabia-Eurasia collision and the forcing of mid-Cenozoic global cooling, *Palaeogeography, Palaeoclimatology, Palaeoecology*, *265*, 52–58, doi:10.1016/j.palaeo.2008.04.021.

Allen, M. B., S. J. Vincent, and P. J. Wheeler (1999), Late Cenozoic tectonics of the Kepingtage thrust zone: Interactions of the Tien Shan and Tarim Basin, northwest China, *Tectonics*, *18*(4), 639, doi:10.1029/1999TC900019.

Altiner, Y., W. Söhne, C. Güney, J. Perlt, R. Wang, and M. Muzli (2013), A geodetic study of the 23 October 2011 Van, Turkey earthquake, *Tectonophysics*, *588*(2013), 118–134, doi:10.1016/j.tecto.2012.12.005.

Altinli, I. E. (1966), Geology of eastern and southeastern Anatolia, *Bulletin of the Mineral Research and Exploration of Turkey*, *66*, 35–75.

Ambraseys, N., and C. P. Melville (1982), *A History of Persian Earthquakes*, 236 pp., Cambridge University Press, Cambridge/GB.

Ambraseys, N. N. (1989), Temporary seismic quiescence: SE Turkey, *Geophysical Journal International*, *96*(2), 311–331, doi:10.1111/j.1365-246X.1989.tb04453.x.

Amos, C. B., K. I. Kelson, D. H. Rood, D. T. Simpson, and R. S. Rose (2010), Late Quaternary slip rate on the Kern Canyon fault at Soda Spring, Tulare County, California, *Lithosphere*, *2*, 411–417, doi:10.1130/L100.1.

Arrowsmith, J. R., and M. R. Strecker (1999), Seismotectonic range-front segmentation and mountain-belt growth in the Pamir-Alai region , Kyrgyzstan (India-Eurasia collision zone), *Geological Society of America*, *111*(11), 1665–1683, doi:10.1130/0016-7606(1999)111<1665.

Arrowsmith, J. R., C. J. Crosby, A. M. Korzhenkov, E. Mamyrov, I. Povolotskaya, B. Guralnik, and A. Landgraf (2016), Surface rupture of the 1911 Kebin (Chon–Kemin) earthquake, Northern Tien Shan, Kyrgyzstan, *Geological Society, London, Special Publications*, doi:10.1144/SP432.10.

Avouac, J.-P. (1993), Analysis of scarp profiles: Evaluation of errors in morphologic dating, *Journal of Geophysical Research*, *98*(B4), 6745, doi:10.1029/92JB01962.

Avouac, J.-P. (2015), From Geodetic Imaging of Seismic and Aseismic Fault Slip to Dynamic Modeling of the Seismic Cycle, *Annual Review of Earth and Planetary Sciences*, *43*(1), 233–271, doi:10.1146/annurev-earth-060614-105302.

Avouac, J.-P., and G. Peltzer (1993), Active tectonics in southern Xinjiang, China: Analysis of terrace riser and normal fault scarp degradation along the Hotan-Qira Fault System, *Journal of Geophysical Research*, *98*(B12), 773–807, doi:10.1029/93JB02172.

Avouac, J.-P., and P. Tapponnier (1993), Kinematic model of active deformation in central Asia, *Geophysical Research Letters*, *20*(10), 895–898.

Avouac, J. P., F. Ayoub, S. Wei, J. P. Ampuero, L. Meng, S. Leprince, R. Jolivet, Z. Duputel, and D. Helmberger (2014), The 2013, Mw 7.7 Balochistan earthquake, energetic strike-slip reactivation of a thrust fault, *Earth and Planetary Science Letters*, *391*, 128–134, doi:10.1016/j.epsl.2014.01.036.

Avouac, J.-P., L. Meng, S. Wei, T. Wang, and J.-P. Ampuero (2015), Lower edge of locked Main Himalayan Thrust unzipped by the 2015 Gorkha earthquake, *Nature Geoscience*, *8*(9), 708–711, doi:10.1038/ngeo2518.

Balescu, S., and M. Lamothe (1994), Comparison of TL and IRSL age estimates of feldspar coarse grains from waterlain sediments, *Quaternary Science Reviews*, *13*(5), 437–444, doi:10.1016/0277-3791(94)90056-6.

Baljinnyam, I., A. Bayasgalan, B. A. Borisov, A. Cisternas, M. G. Dem'yanovich, L. Ganbaatar, V. M. Kochetkov, R. A. Kurushin, P. Molnar, H. Philip, and Y. Y. Vashchilov (1993), *Ruptures of Major Earthquakes and Active Deformation in Mongolia and Its Surroundings*, 1–60 pp., doi:10.1130/MEM181-p1.

Balmino, G., N. Vales, S. Bonvalot, and A. Briais (2012), Spherical harmonic modelling to ultra-high degree of Bouguer and isostatic anomalies, *Journal of Geodesy*, *86*(7), 499–520, doi:10.1007/s00190-011-0533-4.

Banerjee, D., and A. Murray (2001), Equivalent dose estimation using a single aliquot of polymineral fine grains, *Radiation Measurements*, *33*, 73–94.

Barnhart, W. D., G. P. Hayes, R. W. Briggs, R. D. Gold, and R. Bilham (2014), Ball-and-socket tectonic rotation during the 2013 Mw7.7 Balochistan earthquake, doi:10.1016/j.epsl.2014.07.001.

Bemis, S. P., S. Micklethwaite, D. Turner, M. R. James, S. Akciz, S. T. Thiele, and H. Ali (2014), Ground-based and UAV-Based photogrammetry: A multi-scale, high-resolution mapping tool for structural geology and paleoseismology, *Journal of Structural Geology*, *69*, 163–178, doi:10.1016/j.jsg.2014.10.007.

Benedetti, L., R. Finkel, G. King, R. Armijo, D. Papanastassiou, F. J. Ryerson, F. Flerit, D. Farber, and G. Stavrakakis (2003), Motion on the Kaparelli fault (Greece) prior to the 1981 earthquake sequence determined from 36Cl cosmogenic dating, *Terra Nova*, *15*(2), 118–124, doi:10.1046/j.1365-3121.2003.00474.x.

Bilham, R. (2009), The seismic future of cities, *Bulletin of Earthquake Engineering*, *7*(4), 839–887, doi:10.1007/s10518-009-9147-0.

Bilham, R. (2013), Societal and observational problems in earthquake risk assessments and their delivery to those most at risk, *Tectonophysics*, *584*, 166–173, doi:10.1016/j.tecto.2012.03.023.

Bindi, D., K. Abdrakhmatov, S. Parolai, M. Mucciarelli, G. Grünthal, A. Ischuk, N. Mikhailova, and J. Zschau (2012), Seismic hazard assessment in Central Asia: Outcomes from a site approach, *Soil Dynamics and Earthquake Engineering*, *37*, 84–91, doi:10.1016/j.soildyn.2012.01.016.

Bindi, D., A. A. G. Capera, S. Parolai, K. Abdrakhmatov, M. Stucchi, and J. Zschau (2013), Location and magnitudes of earthquakes in Central Asia from seismic intensity data: model calibration and validation, *Geophysical Journal International*, *192*(2), 710–724, doi:10.1093/gji/ggs039.

Bird, P. (2003), An updated digital model of plate boundaries, *Geochemistry, Geophysics, Geosystems*, *4*(3), doi:10.1029/2001GC000252.

Birkeland, P. W. (1984), *Soils and geomorphology.*, Oxford University Press.

Bogdanovitch, K. I., I. M. Kark, B. Y. Korolkov, and D. I. Mushketov (1914), Earthquake in Northern district of Tien-Shan, 22 December 1910 (4 January 1911), *Commission of the Geology Committee, Leningrad (256 pp., in Russian).*

Booker, J. R. (1974), Time dependent strain following faulting of a porous medium, *Journal of Geophysical Research*, *79*(14), 2037–2044, doi:10.1029/JB079i014p02037.

Borsa, A., and J.-B. Minster (2012), Rapid Determination of Near-Fault Earthquake Deformation Using Differential LiDAR, *Bulletin of the Seismological Society of America*, *102*(4), 1335–1347, doi:10.1785/0120110159.

Bøtter-Jensen, L. (1997), Luminescence techniques: instrumentation and methods, *Radiation Measurements*, *27*(5), 749–768, doi:10.1016/S1350-4487(97)00206-0.

Bøtter-Jensen, L., E. Bulur, G. A. T. Duller, and A. S. Murray (2000), Advances in luminescence instrument systems, *Radiation Measurements*, *32*, 523–528, doi:10.1016/S1350-4487(00)00039-1.

Bowman, D., A. Korjenkov, N. Porat, and B. Czassny (2004), Morphological response to Quaternary deformation at an intermontane basin piedmont, the northern Tien Shan, Kyrghyzstan, *Geomorphology*, *63*(1-2), doi:10.1016/j.geomorph.2004.03.007.

Brocher, T. M., A. S. Baltay, J. L. Hardebeck, F. Pollitz, J. R. Murray, A. L. Llenos, D. P. Schwartz, J. L. Blair, D. J. Ponti, J. J. Lienkaemper, E. Victoria, T. E. Dawson, K. W. Hudnut, D. R. Shelly, D. S. Dreger, J. Boatwright, B. T. Aagaard, D. J. Wald, R. M. Allen, W. D. Barnhart, K. L. Knudsen, B. A. Brooks, and K. M. Scharer (2015), The Mw 6.0 24 August 2014 South Napa Earthquake, *Seismological Research Letters*, *86*(2A), 309–326, doi:10.1785/0220150004.

Bronk Ramsey, C. (2009), Bayesian Analysis of Radiocarbon Dates, *Radiocarbon*, *51*(1), 337–360, doi:10.2458/azu_js_rc.v51i1.3494.

Bullen, M., and D. Burbank (2001), Late Cenozoic tectonic evolution of the northwestern Tien Shan: New age estimates for the initiation of mountain building, *Geological Society of America Bulletin*, *113*(12), 1544–1559, doi:10.1130/0016-7606.

Burbank, McLean, Bullen, Abdrakhmatov, and Miller (1999), Partitioning of intermontane basins by thrust-related folding, Tien Shan, Kyrgyzstan, *Basin Research*, *11*(1), 75–92, doi:10.1046/j.1365-2117.1999.00086.x.

Burbank, D. W., and R. S. Anderson (2011), *Tectonic Geomorphology*, John Wiley & Sons, Ltd, Chichester, UK, doi:10.1002/9781444345063.

Burchfiel, B. C., E. T. Brown, D. Qidong, F. Xianyue, L. Jun, P. Molnar, S. Jianbang, W. Zhangming, and Y. Huichuan (1999), Crustal Shortening on the Margins of the Tien Shan, Xinjiang, China, *International Geology Review*, *41*(January), 665–700, doi:10.1080/00206819909465164.

Bürgmann, R., and G. Dresen (2008), Rheology of the Lower Crust and Upper Mantle: Evidence from Rock Mechanics, Geodesy, and Field Observations, *Annual Review of Earth and Planetary Sciences*, *36*(1), 531–567, doi:10.1146/annurev.earth.36.031207.124326.

Burgmann, R., D. Schmidt, R. M. Nadeau, M. D'Alessio, E. Fielding, D. Manaker, T. V. McEvilly, and M. H. Murray (2000), Earthquake Potential Along the Northern Hayward Fault, California, *Science*, *289*(5482), 1178–1182, doi:10.1126/science.289.5482.1178.

Burov, E., M. G. Kogan, H. Lyop-Caen, and P. Molnar (1990), Gravity anomalies , the deep structure , and dynamic processes beneath the Tien Shan, *Earth and Planetary Science Letters*, *96*, 367–383.

Burov, E. B., A. B. Watts, and Others (2006), The long-term strength of continental lithosphere:" jelly sandwich" or "crème brûlée"?, *GSA today*, *16*(1), 4, doi:0.1130/1052-5173(2006)016<4:TLTSOC>2.0.CO;2.

Burtman, V. S. (1975), Structural geology of variscan Tien Shan, USSR, *American Journal of Science*, *275-A*, 157–186.

Burtman, V. S., S. F. Skobelev, and P. Molnar (1996), Late Cenozoic slip on the Talas-Ferghana fault, the Tien Shan, central Asia, *Geological Society of America Bulletin*, *108*(8), 1004–1021, doi:10.1130/0016-7606(1996)108<1004:LCSOTT>2.3.CO;2.

Buylaert, J., A. Murray, K. Thomsen, and M. Jain (2009), Testing the potential of an elevated temperature IRSL signal from K-feldspar, *Radiation Measurements*, *44*(5-6), 560–565, doi:10.1016/j.radmeas.2009.02.007.

Campbell, G. (2015), Active Tectonics of the Tien Shan, Central Asia, Ph.D. thesis, University of Cambridge.

Campbell, G. E., R. T. Walker, K. Abdrakhmatov, J. Schwenninger, J. Jackson, J. R. Elliott, and A. Copley (2013), The Dzhungarian fault: Late Quaternary tectonics and slip rate of a major right-lateral strike-slip fault in the northern Tien Shan region, *Journal of Geophysical Research: Solid Earth*, *118*, 5681–5698, doi:10.1002/jgrb.50367.

Campbell, G. E., R. T. Walker, K. Abdrakhmatov, J. Jackson, J. R. Elliott, D. Mackenzie, T. Middleton, and J.-L. Schwenninger (2015), Great earthquakes in low strain rate continental interiors: An example from SE Kazakhstan, *Journal of Geophysical Research: Solid Earth*, *120*(8), 5507–5534, doi:10.1002/2015JB011925.

Carpenter, B. M., C. Marone, and D. M. Saffer (2011), Weakness of the San Andreas Fault revealed by samples from the active fault zone, *Nature Geoscience*, *4*(4), 251–254, doi:10.1038/ngeo1089.

Carretier, S., J. F. Ritz, J. Jackson, and A. Bayasgalan (2002), Morphological dating of cumulative reverse fault scarps: Examples from the Gurvan Bogd fault system, Mongolia, *Geophysical Journal International*, *148*(2), 256–277, doi:10.1046/j.1365-246X.2002.01599.x.

Carson, E., C. Grützner, D. Mackenzie, R. Walker, A. Mukambayev, A. Moldobaev, and K. Abdrakhmatov (2015), Large thrust faulting earthquakes in Eastern Kazakhstan – first results from paleoseismic trenching, in *6th International INQUA Meeting on Paleoseismology, Active Tectonics and Archaeoseismology*, April, pp. 75–78.

Center for International Earth Science Information Network (CIESIN) (2016), *Gridded Population of the World, Version 4 (GPWv4): Population Density*, NASA Socioeconomic Data and Applications Center (SEDAC), Columbia University, Palisades, NY, doi:10.7927/H46T0JKB.

Charreau, J., Y. Chen, S. Gilder, S. Dominguez, J. P. Avouac, S. Sen, D. Sun, Y. Li, and W. M. Wang (2005), Magnetostratigraphy and rock magnetism of the Neogene Kuitun He section (northwest China): Implications for Late Cenozoic uplift of the Tianshan mountains, *Earth and Planetary Science Letters*, *230*(1-2), 177–192, doi:10.1016/j.epsl.2004.11.002.

Charreau, J., J. P. Avouac, Y. Chen, S. Dominguez, and S. Gilder (2008), Miocene to present kinematics of fault-bend folding across the Huerguosi anticline, northern Tianshan (China), derived from structural, seismic, and magnetostratigraphic data, *Geology*, *36*(11), 871–874, doi:10.1130/G25073A.1.

Cherie, S. G., S. S. Gao, K. H. Liu, A. A. Elsheikh, F. Kong, C. A. Reed, and B. B. Yang (2016), Shear wave splitting analyses in Tian Shan: Geodynamic implications of complex seismic anisotropy, *Geochemistry, Geophysics, Geosystems*, doi:10.1002/2016GC006269.

Chester, F. M., J. P. Evans, and R. L. Biegel (1993), Internal structure and weakening mechanisms of the San Andreas Fault, *Journal of Geophysical Research*, *98*(B1), 771, doi:10.1029/92JB01866.

Clark, D. H., P. R. Bierman, and P. Larsen (1995), Improving in Situ Cosmogenic Chronometers, *Quaternary Research*, *44*(3), 367–377, doi:10.1006/qres.1995.1081.

Cohn, B. S. N., C. R. Allen, R. Oilman, and N. R. Goulty (1982), Preearthquake and postearthquake creep on the imperial fault and the brawley fault zone, in *The Imperial Valley, California, earthquake of October 15, 1979. Geological Survey professional paper. No.1254*, pp. 161–167, United States Geological Survey, Washington, DC.

Colarossi, D., G. Duller, H. Roberts, S. Tooth, and R. Lyons (2015), Comparison of paired quartz OSL and feldspar post-IR IRSL dose distributions in poorly bleached fluvial sediments from South Africa, *Quaternary Geochronology*, *30*, 233–238, doi:10.1016/j.quageo.2015.02.015.

Copley, A., and J. Jackson (2006), Active tectonics of the Turkish-Iranian Plateau, *Tectonics*, *25*(6), doi:10.1029/2005TC001906.

Copley, A., and R. Jolivet (2016), Fault rheology in an aseismic fold-thrust belt (Shahdad, eastern Iran), *Journal of Geophysical Research: Solid Earth*, *121*(1), 412–431, doi:10.1002/2015JB012431.

Cording, A., R. Hetzel, M. Kober, and J. Kley (2014), 10Be exposure dating of river terraces at the southern mountain front of the Dzungarian Alatau (SE Kazakhstan) reveals rate of thrust faulting over the past ∼400ka, *Quaternary Research*, *81*(1), 168–178, doi:10.1016/j.yqres.2013.10.016.

Cowgill, E. (2007), Impact of riser reconstructions on estimation of secular variation in rates of strike-slip faulting: Revisiting the Cherchen River site along the Altyn Tagh Fault, NW China, *Earth and Planetary Science Letters*, *254*(3-4), 239–255, doi:10.1016/j.epsl.2006.09.015.

Crosby, C., J. Arrowsmith, A. Korjenkov, B. Guralnik, E. Mamyrov, and I. Povolotskaya (2007), The Hunt for Surface Rupture From the 1889 Ms 8.3 Chilik Earthquake, Northern Tien Shan, Kyrgyzstan and Kazakhstan, *AGU Fall Meeting Abstracts*.

Cukur, D., S. Krastel, H.-U. Schmincke, M. Sumita, M. N. Çağatay, A. F. Meydan, E. Damcı, and M. Stockhecke (2014), Seismic stratigraphy of Lake Van, eastern Turkey, *Quaternary Science Reviews*, *104*, 63–84, doi:10.1016/j.quascirev.2014.07.016.

Davis, K., D. W. Burbank, D. Fisher, S. Wallace, and D. Nobes (2005), Thrust-fault growth and segment linkage in the active Ostler fault zone, New Zealand, *Journal of Structural Geology*, *27*(8), 1528–1546, doi:10.1016/j.jsg.2005.04.011.

De Grave, J., M. M. Buslov, and P. Van den haute (2007), Distant effects of India-Eurasia convergence and Mesozoic intracontinental deformation in Central Asia: Constraints from apatite fission-track thermochronology, *Journal of Asian Earth Sciences*, *29*(2-3), 188–204, doi:10.1016/j.jseaes.2006.03.001.

Delvaux, D., K. Abdrakhmatov, I. Lemzin, and A. Strom (2001), Landslides and surface breaks af the Ms 8.2 Kemin earthquake (Kyrgyzstan), *Russian Geology and Geophysics*, *42*(10), 1583–1592.

DeMets, C., R. G. Gordon, D. F. Argus, and S. Stein (1990), Current plate motions, *Geophysical Journal International*, *101*(2), 425–478, doi:10.1111/j.1365-246X.1990.tb06579.x.

DeMets, C., R. G. Gordon, D. F. Argus, and S. Stein (1994), Effect of recent revisions to the geomagnetic reversal time scale on estimates of current plate motions, *Geophysical Research Letters*, *21*(20), 2191–2194, doi:10.1029/94GL02118.

Deng, Q., P. Zhang, Y. Ran, X. Yang, W. Min, and Q. Chu (2003), Basic characteristics of active tectonics of China, *Science in China (Series D)*, *46*(4), 356–372, doi:10.1360/03yd9032.

Deng, Q., Y. Ran, X. Yang, W. Min, and Q. Chu (2004), Map of Active Tectonics in China (in Chinese).

Dewey, J. F., M. R. Hempton, W. S. F. Kidd, F. Saroglu, and A. M. C. Sengor (1986), Shortening of continental lithosphere: the neotectonics of Eastern Anatolia – a young collision zone, *Geological Society, London, Special Publications*, *19*(1), 1–36, doi:10.1144/GSL.SP.1986.019.01.01.

Dolan, J. F., L. J. McAuliffe, E. J. Rhodes, S. F. McGill, and R. Zinke (2016), Extreme multi-millennial slip rate variations on the Garlock fault, California: Strain super-cycles, potentially time-variable fault strength, and implications for system-level earthquake occurrence, *Earth and Planetary Science Letters*, *446*, 123–136, doi:10.1016/j.epsl.2016.04.011.

Doğan, B., and A. Karakaş (2013), Geometry of co-seismic surface ruptures and tectonic meaning of the 23 October 2011 Mw 7.1 Van earthquake (East Anatolian Region, Turkey), *Journal of Structural Geology*, *46*, 99–114, doi:10.1016/j.jsg.2012.10.001.

Doğan, U., D. Ö. Demir, Z. Çakir, S. Ergintav, H. Özener, A. M. Akoğlu, S. S. Nalbant, and R. Reilinger (2014), Postseismic deformation following the Mw 7.2 October 23, 2011 Van earthquake (Turkey): Evidence for aseismic fault reactivation, *Geophysical Research Letters*, *41*(7), 2334–2341, doi:10.1002/2014GL059291.

Duller, G. A. T. (2007), Assessing the error on equivalent dose estimates derived from single aliquot regenerative dose measurements, *Ancient TL*, *25*(1), 15–24.

Duller, G. A. T. (2008), Single-grain optical dating of Quaternary sediments: why aliquot size matters in luminescence dating, *Boreas*, *37*(4), 589–612, doi:10.1111/j.1502-3885.2008.00051.x.

Dziewonski, A. M., T.-A. Chou, and J. H. Woodhouse (1981), Determination of earthquake source parameters from waveform data for studies of global and regional seismicity, *Journal of Geophysical Research*, *86*(B4), 2825–2852, doi:10.1029/JB086iB04p02825.

Ekström, G., M. Nettles, and A. Dziewoński (2012), The global CMT project 2004–2010: Centroid-moment tensors for 13,017 earthquakes, *Physics of the Earth and Planetary Interiors*, *200-201*, doi:10.1016/j.pepi.2012.04.002.

Elliott, A. J., M. E. Oskin, D. Banesh, P. O. Gold, A. Hinojosa-Corona, R. H. Styron, and M. H. Taylor (2012a), How quickly do earthquakes get locked in the landscape? One year of erosion on El Mayor-Cucapah rupture scarps imaged by repeat terrestrial lidar scans, *AGU Fall Meeting Abstracts*.

Elliott, A. J., M. E. Oskin, J. Liu-Zeng, and Y. Shao (2015a), Rupture termination at restraining bends: The last great earthquake on the Altyn Tagh Fault, *Geophysical Research Letters*, *42*(7), 2164–2170, doi:10.1002/2015GL063107.

Elliott, J. R., R. J. Walters, P. C. England, J. A. Jackson, Z. Li, and B. Parsons (2010), Extension on the Tibetan plateau: recent normal faulting measured by InSAR and body wave seismology, *Geophysical Journal International*, *183*(2), 503–535, doi:10.1111/j.1365-246X.2010.04754.x.

Elliott, J. R., B. Parsons, J. A. Jackson, X. Shan, R. A. Sloan, and R. T. Walker (2011), Depth segmentation of the seismogenic continental crust: The 2008 and 2009 Qaidam earthquakes, *Geophysical Research Letters*, *38*(6), doi:10.1029/2011GL046897.

Elliott, J. R., E. K. Nissen, P. C. England, J. A. Jackson, S. Lamb, Z. Li, M. Oehlers, and B. Parsons (2012b), Slip in the 2010-2011 Canterbury earthquakes, New Zealand, *Journal of Geophysical Research: Solid Earth*, *117*(B03401), doi:10.1029/2011JB008868.

Elliott, J. R., A. C. Copley, R. Holley, K. Scharer, and B. Parsons (2013), The 2011 Mw 7.1 Van (Eastern Turkey) earthquake, *Journal of Geophysical Research: Solid Earth*, *118*, doi:10.1002/jgrb.50117.

Elliott, J. R., E. A. Bergman, A. C. Copley, A. R. Ghods, E. K. Nissen, B. Oveisi, M. Tatar, R. J. Walters, and F. Yamini-Fard (2015b), The 2013 M w 6.2 Khaki-Shonbe (Iran) Earthquake: Insights into seismic and aseismic shortening of the Zagros sedimentary cover, *Earth and Space Science*, *2*(11), 435–471, doi:10.1002/2015EA000098.

Elliott, J. R., A. J. Elliott, A. Hooper, Y. Larsen, P. Marinkovic, and T. J. Wright (2015c), Earthquake Monitoring Gets Boost from New Satellite, *Eos*, *96*(August 2014), 14–18, doi:10.1029/2015EO023967.

Elliott, J. R., R. Jolivet, P. J. González, J.-P. Avouac, J. Hollingsworth, M. P. Searle, and V. L. Stevens (2016), Himalayan megathrust geometry and relation to topography revealed by the Gorkha earthquake, *Nature Geoscience*, *9*(2), 174–180, doi:10.1038/ngeo2623.

Emre, Ö., T. Y. Duman, S. Özalp, and H. Elmacı (2011), Ekim 2011 Van depremi saha gözlemleri ve kaynak faya ilişkin ön değerlendirmeler. (In Turkish), *Tech. rep.*, Mineral Research and Exploration General Directorate of Turkey, Ankara.

England, P., and J. Jackson (2011), Uncharted seismic risk, *Nature Geoscience*, *4*(6), 348–349, doi:10.1038/ngeo1168.

England, P., and P. Molnar (2005), Late Quaternary to decadal velocity fields in Asia, *Journal of Geophysical Research*, *110*(B12), B12,401, doi:10.1029/2004JB003541.

England, P., and P. Molnar (2015), Rheology of the lithosphere beneath the central and western Tien Shan, *Journal of Geophysical Research: Solid Earth*, *120*(5), 3803–3823, doi:10.1002/2014JB011733.

Erdik, M., Y. Kamer, M. Demircioglu, and K. Sesetyan (2012), 23 October 2011 Van (Turkey) earthquake, *Natural Hazards*, *64*(1), 651–665, doi:10.1007/s11069-012-0263-9.

Evangelidis, C. P., and H. Kao (2013), High-frequency source imaging of the 2011 October 23 Van (Eastern Turkey) earthquake by backprojection of strong motion waveforms, *Geophysical Journal International*, *196*(2), 1060–1072, doi:10.1093/gji/ggt437.

Fattahi, M., R. T. Walker, M. M. Khatib, A. Dolati, and A. Bahroudi (2007), Slip-rate estimate and past earthquakes on the Doruneh fault, eastern Iran, *Geophysical Journal International*, *168*(2), 691–709, doi:10.1111/j.1365-246X.2006.03248.x.

Feng, W., Z. Li, T. Hoey, Y. Zhang, R. Wang, S. Samsonov, Y. Li, and Z. Xu (2014), Patterns and mechanisms of coseismic and postseismic slips of the 2011 Mw 7.1 Van (Turkey) earthquake revealed by multi-platform synthetic aperture radar interferometry, *Tectonophysics*, *632*, 188–198, doi:10.1016/j.tecto.2014.06.011.

Fielding, E. J., P. R. Lundgren, T. Taymaz, S. Yolsal-Cevikbilen, and S. E. Owen (2013), Fault-Slip Source Models for the 2011 M 7.1 Van Earthquake in Turkey from SAR Interferometry, Pixel Offset Tracking, GPS, and Seismic Waveform Analysis, *Seismological Research Letters*, *84*, 579–593, doi:10.1785/0220120164.

Floyd, M. A., R. J. Walters, J. R. Elliott, G. J. Funning, J. L. Svarc, J. H. Murray, Y. Hooper A. J. Larsen, P. Marinkovic, R. Bürgmann, I. A. Johanson, T. J. Wright, and i. Review) (), Afterslip evolution following the 2014 South Napa earthquake exposes variations in fault plane friction, *Nature Geoscience*.

Fonstad, M. A., J. T. Dietrich, B. C. Courville, J. L. Jensen, and P. E. Carbonneau (2013), Topographic structure from motion: a new development in photogrammetric measurement, *Earth Surface Processes and Landforms*, *38*(4), 421–430, doi:10.1002/esp.3366.

Gallovic, F., G. Ameri, J. Zahradnik, J. Jansky, V. Plicka, E. Sokos, A. Askan, and M. Pakzad (2013), Fault Process and Broadband Ground-Motion Simulations of the 23 October 2011 Van (Eastern Turkey) Earthquake, *Bulletin of the Seismological Society of America*, *103*(6), 3164–3178, doi:10.1785/0120130044.

Gao, X., Z. Guo, W. Wang, and Y. Wu (2014), Crustal structure beneath the central tien shan from ambient noise tomography, *Terra Nova*, *26*(6), 469–476, doi:10.1111/ter.12122.

Gebhardt, A. C., L. Naudts, L. De Mol, J. Klerkx, K. Abdrakhmatov, E. R. Sobel, and M. De Batist (2016), An extended history of high-amplitude lake-level changes in tectonically active Lake Issyk-Kul (Kyrgyzstan), as revealed by high-resolution seismic reflection data, *Climate of the Past Discussions*, pp. 1–36, doi:10.5194/cp-2016-3.

Giardini, D., G. Grünthal, K. M. Shedlock, and P. Zhang (1999), The GSHAP global seismic hazard map, *Annals of Geophysics*, *42*(6), doi:10.4401/ag-3784.

Gilligan, A., S. W. Roecker, K. F. Priestley, and C. Nunn (2014), Shear velocity model for the Kyrgyz Tien Shan from joint inversion of receiver function and surface wave data, *Geophysical Journal International*, *199*(1), 480–498, doi:10.1093/gji/ggu225.

Glennie, C. L., A. Hinojosa-Corona, E. Nissen, A. Kusari, M. E. Oskin, J. R. Arrowsmith, and A. Borsa (2014), Optimization of legacy lidar data sets for measuring near-field earthquake displacements, *Geophysical Research Letters*, *41*(10), 3494–3501, doi:10.1002/2014GL059919.

Glorie, S., and J. De Grave (2016), Exhuming the Meso-Cenozoic Kyrgyz Tianshan and Siberian Altai-Sayan: A review based on low-temperature thermochronology, *Geoscience Frontiers*, *7*(2), 155–170, doi:10.1016/j.gsf.2015.04.003.

Glorie, S., J. De Grave, M. M. Buslov, M. A. Elburg, D. F. Stockli, A. Gerdes, and P. Van den haute (2010), Multi-method chronometric constraints on the evolution of the Northern Kyrgyz Tien Shan granitoids (Central Asian Orogenic Belt): From emplacement to exhumation, *Journal of Asian Earth Sciences*, *38*(3-4), 131–146, doi:10.1016/j.jseaes.2009.12.009.

Glorie, S., J. De Grave, M. M. Buslov, F. I. Zhimulev, D. F. Stockli, V. Y. Batalev, A. Izmer, P. Van den haute, F. Vanhaecke, and M. A. Elburg (2011), Tectonic history of the Kyrgyz South Tien Shan (Atbashi-Inylchek) suture zone: The role of inherited structures during deformation-propagation, *Tectonics*, *30*(6), doi:10.1029/2011TC002949.

Gold, P., E. Cowgill, O. Kreylos, and R. D. Gold (2012), A terrestrial lidar-based workflow for determining three-dimensional slip vectors and associated uncertainties, *Geosphere*, *8*(2), 431, doi:10.1130/GES00714.1.

Gold, P. O., M. E. Oskin, A. J. Elliott, A. Hinojosa-Corona, M. H. Taylor, O. Kreylos, and E. Cowgill (2013), Coseismic Slip Variation Assessed from Terrestrial Lidar Scans of the El Mayor-Cucapah Surface Rupture, *Earth and Planetary Science Letters*, *366*, 151–162, doi:10.1016/j.epsl.2013.01.040.

Gold, R. D., N. G. Reitman, R. W. Briggs, W. D. Barnhart, G. P. Hayes, and E. Wilson (2015), On- and off-fault deformation associated with the September 2013 Mw 7.7 Balochistan earthquake: Implications for geologic slip rate measurements, *Tectonophysics*, *660*, 65–78, doi:10.1016/j.tecto.2015.08.019.

Goode, J. K., D. W. Burbank, and B. Bookhagen (2011), Basin width control of faulting in the Naryn Basin, south-central Kyrgyzstan, *Tectonics*, *30*(6), doi:10.1029/2011TC002910.

Goode, J. K., D. W. Burbank, and C. Ormukov (2014), Pliocene-Pleistocene initiation, style, and sequencing of deformation in the central Tien Shan, *Tectonics*, *33*(4), 464–484, doi:10.1002/2013TC003394.

Gosse, J. C., and F. M. Phillips (2001), Terrestrial in situ cosmogenic nuclides: theory and application, *Quaternary Science Reviews*, *20*(14), 1475–1560, doi:10.1016/S0277-3791(00)00171-2.

Grant, L. B., and K. Sieh (1994), Paleoseismic evidence of clustered earthquakes on the San Andreas Fault in the Carrizo Plain, California, *Journal of Geophysical Research*, *99*(B4), 6819–6841, doi:10.1029/94JB00125.

Gregory, L. C. (2012), Active Faulting and Deformation of the Mongolian Altay Mountains, Ph.D. thesis, University of Oxford.

Grützner, C., E. Carson, R. Walker, E. Rhodes, A. Mukambayev, D. Mackenzie, J. Elliott, G. Campbell, and K. Abdrakhmatov (), Assessing the activity of faults in continental interiors: palaeoseismic insights from SE Kazakhstan, *in revision for EPSL*.

Guérin, G., N. Mercier, and G. Adamiec (2011), Dose-rate conversion factors: update, *Ancient TL*, *29*(1), 5–8.

Gülkan, P., A. Gürpinar, M. Celebi, E. Arpat, and S. Gencoğlu (1978), *Engineering Report on the Muradiye-Çaldıran, Turkey, Earthquake of 24 November 1976*, National Academy of Sciences.

Haddon, E., C. Amos, O. Zielke, A. Jayko, and R. Bürgmann (2016), Surface slip during large Owens Valley earthquakes, *Geochemistry, Geophysics, Geosystems*, doi:10.1002/2015GC006033.

Haeussler, P. J., D. P. Schwartz, T. E. Dawson, H. D. Stenner, J. J. Lienkaemper, B. Sherrod, F. R. Cinti, P. Montone, P. A. Craw, A. J. Crone, and S. F. Personius (2004), Surface Rupture and Slip Distribution of the Denali and Totschunda Faults in the 3 November 2002 M 7.9 Earthquake, Alaska, *Bulletin of the Seismological Society of America*, *94*(6B), 23–52, doi:10.1785/0120040626.

Hendrix, M. S., S. A. Graham, A. R. Carroll, E. R. Sobel, C. L. McKnight, B. J. Schulein, and Z. Wang (1992), Sedimentary record and climatic implications of recurrent deformation in the Tian Shan: Evidence from Mesozoic strata of the north Tarim, south Junggar, and Turpan basins, northwest China, *Geological Society of America Bulletin*, *104*(1), 53–79, doi:10.1130/0016-7606(1992)104<0053:SRACIO>2.3.CO;2.

Hill, M. L. (1959), Dual Classification of Faults: GEOLOGICAL NOTES, *AAPG Bulletin*, *43*(1), 217–221.

Holden, N. E. (1990), Total half-lives for selected nuclides, *Pure and Applied Chemistry*, *62*(5), 1483–1504, doi:10.1351/pac199062050941.

Hollingsworth, J., J. Jackson, R. Walker, and H. Nazari (2008), Extrusion tectonics and subduction in the easter South Caspian region since 10 Ma, *Geology*, *36*(10), 763–766, doi:10.1130/G25008A.1.

Hollingsworth, J., S. Leprince, F. Ayoub, and J.-P. Avouac (2012), Deformation during the 1975-1984 Krafla rifting crisis, NE Iceland, measured from historical optical imagery, *Journal of Geophysical Research: Solid Earth*, *117*(B11407), doi:10.1029/2012JB009140.

Holt, W. E., C. Kreemer, a. J. Haines, L. Estey, C. Meertens, G. Blewitt, and D. Lavallée (2005), Project helps constrain continental dynamics and seismic hazards, *Eos, Transactions American Geophysical Union*, *86*(41), 383, doi:10.1029/2005EO410002.

Hubert-Ferrari, A. (2005), Irregular earthquake cycle along the southern Tianshan front, Aksu area, China, *Journal of Geophysical Research*, *110*(B6), B06,402, doi:10.1029/2003JB002603.

Hudnut, K. W., T. M. Brocher, C. S. Prentice, J. Boatwright, B. A. Brooks, T. Brad, J. L. Blair, J. B. Fletcher, J. E. Erdem, C. W. Wicks, J. R. Murray, F. F. Pollitz, J. Langbein, J. Svarc, D. P. Schwartz, D. J. Ponti, S. Hecker, S. Delong, C. Rosa, B. Jones, R. Lamb, A. M. Rosinski, T. P. Mccrink, T. E. Dawson, G. Seitz, S. Ron, C. Glennie, D. Hauser, T. Ericksen, D. Mardock, D. F. Hoirup, J. D. Bray, and S. Jewell (2014), Key recovery factors for the August 24, 2014, South Napa earthquake:, *Tech. rep.*, U.S. Geological Survey Open-File Report, doi:10.3133/ofr20141249.

Hudnutt, K. W., A. Borsa, C. Glennie, and J. B. Minster (2002), High-resolution topography along surface rupture of the 16 October 1999 Hector Mine, California (Mw 7.1) from airborne laser swath mapping, *Bulletin of the Seismological Society of America*, *92*(4), 1570–1576, doi:10.1785/0120000934.

Huntley, D. J., and M. R. Baril (1997), The K content of the K-feldspars being measured in optical dating or in thermoluminescence dating, *Ancient TL*, *15*(1), 11–13.

Huntley, D. J., and R. G. V. Hancock (2001), The Rb contents of the K-feldspar grains being measured in optical dating, *Ancient TL*, *19*(2), 43–46.

Hyndman, R. D., K. Wang, and M. Yamano (1995), Thermal constraints on the seismogenic portion of the southwestern Japan subduction thrust, *Journal of Geophysical Research: Solid Earth*, *100*(B8), 15,373–15,392, doi:10.1029/95JB00153.

Imbrie, J., J. D. Hays, D. G. Martinson, A. McIntyre, A. C. Mix, J. J. Morley, N. G. Pisias, W. L. Prell, and N. J. Shackleton (1984), The orbital theory of Pleistocene climate: Support from a revised chronology of the marine d18O record, in *Milankovitch and Climate: Understanding the Response to Astronomical Forcing*, vol. 1, pp. 269–305, doi:-.

Irmak, T. S., B. Doğan, and A. Karakaş (2012), Source mechanism of the 23 October, 2011, Van (Turkey) earthquake (Mw = 7.1) and aftershocks with its tectonic implications, *Earth, Planets and Space*, *64*(11), 991–1003, doi:10.5047/eps.2012.05.002.

Jackson, J. (2001), Living with earthquakes: know your faults, *Journal of Earthquake Engineering*, *5*(Special Issue 1), 5, doi:10.1142/S1363246901000431.

Jackson, J. (2008), *Surviving natural disasters*, Darwin College Lectures, Cambridge University Press.

Jackson, J., and D. McKenzie (1984), Active tectonics of the Alpine–Himalayan Belt between western Turkey and Pakistan, *Geophysical Journal of the Royal Astronomical Society*, *77*(1), 185–264, doi:10.1111/j.1365-246X.1984.tb01931.x.

Jackson, J. A. (1980), Reactivation of basement faults and crustal shortening in orogenic belts, *Nature*, *283*(5745), 343–346, doi:doi:10.1038/283343a0.

Jain, M., J. Buylaert, K. Thomsen, and A. Murray (2015), Further investigations on 'non-fading' in K-Feldspar, *Quaternary International*, *362*, 3–7, doi:10.1016/j.quaint.2014.11.018.

James, M. R., and S. Robson (2012), Straightforward reconstruction of 3D surfaces and topography with a camera: Accuracy and geoscience application, *Journal of Geophysical Research*, *117*(F03017), doi:10.1029/2011JF002289.

James, M. R., and S. Robson (2014), Mitigating systematic error in topographic models derived from UAV and ground-based image networks, *Earth Surface Processes and Landforms*, doi:10.1002/esp.3609.

Johnson, K., E. Nissen, S. Saripalli, J. R. Arrowsmith, P. Mcgarey, P. Williams, and K. Blisniuk (2014), Rapid mapping of ultrafine fault zone topography with structure from motion, *Geosphere*, *10*(5), 969–986, doi:10.1130/GES01017.1.

Jolivet, R., C. Lasserre, M. P. Doin, S. Guillaso, G. Peltzer, R. Dailu, J. Sun, Z. K. Shen, and X. Xu (2012), Shallow creep on the Haiyuan fault (Gansu, China) revealed by SAR interferometry, *Journal of Geophysical Research: Solid Earth*, *117*(6), 1–18, doi:10.1029/2011JB008732.

Jolivet, R., Z. Duputel, B. Riel, M. Simons, L. Rivera, S. E. Minson, H. Zhang, M. A. G. Aivazis, F. Ayoub, S. Leprince, S. Samsonov, M. Motagh, and E. J. Fielding (2014), The 2013 Mw 7.7 balochistan earthquake: Seismic potential of an accretionary wedge, *Bulletin of the Seismological Society of America*, *104*(2), 1020–1030, doi:10.1785/0120130313.

Kaban, M. K., and T. R. Yuanda (2014), Density Structure, Isostatic Balance and Tectonic Models of the Central Tien Shan, *Surveys in Geophysics*, *35*(6), 1375–1391, doi:10.1007/s10712-014-9298-7.

Kadioğlu, M., Z. Şen, and E. Batur (1997), The greatest soda-water lake in the world and how it is influenced by climatic change, *Annales Geophysicae*, *15*, 1489, doi:10.1007/s005850050564.

Kalmetieva, Z. A., A. V. Mikolaichuk, B. D. Moldobekov, A. V. Meleshko, M. M. Jantaev, A. V. Zubovich, and H. B. Havenith (2009), Atlas of earthquakes in Kyrgyzstan, *Tech. rep.*

Kaneko, Y., Y. Fialko, D. T. Sandwell, X. Tong, and M. Furuya (2012), Interseismic deformation and creep along the central section of the North Anatolian fault (Turkey): InSAR observations and implications for rate-and-state friction properties, *Journal of Geophysical Research*, *118*, 1–15, doi:10.1029/2012JB009661.

Karakhanian, A. S., V. G. Trifonov, H. Philip, A. Avagyan, K. Hessami, F. Jamali, M. Salih Bayraktutan, H. Bagdassarian, S. Arakelian, V. Davtian, and A. Adilkhanyan (2004), Active faulting and natural hazards in Armenia, eastern Turkey and northwestern Iran, *Tectonophysics*, *380*(3-4), 189–219, doi:10.1016/j.tecto.2003.09.020.

Kars, R. H., F. S. Busschers, and J. Wallinga (2012), Validating post IR-IRSL dating on K-feldspars through comparison with quartz OSL ages, *Quaternary Geochronology*, *12*, 74–86, doi:10.1016/j.quageo.2012.05.001.

Klinger, Y., R. Michel, and G. King (2006), Evidence for an earthquake barrier model from Mw∼7.8 Kokoxili (Tibet) earthquake slip-distribution, *Earth and Planetary Science Letters*, *242*(3-4), 354–364, doi:10.1016/j.epsl.2005.12.003.

Klinger, Y., M. Etchebes, P. Tapponnier, and C. Narteau (2011), Characteristic slip for five great earthquakes along the Fuyun fault in China, *Nature Geoscience*, *4*(6), 389–392, doi:10.1038/ngeo1158.

Kober, M., N. Seib, J. Kley, and T. Voigt (2013), Thick-skinned thrusting in the northern Tien Shan foreland, Kazakhstan: structural inheritance and polyphase deformation, in *Thick-Skin-Dominated Orogens: From Initial Inversion to Full Accretion*, pp. 19–42, doi:10.1144/SP377.7.

Kondo, H., V. Özaksoy, and C. Yildirim (2010), Slip history of the 1944 Bolu-Gerede earthquake rupture along the North Anatolian fault system: Implications for recurrence behavior of multisegment earthquakes, *Journal of Geophysical Research: Solid Earth*, *115*(4), 1–16, doi:10.1029/2009JB006413.

Korjenkov, A. M., I. E. Povolotskaya, and E. Mamyrov (2007), Morphologic expression of Quaternary deformation in the northwestern foothills of the Ysyk-Köl basin, Tien Shan, *Geotectonics*, *41*(2), 130–148, doi:10.1134/S0016852107020045.

Kossobokov, V. G., and A. K. Nekrasova (2012), Global Seismic Hazard Assessment Program maps are erroneous, *Seismic Instruments*, *48*(2), 162–170, doi:10.3103/S0747923912020065.

Kreemer, C., W. E. Holt, and A. J. Haines (2003), An integrated global model of present-day plate motions and plate boundary deformation, *Geophysical Journal International*, *154*(1), 8–34, doi:10.1046/j.1365-246X.2003.01917.x.

Kreylos, O., M. Oskin, E. Cowgill, P. Gold, A. Elliott, and L. Kellogg (2013), Point-based computing on scanned terrain with LidarViewer, *Geosphere*, *9*(3), 546–556, doi:10.1130/GES00705.1.

Krüger, F., G. Kulikova, and A. Landgraf (2015), Instrumental magnitude constraints for the 11 July 1889 , Chilik earthquake, in *Seismicity, Fault Rupture and Earthquake Hazards in Slowly Deforming Regions*, edited by A. Landgraf, S. Kuebler, E. Hintersberger, and S. Stein, 432, Geological Society, London, Special Publications, doi:10.1144/SP432.8.

Ku, T.-L., W. B. Bull, S. T. Freeman, and K. G. Knauss (1979), Th230-U234 dating of pedogenic carbonates in gravelly desert soils of Vidal Valley, southeastern California, *Geological Society of America Bulletin*, *90*(11), 1063, doi:10.1130/0016-7606(1979)90<1063:TDOPCI>2.0.CO;2.

Kulikova, G., and F. Kruger (2015), Source process of the 1911 M8.0 Chon-Kemin earthquake: investigation results by analogue seismic records, *Geophysical Journal International*, *201*(3), 1891–1911, doi:10.1093/gji/ggv091.

Kuzucuoğlu, C., A. Christol, D. Mouralis, A.-F. Doğu, E. Akköprü, M. Fort, D. Brunstein, H. Zorer, M. Fontugne, M. Karabiyikoğlu, S. Scaillet, J.-L. Reyss, and H. Guillou (2010), Formation of the Upper Pleistocene terraces of Lake Van (Turkey), *Journal of Quaternary Science*, *25*(7), 1124–1137, doi:10.1002/jqs.1431.

Landgraf, A., A. Dzhumabaeva, K. E. Abdrakhmatov, M. R. Strecker, E. A. Macaulay, J. R. Arrowsmith, H. Sudhaus, F. Preusser, G. Rugel, and S. Merchel (2016), Repeated large-magnitude earthquakes in a tectonically active, low-strain continental interior: the northern Tien Shan, Kyrgyzstan, *Journal of Geophysical Research: Solid Earth*, pp. 1–23, doi:10.1002/2015JB012714.

Lavé, J., and J. P. Avouac (2000), Active folding of fluvial terraces across the Siwaliks Hills, Himalayas of central Nepal, *Journal of Geophysical Research: Solid Earth*, *105*(B3), 5735–5770, doi:10.1029/1999JB900292.

Le Béon, M., J. Suppe, M. K. Jaiswal, Y.-G. Chen, and M. E. Ustaszewski (2014), Deciphering cumulative fault slip vectors from fold scarps: Relationships between long-term and coseismic deformations in central Western Taiwan, *Journal of Geophysical Research: Solid Earth*, *119*(7), 5943–5978, doi:10.1002/2013JB010794.

Lei, J. (2011), Seismic tomographic imaging of the crust and upper mantle under the central and western Tien Shan orogenic belt, *Journal of Geophysical Research*, *116*(B9), 1–20, doi:10.1029/2010JB008000.

Leonard, M. (2010), Earthquake fault scaling: Self-consistent relating of rupture length, width, average displacement, and moment release, *Bulletin of the Seismological Society of America*, *100*(5A), 1971–1988, doi:10.1785/0120090189.

Li, C., G. Dupont-Nivet, and Z. Z. Guo (2011), Magnetostratigraphy of the Northern Tian Shan foreland, Taxi He section, China, *Basin Research*, *23*(1), 101–117, doi:10.1111/j.1365-2117.2010.00475.x.

Li, Y., L. Shi, and J. Gao (2016), Lithospheric structure across the central Tien Shan constrained by gravity anomalies and joint inversions of receiver function and Rayleigh wave dispersion, *Journal of Asian Earth Sciences*, *124*, 191–203, doi:10.1016/j.jseaes.2016.05.003.

Lienkaemper, J. J. (2001), 1857 Slip on the San Andreas Fault Southeast of Cholame, California, *Bulletin of the Seismological Society of America*, *91*(6), 1659–1672, doi:10.1785/0120000043.

Lienkaemper, J. J., J. S. Galehouse, and R. W. Simpson (2001), Long-term monitoring of creep rate along the Hayward fault and evidence for a lasting creep response to 1989 Loma Prieta earthquake, *Geophysical Research Letters*, *28*(11), 2265–2268, doi:10.1029/2000GL012776.

Lienkaemper, J. J., S. B. DeLong, C. J. Domrose, and C. M. Rosa (2016), Afterslip Behavior following the 2014 M 6.0 South Napa Earthquake with Implications for Afterslip Forecasting on Other Seismogenic Faults, *Seismological Research Letters*, *87*(3), 609–619, doi:10.1785/0220150262.

Lin, J., and R. S. Stein (2004), Stress triggering in thrust and subduction earthquakes and stress interaction between the southern San Andreas and nearby thrust and strike-slip faults, *Journal of Geophysical Research: Solid Earth*, *109*(B2), doi:10.1029/2003JB002607.

Lindvall, S. C., T. K. Rockwell, and K. W. Hudnut (1989), Evidence for prehistoric earthquakes on the Superstition Hills fault from offset geomorphic features, *Bulletin of the Seismological Society of America*, *79*(2), 342–361.

Litt, T., and F. S. Anselmetti (2014), Lake Van deep drilling project PALEOVAN, *Quaternary Science Reviews*, *104*, 1–7, doi:10.1016/j.quascirev.2014.09.026.

Litt, T., S. Krastel, M. Sturm, R. Kipfer, S. Örcen, G. Heumann, S. O. Franz, U. B. Ülgen, and F. Niessen (2009), 'PALEOVAN', International Continental Scientific Drilling Program (ICDP): site survey results and perspectives, *Quaternary Science Reviews*, *28*(15-16), 1555–1567, doi:10.1016/j.quascirev.2009.03.002.

Litt, T., F. S. Anselmetti, H. Baumgarten, J. Beer, N. Cagatay, D. Cukur, E. Damci, C. Glombitza, G. Haug, K. Heumann, K. Jens, K. Rolf, K. Sebastian, M. Ola, O. A. Feray, P. Sefer, R. Nadine, S. Marie-Eve, S. Hans-Ulrich, S. Carsten J., S. Mike, S. Mari, T. Mona, V. Yama, W. Luigi, and t. P. S. T. Thomas (2012), Scientific Drilling, *Scientific Drilling*, *14*, 18–29, doi:10.2204/iodp.sd.14.02.2012.

Liu, J., Q. Y. Liu, B. Guo, D. A. Yuen, and H. Z. Song (2007), Small-scale convection in the upper mantle beneath the Chinese Tian Shan Mountains, *Physics of the Earth and Planetary Interiors*, *163*(1-4), 179–190, doi:10.1016/j.pepi.2007.04.019.

Lowe, D. G. (2004), Distinctive Image Features from Scale-Invariant Keypoints, *International Journal of Computer Vision*, *60*(2), 91–110, doi:10.1023/B:VISI.0000029664.99615.94.

Macaulay, E. A., E. R. Sobel, A. Mikolaichuk, A. Landgraf, B. Kohn, and F. Stuart (2013), Thermochronologic insight into late Cenozoic deformation in the basement-cored Terskey Range, Kyrgyz Tien Shan, *Tectonics*, *32*(3), 487–500, doi:10.1002/tect.20040.

Macaulay, E. A., E. R. Sobel, A. Mikolaichuk, B. Kohn, and F. M. Stuart (2014), Cenozoic deformation and exhumation history of the Central Kyrgyz Tien Shan, *Tectonics*, *33*(2), 135–165, doi:10.1002/2013TC003376.

Mackenzie, D., K. Abdrakhmatov, G. Campbell, C. Grützner, E. Carson, and A. Moldobaeb (2015), A transect of quaternary geological slip rates in the Kazakh Tien Shan, in *6th International INQUA Meeting on Paleoseismology, Active Tectonics and Archaeoseismology*, April, pp. 267–270.

Mackenzie, D., J. Elliott, E. Altunel, R. Walker, Y. Kurban, J.-L. Schwenninger, and B. Parsons (2016), Seismotectonics and rupture process of the Mw 7.1 2011 Van reverse-faulting earthquake, eastern Turkey, and implications for hazard in regions of distributed shortening, *Geophysical Journal International*, *206*(1), 501–524, doi:10.1093/gji/ggw158.

Makarov, V. I., D. V. Alekseev, V. Y. Batalev, E. a. Bataleva, I. V. Belyaev, V. D. Bragin, N. T. Dergunov, N. N. Efimova, M. G. Leonov, L. M. Munirova, a. D. Pavlenkin, S. Roecker, Y. V. Roslov, a. K. Rybin, and G. G. Shchelochkov (2010), Underthrusting of Tarim beneath the Tien Shan and deep structure of their junction zone: Main results of seismic experiment along MANAS Profile Kashgar-Song-Köl, *Geotectonics*, *44*(2), 102–126, doi:10.1134/S0016852110020020.

Manighetti, I., M. Campillo, S. Bouley, and F. Cotton (2007), Earthquake scaling, fault segmentation, and structural maturity, *Earth and Planetary Science Letters*, *253*(3-4), 429–438, doi:10.1016/j.epsl.2006.11.004.

Marone, C., and C. H. Scholz (1988), The depth of seismic faulting and the upper transition from stable to unstable slip regimes, *Geophysical Research Letters*, *15*(6), 621, doi:10.1029/GL015i006p00621.

Marone, C. J., C. H. Scholtz, and R. Bilham (1991), On the mechanics of earthquake afterslip, *Journal of Geophysical Research*, *96*(B5), 8441, doi:10.1029/91JB00275.

Mattauer, M. (1986), Intracontinental subduction, crust-mantle decollement and crustal-stacking wedge in the Himalayas and other collision belts, *Geological Society, London, Special Publications*, *19*(1), 37–50, doi:10.1144/GSL.SP.1986.019.01.02.

McCalpin, J. P. (2009), *Paleoseismology*, 2nd ed., Academic Press.

McClusky, S., S. Balassanian, A. Barka, C. Demir, S. Ergintav, I. Georgiev, O. Gurkan, M. Hamburger, K. Hurst, H. Kahle, K. Kastens, G. Kekelidze, R. King, V. Kotzev, O. Lenk, S. Mahmoud, A. Mishin, M. Nadariya, A. Ouzounis, D. Paradissis, Y. Peter, M. Prilepin, R. Reilinger, I. Sanli, H. Seeger, A. Tealeb, M. N. Toksöz, and G. Veis (2000), Global Positioning System constraints on plate kinematics and dynamics in the eastern Mediterranean and Caucasus, *Journal of Geophysical Research*, *105*(B3), 5695–5719, doi:10.1029/1999JB900351.

McKenzie, D. (1972), Active Tectonics of the Mediterranean Region, *Geophysical Journal International*, *30*(2), 109–185, doi:10.1111/j.1365-246X.1972.tb02351.x.

McKenzie, D. P. (1970), Plate Tectonics of the Mediterranean Region, *Nature*, *226*(5242), 239–243, doi:10.1038/226239a0.

McKenzie, D. P., and R. L. Parker (1967), The North Pacific: an Example of Tectonics on a Sphere, *Nature*, *216*(5122), 1276–1280, doi:10.1038/2161276a0.

McKenzie, D. P., D. Davies, and P. Molnar (1970), Plate Tectonics of the Red Sea and East Africa, *Nature*, *226*(5242), 243–248, doi:10.1038/226243a0.

Mejdahl, V. (1979), Thermoluminescence dating: Beta-dose attenuation in quartz grains, *Archaeometry*, *21*(1), 61–72, doi:10.1111/j.1475-4754.1979.tb00241.x.

Mériaux, A.-S., F. J. Ryerson, P. Tapponnier, J. Van der Woerd, R. C. Finkel, X. Xu, Z. Xu, and M. W. Caffee (2004), Rapid slip along the central Altyn Tagh Fault: Morphochronologic evidence from Cherchen He and Sulamu Tagh, *Journal of Geophysical Research: Solid Earth*, *109*(B6), doi:10.1029/2003JB002558.

Middleton, T. A., R. T. Walker, B. Parsons, Q. Lei, Y. Zhou, and Z. Ren (2016), A major, intraplate, normal-faulting earthquake: the 1739 Yinchuan event in northern China, *Journal of Geophysical Research: Solid Earth*, *120*, doi:10.1002/2015JB012355.

Molnar, P., and P. Tapponnier (1975), Cenozoic tectonics of Asia: Effects of a continental collision, *Science*, *189*(4201), 419–426.

Molnar, P., E. T. Brown, B. Burchfiel, D. Qudong, F. Zianyue, L. Jun, G. M. Raisbeck, S. Jianbang, W. Zhangming, F. Yiou, and Y. Huichuan (1994), Quaternary climate change and the formation of river terraces across growing anticlines on the north flank of the Tien Shan, China., *Journal of Geology*, *102*(5), 583–602.

Morelan, A. (2015), Rapid documentation of earthquake surface displacements using structure from motion photogrammetry, in *2015 AGU Fall Meeting*, American Geophysical Union.

Morelan, A. E., C. C. Trexler, and M. E. Oskin (2015), Surface-Rupture and Slip Observations on the Day of the 24 August 2014 South Napa Earthquake, *Seismological Research Letters*, *86*(4), 1119–1127, doi:10.1785/0220140235.

Moro, M., V. Cannelli, M. Chini, C. Bignami, D. Melini, S. Stramondo, M. Saroli, M. Picchiani, C. Kyriakopoulos, and C. A. Brunori (2014), The October 23, 2011, Van (Turkey) earthquake and its relationship with neighbouring structures, *Scientific reports*, *4*, 3959, doi:10.1038/srep03959.

Mousavi, Z., A. Walpersdorf, R. Walker, F. Tavakoli, E. Pathier, H. Nankali, F. Nilfouroushan, and Y. Djamour (2013), Global Positioning System constraints on the active tectonics of NE Iran and the South Caspian region, *Earth and Planetary Science Letters*, *377-378*, 287–298, doi:10.1016/j.epsl.2013.07.007.

MTA (2002), Van Section, in *1:500 000 Scale Geological Maps of Turkey*, Mineral Research & Exploration General Directorate Press, Ankara.

Murray, A., and A. Wintle (2000), Luminescence dating of quartz using an improved single-aliquot regenerative-dose protocol, *Radiation Measurements*, *32*(1), 57–73, doi:10.1016/S1350-4487(99)00253-X.

Murray, A., and A. Wintle (2003), The single aliquot regenerative dose protocol: potential for improvements in reliability, *Radiation Measurements*, *37*(4-5), 377–381, doi:10.1016/S1350-4487(03)00053-2.

Mushketov, I. V. (1981), Materials for investigation of earthquakes in Russia, in *Annex to the 27th volume of tidings of the Imperial Russian Geographical Society.*

Nissen, E., R. T. Walker, A. Bayasgalan, A. Carter, M. Fattahi, E. Molor, C. Schnabel, A. J. West, and S. Xu (2009), The late Quaternary slip-rate of the Har-Us-Nuur fault (Mongolian Altai) from cosmogenic 10Be and luminescence dating, *Earth and Planetary Science Letters*, *286*(3-4), 467–478, doi:10.1016/j.epsl.2009.06.048.

Nissen, E., F. Yamini-Fard, M. Tatar, A. Gholamzadeh, E. Bergman, J. R. Elliott, J. A. Jackson, and B. Parsons (2010), The vertical separation of mainshock rupture and microseismicity at Qeshm island in the Zagros fold-and-thrust belt, Iran, *Earth and Planetary Science Letters*, *296*(3-4), 181–194, doi:10.1016/j.epsl.2010.04.049.

Nissen, E., A. K. Krishnan, J. R. Arrowsmith, and S. Saripalli (2012), Three-dimensional surface displacements and rotations from differencing pre- and post-earthquake LiDAR point clouds, *Geophysical Research Letters*, *39*(16), doi:10.1029/2012GL052460.

Nissen, E., T. Maruyama, J. Ramon Arrowsmith, J. R. Elliott, A. K. Krishnan, M. E. Oskin, and S. Saripalli (2014), Coseismic fault zone deformation revealed with differential lidar: Examples from Japanese Mw ∼7 intraplate earthquakes, *Earth and Planetary Science Letters*, *405*, 244–256, doi:10.1016/j.epsl.2014.08.031.

Nur, A., and G. Mavko (1974), Postseismic Viscoelastic Rebound, *Science*, *183*(4121), 204–206, doi:10.1126/science.183.4121.204.

Okada, Y. (1992), Surface deformation due to shear and tensile faults in a half-space, *Bulletin of the Seismological Society of America*, *82*(4), 1018–1040.

Oreshin, S. (2002), Lithosphere and asthenosphere of the Tien Shan imaged by S receiver functions, *Geophysical Research Letters*, *29*(8), 1–4, doi:10.1029/2001GL014441.

Oskin, M. E., and D. Burbank (2007), Transient landscape evolution of basement-cored uplifts: Example of the Kyrgyz Range, Tian Shan, *Journal of Geophysical Research*, *112*(F03S03), doi:10.1029/2006JF000563.

Özkaymak, Ç., A. Sağlam, and O. Köse (2003), Active Tectonic Characteristics of the East of Lake Van (East Anatolian, Turkey), in *ATAG-7 Active Tectonics Research Group 7th Symposium*, pp. 54–60.

Ozkaymak, C., H. Sozbilir, E. Bozkurt, K. Dirik, T. Topal, H. Alan, and D. Caglan (2011), Seismic Geomorphology of October 23, 2011 Tabanlı-Van Earthquake and Its Relation to Active Tectonics of East Anatolia (in Turkish), *Journal of Geological Engineering*, *35*(2), 175–199.

Palmer, D. (1981), An Introduction to the generalized reciprocal method of seismic refraction interpretation, *Geophysics*, *46*(11), 1508–1518, doi:10.1190/1.1441157.

Pan, B., D. Burbank, Y. Wang, G. Wu, J. Li, and Q. Guan (2003), A 900 k.y. record of strath terrace formation during glacial-interglacial transitions in northwest China, *Geology*, *31*(11), 957, doi:10.1130/G19685.1.

Pan, B., H. Gao, G. Wu, J. Li, B. Li, and Y. Ye (2007), Dating of erosion surface and terraces in the eastern Qilian Shan, northwest China, *Earth Surface Processes and Landforms*, *32*(1), 143–154, doi:10.1002/esp.1390.

Pearce, J. A., J. F. Bender, S. E. De Long, W. S. F. Kidd, P. J. Low, Y. Güner, F. Saroglu, Y. Yilmaz, S. Moorbath, and J. G. Mitchell (1990), Genesis of collision volcanism in Eastern Anatolia, Turkey, *Journal of Volcanology and Geothermal Research*, *44*(1-2), 189–229, doi:10.1016/0377-0273(90)90018-B.

Pigati, J. S., J. A. Rech, and J. C. Nekola (2010), Radiocarbon dating of small terrestrial gastropod shells in North America, *Quaternary Geochronology*, *5*(5), 519–532, doi:10.1016/j.quageo.2010.01.001.

Pittore, M., D. Bindi, S. Tyagunov, M. Wieland, M. Picozzi, M. Pilz, S. Ullah, K. Fleming, S. Parolai, J. Zschau, B. Moldobekov, K. Abdrakhmatov, U. Begaliev, P. Yasunov, A. Ishuk, and N. Mikhailova (2011), Seismic Hazard and Risk in Central Asia, *Tech. rep.*, Deutsches GeoForschungsZentrum GFZ, doi:10.2312/GFZ.b103-11149.

Poupinet, G., J. P. Avouac, M. Jiang, S. Wei, E. Kissling, G. Herquel, J. Guilbert, A. Paul, G. Wittlinger, H. Su, and J. C. Thomas (2002), Intracontinental subduction and palaeozoic inheritance of the lithosphere suggested by a teleseismic experiment across the Chinese Tien Shan, *Terra Nova*, *14*(1), 18–24, doi:10.1046/j.1365-3121.2002.00391.x.

Prescott, J., and J. Hutton (1994), Cosmic ray contributions to dose rates for luminescence and ESR dating: Large depths and long-term time variations, *Radiation Measurements*, *23*(1), 497–500, doi:10.1016/1350-4487(94)90086-8.

Priestley, K., E. Debayle, D. McKenzie, and S. Pilidou (2006), Upper mantle structure of eastern Asia from multimode surface waveform tomography, *Journal of Geophysical Research: Solid Earth*, *111*(10), 1–20, doi:10.1029/2005JB004082.

Ragan, D. M. (2009), *Structural geology: an introduction to geometrical techniques*, Cambridge University Press.

Readhead, M. L. (2002), Absorbed dose fraction for 87Rb β particles, *Ancient TL*, *20*(1), 25–28.

Reid, H. F. (1910), The mechanics of the earthquake, The California Earthquake of April 18, 1906:, *Report of the State Earthquake Investigation Commission*, *2*(87).

Reilinger, R., S. McClusky, P. Vernant, S. Lawrence, S. Ergintav, R. Cakmak, H. Ozener, F. Kadirov, I. Guliev, R. Stepanyan, M. Nadariya, G. Hahubia, S. Mahmoud, K. Sakr, A. ArRajehi, D. Paradissis, A. Al-Aydrus, M. Prilepin, T. Guseva, E. Evren, A. Dmitrotsa, S. V. Filikov, F. Gomez, R. Al-Ghazzi, and G. Karam (2006), GPS constraints on continental deformation in the Africa-Arabia-Eurasia continental collision zone and implications for the dynamics of plate interactions, *Journal of Geophysical Research*, *111*(B05411), doi:10.1029/2005JB004051.

Reilinger, R. E., S. Ergintav, R. Burgmann, S. McClusky, O. Lenk, A. Barka, O. Gurkan, L. Hearn, K. L. Feigl, R. Cakmak, B. Aktug, H. Ozener, and M. N. Toksoz (2000), Coseismic and Postseismic Fault Slip for the 17 August 1999, M = 7.5, Izmit, Turkey Earthquake, *Science*, *289*(5484), 1519–1524, doi:10.1126/science.289.5484.1519.

Reimann, T., S. Tsukamoto, M. Naumann, and M. Frechen (2011), The potential of using K-rich feldspars for optical dating of young coastal sediments – A test case from Darss-Zingst peninsula (southern Baltic Sea coast), *Quaternary Geochronology*, *6*(2), 207–222, doi:10.1016/j.quageo.2010.10.001.

Reimer, P. (2013), IntCal13 and Marine13 Radiocarbon Age Calibration Curves 0-50,000 Years cal BP, *Radiocarbon*, *55*(4), 1869–1887, doi:10.2458/azu_js_rc.55.16947.

Reitman, N. G., S. E. K. Bennett, R. D. Gold, R. W. Briggs, and C. B. DuRoss (2015), High-resolution trench photomosaics from image-based modeling: Workflow and error analysis, *Bulletin of the Seismological Society of America*, *105*(5), 2354–2366, doi:10.1785/0120150041.

Rhodes, E. J. (2015), Dating sediments using potassium feldspar single-grain IRSL: Initial methodological considerations, *Quaternary International*, *362*, 14–22, doi:10.1016/j.quaint.2014.12.012.

Rizza, M., J.-F. Ritz, R. Braucher, R. Vassallo, C. Prentice, S. Mahan, S. McGill, A. Chauvet, S. Marco, M. Todbileg, S. Demberel, and D. Bourlès (2011), Slip rate and slip magnitudes of past earthquakes along the Bogd left-lateral strike-slip fault (Mongolia), *Geophysical Journal International*, *186*(3), 897–927, doi:10.1111/j.1365-246X.2011.05075.x.

Rockwell, T. K., and Y. Klinger (2013), Surface rupture and slip distribution of the 1940 Imperial Valley earthquake, Imperial Fault, Southern California: Implications for rupture segmentation and dynamics, *Bulletin of the Seismological Society of America*, *103*(2A), 629–640, doi:10.1785/0120120192.

Rockwell, T. K., S. Lindvall, T. Dawson, R. Langridge, W. Lettis, and Y. Klinger (2002), Lateral Offsets on Surveyed Cultural Features Resulting from the 1999 Izmit and Duzce Earthquakes, Turkey, *Bulletin of the Seismological Society of America*, *92*(1), 79–94, doi:10.1785/0120000809.

Roecker, S. W., T. M. Sabitova, L. P. Vinnik, Y. A. Burmakov, M. I. Golvanov, R. Mamatkanova, and L. Munirova (1993), Three-dimensional elastic wave velocity structure of the western and central Tien Shan, *Journal of Geophysical Research*, *98*(B9), 15,779, doi:10.1029/93JB01560.

Rosen, P. A., S. Hensley, G. Peltzer, and M. Simons (2004), Updated repeat orbit interferometry package released, *Eos, Transactions American Geophysical Union*, *85*(5), 47, doi:10.1029/2004EO050004.

Sala, R., and J.-M. Deom (2005), *Petroglyphs of South Kazakhstan*, Laboratory of Geoarchaeology, Centre of Geologo-Geographical Research, Ministry of Sciences, Kazakhstan.

Salisbury, J. B., T. K. Rockwell, T. J. Middleton, and K. W. Hudnut (2012), LiDAR and Field Observations of Slip Distribution for the Most Recent Surface Ruptures along the Central San Jacinto Fault, *Bulletin of the Seismological Society of America*, *102*(2), 598–619, doi:10.1785/0120110068.

Salisbury, J. B., D. Haddad, T. Rockwell, J. R. Arrowsmith, C. Madugo, O. Zielke, and K. Scharer (2015), Validation of meter-scale surface faulting offset measurements from high-resolution topographic data, *Geosphere*, *11*(6), 1884–1901, doi:10.1130/GES01197.1.

Saroglu, F., Ö. Emre, and I. Kuşçu (1992), Active Fault Map of Turkey, *Tech. rep.*, General Directorate of Mineral Research and Exploration (MTA), Eskisehir Yolu, 06520, Ankara, Turkey.

Scharer, K. M., J. B. Salisbury, J. R. Arrowsmith, and T. K. Rockwell (2014), Southern San Andreas Fault Evaluation Field Activity: Approaches to Measuring Small Geomorphic Offsets–Challenges and Recommendations for Active Fault Studies, *Seismological Research Letters*, *85*(1), 68–76, doi:10.1785/0220130108.

Schmidt, S., R. Hetzel, J. Kuhlmann, F. Mingorance, and V. a. Ramos (2011), A note of caution on the use of boulders for exposure dating of depositional surfaces, *Earth and Planetary Science Letters*, *302*(1-2), 60–70, doi:10.1016/j.epsl.2010.11.039.

Scholz, C. H. (1974), Post-Earthquake Dilatancy Recovery, *Geology*, *2*(11), 551–554, doi:10.1130/0091-7613(1974)2<551:PDR>2.0.CO;2.

Scholz, C. H. (1994), A reappraisal of large earthquake scaling, *Bulletin of the Seismological Society of America*, *84*(l), 215–218, doi:10.1016/0148-9062(94)90076-0.

Scholz, C. H. (1998), Earthquakes and friction laws, *Nature*, *391*(6662), 37–42, doi:10.1038/34097.

Scholz, C. H., N. H. Dawers, J.-Z. Yu, M. H. Anders, and P. A. Cowie (1993), Fault growth and fault scaling laws: Preliminary results, *Journal of Geophysical Research*, *98*(B12), 951–961, doi:10.1029/93JB01008.

Schwartz, D. P., and K. J. Coppersmith (1984), Fault behavior and characteristic earthquakes: Examples from the Wasatch and San Andreas Fault Zones, *Journal of Geophysical Research: Solid Earth*, *89*(B7), 5681–5698, doi:10.1029/JB089iB07p05681.

Schwartz, D. P., P. J. Haeussler, G. G. Seitz, and T. E. Dawson (2012), Why the 2002 Denali fault rupture propagated onto the Totschunda fault: Implications for fault branching and seismic hazards, *Journal of Geophysical Research: Solid Earth*, *117*(B11304), doi:10.1029/2011JB008918.

Segall, P. (2010), *Earthquake and volcano deformation*, Chapter 3 pp., Princeton University Press.

Selander, J., M. Oskin, C. Ormukov, and K. Abdrakhmatov (2012), Inherited strike-slip faults as an origin for basement-cored uplifts: Example of the Kungey and Zailiskey ranges, northern Tian Shan, *Tectonics*, *31*(4), doi:10.1029/2011TC003002.

Sharp, W. D., K. R. Ludwig, O. A. Chadwick, R. Amundson, and L. L. Glaser (2003), Dating fluvial terraces by 230Th/U on pedogenic carbonate, Wind River Basin, Wyoming, *Quaternary Research*, *59*(2), 139–150, doi:10.1016/S0033-5894(03)00003-6.

Shebalin, N., A. Nikonov, R. Tatevosian, N. Mokrushina, A. Petrossian, N. Kondorskaya, E. Khrometskaya, A. Karakhanian, R. Harutunian, A. Asatrian, S. Piruzian, A. Gassanov, O. Varazanashvili, V. Papalashvili, G. Golinskiy, B. Karryev, B. Pustovitenko, and V. Kulchtiskiy (1997), Caucasus test-area strong earthquake catalogue, in *Historical and prehistorical earthquakes in the Caucasus : [proceedings of the NATO Advanced Research Workshop on Historical and Prehistorical Earthquakes in the Caucasus, Yerevan, Armenia, July 11-15, 1996]*, pp. 210–223, Kluwer Academic Publishing, Dordrecht, Netherlands.

Shen, Z. K., R. W. King, D. C. Agnew, M. Wang, T. A. Herring, D. Dong, and P. Fang (2011), A unified analysis of crustal motion in Southern California, 1970-2004: The SCEC crustal motion map, *Journal of Geophysical Research: Solid Earth*, *116*(11), 1–19, doi:10.1029/2011JB008549.

Sloan, R. A., J. A. Jackson, D. McKenzie, and K. Priestley (2011), Earthquake depth distributions in central Asia, and their relations with lithosphere thickness, shortening and extension, *Geophysical Journal International*, *185*(1), 1–29, doi:10.1111/j.1365-246X.2010.04882.x.

Smith, S. W., and M. Wyss (1968), Displacement on the San Andreas fault subsequent to the 1966 Parkfield earthquake, *Bulletin of the Seismological Society of America*, *58*(6), 1955–1973.

Smith, W., and P. Wessel (1990), Gridding with continuous curvature splines in tension, *Geophysics*, *55*(3), 293–305.

Snavely, N., S. Seitz, and R. Szeliski (2006), Photo tourism: exploring photo collections in 3D, *ACM transactions on graphics (TOG)*, pp. 835–846.

Sobel, E. R., M. Oskin, D. Burbank, and A. Mikolaichuk (2006), Exhumation of basement-cored uplifts: Example of the Kyrgyz Range quantified with apatite fission track thermochronolgy, *Tectonics*, *25*(2), doi:10.1029/2005TC001809.

Steffen, D., F. Preusser, and F. Schlunegger (2009), OSL quartz age underestimation due to unstable signal components, *Quaternary Geochronology*, *4*(5), 353–362, doi:10.1016/j.quageo.2009.05.015.

Steffen, R., H. Steffen, and G. Jentzsch (2011), A three-dimensional Moho depth model for the Tien Shan from EGM2008 gravity data, *Tectonics*, *30*(5), 1–19, doi:10.1029/2011TC002886.

Steinbrugge, K. V., E. G. Zacher, D. Tocher, C. A. Whitten, and C. N. Claire (1960), Creep on the San Andreas Fault, *Bulletin of the Seismological Society of America*, *50*(3), 389–396.

Stirling, M., T. Goded, K. Berryman, and N. Litchfield (2013), Selection of Earthquake Scaling Relationships for Seismic-Hazard Analysis, *Bulletin of the Seismological Society of America*, *103*(6), 2993–3011, doi:10.1785/0120130052.

Stockhecke, M., M. Sturm, I. Brunner, H.-U. Schmincke, M. Sumita, R. Kipfer, D. Cukur, O. Kwiecien, and F. S. Anselmetti (2014), Sedimentary evolution and environmental history of Lake Van (Turkey) over the past 600 000 years, *Sedimentology*, *61*(6), 1830–1861, doi:10.1111/sed.12118.

Suvorov, A. I. (1964), Contribution To the Description of the Aktas Fault Zone, Central Kazakhstan, *International Geology Review*, *6*(3), 507–518, doi:10.1080/00206816409473927.

Szeliga, W., R. Bilham, D. M. Kakar, and S. H. Lodi (2012), Interseismic strain accumulation along the western boundary of the Indian subcontinent, *Journal of Geophysical Research: Solid Earth*, *117*(8), 1–14, doi:10.1029/2011JB008822.

Tadono, T., H. Ishida, F. Oda, S. Naito, K. Minakawa, and H. Iwamoto (2014), Precise Global DEM Generation by ALOS PRISM, *ISPRS Annals of Photogrammetry, Remote Sensing and Spatial Information Sciences*, *II-4*(May), 71–76, doi:10.5194/isprsannals-II-4-71-2014.

Takaku, J., T. Tadono, and K. Tsutsui (2014), Generation of High Resolution Global DSM from ALOS PRISM, *ISPRS - International Archives of the Photogrammetry, Remote Sensing and Spatial Information Sciences*, *XL-4*(4), 243–248, doi:10.5194/isprsarchives-XL-4-243-2014.

Tapponnier, P., and P. Molnar (1979), Active faulting and cenozoic tectonics of the Tien Shan, Mongolia, and Baykal Regions, *Journal of Geophysical Research: Solid Earth*, *84*(B7), 3425–3459, doi:10.1029/JB084iB07p03425.

Thatcher, W. (1983), Nonlinear strain buildup and the earthquake cycle on the San Andreas Fault, *Journal of Geophysical Research: Solid Earth*, *88*(B7), 5893–5902, doi:10.1029/JB088iB07p05893.

Thatcher, W. (2009), How the Continents Deform: The Evidence From Tectonic Geodesy, *Annual Review of Earth and Planetary Sciences*, *37*(1), 237–262, doi:10.1146/annurev.earth.031208.100035.

Thierry, J. M. (1979), Monasteres Armeniens du Vaspurakan, *Revue Etudes Armeniens*, *9*, 137–178.

Thomas, M. Y., J.-P. Avouac, J. Champenois, J.-C. Lee, and L.-C. Kuo (2014), Spatiotemporal evolution of seismic and aseismic slip on the Longitudinal Valley Fault, Taiwan, *Journal of Geophysical Research: Solid Earth*, *119*(6), 5114–5139, doi:10.1002/2013JB010603.

Thompson, S. C., R. J. Weldon, C. M. Rubin, K. Abdrakhmatov, P. Molnar, and G. W. Berger (2002), Late Quaternary slip rates across the central Tien Shan, Kyrgyzstan, central Asia, *Journal of Geophysical Research*, *107*(B9), 2203, doi:10.1029/2001JB000596.

Thomsen, K. J., A. S. Murray, M. Jain, and L. Bøtter-Jensen (2008), Laboratory fading rates of various luminescence signals from feldspar-rich sediment extracts, *Radiation Measurements*, *43*(9–10), 1474–1486, doi:10.1016/j.radmeas.2008.06.002.

Tibaldi, A. (1998), Effects of topography on surface fault geometry and kinematics: examples from the Alps, Italy and Tien Shan, Kazakstan, *Geomorphology*, *24*(2-3), 225–243, doi:10.1016/S0169-555X(98)00018-X.

Tibaldi, A., E. Graziotto, F. Forcella, and V. H. Gapich (1997), Morphotectonic indicators of Holocene faulting in central Tien Shan, Kazakstan, and geodynamic implications, *Journal of Geodynamics*, *23*(1), 23–45, doi:10.1016/S0264-3707(96)00021-X.

Titus, S. J., C. DeMets, and B. Tikoff (2006), Thirty-five-year creep rates for the creeping segment of the San Andreas fault and the effects of the 2004 Parkfield earthquake: Constraints from alignment arrays, continuous global positioning system, and creepmeters, *Bulletin of the Seismological Society of America*, *96*(4 B), 250–268, doi:10.1785/0120050811.

Toda, S. (2005), Forecasting the evolution of seismicity in southern California: Animations built on earthquake stress transfer, *Journal of Geophysical Research*, *110*(B5), B05S16, doi:10.1029/2004JB003415.

Treiman, J. A. (2002), Primary Surface Rupture Associated with the Mw 7.1 16 October 1999 Hector Mine Earthquake, San Bernardino County, California, *Bulletin of the Seismological Society of America*, *92*(4), 1171–1191, doi:10.1785/0120000923.

Üner, S., Ç. Yeşilova, and T. Yakupoğlu (2012), *The Traces of Earthquake (Seismites): Examples from Lake Van Deposits (Turkey)*, 21–32 pp., InTech.

Üner, S., C. Okuldaş, and A. V. Yilmaz (2015), Structural and Sedimentological Properties of Lacustrine Deposits in Pliocene Dorutay Basin (Özalp-Van) (In Turkish), *Bulletin of the Earth Sciences Application and Research Centre of Hacettepe University*, *36*(1), 19–30.

Utkucu, M. (2013), 23 October 2011 Van, Eastern Anatolia, earthquake (MW 7.1) and seismotectonics of Lake Van area, *Journal of Seismology*, *17*(2), 783–805, doi:10.1007/s10950-012-9354-z.

van Calsteren, P., and L. Thomas (2006), Uranium-series dating applications in natural environmental science, *Earth-Science Reviews*, *75*(1-4), 155–175, doi:10.1016/j.earscirev.2005.09.001.

Van Der Woerd, J., P. Tapponnier, F. J. Ryerson, A.-s. Meriaux, B. Meyer, Y. Gaudemer, R. C. Finkel, M. W. Caffee, Z. Guoguang, and X. Zhiqin (2002), Uniform postglacial slip-rate along the central 600 km of the Kunlun Fault (Tibet), from 26Al, 10Be, and 14C dating of riser offsets, and climatic origin of the regional morphology, *Geophysical Journal International*, *148*(3), 356–388, doi:10.1046/j.1365-246x.2002.01556.x.

Vernant, P., F. Nilforoushan, D. Hatzfeld, M. R. Abbassi, C. Vigny, F. Masson, H. Nankali, J. Martinod, a. Ashtiani, R. Bayer, F. Tavakoli, and J. Chéry (2004), Present-day crustal deformation and plate kinematics in the Middle East constrained by GPS measurements in Iran and northern Oman, *Geophysical Journal International*, *157*, 381–398, doi:10.1111/j.1365-246X.2004.02222.x.

Vinnik, L. P., C. Reigber, I. M. Aleshin, G. L. Kosarev, M. K. Kaban, S. I. Oreshin, and S. W. Roecker (2004), Receiver function tomography of the central Tien Shan, *Earth and Planetary Science Letters*, *225*(1-2), 131–146, doi:10.1016/j.epsl.2004.05.039.

Vinnik, L. P., I. M. Aleshin, M. K. Kaban, S. G. Kiselev, G. L. Kosarev, S. I. Oreshin, and C. Reigber (2006), Crust and mantle of the Tien Shan from data of the receiver function tomography, *Izvestiya, Physics of the Solid Earth*, *42*(8), 639–651, doi:10.1134/S1069351306080027.

Walker, R., and J. Jackson (2004), Active tectonics and late Cenozoic strain distribution in central and eastern Iran, *Tectonics*, *23*(5), 1–24, doi:10.1029/2003TC001529.

Walker, R. T., and M. Fattahi (2011), A framework of Holocene and Late Pleistocene environmental change in eastern Iran inferred from the dating of periods of alluvial fan abandonment, river terracing, and lake deposition, *Quaternary Science Reviews*, *30*(9-10), 1256–1271, doi:10.1016/j.quascirev.2011.03.004.

Wallace, R. E. (1977), Profiles and ages of young fault scarps, north-central Nevada, *Geological Society of America Bulletin*, *88*(9), 1267, doi:10.1130/0016-7606(1977)88<1267:PAAOYF>2.0.CO;2.

Walpersdorf, A., I. Manighetti, Z. Mousavi, F. Tavakoli, M. Vergnolle, A. Jadidi, D. Hatzfeld, A. Aghamohammadi, A. Bigot, Y. Djamour, H. Nankali, and M. Sedighi (2014), Present-day kinematics and fault slip rates in eastern Iran, derived from 11 years of GPS data, *Journal of Geophysical Research: Solid Earth*, *119*(2), 1359–1383, doi:10.1002/2013JB010620.

Walters, R. J., J. R. Elliott, Z. Li, and B. Parsons (2013), Rapid strain accumulation on the Ashkabad fault (Turkmenistan) from atmosphere-corrected InSAR, *Journal of Geophysical Research: Solid Earth*, *118*(7), 3674–3690, doi:10.1002/jgrb.50236.

Wang, C., X. Ding, Q. Li, X. Shan, W. Zhu, B. Guo, and P. Liu (2015), Coseismic and postseismic slip models of the 2011 Van earthquake, Turkey, from InSAR, offset-tracking, MAI, and GPS observations, *Journal of Geodynamics*, *91*, 39–50, doi:10.1016/j.jog.2015.08.006.

Wang, Q. (2001), Present-Day Crustal Deformation in China Constrained by Global Positioning System Measurements, *Science*, *294*(5542), 574–577, doi:10.1126/science.1063647.

Wang, Z. (2008), A preliminary report on the Great Wenchuan Earthquake, *Earthquake Engineering and Engineering Vibration*, *7*(2), 225–234, doi:10.1007/s11803-008-0856-1.

Wei, S., E. Fielding, S. Leprince, A. Sladen, J.-P. Avouac, D. Helmberger, E. Hauksson, R. Chu, M. Simons, K. Hudnut, T. Herring, and R. Briggs (2011), Superficial simplicity of the 2010 El Mayor–Cucapah earthquake of Baja California in Mexico, *Nature Geoscience*, *4*(9), 615–618, doi:10.1038/ngeo1213.

Wells, D. L., and K. J. Coppersmith (1994), New Empirical Relationships among Magnitude, Rupture Length, Rupture Width, Rupture Area, and Surface Displacement, *Bulletin of the Seismological Society of America*, *84*(4), 974–1002.

Wesnousky, S. G. (2008), Displacement and Geometrical Characteristics of Earthquake Surface Ruptures: Issues and Implications for Seismic-Hazard Analysis and the Process of Earthquake Rupture, *Bulletin of the Seismological Society of America*, *98*(4), 1609–1632, doi:10.1785/0120070111.

Wesnousky, S. G., and C. H. Jones (1994), Oblique slip, slip partitioning, spatial and temporal changes in the regional stress field, and the relative strength of active faults in the Basin and Range, western United States, *Geology*, *22*(11), 1031, doi:10.1130/0091-7613(1994)022<1031:OSSPSA>2.3.CO;2.

Wessel, P., and W. H. F. Smith (1998), New, improved version of generic mapping tools released, *Eos, Transactions American Geophysical Union*, *79*(47), 579–579, doi:10.1029/98EO00426.

Wesson, R. L. (1988), Dynamics of fault creep, *Journal of Geophysical Research*, *93*(B8), 8929, doi:10.1029/JB093iB08p08929.

Westoby, M., J. Brasington, N. Glasser, M. Hambrey, and J. Reynolds (2012), 'Structure-from-Motion' photogrammetry: A low-cost, effective tool for geoscience applications, *Geomorphology*, *179*, 300–314, doi:10.1016/j.geomorph.2012.08.021.

Wilkinson, M., K. J. W. McCaffrey, G. Roberts, P. A. Cowie, R. J. Phillips, A. M. Michetti, E. Vittori, L. Guerrieri, A. M. Blumetti, A. Bubeck, A. Yates, and G. Sileo (2010), Partitioned postseismic deformation associated with the 2009 Mw 6.3 LAquila earthquake surface rupture measured using a terrestrial laser scanner, *Geophysical Research Letters*, *37*(L10309), doi:10.1029/2010GL043099.

Windley, B. F., M. B. Allen, C. Zhang, Z.-Y. Zhao, and G.-R. Wang (1990), Paleozoic accretion and Cenozoic redeformation of the Chinese Tien Shan Range, central Asia, *Geology*, *18*(2), 128, doi:10.1130/0091-7613(1990)018<0128:PAACRO>2.3.CO;2.

Wintle, A. G. (1973), Anomalous Fading of Thermo-luminescence in Mineral Samples, *Nature*, *245*(5421), 143–144, doi:10.1038/245143a0.

Wintle, A. G., and A. S. Murray (2006), A review of quartz optically stimulated luminescence characteristics and their relevance in single-aliquot regeneration dating protocols, *Radiation Measurements*, *41*(4), 369–391, doi:10.1016/j.radmeas.2005.11.001.

Wright, T. J., J. R. Elliott, H. Wang, and I. Ryder (2013), Earthquake cycle deformation and the Moho: Implications for the rheology of continental lithosphere, *Tectonophysics*, *609*, 504–523, doi:10.1016/j.tecto.2013.07.029.

Yin, A., S. Nie, P. Craig, T. M. Harrison, F. J. Ryerson, Q. Xianglin, and Y. Geng (1998), Late Cenozoic tectonic evolution of the southern Chinese Tian Shan, *Tectonics*, *17*(1), 1–27, doi:10.1029/97TC03140.

Zabelina, I. V., I. Y. Koulakov, and M. M. Buslov (2013), Deep mechanisms in the Kyrgyz Tien Shan orogen (from results of seismic tomography), *Russian Geology and Geophysics*, *54*(7), 695–706, doi:10.1016/j.rgg.2013.06.005.

Zahradnik, J., and E. Sokos (2011), Multiple-point source solution of the Mw7.2 Van earthquake, October 23, 2011, Eastern Turkey., *Tech. rep.*, European-Mediterranean Seismological Centre (EMSC).

Zahradnik, J., and E. Sokos (2014), The Mw 7.1 Van, Eastern Turkey, earthquake 2011: two-point source modelling by iterative deconvolution and non-negative least squares, *Geophysical Journal International*, *196*(1), 522–538, doi:10.1093/gji/ggt386.

Zechar, J. D., and K. L. Frankel (2009), Incorporating and reporting uncertainties in fault slip rates, *Journal of Geophysical Research: Solid Earth*, *114*(12), 1–9, doi:10.1029/2009JB006325.

Zhiwei, L., S. Roecker, L. Zhihai, W. Bin, W. Haitao, G. Schelochkov, and V. Bragin (2009), Tomographic image of the crust and upper mantle beneath the western Tien Shan from the MANAS broadband deployment: Possible evidence for lithospheric delamination, *Tectonophysics*, *477*(1-2), 49–57, doi:10.1016/j.tecto.2009.05.007.

Zhou, Y., J. R. Elliott, B. Parsons, and R. T. Walker (2015a), The 2013 Balochistan earthquake: An extraordinary or completely ordinary event?, *Geophysical Research Letters*, *42*(15), 6236–6243, doi:10.1002/2015GL065096.

Zhou, Y., B. Parsons, J. R. Elliott, I. Barisin, and R. T. Walker (2015b), Assessing the ability of Pleiades stereo imagery to determine height changes in earthquakes: A case study for the El Mayor-Cucapah epicentral area, *Journal of Geophysical Research: Solid Earth*, *120*(12), 8793–8808, doi:10.1002/2015JB012358.

Zhou, Y., R. T. Walker, J. R. Elliott, and B. Parsons (2016), Mapping 3D fault geometry in earthquakes using high-resolution topography: Examples from the 2010 El Mayor-Cucapah (Mexico) and 2013 Balochistan (Pakistan) earthquakes, *Geophysical Research Letters*, doi:10.1002/2016GL067899.

Zielke, O., and J. R. Arrowsmith (2012), LaDiCaoz and LiDARimager–MATLAB GUIs for LiDAR data handling and lateral displacement measurement, *Geosphere*, *8*(1), 206, doi:10.1130/GES00686.1.

Zielke, O., Y. Klinger, and J. R. Arrowsmith (2015), Fault slip and earthquake recurrence along strike-slip faults – Contributions of high-resolution geomorphic data, *Tectonophysics*, *638*, 43–62, doi:10.1016/j.tecto.2014.11.004.

Zimmerman, D. W. (1971), Thermoluminescence dating using fine grains from pottery, *Archaeometry*, *13*(I), 29–52.

Zinke, R., J. Hollingsworth, and J. F. Dolan (2014), Surface slip and off-fault deformation patterns in the 2013 Mw 7.7 Balochistan, Pakistan earthquake: Implications for controls on the distribution of near-surface coseismic slip, *Geochemistry, Geophysics, Geosystems*, *15*(12), 5034–5050, doi:10.1002/2014GC005538.

Zubovich, A. V., X.-Q. Wang, Y. G. Scherba, G. G. Schelochkov, R. Reilinger, C. Reigber, O. I. Mosienko, P. Molnar, W. Michajljow, V. I. Makarov, J. Li, S. I. Kuzikov, T. A. Herring, M. W. Hamburger, B. H. Hager, Y.-M. Dang, V. D. Bragin, and R. T. Beisenbaev (2010), GPS velocity field for the Tien Shan and surrounding regions, *Tectonics*, *29*(6), doi:10.1029/2010TC002772.

Appendix A

Methods – Technical Specifcations

A.1 Van OSL Dating technical specifications

Optically stimulated luminescence dating was performed on quartz grains from sediment samples collected in well packed stainless steel tubes to ensure sample stability in transport. Sample preparation was carried out under low-intensity light emitting diode (LED) light (at ∼588 nm), to yield clean, sand-sized (180–250 μm) quartz, using standard methods including wet-sieving, HCL acid digestion, heavy liquid separation and etching in concentrated HF (40%) to dissolve potassium feldspar minerals and the alpha-dosed outer layer of the quartz grains. At least 12 aliquots were prepared and measured for each sample, mounting the quartz grains as a multigrain monolayer on aluminium disks of ∼4 mm diameter using a silicon oil adhesive. To estimate the burial age of our samples, we need two components, the equivalent dose *De* (integrated radiation required to produce the luminescence signal observed) and the environmental dose rate received during burial.

The equivalent dose (*De*) was recovered using the single aliquot regeneration measurement protocol (*Murray and Wintle*, 2000; *Wintle and Murray*, 2006), conducted on an automated TL/DA-15 Risø luminescence reader (*Bøtter-Jensen et al.*, 2000; *Bøtter-Jensen*, 1997). The sample was bleached with clusters of 870 nm infrared LEDs providing circa 131 mW cm^{-2} at 50°C for 100 s to confirm the absence of any infrared sensitive signal (*Banerjee and Murray*, 2001), before blue light stimulation with clusters of blue LEDs (42 Nichia 470Δ20 nm, ∼34 W cm^{-2}) at a raised temperature of 125°. The natural and regenerative luminescence dose samples were preheated at 260°C for 10 s, while the fixed test dose samples (to calibrate for sensitivity change) were preheated to 240°C for 10 s prior to optical stimulation. Ultraviolet (∼370 nm) OSL emission was measured using an Electron Tubes Ltd 9235QA photomultiplier tube fitted with a blue-green sensitive bialkali photocathode and either two Corning U-340 glass filters or a 7.5 mm Hoya U-340 glass filter.

After measuring the natural luminescence, a calibrated ^{90}Sr/^{90}Y beta source housed in the reader was used to construct the regenerative dose response curve. The luminescences were measured at 6–8 different doses, including a zero dose point and a duplicate measurement of the lowest regenerative dose to check recovery. Following each luminescence measurement, a test dose and second pre-heat are applied to the aliquot to normalise the luminescence measurement and calibrate for sensitivity change (*Murray and Wintle*, 2000). Fitting a dose response curve, we determined the equivalent dose *De* from the natural luminescence.

The 5 cm of sediment at either end of the collection tube (deemed to have been exposed to light), was used to estimate the concentrations of potassium-40, uranium-238 and thorium-232 by inductively coupled plasma mass spectrometry (ICP-MS) with a lithium metaborate/tetraborate fusion. These concentrations are used to estimate an environmental dose rate from the gamma and beta components of the decay chains for ^{40}K, ^{232}Th, ^{238}U, using the attenuation factors estimated by *Adamiec and Aitken* (1998), with corrections for water content (*Zimmerman*, 1971) and grain size *Mejdahl* (1979). We estimate a cosmic

ray dose rate based on data reported by *Prescott and Hutton* (1994), accounting for the geomagnetic latitude and elevation along with the density and thickness of the overburden. Table 2.3 shows the OSL ages determined, with the relevant site and the displacement at that site.

A.2 Karkara Rangefront OSL and IRSL details

A.2.1 Sample Preparation

Samples were treated with HCl and H_2O_2 to remove carbonates and organics respectively, prior to wet sieving to isolate a size fraction for analysis (given per sample in Tables 3.2–3.3). A preliminary density separation was performed to isolate heavy minerals in the fraction < 2.7 g cm^{-3}, then a second separation to isolate quartz (>2.58 g cm^{-3}) and K-feldspar grains (<2.58 g cm^{-3}). The quartz fraction was treated for 45 minutes in 48% HF to etch the outer 10 μm of the grains and remove any remaining feldspar grains. The feldspar was similarly treated with a 15 minute etch in 10% HF. Lastly the samples were dry sieved to re-isolate the original size fraction.

A.2.2 Sample properties and analysis protocols

All luminescence measurements were performed on a Risoe DA20 TL/OSL reader. For quartz measurements, stimulation (40 s at 125°C) was provided by blue LEDs (stimulation wave length 470 nm) at 70% power (delivering c. 72 mW cm^{-2} to the sample) and the resulting OSL signals were detected with an EMI 9235QA photomultiplier tube and a U-340 filter.

For K-feldspar measurements, stimulation was provided by IR diodes (wavelength 870 nm). Detection of the resulting (blue-violet) IRSL was through a combination of Schott BG39 filters and Corning 7-59 filters (detection range 320 – 450 nm). Laboratory irradiations were performed by a 90Sr beta source with a dose rate (at the time of measurement) of 8.58 to 8.44 Gy min^{-1}. This was derived from calibration against the Risoe calibration quartz and has been validated via comparison with an external luminescence dating laboratory.

Analyses were conducted on small (2 mm) aliquots; given the size fraction analysed, these will likely comprise a signal derived from several hundred grains (e.g. *Duller*, 2008). Growth curves were constructed using a saturating exponential fit in the "Analyst" software and the associated errors derived using a Monte Carlo simulation (*Duller*, 2007), incorporating a 1.5% systematic instrument error.

A.2.3 Environmental dose rate determination

For all luminescence samples, the ∼5 cm of material at the ends of the sampling tube provided an estimate of the modern water content and a sub-sample of this was used to obtain, via ICP-MS and ICP-OES estimates, the uranium, thorium and potassium contents of the samples. The D_e for the feldspar also

includes a component due to the internal Rb and K composition. Though there are errors in estimating this component, this makes the K-feldspar IRSL age estimate less sensitive to errors in the external D_e.

The total uranium, thorium and potassium contents of the sample were determined from sub-samples of the sampling tubes using inductively-coupled plasma mass spectrometry at SGS laboratories, Vancouver, Canada. Elemental concentrations were converted to dose rates using the conversion factors of *Guérin et al.* (2011), with appropriate adjustment for grain size (*Mejdahl*, 1979; *Readhead*, 2002) and sample water content (*Aitken*, 1985). An "a value" (effective alpha) of 0.15±0.05 was applied to the estimation of the external alpha dose (*Balescu and Lamothe*, 1994). Dose rates for internal K and Rb were based on the assumption of K-feldspar grain K and Rb concentrations of 12.5±0.5 % and 400±100 ppm respectively (*Huntley and Baril*, 1997; *Huntley and Hancock*, 2001). It was assumed that the as-measured water content was appropriate and a 3% (absolute) uncertainty in water content was propagated into the final dose rate uncertainties. It is assumed that the dose rate remained constant for the duration of burial. Cosmic dose rates were determined following *Prescott and Hutton* (1994) and were based on the current sample burial depth.

A.3 Karkara Rangefront Seismic Reflection Profiles

In each case the precise topographic location of the geophones was captured using a kinematic DGPS profile. We use a Seistronix RAS-24 24 channel receiver with single component geophones. Balancing time and power constraints, we performed the two profiles across the primary scarp as three end-to-end lines each, with 7 shots per line, performed using a sledgehammer and steel plate. Geophone recording was triggered through connection between the sledgehammer and plate.

The data was analysed using the ReflexW Software (Sandmeier Geophysical Research), performing a shallow seismic refraction analysis using the generalised reciprocal method (*Palmer*, 1981). At each shot location, 4-5 hammer strikes were stacked at acquisition time to improve the signal-to-noise ratio. For each shot, first arrivals were picked manually and plotted to create travel time curves. Critical distances were picked manually from the travel time curve, identifying the change from the direct wave to successive head waves. Based on these selected changes, we perform a tomographic inversion for the velocity structure of the medium.

Figure 3.7 showed the resultant velocity model for profile C across the secondary scarp; the upper 4–5 m shows lower velocities, interpreted as unconsolidated gravels, below which we see higher velocity basement material interpreted to be the Neogene sediments. Unfortunately, due to the size of the primary scarp the depth penetration of this method was insufficient to resolve faulting distorted layers in profiles A and B (Figure A.1).

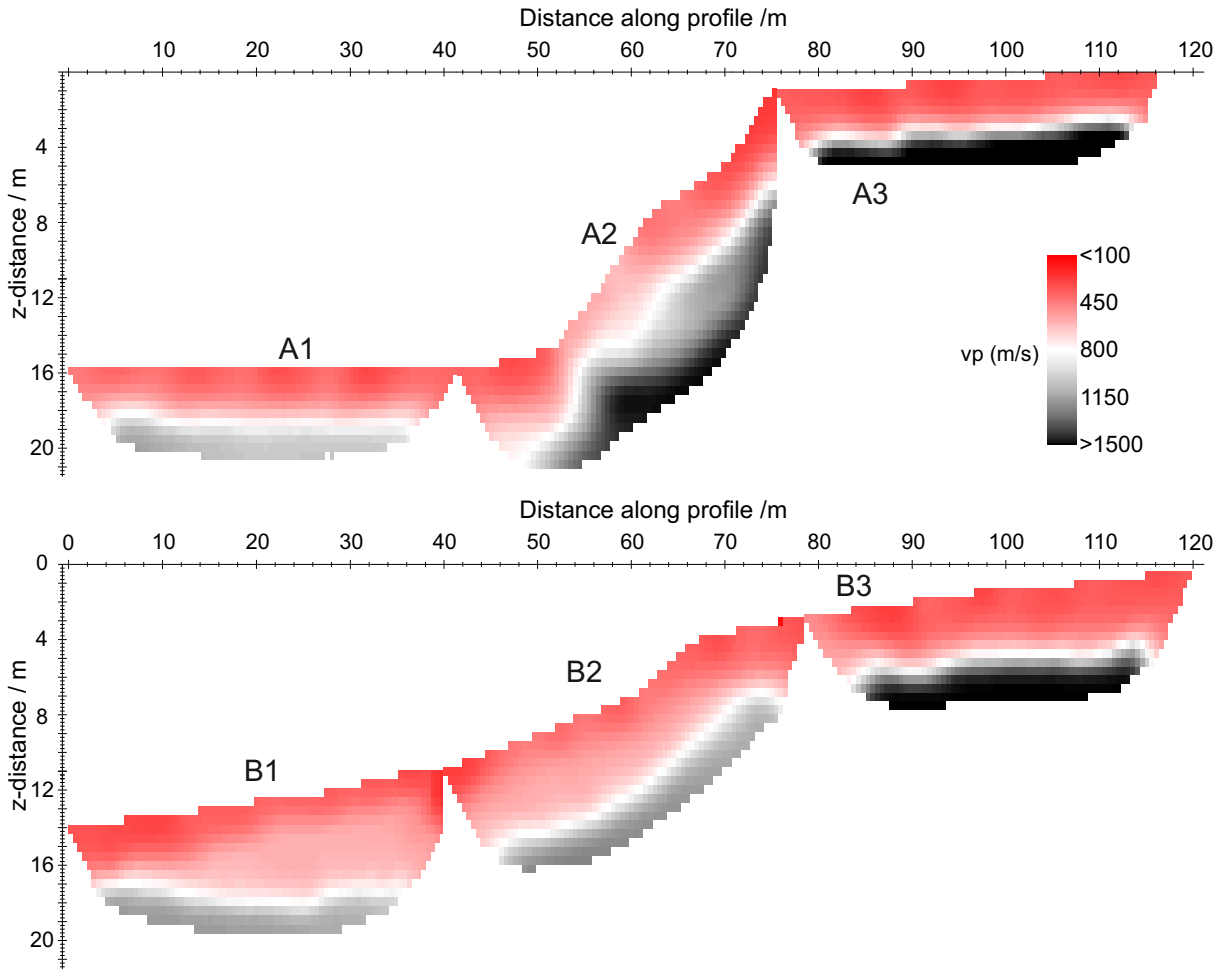


Figure A.1: Hammer seismic refraction model for profiles A and B (locations in Figure 3.6). The high velocity Neogene bedrock is visible at the base of the layer, but no fault relation is resolved. 2x vertical exaggeration.

Appendix B

Matlab Scripts

B.1 Monte-Carlo Throw Estimation

```
% Script provided as a Supplement to:
% Untangling Slip-Distribution and Offset Landform Geometry: Rigorous Quantification of ...
    Fault Slip in 3D
% (Geosphere)
% Authored by:
% David Mackenzie (1), Austin Elliott (1)
%
% (1) Department of Earth Sciences, University of Oxford.
%
% Please cite this work when using this script or an adaptation of it.
%
%%%%%%%%%%%%%%%%%%%%%%%%%%%%%%%%%%%%%%%%%%%%%%%%%%%%%%%%%%%%%%%%%%%%%%%%%%%%%%%
%% An example of throw estimation from a profile by Monte-Carlo Simulation
function [h,N] = MonteCarlo_ThrowEstimate(dip_min, dip_max, params, param_errs, nmax)
% [h,N] = MonteCarlo_ThrowEstimate(dip_min, dip_max, params, param_errs, nmax)
%
% Example code to estimate throw probability distribution function from a
% profile or pair of planes where the orientation of the topographic
% surface is known. I demonstrate here with a uniform distribution for the
% fault dip, and gaussian distributions for the profile delta-z,
% topographic azimuth, and ratio of lateral to dip slip.
%
% Inputs:
%   dip_min, dip_max=> min and max fault dips
%   params     => vector of the gaussian distributed parameters.
%   param_errs => standard errors on each parameter
%   nmax       => number of samples in the PDFs
%
% The gaussian PDF parameters are the vector:
% [delz, slsd, psi, theta]
% Where:
%   delz            => vertical offset measured by profile (HW relative to
%                       FW, ie. +ve for reverse, -ve for normal)
%   slsd            => ratio of lateral slip to dip slip
%   psi             => topographic slope azimuth (in degrees, -180 -- 180)
%   theta           => topographic slope angle (in degrees, 0-90 )
%
% Output:
%   h   => Figure handle
%   N   => nmax samples of the throw PDF (optional!)
%
% NOTE: Requires MATLAB 2015 or later (PDF support)
%
%% Minimal Test Example:
%
% dip_min = 50;
% dip_max = 70;
% % [delz, slsd, psi, theta]
% params = [7.2, 4.5, -32, 7.9];
% param_errs = [0.3, 0.5, 5, 0.5];
% nmax = 1000000;
% [h,N] = MonteCarlo_ThrowEstimate(dip_min, dip_max, params, param_errs, nmax);
%%%%%%%%%%%%%%%%%%%%%%%%%%%%%%%%%%%%%%%%%%%%%%%%%%%%%%%%%%%%%%%%%%%%%%%%%%%%%%%
%% Parse input:
if length(params)~=4 || length(param_errs)~=4
    error('Must supply a 4 element parameter vector and 4 element corresponding error ...
        vector.')
end

delz = params(1);
delz_err = param_errs(1);
slsd = params(2);
slsd_err = param_errs(2);
psi = params(3);
psi_err = param_errs(3);
theta = params(4);
theta_err = param_errs(4);

%% Defaults
```

```
% set number of histogram bins to plot.
nbins = 400;

%% Input checking:
if nargin < 4
    error('Not enough arguments supplied')
elseif nargin == 4
    nmax = 1000000;
elseif nargin > 5
    error('Too many input arguments.')
end
if dip_min < -90 || dip_min > 90 || dip_max > 90 || dip_max < -90 ...
        || dip_max <= dip_min
    error('Dip must be -90 -- 90 and dip_max>dipmin. A dip of <0 implies a scarp against ...
        the topography (uphill side downthrown), while dip>0 is an ordinary scarp with the ...
        downhill downthrown.')
end
if theta < 0 || theta >= 90
    error('Topographic slope angle must be 0 -- 90!')
end
if nmax<=0
    error('nmax must be >0')
end

%% Generate input PDFs
pd_delz = makedist('Normal','mu',delz,'sigma',delz_err);
pd_slsd = makedist('Normal','mu',slsd,'sigma',slsd_err);
pd_psi = makedist('Normal','mu',psi,'sigma',psi_err);
pd_theta = makedist('Normal','mu',theta,'sigma',theta_err);
pd_dip = makedist('Uniform','Lower',dip_min,'Upper',dip_max);

%% Sample pdfs nmax times
dips = random(pd_dip,nmax,1);
delzs = random(pd_delz,nmax,1);
psis = random(pd_psi,nmax,1);
slsds = random(pd_slsd,nmax,1);
thetas = random(pd_theta,nmax,1);

%% Calculate throws
szs = zeros(nmax,1);
szs = delzs./(1+tand(thetas).*(slsds.*sind(psis)./sind(dips) + cosd(psis)./tand(dips)));
% szs = sortrows(szs,1);

%% Calculate stats
meansz = mean(szs);
% Calculate 95% confidence bounds
low = prctile(szs,2.5);
high = prctile(szs,97.5);

% Throw away extreme values (  <0 or >meansz+10*(high-meansz)  )
maxlim = meansz+10*(high-meansz);
minlim = meansz-10*(meansz-low);
szs_trim = szs(szs(:)<maxlim);
szs_trim = szs_trim(szs_trim(:)>minlim);

% recalculate mean and std on trimmed data (will use to overlay estimated
% gaussian for comparison)
szmean = mean(szs);
szstd = std(szs_trim);

% Calculate the mode
[N,edges] = histcounts(szs_trim,nbins);
[~,i] = max(N);
maxp_sz = (edges(i+1)+edges(i))/2;
% estimate of the +/- errors
herr = high - maxp_sz;
lerr = maxp_sz - low;

%% Plot the resultant distribution
h=figure(1);
clf
h1=histogram(szs_trim, nbins, 'Normalization', 'pdf');
% set(h1(1),'FaceColor',[247 236 178]/255,'EdgeColor',150*[1 1 1]/255)
set(h1(1),'FaceColor',170*[1 1 1]/255,'EdgeColor',170*[1 1 1]/255)
```

```
140
141 % Retrieve y auto limits (for plotting dashed lines)
142 ax = gca;
143 ylims = get(ax, 'YLim');
144
145 % Plot a gaussian with the same mean and standard deviation
146 x = minlim:0.1:maxlim;
147 sznormdat = normpdf(x,szmean,szstd);
148 hold on, p2=plot(x,sznormdat, '-r', 'LineWidth', 0.5);
149
150 % Plot 2.5%, 95% and mode lines.
151 hold on, p3 = plot(low*[1 1], ylims, '--b');
152 hold on, p4 = plot(high*[1 1], ylims, '--b');
153 hold on, p5 = plot(maxp_sz*[1 1], ylims, '--k');
154
155 % Trim the x-extent (for throw substantially larger than zero, clip bound
156 % to zero)
157 if meansz-2*(meansz-low)>0
158     xlims = [0 meansz+4*(high-meansz)];
159 elseif meansz+2*(high-meansz)<0
160     xlims = [meansz-4*(meansz-low) 0];
161 else
162     xlims = [meansz-4*(meansz-low) meansz+4*(high-meansz)];
163 end
164 xlim(xlims)
165 xlabel('Throw /m')
166
167 % Annotate with the throw
168 str1 = strcat(mat2str(round(maxp_sz*10)/10), '^{+', mat2str(round(herr*10)/10), '}_{-', ...
        mat2str(round(lerr*10)/10), '} m');
169 strs = {'Throw: ', str1 };
170 annotation('textbox',[0.15,0.45,0.4,0.4],'string',strs,'FontSize',10,'FitHeightToText','on','LineStyle','none')
171 N = szs;
172
173 % Legend:
174 leg = legend([h1,p2,p3,p5],'Throw PDF','Gaussian','95% Bounds','Mode');
175 set(leg, 'Location', 'northeast')
176 end
```

B.2 3D Slip Vector Solving

```
1  % Script provided as a Supplement to:
2  % Untangling Slip-Distribution and Offset Landform Geometry: Rigorous Quantification of ...
       Fault Slip in 3D
3  % (Geosphere)
4  % Authored by:
5  % David Mackenzie (1), Austin Elliott (1)
6  % (1) Department of Earth Sciences, University of Oxford.
7  %
8  % Please cite this work if you use this script or an adaptation of it.
9  %%%%%%%%%%%%%%%%%%%%%%%%%%%%%%%%%%%%%%%%%%%%%%%%%%%%%%%%%%%%%%%%%%%%%%%%%%%%%%%
10
11 function [s, s_err, N, d, derr, sprime, sprime_err] = solve_slipvector_3D(footwalldata, ...
       hangwalldata, dipdiff_tolerance, fstrike)
12 % [s, s_err, N, d, derr, sprime, sprime_err] = ...
13 % solve_slipvector_3D(footwalldata, hangingwalldata)
14 % solve_slipvector_3D(footwalldata, hangwalldata, dipdiff_tolerance)
15 % solve_slipvector_3D(footwalldata, hangwalldata, dipdiff_tolerance, fstrike)
16
17 % ======================================================================
18 % Function takes pairs of pointsets, fits parallel planes to each pair, and
19 % then estimates the best fit slip vector required to give these offsets.
20 %
21 % Each pair must contain one set of xyz points from the hangingwall and
22 % another from the footwall,
23 %
24 % At present no error checking is performed to check for the special cases
25 % where the problem is poorly constrained - this should be clear from the
26 % error estimates however.
27 %
```

```
% Running procedure:
%  - footwalldata => cell array. Each cell contains a matrix of xyz points
%                    corresponding to points in the footwall.
%  - hangwalldata => cell array. Each cell contains a matrix of xyz points
%                    corresponding to points in the hanging wall.
%  - dipdiff_tolerance => tolerance for difference in dip between the
%                    hangingwall and footwall planes (default = 5 degrees).
%  - fstrike => Fault strike in degrees. Necessary to calculate the along
%               strike, strike perpendicular and dip slip components of
%               slip.
%
%   The cells must be in the same order for the two variables, i.e. the
%   i-th cell in each corresponds to the correlative geomorphic surface in
%   the footwall and hangingwall respectively.
%
% Program is run as:
% solve_slipvector_3D(footwalldata, hangingwalldata)
%
% As it runs, the program offers user verification at each stage.
% Execution procedure:
%
% - Run with input dataset pairs
% - For each pair, program will fit a pair of parallel planes to the xyz
%   pointsets
% - The user is then asked to verify or ignore that pair of planes based on
%   a series of plots showing the 3d planes and residuals.
% - Once the normals have been calculated for each case, any tagged as
%   "ignore" are discarded, then the best fit slip vector is calculated by
%   weighted least squares (can easily be replaced by ordinary least squares
%   if required).
%
% Output: [s, s_err, N, d, derr, sprime, sprime_err]
% s = slip vector (x,y,z coordinates)
% s = 1sigma uncertainties in components of s
% N = (nx3) matrix of normal vectors
% d = (nx1) vector of perpendicular separations
% derr = (nx1) vector of perpendicular separation errors
%
% If the fault strike was provided, then the following are also calculated:
% sprime = slip vector in fault coordinates (lateral slip, heave, throw)
% sprime_err = 1sigma uncertainties in components of sprime
%
% For those seeking to reuse the solving portions of the code, there are a
% series of functions:
%   "fit2planesparallel" fits two parallel planes to two sets of points.
%   "fitplane" fits a single plain to a single set of points.
%   "plot_residuals" function generates the analysis plots.
%   "solve_slipvector_3D" (this function) runs the others, then finds the
%       weighted least squares solution for the slip vector.
%
%
% Solution notes:
% - the mean in x,y,z is subtracted from each pair of pointsets to ensure
%   there is no loss of precision due to a large static offset (e.g. with
%   UTM coordinates), but the centers variable retains the positions of the
%   mean location of the pair.
%
% - The solution will be poorly constrained if the plane pairs show little
%   variation of geometry between pairs (reflected by large errors)
%
% - The code assumes none of the planar surfaces are vertical. If precisely vertical
%   planes are included, it will fail. If near vertical planes are used, it
%   may be innaccurate.
%
% - Though written in terms of "hangingwall" and "footwall", it should still function
%   for vertical or near vertical strike slip faults.
% ========================================================================

global FOOT_FIG
global HANG_FIG

%% Defaults
% Weighted (1) or not weighted least squares (0):
weight = 0;
```

```
102
103
104 % check for appropriate Matlab version (>=7.7)
105 V=regexp(version,'[ \.]','split');
106 if (str2num(V{1})<8) || (str2num(V{1})==8 && str2num(V{2})<6),
107   ver
108   error('solve_slipvector_3D: Requires Matlab R2015 or later!');
109 end
110 % Primitive input check: Check same length
111 if length(footwalldata) ~= length(hangwalldata)
112     error('solve_slipvector_3D: input cell-vectors of different lengths');
113 end
114 % Primitive input check: Check same length
115 if length(footwalldata(1,:))>1 || length(hangwalldata(1,:))>1
116     error('solve_slipvector_3D: input cell-vectors must be single column vectors');
117 end
118 if nargin == 2
119     dipdiff_tolerance = 5;
120 end
121 nmax = length(footwalldata);
122
123 %% Loop over all the profiles
124 % Skip/ignore based on user response.
125
126 % Initiate a figure for displaying the plane fits.
127 FOOT_FIG=figure(1);
128 HANG_FIG=figure(2);
129
130 % Initiate results variables
131 plane_separations=zeros(nmax,7);
132 centers=zeros(nmax,2);
133
134 %parfor i=1:nmax
135 for i=1:nmax
136     % Isolate the pair of xyz pointsets
137     footdata = footwalldata{i};
138     hangdata = hangwalldata{i};
139     % Calculate the mean location of the pair of pointsets for later use.
140     centers(i,:) = [mean([footdata(:,1); hangdata(:,1)]) ...
141         mean([footdata(:,2); hangdata(:,2)])];
142
143     % Fit parallel planes through the pointsets
144     [normvec,separation,sep_err,dipdiff] = ...
145         fit2planesparallel(footdata,hangdata);
146
147     % Copy to accumulator, including an index at the end to show hasn't
148     % been 'checked'. Index = 2 for unchecked, 0=ignore, 1=accept.
149     plane_separations(i,:) = [normvec,separation,sep_err,dipdiff, 2];
150
151     % Display the basic results in the terminal. Offset and
152     display(['Angular difference: ' mat2str(round(dipdiff,2))])
153     display(['Offset: ' mat2str(round(separation,2)) ' +/- ' mat2str(round(sep_err,2))])
154
155     % Ask user for input for quality control
156     result = 'x';
157     while (result ~= 'a' && result ~= 'q' && result ~= 'i')
158         result = input('Hit "a" (default) to accept or "i" to ignore this profile (q to ...
                quit)','s');
159         if isempty(result)
160             result = 'a';
161         end
162     end
163     if result == 'q'
164         break
165     elseif result == 'i'
166         plane_separations(i,7) = 0;
167     elseif result == 'a'
168         plane_separations(i,7) = 1;
169     end
170
171 %     % Uncomment to introduce a save to file procedure.
172 %     %Save after every iteration to ensure no loss of work.
173 %     saveas(h,strcat(resultsfolder ,'/',name,'_N',mat2str(i),'_fits.fig'),'fig')
174 %     ...
```

```
    save(strcat(resultsfolder,'/planeoffsets.mat'),'plane_separations','acceptedhists','centers');
end

%% Solve for the slip vector.

if nargin == 4
    % Calculate along strike and strike-perpendicular unit vectors
    strike = fstrike*pi/180;
    %Unit vector along strike
    lhat = [sind(fstrike) cosd(fstrike) 0]
    %Unit vector perpendicular to strike
    qhat = [-cosd(fstrike) sind(fstrike) 0]
    % Project the centers onto the line (for distance along line)
    cprimes = [centers*lhat(1:2)' centers*qhat(1:2)'];

    centers = cprimes(plane_separations(:,7)~=0,:);
else
    centers = centers(plane_separations(:,7)~=0,:);
end

% Remove any ignored data or ones with large dip differences for non-parallel case:
plane_separations = plane_separations(plane_separations(:,7)~=0,:);
centers = centers(plane_separations(:,6)<dipdiff_tolerance,:);
plane_separations = plane_separations(plane_separations(:,6)<dipdiff_tolerance,:);

% Calculate slope angle and azimuth at each pair location for later
% sorting/stats.
azs = atan2d(plane_separations(:,2),plane_separations(:,1));
slopes = 90-asind(plane_separations(:,3));

% Sort data by choice of input (here x-coordinate)
plane_separations = sortrows([centers azs slopes plane_separations],1);

azs = plane_separations(:,3);
slopes = plane_separations(:,4);
centers = plane_separations(:,1:2);
plane_separations = plane_separations(:,5:end);

nmax = length(plane_separations(:,1));

%%%%%%%%%%%%%%%%%%%%%%%%%%%%%%%%%%%%%%%%%%%%%%%%%%%%%%%%%%%%%%%%%%%%%%%%%%%%%%%
%% Solve for the best fit slip vector.
% for separation d, normals ni, and slip vector s, gives:
%       N.s = d    where N is the nmax x 3 matrix of normal vectors.

N = plane_separations(:,1:3);
d = plane_separations(:,4);
derr = plane_separations(:,5);

% Solve by least squares:
if weight
    % Weighted least squares
    [s,s_err] = lscov(N,d,1./(derr.^2));
else
    % Ordinary Least squares
    [s,s_err] = lscov(N,d);
end

residuals = d-N*s;
rmse = rms(residuals);

% Plot separations and predicted separations
figure(FOOT_FIG);
clf
plot(N*s,'-+b')
hold on,errorbar(d,derr,'-+r')

%%%%%%%%%%%%%%%%%%%%%%%%%%%%%%%%%%%%%%%%%%%%%%%%%%%%%%%%%%%%%%%%%%%%%%%%%%%%%%%
%% Calculate return values
if nargin < 4
    extension=nan;
    throw=nan;
    lateral_slip = nan;
    dip = nan;
```

```
248     return
249 end
250 
251 % Rotate into fault coordinates
252 thetad = fstrike-90;
253 theta = thetad*pi/180;
254 R = [cos(theta) -sin(theta) 0; sin(theta) cos(theta) 0; 0 0 1];
255 Nprime = (R*N')';
256 
257 if weight
258     [sprime,sprime_err] = lscov(Nprime,d,1./(derr.^2));
259 else
260     [sprime,sprime_err] = lscov(Nprime,d);
261 end
262 
263 % dip = atan(throw/heave)*180/pi
264 % check = extension*qhat+lateral_slip*lhat+vertical_slip*[0 0 1]
265 
266 end
267 
268 function [normvec,separation,sep_err,dipdiff] = fit2planesparallel(footdata,hangdata)
269 % usage: [normvec,separation,errors] = fit2planesparallel(footdata,hangdata)
270 %
271 % Written by: David Mackenzie
272 % Created: 03/02/14
273 % V2: 17/03/15 (major rebuild)
274 % V3: 07/09/16 (Tidy and comment)
275 %
276 % This function when supplied with two ply files containing xyz points, in
277 % tab separated format, will fit two parallel planes to the data.
278 %
279 % The planes are fitted with the forms (Will FAIL for vertical plane):
280 %
281 % Ax + By + C = z
282 % Ax + By + D = z
283 %
284 % outputs are as follows:
285 % normvec - normalised 3-vector perpendicular to the planes.
286 % separation - distance between the two planes
287 % errors - separation error
288 %
289 % coefficients - a vector [A B C D]
290 % Covariance - Covariance matrix for the estimate of [A B C D]
291 
292 %%
293 % % Test data: Uncomment to use.
294 % testa = 0
295 % testb = -1
296 % testc = 0
297 % testd = 0
298 % testxs = rand(1,1000)*100;
299 % testys = rand(1,1000)*100;
300 % testzs1 = testa*testxs + testb*testys + testc;
301 % testzs2 = testa*testxs + testb*testys + testd;
302 % plydata1 = [testxs' testys' testzs1'];
303 % plydata2 = [testxs' testys' testzs2'];
304 % Ply data is our matrix of datapoints (x,y,z)
305 
306 %% Defaults:
307 global FOOT_FIG
308 global HANG_FIG
309 
310 %% Subtract mean xyz location to avoid computational limits.
311 xmean = mean([footdata(:,1); hangdata(:,1)]);
312 ymean = mean([footdata(:,2); hangdata(:,2)]);
313 zmean = mean([footdata(:,3); hangdata(:,3)]);
314 footdata(:,1:3)=footdata(:,1:3) - ones(length(footdata(:,1)),1)*[xmean,ymean,zmean];
315 hangdata(:,1:3)=hangdata(:,1:3) - ones(length(hangdata(:,1)),1)*[xmean,ymean,zmean];
316 
317 %% Solve Ax=b
318 % M is of form ( x y ? ? ) for each row, where ? ? is 1 0 for plane 1 (P1), and
319 % 0 1 for plane 2 (P2).
320 % b is the vector of z values
321 % x is the vector (A B C D), the coefficients of Ax + By + C = z (P1)
```

```
322 %                                          and Ax + By + D = z (P2)
323
324 M = [footdata(:,1) footdata(:,2) (footdata(:,3)*0+1) (footdata(:,3)*0); ...
325     hangdata(:,1) hangdata(:,2) (hangdata(:,3)*0) (hangdata(:,3)*0+1);];
326 b = [footdata(:,3); hangdata(:,3)];
327
328 % Solve for x using least squares:
329 beta = M\b;
330
331 A=beta(1);
332 B=beta(2);
333 C=beta(3);
334 D=beta(4);
335 coefficients = [A B C D];
336
337 % Calculate the normal vector
338 normaliser = (1/norm([-A -B 1]));
339 normvec = normaliser*[-A -B 1];
340 %covar = inv(M' * M);
341
342 % Generate a plot showing the residuals in the perpendicular directions and
343 % an interactive 3D view, for both the footwall and the hangingwall
344 plot_residuals(footdata,beta(1:3),FOOT_FIG)
345 title('Footwall Data')
346 plot_residuals(hangdata,beta([1,2,4]),HANG_FIG)
347 title('Hangingwall Data')
348
349 %% Calculate Values and Error estimates to return:
350 % Have the normal vector already, normvec. Need to calculate the plane
351 % separations. (HW relative to FW)
352 % Find by (C-D)*[0 0 1]*normvec
353 separation = (C-D)*[0 0 1]*normvec';
354
355 % Calculate the rms error.
356 residuals = M*beta-b;
357
358 % Will take the error in the offset to be rms error in fitting. Alternative
359 % metrics could be used here instead.
360 sep_err = rms(residuals);
361
362 %% Compute the angular difference between the normals
363 % For the case where two planes are fitted independently compared to
364 % parallel fit. Can be used to discriminate between a good and bad fit.
365
366 % planeA
367 [planeA_norm,~,rms_nonpar1] = fitplane(footdata);
368 [planeB_norm,~,rms_nonpar2] = fitplane(hangdata);
369
370 % rms_nonpar = [rms_nonpar1, rms_nonpar2];
371
372 % Calculate the angular difference between the two non-parallel planes.
373 % diffA = (180/pi*acos(planeA_norm*normvec'));
374 % diffB = (180/pi*acos(planeB_norm*normvec'));
375 dipdiff = (180/pi*acos(planeA_norm*planeB_norm'));
376 % dipdiffs = [diffA diffB diffAB];
377 end
378
379 function plot_residuals(data,beta,FIG_HANDLE)
380 % plot_residuals(data,beta,FIG_HANDLE)
381 %
382 % Generate four subplots:
383 %   - 3d view of the data and the plane fitted
384 %   - histogram of the residuals
385 %   - plot of the residuals against distance across the plane (horizontal)
386 %   - plot of residuals against distance along the plane (down slope)
387 %
388 %% Defaults:
389 % set the axis width on the plots to ensure comparable results for the two
390 % planes.
391 xwidth = 1.5;
392
393 % Marker size for plots:
394 msize = 3;
395
```

```
396 % Clear the figure to start
397 figure(FIG_HANDLE)
398 clf
399
400 % Calculate the normal vector
401 A=beta(1);
402 B=beta(2);
403 C=beta(3);
404 normaliser = (1/norm([-A -B 1]));
405 normvec = normaliser*[-A -B 1];
406
407 %% Decimate data to plot %%
408 % Necessary to avoid very large, slow vector plots.
409 ntarget = 1000;
410 reduct_factor = length(data(:,1))/ntarget;
411 n = ceil(reduct_factor);
412 data = data(1:n:end,:);
413
414 %% Estimate Bounds %%
415 % Estimate the bounds of the data
416 xmin = min(data(:,1));
417 xmax = max(data(:,1));
418 ymin = min(data(:,2));
419 ymax = max(data(:,2));
420
421 % Compute grids of x and y coords to calculate z on.
422 xs = xmin:(xmax-xmin)/30:xmax;
423 ys = ymin:(ymax-ymin)/30:ymax;
424 [xg,yg] = meshgrid(xs,ys);
425
426 % Find z values for solution plane.
427 zs = beta(1).*xg + beta(2).*yg + beta(3);
428
429 %% Plotting %%
430 subplot(221)
431 %Plot the plane
432 surf(xs,ys,zs)
433 hold on
434 % Plot the point data as crosses
435 plot3(data(:,1),data(:,2),data(:,3), '+k', 'MarkerSize', msize)
436 xlabel('x'); ylabel('y'); zlabel('z')
437
438 %Calculate the residuals
439 resid1 = C*normaliser - data*normvec';
440 rms1 = rms(resid1);
441 %plot histogram of residuals
442 subplot(222)
443 histfit(resid1,40)
444 xlim([-xwidth xwidth])
445 xlabel('Residual /m')
446 ylims = get(gca,'YLim');
447 hold on
448 % Plot dashed lines at +/- sigma and 2sigma
449 plot([rms1,rms1],[0, ylims(2)*0.8], '--r')
450 plot(-[rms1,rms1],[0, ylims(2)*0.8], '--r')
451 plot(2*[rms1,rms1],[0, ylims(2)*0.8], '--r')
452 plot(-2*[rms1,rms1],[0, ylims(2)*0.8], '--r')
453
454 %% Plot the residuals in the slope parallel and perp. directions
455 % Form a basis set in the plane, such that xprime is horizontal.
456 % yprime is in the plane. Residual (normal) is in the 3rd axis.
457 xprime = cross([0 0 1],normvec);
458 yprime = cross(xprime, normvec);
459
460 %normalise x and y prime.
461 xprime = xprime./norm(xprime);
462 yprime = yprime./norm(yprime);
463
464 % Calculate new bounds
465 projecteddata = [data*xprime'-min(data*xprime') ...
466     data*yprime'-min(data*yprime') resid1];
467 pbaspect([2 1 1])
468
469 % Make a plot of the residuals in the slope parallel and perpendicular
```

```
% directions.
subplot(223)
plot(projecteddata(:,1),projecteddata(:,3), '+b', 'MarkerSize', msize)
xlabel('Distance perpendicular to slope /m')
ylabel('Point residuals /m')
pbaspect([2 1 1])
subplot(224)
plot(projecteddata(:,2),projecteddata(:,3), '+b', 'MarkerSize', msize)
xlabel('Distance parallel to slope /m')
ylabel('Point residuals /m')
pbaspect([2 1 1])
end

function [normvec,intercept,rms_err] = fitplane(data)
% Function to fit a plane to a set of points in a given ascii ply file.
% Written by: David Mackenzie
% Created: 30/01/14
% direct_V2: 17/03/15

%% Test data: Uncomment to use.
% testA = 0
% testB = 0
% testC = 100
% testxs = rand(1,1000)*100;
% testys = rand(1,1000)*100;
% %testgrd = meshgrd(testxs,testys);
% testzs = testA*testxs + testB*testys + testC;
% plydata = [testxs' testys' testzs'];

% Ply data is our matrix of datapoints (x,y,z)

%% Subtract mean xyz location to avoid computational limits.
xmean = mean(data(:,1));
ymean = mean(data(:,2));
zmean = mean(data(:,3));
data(:,1:3)=data(:,1:3) - ones(length(data(:,1)),1)*[xmean,ymean,zmean];

%% Solve Ax=b
% M is of form ( x y 1 ) for each row
% b is the vector of z values
% x is the vector (A B C), the coefficients of Ax + By + C = z

M = [data(:,1) data(:,2) (data(:,3)*0+1)];
b = data(:,3);

beta = M\b;

A=beta(1);
B=beta(2);
C=beta(3);
normaliser = (1/norm([-A -B 1]));
normvec = normaliser*[-A -B 1];
intercept = C;
%covar = inv(M' * M);

% Plot the plane and the data in 3D
xmin = min(data(:,1));
xmax = max(data(:,1));
ymin = min(data(:,2));
ymax = max(data(:,2));

% Compute grids of x and y coords to calculate z on.
xs = xmin:(xmax-xmin)/30:xmax;
ys = ymin:(ymax-ymin)/30:ymax;
[xg,yg] = meshgrid(xs,ys);

% Find z values for solution plane.
zs = beta(1).*xg + beta(2).*yg + beta(3);

%Calculate the residuals
resid = C*normaliser - data*normvec';
rms_err = rms(resid);
end
```